

2016-01-01

Damage Tolerance and Assessment of Unidirectional Carbon Fiber Composites

Mark David Flores

University of Texas at El Paso, markdf@miners.utep.edu

Follow this and additional works at: https://digitalcommons.utep.edu/open_etd



Part of the [Materials Science and Engineering Commons](#), [Mechanical Engineering Commons](#),
and the [Mechanics of Materials Commons](#)

Recommended Citation

Flores, Mark David, "Damage Tolerance and Assessment of Unidirectional Carbon Fiber Composites" (2016). *Open Access Theses & Dissertations*. 842.

https://digitalcommons.utep.edu/open_etd/842

This is brought to you for free and open access by DigitalCommons@UTEP. It has been accepted for inclusion in Open Access Theses & Dissertations by an authorized administrator of DigitalCommons@UTEP. For more information, please contact lweber@utep.edu.

DAMAGE TOLERANCE AND ASSESSMENT OF UNIDIRECTIONAL
CARBON FIBER COMPOSITES:
AN EXPERIMENTAL AND NUMERICAL STUDY

MARK DAVID FLORES
Doctoral Program in Civil Engineering

APPROVED:

Jack Chessa Ph.D., Chair

Cesar Carrasco Ph.D.

David Mollenhaurer Ph.D.

Pavana Prabhakar Ph.D

Charles Ambler, Ph.D.
Dean of the Graduate School

Copyright ©

by

Mark D. Flores

2016

Dedication

This dissertation is dedicated to my parents, Irene and Juan Gabriel Flores. For provided me the strength and determination to pursue my dreams. For making the most difficult decisions easy.

DAMAGE TOLERANCE AND ASSESSMENT OF UNIDIRECTIONAL
CARBON FIBER COMPOSITES:

AN EXPERIMENTAL AND NUMERICAL STUDY

by

MARK DAVID FLORES, M.S.

DISSERTATION

Presented to the Faculty of the Graduate School of

The University of Texas at El Paso

in Partial Fulfillment

of the Requirements

for the Degree of

DOCTOR IN PHILOSOPHY

Department of Civil Engineering

THE UNIVERSITY OF TEXAS AT EL PASO

May 2016

Acknowledgements

I would like to express my most sincere gratitude to the people that provided me valuable knowledge and guidance on this adventure of solving a really complex problem. All ideas start somewhere, almost similar to the initiation of damage of a composite. The onset of a single matrix crack was initiated using criteria developed by Dr. L. Roy Xu who strongly encouraged me into pursuing a PhD. Crack propagation was modeled using a Dr. Jack Chessa law who initially proposed to me the opportunity to work with Air Force Research Laboratory. Crack arrest occurred until the Dr. Eric Jones effect and new cracks begin to coalesce. The underlying stress concentration for the coalescent of new damage were the result of the Dr. David Mollenhauer Phenomenon, who continuously cultivated new ideas. With new responsibilities and challenges, delamination formed causing damage to branch out to Dan Rapping and Kevin Hoos. As the inertial effects of these people begin to take effect on my passion and love for hard work and breaking composites, damage still continued to propagate with Dr. Vipul Ranatunga adding extra failure modes at accelerated speeds. Understanding the physical parameters sufficient to model and characterize damage was done through Dr. Eric Lindgren techniques. A sudden reduction of modulus occurred with the overwhelming task in characterizing damage in a discretized model. As the Dr. Steve Engelstad and Jason Action loading begin to increase to determine my strength, a sudden roaring explosion sounded off due to fiber breakage indicating ultimate failure. Post analyses indicated that Dr. Pavana Prabhakar, Dr. Mark Pankow, Dr. Cesar Carrasco, Steve Thompson, and Dave Roberts were also modes of failure. However, nondestructive evaluation indicated that the predominately mode of failure occurred as a result of the Dr. David Mollenhauer Phenomenon.

Abstract

Composites are beginning to be used in a variety of different applications throughout industry. However, certification and damage tolerance is a growing concern in many aerospace and marine applications. Although compression-after-impact have been studied thoroughly, determining a damage tolerance methodology that accurately characterizes the failure of composites has not been established. An experimental investigation was performed to study the effect of stacking sequence, low-velocity impact response, and residual strength due to compression and fatigue. Digital Image Correlation (DIC) captured the strains and deformation of the plate due to compression. Computational investigations integrated non-destructive techniques (C-Scan, X-Ray) to determine the extent of the damage created by the manufacturing process and impact to accurately create a representative of the pre-existing damage. Fiber/matrix cracking, delamination growth, buckling, as well as other failures mechanisms occur in compression-after-impact laminated specimens examined experimentally. The results from this study provide knowledge of the compression after impact strength of plates, and a basis for validation of detailed modeling of progressive failure from impact damaged composites.

Table of Contents

| | |
|----------------------------------------------------------------------|------|
| Acknowledgements..... | v |
| Abstract..... | vi |
| Table of Contents..... | vii |
| List of Tables | xii |
| List of Figures..... | xiii |
| Chapter 1: Introduction..... | 1 |
| 1.1 Introduction..... | 1 |
| 1.2 Motivation..... | 3 |
| 1.3 Research Objectives..... | 4 |
| 1.4 Overview of Research..... | 6 |
| 1.5 Relevance..... | 7 |
| Chapter 2: Impact Experiments | 9 |
| 2.1 Impact Experiments of Thin Unidirectional Composite Plates | 9 |
| 2.1.2 Material Specifications | 11 |
| 2.1.3 Environmental Conditions | 12 |
| 2.1.4 Test Method | 12 |
| 2.1.4.1 Digital Image Correlation of Impact Event | 13 |
| 2.1.4.2 Optical Profilometry | 15 |
| 2.1.4.3 Nondestructive Evaluation..... | 17 |
| 2.1.5 Results and Discussions..... | 17 |
| 2.1.5.1 Drop Weight Tower..... | 17 |
| 2.1.5.2 DIC – Out-of-Plane Displacements | 22 |
| 2.1.5.3 DIC – Strain Measurements..... | 24 |
| 2.1.5.4 DIC – Permanent Deformation..... | 28 |
| 2.1.5.5 DIC – Crack Initiation of Panel C | 31 |
| 2.1.5.6 DIC – Crack Initiation Using V-Displacements..... | 31 |
| 2.1.5.7 Nondestructive Evaluation – Immersion Ultrasound | 32 |
| 2.1.5.8 Nondestructive Evaluation – C-Scan (10 MHz)..... | 34 |
| 2.1.5.9 Nondestructive Evaluation – X-Ray CT..... | 35 |
| 2.1.5.10 Nondestructive Evaluation – X-Ray CT with Zinc Iodine | 36 |

| | | |
|---------------------------------------------------------------------------------------------------------------------------------------------------------------------------|-----------------------------------------------------------------------|----|
| 2.1.6 | Conclusions for Impact of Thin Plate Unidirectional Composites | 37 |
| 2.1.7 | Future Work for Impact of Thin Plates..... | 38 |
| 2.2 | Impact Experiments of Thick Unidirectional Composite Plates | 39 |
| 2.2.2 | Material Specifications – Lockheed Martin | 40 |
| 2.2.2.1 | Impact Methodology – Lockheed Martin | 40 |
| 2.2.3 | Nondestructive Evaluation – Lockheed Martin | 40 |
| 2.2.3.1 | Nondestructive Evaluation – Infrared Flash Thermography | 41 |
| 2.2.3.2 | Nondestructive Evaluation – Immersion Ultrasound | 42 |
| 2.2.3.3 | Nondestructive Evaluation – X-Ray CT | 44 |
| 2.2.3.4 | Nondestructive Evaluation – X-Ray CT with Zinc Iodine Penetrant | 46 |
| 2.2.3.5 | Nondestructive Evaluation – Optical Profilometry | 54 |
| 2.2.3.6 | Nondestructive Evaluation – Segmentation..... | 55 |
| 2.2.4 | Conclusions for Impact of Thick Plates..... | 56 |
| 2.3 | Discussion..... | 57 |
| Chapter 3: A Theoretical Framework for Modeling Nondestructive Evaluation to Predict the Behavior of Compression Strength After Impact of Unidirectional Composites | | |
| 3.1 | Introduction..... | 58 |
| 3.2 | Discrete Damage Modeling | 60 |
| 3.3 | Modeling NDE for use of Damage Tolerance and Assessment | 63 |
| 3.4 | Pre-Imposing Damage Into a 3D Discrete Damage Model | 65 |
| 3.4.1 | Pre-Imposing Geometric Imperfection | 65 |
| 3.4.1.1 | Pre-Imposing Geometric Imperfection for Thin Composite Plates | 66 |
| 3.4.1.2 | Pre-Imposing Geometric Imperfection for Thick Composite Plates | 68 |
| 3.4.2 | Pre-Imposing Delamination | 68 |
| 3.4.2.1 | Analyzing Delamination for Thin Panels | 70 |
| 3.4.2.2 | Analyzing Delamination of Thick Panels..... | 76 |
| 3.4.3 | Pre-Imposing Matrix Cracks..... | 81 |
| 3.4.3.1 | Analyzing Matrix Cracks..... | 83 |
| 3.5 | Considerations for Optimization..... | 86 |
| 3.5.1 | Mesh Generation..... | 86 |
| 3.5.1.1 | Mesh Generation for Thin Composite Plates..... | 88 |
| 3.5.1.2 | Mesh Generation for Thick Composite Plates | 89 |
| 3.5.1.3 | Mesh Parameters and Degrees of Freedom | 90 |
| 3.6 | Conclusions..... | 91 |

| | | |
|----------------------------------------------------------------------------------------------------------------------------------------------------------------------|-------------------------------------------------------------------------------|-----|
| 3.7 | Future Work | 91 |
| 3.7.1 | Thermal Residual Stress | 91 |
| 3.7.2 | Nonlinearity | 91 |
| 3.7.3 | Reduction of Modulus | 92 |
| Chapter 4: Part I - Numerical and Experimental Investigation of Compression Strength After Impact for Unidirectional Carbon Fiber Composites of Thin Plates | | |
| 4.1 | Compression Strength After Impact of Thin Composite Plates | 93 |
| 4.1.1 | Material Specification..... | 93 |
| 4.1.2 | Sample Preparation | 94 |
| 4.1.3 | Baseline Compression Experiments | 94 |
| 4.1.4 | Impact Experiments | 95 |
| 4.1.5 | Compression Strength After Impact Experiments | 95 |
| 4.1.5.1 | Procedure | 96 |
| 4.1.5.2 | Digital Image Correlation | 96 |
| 4.1.5.3 | DIC Data Capture | 96 |
| 4.2 | Results And Discussion | 97 |
| 4.2.1 | Baseline Compression Experiments | 97 |
| 4.2.2 | Impact Experiments | 99 |
| 4.2.3 | Residual Compression Strength After Impact | 100 |
| 4.3 | Digital Image Correlation | 102 |
| 4.3.1 | DIC: Displacement and Strain Contours | 103 |
| 4.3.2 | DIC: Virtual Strain Gauge vs Actual Strain Gauge Response | 116 |
| 4.4 | Nondestructive Evaluation for Residual Compression Strength after Impact..... | 119 |
| 4.4.1 | NDE: Immersion Ultrasound | 119 |
| 4.4.2 | NDE: 2D X-Ray | 121 |
| 4.4.3 | NDE: 3D X-Ray Computed Tomography | 122 |
| 4.5 | Discrete Damage Modeling (DDM) | 131 |
| 4.5.1 | Modeling Strategy | 131 |
| 4.5.2 | Material Properties..... | 133 |
| 4.5.3 | Model Preparation | 134 |
| 4.6 | DDM Results | 134 |
| 4.6.1 | Out-of-Plane Displacement | 134 |
| 4.6.2 | Strain Contours | 136 |
| 4.6.3 | Damage Evolution | 140 |

| | | |
|---------------------------------------------------------------------------------------------------------------------------------------------------------------------|--------------------------------------------------------------------------|-----|
| 4.7 | Conclusions..... | 144 |
| 4.8 | Future Work..... | 145 |
| Chapter 5: Part II - Numerical and Experimental Investigation of Compression Strength After Impact for Unidirectional Carbon Fiber Composites of Thick Plates | | |
| 5.1 | Introduction..... | 147 |
| 5.1.1 | Material Specification..... | 148 |
| 5.1.2 | Sample Preparation | 148 |
| 5.2 | Methodology | 148 |
| 5.2.1 | Procedure | 149 |
| 5.2.2 | Testing Apparatus | 150 |
| 5.2.3 | Digital Image Correlation | 151 |
| 5.2.3.1 | DIC Data Capture | 153 |
| 5.3 | Results and Discussion | 153 |
| 5.3.1 | Digital Image Correlation Results | 153 |
| 5.3.1.2 | DIC: Profilometry | 156 |
| 5.3.1.3 | DIC: Displacements | 157 |
| 5.3.1.4 | DIC: Surface Strains | 161 |
| 5.3.2 | Nondestructive Evaluation: Post Damage of Compression After Impact | 169 |
| 5.4 | Discrete Damage Model | 172 |
| 5.4.1 | Modeling Strategy | 173 |
| 5.4.2 | Material Properties..... | 174 |
| 5.5 | Discrete Damage Model Results | 175 |
| 5.5.1 | Failure Prediction..... | 179 |
| 5.5.2 | Ballpark Estimates for Real World Problems | 183 |
| 5.6 | Conclusion | 192 |
| 5.7 | Future Work | 193 |
| Chapter 6: Conclusion | | |
| 6.1 | Impact Experiments | 194 |
| 6.2 | Modeling Damage | 194 |
| 6.3 | Compression Strength After Impact | 195 |
| 6.4 | Damage Tolerance and Assessment | 196 |
| 6.5 | Significance of Study | 196 |

| | |
|--------------------------------------------------------------------------|-----|
| References..... | 198 |
| Appendix A: NDE – Immersion Ultrasound | 202 |
| Appendix B: Flash Thermography of Impacted Surface | 213 |
| Appendix C: Flash Thermography of Back Surface..... | 216 |
| Appendix D: Immersion Ultrasound – Amplitude Data | 219 |
| Appendix E: Immersion Ultrasound – Time of Flight Data | 222 |
| Appendix F: Image Segmentation C-Scan/X-Ray CT Analysis of Panel A | 225 |
| Appendix G: Image Segmentation Specimen-1 X-Ray CT Analysis..... | 238 |
| Appendix H: Post Compression Failure C-Scan Images – Time of Flight..... | 248 |
| Appendix I: Post Compression Failure C-Scan Images – Amplitude | 251 |
| Appendix J: Post Compression Failure X-Ray Images | 254 |
| Vita.... | 257 |

List of Tables

| | |
|----------------------------------------------------------------------|-----|
| Table 2.1.1 – Stacking Sequence Table | 12 |
| Table 2.1.5.1 – Drop in Load vs Peak Load Data..... | 19 |
| Table 2.1.5.2 – Strain, Displacement, and Load at Drop in Load | 26 |
| Table 2.1.5.3 – Area of Delaminated Region for each Panel | 34 |
| Table 2.1.5.4 – Zinc Iodide Radio-Opaque Dye Recipe..... | 37 |
| Table 2.2.3.1 – Nondestructive Evaluation Test Matrix..... | 41 |
| Table 2.2.3.2 – Zinc Iodide Radio-Opaque Dye Recipe..... | 47 |
| Table 4.1.1 – Stacking Sequence | 94 |
| Table 4.2.1 – Baseline compression experimental data..... | 97 |
| Table 4.2.2: Impact Experimental Values | 99 |
| Table 4.2.3 – Compression after impact experimental data | 100 |
| Table 4.5.1 – Mechanical Properties of IM7/M65 | 133 |
| Table 5.4.1 – Mechanical Properties of IM7/977-3 | 175 |

List of Figures

| | |
|-----------------------------------------------------------------------------------------------------------------------------------------------------------|----|
| Figure 1.2.1 – Definitions of durability and damage tolerance for commercial aircraft and associated design requirements (Mil-Hbk-17) ¹² | 3 |
| Figure 1.3.1 – Nondestructive Evaluation to Prediction of Behavior..... | 6 |
| Figure 1.4.1 – Damage Tolerance and Assessment Initiative | 7 |
| Figure 2.1.4.1 – ASTM 7136 Impact Fixture | 13 |
| Figure 2.1.4.2 – Cantilever beam mount for mirror | 14 |
| Figure 2.1.4.3 – Optical Stand and High-Speed Cameras | 15 |
| Figure 2.1.4.4 – Nanovea Optical Profilometry Schematic..... | 16 |
| Figure 2.1.4.5 – Nanovea Optical Profilometry Setup | 17 |
| Figure 2.1.5.1 – Composite Panels Load vs Time | 18 |
| Figure 2.1.5.2 – Composite Panel’s Load vs Displacement | 19 |
| Figure 2.1.5.3 – Composite Panel’s Energy vs Time | 20 |
| Figure 2.1.5.4 – Composite Panel’s Velocity vs Time | 21 |
| Figure 2.1.5.5 – Composite Panel’s Displacement vs Time..... | 22 |
| Figure 2.1.5.6 – Out-of-Plane Displacement Contours – Panel B..... | 23 |
| Figure 2.1.5.7 – Out-of-Plane Displacement vs Time | 23 |
| Figure 2.1.5.8 – Maximum Out-of-Plane Displacements – DIC vs Drop Weight Tower | 24 |
| Figure 2.1.5.9 – Major Principle Strains vs Time: Obtained from tracking the maximum out-of-plane displacement pixel point | 25 |
| Figure 2.1.5.10 – Axial Strains vs Time | 27 |
| Figure 2.1.5.11 – Transverse Strains vs Time | 28 |
| Figure 2.1.5.12 – Profilometry scans..... | 29 |
| Figure 2.1.5.13– Horizontal line profiles for impacted surface..... | 29 |
| Figure 2.1.5.14 – Vertical line profiles for back surface | 30 |
| Figure 2.1.5.15 – Profilometry vs. DIC | 30 |
| Figure 2.1.5.16 – Crack Initiation and Propagation of Panel C..... | 31 |
| Figure 2.1.5.17 – Y-Displacement of Panel D..... | 32 |
| Figure 2.1.5.18 – C-Scan Amplitude Data of Panels (5 MHz)..... | 33 |
| Figure 2.1.5.19 – C-Scan Time of Flight Data of Panels (5 MHz)..... | 33 |
| Figure 2.1.5.20 – C-Scan Images: Interfacial Damage for Panel A (10 MHz) | 35 |
| Figure 2.1.5.21 – X-Ray CT images of damage | 36 |
| Figure 2.1.5.22 – X-Ray with penetrant for Panel A..... | 37 |
| Figure 2.2.2.1 – Lockheed Martin Impact Fixture..... | 40 |
| Figure 2.2.3.1 –Infrared Flash Thermography (specimen-1) | 42 |
| Figure 2.2.3.2 – Ultrasonic images of impacted specimen 1, 2, and 3 | 43 |
| Figure 2.2.3.3 – Immersion Ultrasonic Time of Flight image of specimen-1 | 43 |
| Figure 2.2.3.4 – Immersion Ultrasonic Time of Flight image of specimen-2 | 43 |
| Figure 2.2.3.5 – Immersion Ultrasonic Time of Flight image of specimen-3 | 44 |
| Figure 2.2.3.6 – X-Ray Images of specimen-1 | 45 |
| Figure 2.2.3.7 – X-Ray Images of specimen-2 | 45 |
| Figure 2.2.3.8 – X-Ray Images of specimen-3 | 46 |
| Figure 2.2.3.9 – Zinc Iodide Pool | 47 |
| Figure 2.2.3.10 – Ladd Vacuum Evaporator | 47 |
| Figure 2.2.3.11 – X-Ray front images with zinc iodide penetrant for Specimen-1 | 49 |
| Figure 2.2.3.12 – X-Ray side images with zinc iodide penetrant for Specimen-1 | 49 |

| | |
|---------------------------------------------------------------------------------------------------------------------------------------------------------------|-----|
| Figure 2.2.3.13 – X-Ray top images with zinc iodide penetrant for Specimen-1 | 50 |
| Figure 2.2.3.14 – X-Ray front images with zinc iodide penetrant for Specimen-2 | 50 |
| Figure 2.2.3.15 – X-Ray side images with zinc iodide penetrant for Specimen-2 | 51 |
| Figure 2.2.3.16 – X-Ray top images with zinc iodide penetrant for Specimen-2 | 51 |
| Figure 2.2.3.17 – X-Ray front images with zinc iodide penetrant for Specimen-3 | 52 |
| Figure 2.2.3.18 – X-Ray side images with zinc iodide penetrant for Specimen-3 | 52 |
| Figure 2.2.3.19 – X-Ray top images with zinc iodide penetrant for Specimen-3 | 53 |
| Figure 2.2.3.20 – Horizontal profiles of a) specimen-1 b) specimen-2 c) specimen-3 | 55 |
| Figure 2.2.3.21 – Vertical profiles of a) specimen-1 b) specimen-2 c) specimen-3 | 55 |
| Figure 3.2.1 – Schematic of the damage evolution process in a laminated composite | 61 |
| Figure 3.2.2 – Flowchart of a typical DDM simulation | 63 |
| Figure 3.2.3 – Flowchart of model preparation | 64 |
| Figure 3.4.1 – Average line profile for Panel A | 67 |
| Figure 3.4.2 – Discretized representation through the thickness of the composite | 67 |
| Figure 3.4.3 – Arbitrary delamination of a composite interface | 69 |
| Figure 3.4.4 – Surface behavior of plies with delamination | 69 |
| Figure 3.4.5 – Pre-imposed delamination flow chart with a) discretized undamaged composite b) pre-imposed STL image c) interfacial nodal selection | 70 |
| Figure 3.4.6 – Adaptive modal filter technique used for c-scan images | 71 |
| Figure 3.4.7 – C-scan, c-scan filter, and X-Ray CT image of interface 5 for Panel A | 72 |
| Figure 3.4.8 – X-Ray vs C-Scan delamination pattern | 73 |
| Figure 3.4.9 – a) STL creation from a mask being b) superimposed into a discretized model | 75 |
| Figure 3.4.10 – a) STL creation from a mask being b) superimposed into a discretized model | 76 |
| Figure 3.4.11 – Delamination shape of the 8 th interface of the thick composite laminate | 77 |
| Figure 3.4.12 – STL Creation of Damaged Region – Zinc Iodide Alone Back Surface | 78 |
| Figure 3.4.13 – STL Creation of Damaged Region – Zinc Iodide Alone Impacted Surface | 78 |
| Figure 3.4.14 – STL Creation of Damaged Region – Zinc Iodide Filled Back Surface | 78 |
| Figure 3.4.15 – Super-imposed STL into discretized model a) top view, b) side view c) and selection of nodes in each interface | 79 |
| Figure 3.4.16 – Delamination pattern in discrete damage model | 80 |
| Figure 3.4.17 – Immersion Ultrasound image vs DDM initial delamination | 80 |
| Figure 3.4.18 – Pre-imposing cracks into DDM of a 45° ply a) selected elements of delaminated region b) pre-imposed crack within the delaminated region | 81 |
| Figure 3.4.19 – Crack identification using X-ray CT for thin composite plates | 84 |
| Figure 3.4.20 – Crack identification using X-ray CT for thick composite plates | 84 |
| Figure 3.4.21 – Discretized model of pre-imposed cracks and delamination | 85 |
| Figure 3.4.22 – Pre-imposed cracks and delamination for thick composite plates | 85 |
| Figure 3.5.1 – Unstructured mesh of thin composite plate | 89 |
| Figure 3.5.2 – Unstructured mesh of thick composite plate | 90 |
| Figure 3.5.3 – Unstructured mesh of damage region of thick composite plate | 90 |
| Figure 4.1.1 – ASTM 7137 Experimental Setup | 95 |
| Figure 4.2.1 – Maximum load: undamaged compression specimens | 98 |
| Figure 4.2.2 – Load vs displacement: undamaged compression specimens | 99 |
| Figure 4.2.3 – Strain vs strain: undamaged compression specimens | 99 |
| Figure 4.2.4 – Load vs displacement: compression strength after impact | 100 |
| Figure 4.2.5 – Stress vs strain: compression strength after impact | 101 |
| Figure 4.2.6 – Compression strength after impact: Undamaged vs damaged | 101 |
| Figure 4.3.1 – Panel A: DIC images of displacements, 3 seconds prior to failure | 104 |

| | |
|-------------------------------------------------------------------------------------------------------|-----|
| Figure 4.3.2 – Panel A: DIC images of strains, 3 seconds prior to failure | 105 |
| Figure 4.3.3 – Panel B: DIC images of displacements, 3 seconds prior to failure | 107 |
| Figure 4.3.4 – W Displacements: Panel B impacted surface 5 seconds prior to failure..... | 108 |
| Figure 4.3.5 – Panel B: DIC images of strains, 3 seconds prior to failure | 109 |
| Figure 4.3.6 – Panel C: DIC images of displacements, 3 seconds prior to failure | 111 |
| Figure 4.3.7 – Panel C: DIC images of strains, 3 seconds prior to failure | 112 |
| Figure 4.3.8 – Panel D: DIC images of displacements, 3 seconds prior to failure | 114 |
| Figure 4.3.9 – Panel D: DIC images of strains, 3 seconds prior to failure | 115 |
| Figure 4.3.10 – DIC Strain Location | 116 |
| Figure 4.3.11– Axial Strain (ϵ_{yy}) vs time: Panel A | 117 |
| Figure 4.3.12 – Axial Strain (ϵ_{yy}) vs time: Panel B | 117 |
| Figure 4.3.13 – Axial Strain (ϵ_{yy}) vs time: Panel C | 118 |
| Figure 4.3.14 – Axial Strain (ϵ_{yy}) vs time: Panel D | 118 |
| Figure 4.4.1 – C-Scan amplitude data: Post compression test damage | 120 |
| Figure 4.4.2 – C-Scan time of flight: Compression after impact damage | 121 |
| Figure 4.4.3 – X-Ray: Compression after impact damage | 122 |
| Figure 4.4.4 – X-Ray: Panel A front images | 123 |
| Figure 4.4.5 – X-Ray: Panel A side images..... | 124 |
| Figure 4.4.6 – X-Ray: Panel A top images | 124 |
| Figure 4.4.7 – X-Ray: Panel B front images | 125 |
| Figure 4.4.8 – X-Ray: Panel B side images..... | 126 |
| Figure 4.4.9 – X-Ray: Panel B top images | 126 |
| Figure 4.4.10 – X-Ray: Panel C front images | 127 |
| Figure 4.4.11 – X-Ray: Panel C side images..... | 128 |
| Figure 4.4.12 – X-Ray: Panel C top images | 128 |
| Figure 4.4.13 – X-Ray: Panel D front images | 129 |
| Figure 4.4.14 – X-Ray: Panel D side images..... | 130 |
| Figure 4.4.15 – X-Ray: Panel D top images..... | 130 |
| Figure 4.5.1 – Property degradation approach to fiber fracture | 133 |
| Figure 4.5.2 – DDM model for Panel A | 134 |
| Figure 4.6.1 – Panel A Out-of-Plane Displacements: Impacted Surface | 135 |
| Figure 4.6.2 – Panel A Out-of-Plane Displacements: Back Surface | 136 |
| Figure 4.6.3 – Axial Strain Panel A Impacted Surface for both simulation and experiment | 137 |
| Figure 4.6.4 – Axial Strain Panel A Back Surface for both simulation and experiment..... | 137 |
| Figure 4.6.5 – Transverse Strain Panel-A Impacted for both simulation and experiment | 138 |
| Figure 4.6.6 – Transverse Strain Panel-A Back for both simulation and experiment | 138 |
| Figure 4.6.7 – Shear Strain Panel-A Impacted for both simulation and experiment..... | 139 |
| Figure 4.6.8 – Shear Strain Panel-A Back Surface for both simulation and experiment | 139 |
| Figure 4.6.9 – 3D Representation of initial delamination | 140 |
| Figure 4.6.10 – Frontal image (impacted surface) of initial delamination and transverse matrix cracks | 140 |
| Figure 4.6.11 – Sequence of damage events for Panel A | 141 |
| Figure 4.6.12 – Ultimate failure of simulation | 142 |
| Figure 4.6.13 – Damage at ultimate failure for a) Simulation b) Experiment, X-Ray CT | 143 |
| Figure 4.6.14 – Damage at ultimate failure for a) Simulation b) Experiment, Immersion Ultrasound.. | 143 |
| Figure 4.6.15 – Damage at ultimate failure for a) Simulation b) Experiment, Immersion Ultrasound.. | 144 |
| Figure 5.2.1 – Compression fixture with strain gauge location of impacted surface and DIC window. | 149 |
| Figure 5.2.2 – Swivel Plate..... | 150 |
| Figure 5.2.3 – Experimental setup for impacted surface | 151 |

| | |
|----------------------------------------------------------------------------------------------------------|-----|
| Figure 5.2.4 – DIC Calibration Prior to Each Test | 152 |
| Figure 5.2.5 – Camera setup of back surface..... | 152 |
| Figure 5.3.1 – Load vs Displacement | 153 |
| Figure 5.3.2 – Load vs Displacement | 154 |
| Figure 5.3.3 – Impacted Surface DIC strain gauge location and setup | 155 |
| Figure 5.3.4 – Back Surface DIC strain gauge location and correlation setup..... | 155 |
| Figure 5.3.5 – Profilometry obtained through DIC | 156 |
| Figure 5.3.6 – Profilometry obtained through the Nanovea Optical Profilometer | 156 |
| Figure 5.3.7 – Profilometry of back surface obtained through DIC | 157 |
| Figure 5.3.8 – U: Longitudinal displacements from DIC | 158 |
| Figure 5.3.9 – V: Transverse displacements from DIC | 159 |
| Figure 5.3.10 – W: Out-of-plane displacements from DIC | 160 |
| Figure 5.3.11 – Axial strain contours from DIC measurements..... | 163 |
| Figure 5.3.12 – Transverse strain contours from DIC | 164 |
| Figure 5.3.13 – Shear strain contours from DIC | 165 |
| Figure 5.3.14 – Major principal strain contours from DIC..... | 166 |
| Figure 5.3.15 – Minor principal strain contours from DIC | 167 |
| Figure 5.3.16 – Physical and virtual strain gauge location respect to fixture and DIC window | 168 |
| Figure 5.3.17 – Compressive strains obtained from virtual DIC and physical strain gauges..... | 169 |
| Figure 5.3.18 – Ultrasound amplitude data for specimen-4 | 170 |
| Figure 5.3.19 – Ultrasound time-of-flight data for specimen-4..... | 171 |
| Figure 5.3.20 – 2D X-ray image of specimen-4 | 172 |
| Figure 5.4.1 – Property degradation approach to fiber fracture | 174 |
| Figure 5.5.1 – Out-of-plane comparisons between simulation and DIC | 176 |
| Figure 5.5.2 – Axial strain comparisons between simulation and DIC | 177 |
| Figure 5.5.3 – Transverse strain comparisons between simulation and DIC | 178 |
| Figure 5.5.4 – Shear strains comparisons between simulation and DIC | 179 |
| Figure 5.5.5 – 3D Representation of initial delamination | 180 |
| Figure 5.5.6 – Frontal image of initial delamination and open transverse matrix cracks..... | 180 |
| Figure 5.5.7 – Sequence of damage growth for cracks, delamination, and fiber breakage | 181 |
| Figure 5.5.8 – Transverse matrix crack and progressive fiber failure | 182 |
| Figure 5.5.9 – Three dimensional representation of the pre-imposed delamination | 183 |
| Figure 5.5.10 – Comparison of delamination between the a) simulation and b) Olympus Omniscan Probe | 184 |
| Figure 5.5.11 – Out-of-plane comparisons between simulation and DIC | 185 |
| Figure 5.5.12 – Axial strain comparisons between simulation and DIC | 186 |
| Figure 5.5.13 – Transverse strain comparisons between simulation and DIC | 187 |
| Figure 5.5.14 – Shear strain comparisons between simulation and DIC | 188 |
| Figure 5.5.15 – Comparison of ultimate failure between a) simulation and b) experiment | 189 |
| Figure 5.5.16 – Comparison of ultimate failure between a) simulation and b) experiment (c-scan) | 190 |
| Figure 5.5.17 – Comparison of ultimate failure between a) simulation and b) experiment (X-Ray).... | 191 |
| Figure 5.5.17 – Load vs displacement curves for simulation and experiments..... | 192 |

Chapter 1: Introduction

1.1 Introduction

Damage tolerance testing is important for investigating the composite's strength performance when subjected to low velocity impact. As documented in numerous investigations, impact damage may not be visible to the naked eye, although its effect on the residual strength and reliability is important [1,2,3]. The impact event is known to cause several failure modes in the composite such as permanent deformation, fiber/matrix cracking, and delamination. Due to interlaminar damage, the composite's mechanical properties degrade because areas in the composite are free to exhibit local instabilities [4,5]. The complexity of the problem lies in the interaction of various modes of damage such as matrix cracking, delamination, and fiber failure, which cooperatively lead to a loss of load carrying capacity and loss of integrity [5,6,7]. If the load-bearing capacity of the structure is compromised, proper actions must be taken to ensure catastrophic failure does not occur. Therefore, many composites are designed for damage tolerance such that the growth of damage is minimal and still maintains its load bearing capacity.

Many composite structures experience damage in some form during its lifetime. Impact events could cause significant damage that cannot be seen with the naked eye. For example, airframe structures could suffer damage from a tool drop, which would require maintenance to repair the structure if considerable damage was present. Although there is no adopted definition of Barely Visible Impact Damage (BVID), it implies that in the presence of an indent of considerable size, the composite could have undetectable damage that cannot be seen with the naked eye. BVID requires nondestructive techniques to assess the damage of the composite. The categories of damage are outlined in FAA-AC-23-14A [8], which provides insight into the assessment and design guidance to ensure damage tolerant designs are applied to structural applications. This work primarily focuses on low-velocity impact (LVI). Under LVI, an impacted plate deforms according to plate theory, as the impact duration is longer than the time needed for flexural waves to reach the boundaries [9,10].

Composite response to damage, including the various degrees of damage and its influence on residual strength, cannot yet be analyzed with any high level of accuracy. Hence, design guidance relies

very heavily on experiments. Reducing the amount of variability to obtain more accurate models to predict failure and strength would give a significant advantage for creating structures using composite materials. Advancements in nondestructive techniques such as immersion ultrasound, thermography, X-Ray, and C-scanning techniques provide qualitative information about the damage of the material. With combined efforts in experimentation, nondestructive evaluation (NDE), and computational analysis, there exists the possibility of modeling and predicting the residual strength of damaged composites. Obtaining a high-resolution representation of damage in composite structures, utilizing existing or improved nondestructive evaluation, could be significantly improve the accuracy of modeling failure. In addition, this could enable engineers to design more resistant composites and increase the mission life of composite structures.

Using NDE to classify and identify delamination, fiber/matrix cracks, and permanent deformation can be used to create high-fidelity models to accurately predict the failure of composites. Using a progressive discrete damage model that uses fracture mechanics can be used to determine how delamination and matrix crack grow when applying load. Any predictive approach for simulating structural fracture in fiber composites needs to quantify: (1) all possible fracture modes, (2) the types of damage they initiate, and (3) the coalescence and propagation of the damage for imminent structural failure [4].

Damage tolerance design consists of several experiments in a controlled environment to ensure composites can be used in structural applications. However, structures used in many industries (aerospace, marine, energy, automotive, etc.) are often not used in a controlled environment. Damage can occur in various forms in these structures. Developing high fidelity models and methodologies for the industry would improve the certification process of composites for structural applications.

The aircraft's ability to survive even after exposure to severe damage to the vital and load-carrying parts of the aircraft construction is imperative not only for combat aircraft, but also civil aircraft [10]. All aerospace vehicles must be designed such that the structural integrity of the platform is ensured. The complexity of damage could range from matrix cracking, to fiber failure and delamination.

The definition for damage tolerance can be qualified by the ability of the structure to sustain design limit loads in the presence of damage [12].

1.2 Motivation

Individuals are beginning to rely more on composites as their usage increases in structural applications. Composite materials have become prevalent throughout the aerospace, marine, and automotive industries due to their weight to strength properties. Composites experience some form of damage during its lifetime, which could degrade the mechanical properties and reduce the lifespan of the structure. Damage in composites could lead to catastrophic failure, which leads to the cost of lives. Figure 1.2.1 graphically displays the design requirements when discussing damage tolerant design [13]. The figure assumes that a damage threshold is accepted up to a point where the design load level is unable to maintain the material properties to ensure safety [14]. The safety factor is usually determined by good design practices and lessons learned from the aerospace industry [15,16].

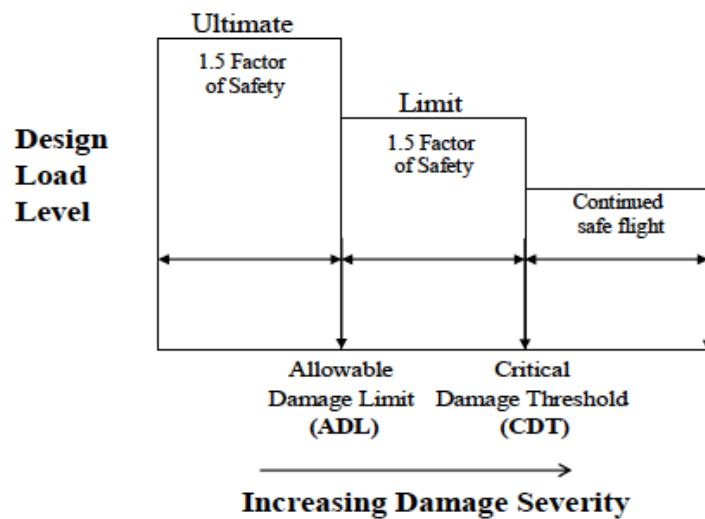


Figure 1.2.1 – Definitions of durability and damage tolerance for commercial aircraft and associated design requirements (Mil-Hbk-17)¹²

The purpose of this research is to quantify the evolution of damage knowing the damage state of the material system. Nondestructive evaluation characterizes the amount of damage seen in the composite. The information provided by nondestructive techniques is integrated into a progressive discrete damage model to predict the failure modes of the composite structure. It is essential, in the

context of safety (aviation, civil, marine, or automotive), that composite structures sustain their design limit loads even with the presence of damage.

Simulating the critical damage that drives the failure of post-impacted composites has not been studied to any degree so far. Integrating experimentation, simulation, and nondestructive evaluation is a challenging task. Individually, each discipline comes with sets of assumptions and limitations requiring extensive amounts of research. Performing an experiment heavily depends on the boundary conditions that were applied. However, what is an appropriate boundary condition? Computational modeling provides insight into the boundary conditions to capture the physics of the experiment. However the underlying boundary conditions are only as good as what the model can predict to an experimental outcome. Nondestructive evaluation provides visualization and understanding of the failure mechanisms of the experiment. However, each nondestructive technique has limitations on what it can capture in the form of damage. An ill posed problem could arise if a wrong assumption about the failure were applied to the model.

There is limited research that simulates the physics of damage growth of known damage in a 3-dimensional composite material system. If models could accurately predict the behavior of failure for an impacted composite laminate while under compressive loading, then it could be used as an analysis tool pack that determines critical damage. This ultimately means that accurately determining the dominating failure mechanisms in the model could be beneficial not only to in the modeling industry but also for nondestructive evaluation. Integrating these disciplines is needed to create high fidelity models that could accurately predict the damage growth and failure. Therefore, by integrating these disciplines, more knowledge can be obtained about the failure and fracture mechanics of any composite system.

1.3 Research Objectives

The goal of this research is to utilize existing and new nondestructive techniques in assessing impact damage of composite plates and pre-impose realistic damage into a three-dimensional discrete model. Some of the nondestructive techniques consist of, but are not limited to, X-ray Computed Tomography, thermography, and ultrasound. Although, compression-after-impact has been studied extensively, determining a damage tolerance methodology that accurately characterizes the failure of

composites has not been established at any level from microscale, mesoscale, and component. A computational and experimental investigation was performed to study the effect of stacking sequence, low-velocity impact response, and residual strength due to compression. The latest non-destructive techniques (C-Scan, Thermography, X-ray) for determining the extent of the damage created by the impact event are utilized to accurately create representative damage models. Digital Image Correlation (DIC) captured the strains and deformation of the plate due to impact and compression. Fiber/matrix cracking, delamination growth, buckling, as well as other failures mechanisms, differ between an impact event and compression-after-impact. The results of this study provide comprehensive knowledge of the end-to-end testing of compression strength of plates and compression-after-impact.

The wider objective is to use nondestructive techniques to gather information about the damage and pre-impose realistic damage into some form of computational modeling. A major challenge in computational investigations is determining the underlying mechanisms that cause failure in composite structures. With more detailed information on damage as a result of the out-of-plane impact; damage evolution and failure can be modeled more realistically when applying in-plane loading.

Giving engineers the tools to evaluate structures and determine the structure's integrity is key to predicting the residual strength of the composite. In addition, if a model could blindly predict the failure mechanism before conducting an experimental test (repair), this would also allow engineers to develop better design requirements for composite materials. Figure 1.3.1 depicts the approach to help mitigate this problem. First nondestructive evaluation detects the damage. Then the nondestructive evaluation is given to a computational investigator such that the engineer can pre-impose the NDE into a discretized model. Then a finite element analysis package is used to accurately predict the behavior of delamination and fiber/matrix crack growth in order to obtain the structure's residual strength. Capturing the complexity of the damage and its propagation would provide insight in the behavior of failure for any composite material system.

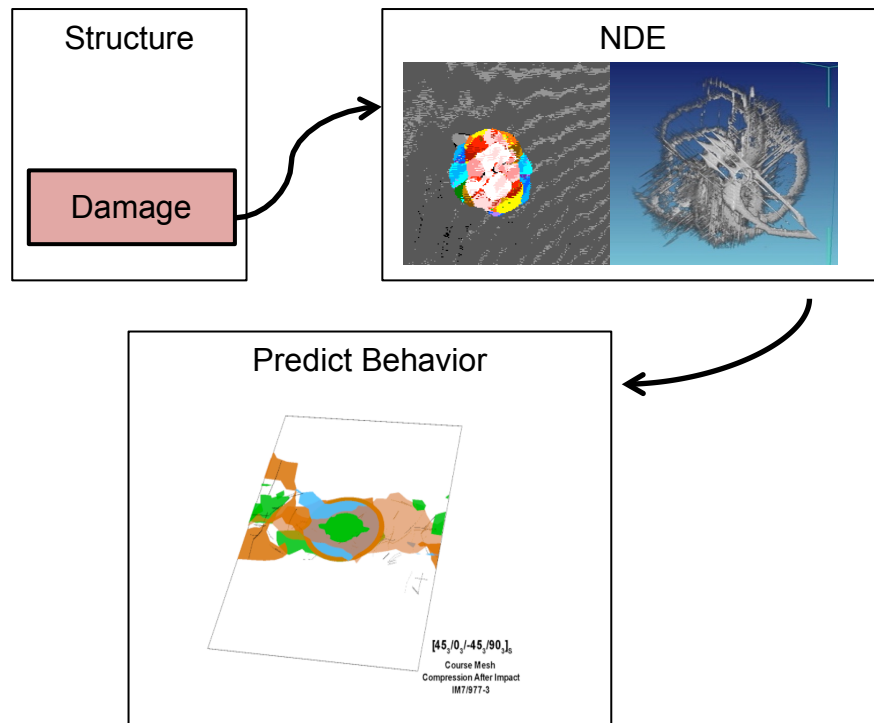


Figure 1.3.1 – Nondestructive Evaluation to Prediction of Behavior

1.4 Overview of Research

In many industries, the collaboration between engineers and mathematicians has been well established when trying to create analytical methods to solving complex problems. In most cases, mathematicians accommodate engineers in testing and engineers help mathematicians develop numerical methods to help predict the underlying physics of a system. For damage tolerance and assessment of composite performance, the utilization of nondestructive techniques has not been explored in great detail in determining the behavior of failure in modeling. Therefore, the purpose of this research is integrating nondestructive evaluation data into finite element analysis to predict the failure modes of compression strength after impact experiments for unidirectional carbon fiber polymer composites. Figure 1.4.1 represents three of disciplines being integrated with each other to understate the behavior of composite for damage tolerance and assessment.

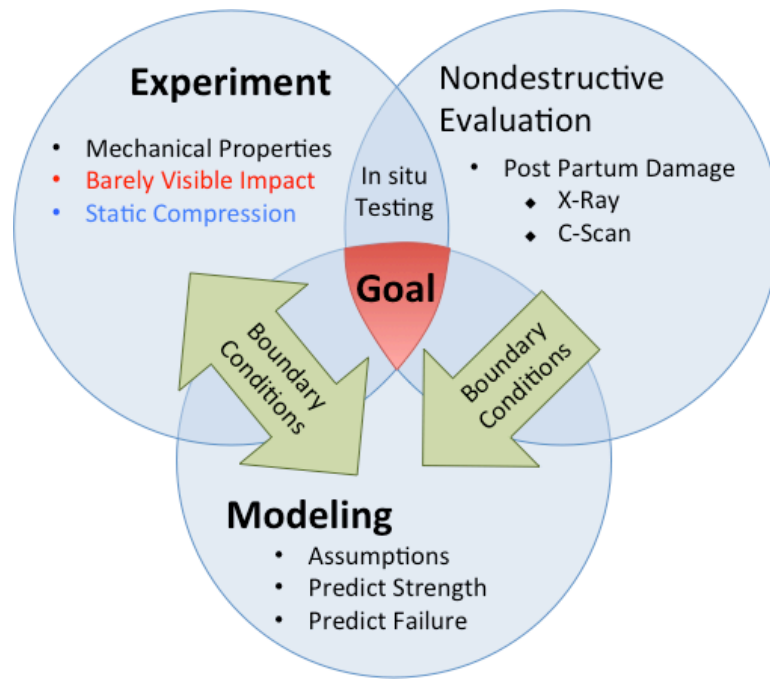


Figure 1.4.1 – Damage Tolerance and Assessment Initiative

Nondestructive techniques have primarily been used to analyze the damage of composites for damage tolerance and assessment after an experiment. In some cases, experiments have been conducted where nondestructive evaluation is integrated with the experiment. However, the driving goal is to use nondestructive techniques (NDT) data from an impact event and use it as an underlying boundary condition of the model. Developing the capability to insert damage into a computational framework requires several technologies and high fidelity analysis tool packs that have not been created in any industry. By incepting realistic damage into a model may allow us to determine what failure mechanism are more predominant than other.

1.5 Relevance

A computational and experimental investigation on compression strength after impact is revisited. The computational effort provides a mechanism to pre-impose realistic damage into a discrete damage model in the form of delamination and open cracks. The research helps study:

- 1) The identification of critical damage
- 2) Evaluation of critical damage on structures
- 3) Quantify growth rates and the effects on residual strength

- 4) Evaluate industrial design criteria and certification
- 5) Identify potential threats to structures

The research could reduce the cost of certification of future composite materials and composite systems. The modeling efforts could be used as a method to aid in the design process for evaluating the mechanisms that drive failure. The tools could be utilized as design guidance for damage tolerance. Integrating nondestructive evaluation into discrete damage modeling could provide a significant amount of understanding on the behavior of failure for complex material structures.

Chapter 2: Impact Experiments

Chapter 2 discusses two types of experimental impact tests that were conducted for damage tolerance and assessment. Section 2.1 discusses the impact behavior of composite plates that were impacted with a ½” (12.7 mm) hemispherical tupper at 10 J (7.38 ft-lbs) which used the ASTM 7136 standard method for impacting composites. Section 2.2 discusses the impact damage of composite plates that were impacted with a 1” (25.4 mm) hemispherical tupper at 55 ft-lbs (75J) which used Lockheed Martin Damage Tolerance and Assessment guidelines. The width, length, and thickness of the composite plates discussed in Section 2.1 (6”x4”x1/8”) are less than the composite plates discussed in Section 2.2 (13”x11”x0.178”). Therefore, the composite plates discussed in Section 2.1 may be referred to as the “thin” and “small” composite plates versus Section 2.2 “thick” and “large” composite plates.

2.1 Impact Experiments of Thin Unidirectional Composite Plates

Damage tolerance testing is important in investigating the composite’s strength performance to low velocity impact. As documented in numerous investigations, impact damage may not be visible to the naked eye, although its effect on the residual strength and reliability is important [17-20]. Transverse impact events are known to cause several failure modes in the composite such as permanent deformation, fiber/matrix cracking, and delamination. Due to interlaminar damage, the composite’s mechanical properties degrade because the area in the composite is free to exhibit local instabilities. The complexity of the problem lies in the interaction of various modes of damage such as matrix cracking, delamination and fiber failure, which cooperatively lead to a loss of load carrying capacity and/or loss of integrity.

Many composite structures experience damage due to impact in their lifetime that unfortunately degrades the strength. Guidelines for impact testing of composites start with ASTM D7136, “Standard Test Method for Measuring the Damage Resistance of Fiber-Reinforced Polymer Matrix Composites to a Drop Weight Impact Event”. In this standard, composite plates are impacted using a hemispherical striker tip at energy levels that cause nearly undetectable damage also known as Barely Visible Impact Damage (BVID). However, it’s difficult to infer the amount of damage the composite has simply

through BVID alone. The impact event could cause damage in the form of delamination, transverse matrix cracks, debonding, and fiber breakage. In order to evaluate the types of damage that exist within the composite as result of impact requires nondestructive techniques. Nondestructive techniques most common used but not limited to is immersion ultrasound, infrared flash thermography, and X-Ray.

High-speed cameras have been used in the ballistic industry to capture the impact event for a variety of different materials and projectiles [17]. Takeda used high-speed photography for glass/epoxy cross-ply composite laminates to monitor a high velocity impact and the onset and propagation of damage [21]. By shining a light through the translucent composite, Takeda captured crack-delamination propagation with a frame rate of 40,000 frames per second. From the shadow fringes that occurred during the experiments, Takeda was able to approximate the velocity and energy of the impact. After observing the initiation of damage, the growth of the damage was determined by taking the difference in time. During Takeda's experiments, crack initiation begins at a high velocity and after the impact response time increases, velocity of the crack begins to decrease until the crack arrests [22]. Using high-speed photography and Shadow-Moire technique, Chai recorded the failure propagation in graphite/epoxy composite panels subjected simultaneously to compressive in-plane loading and low velocity transverse impact [23]. Similar findings were made with Takeda; however, the significant difference was the damage was more severe due the initial boundary conditions that lead to faster crack propagation speeds and delamination. Malvern used high-speed cameras to capture ballistic impacts for composites [24].

Namala investigated low-velocity impact using digital image correlation for glass/epoxy laminate to capture the strains and displacements on the impacted surface of the plate. Namala conducted impact experiments using several velocities on cross-ply and unidirectional composites [25]. The experiments captured out-of plane displacements and strains using a camera speed of 60,000 frames per second and 3-D digital image correlation.

The strain rate sensitivity of a material's properties is a factor generally neglected in low velocity impact studies [26]. Design failure strains of 0.5% are used to guard against impact failure, resulting in a failure to take advantage of the excellent in-plane strength and stiffness properties of composite [27].

Literature is lacking in obtaining experimental strain measurements of composites during impact as strain gauges tend to debond from the specimen. Since, delamination growth rates depend on strain energy release rates for residual strength after impact tests [28,29], DIC could provide information on the strain threshold of a composite during impact as well as determine residual strain that may remain in the composite after impact.

In this work, 3D digital image correlation was performed using two high-speed digital cameras at 20,000 frames per sec to capture the out-of-plane deformations and in-plane strains. Understanding the amount of damage that results from a low-velocity impact event is crucial in determining its residual strength after impact. The impact event is known to cause transverse matrix cracks, fiber breakage, and delamination. Nondestructive techniques have provided ways to visualize the damage after impact such as transverse matrix cracks, fiber breakage, and delamination. Using high-speed 3-D digital image correlation, deformations and strains were recorded. The high-speed cameras were also able to capture transverse matrix crack initiation and propagation.

2.1.2 Material Specifications

Carbon fiber reinforced polymers of IM7/977-3 were produced using a standard autoclave approach. Panels consisting of four different stacking sequences with 24 plies were provided by Air Force Research Laboratory (AFRL). Each of the panels had a dimension of 24 in x 24 in with a nominal cured thickness of 1/8 inch (3.2 mm). Each panel was C-Scanned to determine if they were any initial defects in the panel. A waterjet process was used to cut the panels into 6 in x 4 in (101.6 mm x 152.4 mm) specimens for impact testing according to ASTM 7136. After the waterjet was completed, the specimens were C-scanned a second time to determine if delamination, damage or other flaws occurred through the cutting process. Table 2.1.2 is a table of the alpha numeric that represents each stacking sequence and is referred to as such through out this study. The stacking sequences were chosen because they are commonly known composite layouts that are used in airframes in aeronautical structures.

Table 2.1.1 – Stacking Sequence Table

| # | Stacking Sequence |
|---|-----------------------------------------------|
| A | $[-45/90/45/90/-45/0/45/90/90/-45/90/45]_s$ |
| B | $[-45/45/-45/45/0/45/90/-45/45/-45/45/-45]_s$ |
| C | $[-45_3/90_3/45_3/0_3]_s$ |
| D | $[-45/90/45/0]_{3s}$ |

2.1.3 Environmental Conditions

Each specimen went through a 50 °C heating cycle for 24 hours prior to testing to dry the specimen from any moisture that it obtained through nondestructive testing and environmental conditions such as humidity. The specimens were placed into a desiccator to cool down to room temperature until the experiment.

2.1.4 Test Method

Several composite plates consisting of different stacking sequences were impacted using a drop weight tower in accordance to ASTM 7136. During a subset of those impact experiments, high-speed photography was used to capture the back surface of the composite during the impact event. Using two digital cameras, displacements and strains were calculated using digital image correlation. After the experiments were completed, each composite went through immersion ultrasound to get a representation of the delamination area. Optical profilometry was performed to obtain line and area profiles of the permanent deformation.

Composite plates with the dimension of 152.4 mm x 101.6 mm (4" x 6") were clamped onto a 76.2 mm x 127 mm (3" x 5") fixture with a rectangular open frame using 4 push clamps. Figure 2.1.4.1 is a picture of the ASTM 7136 impact fixture showing how the specimens are clamped. This impact fixture was fixed to a steel base inside the drop weight tower. The composite fixture was aligned to the center of the steel base's 76.2 mm (3") circular opening. The impact event was introduced using an INSTRON/CEAST drop weight tower with a 12.7 mm (1/2") diameter hemispherical tupper with a mass of 5.439 kg. The drop weight tower was calibrated using a 22kN (4.945 kip) transducer to measure the forces. Each impact occurred in the center of the composite. Each plate was impacted with 10 joules (7.37 ft-lb) of energy, which was enough energy to create BVID. Additional tests were conducted to capture the deformation using high-speed cameras during impact.

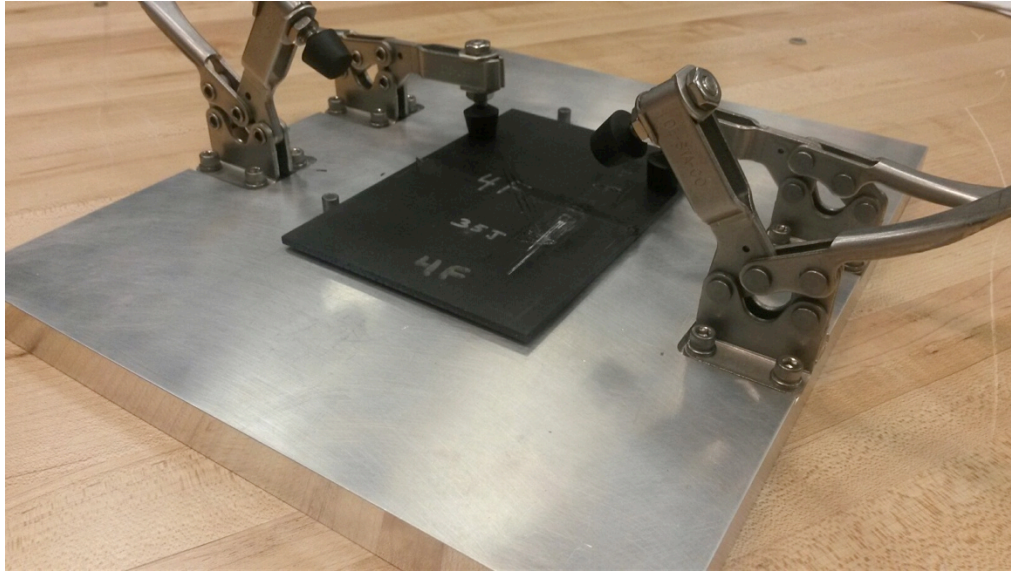


Figure 2.1.4.1 – ASTM 7136 Impact Fixture

2.1.4.1 Digital Image Correlation of Impact Event

A mount and stand was designed in order to capture the impact event using high-speed photography. The mount used a cantilever beam to hold a flat mirror at approximately a 45° angle as seen in Figure 2.1.4.2. The mount was positioned through the side of the drop weight tower. The mount was designed to reduce any vibration that might occur during the impact event and capture the back surface of the composite under impact. An optical stand was constructed to hold two 1-megapixel Photron FASTCAM SA-5 high-speed digital cameras (Figure 2.1.4.3). The camera lenses used were 50 mm with the aperture set at 2.8 and were placed in a 24.5° angle between each other with respect to the mirror to obtain accurate strain data. The experiments were calibrated by placing a predefined grid pattern a distance away from the cameras. The grid pattern was a 135 mm x 108 mm panel manufactured by GOM to calibrate optical measurements for digital image processing within the ARAMIS DIC software. The distance of the grid pattern to the camera was approximately the same distance between the cameras and the mirrors. Images were taken after translating and rotating the grid pattern several times to perform calibration. Both of the cameras were able to locate the fiducial marks on the grid pattern to calibrate the system. Initial assumptions were made when capturing the images through DIC. Since two cameras were being used, it would compensate for any distortion effects caused

from the angle of the mirror. Due to space limitations the system was not able to be calibrated through the reflection of the mirror, therefore the aberration of the mirror are not taken into account in the correlation of the images. Due to limitation of space, the calibration was done without the mirrors. Future experiments would consider calibrating the test with respect to the mirror. Two light sources were used to ensure adequate lighting with minimal vibration. The specimens were spray painted white and a black speckle pattern was applied using an airbrush. Each DIC test took 5 still frames prior to testing. During the impact event, the frames of the un-deformed and deformed images were captured with the Photron FASTCAM viewer software and then imported into the ARAMIS software for correlation.

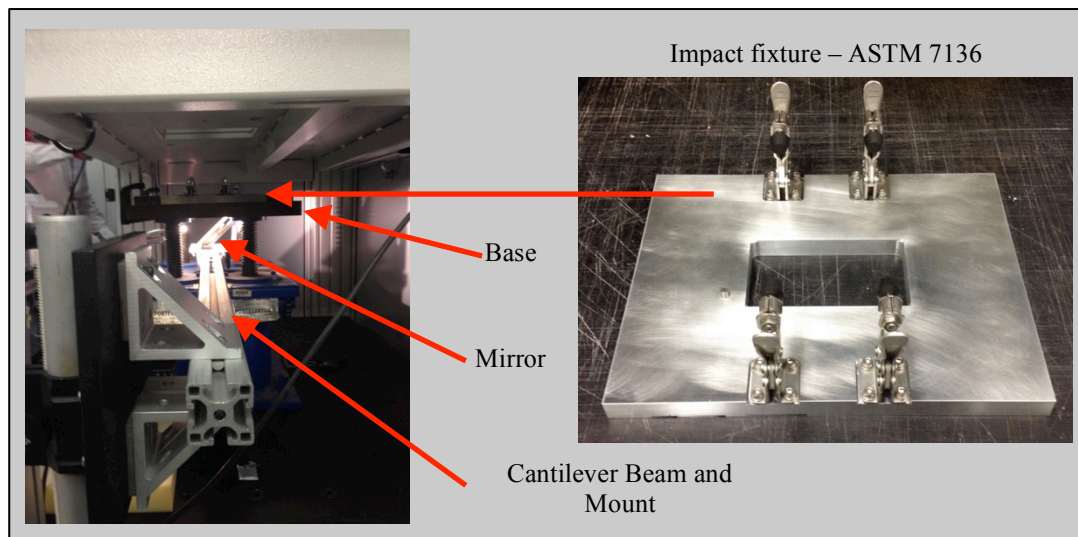


Figure 2.1.4.2 – Cantilever beam mount for mirror

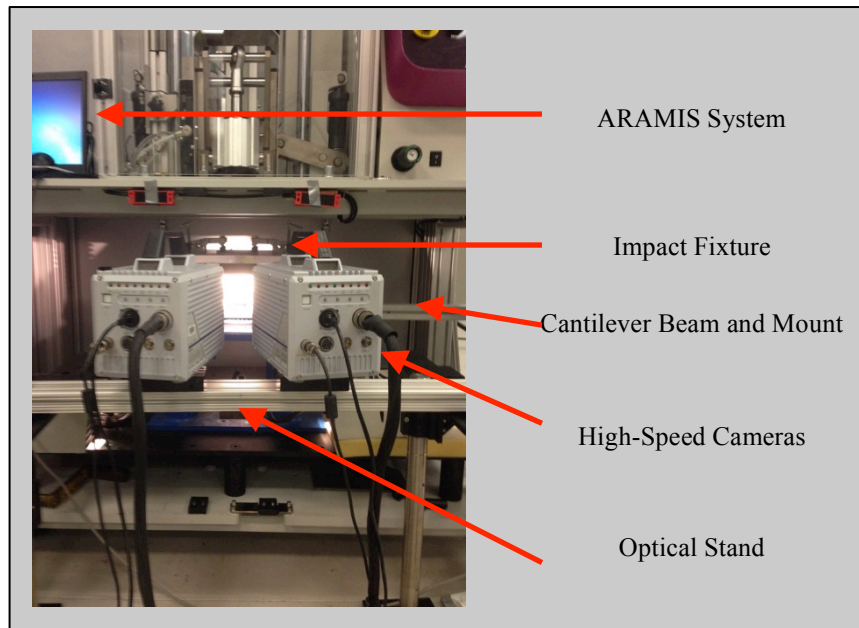


Figure 2.1.4.3 – Optical Stand and High-Speed Cameras

The camera speed was set at 20,000 frames per second (fps) to capture the impact event with enough field of view to measure strain and displacements. The optimal speed of 20,000 fps proved to be beneficial since it required less light with the speckled composite samples. Both cameras were connected to the photocell trigger of the drop weight tower to initiate capturing the images automatically during the impact event. The field of view of the 101.6 mm x 152.4 mm (4" x 6") specimens was approximately a 63.5 mm by 88.9 mm (2.5" x 3.5") window. Higher speeds required more light, lowered the field of view available to perform digital image correlation, and reduced the amount of resolution needed for an adequate correlation. The calibration deviation of the tests was 0.028 pixels with a camera angle 24.5°. The angle variance was -15.5°/17.7° and the height variance was 23 mm.

2.1.4.2 Optical Profilometry

A Nanovea Optical Profilometer was used to measure the permanent deformation of composite after the impact event. Figure 2.1.4.4 shows how optical profilometry works. The Nanovea Optical Profilometer uses a chromatic confocal technique to measure the vertical variations of a surface. The optical probe uses a white light emanating from a light emitting diode to capture depths of 3.5 mm (0.138"). An optical base was constructed to ensure the center of the impact would be captured for both the impacted surface and back surface of the composite as seen in Figure 2.1.4.5. The reflection of the

light passes through a beam splitter where it is analyzed and processed by the spectrometer. From the spatial filter, the signal is processed into height data. The process could be used to obtain area profiles or line profiles. Horizontal and vertical line profiles each with a length of 76.2 mm (3”) were recorded. The scan used 20-micrometer steps with a 1000 Hz sampling rate. Surface roughness could have attributed to the noise in the profilometry data therefor smoothing was performed using a robust local linear regression to remove any outliers that exist in the data. Outliers could exist from the mechanical gears used to move the probe and any surface cracks that could cause interruption in the collection.

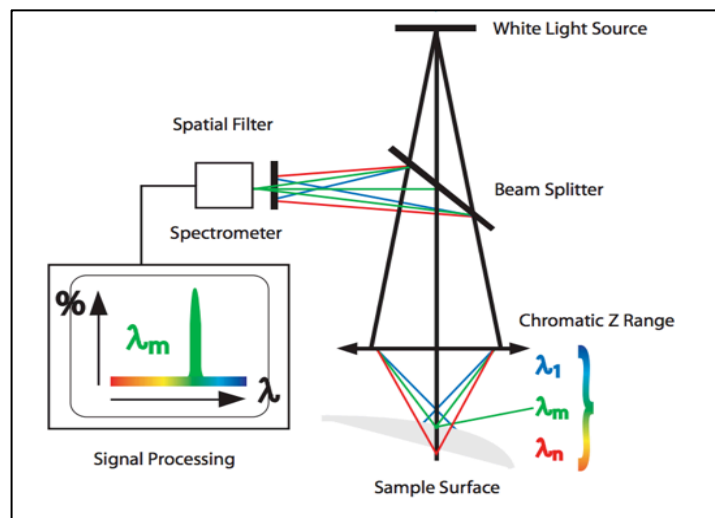


Figure 2.1.4.4 – Nanovea Optical Profilometry Schematic

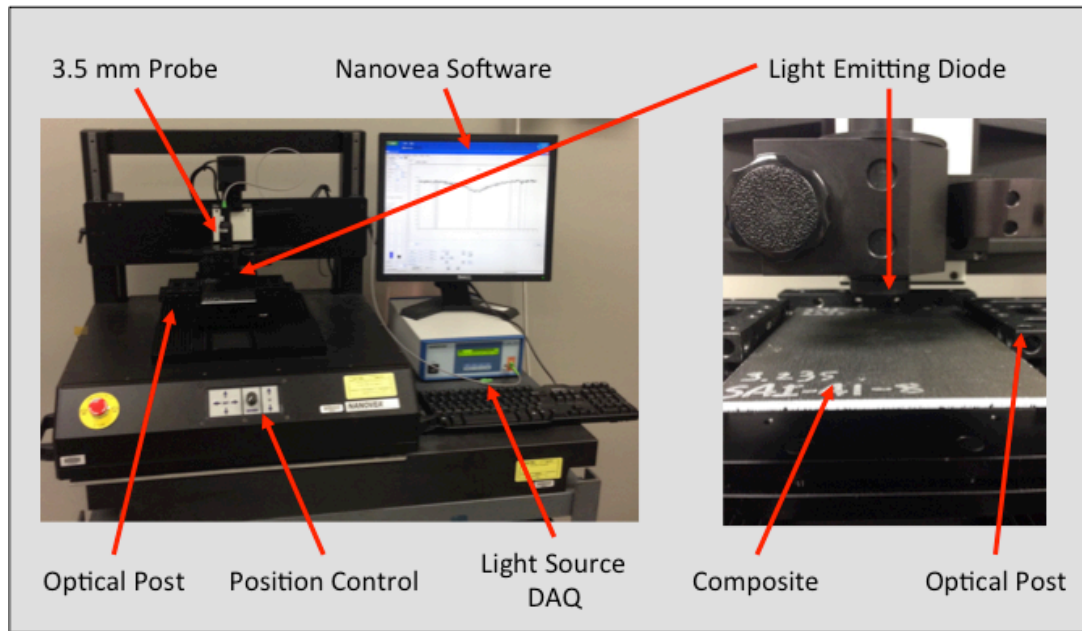


Figure 2.1.4.5 – Nanovea Optical Profilometry Setup

2.1.4.3 Nondestructive Evaluation

Each of the specimens went through immersion ultrasound to determine the amount of internal damage that occurred for each of the specimens. Using a 5 MHz frequency, amplitude and time-of-flight data was recorded. Amplitude data provides a general area of delamination through the thickness while time-of-flight data provides depth where the delamination is present. A total of 3 specimens for each stacking sequences went through immersion ultrasound using a 10 MHz frequency. One specimen from each stacking sequence went through X-Ray CT. More details of these nondestructive techniques is discussed in Chapter 4. The basic premise behind using a 10 MHz sampling frequency is to obtain a higher resolution image of the damage. The 5 MHz is a common probe that has been utilized in the industry. X-Ray CT was used to obtain information of the delaminated regions, cracks, and fiber breakage.

2.1.5 Results and Discussions

2.1.5.1 Drop Weight Tower

The hysteresis of the impact load followed similar patterns seen in previous studies [17,18,30,31]. The load-time impact responses were identical across each of the panels. During the loading phase of the impact, a sharp drop in load is observed possibly indicating crack initiation or a

damage threshold load [30]. Figure 2.1.5.1 is a graphical representation of the load versus time for each panel. The composites from Panel C had a lower drop in force than the other Panels which may have been attributed to the amount of 0° plies it had in the center of the composite. The average peak load for Panel A, B, C, and D are 5.601, 5.452, 4.733, and 5.588 kN, respectively. The minor fluctuations prior to the drop in maximum load are attributed to the vibration of the specimen. After the drop in load occurs, the fluctuations increased primarily due to the elastic wave response, crack initiation, and vibration in the specimen.

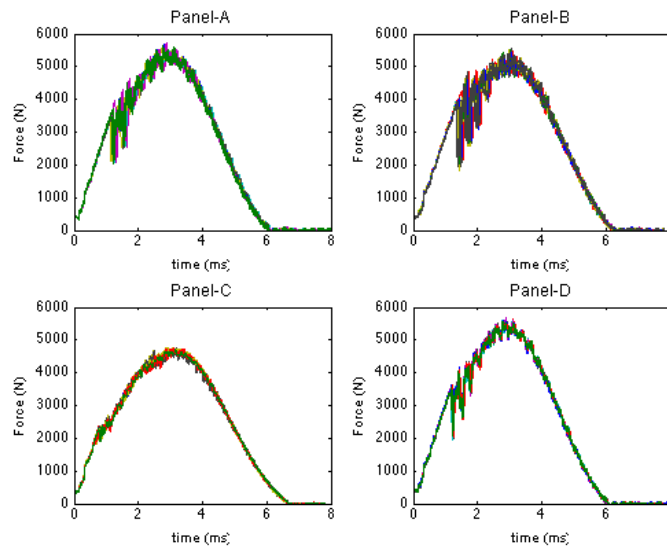


Figure 2.1.5.1 – Composite Panels Load vs Time

The load versus deflection curve (Figure 2.1.5.2) also shows the change in slope during the loading phase and the drop in load. The load appears to increase linearly with respect to time and displacement during the loading phase until the load drops. The change in slope during the loading phase would indicate degradation in the stiffness as a result of damage. The change in slope for Panel C is more easily seen versus the other panels. This could be attributed to Panel C being more flexible than the other panels. Panel C had more damage than the other panels with respect to delamination, transverse matrix cracks, and permanent deformation. Although Panel A, B, and D possess flexural stiffness, they are also more rigid than Panel C. Crack growth for Panel C appeared to be dominated by the flexural stiffness. However, crack growth for Panel A, B, and D appeared to be dominated by the shear stiffness. The dramatic drop in load in Panel A, B, and D could also be attributed to the sudden

unstable growth in delamination. The small drop in load in Panel C could be the result of crack opening occurring on the back surface.

The derivative of the load versus time plot was used to find the time in which the initial drop in load occurred. Table 2.1.5.1 shows the average load, velocity (V) and displacement (w) for each panel for the drop in load time (t) and the peak load time. Figure 2.1.5.3-5 shows the time hysteresis curves for energy, velocity, and deflection as measured from the drop weight tower.

Table 2.1.5.1 – Drop in Load vs Peak Load Data

| Panel | Drop in Load | | | | Peak Load | | | |
|-------|--------------|--------------|------------|-----------|-----------|--------------|------------|-----------|
| | t (ms) | Load (kN) | V (m/s) | w (mm) | t (ms) | Load (kN) | V (m/s) | w (mm) |
| A | 1.186 | 3.345 | 1.488 | 2.073 | 2.839 | 5.601 | 0.194 | 3.565 |
| B | 1.427 | 3.741 | 1.347 | 2.426 | 3.023 | 5.452 | 0.082 | 3.646 |
| C | 0.628 | 1.751 | 1.731 | 1.119 | 3.109 | 4.733 | 0.177 | 3.839 |
| D | 1.109 | 3.000 | 1.514 | 1.937 | 2.858 | 5.588 | 0.169 | 3.578 |

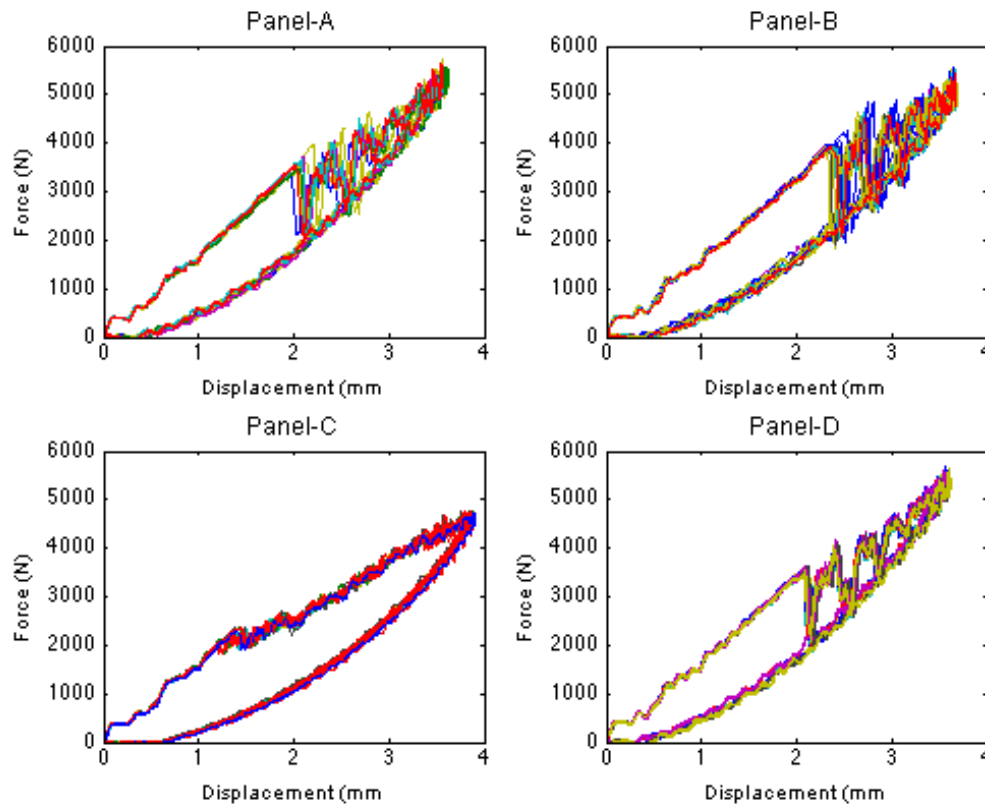


Figure 2.1.5.2 – Composite Panel's Load vs Displacement

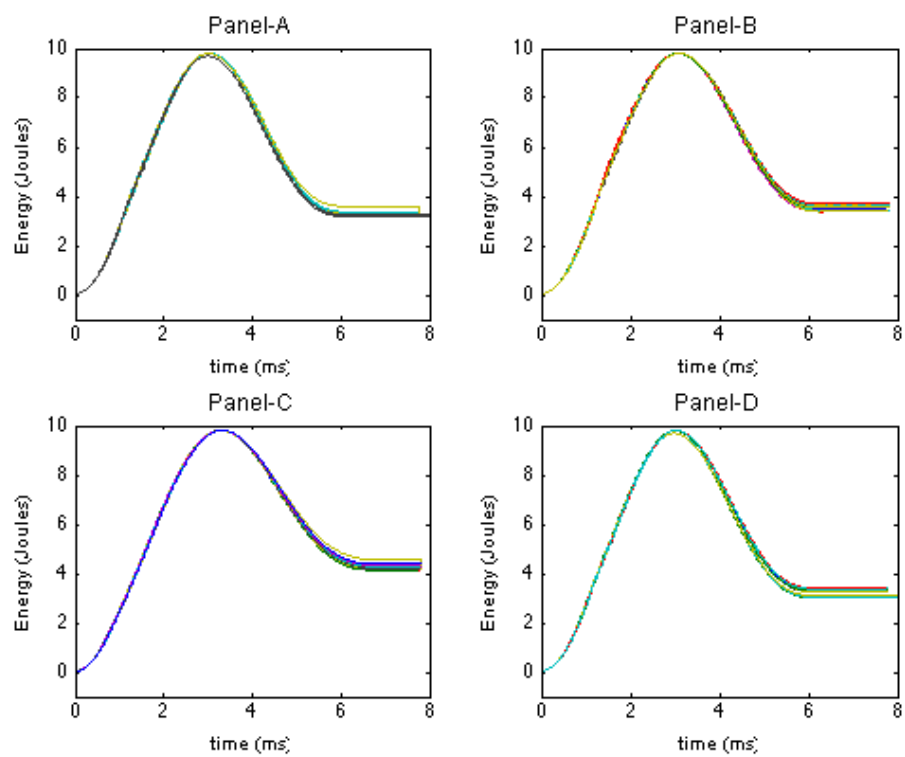


Figure 2.1.5.3 – Composite Panel's Energy vs Time

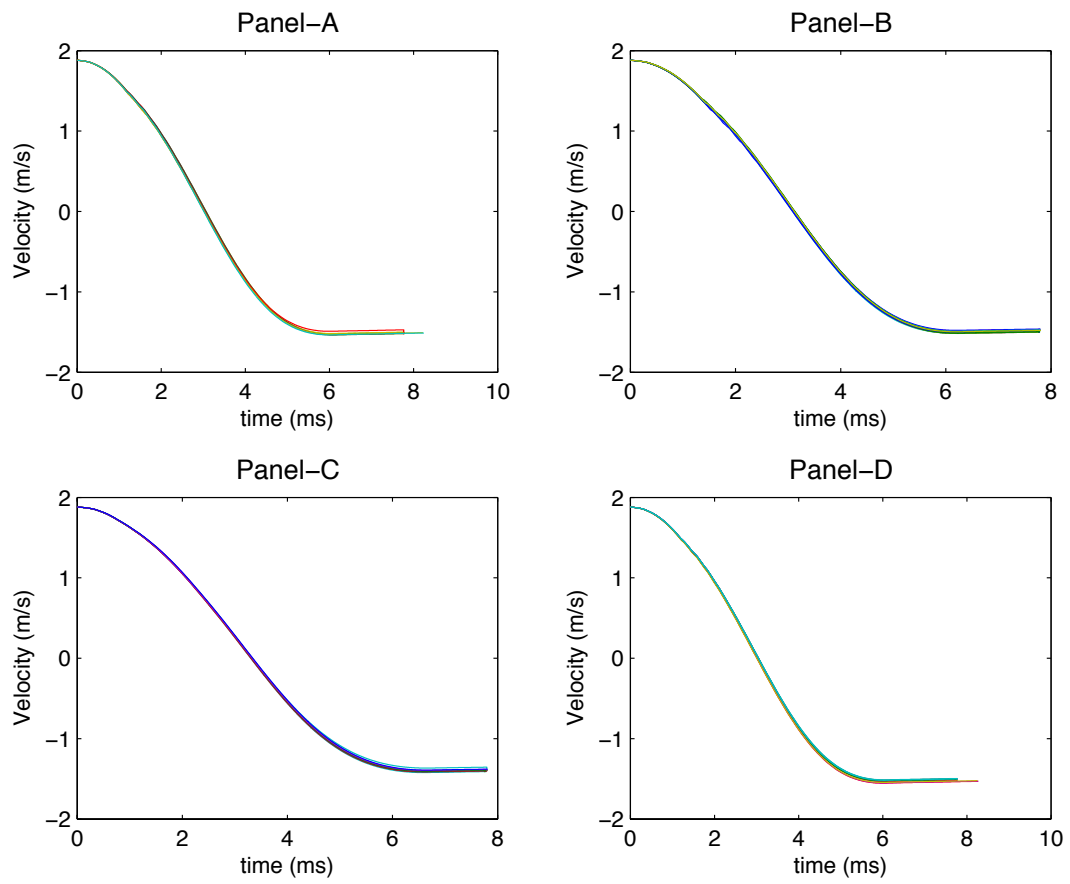


Figure 2.1.5.4 – Composite Panel's Velocity vs Time

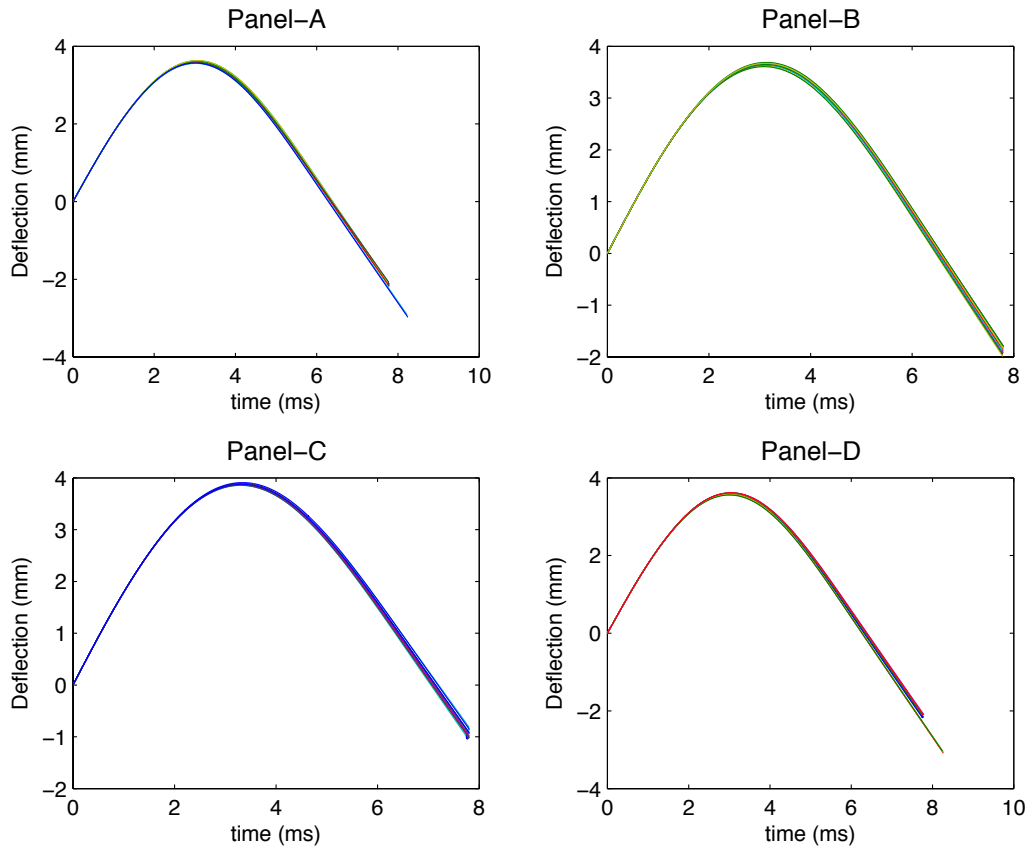


Figure 2.1.5.5 – Composite Panel's Displacement vs Time

2.1.5.2 DIC – Out-of-Plane Displacements

Digital image correlation was able to capture the initial contact of the impact showing a concentration of out-of-plane displacements until it reached its maximum displacement. Contact mechanics have shown that tensile stresses are generated at the periphery of the area of contact, at which sufficient impact velocities are large enough to cause failure at the fiber/matrix interface [4]. Approximately a 63.5 mm by 88.9 mm window was used to capture digital image correlation data. Each panel had similar contours as those shown in Figure 2.1.5.6. The out-of-plane displacement contours show residual displacements after the impact possibly indicating permanent deformation of the composite panel. Initial contact occurred between the 129-133rd frames and is considered the initial time (0 seconds). The maximum out-of-plane displacement occurred between the 185-195th frames for each of the panels, which happened approximately in 3 ms after initial contact. The coordinate location of this point was recorded. Then the out-of-plane displacements were graphed using the point location

through all the frames as seen in Figure 2.1.5.7. The comparison of the out-of-plane displacement between DIC and the drop weight tower were within 5% as seen in Figure 2.1.5.8.

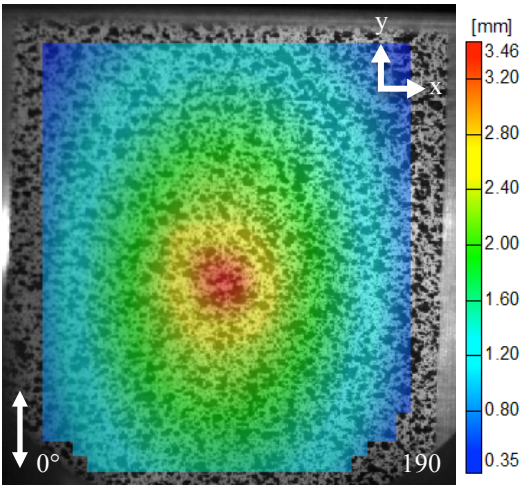


Figure 2.1.5.6 – Out-of-Plane Displacement Contours – Panel B

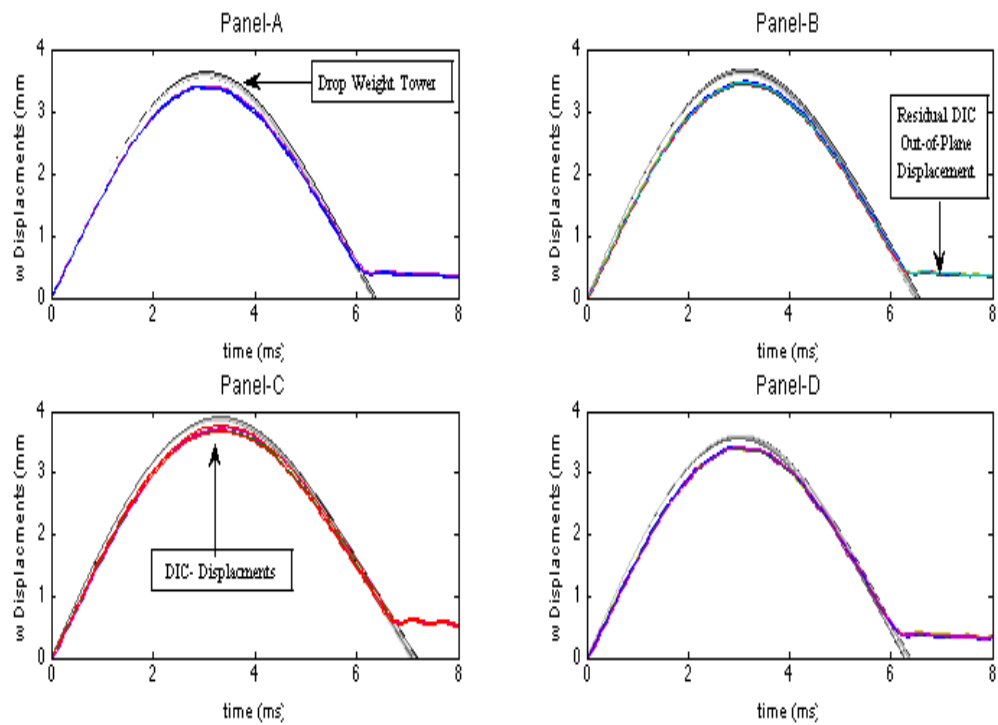


Figure 2.1.5.7 – Out-of-Plane Displacement vs Time

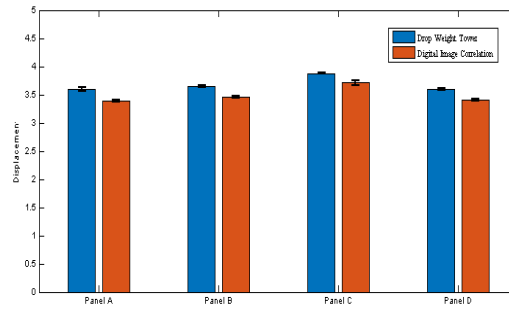


Figure 2.1.5.8 – Maximum Out-of-Plane Displacements – DIC vs Drop Weight Tower

The displacements in the x and y were similar among all the panels. The width of the window was not adequate to capture a full field of view of the x displacement contours of the impact event. However, the length of the window was adequate enough to capture a full field of view of the y displacement contours of the impact event. The full field of view of the y-displacements is discussed later.

2.1.5.3 DIC – Strain Measurements

Previous studies examined the effects of strain during impact using strain gauges placed on the impact and back surface of the composite [25]. The ARAMIS system uses a linear strain method to compute the strains [33]. Axial strains, longitudinal strains, shear strains, major principle strains and minor strains were calculated using the ARAMIS software. Strain computation for the curvature radii of the specimen that are smaller or equal to the facet was not performed [33]. Even though only the surface strains were captured during the impact event, the impact studies discovered new parameters such as the damage threshold strain, surface cracking, and crack opening.

The contours for the major strains were similar in pattern to the ones seen in the out-of-plane displacements during initial contact. During the loading phase the major principle strains increase linearly until it reaches the load drop. After the load drops the slope increases dramatically until it reaches peak effective major principle strain. After maximum major principle strain is reached, the major principle strain begins to decrease to a final state. It was observed through the contours that the concentration became more pronounced during the impact event possibly capturing the initiation of a crack. X-Ray CT was performed to verify that DIC did capture a surface crack. The final state indicates

possible residual strains that occur in the composite after impact. The major principle strains were graphed using the maximum out-of-plane displacement coordinates as seen in Figure 2.1.5.9. The residual strains could be implemented into models to accurately predict failure strength of the composite after impact. Panel C stacking sequence had more 0° plies in the midplane of the composite causing it to deform more and have higher major principle strains. The increase in slope occurred around the same time the initiation of crack occurred for the load versus time plots. The times for the change in slopes were 1.217, 1.400, 0.690, and 1.181 ms.

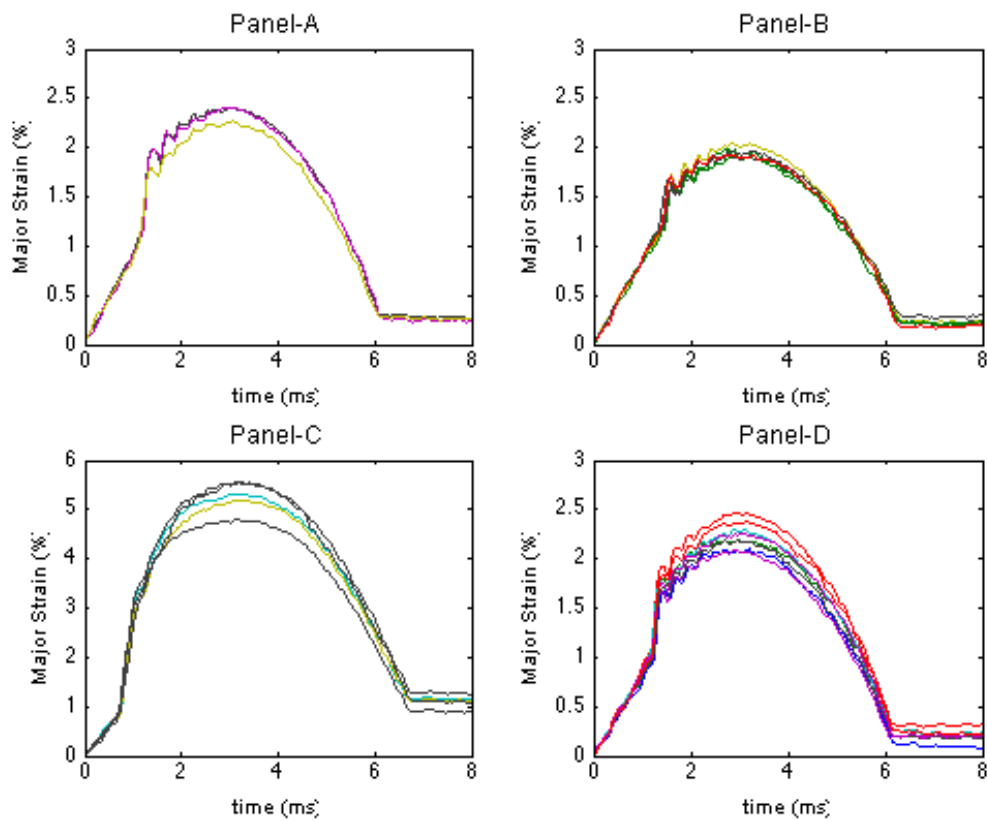


Figure 2.1.5.9 – Major Principle Strains vs Time: Obtained from tracking the maximum out-of-plane displacement pixel point

The damage threshold strains can be defined similarly to the damage threshold load where the delamination threshold is associated with the sudden increase in slope during the loading phase. The major principle strains are similar to the ones shown in literature [24, 33, 34], however, the residual strains and deformation that digital image correlation capture on the back surface of the composite

specimen are absent from literature. The dramatic increase in slope shown in Figure 2.1.5.9 is due to crack initiation where the effective major principle strain is calculated from the effective movement of the crack opening. The increase in slope occurs at approximately the same time in which the composite also had its damage threshold load (Table 2.1.5.2).

Table 2.1.5.2 – Strain, Displacement, and Load at Drop in Load

| Panel | Drop Weight Tower | | | | Digital Image Correlation | | |
|-------|-------------------|---------------|------------|-----------|---------------------------|-------------------|-----------|
| | t (ms) | Force (kN) | V (m/s) | w (mm) | t (ms) | ϵ (%) | w (mm) |
| A | 1.186 | 3.345 | 1.488 | 2.073 | 1.217 | 1.106 | 1.886 |
| B | 1.427 | 3.741 | 1.347 | 2.426 | 1.400 | 1.161 | 2.223 |
| C | 0.628 | 1.751 | 1.731 | 1.119 | 0.690 | 0.871 | 1.175 |
| D | 1.109 | 3.000 | 1.514 | 1.937 | 1.181 | 1.052 | 1.927 |

Strain measurements of the back surface provided a great deal of information for axial strains and transverse strains. Figure 2.1.5.10-11 is a graphical representation of the axial strains and transverse strains with respect to time. The axial strain curves and transverse strain curves are nearly identical to the major principle strain. Figure 2.1.5.12 shows the minor strains that occurred during the experiment. The length of the rectangular opening from the impact fixture is 5" (127mm) and the width is 3" (76.2mm). The axial strains are in the y-direction along the length of the rectangular opening. Due the underlying boundary conditions, the axial strains are more dominate in the y-direction of the specimen.

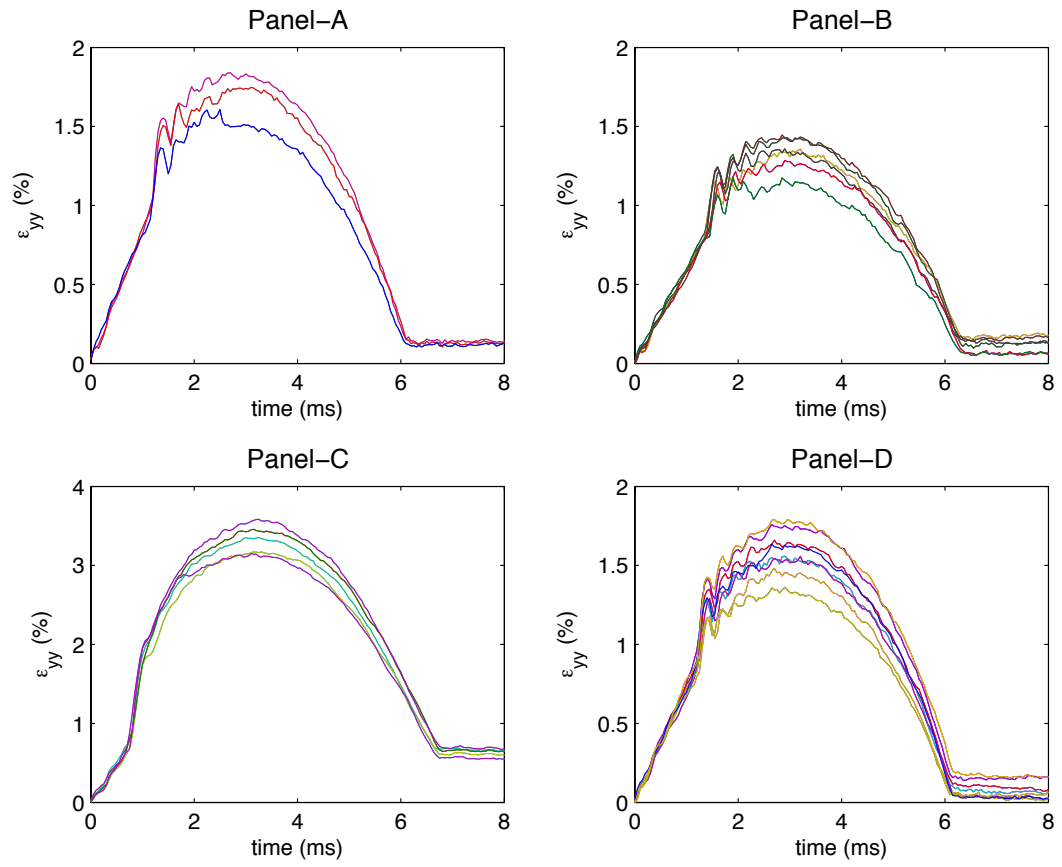


Figure 2.1.5.10 – Axial Strains vs Time

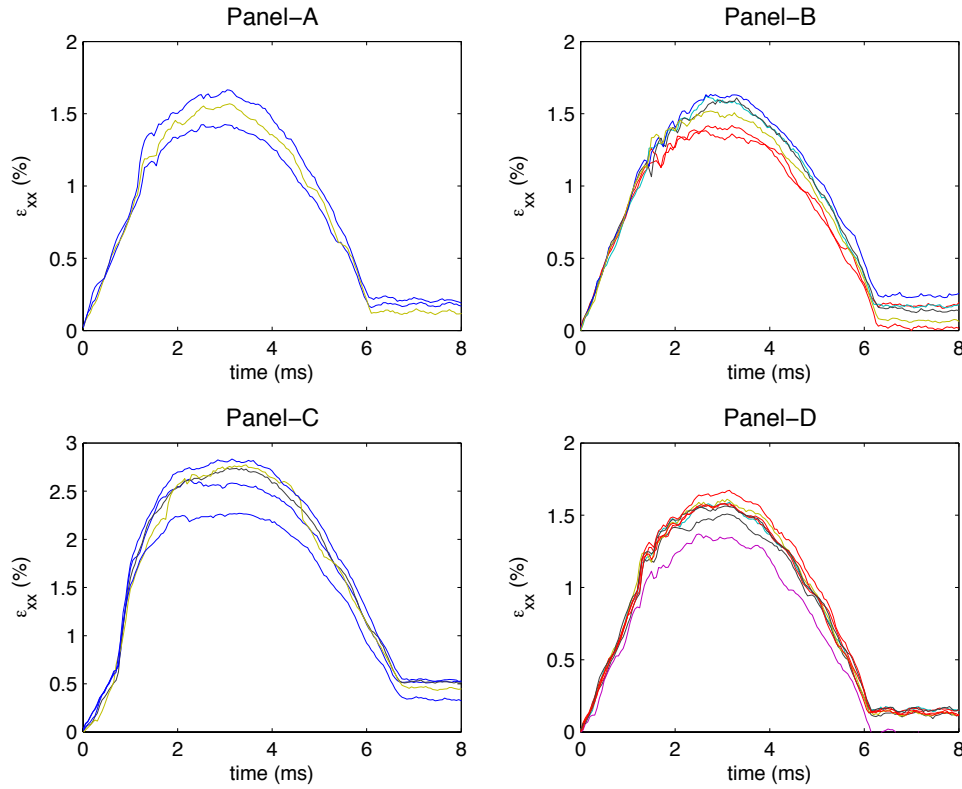


Figure 2.1.5.11 – Transverse Strains vs Time

2.1.5.4 DIC – Permanent Deformation

Both the horizontal and vertical line profiles were measured using profilometry. Figure 2.1.5.12 shows the lateral displacement of the profilometry probe to obtain height data for the horizontal and vertical line. Figure 2.1.5.13 represents the horizontal line profiles from the impacted surface of the composite and Figure 2.1.5.14 represents the vertical line profiles from the back surface. The 3.5 mm probe scanned 76.2 mm (3”) in length with sampling height data every 20 microns. For future studies, area profiles would be performed and then turned into a discretized model. This study does not consider simulating the impact event. However, modeling strength after impact requires an accurate representation of the morphology to capture the strain response of the material during compressive loading.

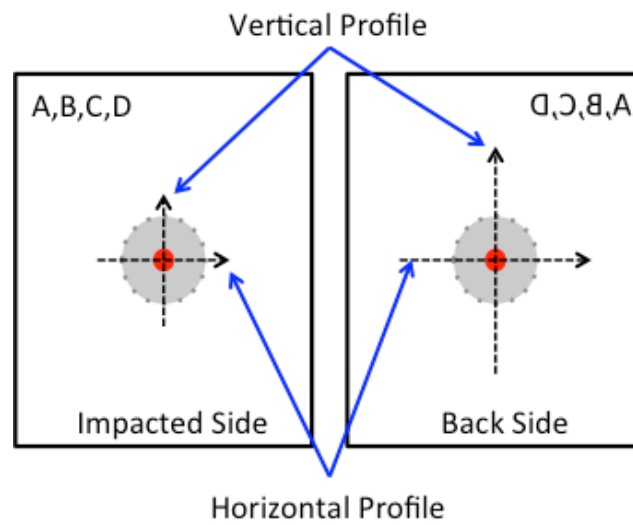


Figure 2.1.5.12 – Profilometry scans

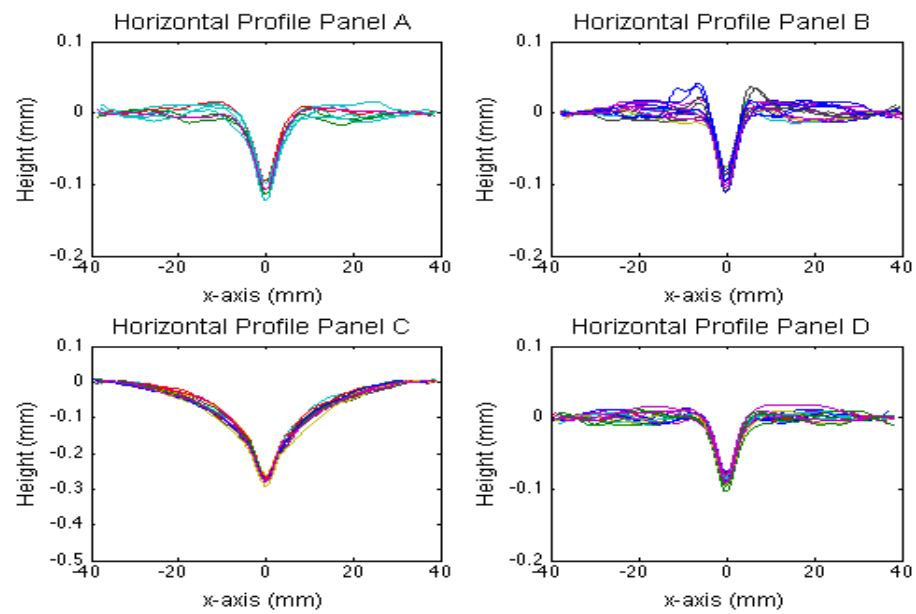


Figure 2.1.5.13– Horizontal line profiles for impacted surface

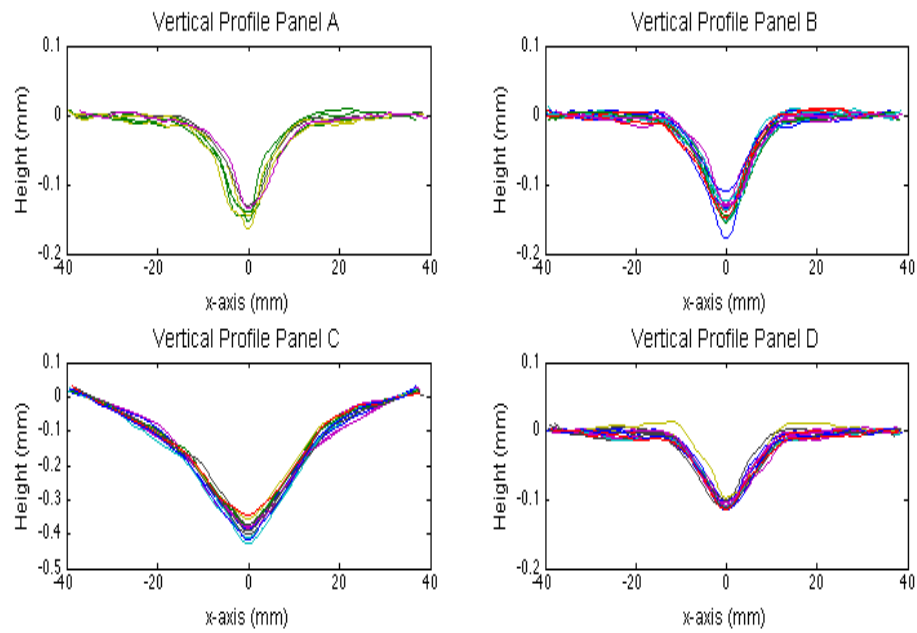


Figure 2.1.5.14 – Vertical line profiles for back surface

Out-of-plane displacements were measured after the impact event using digital image correlation to record any residual displacements that occurred. Averaging of the last few frames was done to reduce any noise from the vibration. Given the speckle size, the facet size used for the correlation, and the DIC calibration was without the mirror; the out-of-plane displacements were within a 10% error of each other for the back surface. Figure 2.1.5.15 is a plot showing the differences between digital image correlation and profilometry.

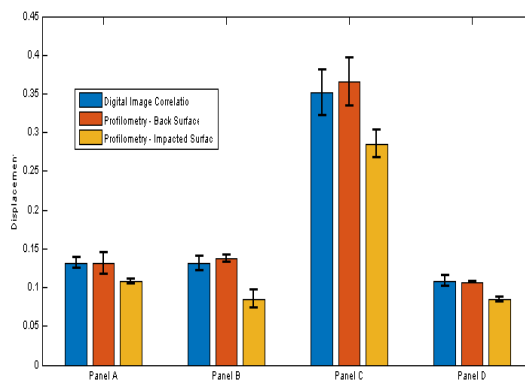


Figure 2.1.5.15 – Profilometry vs. DIC

2.1.5.5 DIC – Crack Initiation of Panel C

Digital image correlation and high-speed photography may also be used to capture the back splitting of crack initiation and propagation. Although, DIC cannot quantify matrix crack and fiber breakage, X-Ray indicated that the back splitting represents a transverse matrix crack on the back surface ply of the composite. Panel C was the easiest to detect crack initiation using high-speed photography since the crack could be seen on the back surface of the composite. For each of the tests, initial contact occurred at approximately frame 130 (0 s), then crack initiation occurred at approximately frame 144 (0.6 ms), followed by crack propagation until the maximum deformation around frame 190 (3 ms). Figure 2.1.5.16 represents the event after a couple of frames of crack initiation to the frame that represents the maximum out-of-plane displacement. Target stiffness is a dominant parameter and controls the mode of fracture. This precipitates failure at the fiber/matrix interphase [31,32].

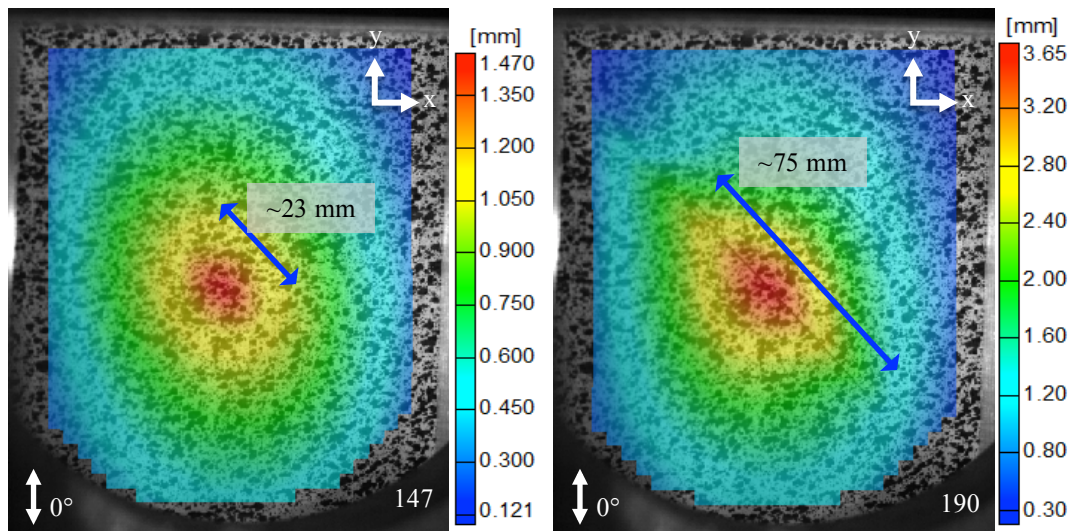


Figure 2.1.5.16 – Crack Initiation and Propagation of Panel C

2.1.5.6 DIC – Crack Initiation Using V-Displacements

For Panel A, B, and D, y-displacements formed a symmetric pattern about the y-axis from initial contact through 150-155th frame (1.25 ms). The y-displacement begins to change around the center of impact region as the y-displacement contours begin to show a rapid variation oriented transverse to the fiber direction between each frame as seen in Figure 2.1.5.17. The discontinuity of the y-displacement contours is an indication that a crack formed on the surface. The change in contours could have

indicated that cracking was initiated. The major principle strain contours indicated a strain concentration possibly also indicating crack initiation. The contour change correlated to the timing of the damage threshold load and damage threshold strain.

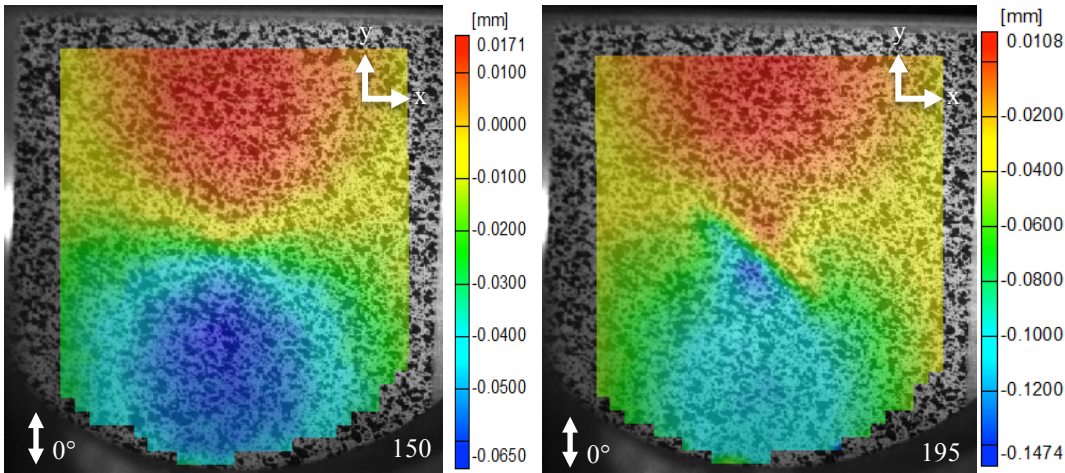


Figure 2.1.5.17 – Y-Displacement of Panel D

2.1.5.7 Nondestructive Evaluation – Immersion Ultrasound

Each of the panels went through immersion ultrasound (pulse echo) to obtain the amount of delamination from impact. The projected area of delamination was calculated using image processing and analysis. The approximate size of a pixel was calculated for each image and filtering techniques were used to create a border around the delamination. The delaminated areas were calculated by using the area of the pixels inside the boundary. Figure 2.1.5.18 shows the amount of delamination that occurred from impact for each panel. Panel A, B, and D had similar damage patterns. Panel C had substantially more damage than in the other panels. Panel C also had cracks that could be seen on the back surface of composite specimen. Table 2.1.5.3 is a chart of the average and standard deviations of the delaminated areas of the composite. Figure 2.1.5.19 shows the time of flight for each of the panels. The shapes and damage for each of the specimens had remarkable repeatability. Appendix A is the immersion ultrasonic data that was conducted on the specimens.

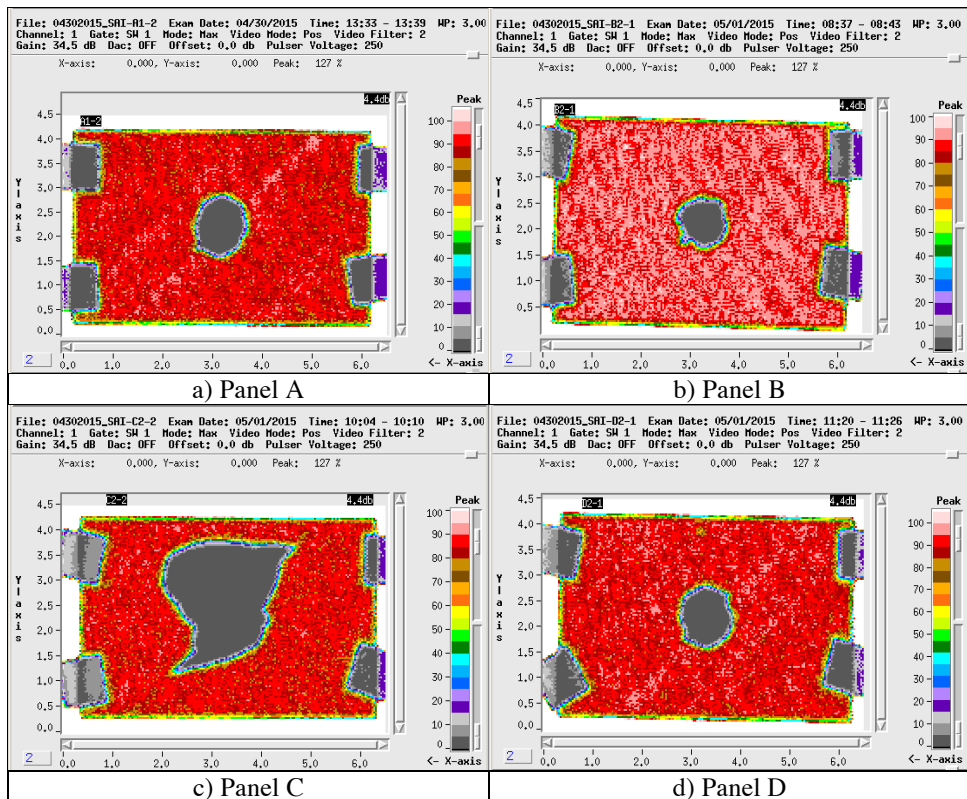


Figure 2.1.5.18 – C-Scan Amplitude Data of Panels (5 MHz)

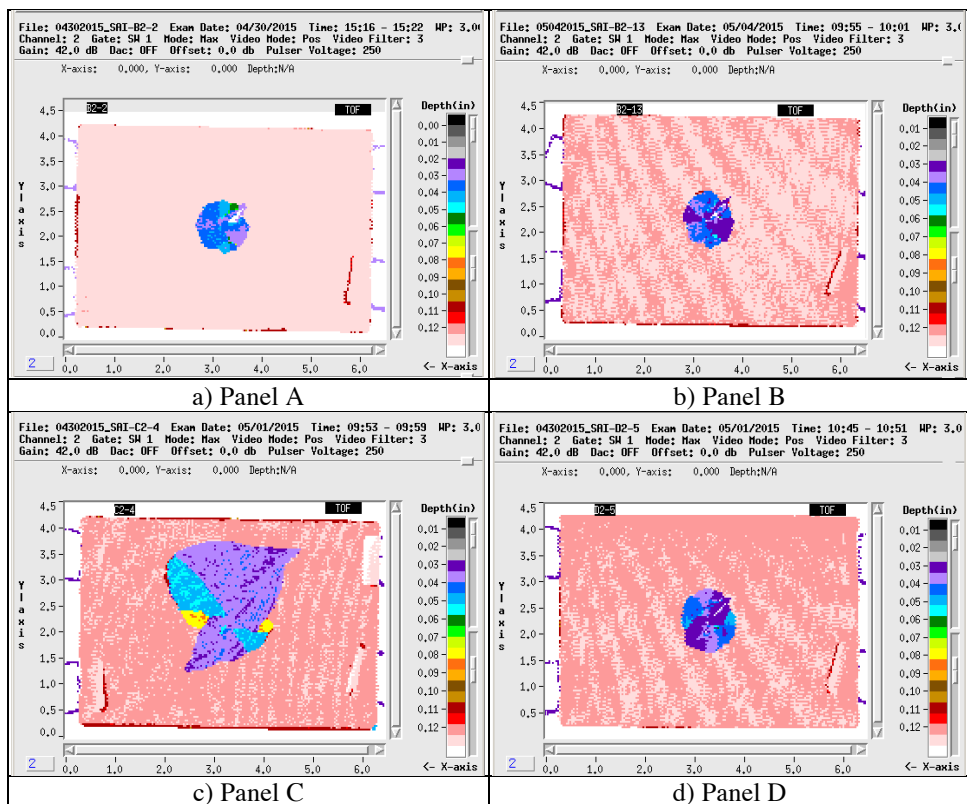


Figure 2.1.5.19 – C-Scan Time of Flight Data of Panels (5 MHz)

Table 2.1.5.3 – Area of Delaminated Region for each Panel

| Panel | Area mm² (in²) | Standard Deviation mm² (in²) |
|--------------|-------------------------------------------------|---------------------------------------------------------------|
| A | 704.87 (1.093) | 82.41 (0.127) |
| B | 571.43 (0.886) | 73.55 (0.114) |
| C | 2545.36 (3.945) | 363.38 (0.563) |
| D | 636.85 (0.987) | 87.88 (0.136) |

2.1.5.8 Nondestructive Evaluation – C-Scan (10 MHz)

Three specimens of each stacking sequence went through c-scan imaging with a 10 MHz probe to obtain a higher resolution image of the impacted region. The images were gated 2048 times to reconstructed 2D gated images into three dimensional computer aided design drawing of damage to pre-imposse into a discrete damage model, which is discussed in Chapter 4. The waveform data was gated to identify interfacial delamination within the composite. Figure 2.1.5.20 shows c-scan images of the interfacial delamination for Panel A. C-Scan were performed on both the impacted and back surfaces. The impacted c-scan images begin to lose information of the damage after interface 10 while the back c-scan images begin to lose information before the 21st ply. The industry usually uses a 5 MHz probe to detect delamination of a composite. Appendix F has a side-by-side comparison of the images obtained from the 10 MHz c-scan and X-Ray CT.

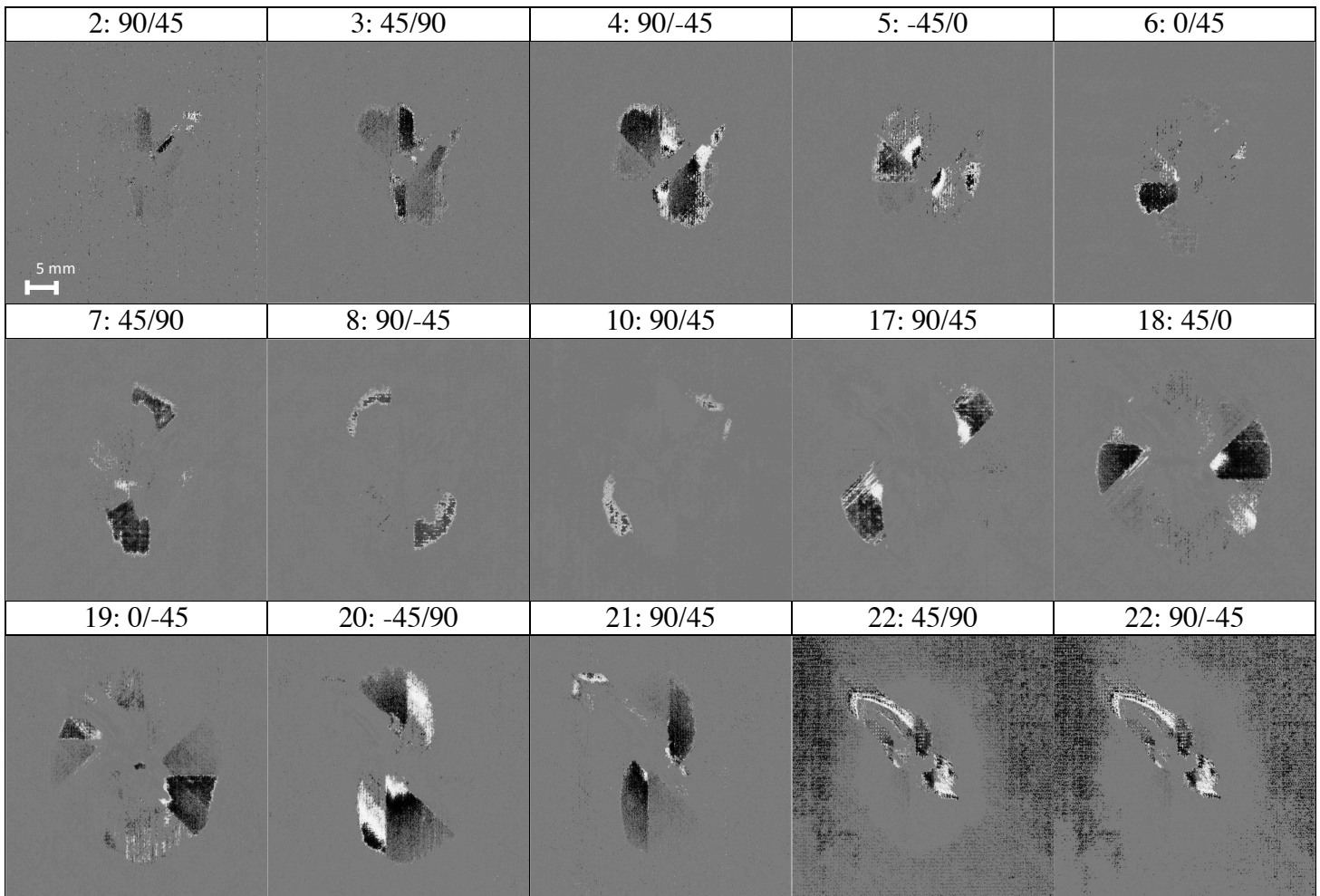


Figure 2.1.5.20 – C-Scan Images: Interfacial Damage for Panel A (10 MHz)

2.1.5.9 Nondestructive Evaluation – X-Ray CT

A total of four specimens, one from each stacking sequence went through X-Ray CT to visualize the amount of damage that occurred post impact. The purpose of performing X-Ray CT was to determine a layer-by-layer representation of delamination and cracks that was caused by impact. A frontal image of the X-Ray CT is shown in the Figures 2.1.5.20 at a specific interface through the thickness of the composite. The resolution of the X-Ray CT images is 0.05, 0.05, 0.1, and 0.05 mm for panels A, B, C, and D respectively. Since the amount of damage for panel C was significantly larger than the other composites, a larger resolution image was needed to capture the full field of damage. More information about the X-Ray CT images could be viewed in Appendix F.

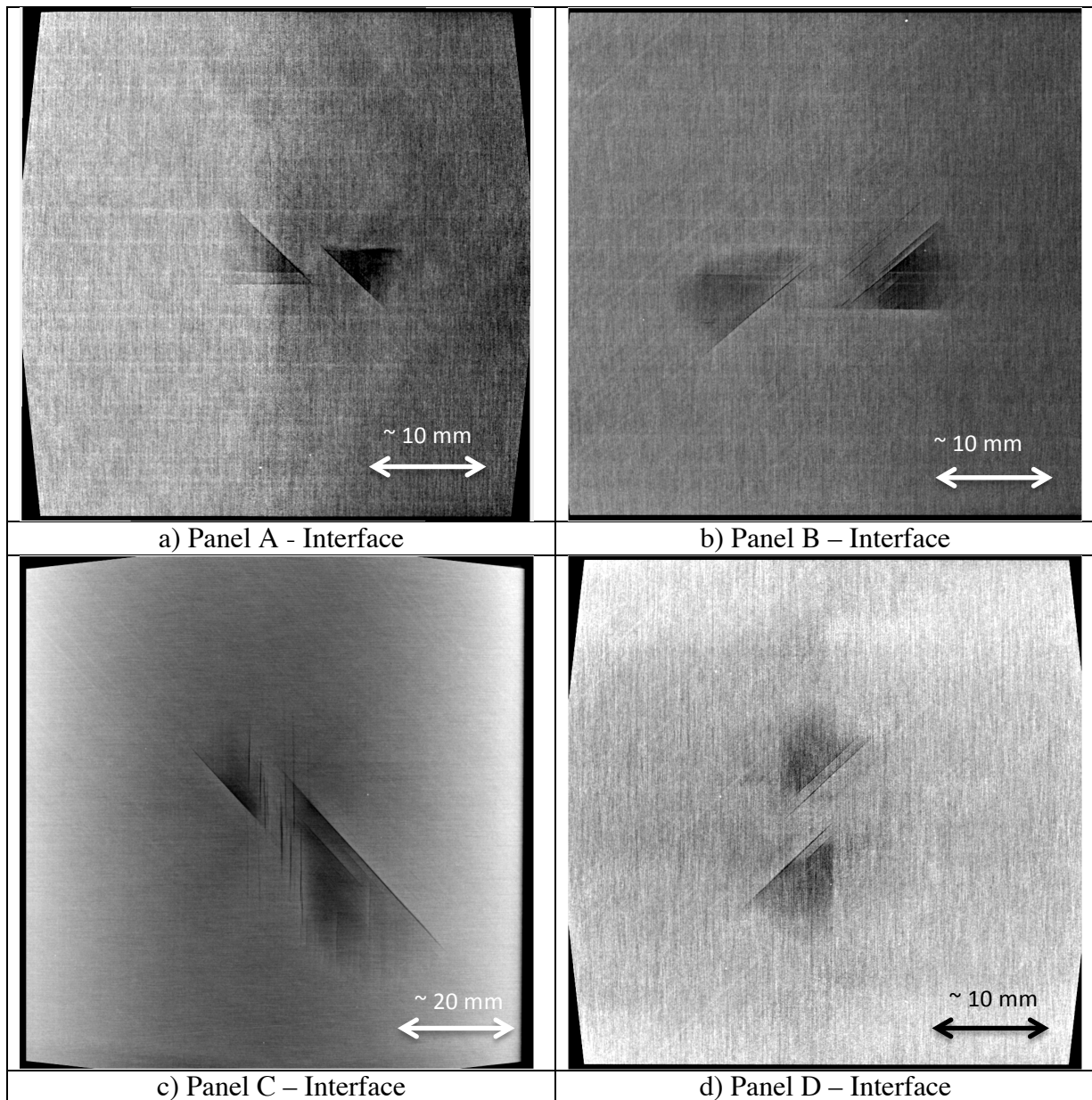


Figure 2.1.5.21 – X-Ray CT images of damage

2.1.5.10 Nondestructive Evaluation – X-Ray CT with Zinc Iodine

One specimen from panel A was cut into a smaller 30.8 mm x 30.8 mm (1.5 in x 1.5”) piece using a diamond saw. Using a diamond core drill, a ¼” diameter hole was cut out of the center of a specimen. Dye penetrant, zinc iodine, was put into the hole with a cotton swab and put into a vacuum to allow the penetrant to wick into the damaged regions of the specimen. Table 2.1.5.4 lists the chemicals used in making the penetrant. The purpose of performing these techniques is to visualize the amount of damage that occurred in the specimen with higher resolution. Software used threshold techniques to

extract the damage region of the composite. Figure 2.1.5.22 shows the damaged region of the composite. This gives us a 3D representation of the damage that occurs which could possibly be used for modeling. This process is important as it extracts the amount of cracks that are present in the specimen giving detailed information on the location, length, and size of the crack.

Table 2.1.5.4 – Zinc Iodide Radio-Opaque Dye Recipe

| | |
|--------------------------------|----------|
| Zinc Iodide (Powder) | 60 grams |
| Distilled Water | 10 mL |
| Isopropyl Alcohol | 10 mL |
| Kodak 'Photo-flo 600' Solution | 1 mL |

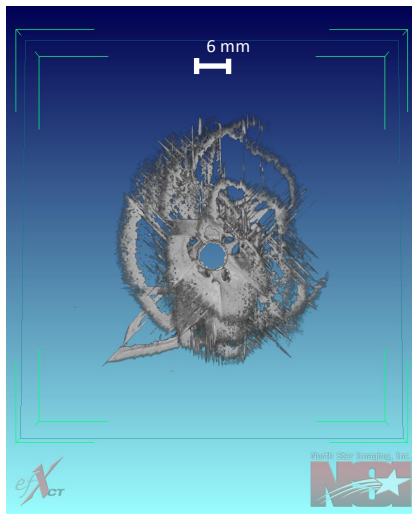


Figure 2.1.5.22 – X-Ray with penetrant for Panel A

2.1.6 Conclusions for Impact of Thin Plate Unidirectional Composites

Using high-speed photography and 3-D digital image correlation, the displacements and strains were captured. Digital image correlation provided more in depth knowledge of what occurs in the impact of composites. DIC out-of-plane displacements correlated well between the drop weight tower and profilometry. DIC was able to capture the out-of-plane displacements and the final permanent deformation seen in profilometry. The damage threshold load and the damage threshold strain occurred at approximately the same time. Although the drop weight tower can calculate the deflection from the force transducer, it does not have the capability to measure the indent or permanent deformation of the

specimen post impact. DIC was able to capture final out-of-plane displacement of the back surface and correlated well with the height data obtained from profilometry data. The next step is to determine the residual stresses that may occur within the composite to accurately model its strength after impact. DIC captures the final strain state, which could be used in conjunction with modeling.

2.1.7 Future Work for Impact of Thin Plates

Compression after impact experiments is conducted to measure the residual strength of the composite panels. A computational framework is being established to optimize modeling efforts in predicting the failure of composite after impact. The profilometry data from this study would be used to create a discretized model of the permanent deformation of the impact. The NDE would be used to map the delamination and discrete matrix cracks from the impact event. The residual strains would be used in the impact regions to accurately represent the weaken region of the composite. The load hysteresis, major principle strain, and displacement contours could be used to map crack initiation and growth to determine the underlying fracture mechanics of the system. The overall objective is to create a realistic model with realistic damage to predict a composite's failure strength after impact.

The damage threshold strain could provide more information about the impact resistance of unidirectional carbon fiber composites. Nondestructive techniques could be used to quantify the reduction of modulus of the impacted region for a threshold strain. Currently airframe structures are designed using a no growth criteria for delamination and transverse matrix cracks. New criteria would need to be developed to understand the threshold strain for a composite under impact and how it influences the composite under residual loading. With supplemental information on the damage (delamination, cracks), analytical models could be constructed in determining critical damage for damage tolerance design.

2.2 Impact Experiments of Thick Unidirectional Composite Plates

In accordance to the Lockheed Martin Aero Composite Durability and Damage Tolerance Test Methodology [36], six 13 in x 11 in x 0.177 in (330.2 mm x 279.4 mm x 4.5 mm) panels were impacted with a 1 in (25.4 mm) hemispherical tupper to induce barely visible damage (BVID). Initial ultrasonic data was captured using an Olympus Omniscan MX phased array hand-held probe to obtain time of flight damage of the composite structure [37]. Approximate damages lengths and depths were recorded. Preliminary compression tests performed at Intec found the residual strength after impact failure load was 48 kips with a standard deviation of 5.8 kips. The maximum failure load was recorded to be 57.4 kips. The first objective of this study is to perform nondestructive evaluation on the six impacted specimens. The second objective of this study is to perform digital image correlation of compression after impact tests for three of the impacted specimens, which is discussed in a Chapter 5.

The collaborative effort between Lockheed Martin and Air Force Research Laboratory are part of the Composite Performance RT Damage Tolerance Assessment Methodologies Project. The objective of the project is to:

1. Develop high fidelity matrix and fiber damage simulation methodologies for use in laminated polymer matrix composites.
2. Unify cohesive zone modeling methods for both static and fatigue damage evolution and integrate into in-house stress and analysis tools for demonstration.
3. Insert nonlinear analysis capability into in-house codes to address critical compression loading induced damage evolution.
4. Assess high fidelity toolsets against real world problems, such as compression strength after impact and certification by analysis.

The section outlines the nondestructive techniques used to obtain high-fidelity images of the damage of the impacted composites. Subsequent chapters demonstrate how nondestructive techniques were used to accurately predict the compression strength after impact. It is important to note that AFRL received six damaged specimens with no experimental data of the impact event.

2.2.2 Material Specifications – Lockheed Martin

Carbon fiber reinforced polymers of IM7/M65 were produced and manufactured by Lockheed Martin Company. Each of the panels had the dimensions of 13 in x 11 in (330.2 mm x 304.8 mm) with a nominal cured thickness of 0.177 in (4.5 mm).

2.2.2.1 Impact Methodology – Lockheed Martin

Six 13 in x 11 in composite panels were subjected to an impact test using a 1 in hemispherical tupper by Lockheed Martin in accordance to the Composite Durability and Damage Tolerance Test Methodology. Lockheed Martin Aero Team and internal test methods per specifications 5PTPTT01-B have been used on several legacy programs. Similar test methods were also derived through NASA-RP-1142 12Lx10W test procedures.

The support fixture shown in Figure 2.2.2.1 displays the boundary conditions of the experiment. The specimens were clamped into the impact fixture using a 20 ft-lb (27.116 Nm) torque. The support fixture is capable of holding larger specimens. A drop weight tower with specifications outlined in ASTM 7136 was used for impact. Each of the specimens was impacted 55 ft-lb (~75 J) of energy.

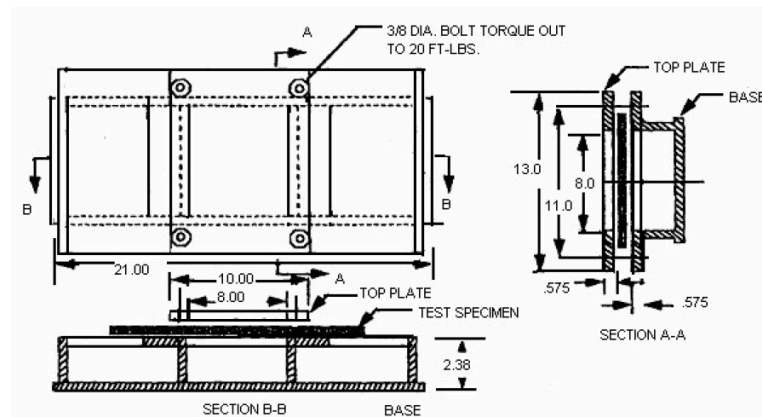


Figure 2.2.2.1 – Lockheed Martin Impact Fixture

2.2.3 Nondestructive Evaluation – Lockheed Martin

Each of the specimens was evaluated using several nondestructive techniques. However, in order to obtain high-fidelity images of the damage from the impact, some of the specimens needed to be cut smaller. Only three specimen went through a serious of nondestructive techniques to obtain high

resolution images of the damage while the other three were subjected to compression testing to determine the residual compression strength after impact. Table 2.2.3.1 is the nondestructive evaluation test matrix that was been performed on the composite specimens provided by Lockheed Martin for the damage tolerance assessment initiative. Infrared flash thermography (IFT), immersion ultrasounds (UT), and X-Ray CT techniques (X-Ray, X-Ray w/ ZnI) were performed on each of the specimens as outlined in Table 2.2.3.1. Three of the specimens were put through compression tests to obtain the residual strength after impact of the specimen (RSAI).

Table 2.2.3.1 – Nondestructive Evaluation Test Matrix

| Specimen | IFT | UT | Post Cut UT | ZnI | X-Ray | RSAI |
|-------------|-----|----|----------------|-----|-------|------|
| Specimen-1 | X | X | X | X | X | |
| Specimen -2 | X | X | X | X | X | |
| Specimen -3 | X | X | X | X | X | |
| Specimen -4 | X | X | | | | X |
| Specimen -5 | X | X | | | | X |
| Specimen -6 | X | X | | | | X |

2.2.3.1 Nondestructive Evaluation – Infrared Flash Thermography

Each of the specimens went through infrared flash thermography (IFT). The camera settings had a capture frequency of 60 Hz with a camera frequency of 200 Hz. The acquisition length was 900 frames within a 15 second time window. The flash timing occurred every 10 frames with an offset of 4.2 frames for duration of 4.9 seconds. Flash Thermography was used to identify the location of the damaged region prior to performing immersion ultrasound. Images for flash thermography for the impacted side and backside could be found in Appendix B and Appendix C. Figure 2.2.3.1 shows the IFT images for specimen 1. A sticker was placed on each panel 4 inches in length and width from the corner edge to determine the location of the impact region. IFT is a nondestructive used to obtain information of delamination and transverse matrix cracks. Although the panel is large, transverse matrix could be seen in many of the images.

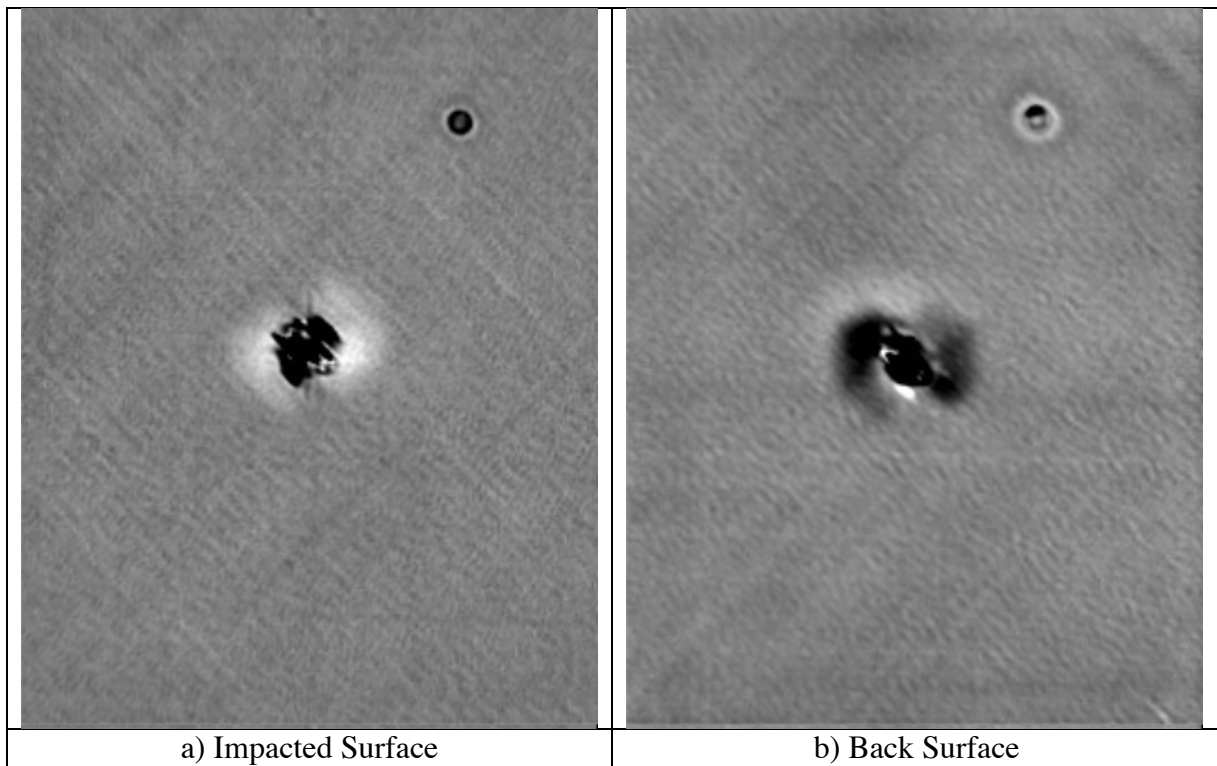


Figure 2.2.3.1 –Infrared Flash Thermography (specimen-1)

2.2.3.2 Nondestructive Evaluation – Immersion Ultrasound

Immersion ultrasound, with a 5 MHz probe, was performed on the back surface for each of the panels. A marker sticker was placed in the same region as the flash thermography images to visually identify the location of the impacted region. Pulse echo was performed to get a generalized area of the damage of the composite. Time of flight was also recorded to visualize the depth of damage. The images could be viewed in Appendix D and Appendix E.

After thermography and immersion ultrasound was performed, specimens 1, 2, and 3 were cut into smaller pieces using a diamond saw. The specimens were cut into rectangle plates such that there was a 1-inch clearance between the cut and delamination found from the immersion ultrasounds. After the specimens were cut, immersion ultrasound was performed again to get a visualization of the damage region with more accuracy. Figure 2.2.3.2 shows the amplitude waveform of the ultrasound for specimen 1, 2, and 3. The time of flight damage for specimen 1-3 could be seen in Figure 2.2.3-5.

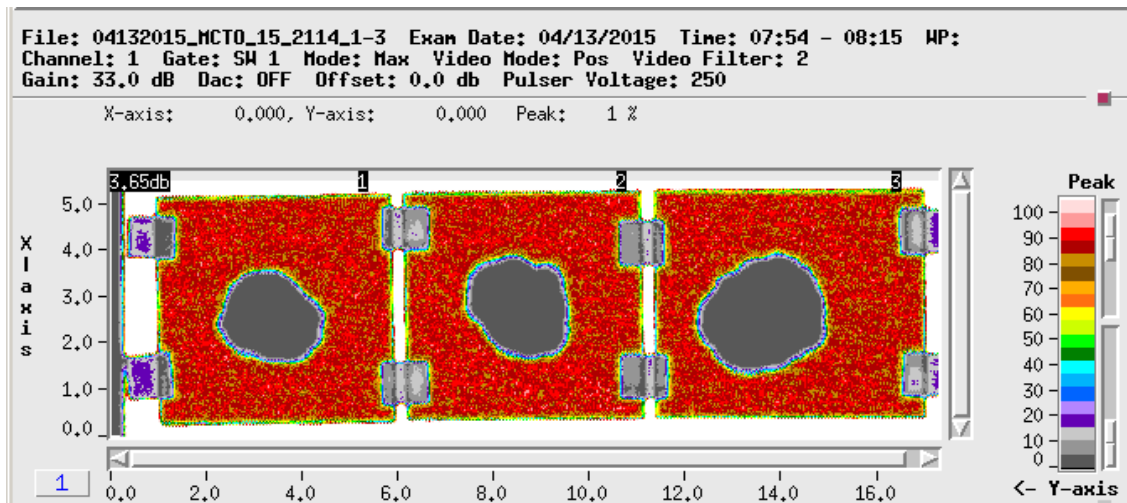


Figure 2.2.3.2 – Ultrasonic images of impacted specimen 1, 2, and 3

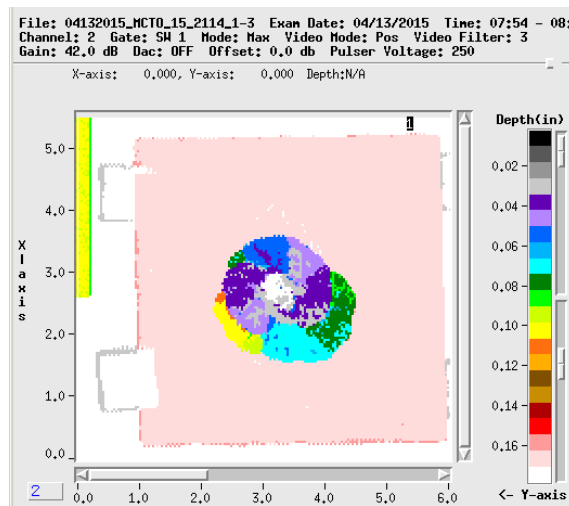


Figure 2.2.3.3 – Immersion Ultrasonic Time of Flight image of specimen-1

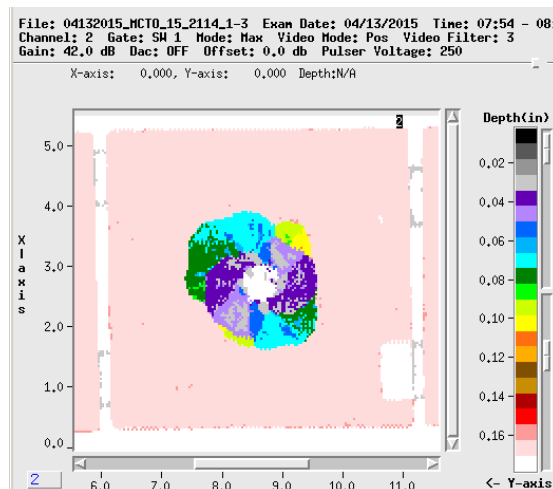


Figure 2.2.3.4 – Immersion Ultrasonic Time of Flight image of specimen-2

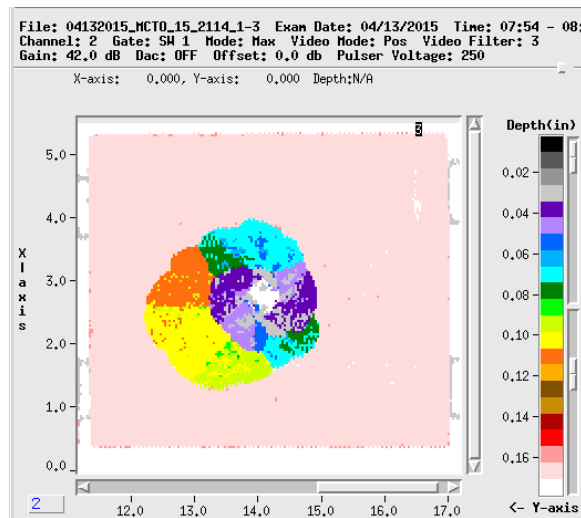


Figure 2.2.3.5 – Immersion Ultrasonic Time of Flight image of specimen-3

2.2.3.3 Nondestructive Evaluation – X-Ray CT

The specimens were cut again where the cut was about ¼” away from the damage region. The purpose of cutting the specimens smaller is to obtain a high-resolution image of the damage from X-Ray Computed Tomography scanning techniques. The specimens went through X-Ray CT scanning to obtain volumetric data about the amount of damage present in the composite. From the X-Ray CT, delamination, transverse matrix cracks, and fiber breakages were observed in each of the specimens. Images of the X-Rays can be seen in Figure 2.2.3.6-8 where the front, side, and top images of the specimen showing different damage modes within the composite. In each of the X-ray figures, the top and side angles of the images are located near the center of the impacted region. The front represents the image nearest the center of the composite through the thickness or midplane of the composite. Other damage was observed around the impact crater such as delamination and transverse matrix cracks. Crushing of the first plies of the impacted surfaced was observed however more cracks and delamination were present in subsequent plies. For specimens 1, 2, and 3, particulates were also observed which could have come from manufacturing process and are represented in Figure 2.2.3.6 and Figure 2.2.3.7 as bright white spots in the image.

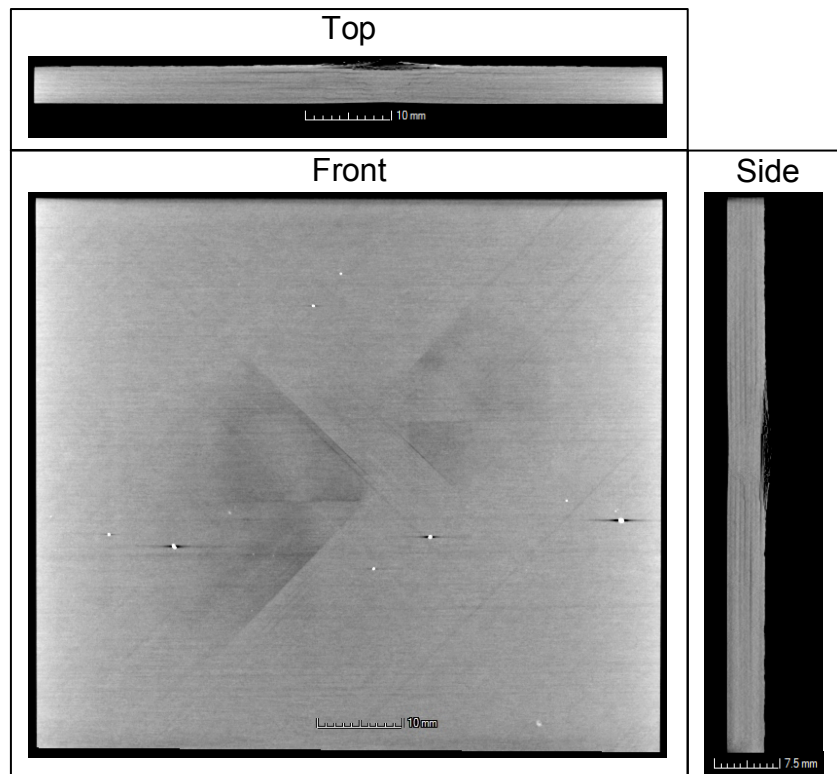


Figure 2.2.3.6 – X-Ray Images of specimen-1

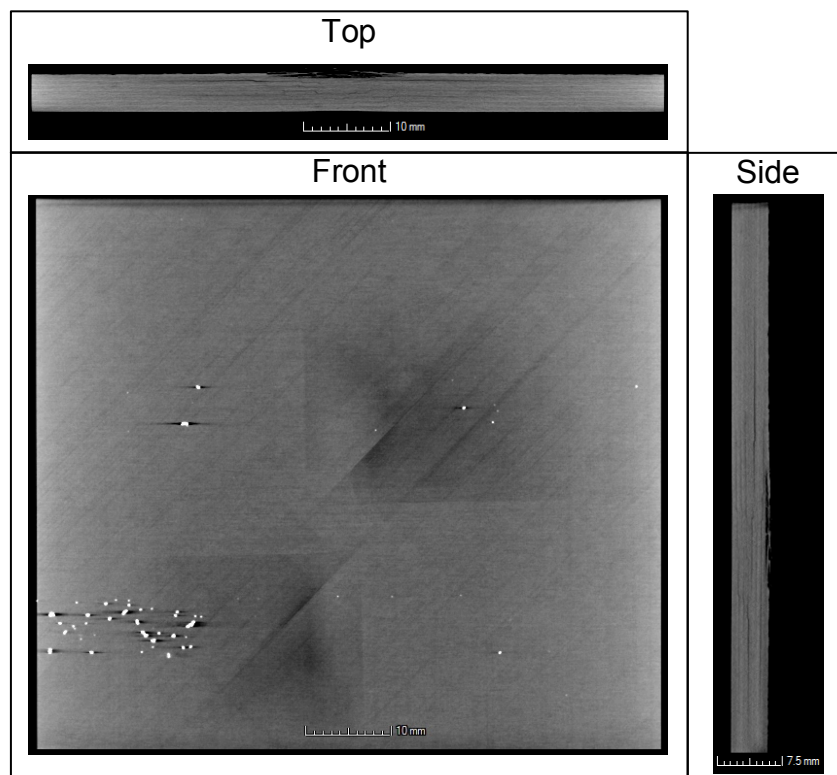


Figure 2.2.3.7 – X-Ray Images of specimen-2

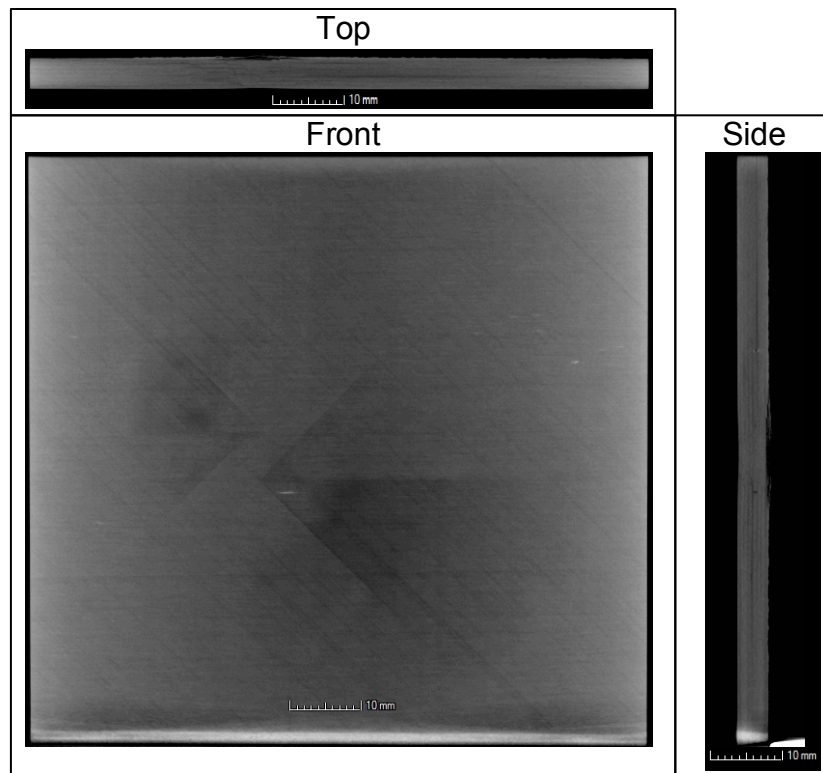


Figure 2.2.3.8 – X-Ray Images of specimen-3

2.2.3.4 Nondestructive Evaluation – X-Ray CT with Zinc Iodine Penetrant

Each of the specimens had a small indentation of barely visible damage. Fiber breakage could be seen with the naked eye on the backside of the composite. From the X-Ray scans mentioned in the previous section, it was determined that there was enough damage through the composite to inject a zinc-iodide solution into the back surface. A pool was created around the impact region where the zinc-iodide solution could be placed as shown in Figure 2.2.3.9. The recipe for the zinc iodide solution is shown in Table 2.2.3.2. Then the specimen was put into a rubber mount and placed into a Ladd Vacuum Evaporator shown in Figure 2.2.310.

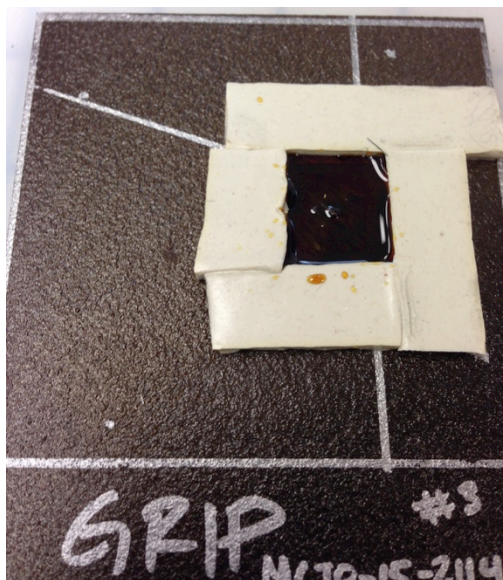


Figure 2.2.3.9 – Zinc Iodide Pool



Figure 2.2.3.10 – Ladd Vacuum Evaporator

Table 2.2.3.2 – Zinc Iodide Radio-Opaque Dye Recipe

| | |
|--------------------------------|----------|
| Zinc Iodide (Powder) | 60 grams |
| Distilled Water | 10 mL |
| Isopropyl Alcohol | 10 mL |
| Kodak 'Photo-flo 600' Solution | 1 mL |

The specimens were put into a vacuum and through observation air bubbles within the composite begin to surface indicating that the penetrant was seeping into the damage zone. In the middle of the vacuum process, the system was bled to keep the liquid from boiling. After being approximately 2-5 minutes in a vacuum, the process was halted, and the liquid was allowed to rest for approximately 2 minutes inside the chamber. In some cases the procedure had to be halted since the liquid would boil instead of penetrating through the composite. The samples were taken out of the vacuum, additional penetrant was poured into the pool with a pipette, rested for approximately 15 minutes, and then replaced into the Ladd Vacuum Evaporator. This procedure was done a total of three times to ensure enough penetrant entered the damaged region of the composite.

The specimens were put into a THELCO laboratory oven at 50°C to dry the composite for 24 hours. Since the time to perform X-Ray CT scan could take up 4 hours, the basic rule of thumb is to dry the penetrant before performing X-Ray CT scanning to reduce any artifacts arising as a result of the liquid moving. The zinc iodide solution appeared brighter in the X-Ray CT images showing the level of damage in the composite that resulted from impact. X-Ray CT images of the damage could be seen in Figures 2.2.3.11-19. The sequence of side and top images show where the damage begins to occur and spans toward the center of the impact region. The sequence of front images begins from the impacted surface and goes towards the back surface. The location, size, and orientation of transverse matrix cracks were observed more dominantly in the front images of the X-Ray CT images. A small circular undamaged region where the impactor struck the composite is seen in the front, side, and top images. Although damage may exist in this region, the X-Ray images indicate no delamination and transverse matrix cracks occur at the surface of the impact to the last few plies where fiber breakages begin to appear. Observing the side and top images, the maximum area of delamination appears to occur around the midplane of the composite. As the images approach the center of the impact, the damage appears to be conical which is represented in most impacts.

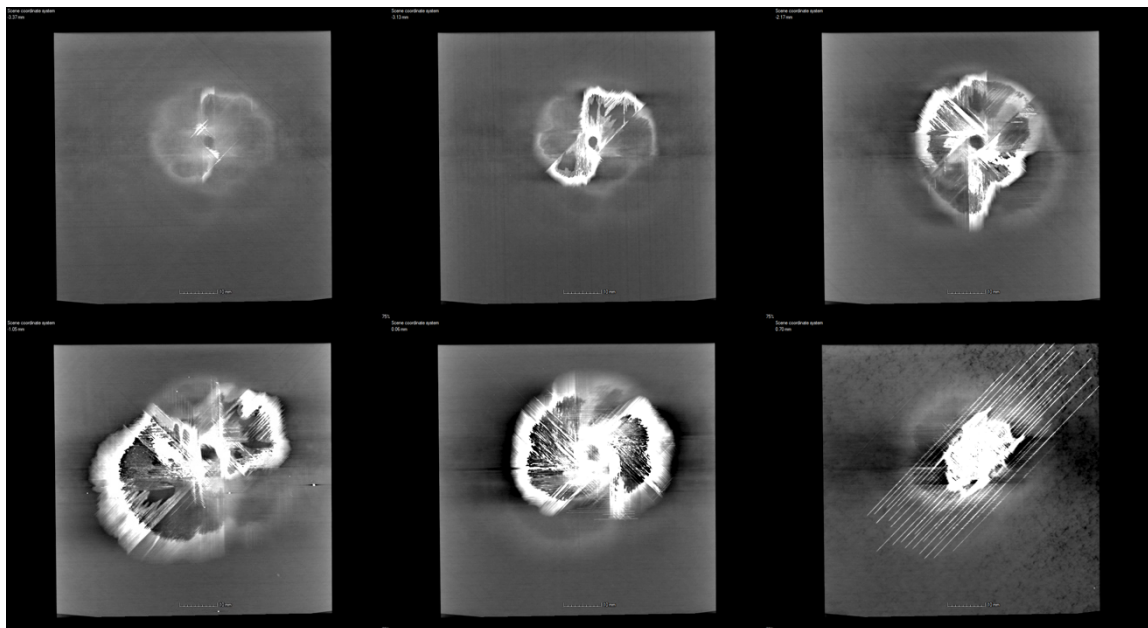


Figure 2.2.3.11 – X-Ray front images with zinc iodide penetrant for Specimen-1

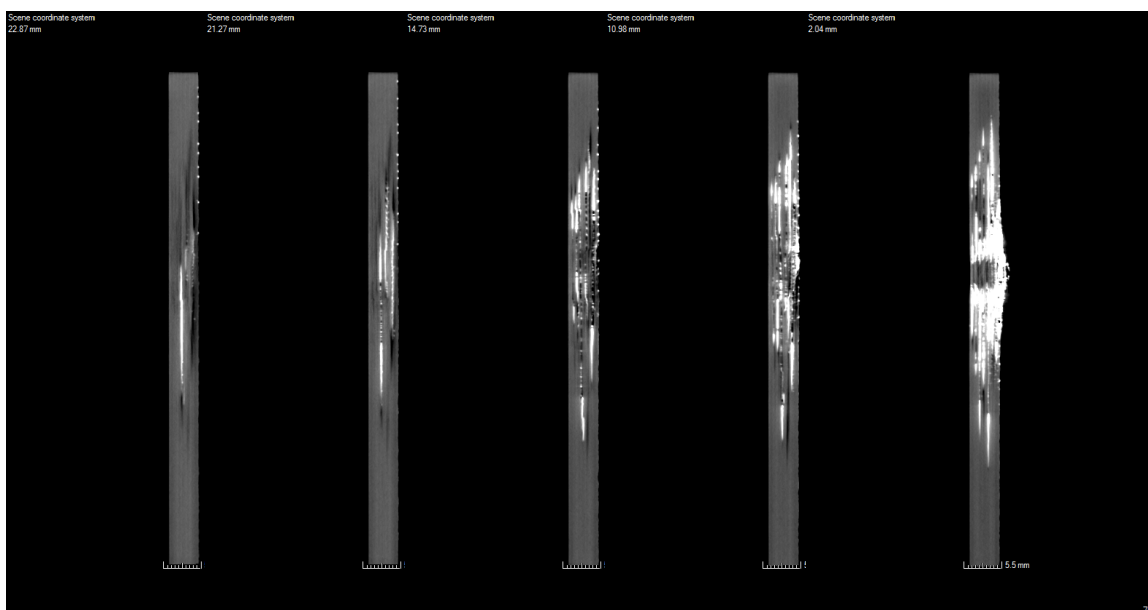


Figure 2.2.3.12 – X-Ray side images with zinc iodide penetrant for Specimen-1

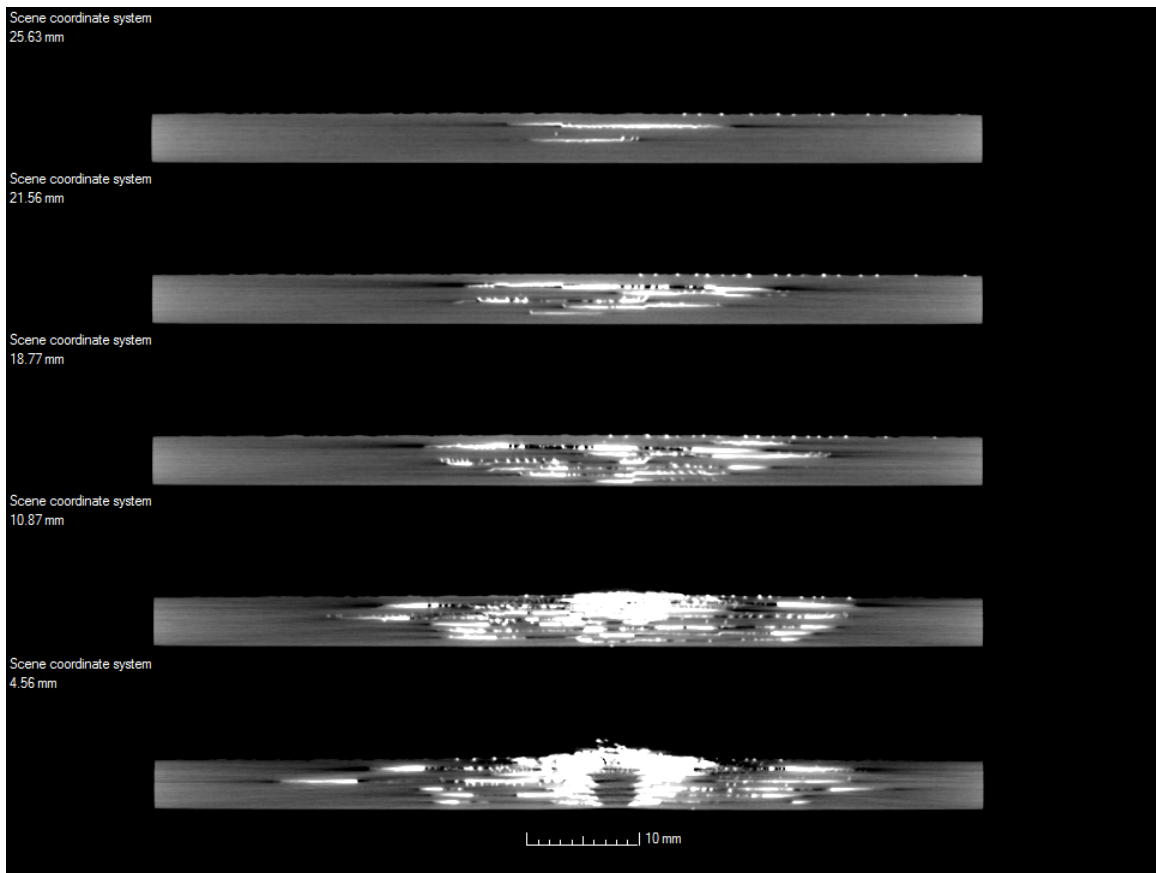


Figure 2.2.3.13 – X-Ray top images with zinc iodide penetrant for Specimen-1

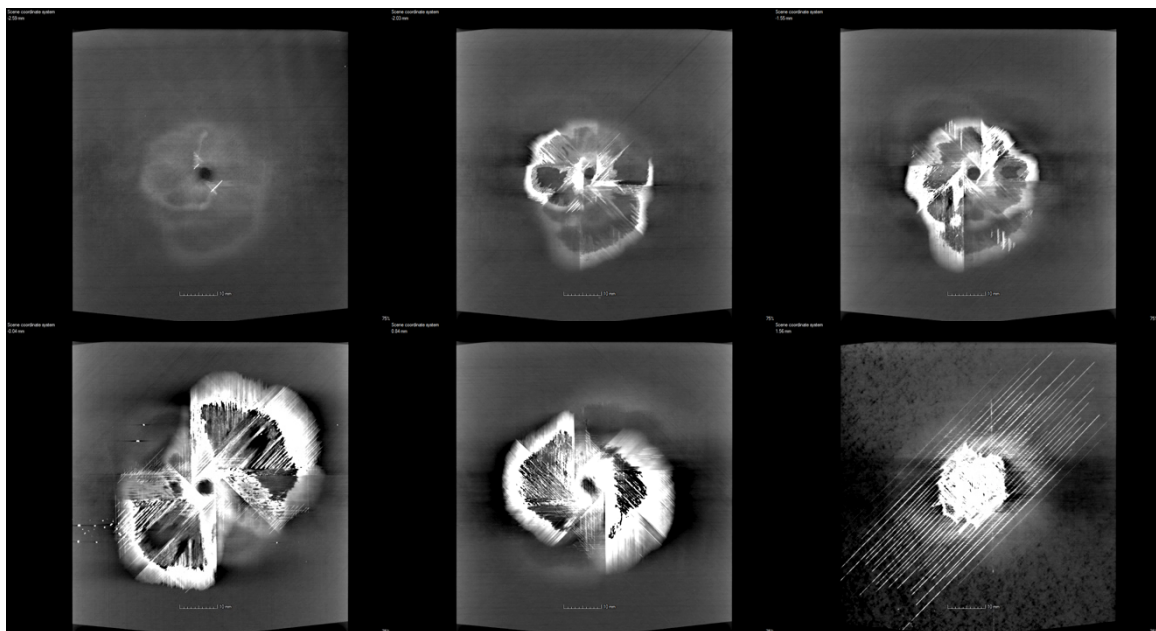


Figure 2.2.3.14 – X-Ray front images with zinc iodide penetrant for Specimen-2

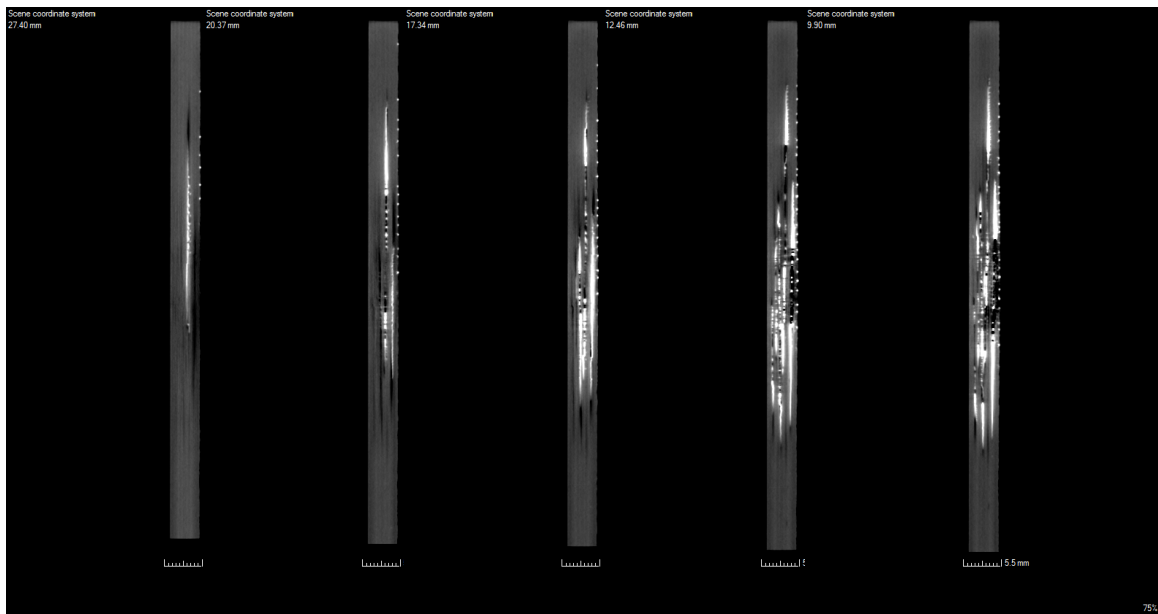


Figure 2.2.3.15 – X-Ray side images with zinc iodide penetrant for Specimen-2

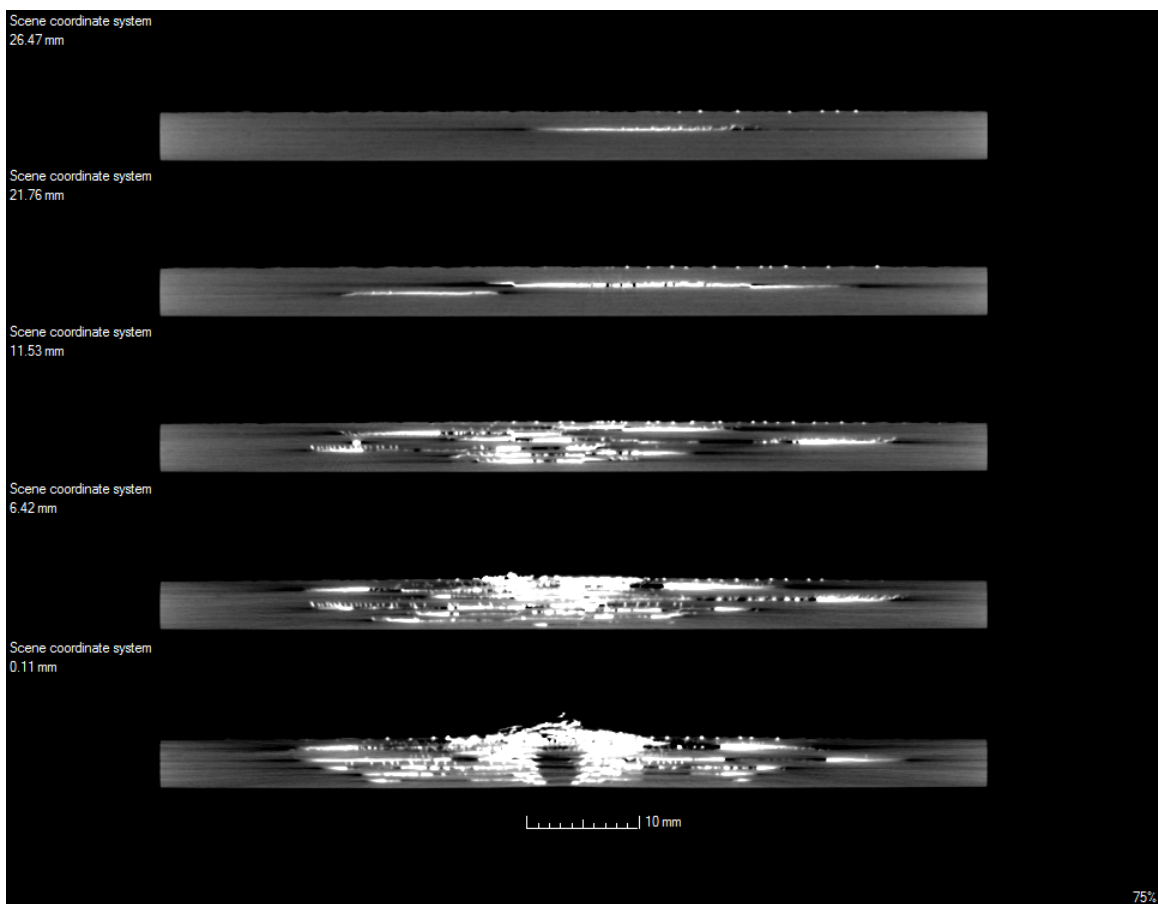


Figure 2.2.3.16 – X-Ray top images with zinc iodide penetrant for Specimen-2

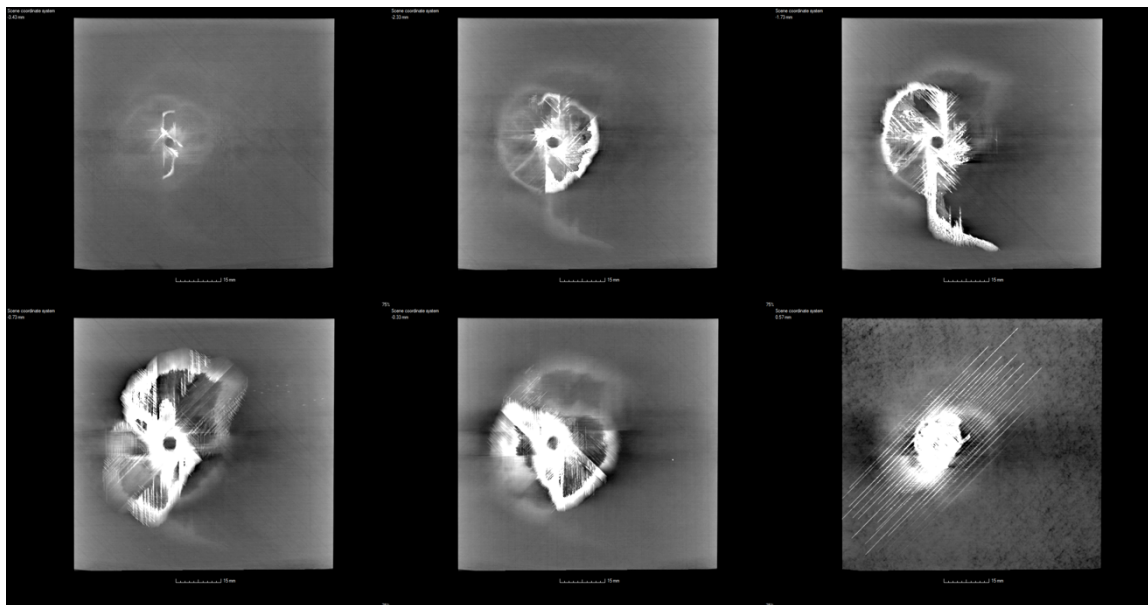


Figure 2.2.3.17 – X-Ray front images with zinc iodide penetrant for Specimen-3

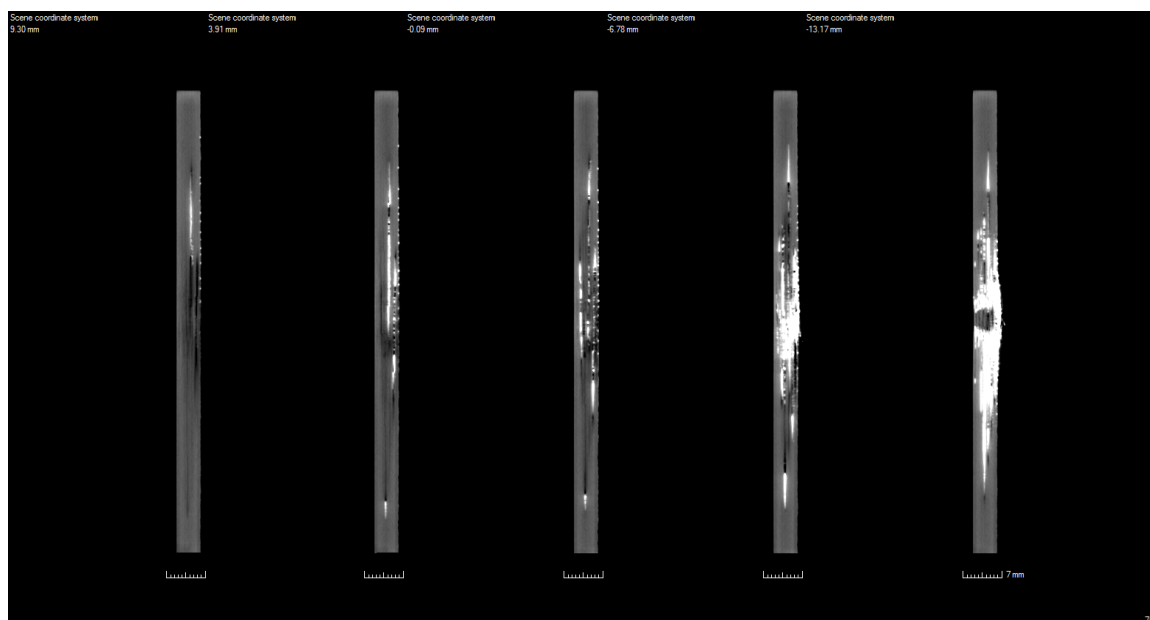


Figure 2.2.3.18 – X-Ray side images with zinc iodide penetrant for Specimen-3

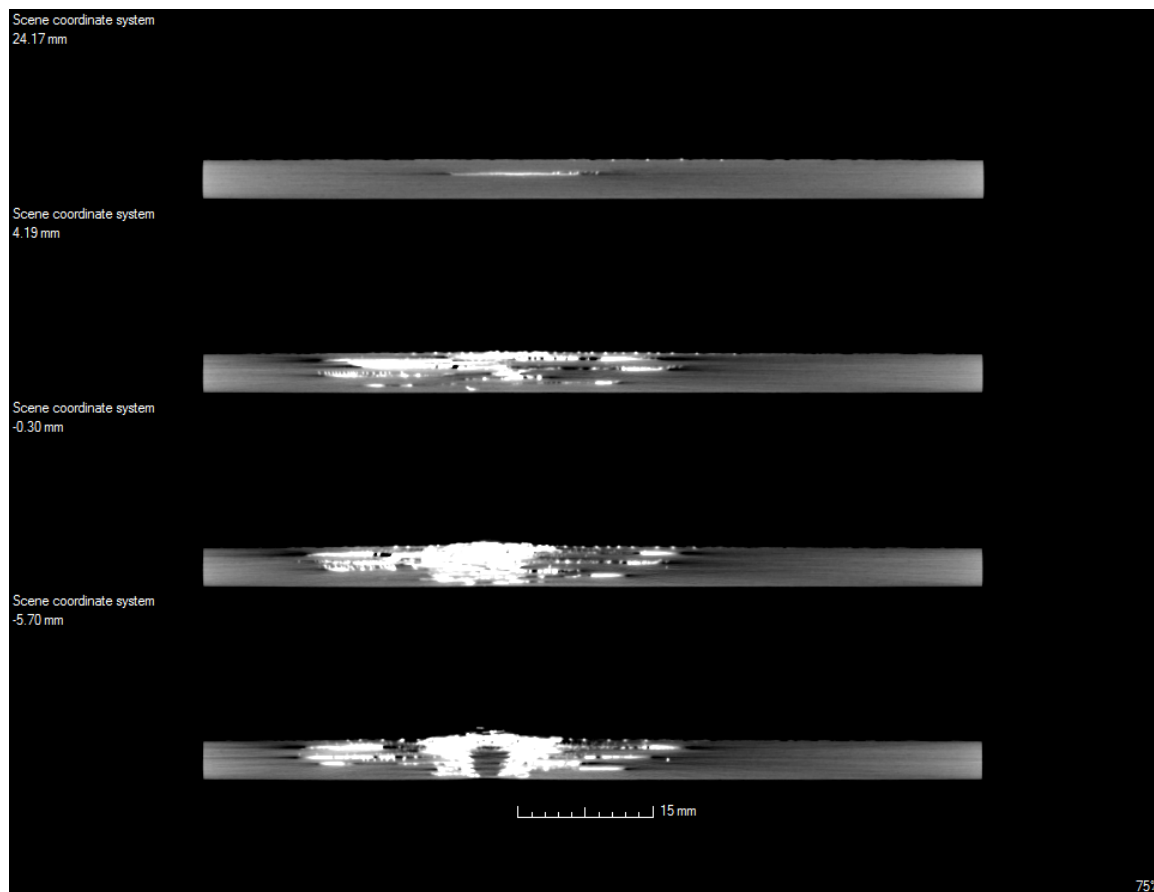


Figure 2.2.3.19 – X-Ray top images with zinc iodide penetrant for Specimen-3

Zinc iodide was used as a contrast agent in the polymer matrix composite specimen. Though better visualization of damages (crack and/or delamination) in CT images, the presence of contrast agent can cause incorrect CT numbers in the reconstructed image [38,39]. Beam hardening artifacts, streaks and dark bands adjacent to areas of high-density contrast agent, were observed in the images as shown in Figure 2.2.3.13-19.

The procedure for penetrating the composite with zinc iodide solution may need some modification to ensure each gap is filled in the composite. The complexity of the damage may have prevented certain areas to be filled such as delamination due to insufficient ZnI and/or inadequate capillary effects from the vacuum. Another possibility is that the procedure on penetrating the composite with a zinc iodide solution needed to be done for a longer period of time. The process of allowing it to settle and re-implementing may need to be done more often. Even though gaps can still be seen in the

X-Ray images, the application still proved to be a viable procedure in visualizing the extent of damage of the composite structure.

2.2.3.5 Nondestructive Evaluation – Optical Profilometry

Profilometry was performed using a Nanovea Optical Profilometer to obtain the permanent deformation of the depth of the impact crater for specimen-1-3. Nanovea uses a white light emitting diode, confocal chromatic image techniques, and spectral filtering to obtain profiles with an accuracy of 20 micrometers. The back surface did not undergo profilometry due the amount of damage that was present. Fiber breakage on the back surface would not allow the reflection of the LED to be captured by the spectral analyzer to obtain a sufficient and adequate profile. Figure 2.2.3.20-21 represents the vertical and horizontal profiles found in the specimens. The maximum depth of the composite was 0.15 +0.0102mm.

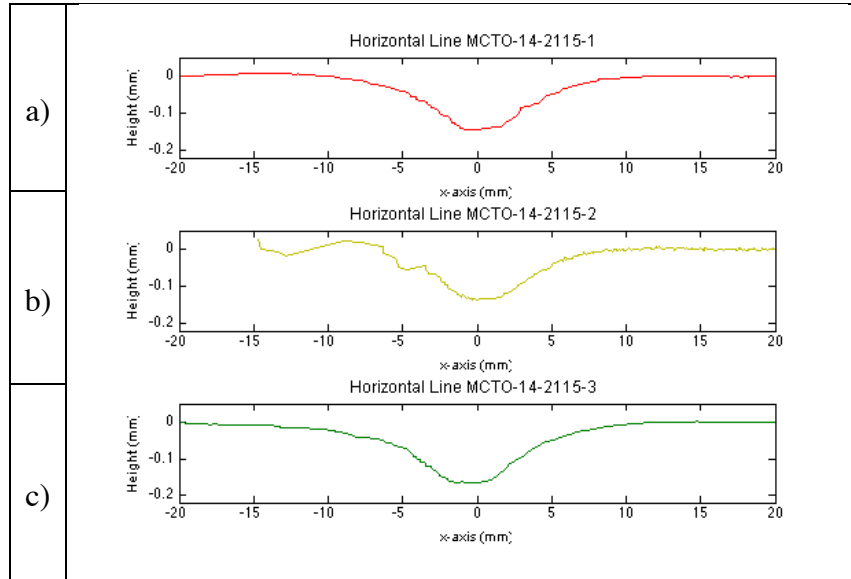


Figure 2.2.3.20 – Horizontal profiles of a) specimen-1 b) specimen-2 c) specimen-3

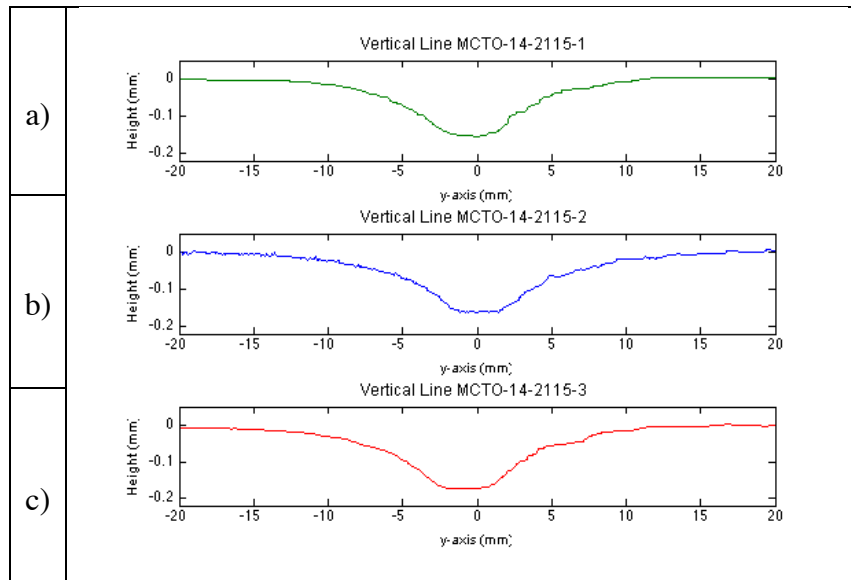


Figure 2.2.3.21 – Vertical profiles of a) specimen-1 b) specimen-2 c) specimen-3

2.2.3.6 Nondestructive Evaluation – Segmentation

Image segmentation techniques are essential when extracted damage from nondestructive evaluation. Segmentation is discussed in more detail in the modeling section in how the images were used to extract delamination patterns, crack locations, and permanent deformation for the use of high-fidelity 3D discrete damage models.

2.2.4 Conclusions for Impact of Thick Plates

Lockheed Martin impacted six composite specimens. Each of the specimens went through a series of nondestructive techniques to characterize the amount of the damage the composite. Chapter 4 proposes methods to use nondestructive evaluation to modeling and predicting the compression strength after impact behavior. Chapter 5 discusses the results of compression strength after impact experiments and models.

2.3 Discussion

The purpose of this section is to discuss the differences between thin and thick plates. For the AFRL samples, the specimens were thinner, had smaller dimensions (6"x4"), and impacted with a ½" hemispherical tupper. The Lockheed Martin specimens were thicker, had larger dimensions (11"x13"), and impacted with a 1" hemispherical tupper. Each showed different levels of damage to various degrees. The thinner specimens had delamination, transverse matrix cracks, and permanent deformation. The thicker specimens had the same damage with the addition of fiber breakage. It is important to note that experimental recorded data of the impact events was obtained for the thin plates. However, if recorded data was gathered for the impact events for the thick plates, the data was not shared. In many real problem scenarios, maintenance engineers do not have the luxury of knowing information from the impact event. Chapter 4 and 5 goes into detail to the modeling capabilities and discuss limitations in modeling the problem.

Chapter 3: A Theoretical Framework for Modeling Nondestructive Evaluation to Predict the Behavior of Compression Strength After Impact of Unidirectional Composites

In chapter 2, nondestructive techniques were discussed to characterize the amount of damage that occurred after an impact event. Chapter 3 presents a theoretical framework for discrete damage modeling and how nondestructive evaluation could be used to artificially pre-impose damage into a 3D high-fidelity model to predict the behavior of compression after impact for unidirectional carbon fiber composites.

3.1 Introduction

Using nondestructive evaluation (NDE) has been an incredibly useful tool in understanding the behavior of materials from the medical industry to the aerospace industry. It provides engineers with tools for designing and optimizing structural applications. The use of nondestructive evaluation with integrated finite element modeling has reduced the time for several materials to reach the market. Nondestructive evaluation with integrated discrete damage modeling could provide an overall understanding of the behavior of composites at the microscale, mesoscale, and component level.

Chawla was able to recreate a 3D microstructure that accurately represented the orientation, aspect ratio, and distribution of SiC particles in reinforced aluminum composites. Through finite element modeling of the 3D microstructure, local regions within the microstructure were used to accurately predict the Young's modulus of the composite. The 3D microstructure models were most accurate in predicting the uniaxial deformation of the composite [40,41]. Coleri developed FE models using x-ray computed tomography images of asphalt concrete samples to study the heterogeneous viscoelastic properties of full-scale accelerated pavement test sections and found that the displacements are similar to the in-situ rutting performance rankings Heavy Vehicle Simulator [42]. Dudek simulated solder joints from high resolution x-ray tomography to capture the effects of pore size, distribution, shape, and location on localized stresses and strains in the joint [43]. Hoyt integrated micro-computed tomography, FEA, and experiments to understand the monotonic and fatigue behavior of any novel microstructure [44]. Stienen developed a methodology of coupling 3D imaging, nano-indentation and

FEA to calculate more realistic stress fields around inclusions embedded in a steel matrix submitted to mechanics loadings typical of service conditions [45]. Groeber developed an FE framework to study the effects of grain size of alloys or poly-crystals [46-52]. Nondestructive evaluation has been used for material characterization for many material systems [53-56].

Nondestructive evaluation and finite element analysis have been used to understand how defects affect the mechanical properties of materials. Defects such as pores could have a significant influence on how damage grows ranging from a nanoscale to mesoscale part of a structure. Mikkola created a 2D FE-based mesoscale approach to model grain size, defect size, mechanical properties of individual grains and mechanical properties of the bulk material of high strength steel. The study found that micro-crack initiation near a defect was highly dependent on the orientation of the adjacent grains so that only a small fraction of defects of given size would be expected to result in fatigue cracking [57]. Independent of grain orientation, the defect creates a zone of high local stress and strains which controls the position of crack initiation. Shigang investigated the manufacturing defects of C/C composites using a micro-resolution computed tomography. From the numerical simulation results, manufacturing defects such as voids have great effects on the mechanical performance of the C/C composite [58].

For component level testing, Kline proposed a method of integrating NDE-derived engineering properties with finite element analysis for structural composite materials using ultrasonic and x-ray techniques. The method relied upon a point-by-point analysis of x-ray intensity levels from digitized radiographs. Then local moduli were then used as inputs into a finite element code to predict the specimen's responses to several different loading conditions [59]. Many ultrasonic studies have used inversed methods to extract mechanical problems, which could also be incorporated into a model to ensure an accurate behavior of the material under loading [60-61].

Panettieri created a 3D model incorporating the morphology and theoretical delamination patterns obtained from previous impact simulations and NDE techniques [62-63]. Using a cohesive zone methodology to model initialized damage with the intent of characterizing the behavior of delamination. Panettiera also provides a simulation-based initialization technique, which has the potential of gathering information of damage on complex structures. The only limitation of this

technique is that it only considers the effects of delamination. More research needs to be developed on how fiber/matrix cracks affect the strength of the composite.

Nondestructive techniques provide a great deal of information about the damage state of a material. The medical industry has greatly benefitted from using software packages like Simpleware and Mimics to create simulations based on nondestructive evaluation to optimize design and reduce the time for the designs to reach market. With the aid of nondestructive evaluation, the capability to certify composites could dramatically reduce the cost of experiments for new designs. Accurately modeling crack propagation, delamination growth, and fiber breakage could be dependent on several parameters. The aim of this research is to integrate nondestructive evaluation and discrete damage modeling to predict the failure of unidirectional carbon fiber composites under compressive loading. Many composites experience damage during its lifetime, which may reduce the load bearing capacity of the structure causing catastrophic failure. Nondestructive evaluation is used to assess the amount of damage to the composite. The damage is pre-imposed into a discrete damage model to determine the effects of cracks, delamination, deformation, and fiber breakage under compressive loading. Although material characterization has heavily focused on the microstructure of composites, nondestructive evaluation and finite element methods proposed in the work model realistic damage of composite structures. The proposed FE tool uses discrete damage modeling to characterize the growth of pre-existing cracks and delamination developed by Iarve [64].

3.2 Discrete Damage Modeling

A simplified damage progression sequence of coupled transverse matrix cracking and interlaminar delamination is shown in Figures 3.2.1 a-d for the case of a laminate plate subjected to a tensile load. Initially, the laminate is undamaged, Figure 3.2.1.a. As a result of the load application, transverse matrix cracks form in different plies of the laminate, as shown in Figure 3.2.1.b. In the absence of a stress concentration, the locations of the initial matrix cracks are random, and cannot be known a priori. As the load increases, new cracks appear, and the spacing between them becomes increasingly deterministic. At some value of the applied load, delamination initiates from the matrix cracks (Figure 3.2.1.c). These delaminations can connect matrix cracks in adjacent plies, which can

cause disintegration of the laminate. The failure scenario outlined above is intended for illustration purposes only and as it simplifies the actual damage progression and failure process. Finally, fiber failure occurs and the laminate separates in two parts.

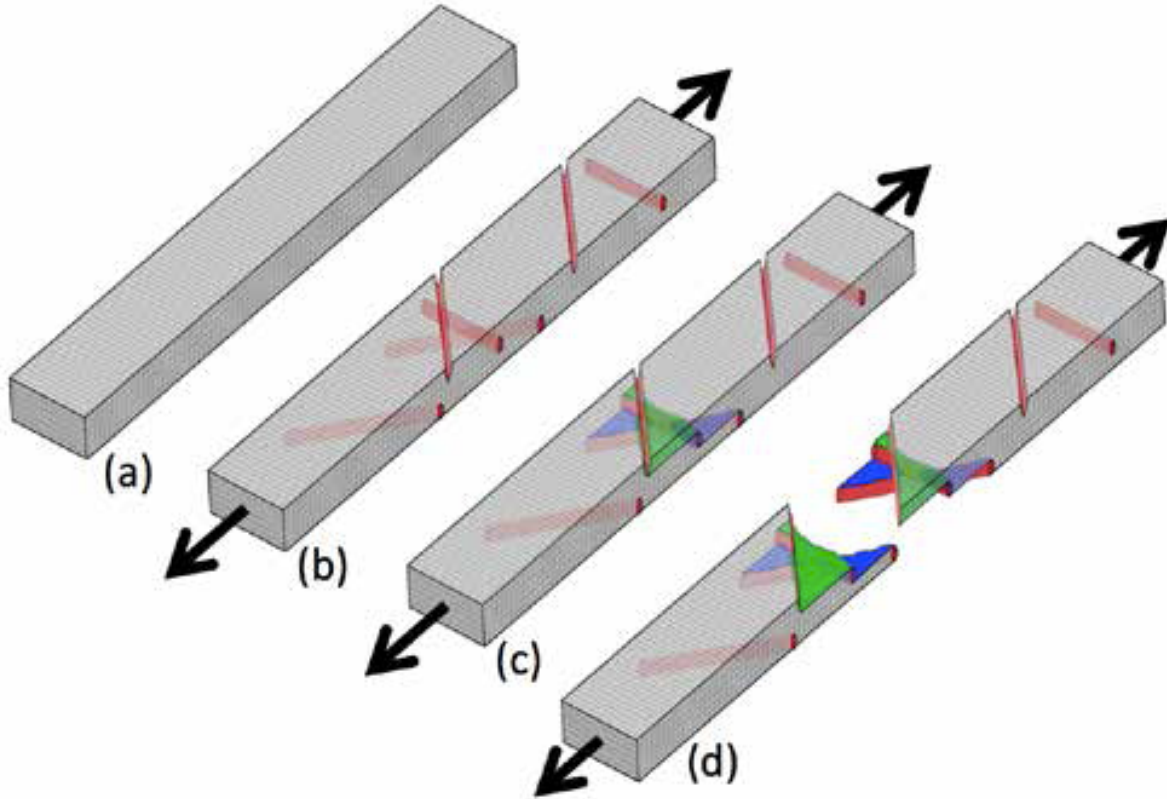


Figure 3.2.1 – Schematic of the damage evolution process in a laminated composite

The DDM approach proposed herein for modeling networks for multiple parallel transverse matrix cracks within individual plies of a laminate and delaminations between plies couples a Regularized eXtended Finite Element Method (Rx-FEM), also called Mesh Independent Crack (MIC) modeling [65-68], where the step function used in traditional x-FEM approaches to construct local enrichment for a crack discontinuity is replaced with a continuous function that is approximately by the same shape functions as those used for initial displacement approximation. The surface of each crack is replaced with a gradient zone (a volume where the gradient of the approximate step function is nonzero), and the surface fracture energy is replaced with the cohesive energy in the gradient zone.

A flow chart of a typical simulation is shown in Figure 3.2.2. A simulation begins without any initial matrix cracks. As the load increases, matrix cracks are inserted according to a failure criterion. In

the present paper, the LaRC03 in-plane stress-based failure criterion [69], as well as the 3D LaRC04 criterion [70], are used. The criterion is evaluated at each integration point of a discretized element and, if the criterion is exceeded, a matrix crack oriented in the fiber direction is added. LaRC04 predicts the crack angle with respect to ply surface, which is 90° under tensile normal stresses whereas in shear and compression dominated loading states can significantly differ from 90° . The crack is inserted using the displacement enrichment necessary to model the displacement jump. The magnitude of the jump is initially zero and is controlled by an interface cohesive law developed by Turon [71]. The same cohesive law is used at the ply interfaces to represent potential delamination surfaces. Fiber failure uses a Progressive Fiber Failure (PFF) methodology based on the uniform degradation of the element stiffness when the fiber failure mode is detected [73-74]. The PFF method continuously degrades stiffness in a given integration point as a function of normal strain in the fiber direction. The degradation begins after a threshold value corresponding to the tensile strength of unidirectional coupons is reached. A Newton-Raphson procedure is applied to find the equilibrium solution at each load step of the implicit incremental solution combining softening mechanisms from cohesive interface matrix damage models and stiffness degradation from fiber failure models.

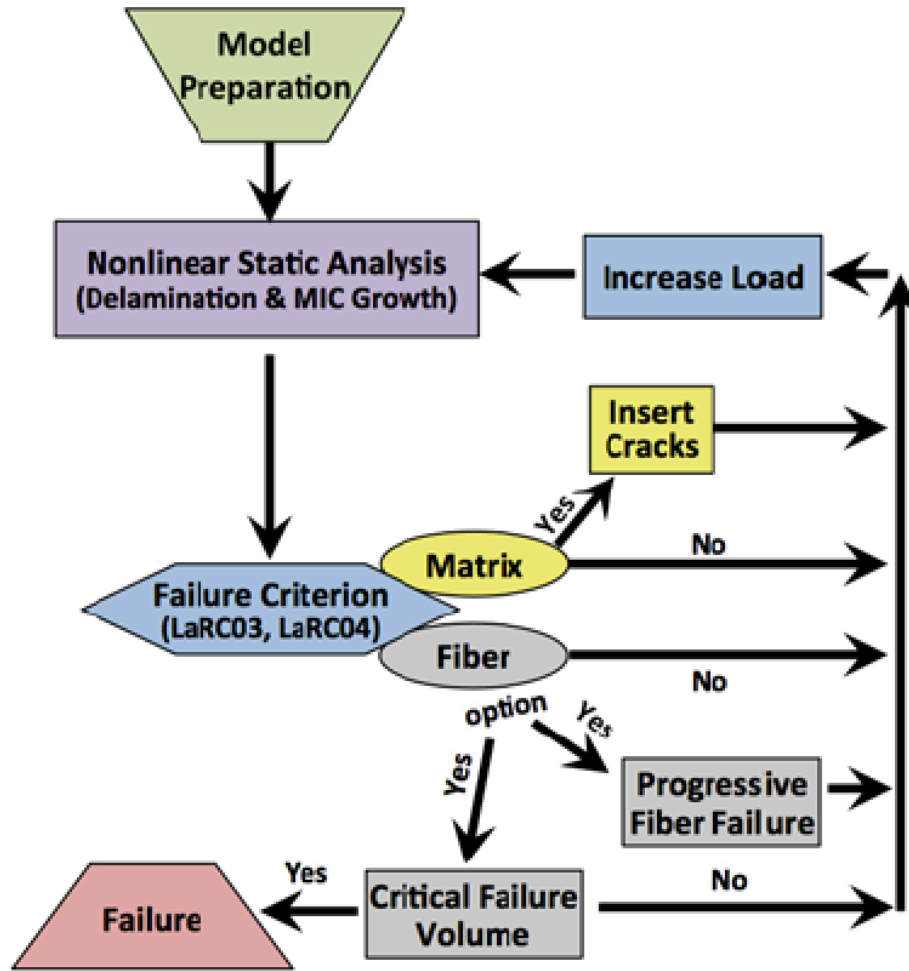


Figure 3.2.2 – Flowchart of a typical DDM simulation

3.3 Modeling NDE for use of Damage Tolerance and Assessment

This work proposes a methodology of pre-imposing realistic damage into a discrete damage model. Figure 3.3.1 is a flow chart of the modeling preparation, which considers the scenario that there is no information on how the damage was created on the composite. It begins with a composite flat plate. The flat plate is discretized into smaller elements that represent the laminated composite. The discretized composite goes through a series of steps to pre-impose realistic damage. It first superposes an out-of-plane translation of the nodes through the thickness of composite to represent the permanent plastic deformation obtained from profilometry. The interfacial node translations are a linear interpolation of the impacted and back surface profiles. For delamination, computer aided design tools were created to superimpose 3D reconstructed NDE data (x-ray CT, C-Scan) such that it would create

node sets from the translated interfacial nodes. Most matrix cracks in post-impacted composites are within the regions associated with delaminated interfaces. Nodes were selected within the delaminated areas in conjunction with the location of the cracks obtained from x-ray CT scans.

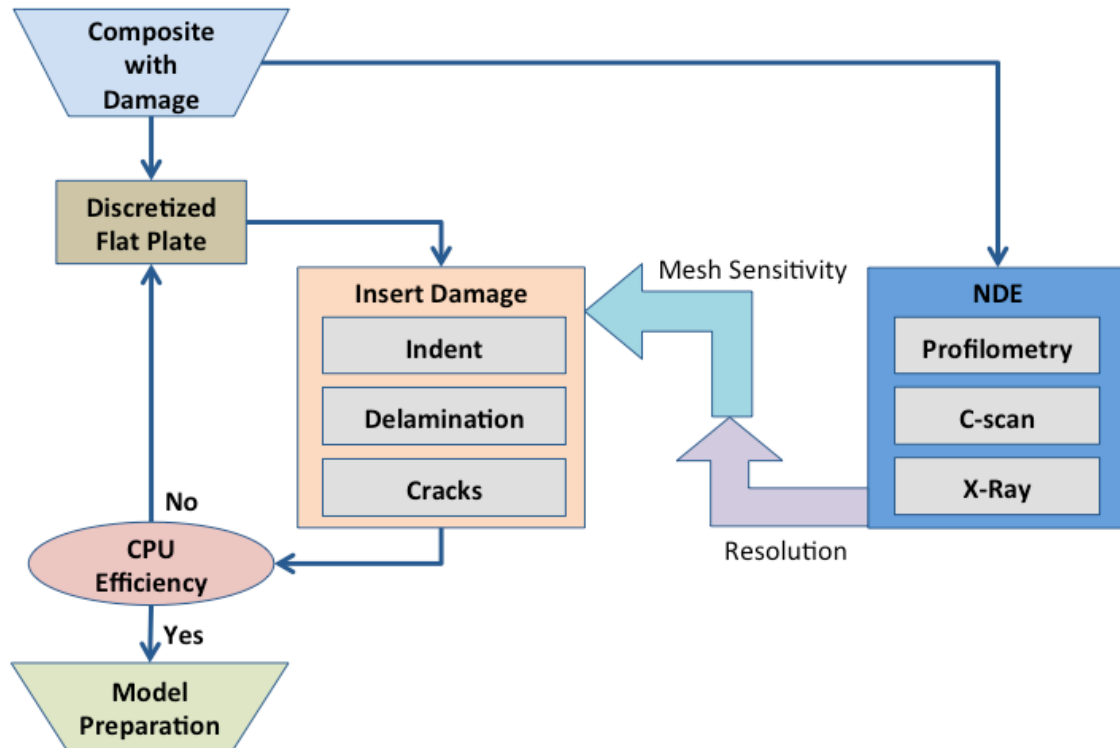


Figure 3.2.3 – Flowchart of model preparation

It is important to understand the dominant factors that affect the behavior of composites while also reflecting on the limitations on the resolution of the images presented from nondestructive evaluation. In this study, mesh sensitivity was not explored, but the basic premise is that the model preparation takes into account the resolution needed to predict the behavior of failure. Currently, they are limitations to BSAM as well. First is that it has yet to be parallelized such that memory would not be an issue in running large problems. Therefore, the mesh sensitivity was dependent upon the amount of degrees of freedom BSAM could solve with the available 128 GB of computer RAM, which correlates to a maximum of 1.4 million degrees of freedom for a tractable model. Once modeling preparation is complete, boundary conditions are applied such as constraints and loads with the VTMS/BSAM software [75].

3.4 Pre-Imposing Damage Into a 3D Discrete Damage Model

Damage from an impacted composite can come in the form of permanent deformation, transverse matrix cracks, delamination and fiber breakage. There are other forms of damage due to chemical degradation, moisture, high-temperature and radiation. These forms of damage add another layer of complexity to the problem and are not discussed in any context. This section primarily focuses on inserting damage in terms of permanent deformation, transverse matrix cracks and delamination for compression after impact studies. The following sections covers how nondestructive evaluation was used to pre-impose damage into a 3-dimension discrete damage model.

3.4.1 Pre-Imposing Geometric Imperfection

The threshold of detectability based on the residual indentation is known as barely visible impact damage (BVID). There is no consensus on the standard value for BVID, even though it has been assumed that the strength degradation is proportional to the residual indentation depth based on data for impactors 1" or smaller (FAA-AC-20-107B). Although the morphology alone does not determine the compression after impact strength, it could be used to design strain levels sufficiently low such that large planar damage does not pose a safety threat. Guidance for assessing morphology is heavily reliant on good design practice.

For thin composites, the deformation could be anywhere from 50% to 100% of the ply thickness. In Section 2.1, the magnitude of the indent on the impact surface was slightly lower than the back surface. The indent was one ply thickness deep into the composite. Although it may appear to be small at a mesoscale, it could play a role in the failure of the composite. The region where deformation is present is also a region that has delamination so the connections between plies could experience local instabilities from the curvature.

For thick composites, the through thickness deformation is worse than it is for thin composites. In Section 2.2, the indent of the impact surface was close to one ply thickness while the back surface was six times one ply thickness. This indicates that the amount of permanent deformation gets progressively worse through the thickness of the composite. The amount of permanent deformation could be more severe for thicker composites especially in determining design guidance for damage

tolerance. To induce BVID on thicker composites, it would require higher energy impacts, which inevitably means more damage.

For the thinner composite, the impact energy was 10 J versus 75 J for the thicker composite. The amount of damage that occurs at this energy level is dramatically different and could have different compressive failure modes. The amount of damage through the thickness of the composite cannot be easily quantified by looking at the indent alone, and that includes the morphology. In many cases, industries do not have the capability to measure the morphology of the back surface of composite structures due to the limitation of NDE. The underlying reasons for modeling the morphology is to determine if the stresses localized in the area would cause delamination and crack propagation. Therefore it is important to pre-impose the indent into the model to determine if it affects the behavior of delamination growth.

3.4.1.1 Pre-Imposing Geometric Imperfection for Thin Composite Plates

In Section 2.1, optical profilometry was performed on the impacted and back surface to record the morphology of the permanent deformation caused as a result of the impact. Horizontal and vertical lines were created for the impacted and back surface. For each of the panels, the height data was averaged to create a common profile. Averaging the profilometry data is important because noise could exist in the collection if there is a rough surface. Also the more complicated the profilometry lines are, the harder it is to create a discretized model to accommodate the indent. Incorporating jagged lines that may have existed in the line profiles could lead to modeling errors arising in the discretized elements themselves. Careful consideration was taken to ensure the Jacobians (the gradient of the element's shape functions) were sufficient to minimize errors.

To minimize the amount of error that existed and still maintain some curvature representative of the indent, smoothing and averaging were done. Using Matlab, a robust local regression using weighted linear least squares and a 2nd-degree polynomial model was used to smooth the line profiles. Averaging was done based on each height about an ordinary x-coordinate point for each of the profiles. Side studies were done to find the optimal regression parameters necessary to maintain the shape of the profilometry. The points of the line profile were rotated 180 degrees to capture the indent. Then a linear interpolation

of the nodes between the impacted surface and back surface was done creating nodes representing each interface of the composite.

Using an open source meshing code, GMSH, a 3-dimensional unstructured mesh was created using the dimensions specified in ASTM 7136/7. Using a Matlab script, the interpolated positions of the nodes were translated to the element nodes such that they conformed to the morphology obtained from profilometry. Figure 3.4.1 represents the average line profile that was used to extract the impacted surface indent for Panel A. The same process was done for the each of the panels including their back surface line profiles. Figure 3.4.2 is a representative discretized model to help visualize the geometric imperfection for a thin composite plate.

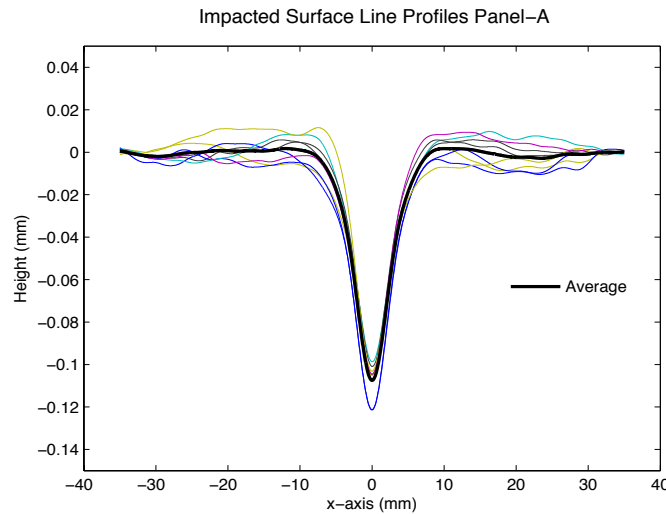


Figure 3.4.1 – Average line profile for Panel A

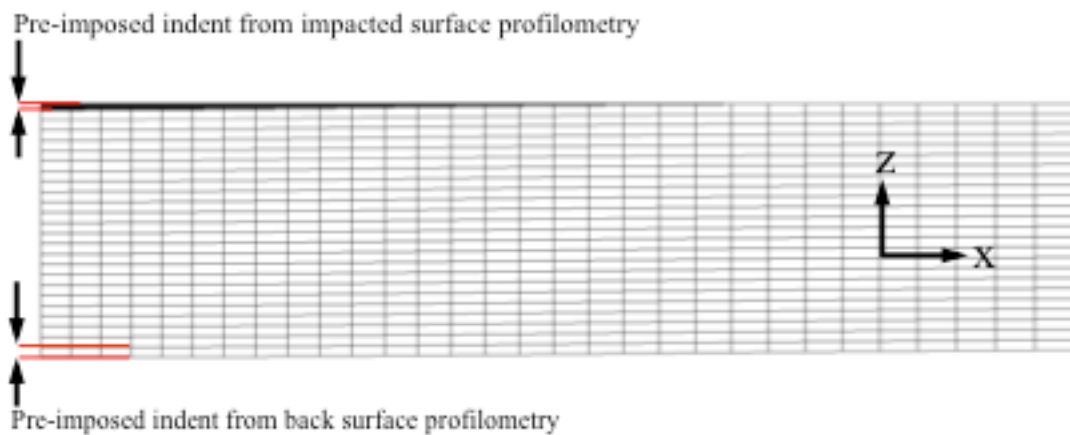


Figure 3.4.2 – Discretized representation through the thickness of the composite

3.2.1.2 Pre-Imposing Geometric Imperfection for Thick Composite Plates

The line profiles for the back surface of the panels could not be obtained through optical profilometry due to the amount of fiber breakage. The line profiles were obtained using 3-D digital image correlation from the compression after impact tests. Digital image correlation uses the speckle pattern to calculate coordinates given a 3-dimensional domain. As a result, Cartesian coordinates could be tracked to find displacements and strains. The maximum out-of-plane displacement pixel for each of the specimens was found from compression strength after impact tests before applications of load. Horizontal and vertical line profiles were obtained from extracting the z-coordinate position information. The same procedure from the previous section was done to pre-impose the geometric imperfection into the model for the thick composite plate (Figure 3.4.2).

3.4.2 Pre-Imposing Delamination

Modeling delamination in a composite requires identifying the underlying interfacial nodes of the discretized composite plate with or without geometric imperfections such as an indent. Once the interfacial nodes are identified, the alternate nodes that remain are the interfacial nodes that make up the undamaged region of the composite. Using VTMS pre-processing tool package, connections were created to model interfaces between each ply. Cohesive zone method is used to model the interface between plies. Figure 3.4.3 is a schematic of an interface of a composite layup. The delaminated region is a set of nodes with low cohesive zone properties that represents delamination in the model. Delaminations represent a disbonding of the layers in the region in question. For the purpose of this study, however, the traction properties of the cohesive zone were set extremely low with relatively low fracture energy values. The properties for delamination growth used the same material properties determined by standard testing.

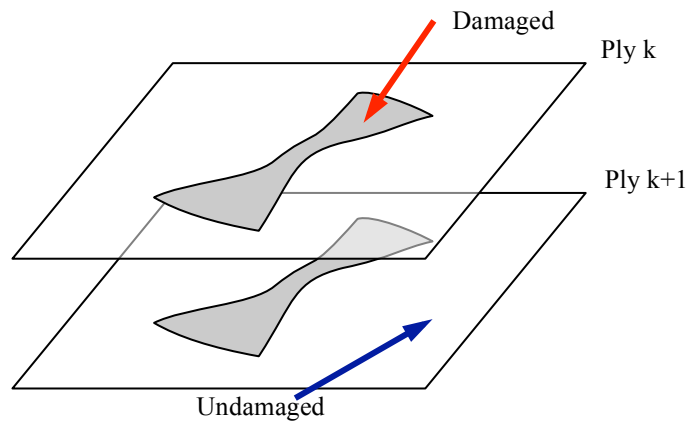


Figure 3.4.3 – Arbitrary delamination of a composite interface

The benefit of having arbitrarily low cohesive zone model properties in delaminated interfaces is to ensure there is no interpenetration of the nodes or elements between adjacent plies. Figure 3.4.4 shows a simple illustration of the effects of penetrating discretized nodes if delamination was modeled with no cohesive zone. The model maintains contact to ensure the behavior of delamination is accurately modeled under loading. The penalty stiffness and damage parameter are the same for both the damaged (weak) and undamaged (strong) interface.

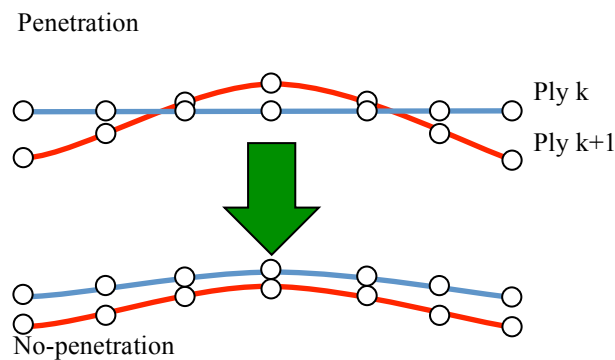


Figure 3.4.4 – Surface behavior of plies with delamination

The delamination patterns for the models were determined using nondestructive techniques such as X-ray CT and C-Scan. A 3D reconstruction of the NDE was performed to create a STereoLithographic (STL) file, which is a 3D computer aided design tool well known in CAD, 3-D printing and additive manufacturing industries. Figure 3.4.5 is a flow chart of how a basic STL is used to

select nodes of the interfaces that connect adjacent plies. It starts with a discretized composite plate (Figure 3.4.5.a). Then an STL is superimposed on the model (Figure 3.4.5.b). VTMS does a search for all of nodes and elements that represent one ply interface (Figure 3.4.5.c).

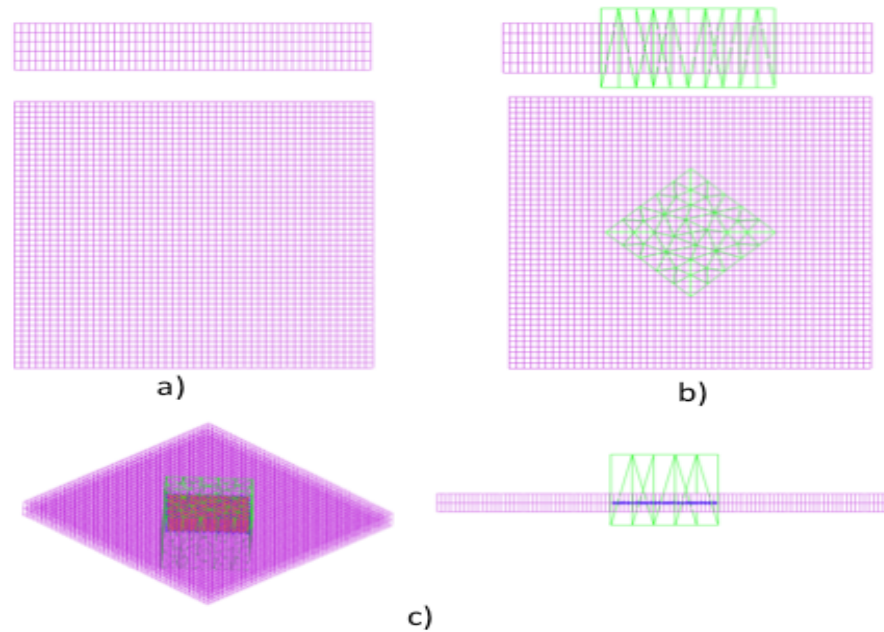


Figure 3.4.5 – Pre-imposed delamination flow chart with a) discretized undamaged composite b) pre-imposed STL image c) interfacial nodal selection

Image segmentation was used to extract delamination patterns for each interface of the composite layup. This section outlines the processes that were used to extract the delamination such that it could be utilized in the model. The following sections are dedicated to the processes that were developed and designed to pre-imposed STL into models to create realistic damage from nondestructive techniques.

3.4.2.1 Analyzing Delamination for Thin Panels

C-Scans were performed on the composites using a 10 MHz probe on both the impacted surface and back surface. The pulse echo waveform was gated 2048 times and outputted as compressed grayscale tiff images with a 0.1 mm resolution in the x and y with a time of flight of 0.002 seconds. Grayscale images have integer scales from 0 (white) to 255 (black), which define one pixel of the

picture. One advantage to gating the waveform 2048 times is that filters could be developed to create a 3-dimensional representation of the damage.

Since information from c-scan images only provides time-of-flight data through the thickness of the composite, the 2-D images were reconstructed to visualize the damage more thoroughly to apply threshold techniques to extract 3-D dimensional volumes of the damage. Then the 3-D dimensional volumes of the damage could then be utilized in a computational software package. The methodology to analyze the C-Scan images took several steps. First, a mean filter was applied to the image to reduce any speckle noise that was occurring. A modified mode filter was applied which incorporated the modal distribution of pixels, maximum and minimum scale integers. An adaptive filtering technique was used through the thickness to accommodate the spatial difference to obtain a 3-D representation of the time-of-flight data. Figure 3.4.6 is an example of the filter that was applied to an interfacial region of the composite.

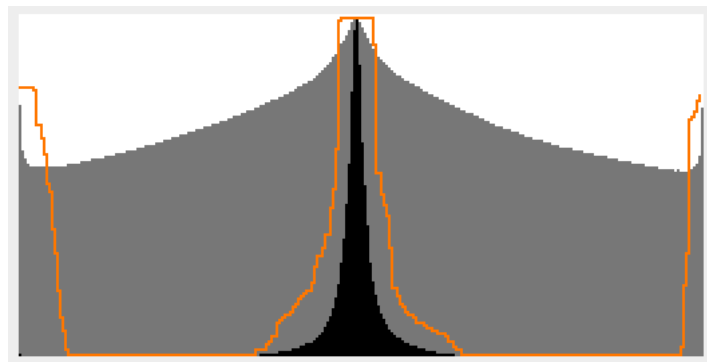


Figure 3.4.6 – Adaptive modal filter technique used for c-scan images

Extracting the delamination patterns and outputting the volumes as an STL required software packages like Simpleware or ImageJ or VG Studio. The filters used may have provided information about the delaminated regions of the composite, but are specific to the spatial resolutions used for X-Ray images. Even though the software analyzes x-ray data, Figure 3.4.7 shows how applying filters makes a significant difference in the image when trying to identify delamination and is highly detailed

comparatively to an x-ray image. As a result, the Simpleware software could identify scale integers in the image needed to apply thresholds to find patterns.

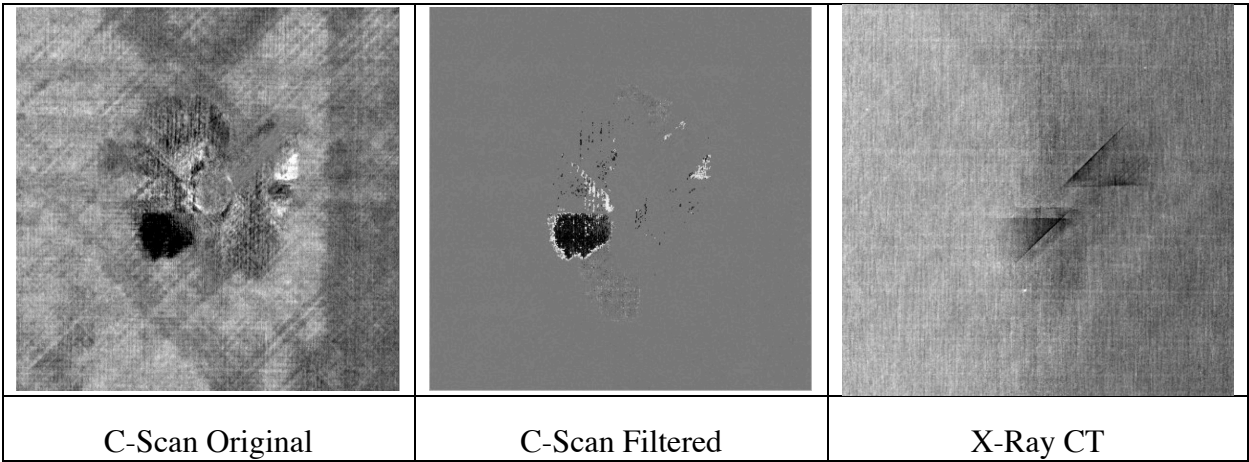


Figure 3.4.7 – C-scan, c-scan filter, and X-Ray CT image of interface 5 for Panel A

The shape and area of the delamination pattern begin to degrade further into the images. This is a common limitation that is known with c-scan. The benefit of using c-scan is that it’s a relatively quicker process of getting information than x-ray CT. Appendix F shows side by side comparison of interfacial damage between plies for c-scan, c-scan filtered and X-Ray. Although not discussed in this paper, the parameters sufficient to create a high-resolution representation of damage using c-scan are currently being investigated. Future models could incorporate c-scan images to address the needs of industry.

X-ray CT scanning was used to extract delamination patterns for the model with a 0.05, 0.05, 0.1, and 0.05 mm resolution for Panels A-D. The x-ray CT scans used a 75kV/100mA beam to extract spatial information about the composite structure. x-ray CT images provide detail about the delamination pattern through the thickness of the composite. VG studio was the software used to reconstruct the waveform data from the x-ray machine. The VG studio software has the capability to create regions of interest to identify areas of delamination. From the created regions of interests, a 2-D representation of the delaminated interface could be seen through the thickness of the composite. Figure 3.4.9 shows the difference between x-ray delamination patterns of Panel A. Figure 3.4.8 also shows the amount of delaminated regions that are missing in the c-scan comparatively to x-ray CT. VG studio also has the capability to read series of images and was used to analyze the c-scan images. Using the same

techniques, regions of interest were created by the filter c-scan images and a 2-D representation of the delaminated interface was extracted into a 3D surface.

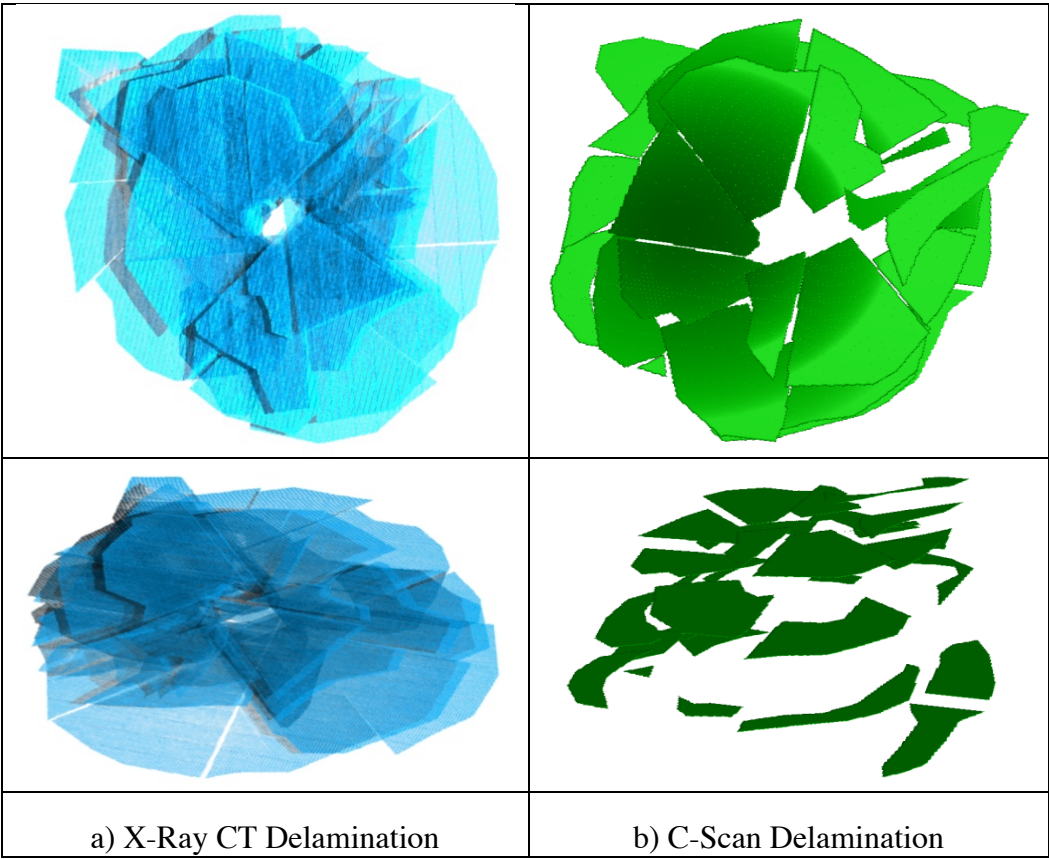


Figure 3.4.8 – X-Ray vs C-Scan delamination pattern

The Simpleware software was the primary tool to extract STL. Simpleware is similar software to VG studio. The only difference is that regions of interests are now called masks. A mask is simply a subcomponent/part of the software that applies certain functions to the images to extract, calculate and export information. Within the mask, threshold techniques could be applied to scale integers of the pixelated information to extract delamination patterns. Since delamination is more on the dark scale side of the gray-scale image, it is easier to extract patterns out of the images in a systematic process. The delaminated regions were found for each interface of the composite. Using a lasso tool, a polygonal surface shape was created. The lasso tool could also implement threshold techniques to ensure that undamaged regions were not selected within the shape. The polygonal surface representing the

delamination region was extruded through the thickness of the composite to form a 3-D volume. Once the 3-D volume is created, it could be exported as an STL. Most CAD software has the capability of reading in images and drawing shapes on images. The shapes could be extruded to form 3D parts, STLs and models.

Once volumetric information of the extracted delaminated regions was performed, Simpleware created a model out of each interface of the composite. A model within the Simpleware software is part of the interface, which allows the user to create STLs or finite element models for the use of computational software like ABAQUS. Using the modeling interface, smoothing and decimation were performed. Smoothing helps reduce sharp edges or sharp volumes. Sharp volumes are tiny volumes within the large volume that are difficult to mesh or interpret. However, for the use of VTMS pre-processing software, it would make it difficult to find element or nodes within the sharp volume. The facet size of the STL is dictated by the resolution of the images. Therefore, decimating was useful to reduce the number of facets it has within the volume. STL image files could get large depending the resolution of the x-ray images. VTMS searching algorithm tries to find every node and element within a set of facets of sub-facets of a volume in the discretized model. By reducing the number of facets, the search processing time is dramatically reduced.

Once the STL is created, it is superimposed on the model. The STL selects all the nodes and elements of the discretized model, and node sets are defined to represent a weak cohesive surface. The nodes outside the selected regions that are undamaged are defined as a strong cohesive surface. Figure 3.4.9 shows the mask, the delaminated region of an interface and how that volumetric data was superimposed over the discretized model.

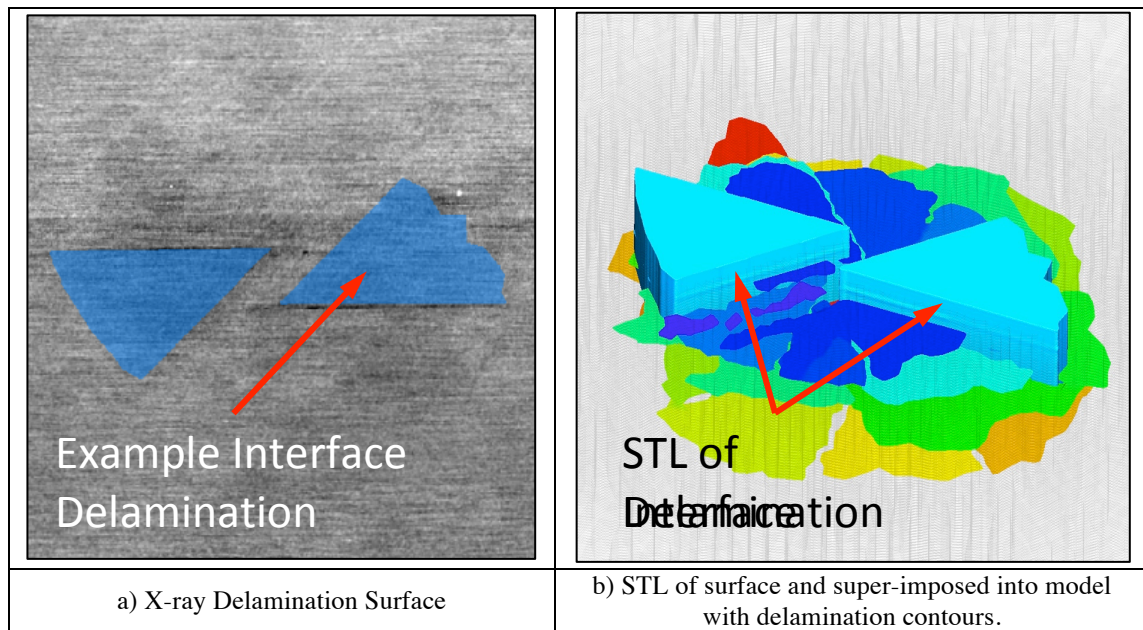


Figure 3.4.9 – a) STL creation from a mask being b) superimposed into a discretized model

The greatest attribute of using an STL of a damaged region to select nodes and elements of a discretized model is that it could be applied to any mesh. Mesh sensitivity is discussed in a later section. Figure 3.4.10 shows a side-by-side comparison between the model and a c-scan of a composites back surface using a 5 MHz probe. Many finite element models attempt to mesh the damage region, which could be problematic with elemental connectivity issues. Due to the complexity of the shape, tetrahedral meshes are used instead of hexahedral meshes, which adds to the computational cost. The process of selecting nodes to an already discretized model gives the extra capability to already existing discretized structures.

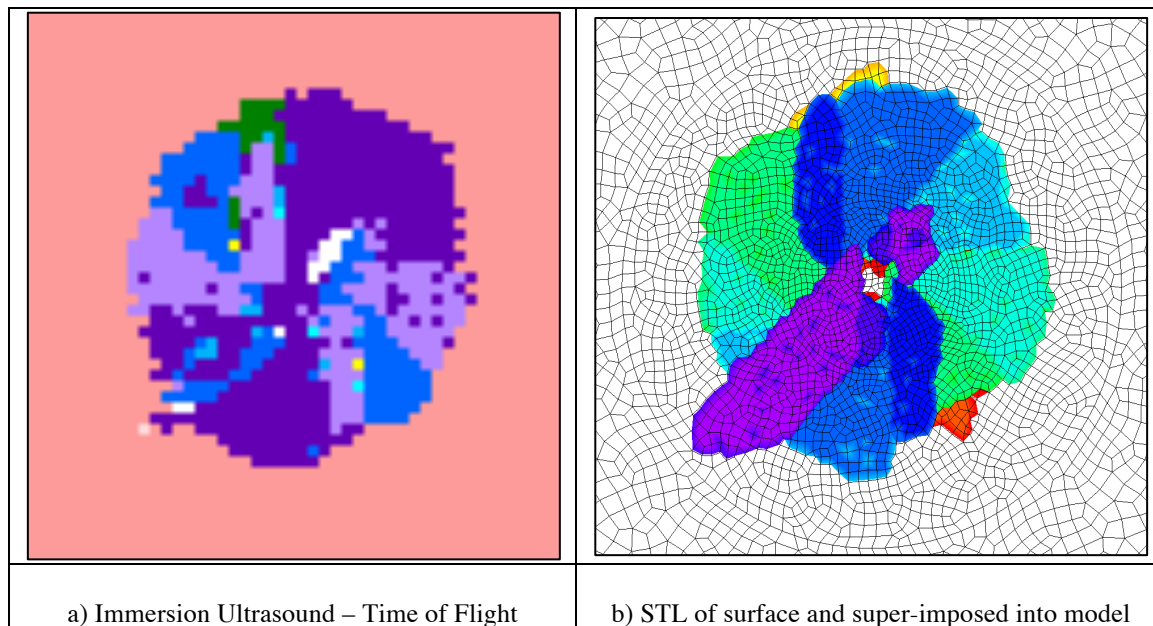


Figure 3.4.10 – a) STL creation from a mask being b) superimposed into a discretized model

3.4.2.2 Analyzing Delamination of Thick Panels

The analysis was done on specimen-1 using VG studio, which is a post-processing tool for x-ray images. Side by side comparisons was done with the x-ray and x-ray with zinc iodide penetrant to try to get a full understanding of the damage of the impact region of the composite. C-scans of both the impacted and back surface were also useful in verifying the depth correlated to the correct interface for delamination. The process is not fully automated, therefore it requires a lot of interpretation to determine the shape, size and area of the delamination. Figure 3.4.11 is an image of the delamination for both the untreated and treated sample. Appendix C gives a more detailed account of delamination for each ply interface.

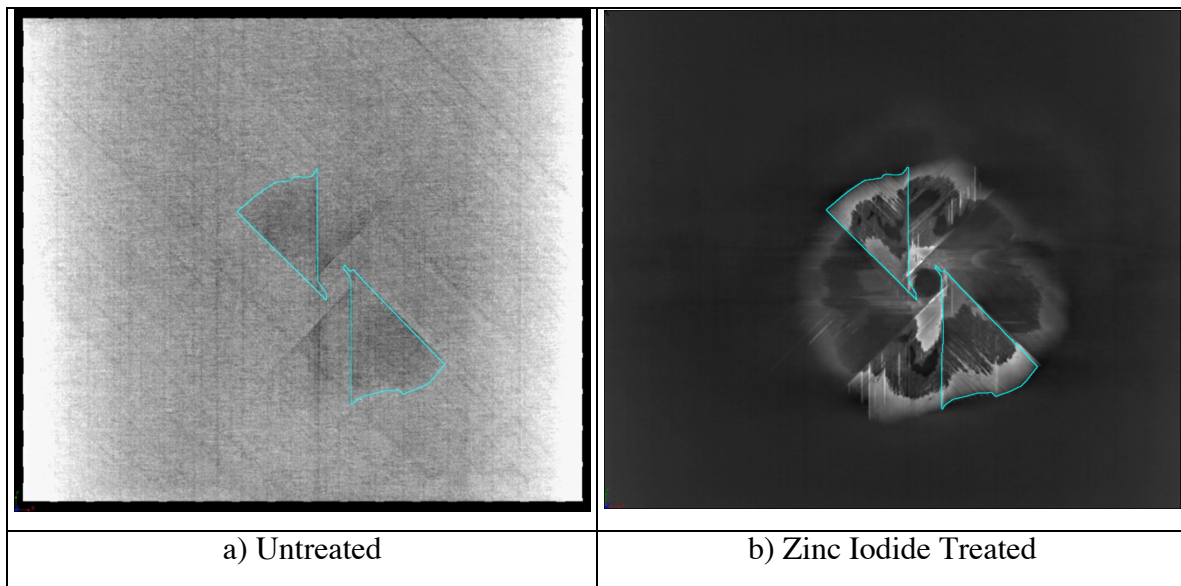


Figure 3.4.11 – Delamination shape of the 8th interface of the thick composite laminate

VG Studio took the waveform data from X-ray CT scans (70kV/120mA), reconstructed the data and extracted tiff images of the front, top and right sides of the specimens. The front images were exported to the Simpleware software to extract the volumetric data of the damage. The resolutions for the x-ray images were 0.08, 0.08, and 0.1 mm for the specimen Specimen-1, 2 and 3 respectively. Since the damage region of Specimen 3 was larger than the other two, it required a larger voxel size to obtain a high-resolution image of the damage. Threshold techniques were used to detect the brightness of the zinc iodine using Simpleware. From the newly created mask, several models could be constructed to develop STL images. The initial STL image is the damage represented through the zinc iodide alone (Figure 3.4.12-13). Due to the capillary action, the zinc iodide penetrant was not able to wick through each delaminated region. Therefore, the region needed to be filled to obtain an accurate representation of the delamination (Figure 3.4.14), which was done using the Simpleware software.

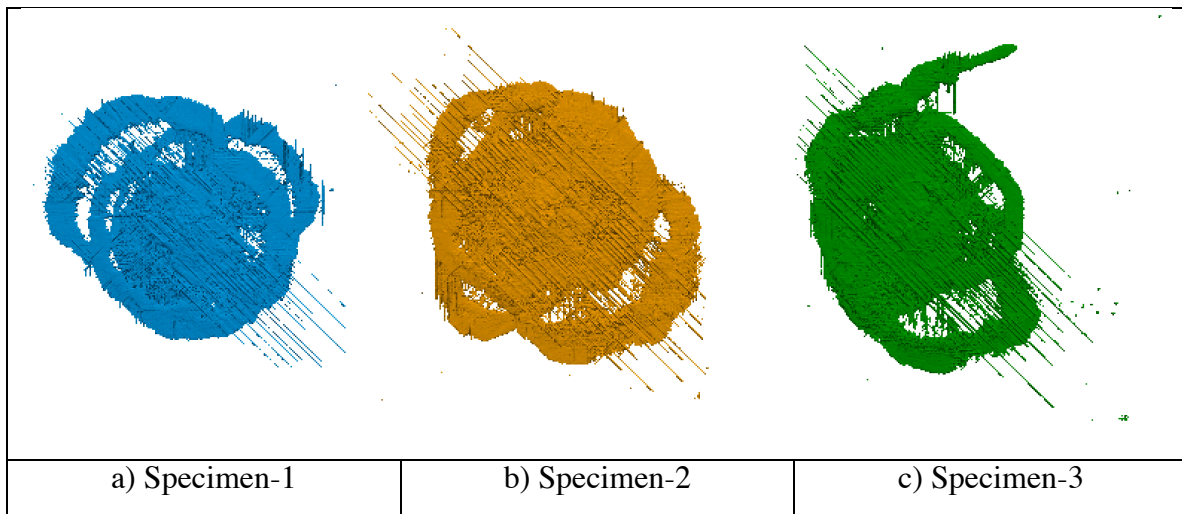


Figure 3.4.12 – STL Creation of Damaged Region – Zinc Iodide Alone Back Surface

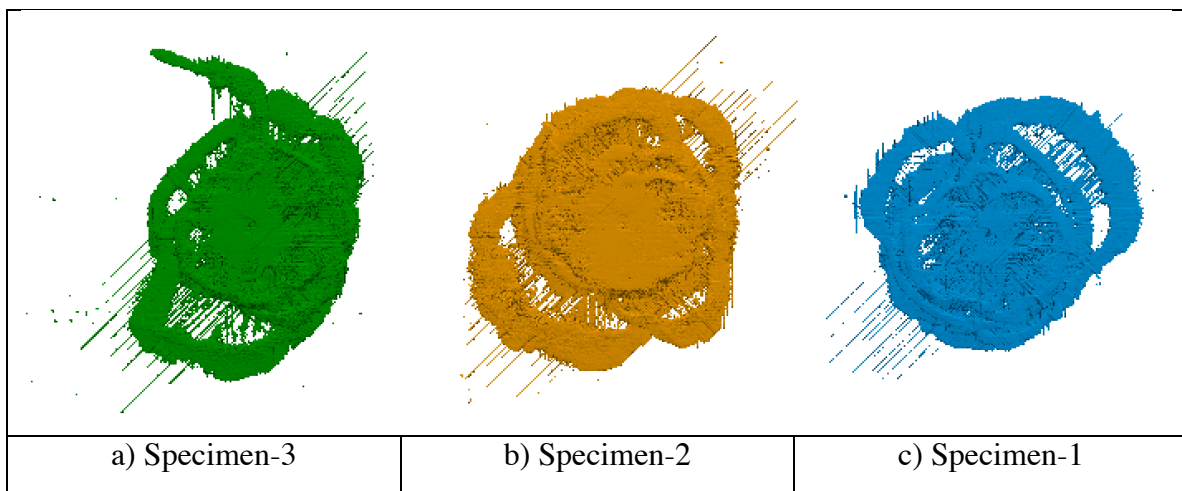


Figure 3.4.13 – STL Creation of Damaged Region – Zinc Iodide Alone Impacted Surface

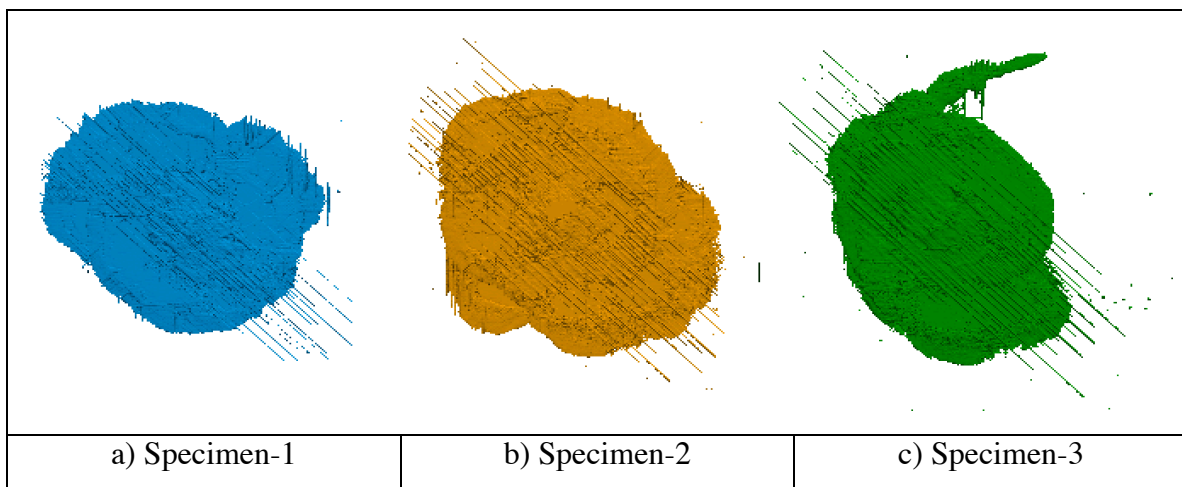


Figure 3.4.14 – STL Creation of Damaged Region – Zinc Iodide Filled Back Surface

The STL was superimposed on the model during pre-processing and setup as shown in Figure 3.4.15. Within the VTMS architecture the STL searched all the discretized elements nodes that were inside the STL, similar to the process outlined in the previous section except the whole volume is searched at once, rather than on an interface-by-interface basis. Node and element sets were created to apply mechanical properties to.

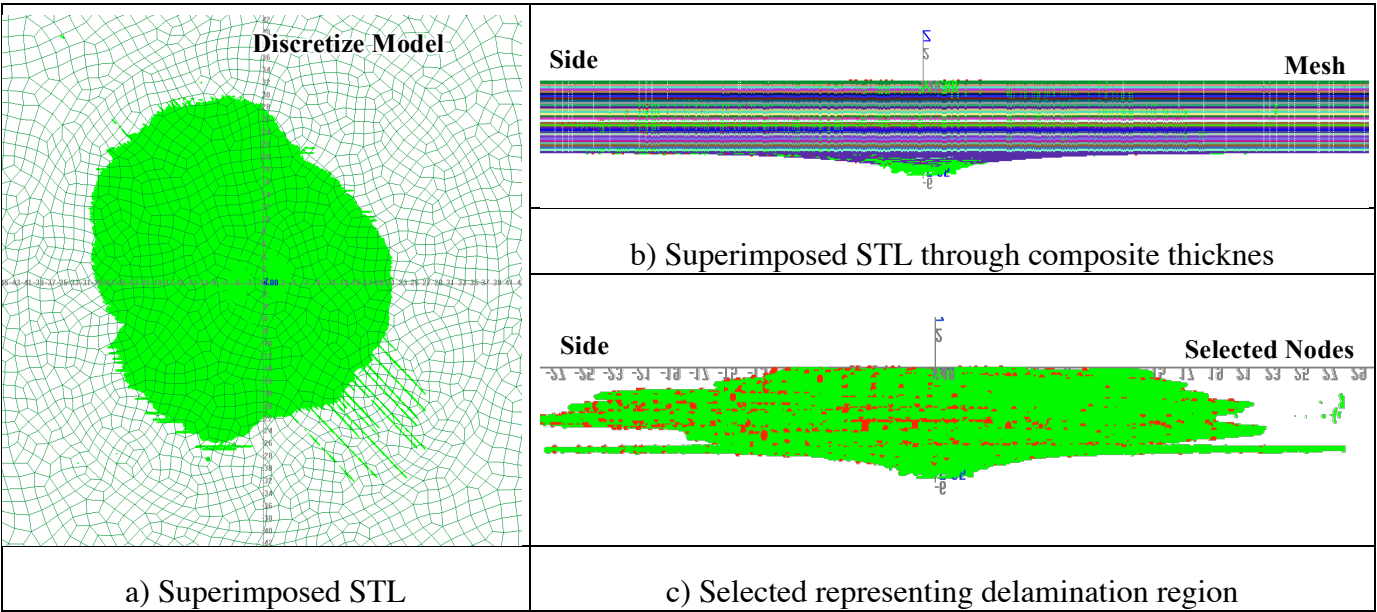


Figure 3.4.15 – Super-imposed STL into discretized model a) top view, b) side view c) and selection of nodes in each interface.

The technique does not automatically ensure that the delaminated patterns are correct for each interface. The process done using the VG Studio software where each interface is accounted for is the correct path forward. However, the time required to obtain such resolution could take a while on top of the time to perform x-ray. Manipulating the STL through the Simpleware S/W provided a quick time solution comparatively to VG Studio. Therefore, for the thick composite plate, the STL from Simpleware was used to pre-impose delamination into the model. It is a crude estimation for delamination and a simple way to superimpose damage into the model. Figure 3.4.16 represents the contours generated by the using STL created by Simpleware. Figure 3.4.17 shows how it differs from immersion ultrasound. The process has remarkable potential in modeling delamination even if you have a crude estimation of what the damage may be.

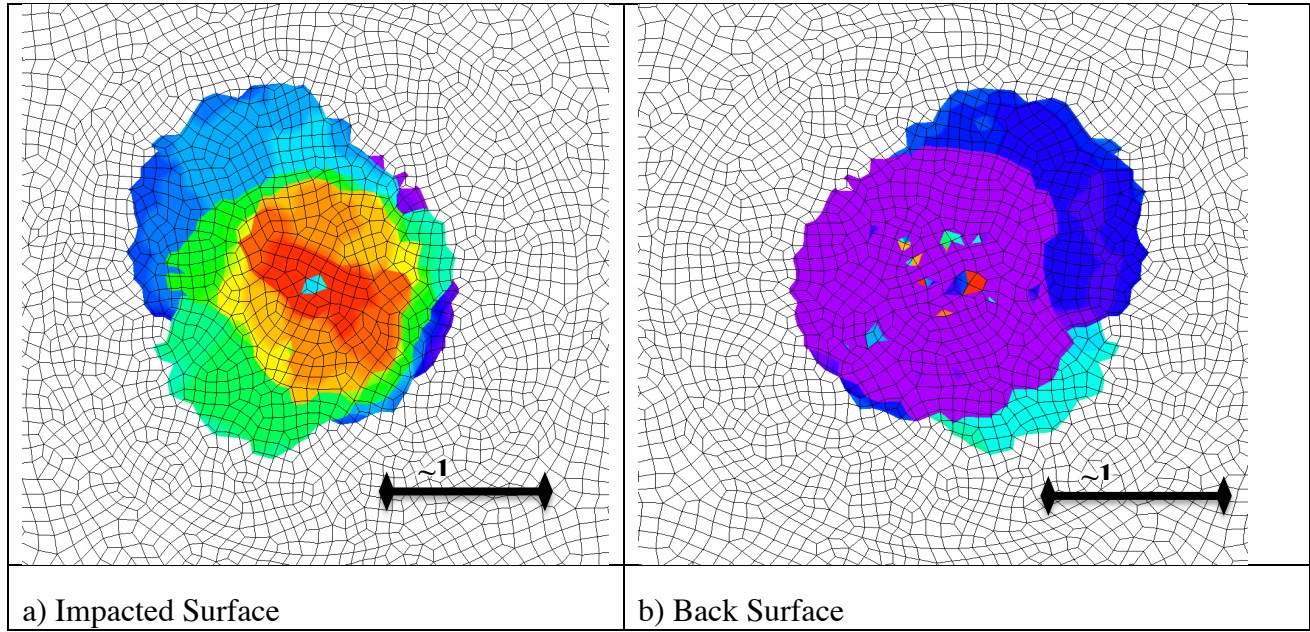


Figure 3.4.16 – Delamination pattern in discrete damage model

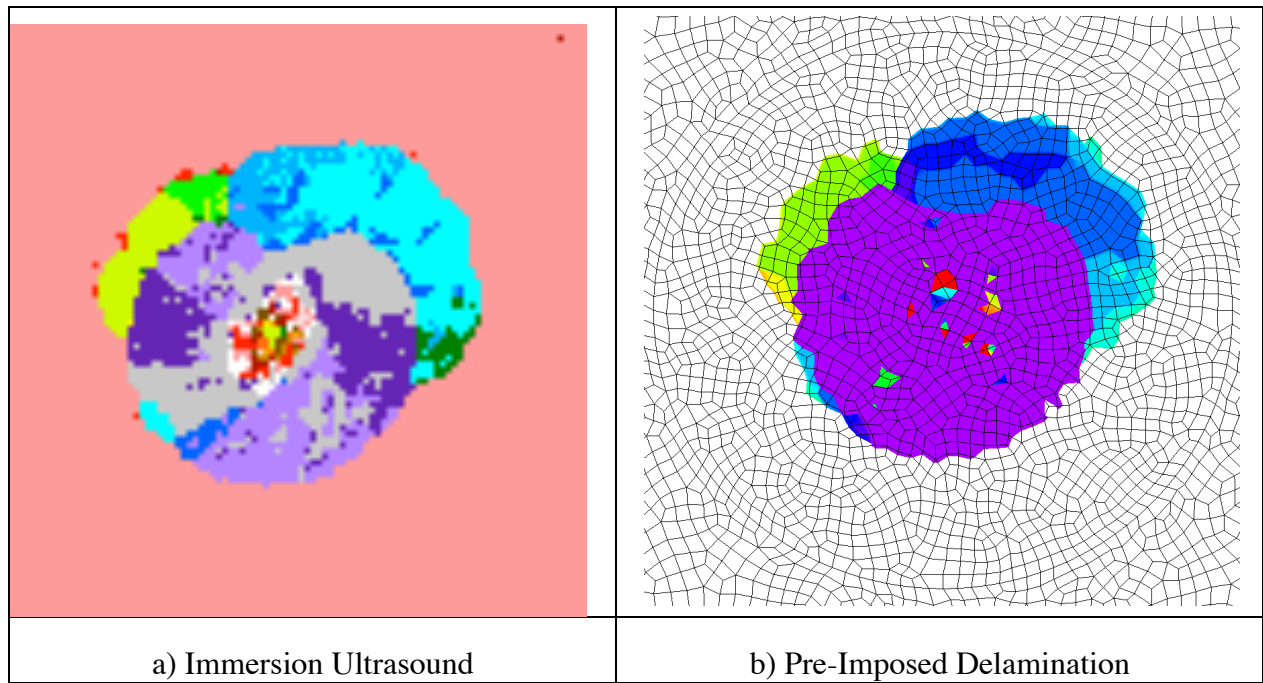


Figure 3.4.17 – Immersion Ultrasound image vs DDM initial delamination

3.4.3 Pre-Imposing Matrix Cracks

Pre-imposing cracks into a discrete damage model requires a two-step process. The first step is modeling an open matrix crack of a given length, location and orientation. Figure 3.4.18 is a theoretical representation of inserting pre-imposed cracks into the model during pre-processing. The location of a single matrix crack must be embedded inside a single element. The orientation of the matrix crack was determined by the fiber orientation of the ply. The matrix crack length was constrained by the delaminated region of elements. The elements were selected in the STL as shown in Figure 3.4.18.a. A matrix crack is inserted (using LARC04 failure criteria) into to the model such that it can only open in a “crack-limited” region. The mechanical properties for the criteria are set to an arbitrarily small value to ensure a crack opening in the first load step. The crack opens within the first step and does not extend beyond the crack region.

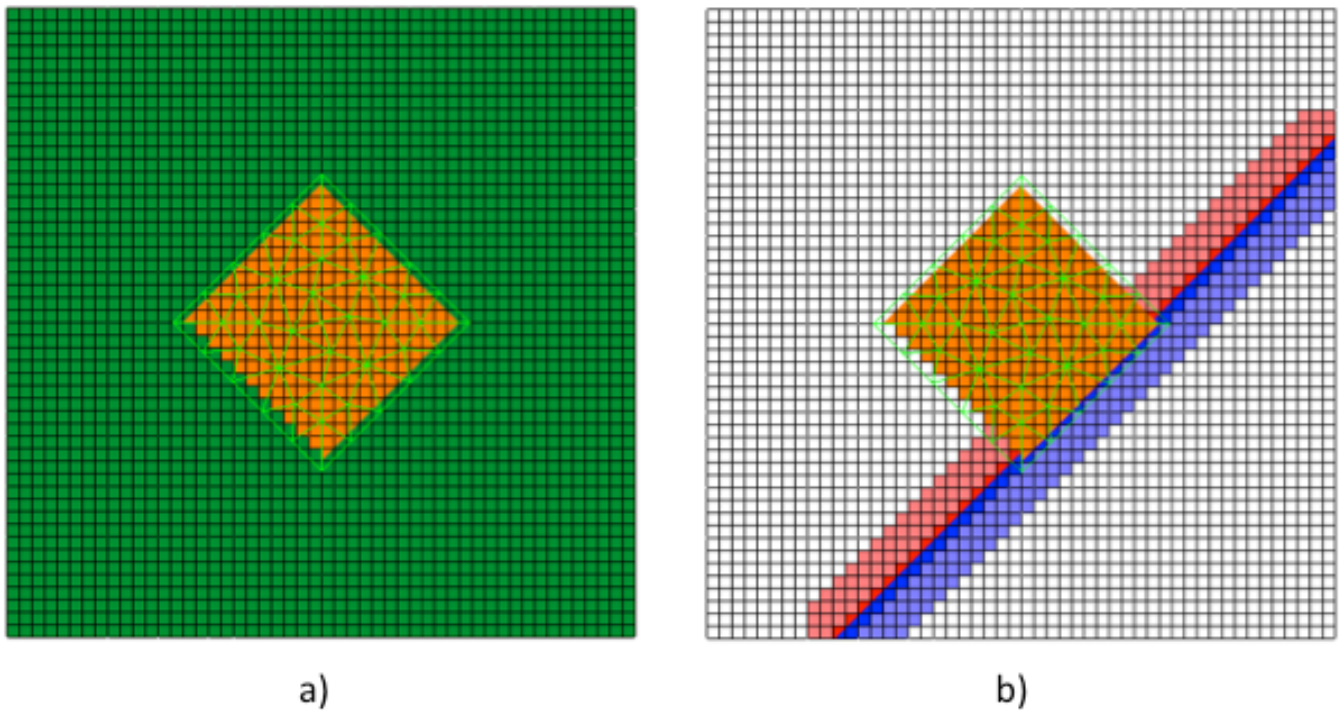


Figure 3.4.18 – Pre-imposing cracks into DDM of a 45° ply a) selected elements of delaminated region
b) pre-imposed crack within the delaminated region

In Step 2, the crack-limited region is removed and replaced with an exclusion box around the perimeter of the damage region. The exclusion box is larger than the delaminated region but smaller than the composite width. Cracks are allowed to extend beyond the borders of the exclusion box, but initiation outside the box is not allowed. This minimizes the effects of 3D interlaminar stresses at the free-edges, which, in CSAI, do not generally play a role. Open matrix cracks can still propagate beyond the exclusion. The crack propagation follows a cohesive zone model and given properties which coincide with an undamaged specimen.

Several assumptions must be made when pre-imposing matrix cracks into the discrete damage model. The cracks are modeled for a flat plate. Since the indent is in the center of the specimen, the crack does not take into account the curvature of the indent. The Rx-FEM representation in BSAM requires a minimum 6-element band to represent cracks. Additionally, this 6-element band requirement extends to the edges of the laminate. Crack arrest could occur due to the coarseness of the mesh and not the underlying physics of crack propagation. If cracks are too close to one another, the BSAM algorithm continues to the next matrix crack until there exist a crack six elements away from its initial adjacent crack.

Delamination growth is assisted through matrix cracks therefore a coupled system is needed to model the behavior of failure. X-ray CT was used to identify potential cracks that could affect the overall behavior of the material. The Simpleware and ImageJ software could be used to identify the crack location. The center of each specimen was found and recorded. After the center of the impacted region was identified, the center location of the crack was also recorded. The process requires the user to span each of the images and identify cracks. The delamination patterns differ through the thickness of the composite and the refraction of the beam could make it difficult to identify delamination for certain interfaces. For matrix cracks, the refractions provide a clear dark line in the images. However, the X-ray images also provide dark regions of interest for delamination. This makes it challenging for applying a unified threshold technique in identifying delamination patterns and matrix cracks simultaneously. The X-ray CT would have to be configured such that it could extract matrix cracks with the resolution set to

the width of the crack opening. Then threshold techniques could be applied to extract transverse matrix cracks alone.

Therefore, identifying cracks was based on engineering judgment. The rule of thumb was that the most significant cracks were the ones assisting the propagation of delamination. There are individual cases where no delamination could be present where the interface is between two similar plies with the same orientation. Additionally, the images did not provide clear differences in the location of a matrix crack for similar adjacent plies. For simplicity, it was assumed that the location and orientation of a matrix crack were the same for similar adjacent plies unless the images showed clear differences between delamination and matrix crack. This problem does not occur as often as adjacent plies with different orientations. The crack-limiting region was determined by the larger delamination pattern of the interface before or after the similar adjacent plies.

Future capability of the Simpleware S/W could provide better avenues for identifying cracks by measuring crack opening, length and orientation. The processes could lead to better ways of identifying cracks. There is also the possible capability of superimposing crack information into the STL used for delamination making the system more automated.

3.4.3.1 Analyzing Matrix Cracks

Cracks were identified using X-ray CT. Simpleware and ImageJ are useful tools to mark the locations of the cracks. Figure 3.4.19-20 shows the amount of cracks that could be seen through the front images for the thin and thick plates. The long striations are labeled as cracks. Delamination and cracks have the same pixel contrast therefore it is difficult to extract cracks out of x-ray CT using threshold techniques. Transverse matrix cracks were recorded by location, ply and orientation. The origin was approximately the center of the impact crater. The location of the matrix crack could be any point along the opened crack. Individual cracks were given more priority to others if they were responsible for assisting the growth of delamination.

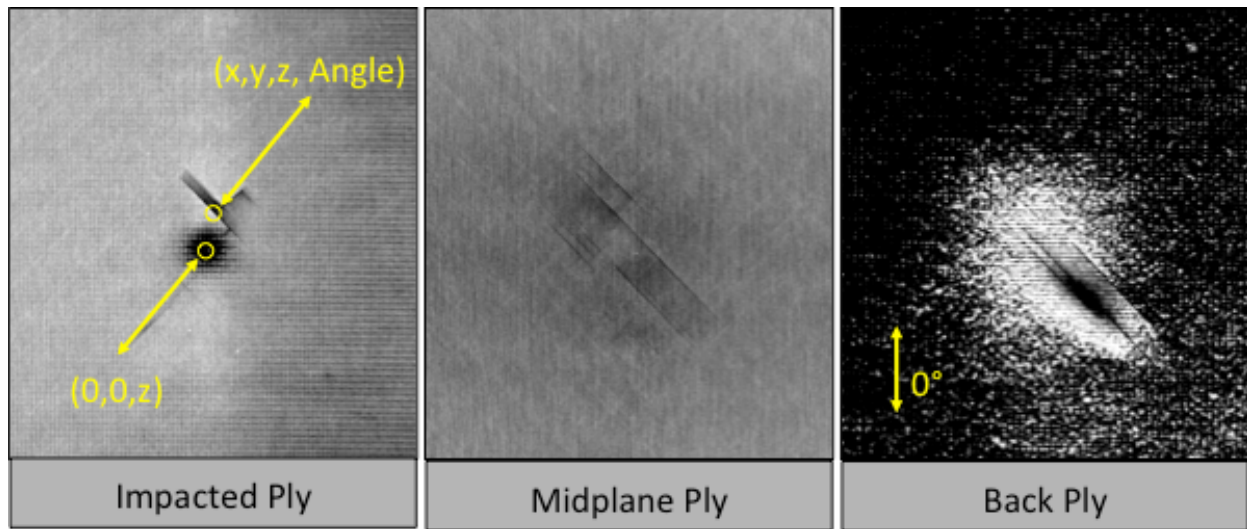


Figure 3.4.19 – Crack identification using X-ray CT for thin composite plates

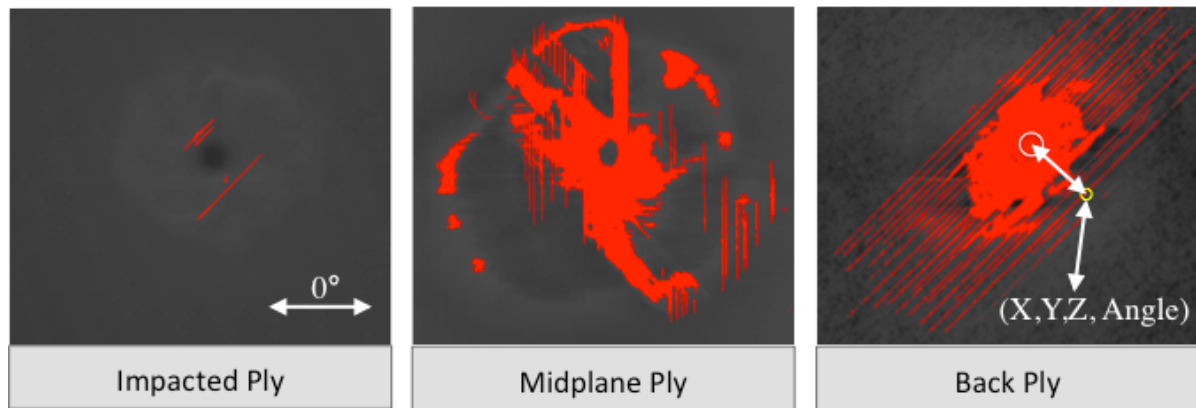


Figure 3.4.20 – Crack identification using X-ray CT for thick composite plates

Since the unstructured mesh does not align to the shape of the delamination pattern, a process of identifying the nodal coordinates to pre-impose matrix cracks needed to be developed. In many cases, matrix cracks were not considered if there were too close to the edges of the delaminated region. As a result, the crack would not insert due to the element selection process. The crack-limiting region had to be extended a few elements outward from the delamination pattern. The nodal coordinates were at least one element away from the edge of the crack-limiting region. Due to the selection process of the elements, the matrix cracks do not automatically align to the edges of the delaminated regions. Even though the process inserts a rough estimation of damage; it still provides remarkable potential as shown in Figure 3.4.21-22 for thin and thick composite plates.

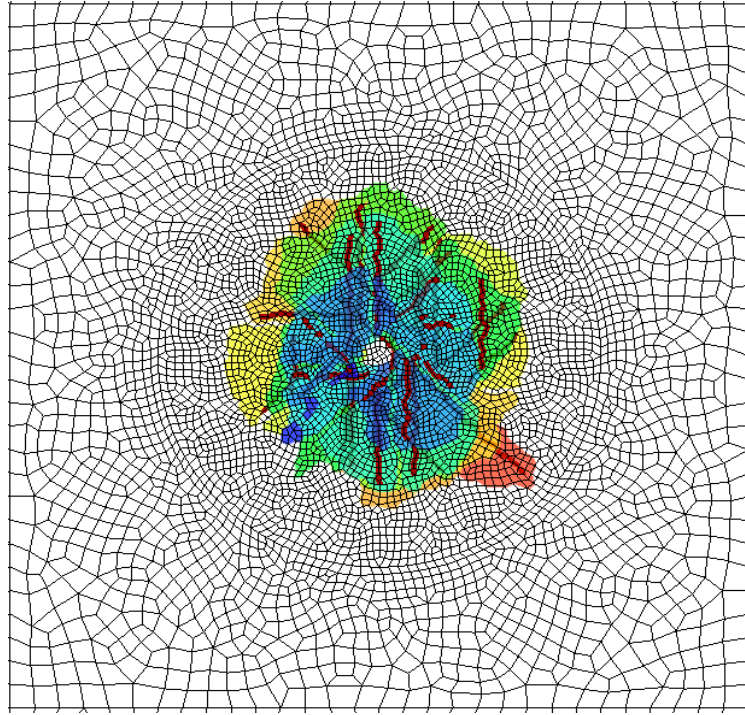


Figure 3.4.21 – Discretized model of pre-imposed cracks and delamination

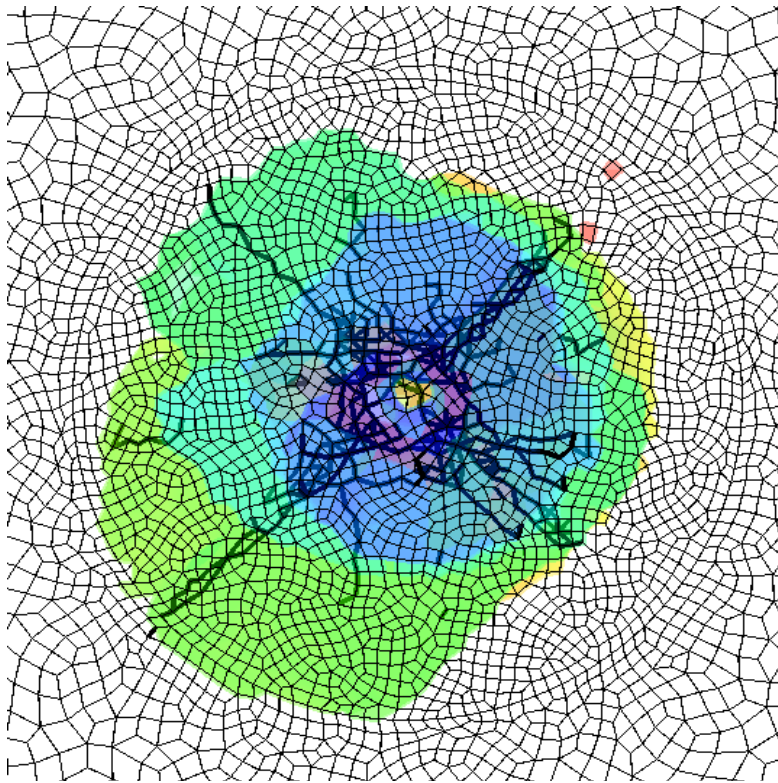


Figure 3.4.22 – Pre-imposed cracks and delamination for thick composite plates

3.5 Considerations for Optimization

The complexity of pre-imposing damage into the discrete damage model is challenging. Special consideration in mesh sensitivity should be noted. How the boundary conditions were applied and how they differ from the experiment. There are limitations in what types of damage nondestructive techniques can provide including resolution. Integrating nondestructive evaluation into discrete damage modeling is not automated and requires a significant amount of interpretation to ensure the damage is properly represented. This section discusses optimization techniques for discrete damage modeling.

3.5.1 Mesh Generation

Usually, the computational power of computers is a constraint on the number of degrees of freedom to solve complex problems. Mesh size is important to verify that the physics of the system is being captured. However, mesh size does not guarantee an improvement in the underlying results not to mention the propagation of damage. Different mesh size could yield different results for damage progression. Even if the limitation of mesh size was not there, could nondestructive evaluation support the modeling assumptions for the propagation of damage growth? Therefore, the assumptions of progressive damage failure are heavily dependent on the NDE assessment of damage. Since there are limitations in what NDE can capture, should similar restrictions be applied to the model?

It is imperative that nondestructive evaluation is used to develop mesh methods. The problem could become ill posed when the primary assumptions of failure of the model are constrained to the physical interpretation of a particular nondestructive technique. Compression after impact is an extremely complex mathematical problem when the system begins to incorporate cracks, delamination and progressive fiber failure. The mesh could be sensitive to the initiation and growth of damage, thereby affecting its capability to converge. The mesh size may have captured similar behavior seen in experiments, but more research needs to go into developing mesh methods. Nondestructive techniques define many of the boundary conditions and initial conditions of the problem when it comes to damage. The primary purpose is to ensure that the progression of failure could be identified by not only the model but captured through nondestructive techniques.

X-ray was a beneficial tool for identifying cracks in the composite. If cracks were the determining factor for failure, then the distance between adjacent cracks would determine the mesh size. BSAM's current limitation is that initiation of a crack must be six elements away from an adjacent crack. If the required distances between adjacent cracks begin to be too small, then the problem becomes computationally expensive. Homogenized crack mesh methods would need to be developed if the distance between adjacent cracks became too small. Therefore, many of the cracks are not represented in the model depending on the coarseness of the mesh.

If delamination is the determining factor for failure, then the mesh is determined using either the voxel length of the x-ray images or pixel length from c-scans. Numerous studies have been performed on the effects of delamination growth given a mesh size (Turon, Pienettire). The instantaneous failure of composites makes it somewhat ambiguous on what mesh size is needed for delamination growth.

If the permanent deformation is the determining factor for failure due to the localized stresses that occur at the indent, then a mesh size is determined by profilometry. Optical profilometry could obtain profiles at a 20-micron level. However, a mesh with a 20-micron size could be computationally expensive to use. Digital image correlation provides profilometry that is determined by the camera's pixel resolution and the correlation step of the test. However, using the pixel size of the images might be too coarse to capture the failure mechanisms that occur during compression after impact tests.

If fiber damage is the determining factor for failure, mesh size is determined by using the volume of the material representing fiber failure. However, NDE techniques are currently challenged in differentiating between matrix and fiber damage. The basic construct is that pre-imposed damage in the form of continuum damage techniques could give a realistic representation of the mechanical properties in the damaged region. Reducing the stiffness in the impacted region is the only way to model fiber damage if fiber damage exists. However, a reduced stiffness also means that there could be matrix damage. Pre-imposing fiber/matrix damage into the model must identify which is being pre-imposed into the model and how they affect each other.

The challenges of mesh sensitivity are documented regarding nondestructive evaluation. The near-term approach combines mesh methods between delamination and matrix cracks. The ultimate goal

is to come up with a viable mesh that captures the failure mechanism and be computationally tractable. The defining parameters and tolerances to accurately mesh and constraint a model could use the resolution of the nondestructive techniques as a benchmark.

It is important to note computational efficiency, which also correlates to mesh sensitivity. Pre-imposing cracks into the model add extra degrees of freedom. Therefore, if the mesh is too fine, the degrees of freedom makes the problem more computationally expensive. There is always a limitation to CPU usage and capability. Therefore more studies for mesh size need to be explored to predict the behavior of failure. However, all of these mesh consideration are for discussion. The following sections discuss some of the mesh parameters that were considered for the specific specimens examined in this work.

3.5.1.1 Mesh Generation for Thin Composite Plates

The unstructured mesh was generated using open source software GMSH (reference). The specimen's dimensions are 101.6 mm x 152.4 mm x 3.2 mm (4" x 6" x 1/8"). Mesh refinement was done in the center of the specimen to capture the initial damage state. The characteristic length for the damaged region is 1 mm². The GMSH script utilized a Box Field to perform the mesh refinement in the damage region. The square box had a length of 38.1 mm (1.5") and was located in the center of the plate. Figure 3.5.1 shows the frontal view of the mesh used for the problem. The total number of element per ply was 7847, which equates to 564,984 degrees of freedom assuming no pre-inserted cracks.

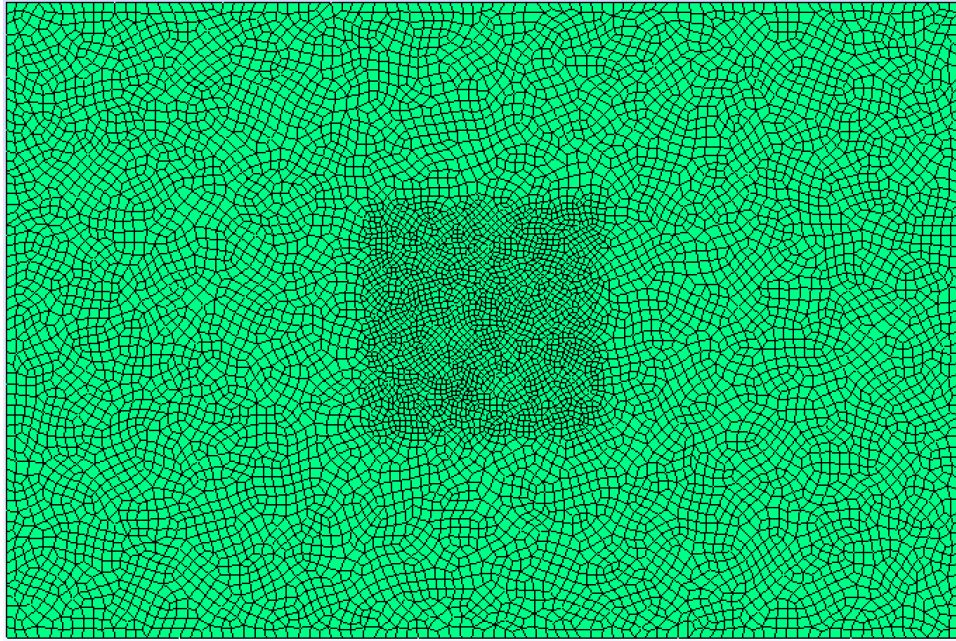


Figure 3.5.1 – Unstructured mesh of thin composite plate

3.3.1.2 Mesh Generation for Thick Composite Plates

The unstructured mesh was generated using open source software GMSH. The specimen's dimensions are 254 mm x 304.8 mm x 4.4 mm (10" x 12" x 0.173"). The specimen is partitioned into two regions. The first region in the center was used to capture the amount of initial damage. The thicker composite has 32 plies, which reduces the amount of elements each ply could have. Figure 3.5.2-3 shows the frontal view of the mesh used for the problem. The total number of elements per ply was 6340. The characteristic length used is closer to the composite thickness of the specimen.

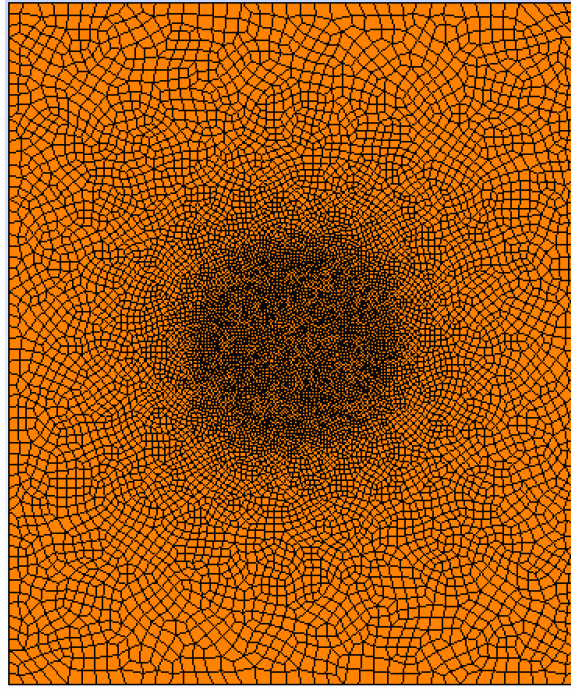


Figure 3.5.2 – Unstructured mesh of thick composite plate

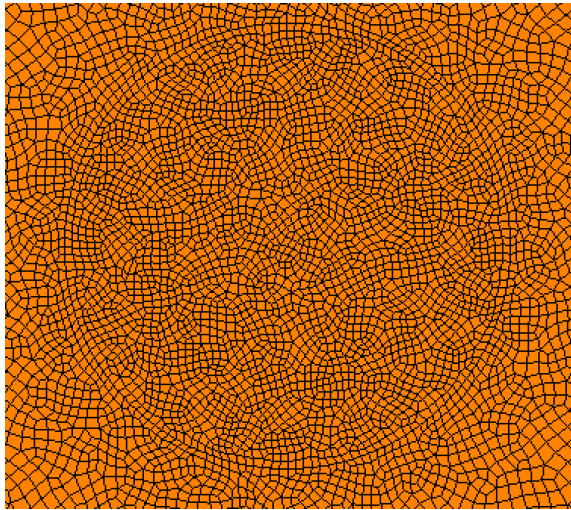


Figure 3.5.3 – Unstructured mesh of damage region of thick composite plate

3.5.1.3 Mesh Parameters and Degrees of Freedom

The mesh parameters in this study were arbitrary due to the limitation of the BSAM and computational capacity of the computer. The methodology was based on the total degrees of freedom of the entire model and memory.

3.6 Conclusions

In this paper, the capability to pre-impose realistic damage into a discrete damage model is proposed. The model takes into consideration the morphology, delamination and transverse matrix cracks. The morphology was obtained through profilometry and interfacial z-coordinate nodes were interpolated through the thickness of the composites. The discretized model conformed to the interpolated nodes. The delamination patterns were acquired by analyzing X-ray CT images with Simpleware software to extract an STL of the damage. The STL was then used to select interfacial nodes representing delamination. Transverse matrix cracks were found using X-ray CT. The damage acquired from nondestructive evaluation and inserted into a discrete damage model. The initial steps showed remarkable potential to solving real world problems with real world damage. Chapter 4 and 5 discusses the effect of damage on the compression strength after impact.

3.7 Future Work

3.7.1 Thermal Residual Stress

During the cure process, composites have thermal residual stresses in the composite. Currently the models do not consider any effects from the cure process. The complexity would involve several modeling steps. The first step would have to consider the thermal residual stress problem and appropriately applying the boundary conditions. The second step involves modeling the impact event. The third step would involve modeling the compression strength after impact. Each of these steps has added levels of complexity. Due to time constraints of the project, thermal residual stresses were not considered for the model. It is also important to note that thermal residual stress problems are difficult to understand when pre-imposed damage is incorporated. Research has not been explored to any detail about the thermal residual stresses when defects or damage are present in the material.

3.7.2 Nonlinearity

The current models incorporate an elastic Newton-Raphson approach to solving the boundary value problem. The reason for using the linear algorithm was the geometric imperfection of the permanent deformation. However, large displacements still occur even with a small indent. Future models will incorporate a Lagrangian geometric nonlinear algorithm to capture the large displacements.

3.7.3 Reduction of Modulus

Localized damaged in the impacted region does not affect the global stiffness of the composite, however, it can reduce the strength significantly. Future models to incorporate realistic fiber breakage will be explored. If nondestructive techniques could determine theoretical reduction of effective modulus then computational models could therefore use that as a basis to pre-impose damage through a continuum damage mechanics approach. Another methodology is the dislocation of nodes in a ply to represent a geometry imperfection within the ply that causes failure of a discretized homogenized element. The capability to artificially pre-impose a reduced stiffness into the discrete damage model could be all that is needed to predict the composite's residual strength.

Chapter 4: Part I - Numerical and Experimental Investigation of Compression Strength After Impact for Unidirectional Carbon Fiber Composites of Thin Plates

4.1 Compression Strength After Impact of Thin Composite Plates

Compression tests were conducted on five undamaged specimens for each stacking sequence to determine the baseline compression strength of the materials. Nondestructive evaluation was performed on one impacted specimen from each stacking sequence. The post-impacted specimens have recorded data from Digital Image Correlation (DIC) from the impact event described in Chapter 2.1. The primary goal is to create a model that could predict the behavior of failure. Using all the information from nondestructive evaluation and impact tests, a high fidelity model is constructed to determine if it could blindly predict the outcome of the compression after impact tests. The primary focus of this experimental-numerical study is to determine what parameters are necessary to predict the compression after impact strength of composites. The section goes into detail about the experimental tests and the finite element modeling conducted.

4.1.1 Material Specification

Carbon fiber reinforced polymers of IM7/977-3 were produced using a standard autoclave approach. Panels consisting of four different stacking sequences with 24 plies were provided by Air Force Research Laboratory (AFRL). Each of the panels had a dimension of 24" x 24" (609.6 mm x 609.6 mm) with a nominal cured thickness of 1/8" (3.2 mm). Each of the panels was C-Scanned to determine if there were any initial defects in the specimens. A waterjet process was used to cut the panels into 6" x 4" (152.4 mm x 101.6 mm) specimens according to ASTM 7136. After the waterjet was completed, the specimens were C-scanned a second time to determine if delamination, damage or other flaws occurred through the cutting process. Throughout this study, each stacking sequence is referred as the alpha numeric shown in Table 4.1.1.

Table 4.1.1 – Stacking Sequence

| Panel # | Stacking Sequence |
|---------|-----------------------------------------------|
| A | $[-45/90/45/90/-45/0/45/90/90/-45/90/45]_s$ |
| B | $[-45/45/-45/45/0/45/90/-45/45/-45/45/-45]_s$ |
| C | $[-45_3/90_3/45_3/0_3]_s$ |
| D | $[-45/90/45/0]_{3s}$ |

4.1.2 Sample Preparation

The specimens were immersed in water to perform c-scans using a 10 MHz probe to determine if there were any defects. As a result of being exposed to water and other conditions such as humidity, the specimens were dried before testing. Each of the specimens were put into a THELCO laboratory oven at 50°C to dry off the specimens for a day to evaporate any residual water that may have been present. Once the specimens were dried, they were put into a desiccator to prevent any effects of humidity. The specimens were taken out of the desiccator once testing was about to commence.

4.1.3 Baseline Compression Experiments

Static compression tests of 5 undamaged composites for each of the panels were conducted using a 50 kip MTS load frame. The dimensions of the composites were 6" x 4" (152.4 mm x 101.6 mm) with a nominal cure thickness of 1/8" (3.2 mm). The composite plates were compressed with a displacement load rate of 0.05 in/min. Each specimen is strain gauged and prepared in accordance to ASTM 7137. The fixture utilized for compression testing follows the standards developed by ASTM 7137. The Experimental setup is shown in Figure 4.1.1.



Figure 4.1.1 – ASTM 7137 Experimental Setup

4.1.4 Impact Experiments

Chapter 2.1 discussed the impact experiments in great detail. Digital image correlation was performed on a subset of the experiments to record the strains and displacements of the specimens. The damage threshold strain (DTS) was discovered which could be used to design future experiments. The DTS is the back surface strain of the specimen where damage initiates during the impact event.

4.1.5 Compression Strength After Impact Experiments

The impacted specimens are mounted into a compression fixture in accordance to ASTM 7137, “Standard Test Method for Compressive Residual Strength Properties of Damaged Polymer Matrix Composite Plates.” The progressive compression failure primarily starts from the impact damage region. Initially, as the compressive load increases, delamination formed the by the impact propagates in a local buckling form. Unlike impact-induced delamination, its propagation is mainly opening-dominated. An inclined angle around 30-45 degrees (with respect to the compressive loading direction) was observed from the two vertical edges of the failed specimen. These results are similar to previous compressive failure results by Daniel and Ishaii [77], Tsai and Sun [78], Oguni and Ravichandran [79]. From load-displacement curve for a compressive experiment of an impacted specimen, the initial non-linear part is

caused by the initial compliance in the test machine and CSAI compressive fixture. Then a long linear load-displacement part was recorded. The failure mode starts from an opened, impact-induced delamination (shear-dominated), followed by a sudden propagation of the longitudinal matrix crack and a final shear crack appeared along the specimen edge based on the recorded high-definition video.

4.1.5.1 Procedure

Four 350-ohm resistance strain gauges were applied to each of the composites in accordance to ASTM 7137 and calibrated to 30,000 microstrain. The samples were carefully put into the compression fixtures specified to the standard. The specimens were clamped into the compression fixture using a torque wrench at 75 in-lbs. The fixture was placed onto the actuator of the MTS 50 kip (222 kN) load frame. The crosshead was moved to the appropriate height to accommodate for the test. The actuator was moved to create just enough traction between the top compression and the crosshead. Alignment was checked at 35 lbs (155 N) and 100 lbs (444) to ensure it was within the 10% error allowable. If the conditions were not met, metallic spacers were used to aid in the adjustment in the alignment. Once this was complete, all the cameras were positioned and calibrated. The specimen was once again loaded to 35 lbs (155 N) to verify if there were any eccentricities in the strain gauges and a still image was captured. Finally, the tests began to put a compression load using a displacement control of 0.05 in/min (1.27 mm/min).

4.1.5.2 Digital Image Correlation

Digital image correlation was performed on both the impacted and back surface of the composite specimen. Cameras were set to the recommended 25 degree separation to ensure accurate strains and out-of-displacements were obtained. The impacted surfaces used 35 mm lenses and the back surface used 20 mm lenses. Prior to testing, a standard process of DIC calibration was conducted.

4.1.5.3 DIC Data Capture

Each camera was set to capture 5 frames per second of the experiment. Load and displacement data from the MTS load frame was captured using National Instruments USB-9162 Data Acquisition device and connected into the analog reader that is provided with the Correlated Solution, Inc. software.

The strain gauges were put into the remaining outputs of the DAQ to record strain data. The strain gauges were calibrated for 30,000 microstrain per volt.

4.2 Results And Discussion

4.2.1 Baseline Compression Experiments

Baseline tests indicated that the ultimate compression load of the composite Panels A, B, C, and D were 90.75 ± 2.12 kN (20.4 ± 0.5 kip), 104.29 ± 3.88 kN (23.4 ± 0.9 kip), 89.22 ± 8.74 kN (20.1 ± 2.0 kip), and 106.97 ± 8.81 kN (24.0 ± 2.0 kip) respectively. Table 4.2.2 shows the experimental data of the baseline compression tests. The ultimate compressive strength (F^{CAI}) of the composites was calculated using the equation $F^{CAI} = P/A$, where P is the ultimate compression load and A is the cross-sectional area of the specimen. The effective modulus is calculated using, $E^{CAI} = (P_{3000} - P_{1000}) / ((\epsilon_{3000} - \epsilon_{1000}) * A)$, taking the applied force corresponding to 1000 and 3000 microstrain. The same equations were used for the compression after impact experiments. Figure 4.2.1 is a bar chart of the maximum load for the experiments conducted and Figure 4.2.2 is the load displacement curves. Figure 4.2.3 is the stress versus strain curves obtained from experiment.

Table 4.2.1 – Baseline compression experimental data

| Panel # | Load kN (kip) | Strength MPa (ksi) | Effective Modulus GPa (ksi) |
|---------|--------------------------------------|-----------------------------------------|------------------------------------------|
| A | 90.75 ± 2.12 (20.4 ± 0.5) | 279.095 ± 6.209 (40.5 ± 0.9) | 34.666 ± 0.525 (5027.9 ± 76.2) |
| B | 104.29 ± 3.88 (23.4 ± 0.9) | 320.782 ± 11.932 (46.5 ± 1.7) | 35.356 ± 0.463 (5128.0 ± 67.1) |
| C | 89.22 ± 8.74 (20.1 ± 2.0) | 274.435 ± 26.886 (39.8 ± 3.9) | 57.119 ± 0.645 (8284.4 ± 93.6) |
| D | 106.97 ± 8.81 (24.0 ± 2.0) | 329.009 ± 27.084 (47.7 ± 3.9) | 57.093 ± 0.450 (8280.6 ± 64.5) |

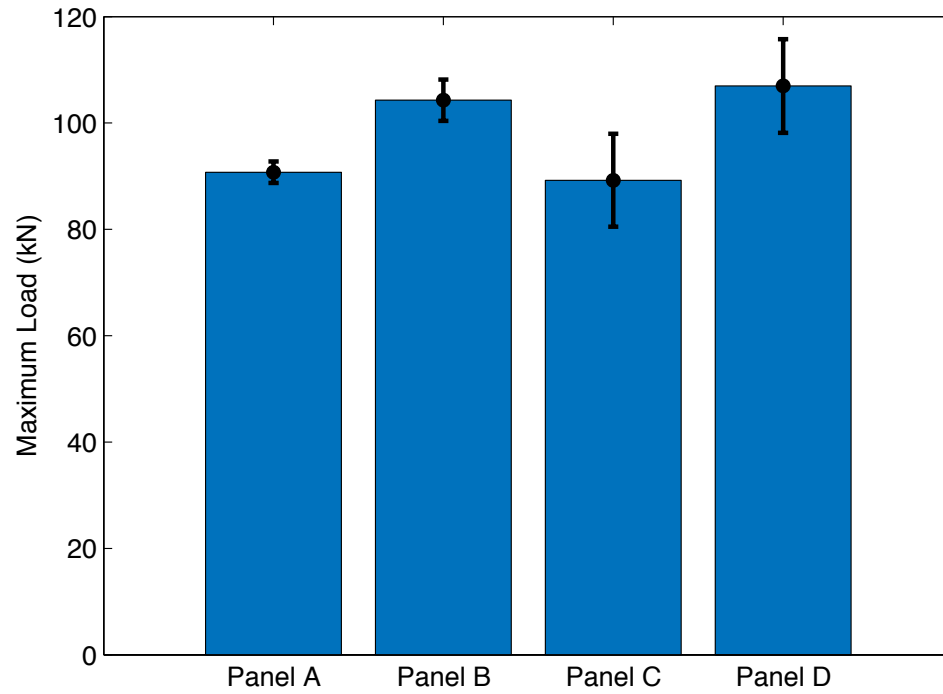


Figure 4.2.1 – Maximum load: undamaged compression specimens

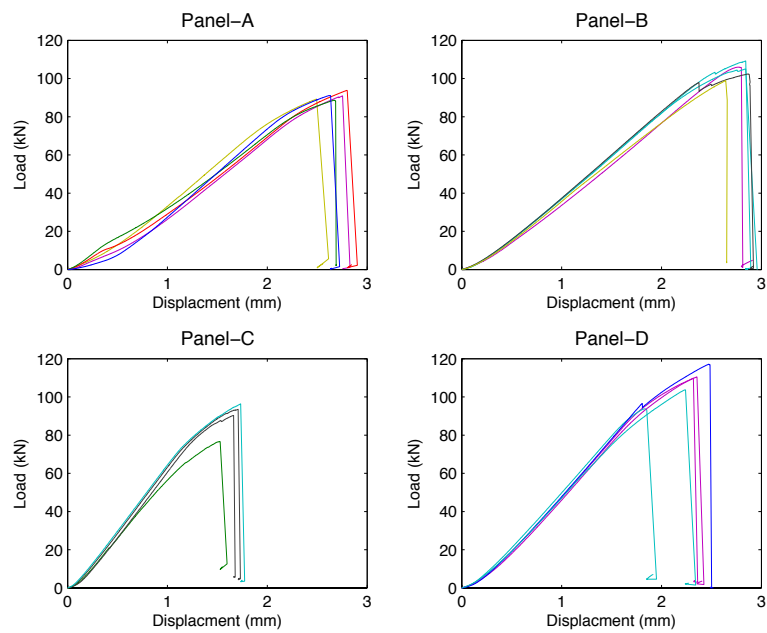


Figure 4.2.2 – Load vs displacement: undamaged compression specimens

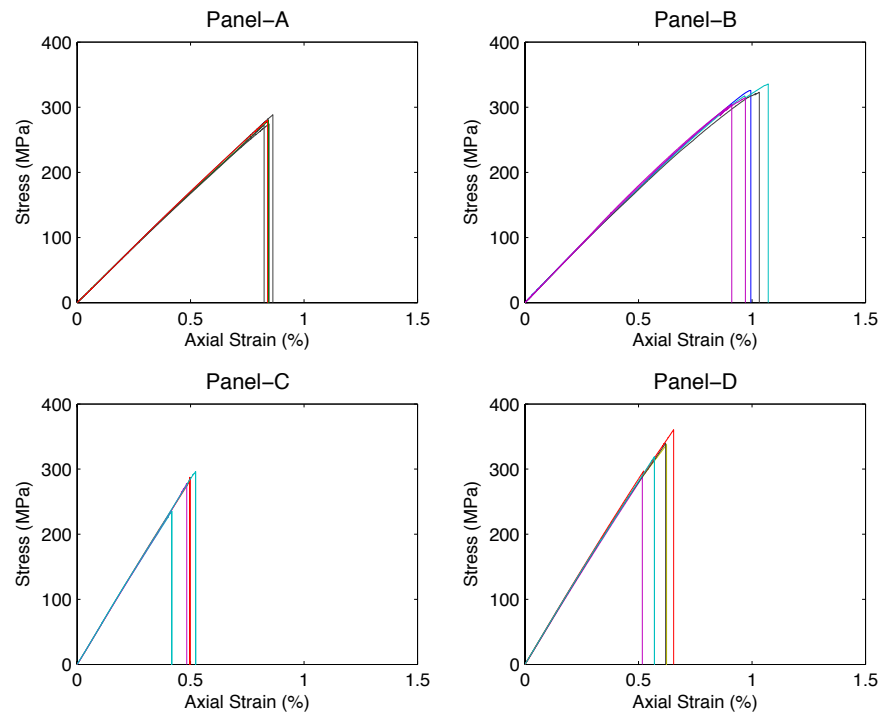


Figure 4.2.3 – Strain vs strain: undamaged compression specimens

4.2.2 Impact Experiments

Each of the stacking sequences were impacted with ½” (12.7mm) hemispherical tupper with 10J of energy. Section 3.1 discusses in detail the recorded data capture from the experiments. The speed of the tupper prior to impact was 1.888 m/s (74.33 in/s). The mass of the tupper was 5.198 kg. Table 4.2.1 lists some of the information obtained from the experiments such as maximum load, damage threshold load (DTL), and damage threshold strain (DTS). The area was calculated using the amplitude data of the c-scan images.

Table 4.2.2: Impact Experimental Values

| Panel | Maximum Load kN | DTL kN | DTS % | Area mm ² |
|-------|--------------------|-----------|----------|-------------------------|
| A | 5.601 | 3.345 | 1.106 | 704.87 |
| B | 5.452 | 3.741 | 1.161 | 571.43 |
| C | 4.733 | 1.751 | 0.871 | 2545.36 |
| D | 5.588 | 3.000 | 1.052 | 636.85 |

4.2.3 Residual Compression Strength After Impact

One specimen from each of the stacking sequences was selected for compression strength after impact testing. Table 4.2.3 displays the experimental data for the compression after impact tests. Figure 4.2.4 is a graph showing the load vs displacement. The strength vs strain is shown in Figure 4.2.5. The reduction of strength for Panels A, B, C, D were 31.440%, 31.139%, 22.906%, and 26.018% (Figure 4.2.6).

Table 4.2.3 – Compression after impact experimental data

| Panel # | Load kN (kip) | Strength MPa (ksi) | Effective Modulus GPa (ksi) | Reduction % |
|---------|------------------|-----------------------|--------------------------------|----------------|
| A | 62.211 (13.986) | 191.348 (27.753) | 35.582 (5160.720) | 31.440 |
| B | 71.817 (16.145) | 220.894 (32.038) | 37.034 (5371.444) | 31.139 |
| C | 68.786 (15.464) | 211.572 (30.686) | 58.594 (8498.358) | 22.906 |
| D | 79.137 (17.791) | 243.407 (35.303) | 58.164 (8436.048) | 26.018 |

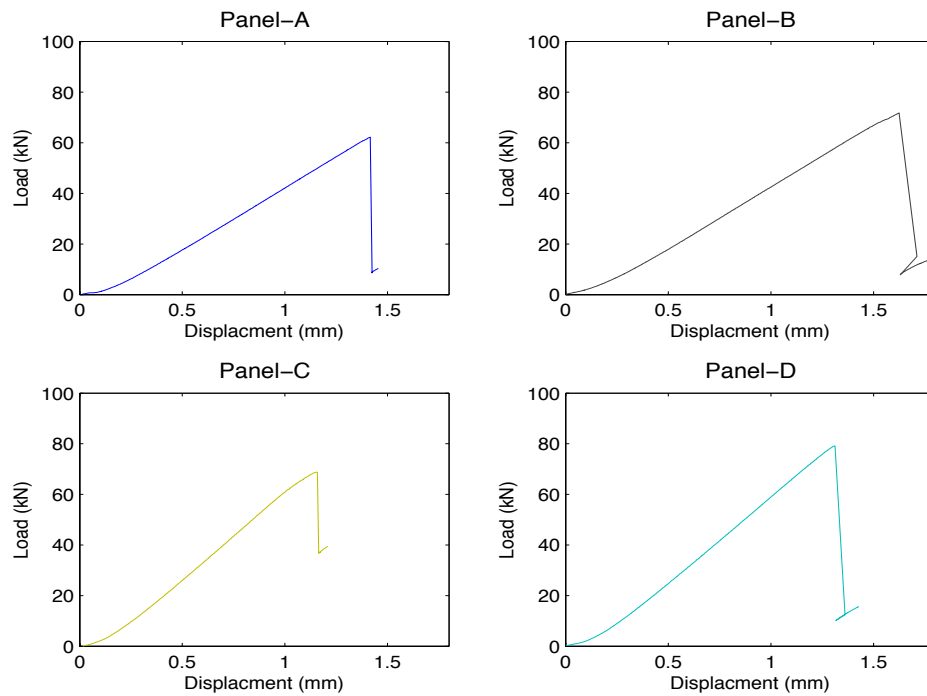


Figure 4.2.4 – Load vs displacement: compression strength after impact

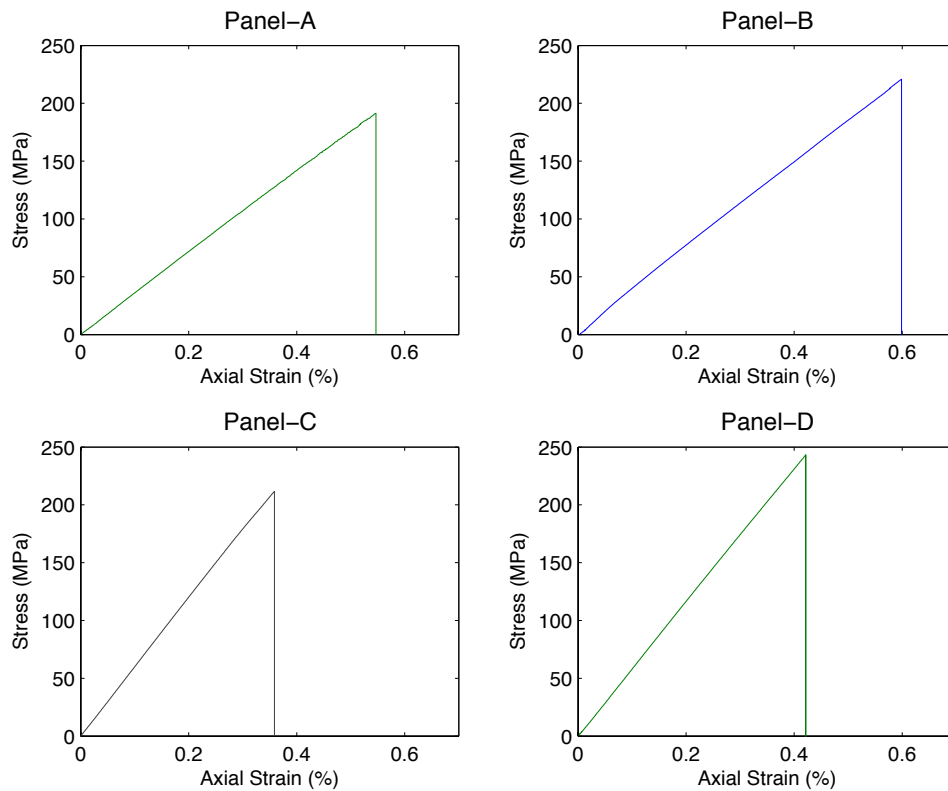


Figure 4.2.5 – Stress vs strain: compression strength after impact

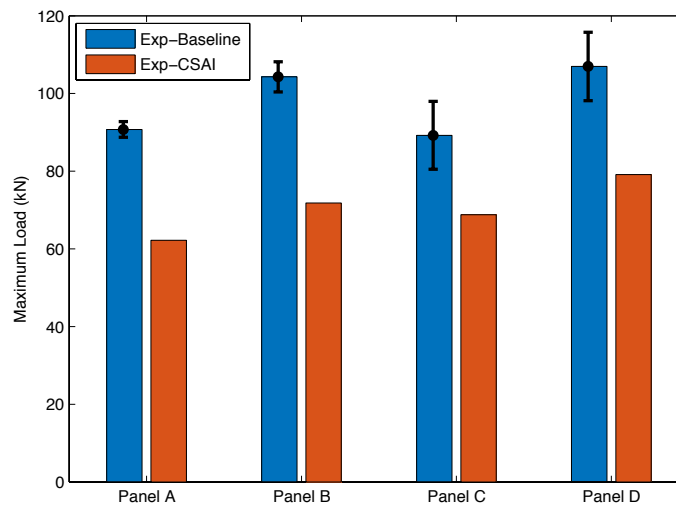


Figure 4.2.6 – Compression strength after impact: Undamaged vs damaged

Although there was a reduction of compression strength of the specimen, there was no significant reduction of modulus of the overall specimen. The difference in modulus between the

impacted specimens and the baseline undamaged specimens was 2.642%, 4.747%, 2.582%, and 1.877% respectively. The average axial ultimate strain (physical strain gauges) for panel A-D of the baseline undamaged experiments were 2.359%, 1.695%, 2.530%, and 2.342%. The residual axial ultimate strain was 0.547%, 0.599%, 0.359% and 1.877%. The reduction of strain from the baseline experiments was calculated to be 76.819%, 64.681%, 85.821%, and 19.868%. Panel D had the lowest drop in compressive strain, however did not have the lowest drop in compressive strength. Panel C had a larger delaminated region, the lowest drop in compressive strength, and the highest drop in strain. Panel A and Panel B had a similar reduction of strength.

4.3 Digital Image Correlation

Digital image correlation was performed on the impacted and back surface of the specimens for compression tests. The angles between the cameras were within 25° to the distance of the surface of the specimen to ensure accurate strain measurements. When correlating the images, the orientation of the cameras shows that the actuator from the MTS load frame comes from the bottom. The crosshead is located on the top. The speckle pattern was sprayed over the 350-ohm resistant strain gauges. The 350-ohm strain gauges were placed on the composite in accordance to ASTM 7137 to ensure alignment was met. The DIC strain gauges were placed so they could be compared to previous experimental strains.

Even though the knife edges of the compression fixture was used to minimize the effects of buckling, DIC and the strain gauges indicated that each of the specimens experience some form of bending deformation. The contours show the complexity of the how stacking sequences affects the overall compression strength of the composites. Although there are similarities among some of the Panels, it is difficult to infer the behavior of failure. Each of the images shown below are taken 3 seconds prior to failure. To analyze the displacement data, rigid body motion was removed from the computation. The axial, transverse, and out-of-plane displacements were recorded. Axial displacement is in relation the loading direction, which is in the y-direction.

4.3.1 DIC: Displacement and Strain Contours

Full-field displacement and strain contours for specimen A with stacking sequence $[45/90/45/90/-45/0/45/90/90/-45/90/45]_s$ are shown in Figures 4.3.1-2. U-displacements indicate slight variations in the global response 3-seconds before failure and include a discontinuity coincident with a surface matrix crack on the back surface of the specimen. V-displacements are relatively smoothly varying, while also showing a slight asymmetry of behavior. The asymmetry in both the U and V displacements may indicate a slight side-to-side bending of the specimen. Out-of-plane displacements (W) show evidence of both global buckling (smooth contour variations across specimen faces) and local, sub-laminate buckling localized around the center of the specimen. Additionally, the back surface W displacement displays a discontinuity associated with the surface matrix crack also observed in the U-displacement field.

Axial (ϵ_{yy}), transverse (ϵ_{xx}), and shear (γ_{xy}) strains (Figure 4.3.3) are, in general, smoothly varying with, as may be expected, local extreme variations around the impact damage. The only discernable clear, global trend is that axial strain on the impacted side is more compressive on average than on the back face. This could indicate a global propensity for the specimen to bend away from the impacted surface.

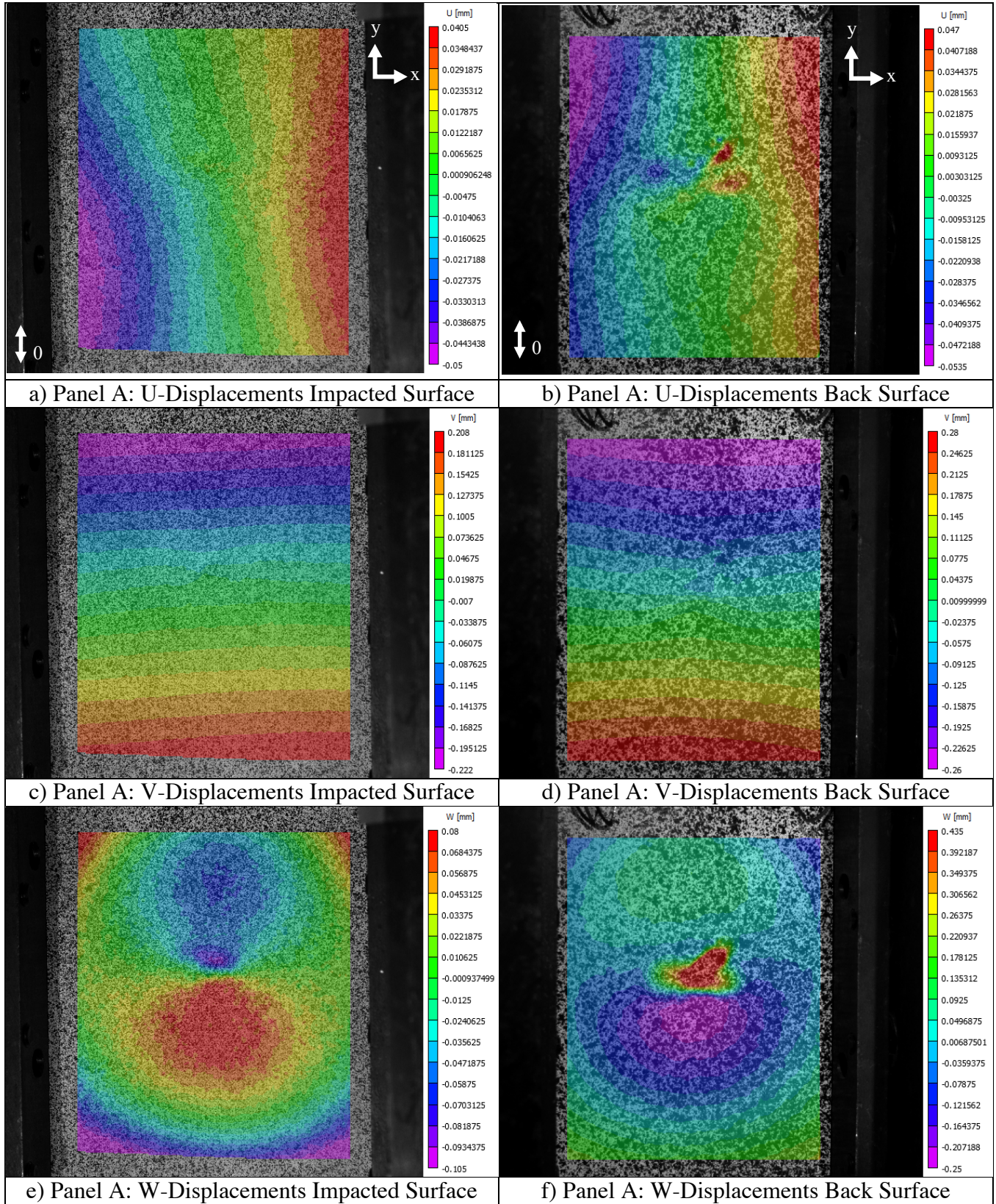


Figure 4.3.1 – Panel A: DIC images of displacements, 3 seconds prior to failure

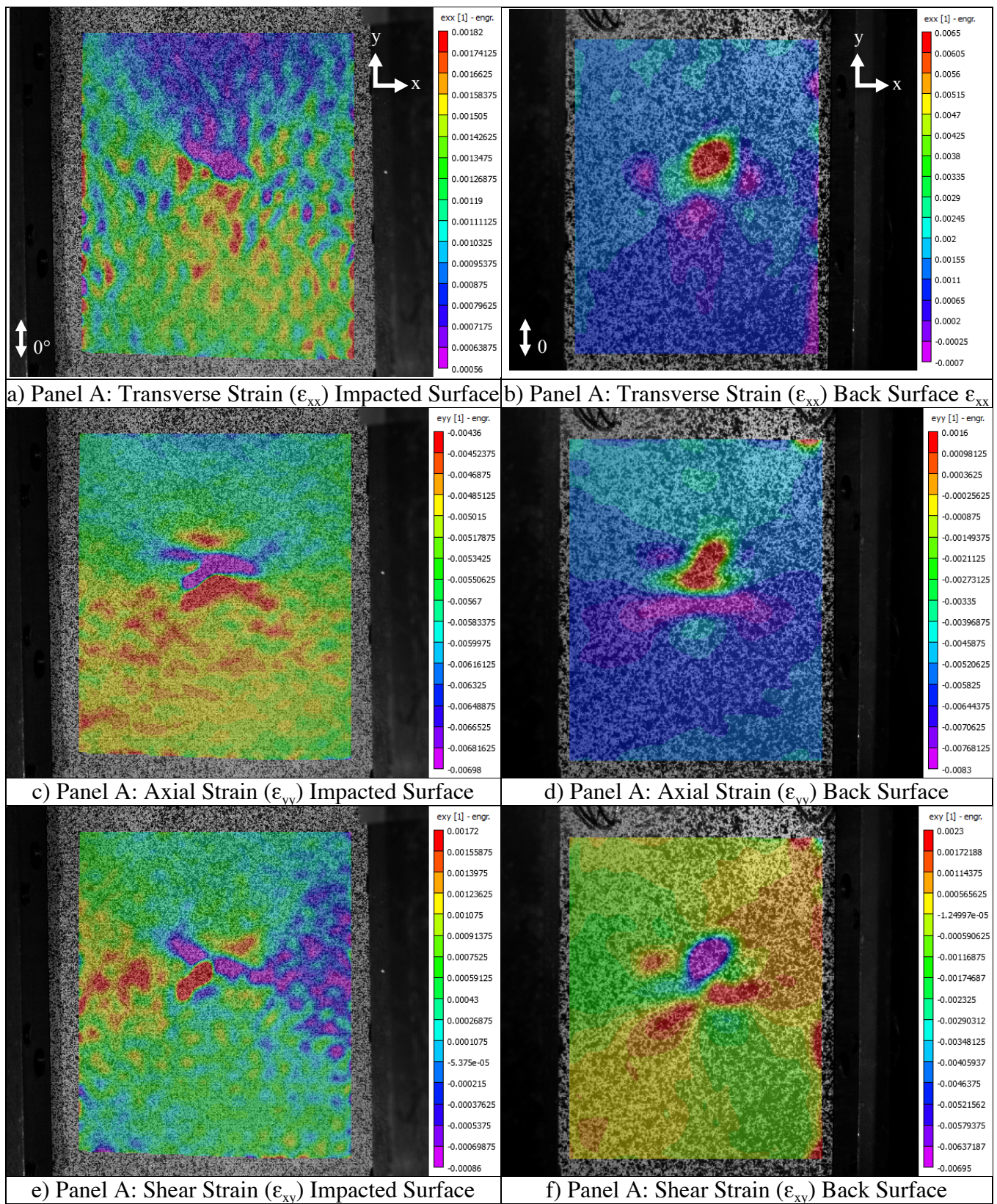


Figure 4.3.2 – Panel A: DIC images of strains, 3 seconds prior to failure

Full-field displacement and strain contours for specimen B with stacking sequence $[-45/45/-45/45/0/45/90/-45/45/-45/45/-45]_s$ are shown in Figures 4.3.3-5. U-displacements indicate slight variations in the global response 3-seconds before failure and include a discontinuity coincident with a surface matrix crack on the back surface of the specimen. V-displacements are relatively smoothly varying, while also showing a slight asymmetry of behavior. The asymmetry in both the U and V displacements may indicate a slight side-to-side bending of the specimen. Out-of-plane displacements (W) show evidence of both global buckling (smooth contour variations across specimen faces) and local, sub-laminate buckling localized around the center of the specimen. Additionally, the impacted surface W displacement displays a discontinuity associated with the surface matrix crack also observed in the U-displacement field. Figure 4.3.4 shows out-of-plane displacement 5 seconds prior to failure. This pattern, which is different than at 3-seconds prior to failure, indicates that the specimen experiences a change in the global buckling mode in the last phases of testing.

Axial (ϵ_{yy}), transverse (ϵ_{xx}), and shear (γ_{xy}) strains (Figure 4.3.5) are, in general, smoothly varying with, as may be expected, local extreme variations around the impact damage. Similar to Panel A, the global trend is that axial strain on the impacted side is more compressive on average than on the back face. This could indicate a global propensity for the specimen to bend away from the impacted surface.

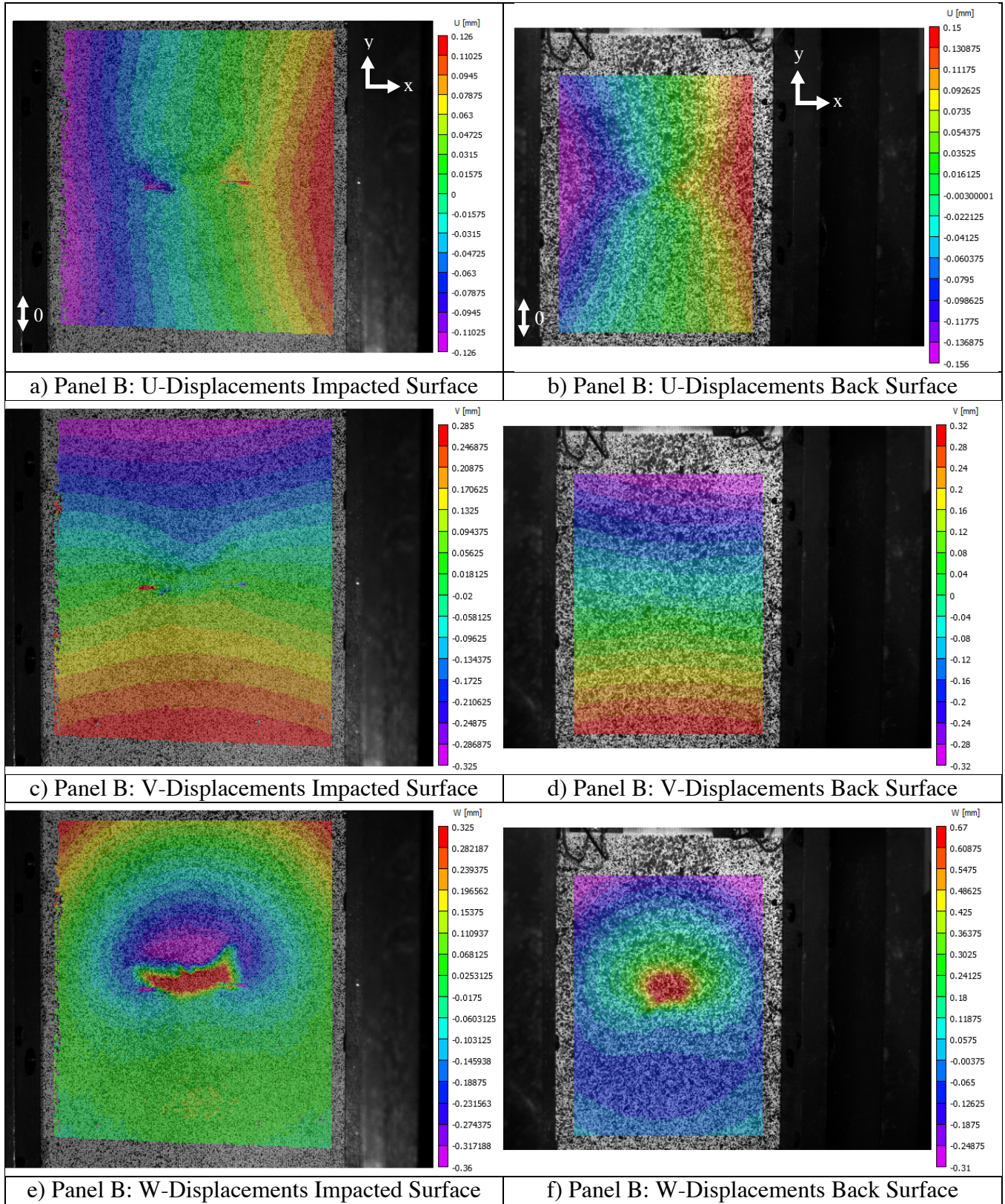


Figure 4.3.3 – Panel B: DIC images of displacements, 3 seconds prior to failure

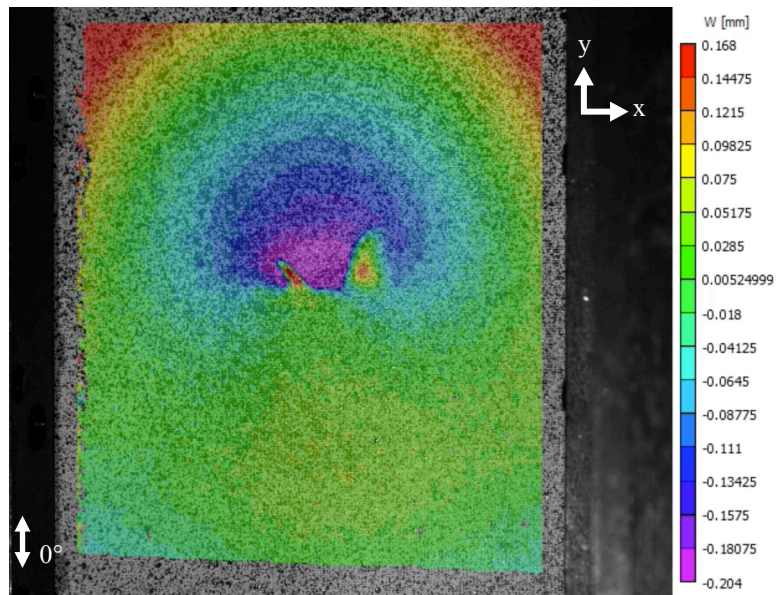


Figure 4.3.4 – W Displacements: Panel B impacted surface 5 seconds prior to failure

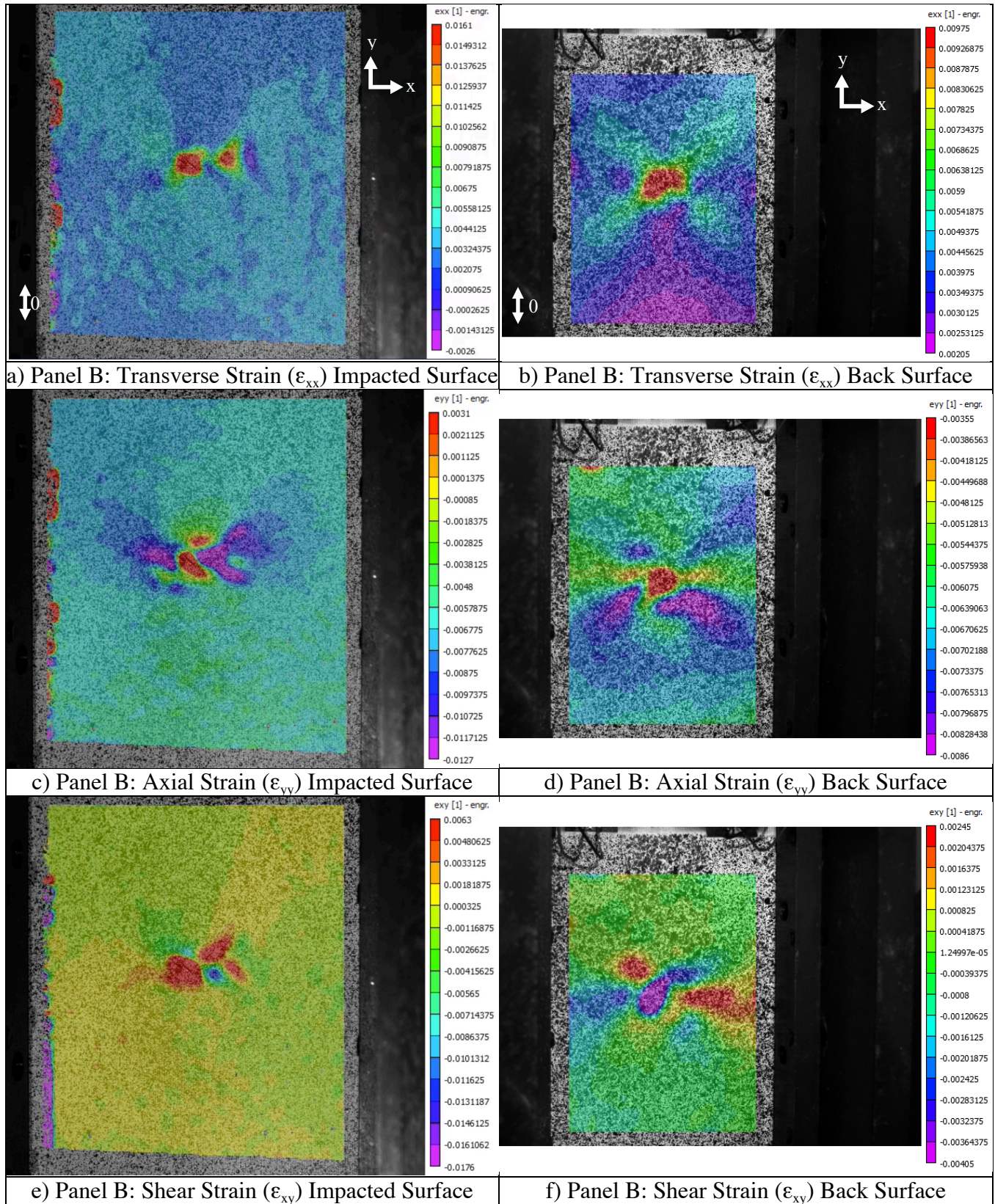


Figure 4.3.5 – Panel B: DIC images of strains, 3 seconds prior to failure

It is difficult to infer any behavior for Panel C, $[-45_3/90_3/45_3/0_3]_s$, due to the amount of internal and external damage present in of the specimen. The discontinuity in the u-displacement for the back surface show the large transverse matrix crack created from the impact event (Figure 4.3.6.b). Even though the v-displacements are smoothly varying through out the specimen for both the impacted and back surfaces, the out-of-plane displacements still indicated buckling behavior (Figure 4.3.6.c-d). Panel C exhibits a primary bilateral buckling mode behavior throughout the entire experiment (Figure 4.3.6.e).

Due to the large amount of internal and external impact damage present in Panel C, the strains are dominated by local variations, especially associated with the large surface crack on the back face of the specimen. The strains did not correlated well enough to determine the pre-dominate modes of failure (Figure 4.3.7). Panel C was more flexible in bending, generating behavior that was significantly different than Panels A, B, and D.

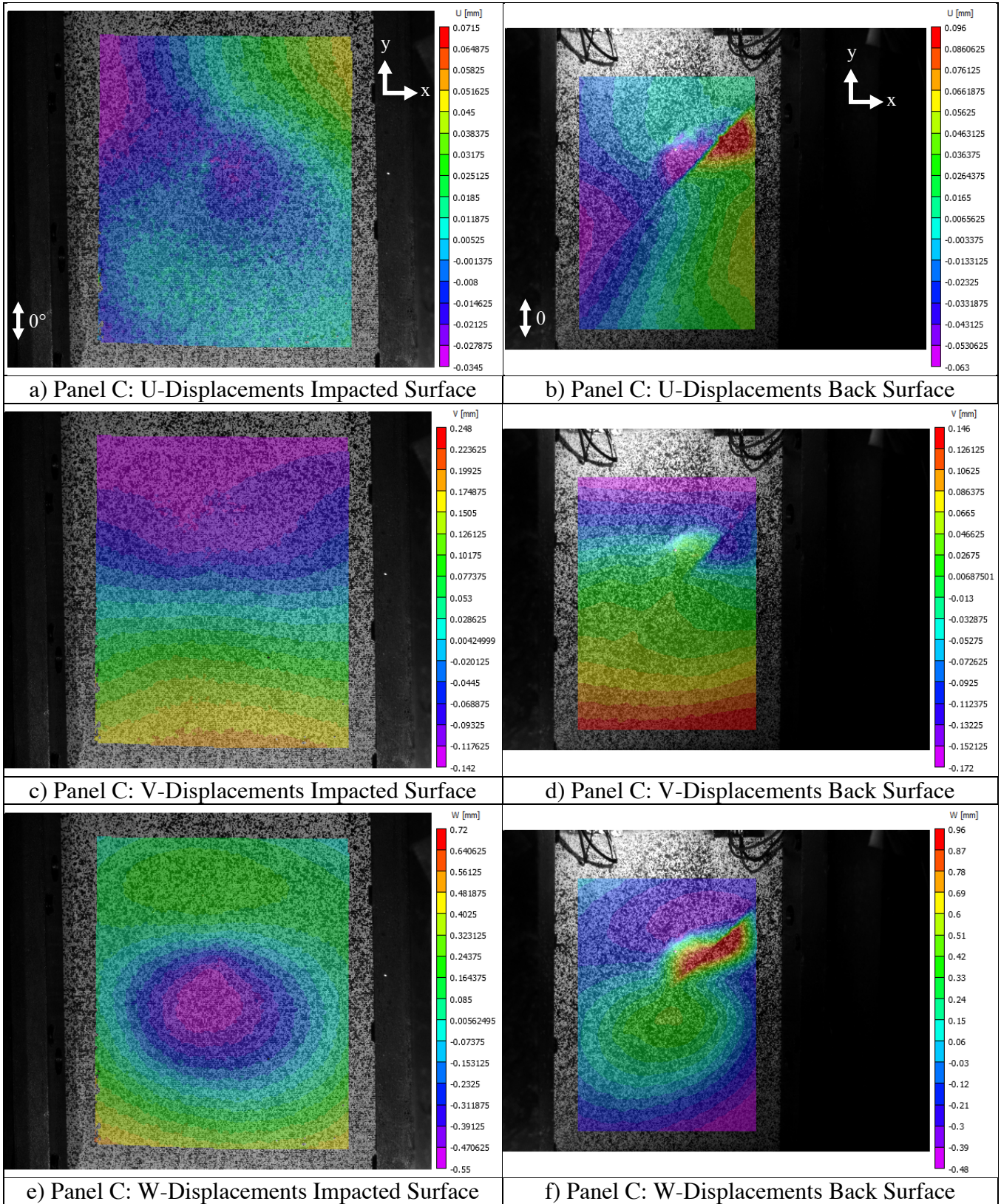


Figure 4.3.6 – Panel C: DIC images of displacements, 3 seconds prior to failure

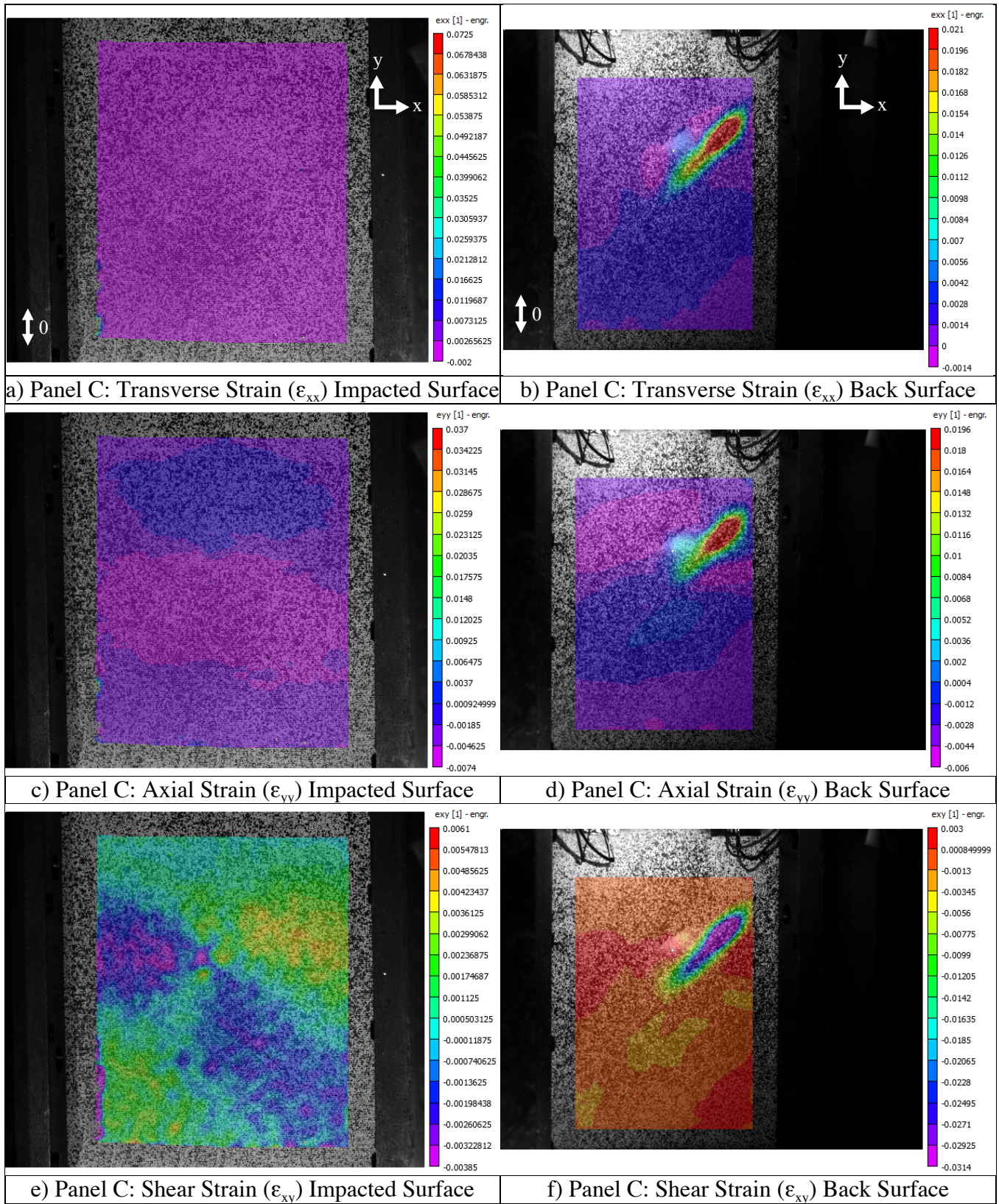


Figure 4.3.7 – Panel C: DIC images of strains, 3 seconds prior to failure

Full-field displacement and strain contours for specimen D with stacking sequence $[-45/90/45/0]_{3s}$ are shown in Figures 4.3.8-9. U-displacements indicate slight variations in the global response 3-seconds before failure and include a discontinuity coincident with a surface matrix crack on the back surface of the specimen. V-displacements are relatively smoothly varying, while also showing a slight asymmetry of behavior. The asymmetry in both the U and V displacements may indicate a slight side-to-side bending of the specimen. Out-of-plane displacements (W) show evidence of both global buckling (smooth contour variations across specimen faces) and local, sub-laminate buckling localized around the center of the specimen. Additionally, the impacted surface W displacement displays a discontinuity associated with the surface matrix crack also observed in the U-displacement field.

Axial (ϵ_{yy}), transverse (ϵ_{xx}), and shear (γ_{xy}) strains (Figure 4.3.9) are, in general, smoothly varying with, as may be expected, local extreme variations around the impact damage. Similar to Panel A and B, the global trend is that axial strain on the impacted side is more compressive on average than on the back face. This could indicate a global propensity for the specimen to bend away from the impacted surface.

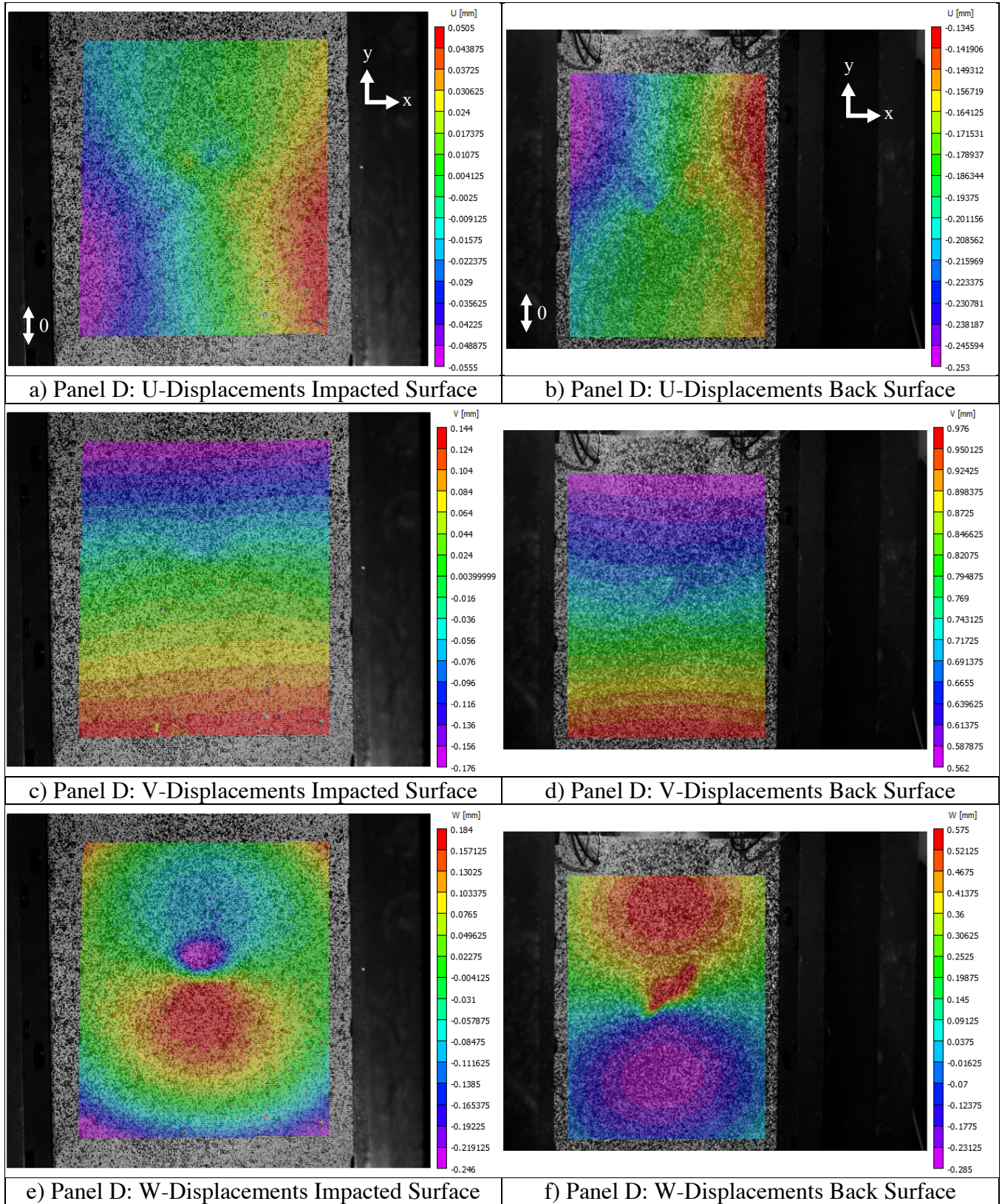


Figure 4.3.8 – Panel D: DIC images of displacements, 3 seconds prior to failure

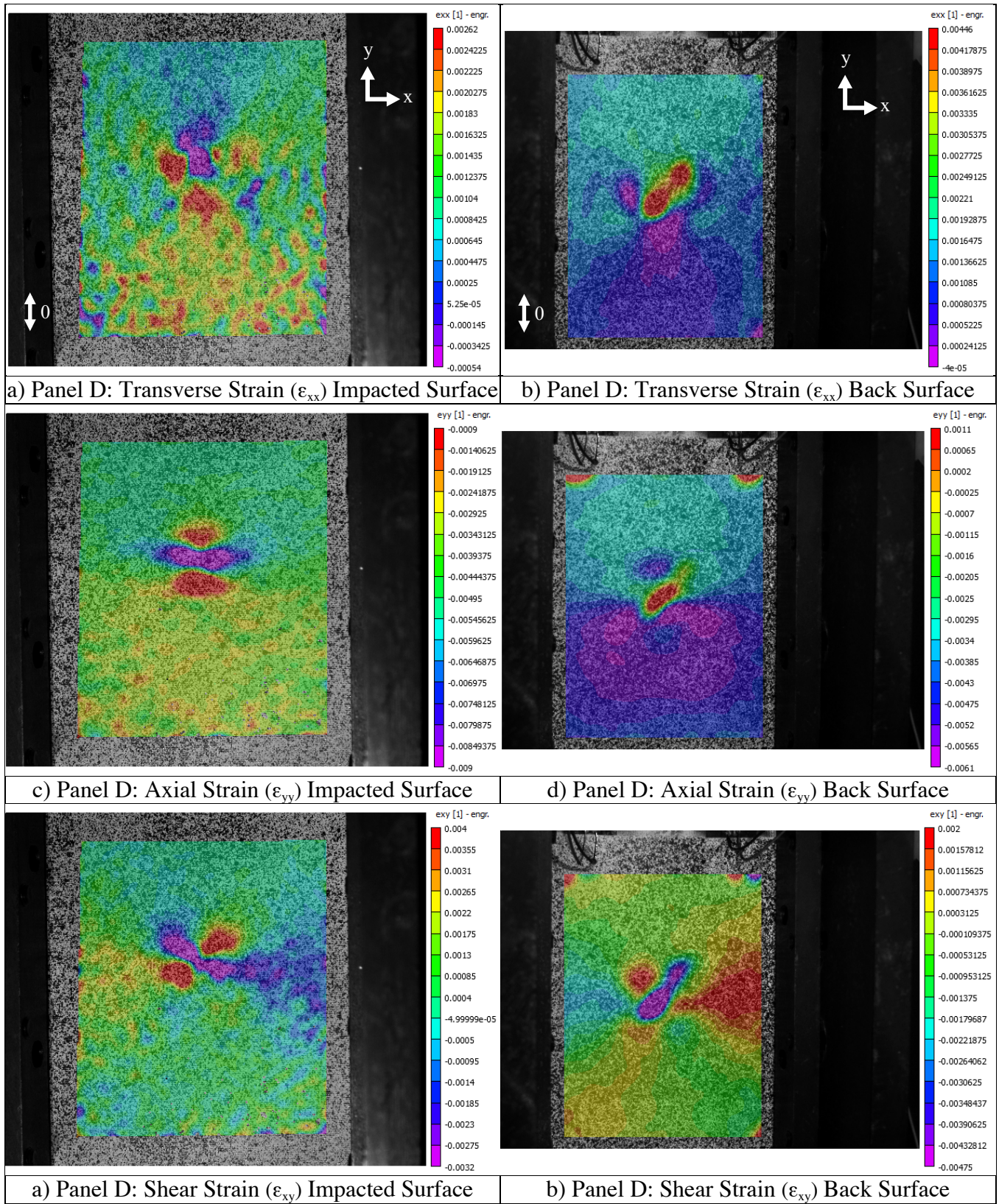


Figure 4.3.9 – Panel D: DIC images of strains, 3 seconds prior to failure

Even though the responses between displacement contours for each stacking sequence appear to behave differently, the strains appear to be similar with the exception of Panel C. Transverse matrix cracks could effect how the images are correlated when calculating displacements, however, unexpectedly the global strains do not seem to be affected by the presence of transverse matrix cracks. Panel B, also indicated that in the presence of a transverse matrix crack, the overall behavior of composite was a primary buckling mode. This likely means that the opening of a crack does not influence the overall buckling mode of the composite specimens. It could be that the stacking sequence plays a bigger role in determining the buckling mode behavior than the amount of damage present in the composite. All the specimens failed catastrophically and there were no indications of damage growing throughout the test.

4.3.2 DIC: Virtual Strain Gauge vs Actual Strain Gauge Response

Using DIC strain data, virtual strain gauges were placed near the physical 350-ohm strain gauges placed on the specimen to obtain real-time information on the strain. The virtual strain gauges correlated well with the experimental strain gauges. Figure 4.3.10 displays the locations of the strain gauges within the DIC window. The variables R0, R1, R2, refer to the left, right, and center virtual strain gauges that were placed in the correlated images, while E1 and E2 represent the actual strain gauge locations. Figure 4.3.11-4.3.14 shows strains obtained from DIC and experiment for both the impacted and back surfaces of the compression after impact tests.

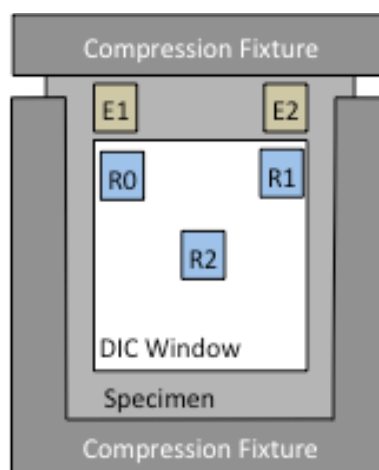


Figure 4.3.10 – DIC Strain Location

The axial strains from the experiment correlated well with those obtained from DIC. For each of the experiments, the virtual strain gauges appeared to experience the same behavior as the experimental ones. The center strain gauges indicated that there were higher localized strains near the indent for the impacted surface. However, for the back surface the center strain gauges were lower than the far-field strain gauges both actual and virtual. For the impacted surface, the localized axial strains near the center reached a value of 1% strain until ultimate failure.

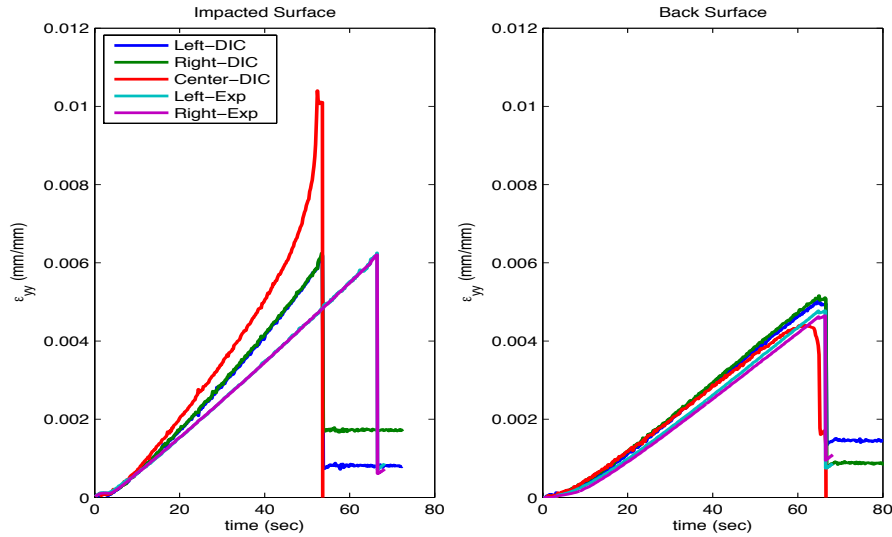


Figure 4.3.11– Axial Strain (ϵ_{yy}) vs time: Panel A

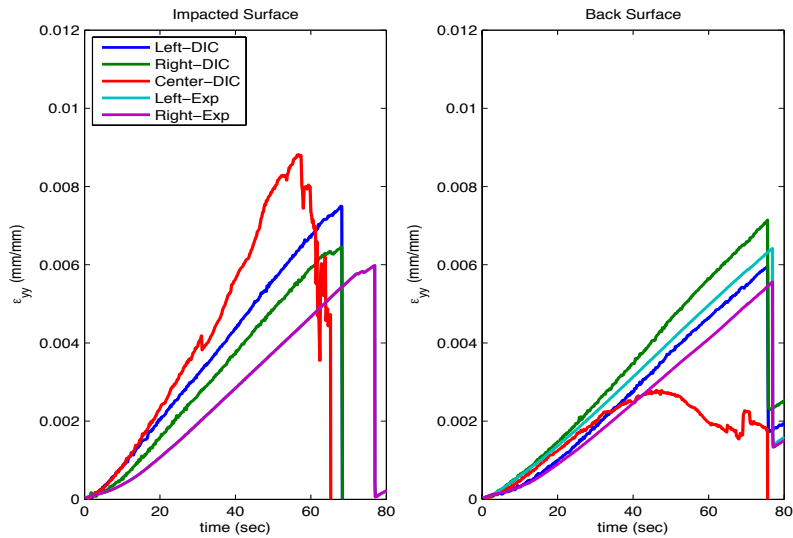


Figure 4.3.12 – Axial Strain (ϵ_{yy}) vs time: Panel B

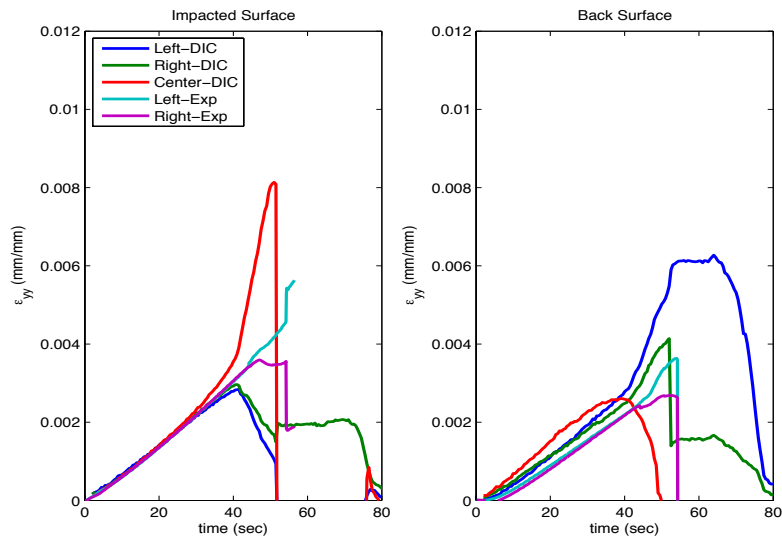


Figure 4.3.13 – Axial Strain (ϵ_{yy}) vs time: Panel C

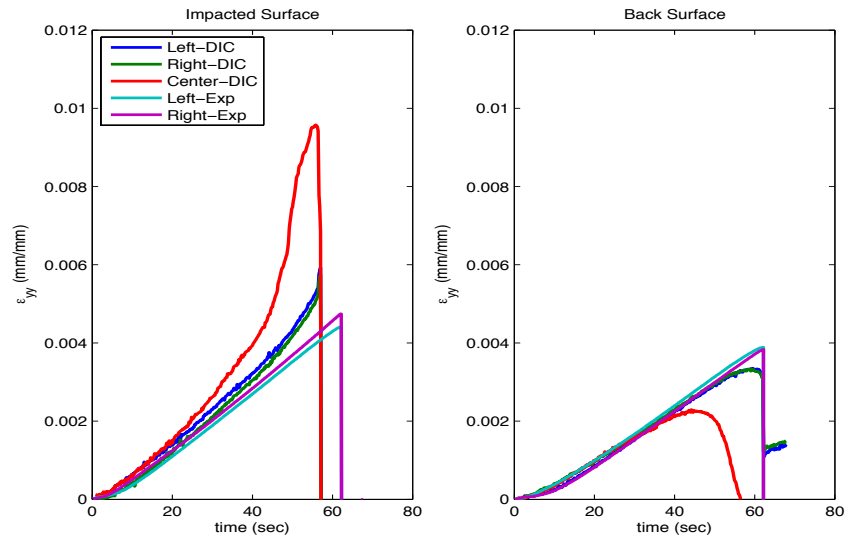


Figure 4.3.14 – Axial Strain (ϵ_{yy}) vs time: Panel D

4.4 Nondestructive Evaluation for Residual Compression Strength after Impact

Each of the specimens went through a series of nondestructive evaluation to characterize the amount damage after compressive loading. The samples went through immersion ultrasound, X-Ray, and X-Ray CT.

4.4.1 NDE: Immersion Ultrasound

Each of the specimens went through immersion ultrasound using a 5 MHz probe. Each of the specimens was rotated 90 degrees during the scans. The amplitude data representing the damage could be seen in Figure 4.4.1. The time of flight data shows the depth of delamination of the composite as shown in Figure 4.4.2. Failure of the composite occurred through the center of each of the composite. Panel C had the largest delaminated region, post impact, so the dominated mode of failure could have resulted from delamination. Immersion ultrasound was able to identify the locations of the strain gauges, which are the white regions in the image in the amplitude data. Immersion Ultrasound has limitation for characterizing damage in that it can only measure delamination. During the test, the samples failed catastrophically with no indication of initiation of new failure events or growth of impact-induced damage.

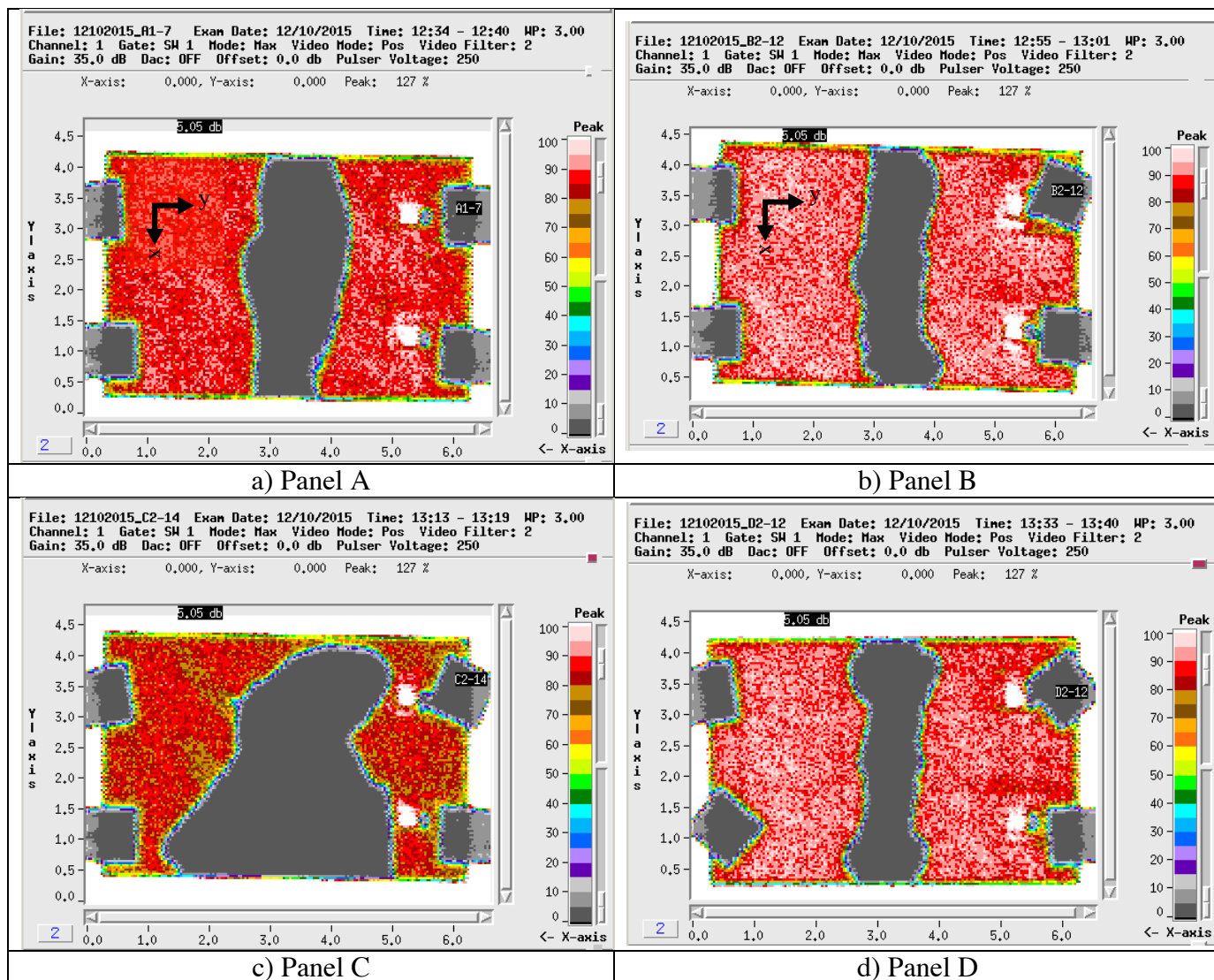


Figure 4.4.1 – C-Scan amplitude data: Post compression test damage

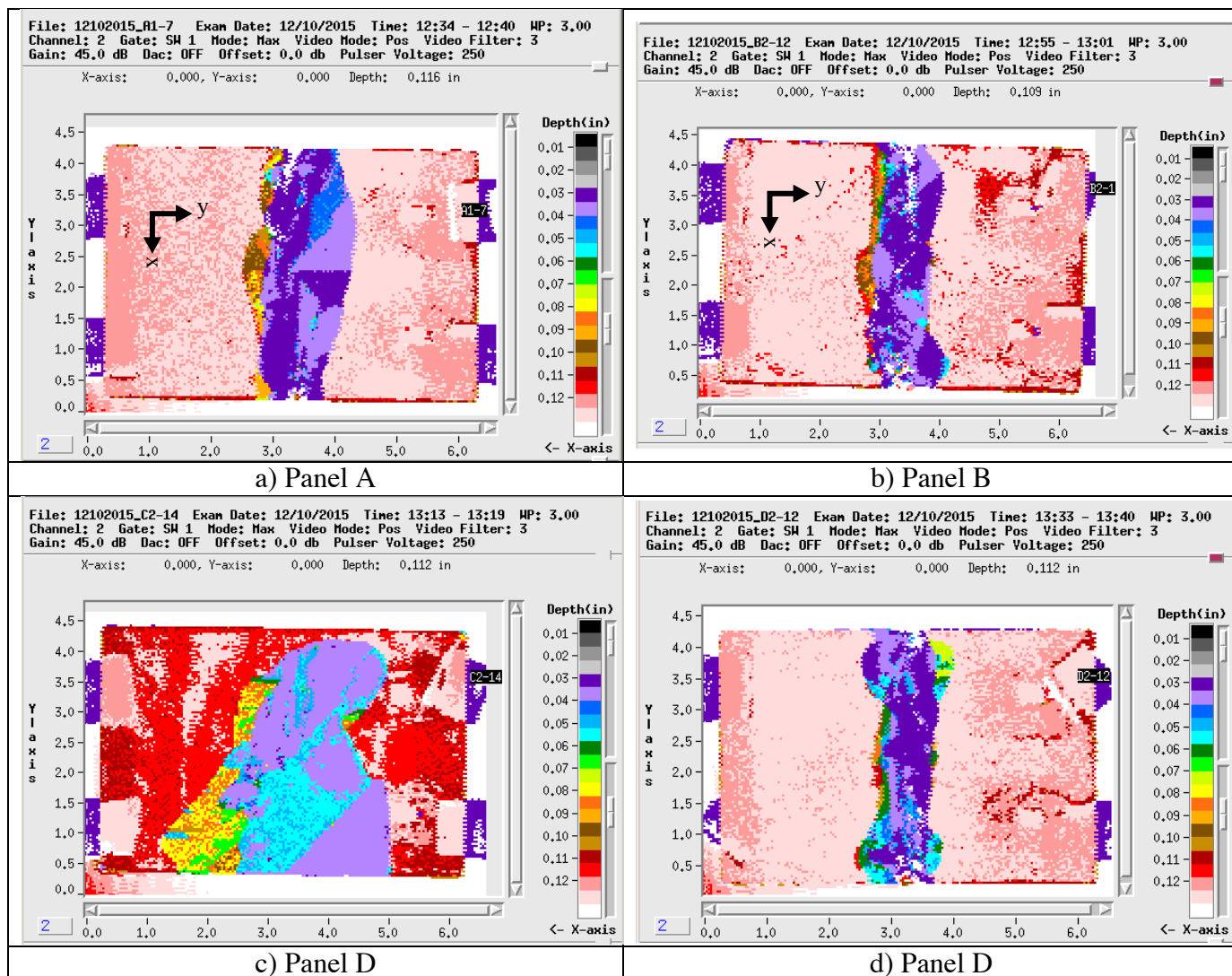


Figure 4.4.2 – C-Scan time of flight: Compression after impact damage

4.4.2 NDE: 2D X-Ray

Immersion Ultrasound can only visualize regions of delamination. Therefore, 2D X-Ray was performed on the panels to see if any damage could be seen within the composite, as shown in Figure 4.4.3. The X-ray beam parameters used were 24 kV, 3.0 mA and 30000 msec. Even though it is a crude estimation of the damage, transverse matrix cracks and fiber breakage could be seen in each of the images. Transverse matrix cracks could be seen more in Panel C. Additionally, many of the matrix cracks visible in this figure are near the edges where the anti-buckling mechanisms of the compression fixture was located. Fiber breakage also occurred in these regions as well. Each of the images was able

to capture the strain gauges that were applied to the composite during the compression testing. Even with X-Ray it is hard to determine the underlying mechanisms that attributed to failure.

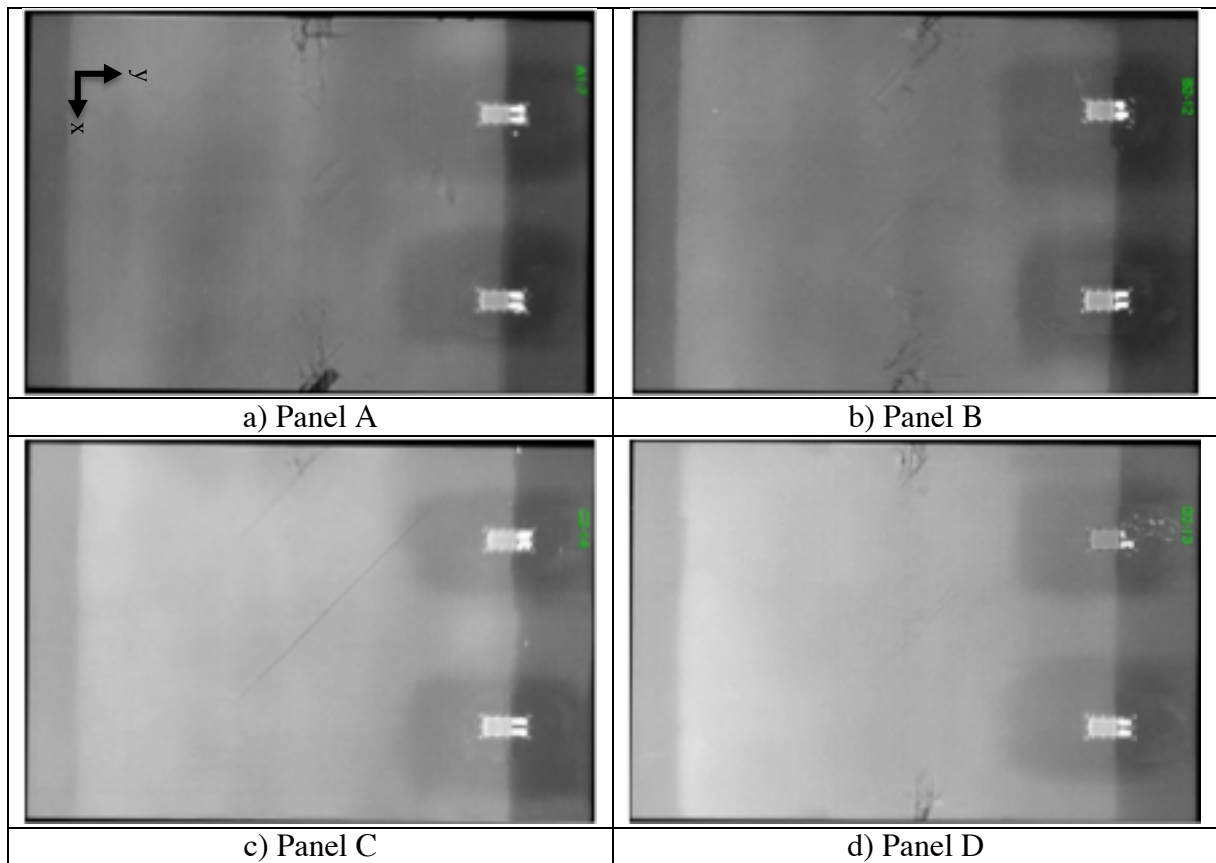


Figure 4.4.3 – X-Ray: Compression after impact damage

4.4.3 NDE: 3D X-Ray Computed Tomography

X-Ray CT proved to be better at characterizing the amount and type of damage that occurred from compression. A panel scan was performed on each of the specimens. Delamination, matrix cracks, and fiber breakage could be seen through the thickness of the composite. Figure 4.4.4-15 shows images of the X-Ray CT for each of the Panels. The front, side, and top view images from X-Ray CT scans provides the capability to see the damage in 3-dimensions. For the front images, just 3 sections were selected. The first section is a depth away the impact surface, the second section is near the midplane and the third section is a depth in the composite away from the back surface. From the front image, it's difficult to conclude that failure is driven by delamination. In many cases, the ply closer to the impacted

surface appears to exhibit fiber failure. Other cases, delamination appears to drive the failure. For the side images, 5 sections were selected close to the region of the impacted region with the center of the indent. For the top image, 5 sections were selected again.

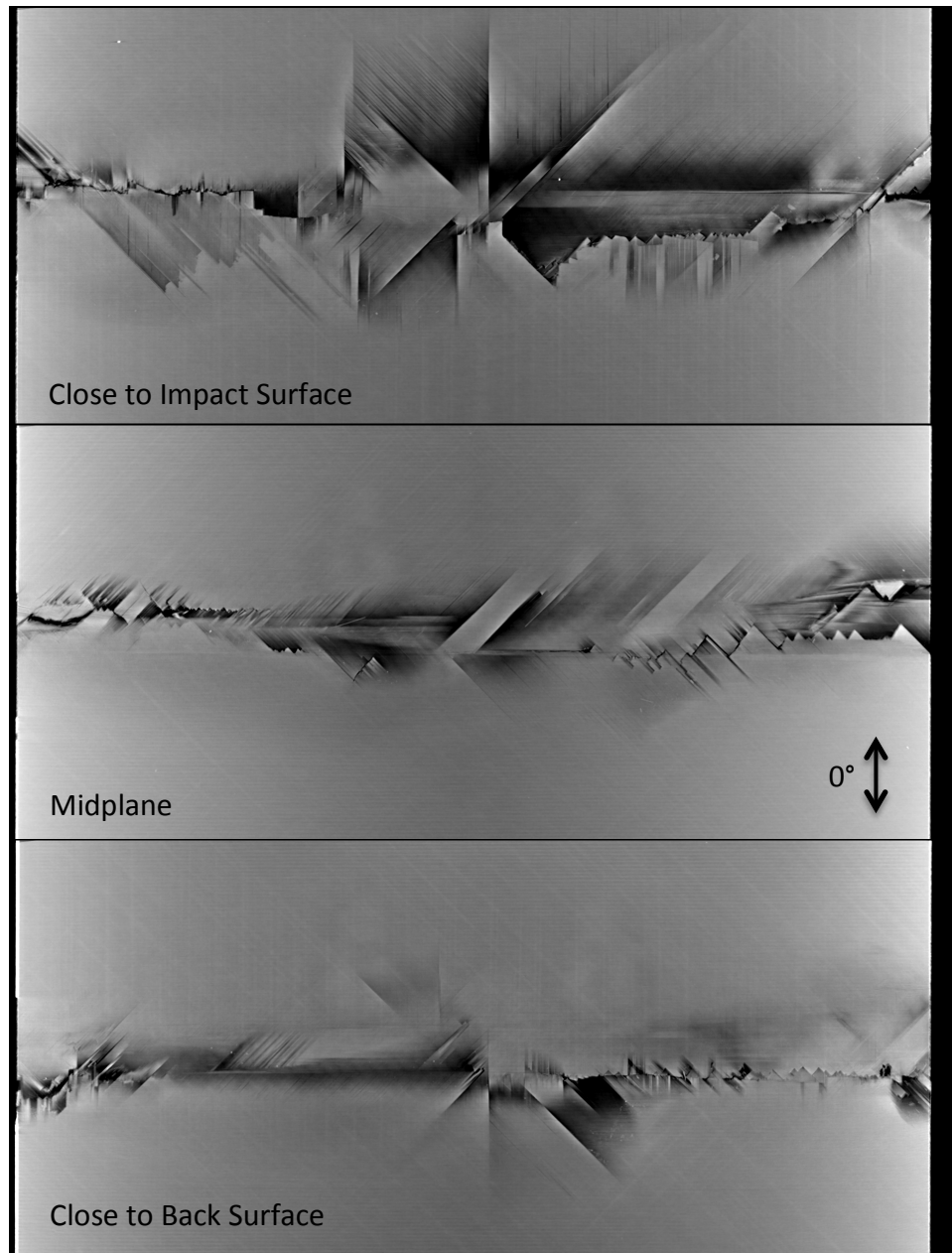


Figure 4.4.4 – X-Ray: Panel A front images

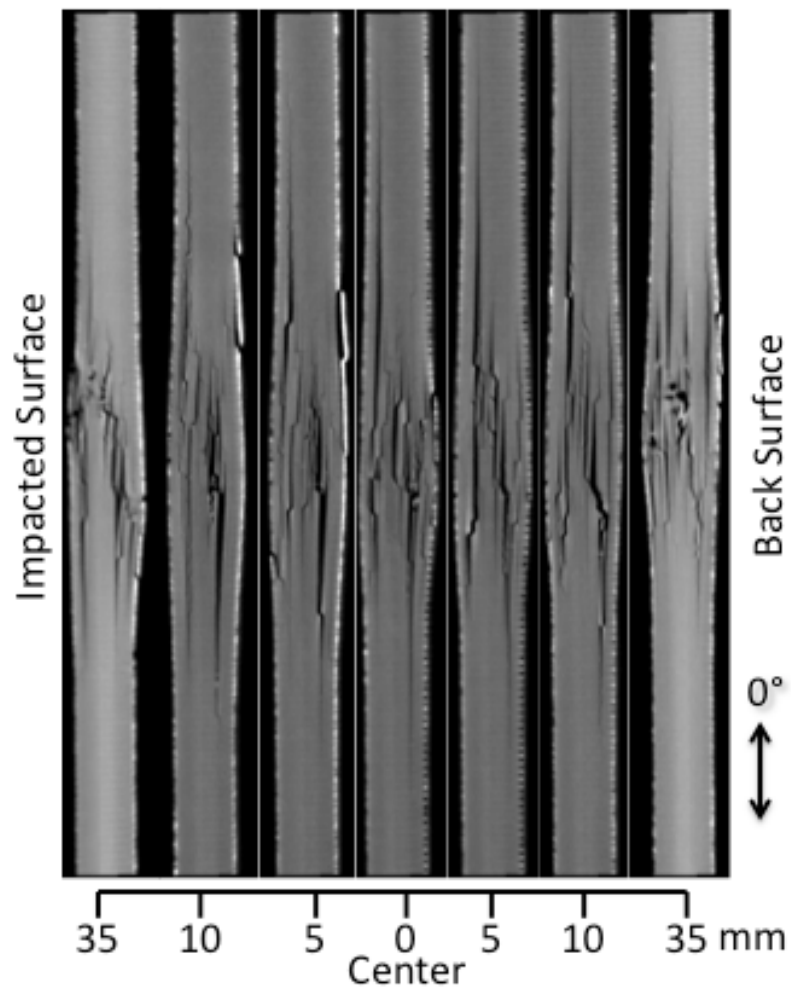


Figure 4.4.5 – X-Ray: Panel A side images

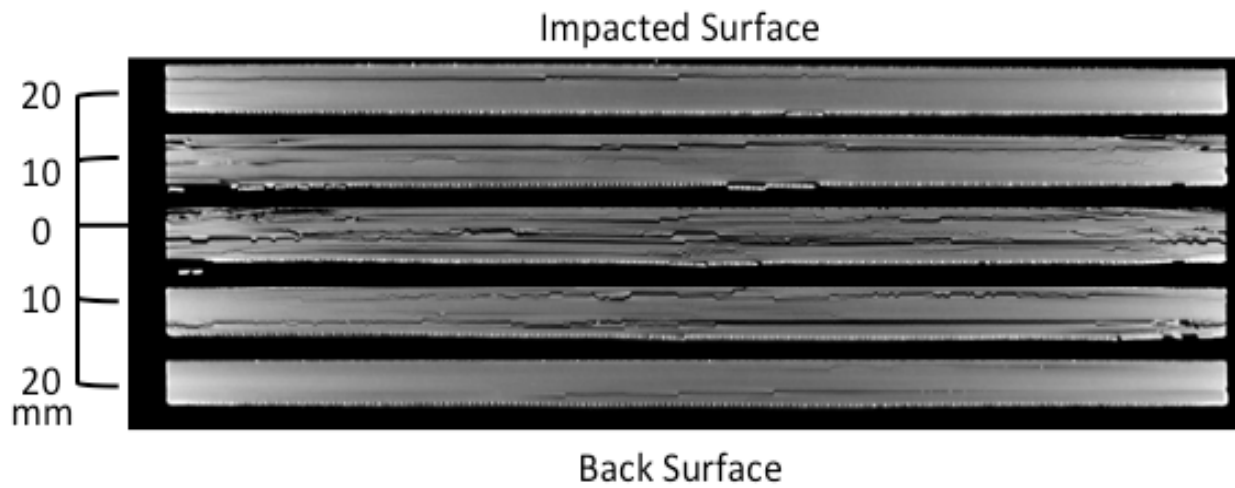


Figure 4.4.6 – X-Ray: Panel A top images

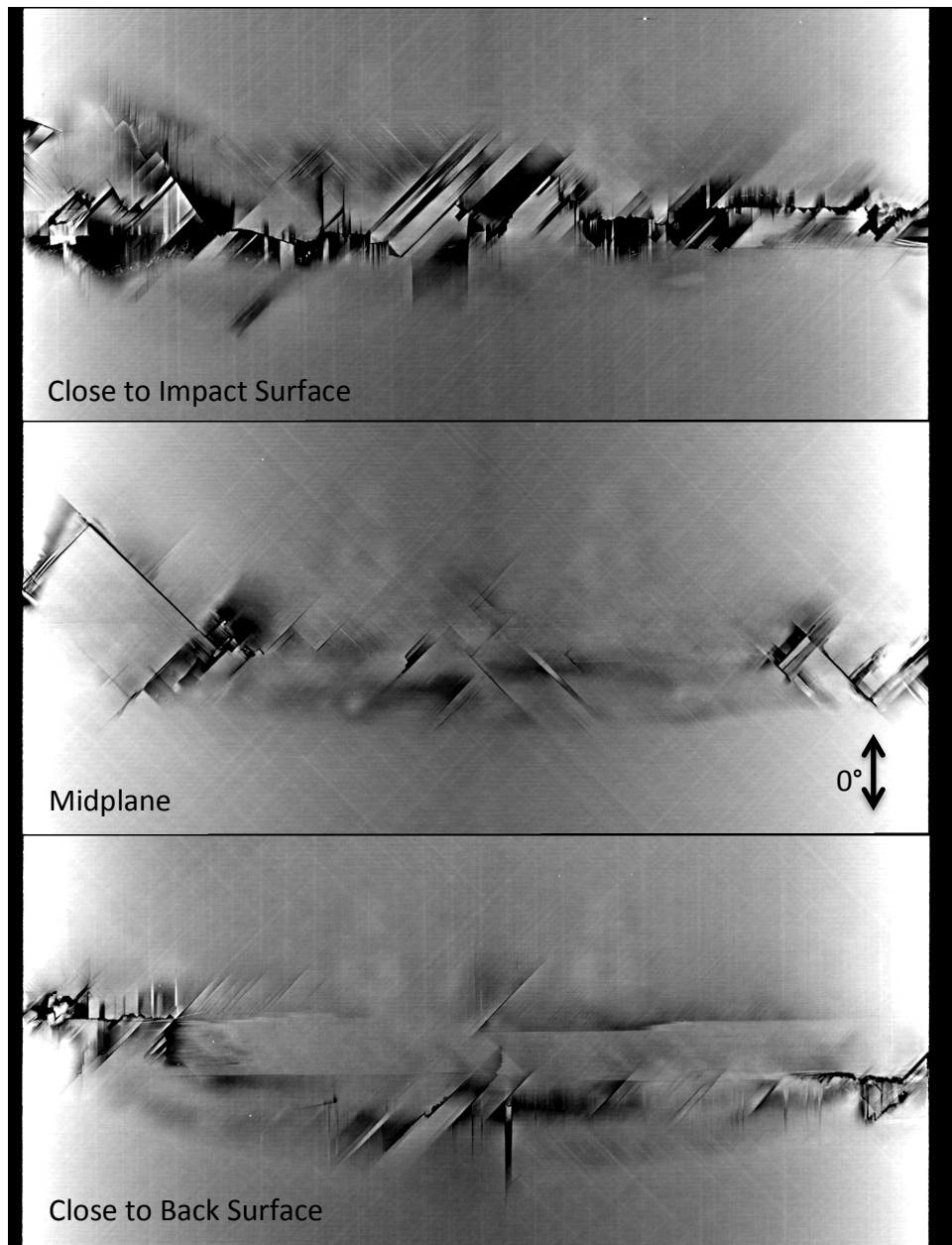


Figure 4.4.7 – X-Ray: Panel B front images

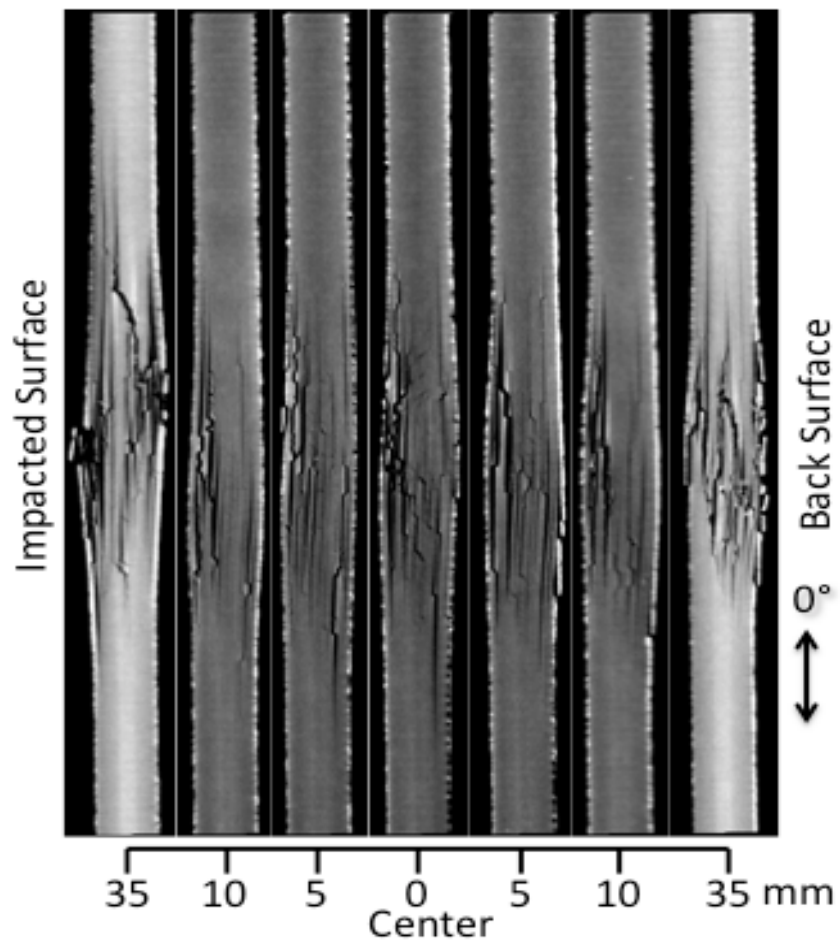


Figure 4.4.8 – X-Ray: Panel B side images

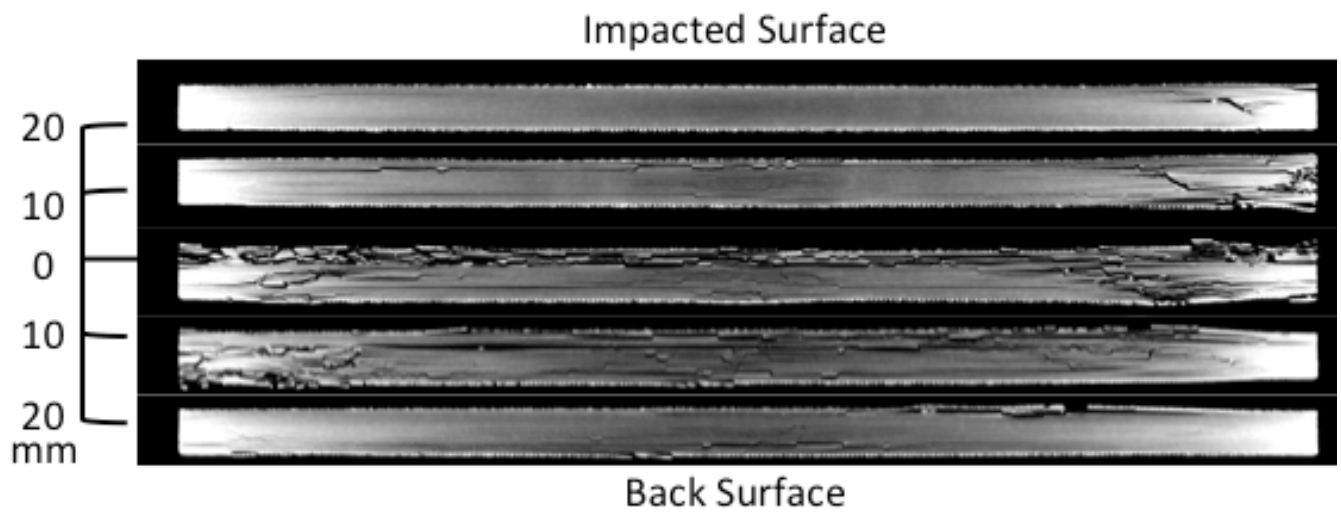


Figure 4.4.9 – X-Ray: Panel B top images

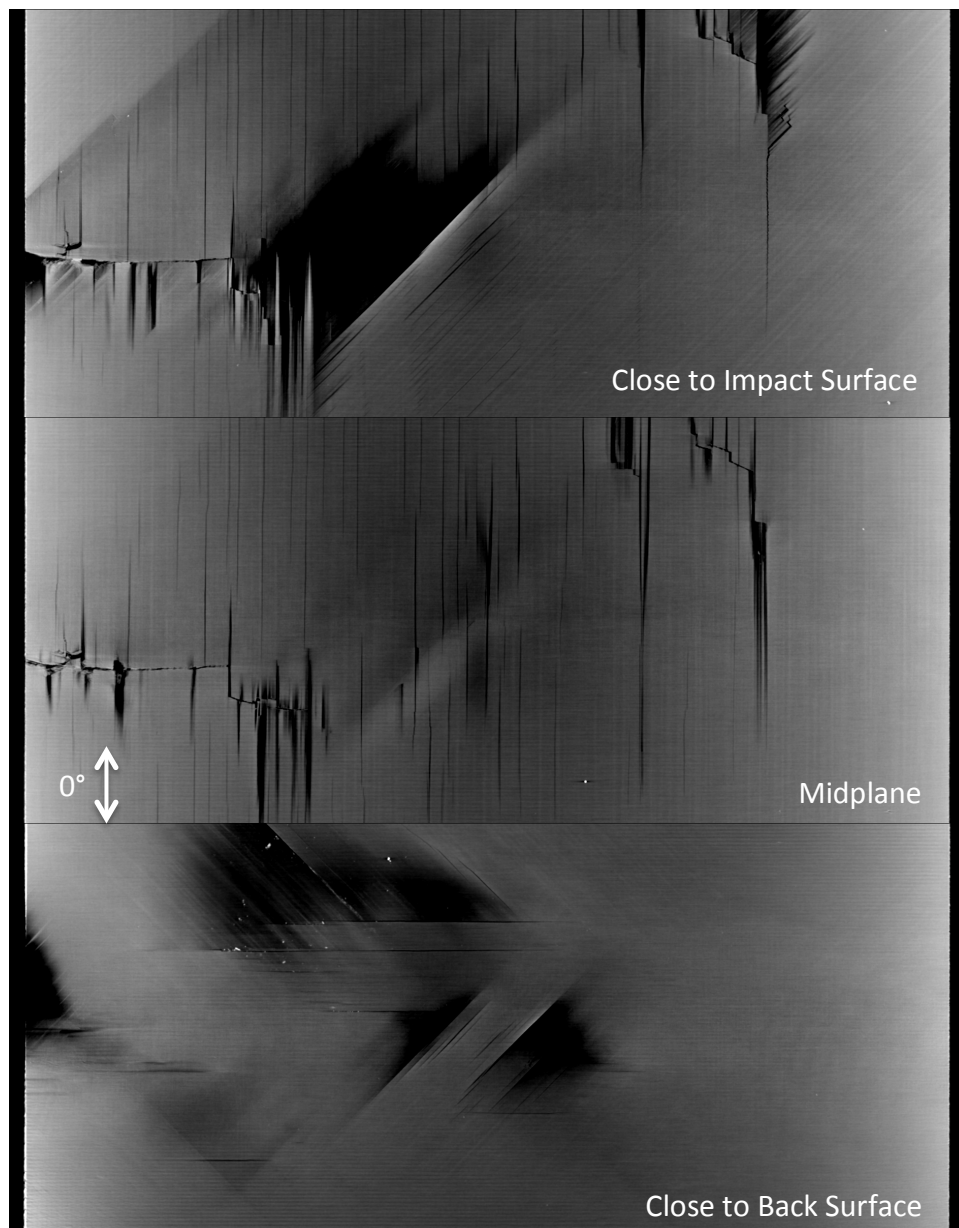


Figure 4.4.10 – X-Ray: Panel C front images

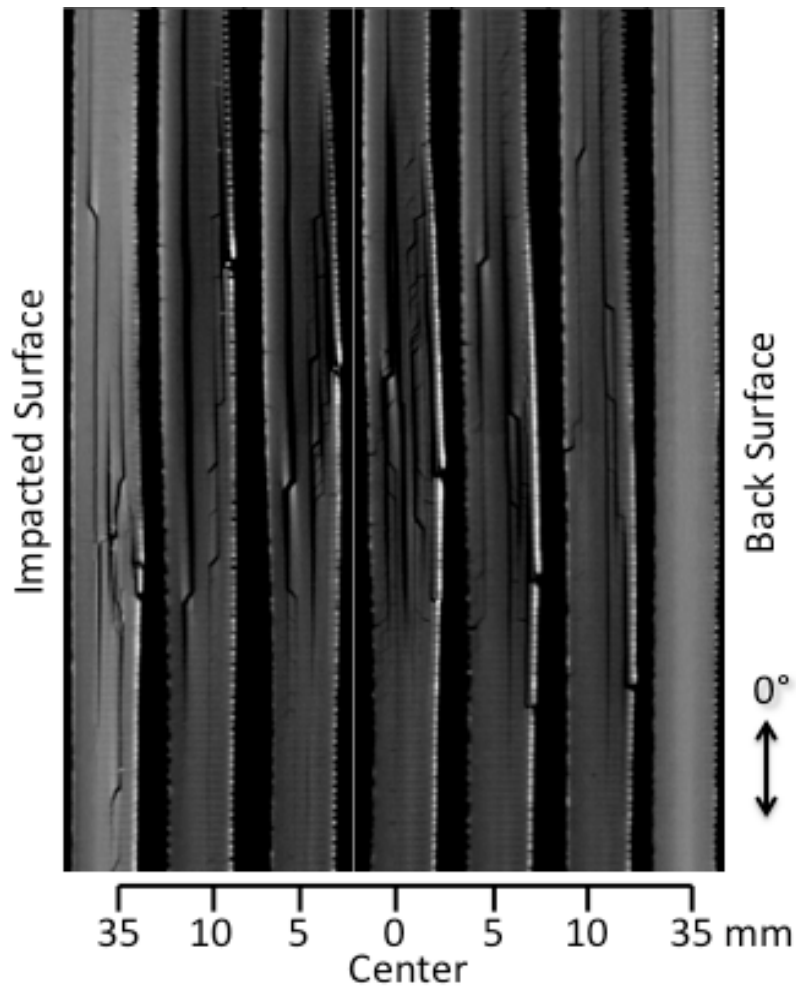


Figure 4.4.11 – X-Ray: Panel C side images

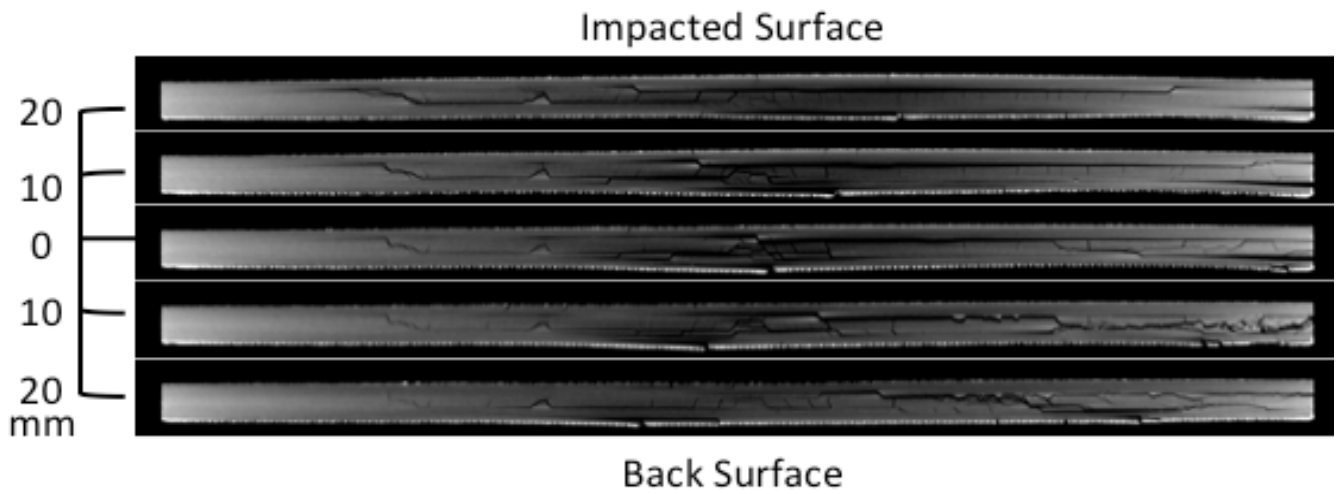


Figure 4.4.12 – X-Ray: Panel C top images

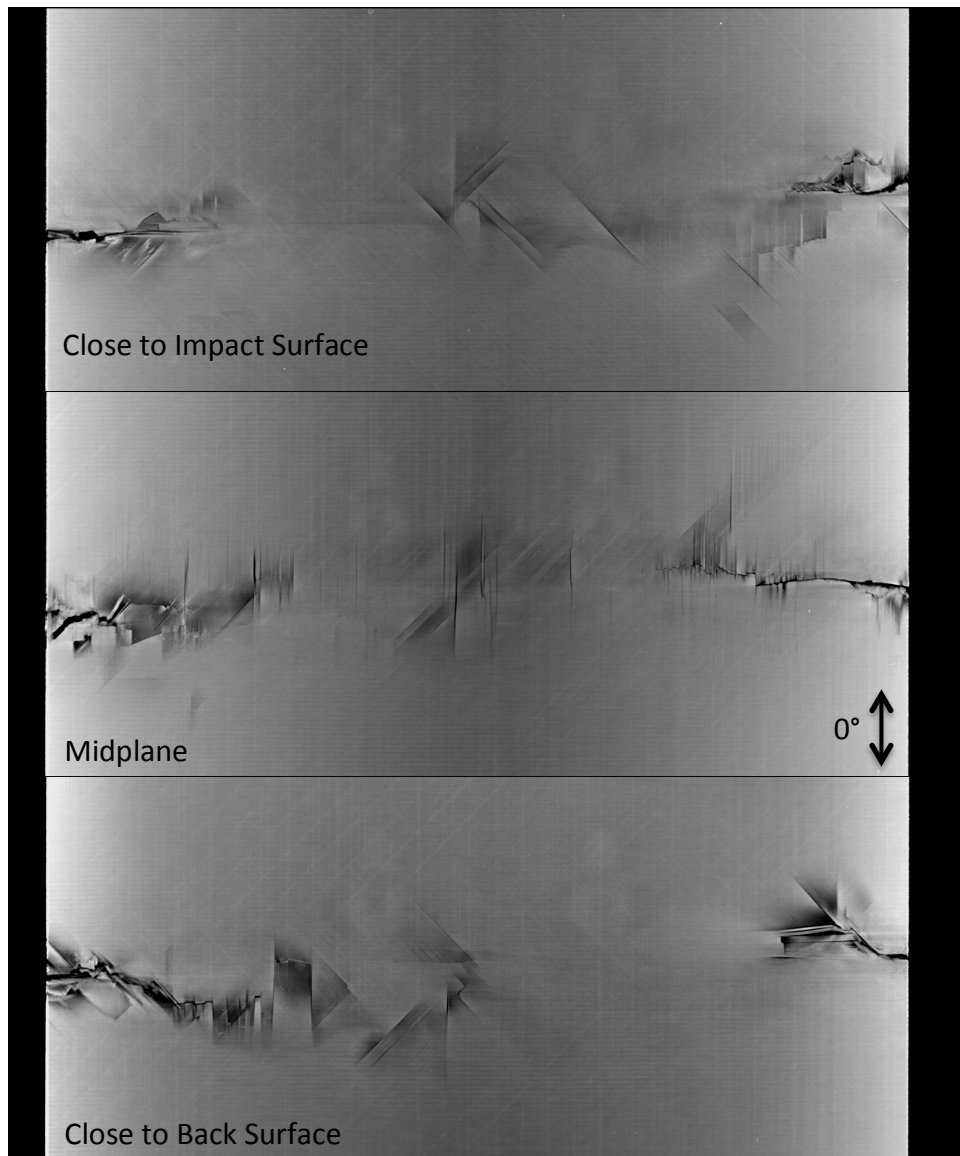


Figure 4.4.13 – X-Ray: Panel D front images

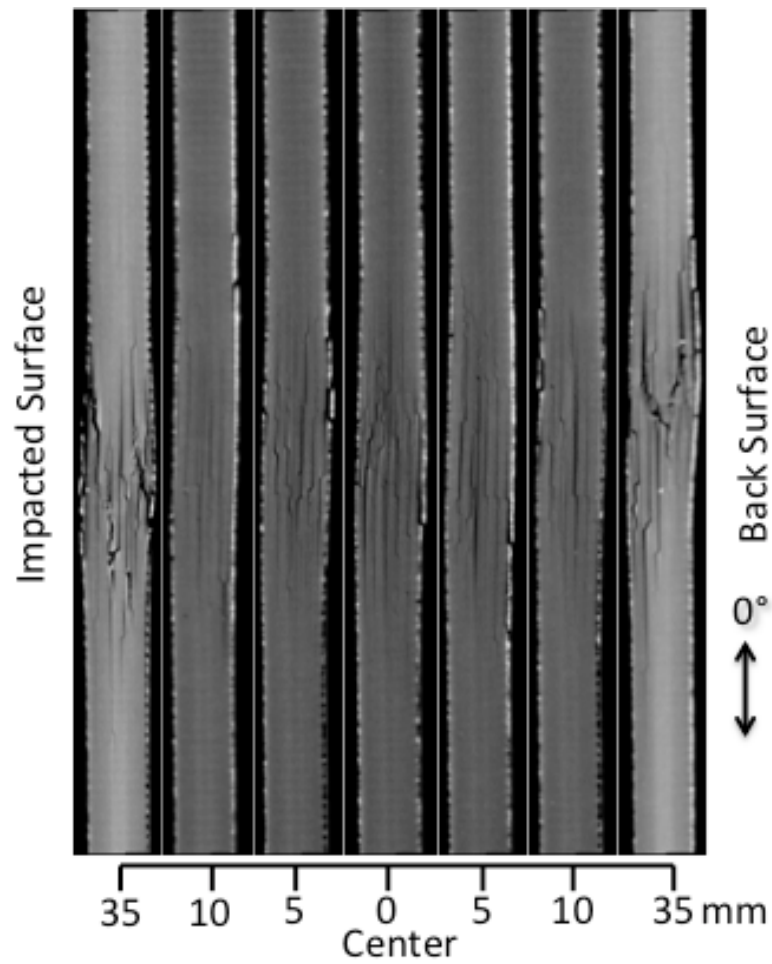


Figure 4.4.14 – X-Ray: Panel D side images

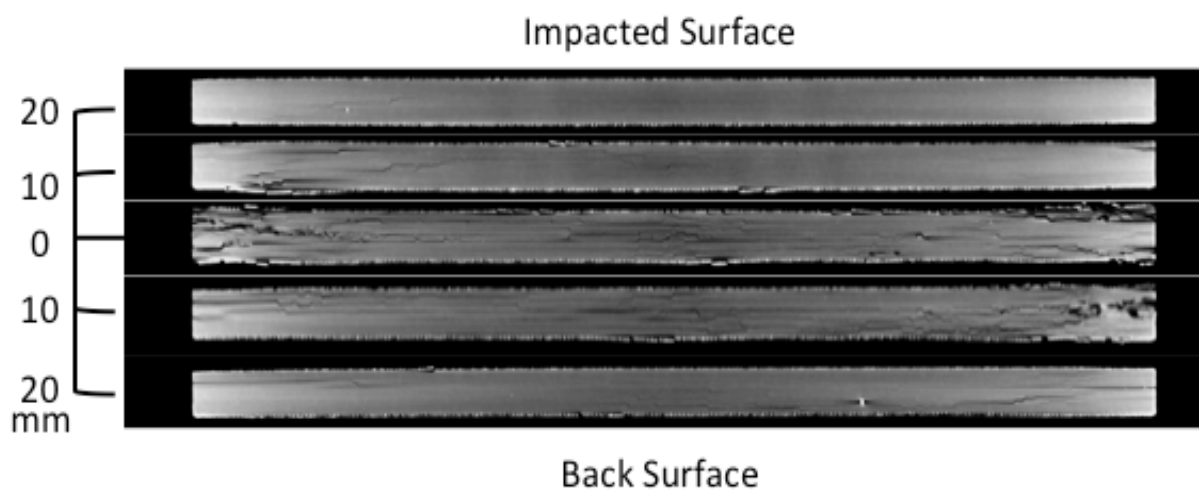


Figure 4.4.15 – X-Ray: Panel D top images

4.5 Discrete Damage Modeling (DDM)

The DDM approach consists of Mesh-independent Crack (MIC) modeling of matrix cracks in each ply of the laminate, and modeling the delamination between the plies by using a cohesive formulation at the ply interface. The matrix cracks are modeled by using the Regularized eXtended Finite Element Method (Rx-FEM) proposed in Chapter 4. The regularized formulation deals with continuous enrichment functions, and replaces the Heaviside step function with a continuous function changing from 0 to 1 over a narrow volume of the so called gradient zone. The formalism tying the volume integrals in the gradient zone to surface integrals in the limit of mesh refinement was discussed in [67,76]. The simulation begins without any initial matrix cracks, which then are inserted based on a failure criterion during the simulation. The LaRC04 failure criterion is chosen in the present work. The propagation of each MIC is performed by a cohesive zone formulation. Simulating delamination between the plies is done using the same cohesive zone formulation, however, the cohesive elements between the interfaces are inserted during initial model preparation. After the failure criterion is met at a certain location a MIC

As discussed in Chapter 4, a discrete damage modeling framework is being implemented to investigate the damage modes such as matrix cracking, delamination and fiber breakages. For the use of damage tolerance, the cracks and delamination are pre-determined entities from nondestructive evaluation.

4.5.1 Modeling Strategy

The morphology, delamination, and transverse matrix cracks were quantified using nondestructive evaluation and pre-imposed into a three-dimensional discrete damage model. Morphology of the impacted and back surface was obtained through optical profilometry and a linear interpolation of nodes was done through the thickness of the composite. The interfacial nodes between plies were selected and given arbitrary weak properties. Coordinate points inside a mesh were selected with the delamination region to pre-impose transverse matrix cracks into the model.

Modeling the delamination between plies uses a cohesive formulation at the ply interface developed by Turon [71]. Using equation 5.1, the initial stiffness (K) is 10^6 and the damage parameter (d) is 10^{-7} . The cohesive force for tension (Y_t) and compression (Y_c) is 60 N and 200 N for damage initiation. The same material properties were used to model crack growth. According to Turon the cohesive forces τ resisting the opening displacement jump Δu at an arbitrary crack surface point is

$$\boldsymbol{\tau} = (1 - d)K\Delta\mathbf{u} + dK\langle\Delta u_n\rangle\mathbf{n} \quad (5.1)$$

The second term in the equation prevents interpenetration of the crack surfaces. The brackets $\langle x \rangle = (x + |x|)/2$ represents the McAuley operator and vector \mathbf{n} is the unit vector to the crack surface. The damage parameter controls the crack opening and displays the length of the cracks.

A Progressive Fiber Failure (PFF) approach was used to address fiber failure in composite laminates. The stiffness tensor at a given stress level is defined as $C = (1-d)C_0$, where C_0 is the initial stiffness. The damage variable, d , is defined based on the stress strain relationship proposed by Maimi et al [73-74], and is shown in Figure 4.5.1. Determination of the numerical values of the parameters defining the cohesive curve in Figure 4.5.1 for IM7/977-3 in tension, for example, include the fracture toughness, $G_x = 80.0$ N/mm and coefficients $f_x = 0.2$, $f_G = 0.4$ as well as the characteristic length, has been addressed in [72]. The initiation stress value, X_T , represents the fiber direction strength measured on standard unidirectional couple type tests. In our simulations, two values of the failure initiation strength are: (i) $X_T = 3116$ N/mm² obtained for typical 24-ply unidirectional coupon with total volume of $V_0 = 49548.288$ mm³ and $X = 3116$ N/mm³ scaled strength for a 1 mm³ of stressed volume.

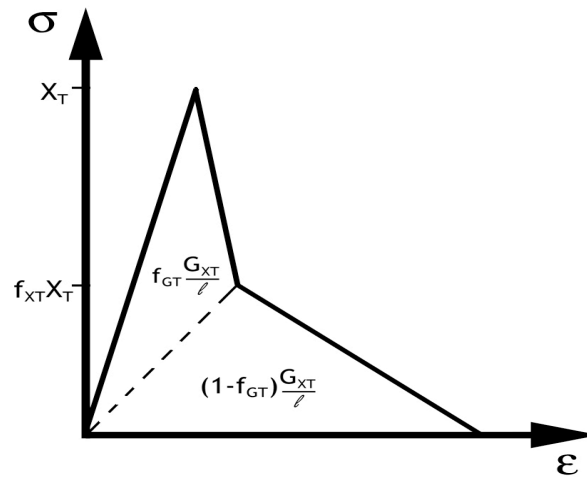


Figure 4.5.1 – Property degradation approach to fiber fracture

4.5.2 Material Properties

The mechanical properties for IM7/977-3 were obtained through an Air Force Research Laboratory program to model and characterize open hole specimens. Table 4.5.1 outlines the mechanical properties for IM7/977-3.

Table 4.5.1 – Mechanical Properties of IM7/M65

| | |
|---------------------------------------------------------|----------|
| Longitudinal Elastic Modulus, E11 (MPa) | 137417 |
| Transverse Elastic Modulus, E22&E33 (MPa) | 8694 |
| In-Plane Shear Modulus Major, G12 & G13 (MPa) | 5000 |
| In-Plane Shear Modulus Minor, G23 (MPa) | 3500 |
| Tensile Longitudinal Ultimate Strength, X^T (MPa) | 2905 |
| Compression Longitudinal Ultimate Strength, X^C (MPa) | 1680 |
| Shear Strength, S (MPa) | 100 |
| Tensile Transverse Ultimate Strength, Y^T (MPa) | 100 |
| Compression Transverse Ultimate Strength, Y^C (MPa) | 240 |
| Poisson's Ratio Major, ν_{12} * & ν_{13} | 0.32 |
| Poisson's Ratio Major, ν_{23} | 0.496 |
| Mode I Fracture Energy, GIC (N/mm) | 80 |
| Mode II Fracture Energy, GIIC (N/mm) | 24 |
| Longitudinal Thermal Expansion, α_{11} | 0.00 |
| Transverse Thermal Expansion, α_{22} | 30.0E-06 |

4.5.3 Model Preparation

Due to the 1.4 million degrees of freedom limitation previously discussed, the mesh was more refined near the impacted region to adequately represent the damage obtained from NDE (Figure 4.5.2). The 3D specimen was fixed in the x on one edge and loaded on the opposite edge. The corner nodes were constrained in the y for the model. The impacted and back surface nodes were selected using an STL and then constrained in the z representing the ASTM 7137 fixture used in experiments. The side edges are not constrained and remain traction free.

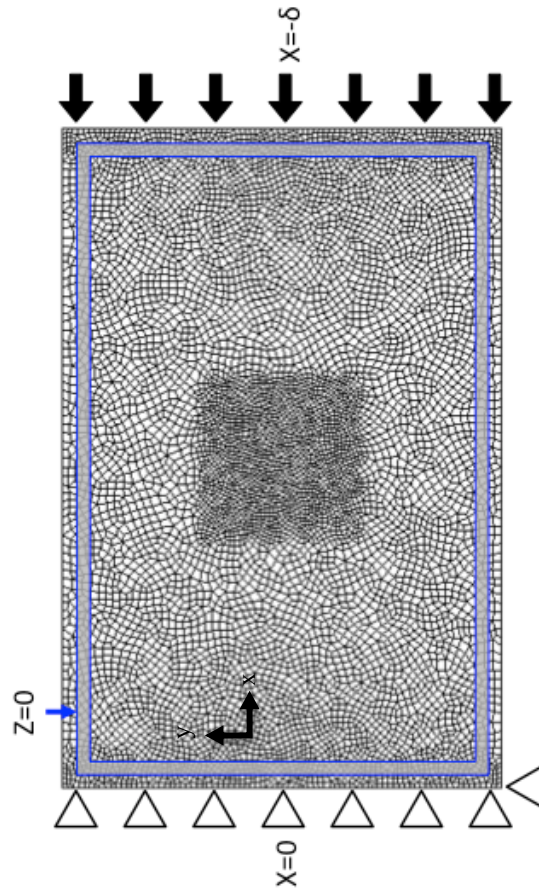


Figure 4.5.2 – DDM model for Panel A

4.6 DDM Results

4.6.1 Out-of-Plane Displacement

The composites experienced non-linear behavior in the form of sublaminar buckling and as a result was not captured in the simulation. The discrete damage model only took into consideration small

displacements, therefore it was only able to capture the out-of-plane deformation in terms of morphology. Figures 4.6.1-2 shows a side-by-side comparison between the simulation and the DIC for the impacted and back surfaces.

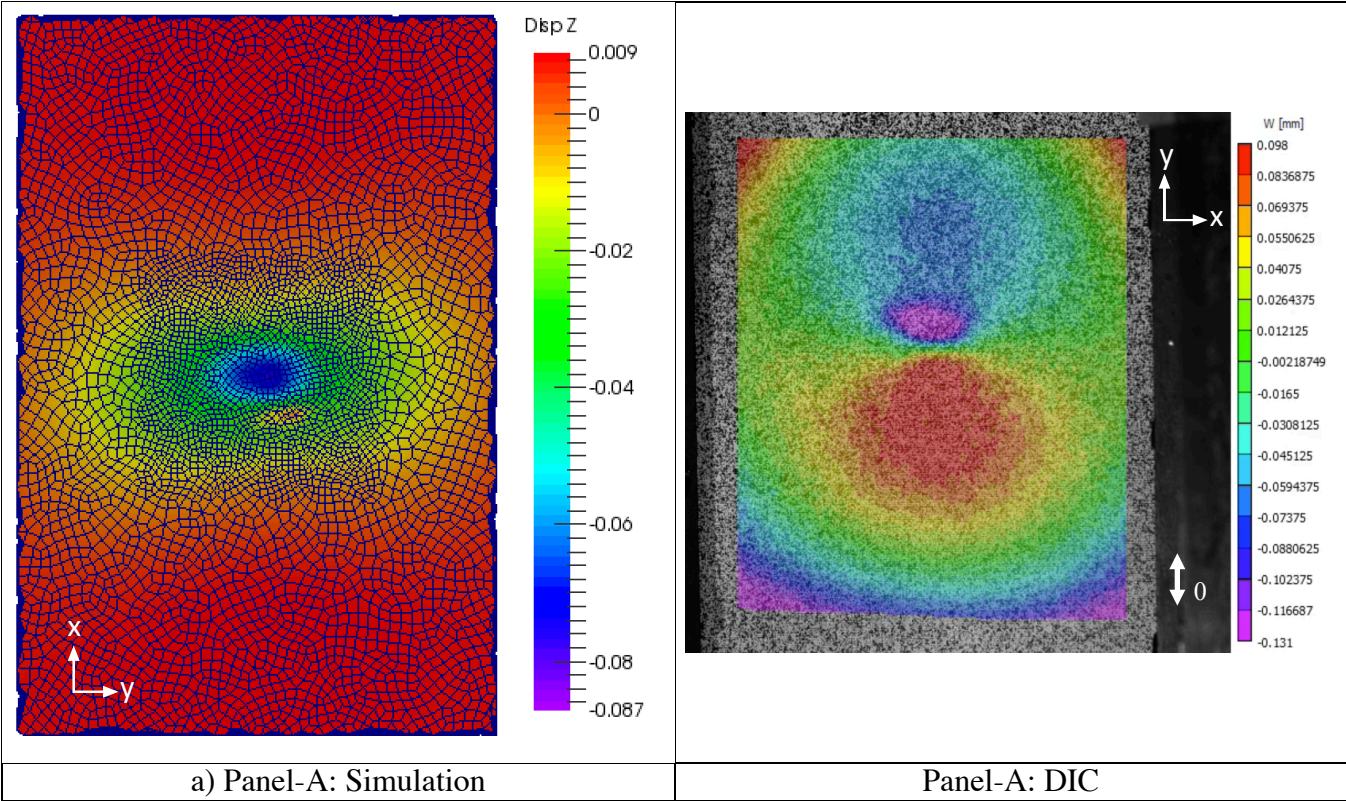


Figure 4.6.1 – Panel A Out-of-Plane Displacements: Impacted Surface

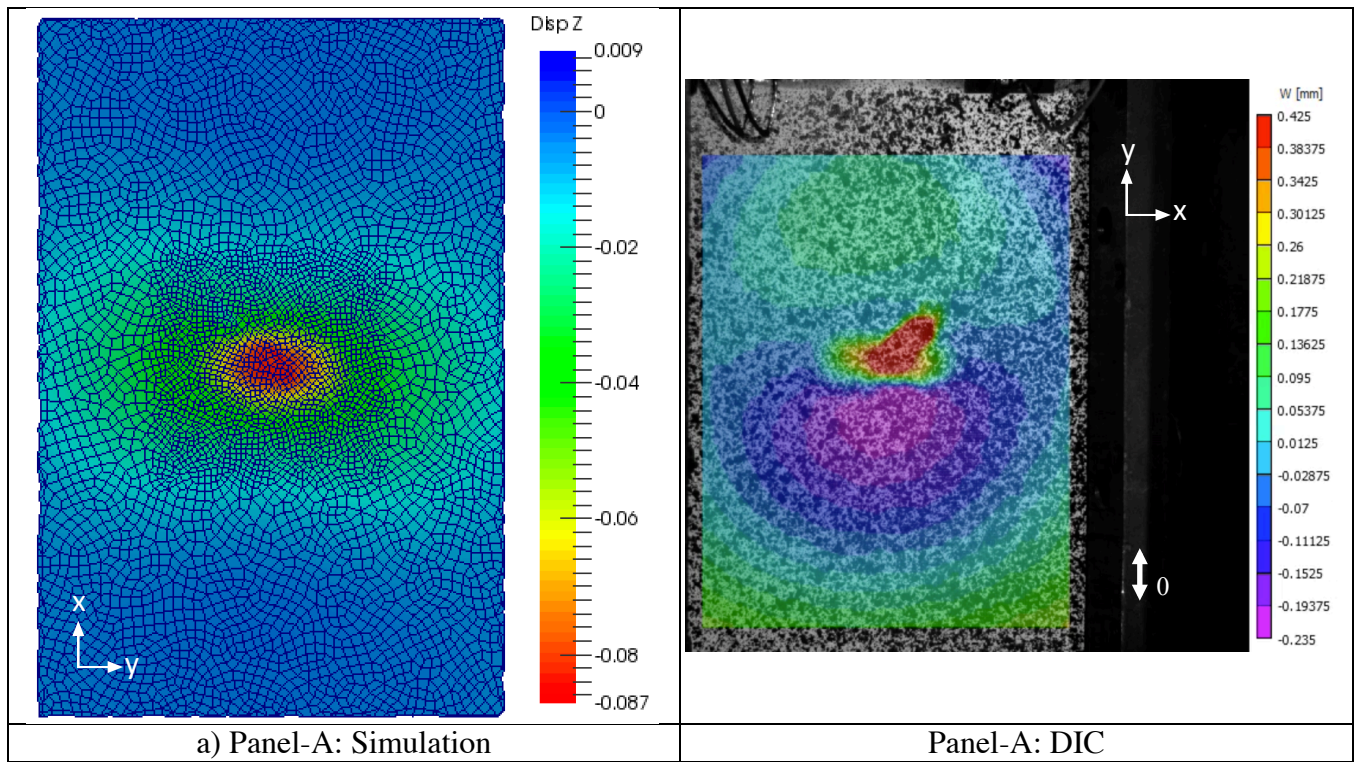


Figure 4.6.2 – Panel A Out-of-Plane Displacements: Back Surface

4.6.2 Strain Contours

There was good agreement for the axial strain between the simulation and experiment. Note that the axial strains for the simulation are in the x-direction, while axial strains in the experiment are in the y-direction. For the impacted side (Figure 4.6.3), the contours indicated compression strains in the center surround by tensile strains. The contours for the back surface (Figure 4.6.4) show how the surface crack influences the behavior of the material. Although the simulation strains were off by 10% of the experiment, modeling the morphology appeared to capture the strains seen in the experiment (Figure 4.6.5-8).

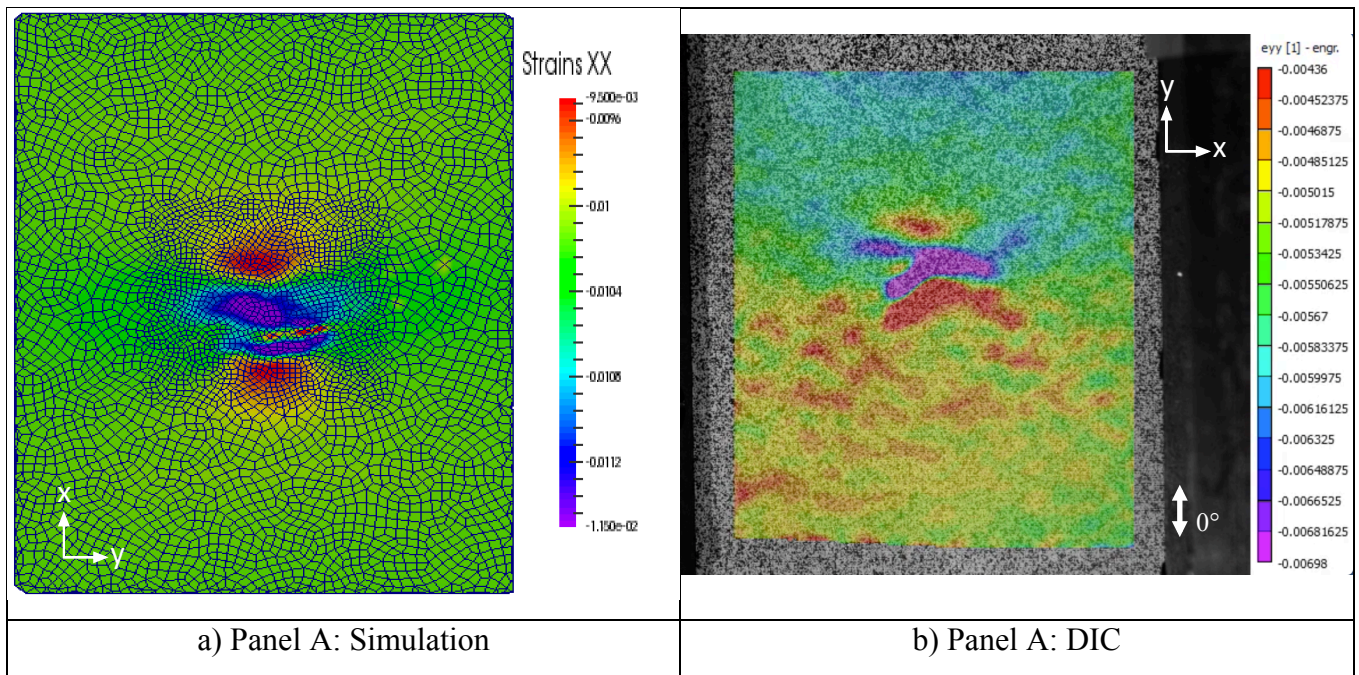


Figure 4.6.3 – Axial Strain Panel A Impacted Surface for both simulation and experiment

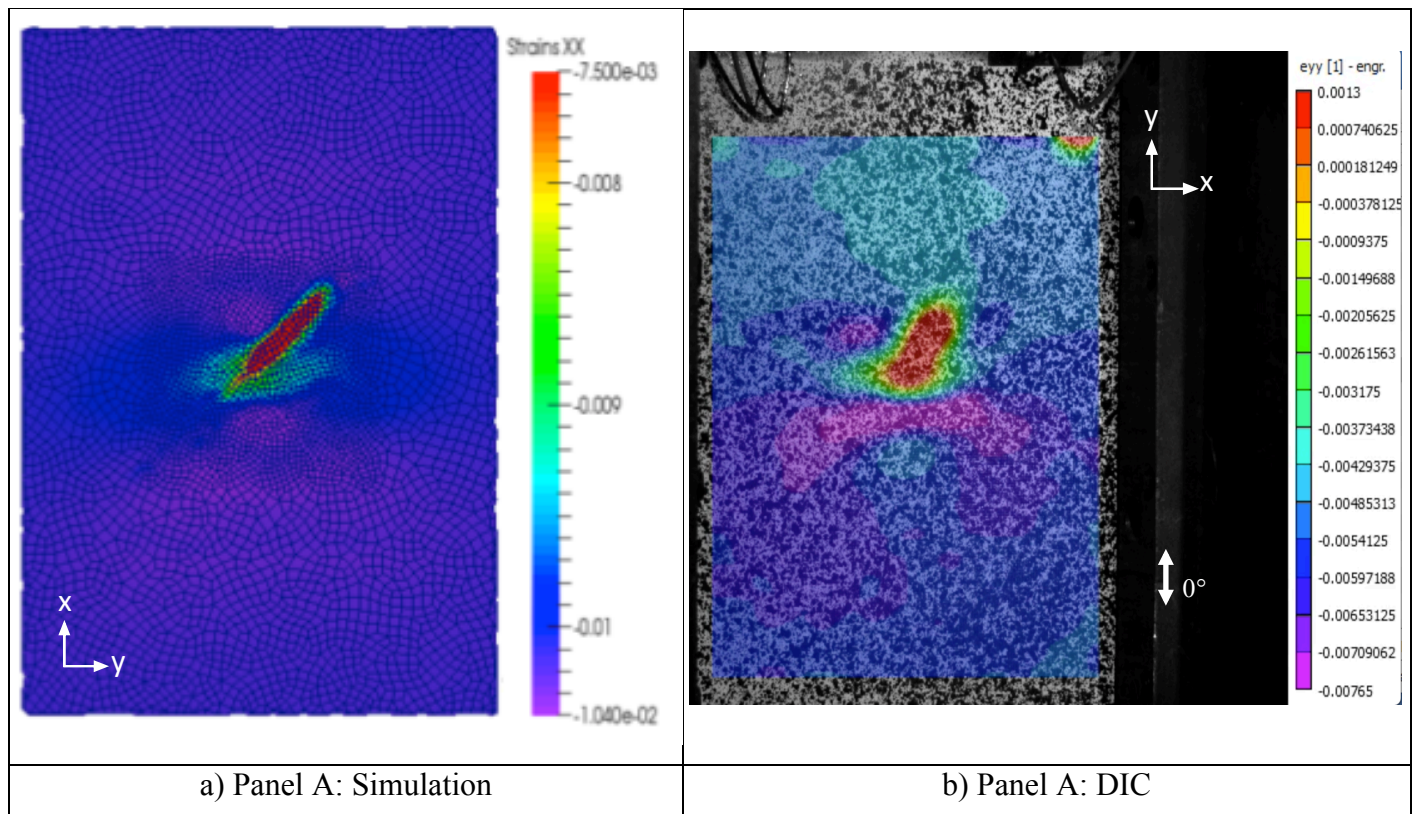


Figure 4.6.4 – Axial Strain Panel A Back Surface for both simulation and experiment

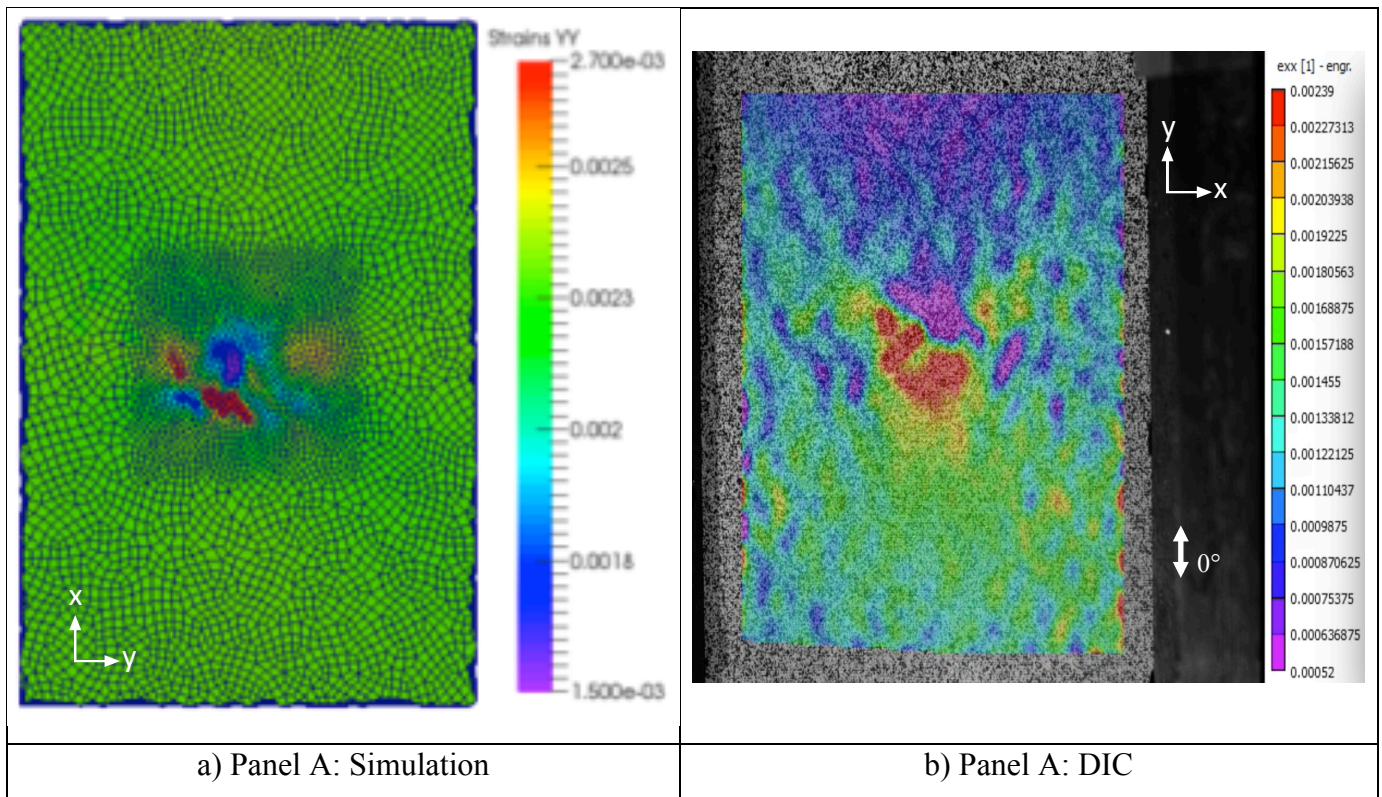


Figure 4.6.5 – Transverse Strain Panel-A Impacted for both simulation and experiment

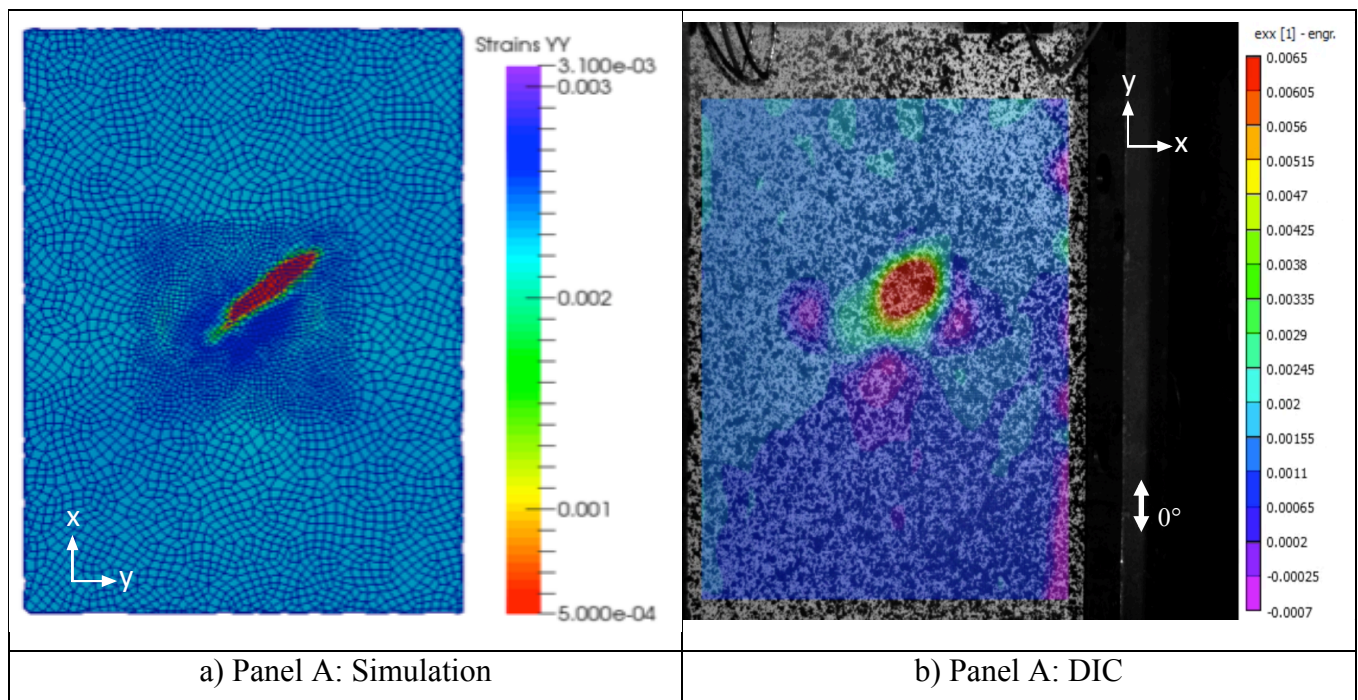


Figure 4.6.6 – Transverse Strain Panel-A Back for both simulation and experiment

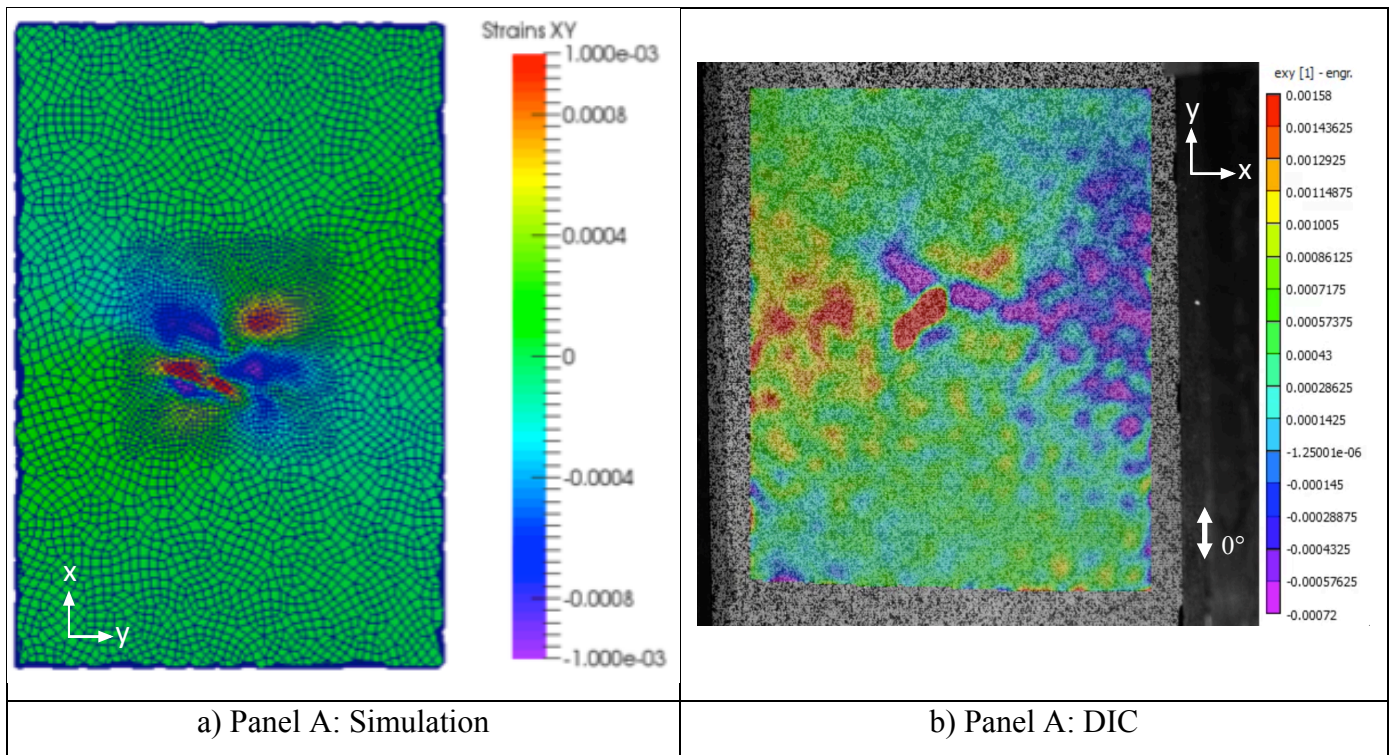


Figure 4.6.7 – Shear Strain Panel-A Impacted for both simulation and experiment

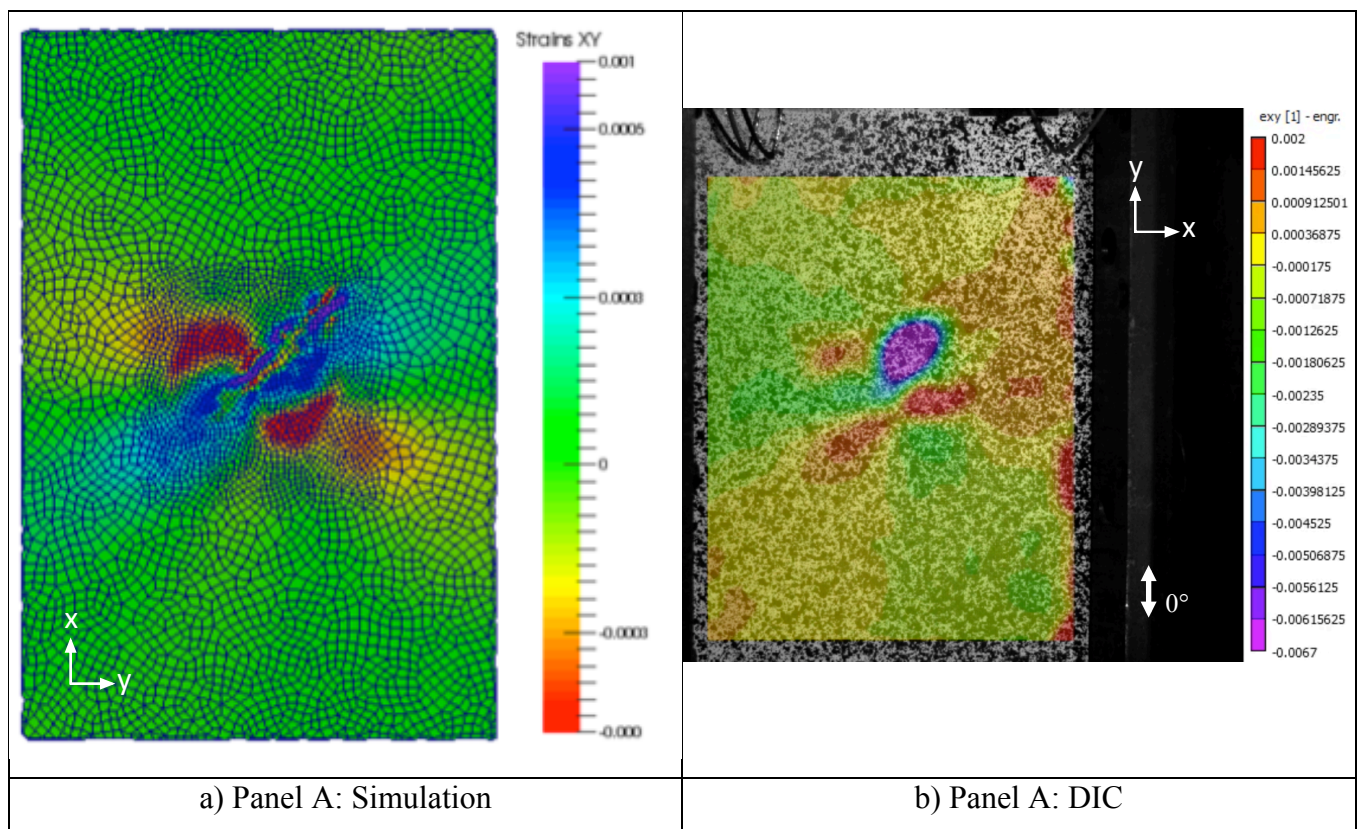


Figure 4.6.8 – Shear Strain Panel-A Back Surface for both simulation and experiment

4.6.3 Damage Evolution

The proposed method was able to pre-impose damage in the form of delamination, transverse matrix cracks, and morphology. Figure 4.6.9 shows the amount of delamination in the 3D discrete damage model obtained from X-Ray CT. Figure 4.6.10.a shows a frontal view of the delamination. Pre-imposed cracks were incorporated into the model (Figure 4.6.10.b) by selected nodal points within the mesh. The cracks were allowed to open to the boundaries of the delaminated regions (Figure 4.6.10.c).

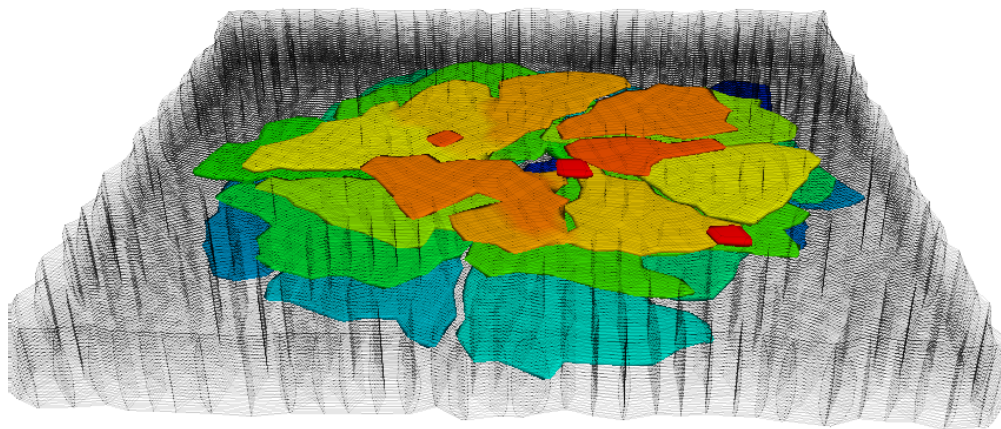


Figure 4.6.9 – 3D Representation of initial delamination

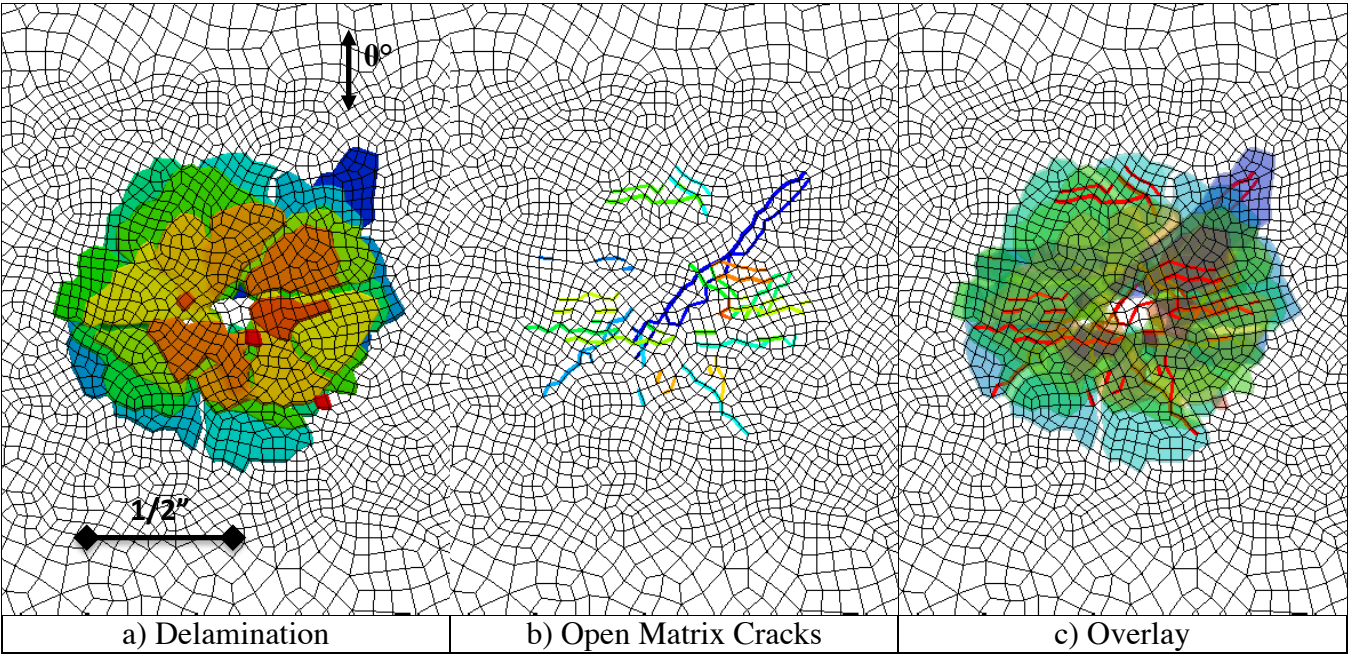


Figure 4.6.10 – Frontal image (impacted surface) of initial delamination and transverse matrix cracks

After the 30th step (displacement load of 0.635 mm), new cracks have formed (red) and the original cracks have continued to propagate slightly (Figure 4.6.11.a). Similar damage growth happens at a displacement load of 1.059 mm (Figure 4.6.11.b). After the 70th step (displacement load of 1.482 mm), new cracks have formed and propagated (Figure 4.6.11.c). However, progressive fiber failure (black) has started in some of the elements. The reduction of the stiffness matrix seemed to be more predominately in the 0° plies and surround transverse matrix cracks. Fiber damage continued to grow until it reached the 78th step (displacement load of 1.651 mm, Figure 4.6.11.d) until ultimate failure of the specimen occurred at 82nd step (1.736 mm, Figure 4.6.12). Through out the simulation delamination grew slightly, but not significant to conclude that is was the dominating mode of failure.

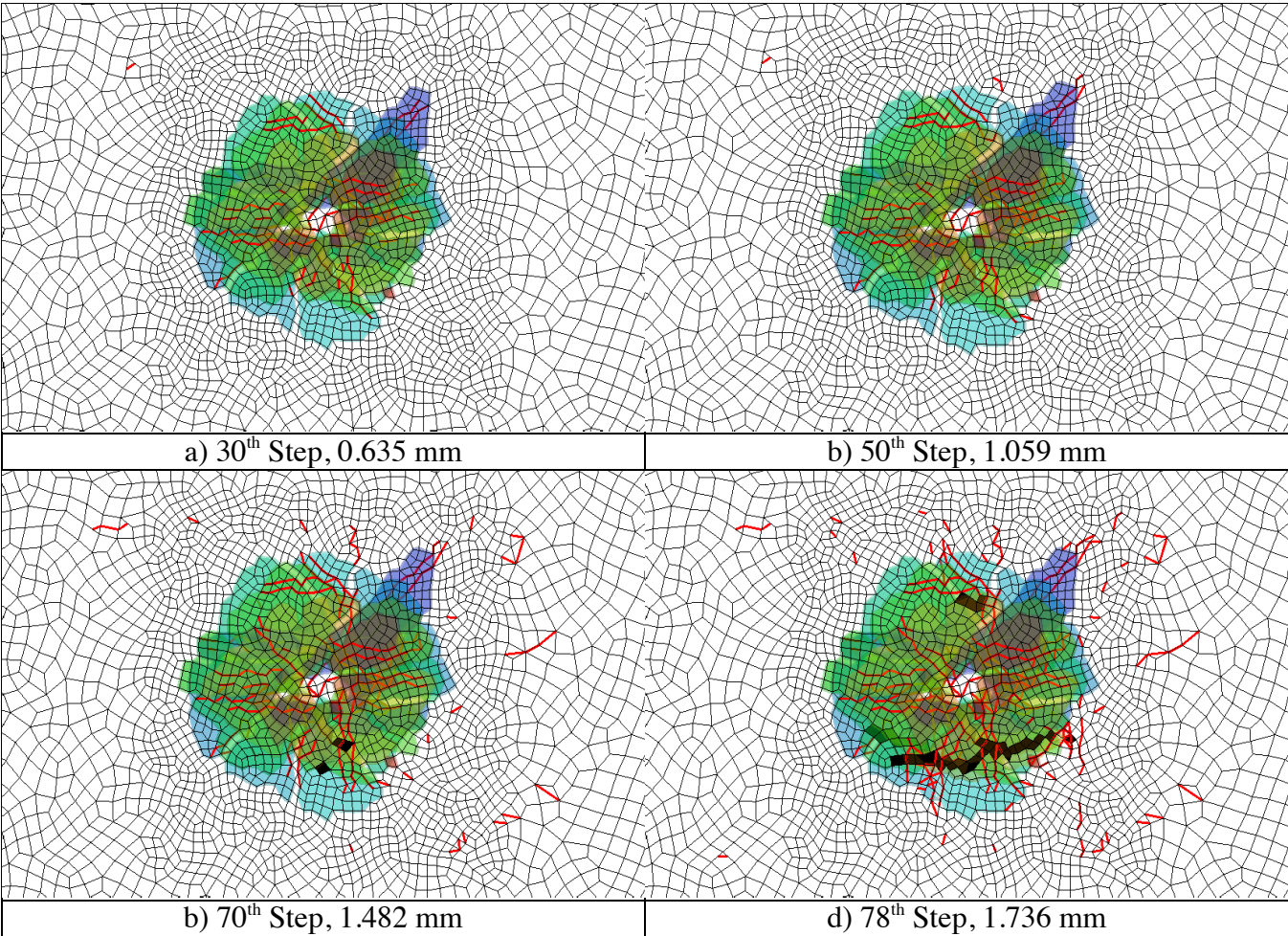


Figure 4.6.11 – Sequence of damage events for Panel A

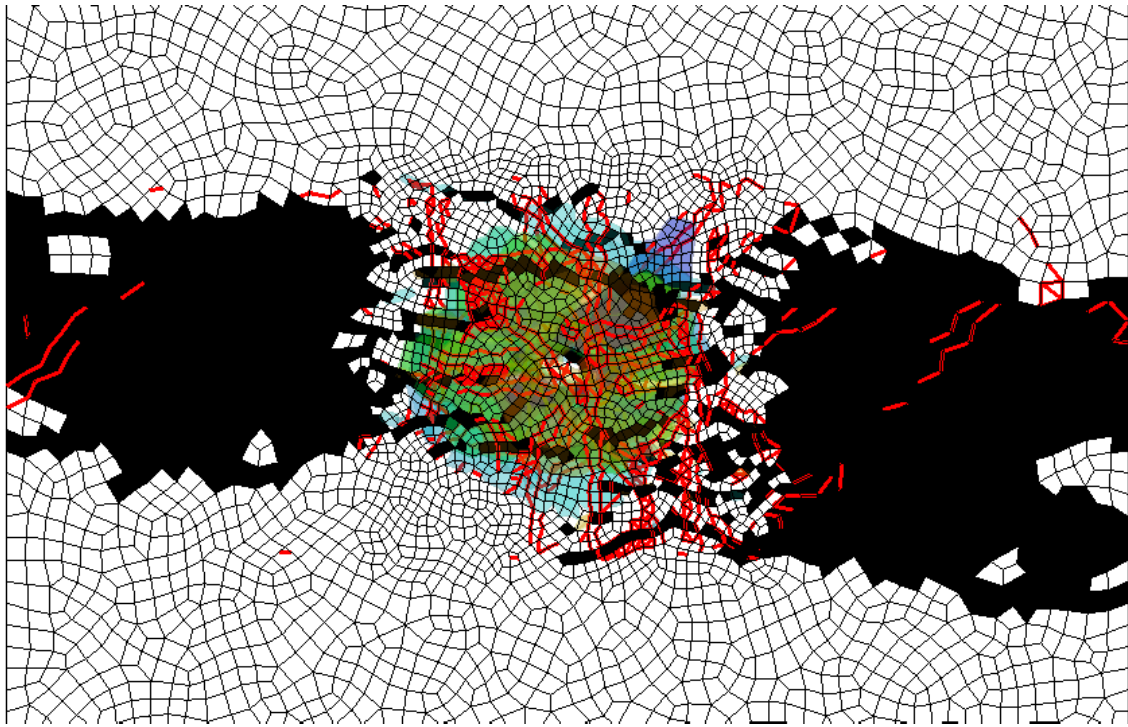


Figure 4.6.12 – Ultimate failure of simulation

Although the damage appeared to be driven by fiber breakage (a reduction of the element stiffness) and transverse matrix cracks, X-Ray CT images of the post failure shows that fiber breakage is present through thickness of the composite. Figure 4.6.13 shows the difference between a panel scan using X-Ray CT versus the simulation. The grey and dark regions represent the elements that failed due to fiber damage. The color map represents the delamination of the specimen. Delamination did grow within the region; however, it did not grow significantly enough to cause failure. Transverse matrix cracks initiated and propagated through out the simulation and show remarkable similarities in the X-Ray CT images. Failure of the 0° plies was observed at step 50 near the modeled specimen's edges, but did not contribute to the ultimate failure of the specimen. The specimen was still able maintain its load bearing capacity. Figure 4.6.14 is a side-by-side comparison of the damage between simulation and an ultrasonic image. Even though immersion ultrasound only has the capability to quantify delamination, the shape of the damage has remarkable similarities with the damage from the simulation.

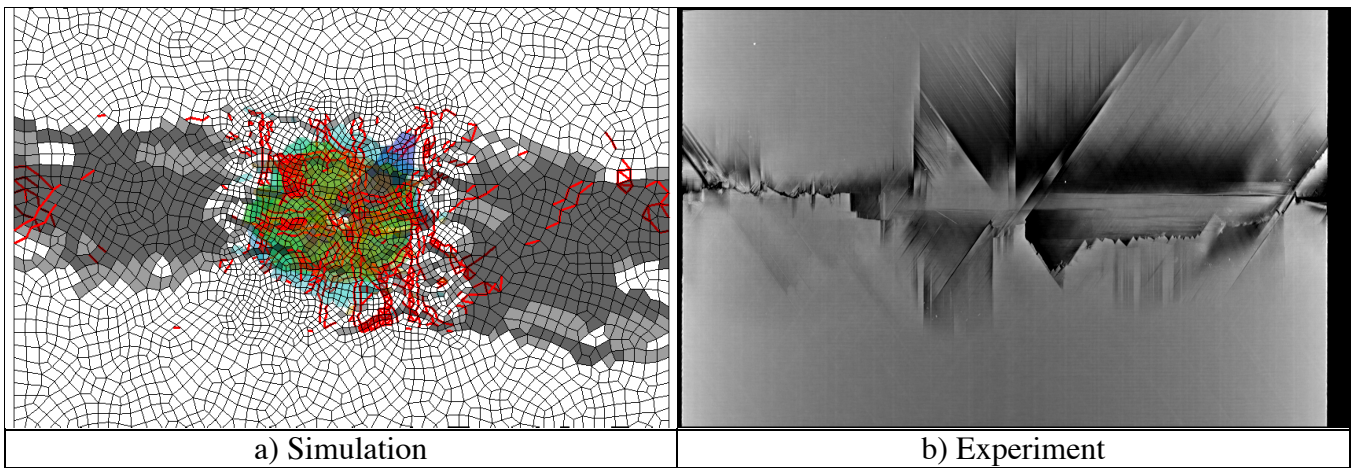


Figure 4.6.13 – Damage at ultimate failure for a) Simulation b) Experiment, X-Ray CT

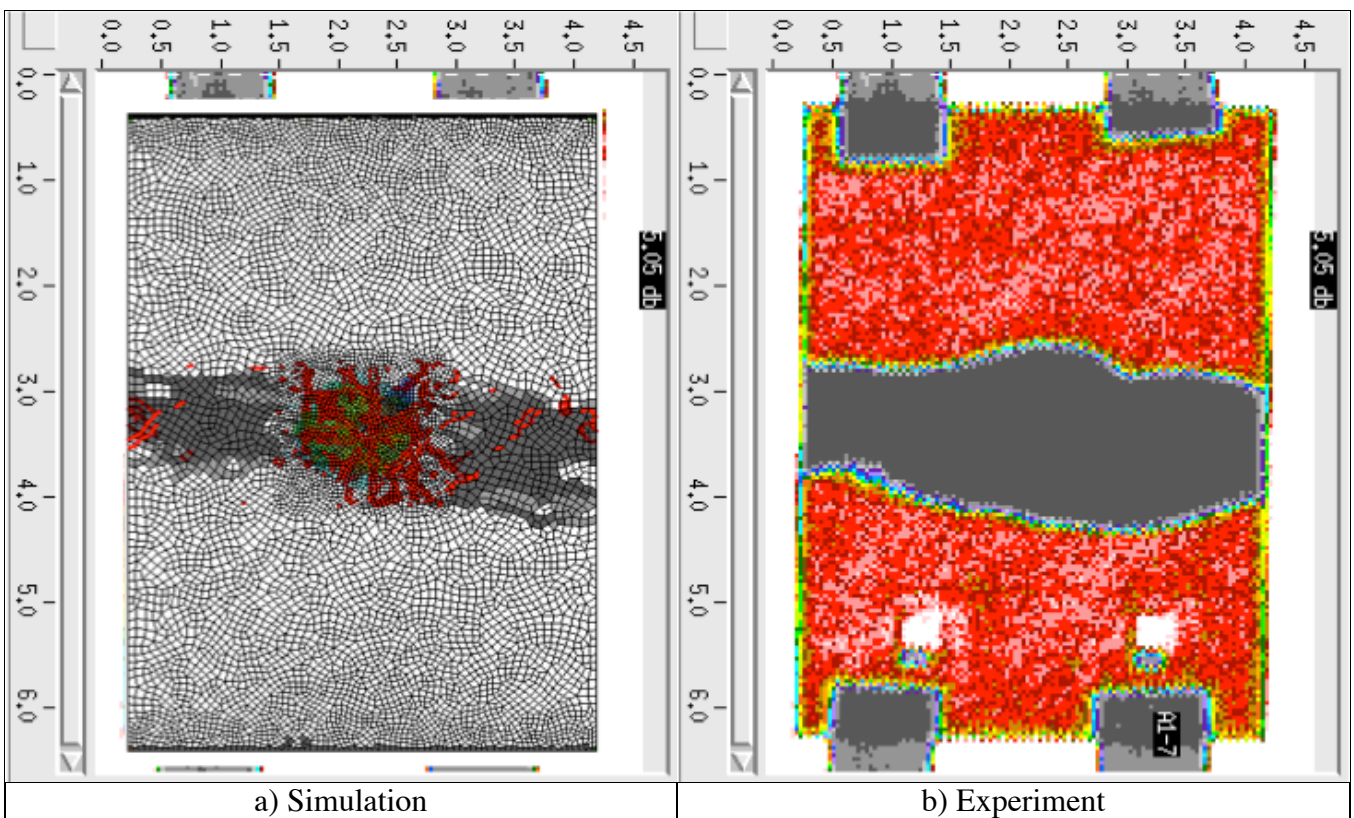


Figure 4.6.14 – Damage at ultimate failure for a) Simulation b) Experiment, Immersion Ultrasound

Even though the model was able to characterized damage and the growth of damage, it failed in predicting the ultimate load of the experiment. Figure 4.6.15 is a graphical representation of the load versus displacement data between the simulation and experiment. The average strain for the simulation was calculated by dividing the length of the specimen to the displacement. The effective modulus for the

experiment (34.666 GPa) and simulation (32.762 GP) were within 6%. The simulation over-predicted the experiment by 100%, nearly twice the experimental value.

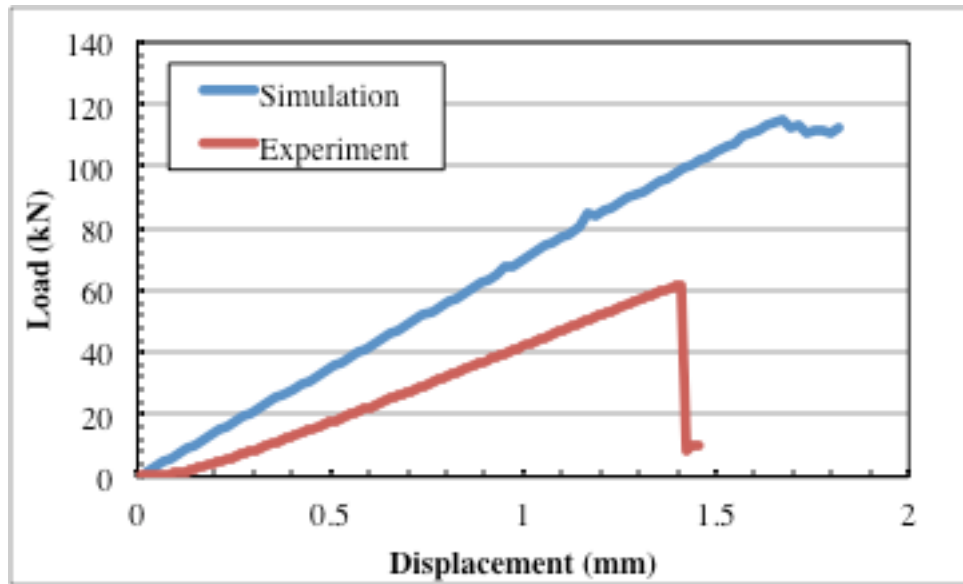


Figure 4.6.15 – Damage at ultimate failure for a) Simulation b) Experiment, Immersion Ultrasound

Several conclusions could be made to the reasoning behind this. The simulation did not take into account large displacements that were occurring and as a result were not capturing the buckling behavior of thin composite plates. However, would it be sufficient to reduce the strength by half? The modulus of the simulation and the experiment were within 6%, which means that the global stiffness of the composite does not affect the residual strength. However, the local reduction of modulus in the impacted region was not modeled. BSAM currently does not have the capability to model the reduction of modulus, which would represent fiber/matrix damage in the model. It could also be that the governing laws that dictate delamination growth are insufficient for modeling compression after impact driven growth.

4.7 Conclusions

Compression after impact test for four different stacking sequences were conducted to understand the performance of thin unidirectional carbon fiber composites. Each of the panels were impacted with 10 Joules of energy using a drop weight tower. Damage in the form of transverse matrix

cracks and delamination formed which reduced the compression strength of the composite plates. The reduction of strength for Panel A-D were 24.2%, 31.1%, 22.9%, and 26.0%. Although the models were not able to predict the failure strength of the composite, it did remarkably well in predicting the damage pattern. The simulation found that the dominating mode of failure was fiber breakage, which is contrary to what literature has provided.

Although the simulation indicated that the failure of the composite specimens was due to fiber breakage, more research needs to go into incorporating nonlinearity to take into account of large displacements. However, simply adding nonlinearity to the problem may not be sufficient enough to drop the predictive strength by 50%. A methodology that allows pre-imposed damage in the form of a reduced stiffness could be key in understanding the failure of impacted composite under compression. Literature has indicated that delamination is the dominating factor for compression after impact experiments. One key discussion point behind this assumption is that it has been based on ultrasonic images. The underlying problem of that assumption is that delamination is the only damage parameter that could be quantified using ultrasonic techniques. As nondestructive techniques become sophisticated enough to quantified all the damage in the impacted composite material, so to will the modeling tools for predict their strength. X-Ray CT provided remarkable insight that the composite did have fiber breakage.

4.8 Future Work

The current model considered only small deformation, or linear theory. The model was not able to capture the nonlinearity that occurs with thin plates. The large displacement that occurred can be seen through digital image correlation. Although there were a few similarities between the model and the experiment, a nonlinear algorithm that captures the large deformation caused from sublaminate buckling would be beneficial.

Using nonlinearity to take into the geometrical displacements of the model still may not be sufficient to accurately predict the overall strength of the composite. DDM currently uses continuum damage mechanics to model the progressive fiber failure. Although X-Ray CT and immersion ultrasound could not identify fiber failure in the impacted composite, some fiber damage appeared to

have occurred in the region. Therefore a methodology to pre-impose fiber damage needs to be incorporated if the goal is to model the failure accurately.

Chapter 5: Part II - Numerical and Experimental Investigation of Compression Strength After Impact for Unidirectional Carbon Fiber Composites of Thick Plates

The collaborative effort between Lockheed Martin and Air Force Research Laboratory (AFRL) is part of the Composite Performance Research Team Damage Tolerance Assessment Methodologies Project. The objective of the project is to:

1. Develop high fidelity matrix and fiber damage simulation methodologies for use in laminated polymer matrix composites.
2. Unify cohesive zone modeling methods for both static and fatigue damage evolution and integrate into in-house stress analysis tools for demonstration.
3. Insert nonlinear analysis capability into in-house codes to address critical compression loading induced damage evolution.
4. Assess high fidelity toolsets against real world problems, such as compression strength after impact and certification by analysis.

Chapter 5 discusses the compression strength after impact experiments, which used digital image correlation to capture the surface strains of the impacted and back surface. Section 5.2 discusses the computational results from the discrete damage model.

5.1 Introduction

Composite performance is a growing field in industry as their use in applications continues to grow. Chapter 5 is a collaborative effort between Lockheed Martin and AFRL to understand the mechanisms that drive failure for composite structures. The collaboration provides a near-real world scenario of testing damaged composites used for airframes. Each of the composites were impacted with a 1” diameter hemispherical tupper with 55 ft-lb. The specimens were then sent to AFRL to be studied. Six specimens were put through a series of nondestructive evaluation. Three of the six specimens were saved for compression testing. This section examines details about the experimental tests and the finite element modeling conducted.

5.1.1 Material Specification

Six IM7/M65 carbon fiber composited specimens were procured through Lockheed Martin. The panels were 13" x 11" with a nominal cured thickness of 0.173". The stacking sequence of the panels were $[45/90/-45/0]_{4s}$. Each of the specimens were impacted with a 1" diameter hemispherical tupper using a drop weight tower with an energy of 55 ft-lbs. Specimen-4, specimen-5, and specimen-6 were cut into 12" x 10" using a water jet process in accordance with the specifications developed by the Lockheed Martin Aero Composite Durability and Damage Tolerance Test Methodology.

5.1.2 Sample Preparation

After each of the specimens were cut, they were put into a THELCO laboratory oven at 50°C to remove excess water from the specimen. Each specimen was taken out one day out prior to testing and spray painted flat white (rust-oleum). The paint was allowed to dry for one day in a controlled environment with low humidity. One day before compression testing, each specimen was spray painted with a flat black (rust-oleum) to form a speckle pattern. This area is referred to as the digital image correlation window. Specimens were dried prior to compression testing.

5.2 Methodology

The compression fixture had a 5"x7" window where the digital image correlation (DIC) window could be viewed. A speckle pattern was painted onto the specimen using flat black rust-oleum spray paint in the DIC window area. Two 350-ohm resistance strain gauges were applied onto the impacted surface of the specimens, and calibrated for 30,000 microstrain. The location of the strains can be seen in Figure 5.2.1 and are labeled as the far field strain gauges.

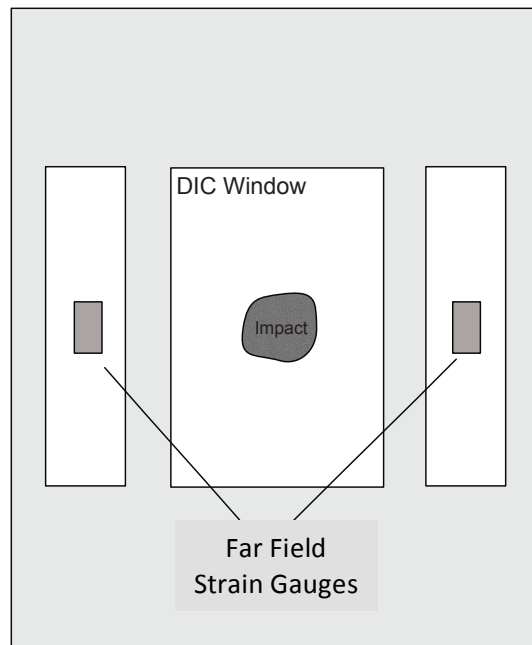


Figure 5.2.1 – Compression fixture with strain gauge location of impacted surface and DIC window

5.2.1 Procedure

The samples were carefully placed into the compression fixtures provided by Lockheed Martin. The strain gauge output wires went through 1” slots next to the DIC window. The specimens were clamped into the compression fixture using a torque wrench at 75 in-lbs. The fixture was placed on a swivel plate, which was connected to the test frame. The crosshead was moved to the appropriate height to accommodate the fixture and specimen. The actuator was moved to apply a small amount of load to stabilize the fixture and specimen. Once this was complete, all the cameras were positioned and calibrated. The specimens were initially loaded to 100 lbs to verify if there were any eccentricities in the strain gauges and a still image was captured. Finally, the test began by putting a compression load on the specimen with a displacement rate of 0.05 in/min until the specimen reached ultimate failure. Each camera was set to capture an image at one second intervals.

5.2.2 Testing Apparatus

A 200 kip (900 kN) MTS load frame was used to perform compression testing of the composite panels. Fixtures needed to be designed to accommodate the swivel plate provided by Lockheed Martin. Using a swivel plate ensured the compression fixture was aligned throughout loading of the test. During test setup the bottom swivel plate was twisted on first, then the top swivel plate laid on the bottom swivel plate as seen in Figure 5.2.2. The compression fixture constrains the composite's impacted and back surfaces, while the side edges remain traction free as shown in Figure 5.2.3. The crosshead of the MTS load frame remained fixed and the actuator applied the displacement-controlled load specified by ASTM 7137 of 0.05 in/min.

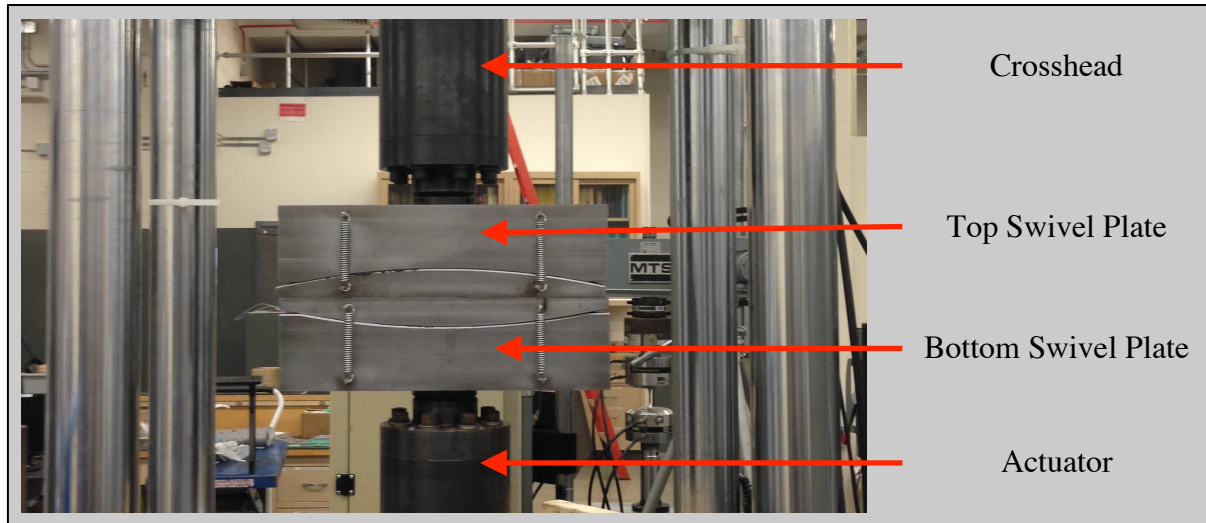


Figure 5.2.2 – Swivel Plate

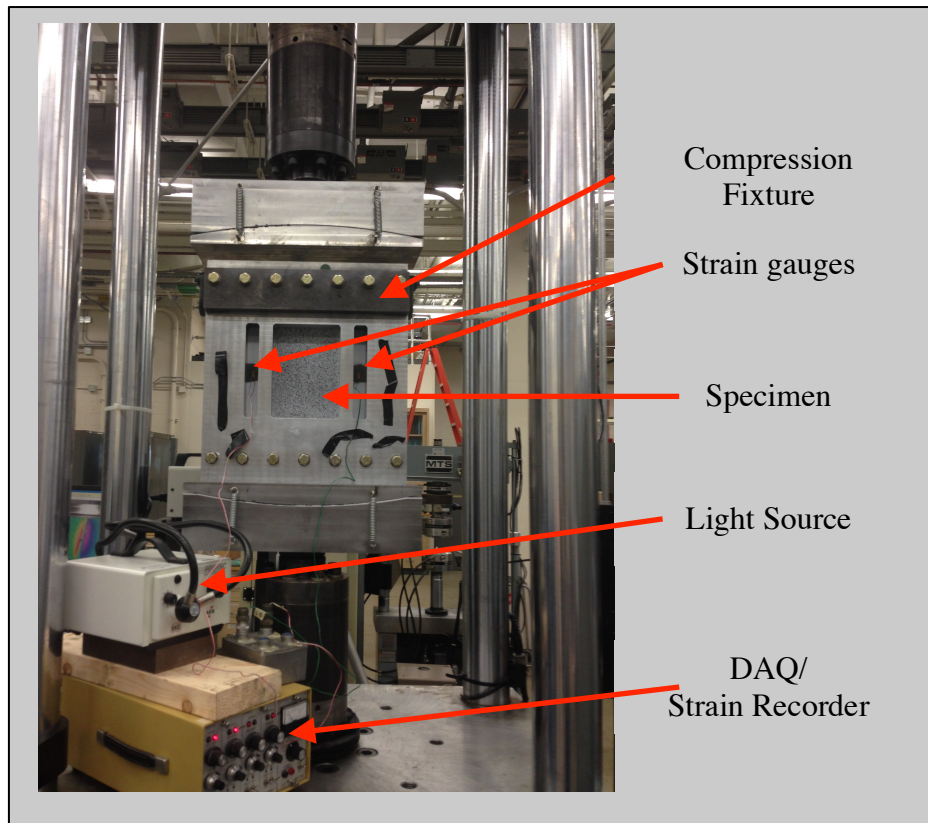


Figure 5.2.3 – Experimental setup for impacted surface

5.2.3 Digital Image Correlation

Digital image correlation was performed on both the impacted and back surface of the composite specimen. Each of the Point Grey Grasshopper Firewire Cameras (4 & 5 MP, with C to F mount adapters), on the composite specimen, were at an angle of 25 degrees from each other to ensure accurate strains and out-of-displacements were obtained during testing. The impacted surfaces was imaged with 35 mm lenses (5 MP) and the back surface was imaged using 20 mm lenses (4 MP). Prior to testing, still images of panels with fiducial marks were taken in several configurations to obtain calibration files to perform 3D DIC. Figure 5.2.4 shows the experiment setup of the impacted surface during calibration and the calibration panel. Figure 5.2.5 shows the camera setup for the back surface of the test.

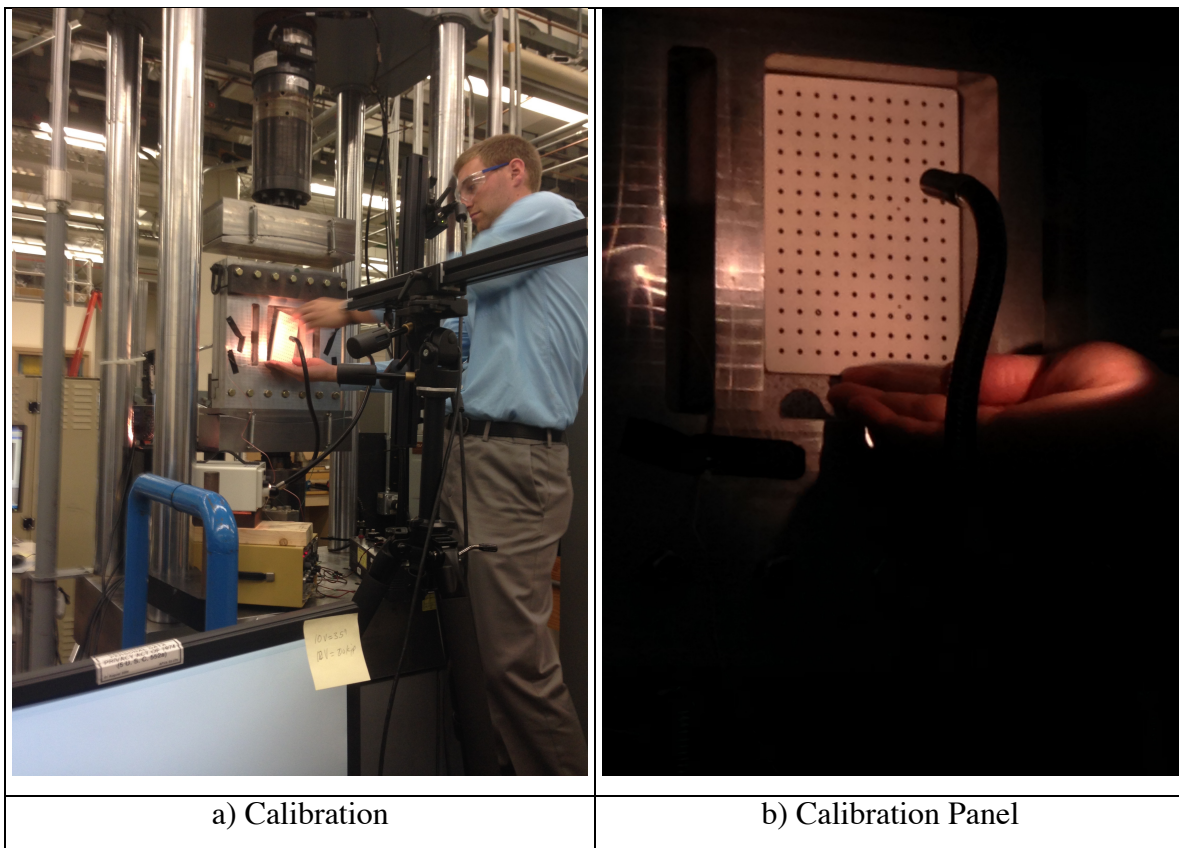


Figure 5.2.4 – DIC Calibration Prior to Each Test



Figure 5.2.5 – Camera setup of back surface

5.2.3.1 DIC Data Capture

Load and displacement data from the MTS load frame was captured using National Instruments USB-9162 Data Acquisition device and connected into the analog reader that is provided with the correlated solution software. The strain gauges were put into the remaining outputs of the DAQ to record strain data. The strain gauges were calibrated for 30,000 microstrain per volt. The load and displacement were calibrated to 200 kip per 10 V and the 2.3 inches per volt.

To verify alignment, the specimens were loaded to 100 lbs. Still images were taken for DIC while strain was recorded for real time information of the alignment. During the compression tests, the cameras were set to sample every second.

5.3 Results and Discussion

Previous tests were performed by Lockheed Martin/Intec to determine the residual strength after impact for IM7/M65. The mechanical tests conducted in the present study were in good correlation with the information Lockheed Martin provided. The average failure load of the tests was 50.045 ± 0.665 kips. Although only three tests were conducted, the average failure was close to Intec assessment of 48 ± 5.8 kips. Figure 5.3.1 represents the load versus displacement curves obtain from the load frame.

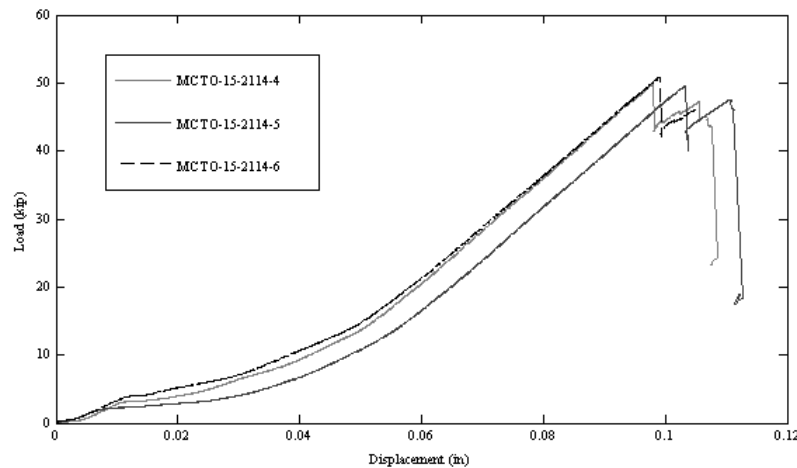


Figure 5.3.1 – Load vs Displacement

5.3.1 Digital Image Correlation Results

During compression testing, DIC was performed on the impacted and back surface of the specimens. Figure 5.3.2 is a photo of the camera stand that was used for the impacted and back surface.

The angles between the cameras were approximately 25° between each other. When correlating the images for the back surface, the orientation of the cameras shows that the actuator comes from the left side of the images. When correlating the images for the impacted surface, the actuator comes from the right side of the images. The boundary conditions of the crosshead, actuator, strain gauges (virtual DIC) and lines can be seen in Figure 5.3.3 and Figure 5.3.4. The DIC strain gauges were placed so they could be compared to previous experimental strains. Line profiles were obtained to get a representation of the permanent deformation of the samples for modeling purposes. In the figures, it's important to know the location of the crosshead of the load frame and the actuator since the configuration for the camera setups is slightly different. For the back surface, the actuator moves from the left of the screen while the impacted surface the actuator moves from the right. The crosshead is fixed in position while the actuator is applying the load to the specimens in compression.

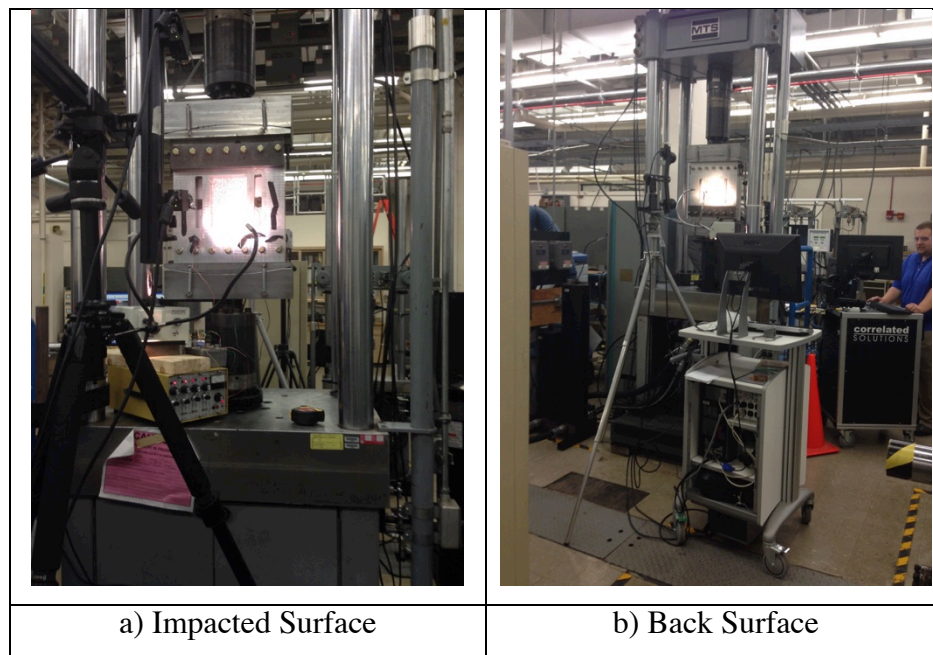


Figure 5.3.2 – Load vs Displacement

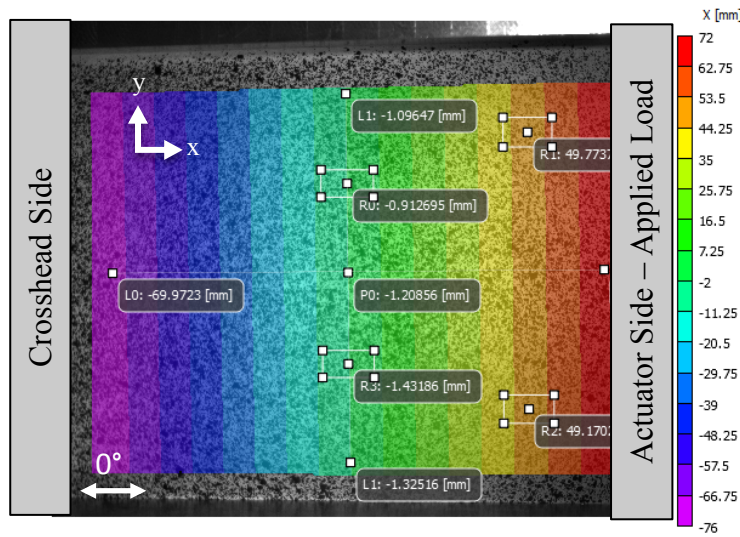


Figure 5.3.3 – Impacted Surface DIC strain gauge location and setup

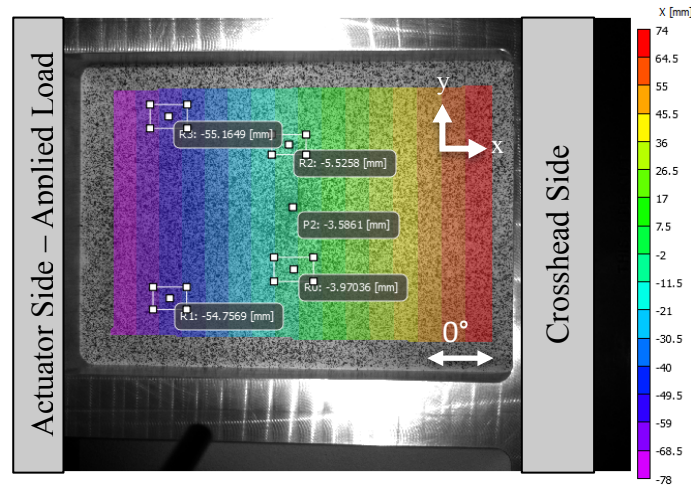


Figure 5.3.4 – Back Surface DIC strain gauge location and correlation setup

The axial strains (ϵ_{xx}) for the impacted and back surface are with respect to the x-coordinate direction, which represents loading direction (along the 0° ply). The load is applied through the actuator, while the crosshead is fixed. The transverse strains (ϵ_{yy}) are perpendicular to the axial strains, which are in the y-coordinate direction for each of the tests. For the duration of the study, axial strains may be referred to strains in the loading direction.

5.3.1.2 DIC: Profilometry

Using z-coordinate data obtained from DIC, line profiles of the permanent deformation were created. Although noisy, the profiles obtained correlated well with optical profilometry done on specimen-1, specimen-2, and specimen-3 in the previous section. Figure 5.3.5 represents the line profiles of the impacted surface obtained from DIC. Although they are not as accurate as optical profilometry shown in Figure 5.3.6, the maximum indent calculated from both were within approximately 0.15 mm.

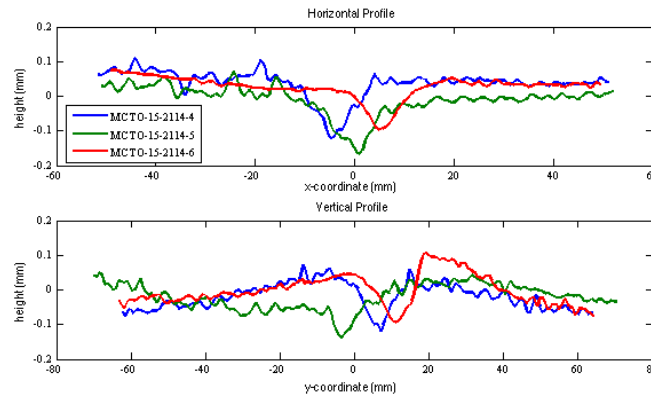


Figure 5.3.5 – Profilometry obtained through DIC

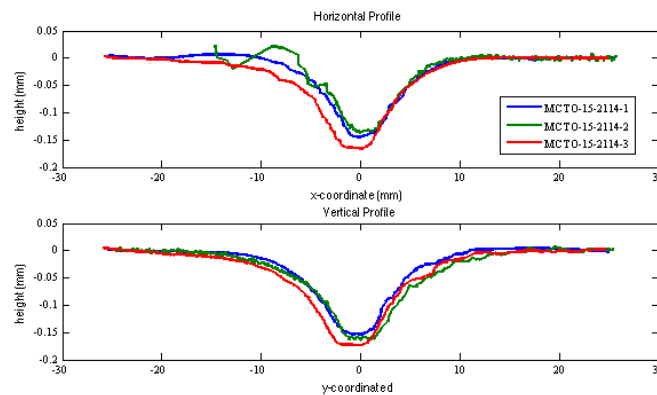


Figure 5.3.6 – Profilometry obtained through the Nanovea Optical Profilometer

Since optical profilometry could not obtain information on the back surface, DIC proved to be a useful tool in acquiring height data of the permanent deformation. For the back surface, the maximum z-coordinated value was found in the first correlated image. Then vertical and horizontal lines profiles were measured from the z-coordinates that the DIC provided. Figure 5.3.7 represents the DIC data for

the back surface with the average profile. The average permanent deformation of the back surface was 0.948 ± 0.359 mm.

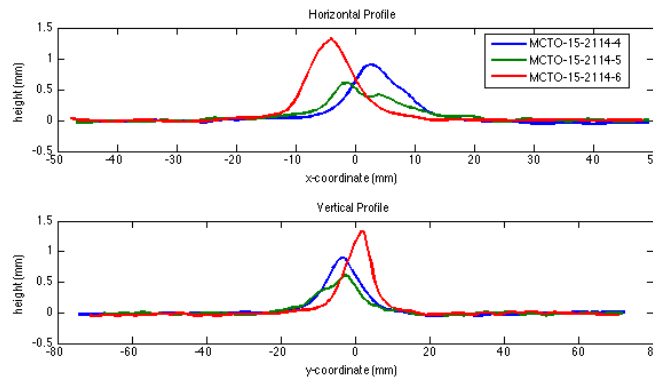


Figure 5.3.7 – Profilometry of back surface obtained through DIC

5.3.1.3 DIC: Displacements

To analyze the displacement data, rigid body motion was removed from the computation. The axial, transverse, and out-of-plane displacements were recorded. The axial displacement contours are in relation to the loading direction. Figure 5.3.8-10 below were taken 10 seconds before ultimate failure of the composite. The contours also show good agreement with each other. Additionally, repeatability is shown between each of the experiments. Several discontinuities show up in the axial and transverse displacement contours. For the axial displacements (x-direction) the impacted and back surface have similar contours. For the transverse displacements (y-direction) the contours are different between the impacted and back surfaces. For the impacted surface the transverse displacements appear to have a concentration near the center of the impact region. For the back surface, discontinuities appear around the impacted regions. The discontinuities in the back surface displacements can be attributed to the amount of fiber breakage that is present. Even though the DIC was able to provide correlation between the various points in this region, errors may exist that could influence the indicated discontinuities in the damaged area. Figure 5.2.4.9 show the out-of-plane displacements. For the impacted surface, the out-of-plane deformation shows the depth of the impact crater. For the back surface, the out-of-plane deformation shows the height of the damage as a positive, hill-like displacement.

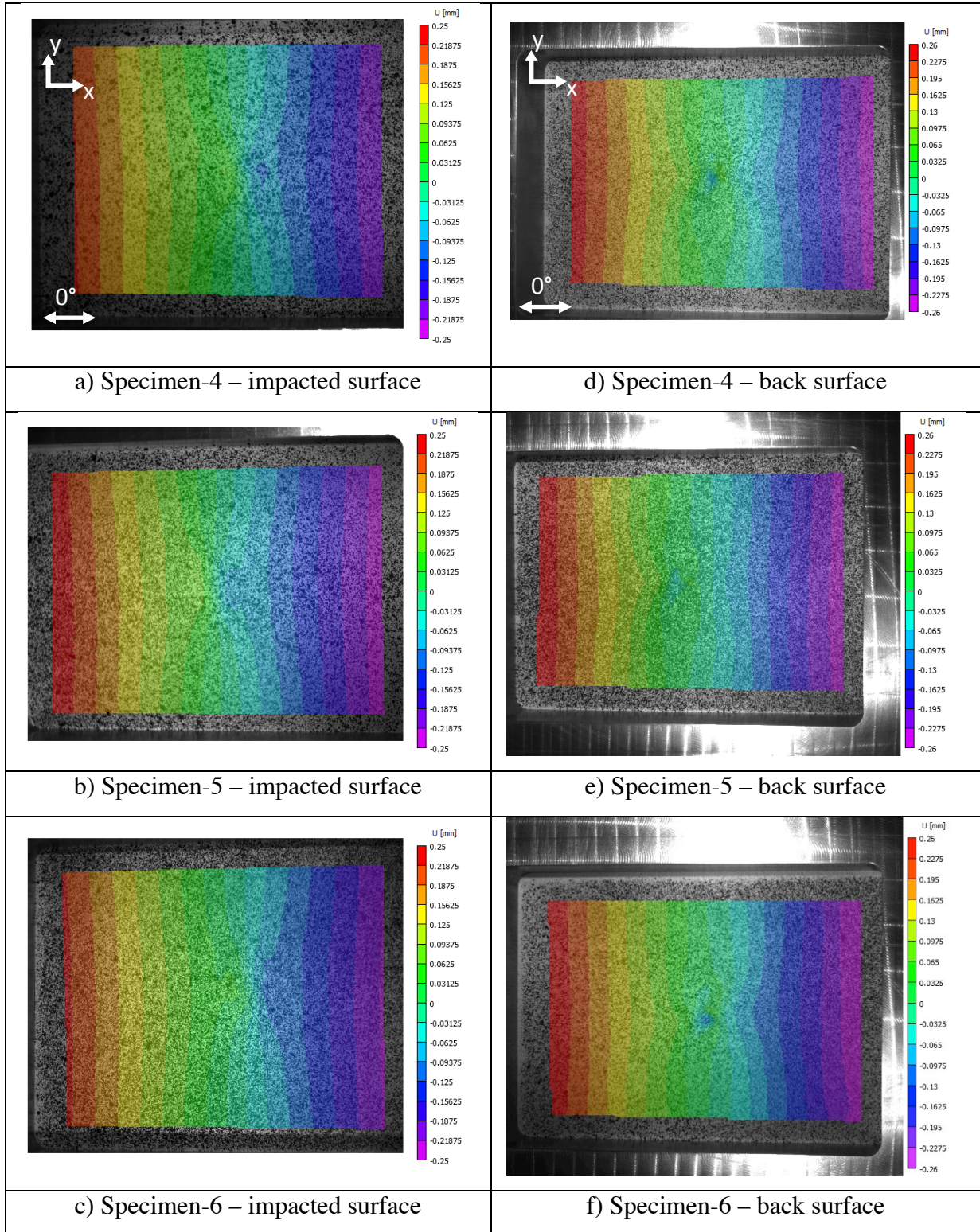


Figure 5.3.8 – U: Longitudinal displacements from DIC

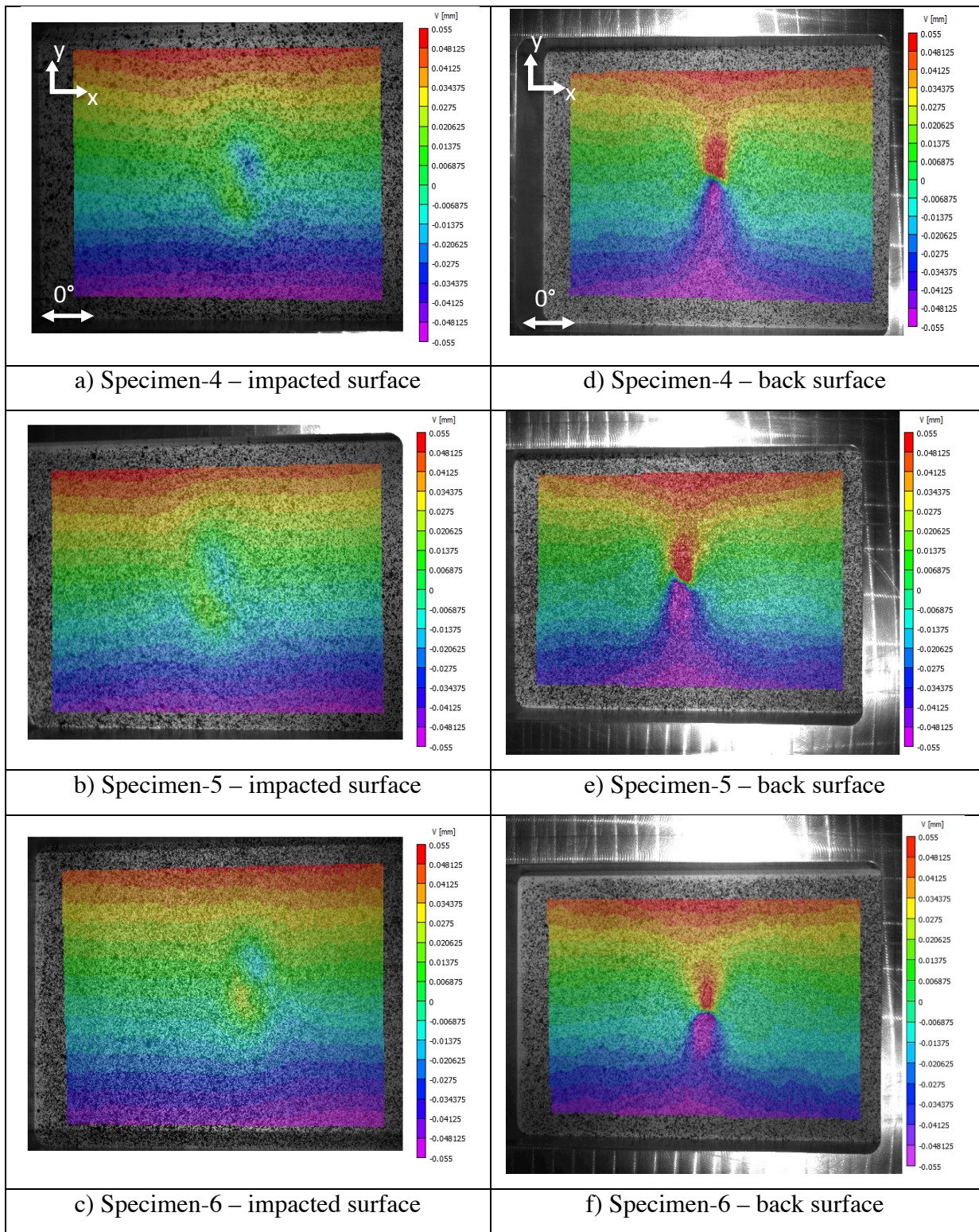


Figure 5.3.9 – V: Transverse displacements from DIC

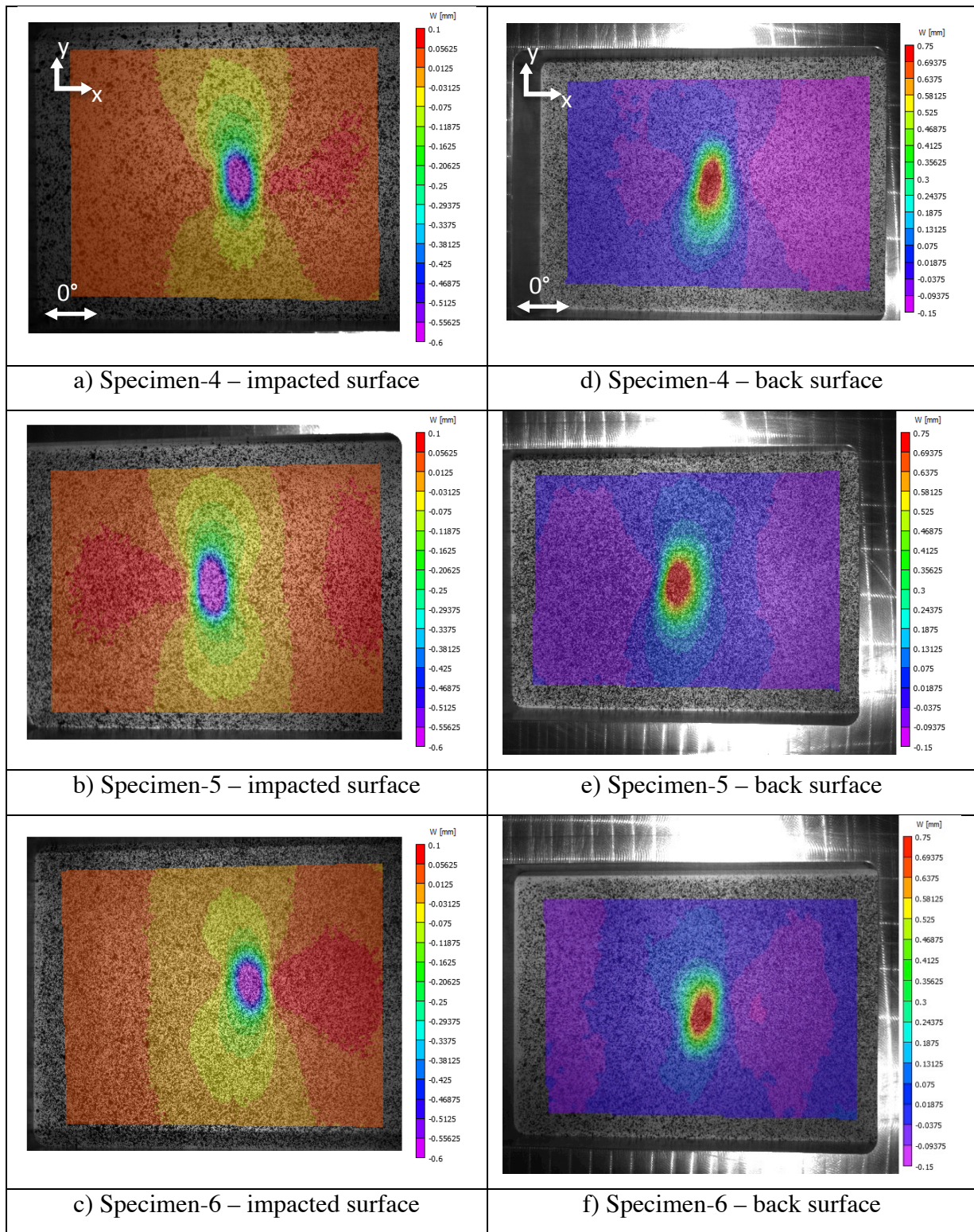


Figure 5.3.10 – W: Out-of-plane displacements from DIC

5.3.1.4 DIC: Surface Strains

For each of the tests the longitudinal strain measurements correlated well between tests. Digital Image Correlation provided contours of the impacted surface. Compressive strains were located in the center of the impact region while surrounded by tensile strains along the edges of the crater with respect to the loading direction. The compression strains in the loading direction are different in magnitude, almost to the order of 10. Figure 5.2.4.11 is the graphical representation of the contours for specimen-4, specimen-5, and specimen-6. The correlated images below were taken 10 seconds before ultimate failure of the composite.

When observing the back surface, tensile strains were located in the center of the permanent deformation region while surrounded by compressive strains with respect to the loading direction. The contours take up a larger area due there being more permanent deformation on the back surface than there is on the impacted surface.

The transverse strains from DIC also show a concentration of compression strains in the center where the impact crater is present, as shown in Figure 5.2.4.12 at 10 seconds before failure. The contour of the compression strain appears to be in the shape of an X. Tensile strains are seen outside the compression region toward the sides of the specimen. The tensile strains concentrated around the impact region appeared to be greater in magnitude than the compression strains.

When analyzing the back surface of the transverse strains, there is a tensile strain concentration in the impacted region. The contours also show compressive strains surround the impacted region on the longitudinal and transverse edges of the impacted region. The tensile strains in the center are larger in magnitude than the compressive strains.

The shear strains were in good correlation between each of the tests. Although there does not appear to be a specific location where the strains are coalescing, the contours are identical. Figure 5.2.4.13 represents the shear strain contours 10 seconds before the ultimate failure of the specimen. The negative shear strains are nearly equal in magnitude to the positive shear strains. The shear strain contours for the back surface look similar to the impacted surface. The shear strains on the impacted surface are greater in magnitude to the back surface.

Major and Minor principal strains were also calculated. Figure 5.2.4.14 and Figure 5.2.4.15 represent the contours at 10 seconds before ultimate failure. Major principal strain contours seem to indicate that tensile strains that surround the impact crater play a significant role in the failure of the composite. However, the minor principal strain contours seem to indicate that the compression strains in the impact region play a significant role in the failure of the composite as well. The minor principal strains look similar to the contours seen in longitudinal strain. The same observation was seen in the back surface. However, the magnitude of the principal strains was larger on the back surface than the impacted surface. This is primarily due to the amount of permanent deformation that is present.

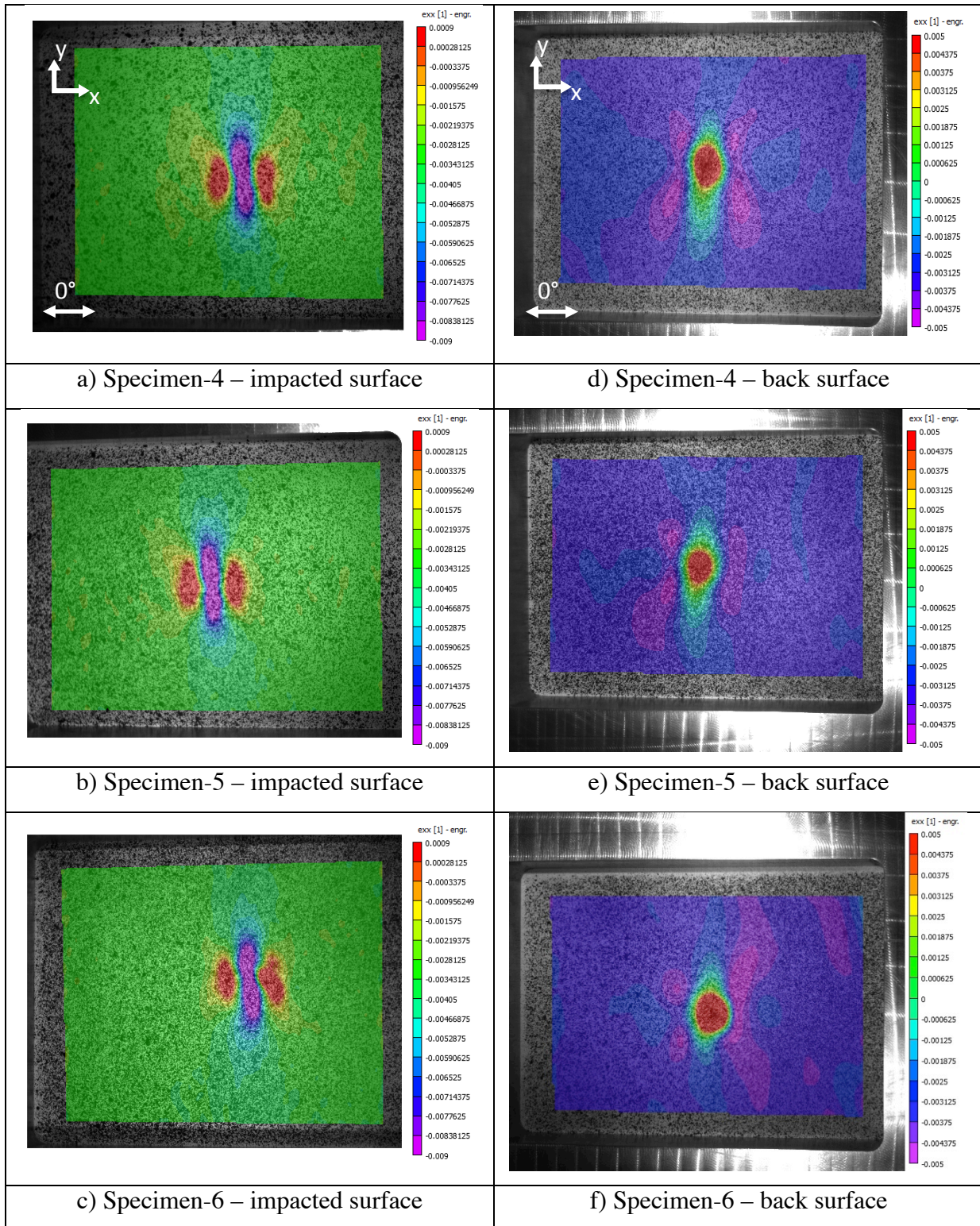


Figure 5.3.11 – Axial strain contours from DIC measurements

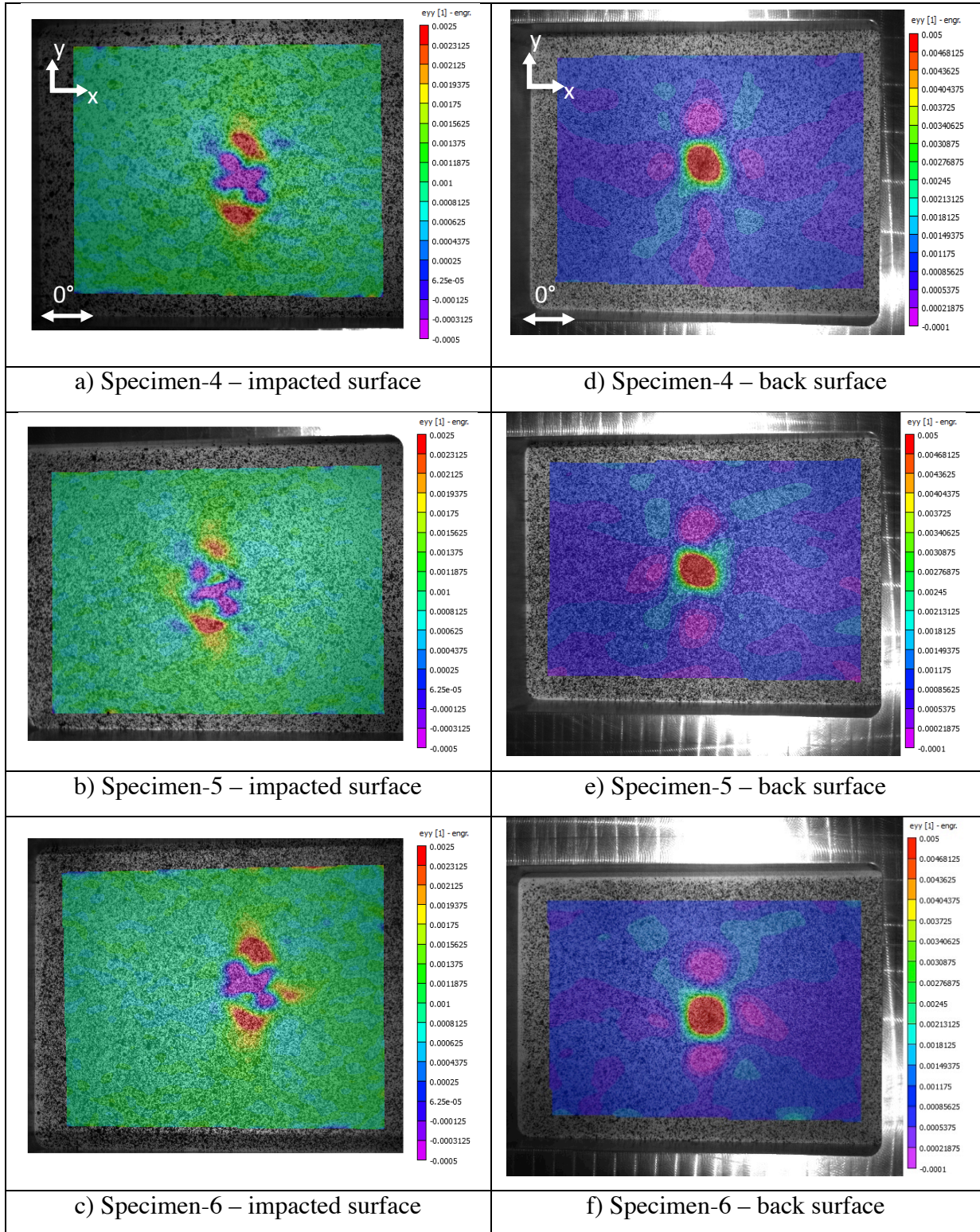


Figure 5.3.12 – Transverse strain contours from DIC

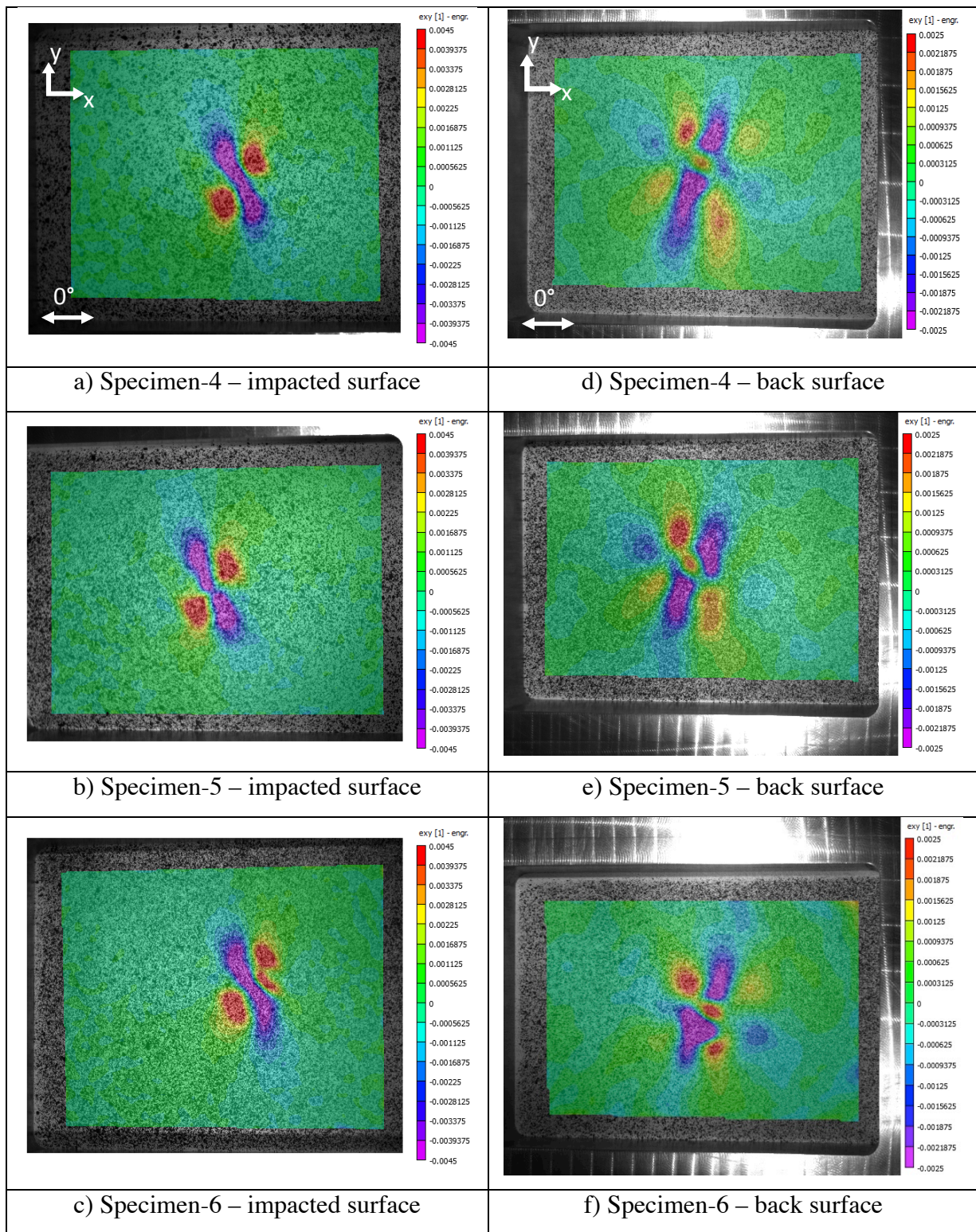


Figure 5.3.13 – Shear strain contours from DIC

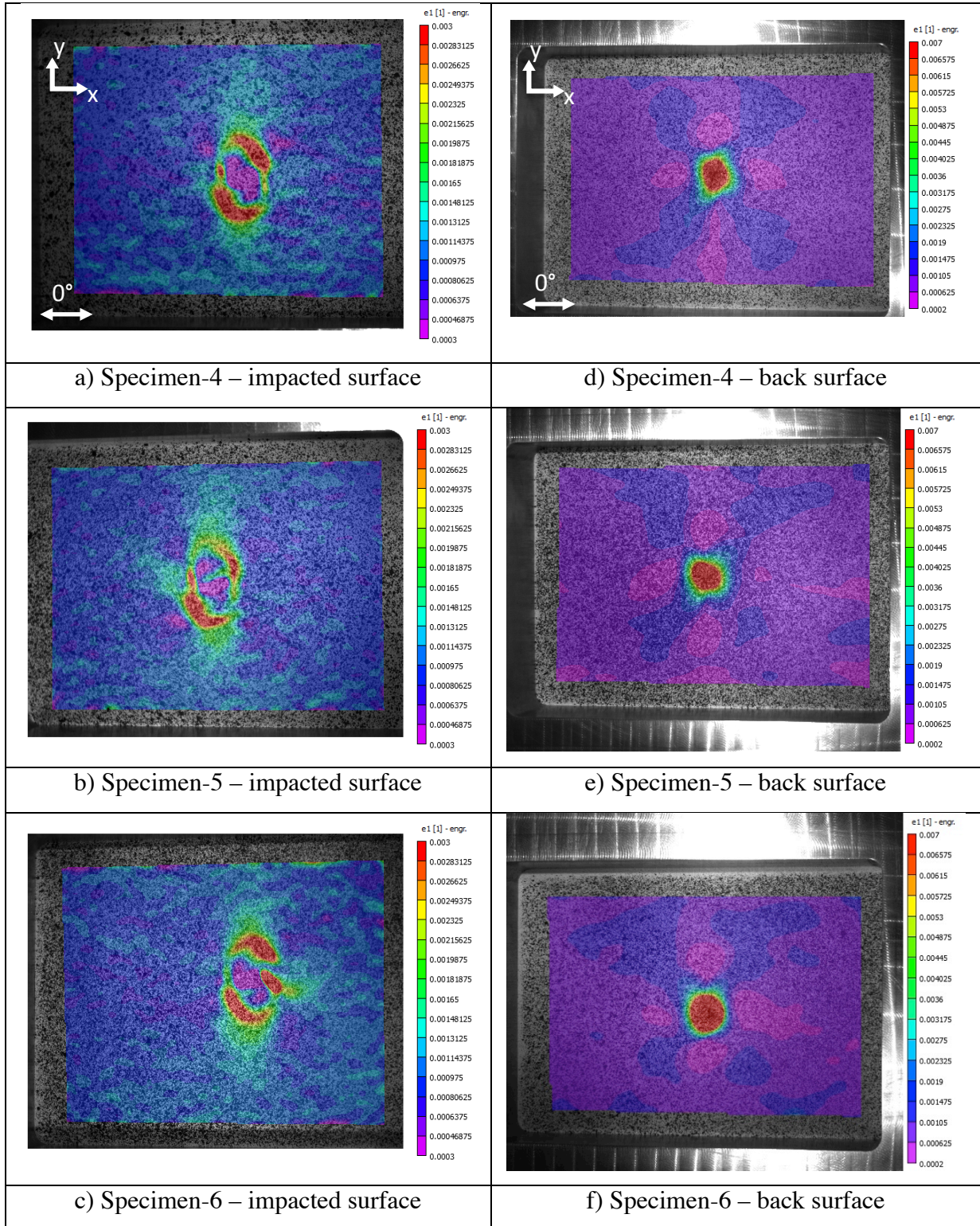


Figure 5.3.14 – Major principal strain contours from DIC

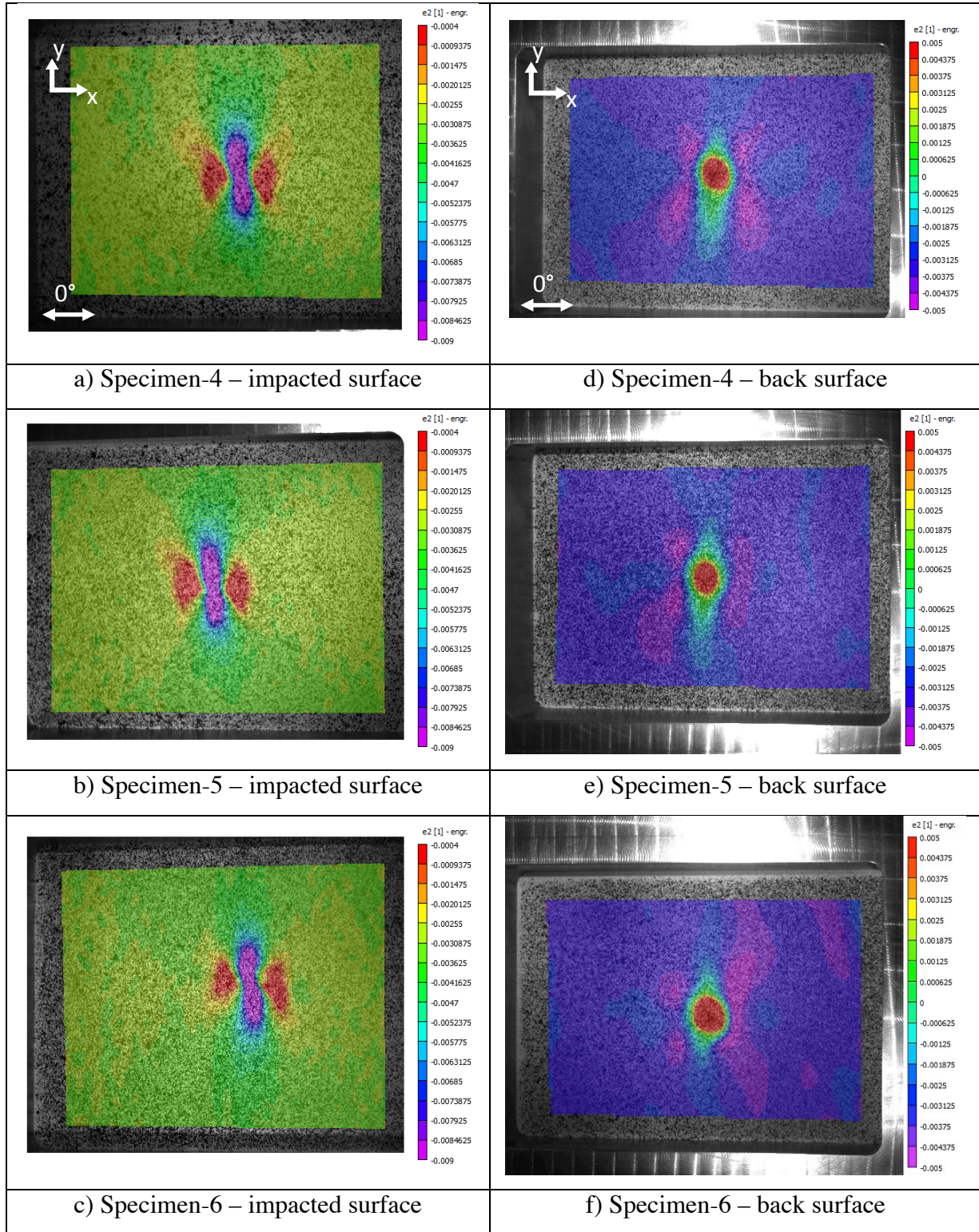


Figure 5.3.15 – Minor principal strain contours from DIC

Virtual strain gauges were placed as seen in Figure 5.3.16. Strain gauge Location 1 (Loc1) is 1" away from the center of the impact in width and on the right side of the specimen. Strain gauge Loc2 is 1.5" away from the center in width and 2" away from the center in length. Strain gauges Loc3 and Loc4 are a reflection of Loc1 and Loc2 for redundancy. Actual 350-ohm strain gauges were placed also on the specimen outside the DIC window. Figure 5.3.16 shows the strains with respect to the loading direction for Loc1, Loc2, Loc3, and Loc4.

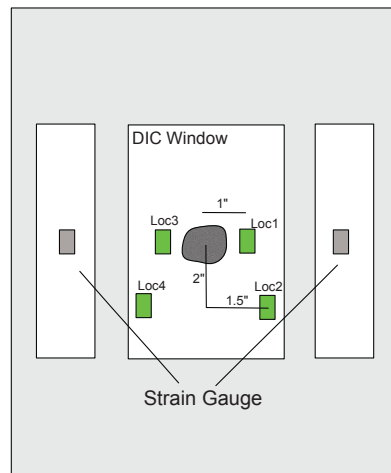


Figure 5.3.16 – Physical and virtual strain gauge location respect to fixture and DIC window

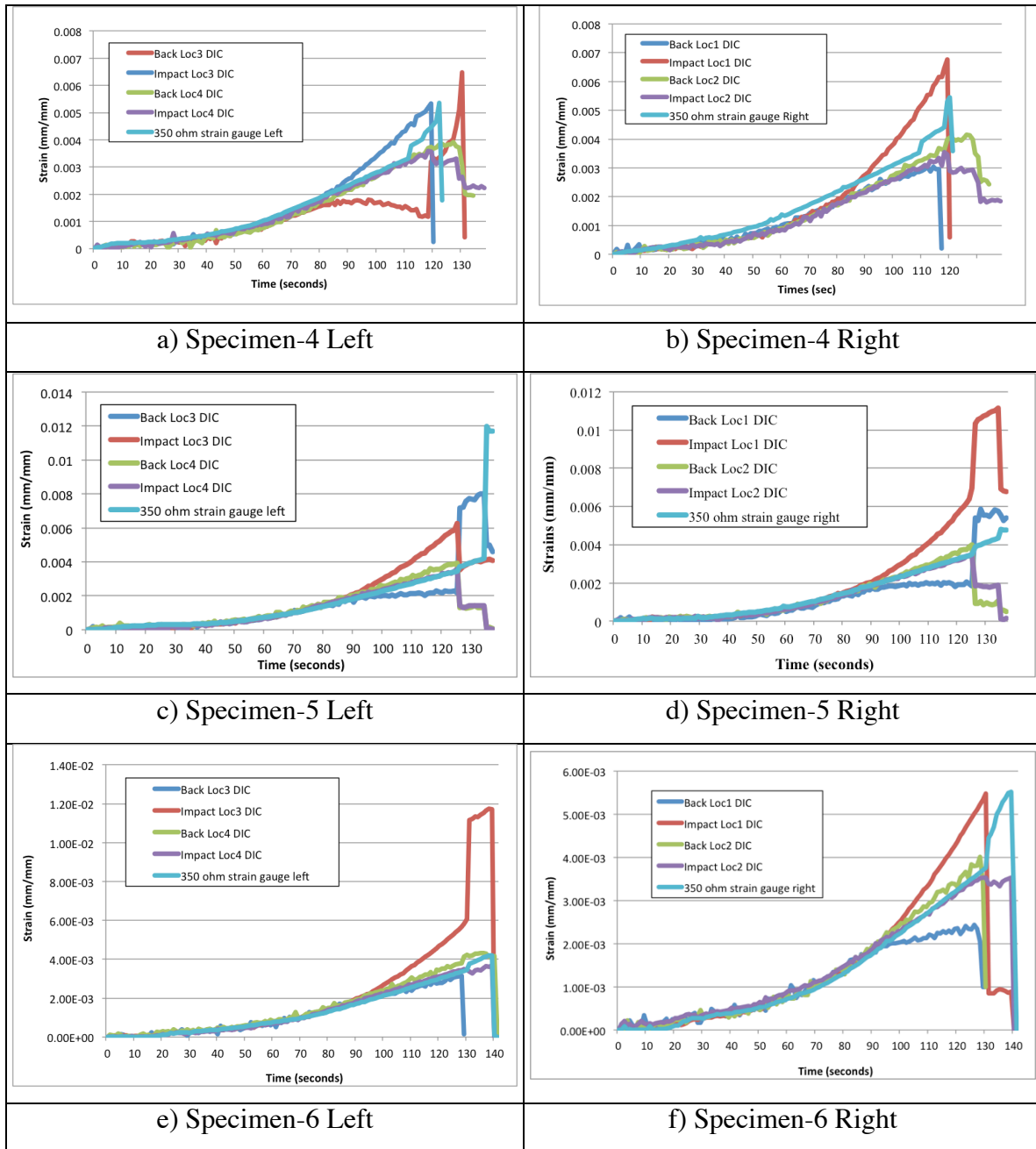


Figure 5.3.17 – Compressive strains obtained from virtual DIC and physical strain gauges

5.3.2 Nondestructive Evaluation: Post Damage of Compression After Impact

Each of the specimens went through immersion ultrasound and X-ray to capture the damage caused through compressive loading. The following sections discuss briefly the techniques used to characterize the post-impact damage. Immersion ultrasound can only capture delamination. Figure 5.3.18-20 show images of the nondestructive techniques performed on specimen-4. Appendix H and

Appendix I show the time of flight images and the amplitude data for specimen-4, specimen-5, and specimen-6. The specimens also went through the X-ray, which can be seen in Appendix J.

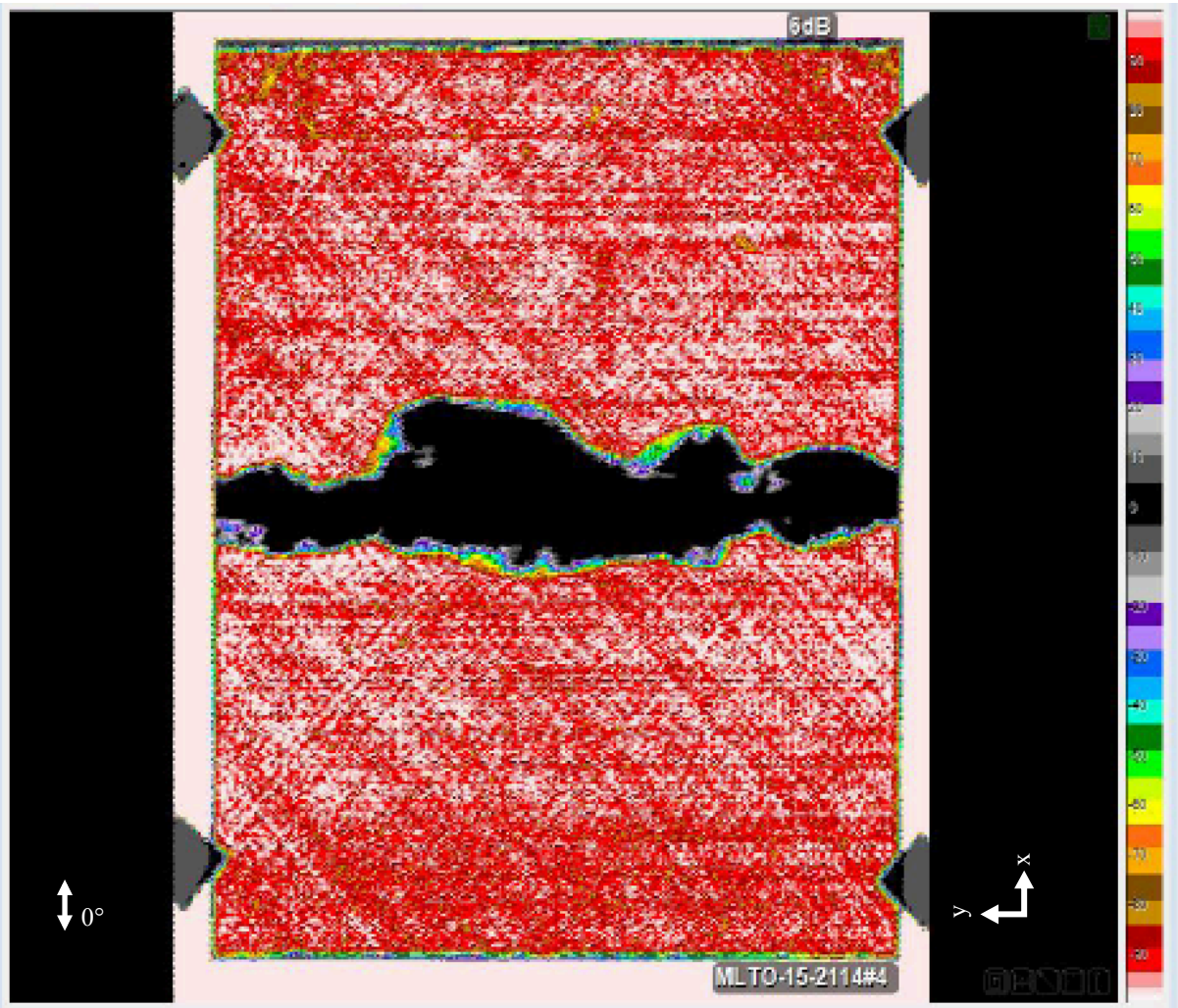
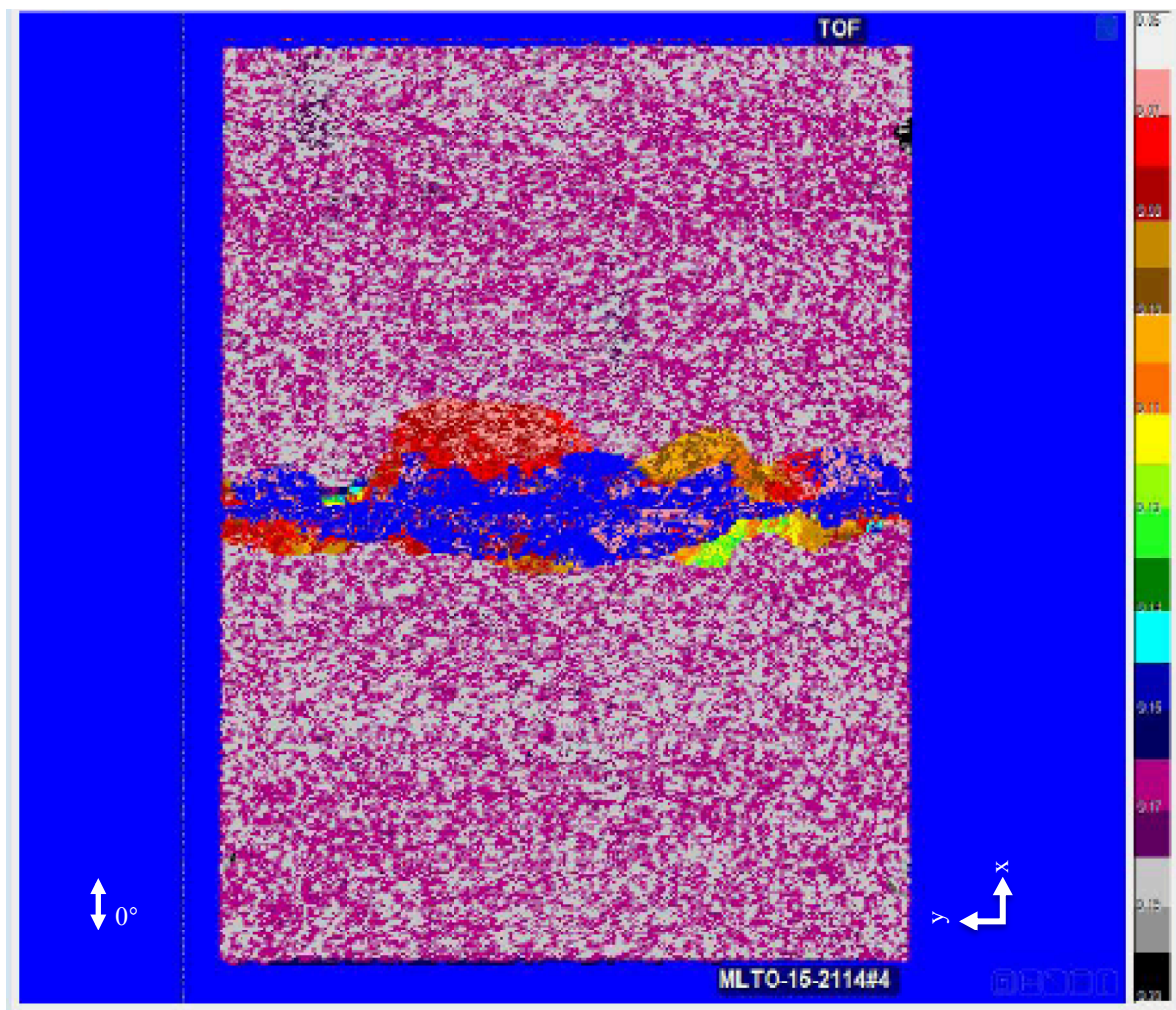


Figure 5.3.18 – Ultrasound amplitude data for specimen-4



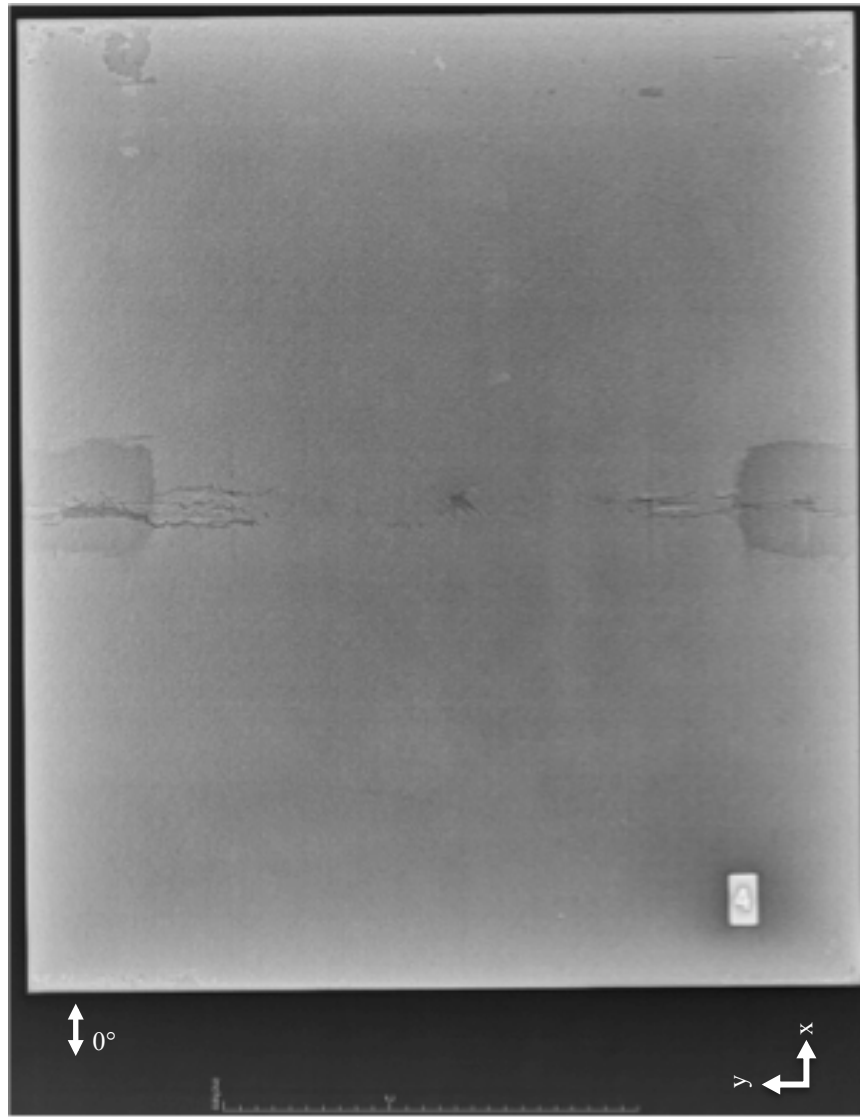


Figure 5.3.20 – 2D X-ray image of specimen-4

5.4 Discrete Damage Model

The DDM approach consists of Mesh-independent Crack (MIC) modeling of matrix cracks in each ply of the laminate, and modeling the delamination between the plies by using a cohesive formulation at the ply interface. The matrix cracks are modeled by using the Regularized eXtended Finite Element Method (Rx-FEM) proposed in Chapter 4. The regularized formulation deals with continuous enrichment functions, and replaces the Heaviside step function with a continuous function changing from 0 to 1 over a narrow volume of the so called gradient zone. The formalism tying the volume integrals in the gradient zone to surface integrals in the limit of mesh refinement was discussed

in [67,76]. The simulation begins without any initial matrix cracks, which then are inserted based on a failure criterion during the simulation. The LaRC04 failure criterion is chosen in the present work. The propagation of each MIC is performed by a cohesive zone formulation. Simulating delamination between the plies is done using the same cohesive zone formulation, however, the cohesive elements between the interfaces are inserted during initial model preparation. After the failure criterion is met at a certain location a MIC is inserted.

As discussed in Chapter 4, a discrete damage modeling framework is being implemented to investigate the damage modes such as matrix cracking, delamination and fiber breakages. For the use as a damage tolerance tool, the cracks and delamination are pre-determined entities from nondestructive evaluation.

5.4.1 Modeling Strategy

The morphology, delamination, and transverse matrix cracks were quantified using nondestructive evaluation and pre-imposed into a three-dimensional discrete damage model. Morphology of the impacted and back surface was obtained through use of the optical profilometry of the impacted surface only (the DIC back surface profile was not used), and a linear interpolation of nodes was done through the thickness of the composite. The interfacial nodes between plies were selected and given arbitrarily weak properties. Coordinate points inside a mesh were selected with the delamination region to pre-impose transverse matrix cracks into the model.

Modeling the delamination between plies uses a cohesive formulation at the ply interface developed by Turon [71]. Using equation 5.1, the initial stiffness (K) is 10^6 and the damage parameter (d) is 10^{-7} . The cohesive force for tension (Y_t) and compression (Y_c) is 60 N and 200 N for damage initiation. The same material properties were used to model crack growth. According to Turon the cohesive forces τ resisting the opening displacement jump Δu at an arbitrary crack surface point is

$$\boldsymbol{\tau} = (1 - d)K\Delta\mathbf{u} + dK\langle\Delta u_n\rangle\mathbf{n} \quad (5.1)$$

The second term in the equation prevents interpenetration of the crack surfaces. The brackets $\langle x \rangle = (x + |x|)/2$ represents the McAuley operator and vector \mathbf{n} is the unit vector to the crack surface. The damage parameter controls the crack opening and displays the length of the cracks in the model.

A Progressive Fiber Failure (PFF) approach was used to address fiber failure in composite laminates. The stiffness tensor at a given stress level is defined as $C=(1-d)C_0$, where C_0 is the initial stiffness. The damage variable, d , is defined based on the stress strain relationship proposed by Maimi et al [73-74], and is shown in Figure 5.4.1. Determination of the numerical values of the parameters defining the cohesive curve in Figure 5.4.1 for IM7/977-3 in tension, for example, include the fracture toughness, $G_X=80.0$ N/mm and coefficients $f_X=0.2$, $f_G=0.4$ as well as the characteristic length, has been addressed in [72]. The initiation stress value, X_T , represents the fiber direction strength measured on standard unidirectional couple type tests. In the simulation, two values of the failure initiation strength are: (i) $X_T=3116$ N/mm² obtained for typical 24-ply unidirectional coupon with total volume of $V_0=49548.288$ mm³ and $X=3116$ N/mm³ scaled strength for a 1 mm³ of stressed volume.

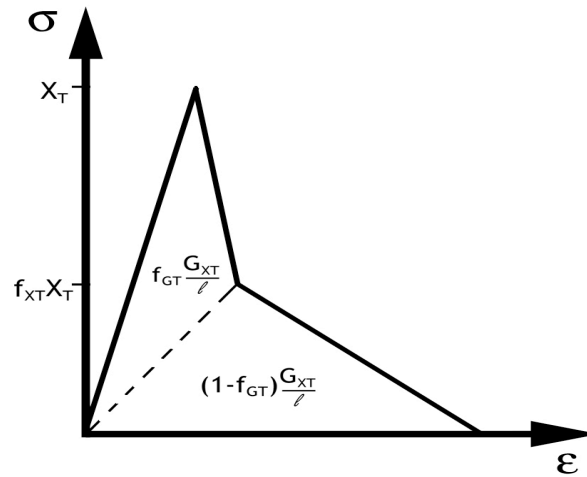


Figure 5.4.1 – Property degradation approach to fiber fracture

5.4.2 Material Properties

The mechanical properties for IM7/977-3 were obtained through an Air Force Research Laboratory program to model and characterize open hole specimens. Table 5.4.1 outlines the mechanical properties for IM7/977-3 and were used in lieu of IM7/M65 properties, which were unavailable..

Table 5.4.1 – Mechanical Properties of IM7/977-3

| | |
|---------------------------------------------------------|----------|
| Longitudinal Elastic Modulus, E11 (MPa) | 137417 |
| Transverse Elastic Modulus, E22&E33 (MPa) | 8694 |
| In-Plane Shear Modulus Major, G12 & G13 (MPa) | 5000 |
| In-Plane Shear Modulus Minor, G23 (MPa) | 3500 |
| Tensile Longitudinal Ultimate Strength, X^T (MPa) | 2905 |
| Compression Longitudinal Ultimate Strength, X^C (MPa) | 1680 |
| Shear Strength, S (MPa) | 100 |
| Tensile Transverse Ultimate Strength, Y^T (MPa) | 100 |
| Compression Transverse Ultimate Strength, Y^C (MPa) | 240 |
| Poisson's Ratio Major, ν_{12} * & ν_{13} | 0.32 |
| Poisson's Ratio Major, ν_{23} | 0.496 |
| Mode I Fracture Energy, GIC (N/mm) | 80 |
| Mode II Fracture Energy, GIIC (N/mm) | 24 |
| Longitudinal Thermal Expansion, α_{11} | 0.00 |
| Transverse Thermal Expansion, α_{22} | 30.0E-06 |

5.5 Discrete Damage Model Results

The modeled laminate ply that represents the impacted surface is at the coordinate origin and the back surface is toward the positive z-direction. This is important to understand when considering the differences between the model and DIC orientation of the coordinate system that is used to calculate displacements. For instance, the coordinate system of the model coincides with the coordinate system for the back surface DIC data. The difference between the model and DIC for the impacted surface is that the z-coordinate reference is in opposite direction. The loading direction is also different in the model with respect to DIC.

The contours were in good agreement to what was seen in the experiments. Although a linear elastic simplification was used (primarily due to limitations with the research finite element code), modeling results appear to capture the complexity of the problem. The out-of-plane displacement contours for the impacted surface match with the contours obtained from DIC.

The strain contours appear to be similar with and without the pre-imposition of cracks. Simply pre-imposing the permanent deformation appears to be beneficial to obtaining accurate strains from the

experiments. The strains in the model also show the complexity of the problem for both the impacted and back surfaces that were capture by DIC. One observation was the influence of cracks on the strain contours for the back surface. In most cases, the DIC contours are significantly smoother than the strain contours of the simulations.

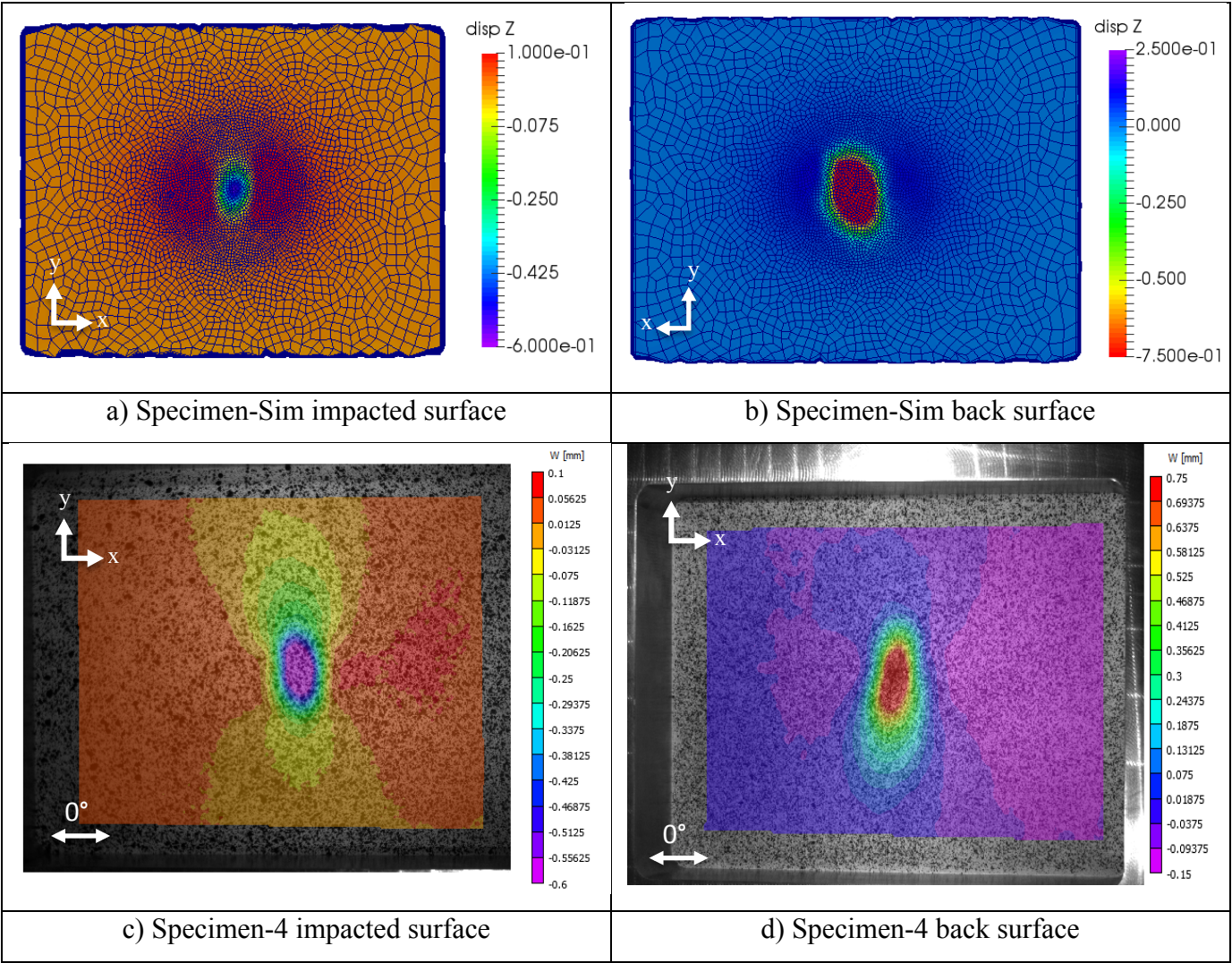


Figure 5.5.1 – Out-of-plane comparisons between simulation and DIC

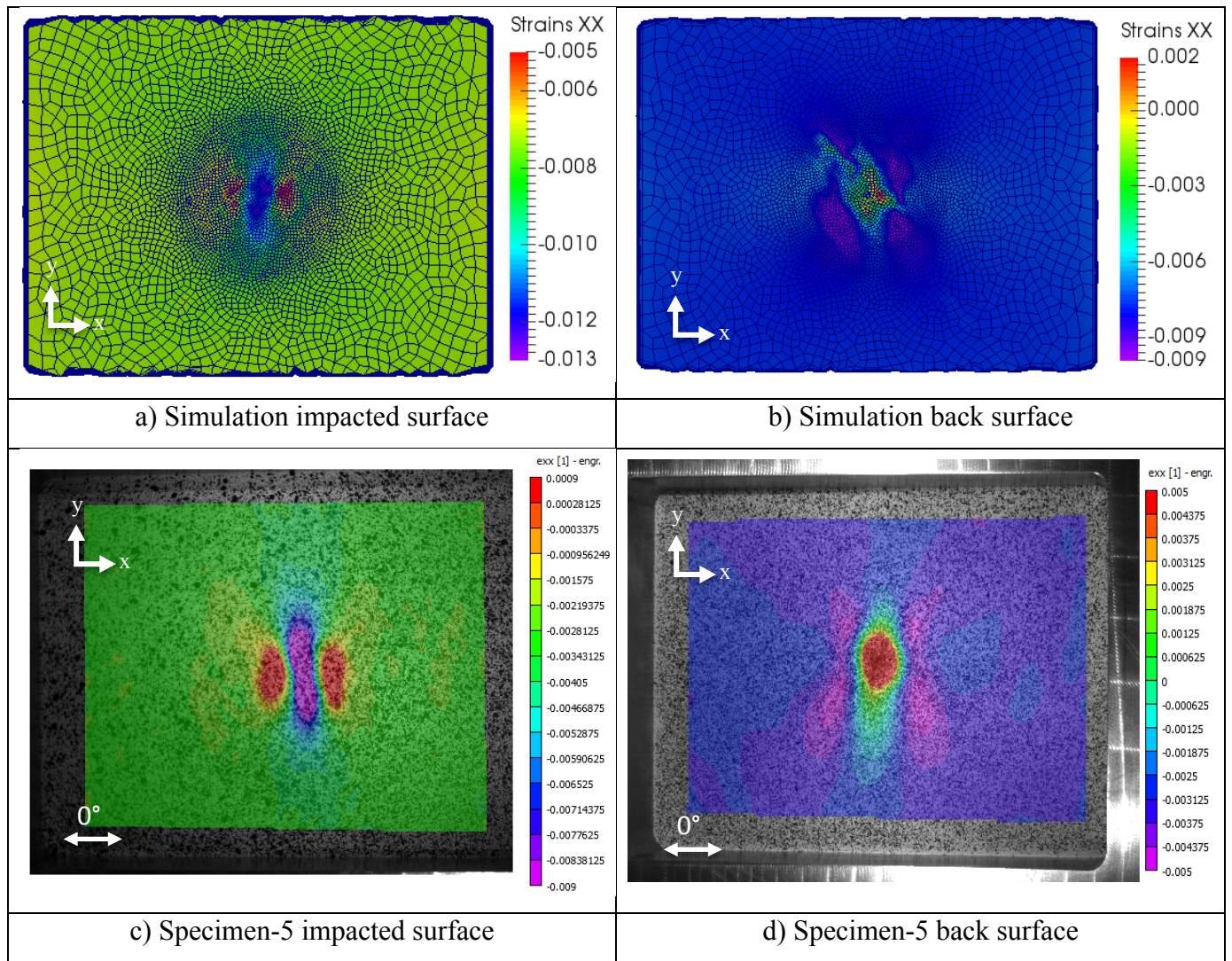


Figure 5.5.2 – Axial strain comparisons between simulation and DIC

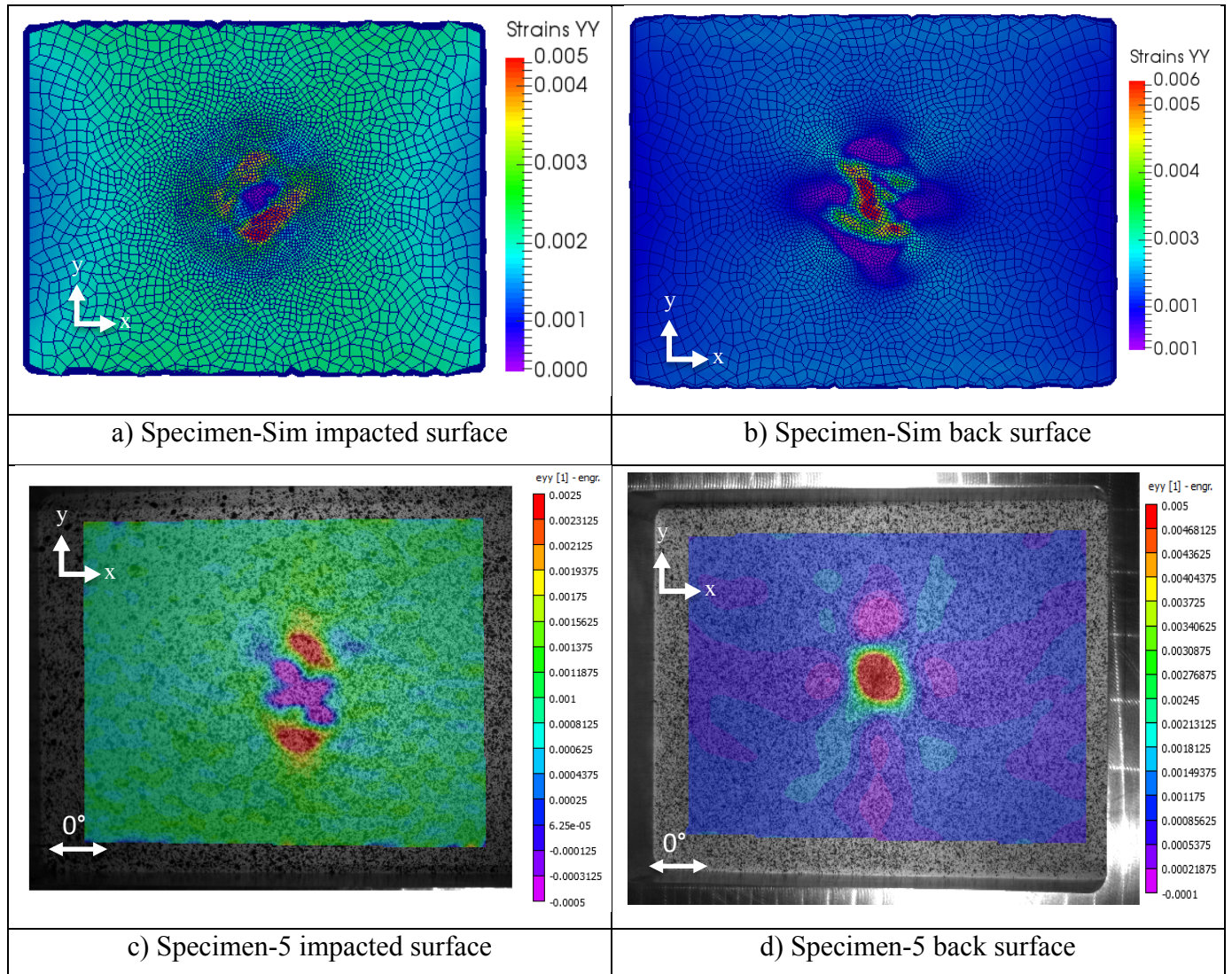


Figure 5.5.3 – Transverse strain comparisons between simulation and DIC

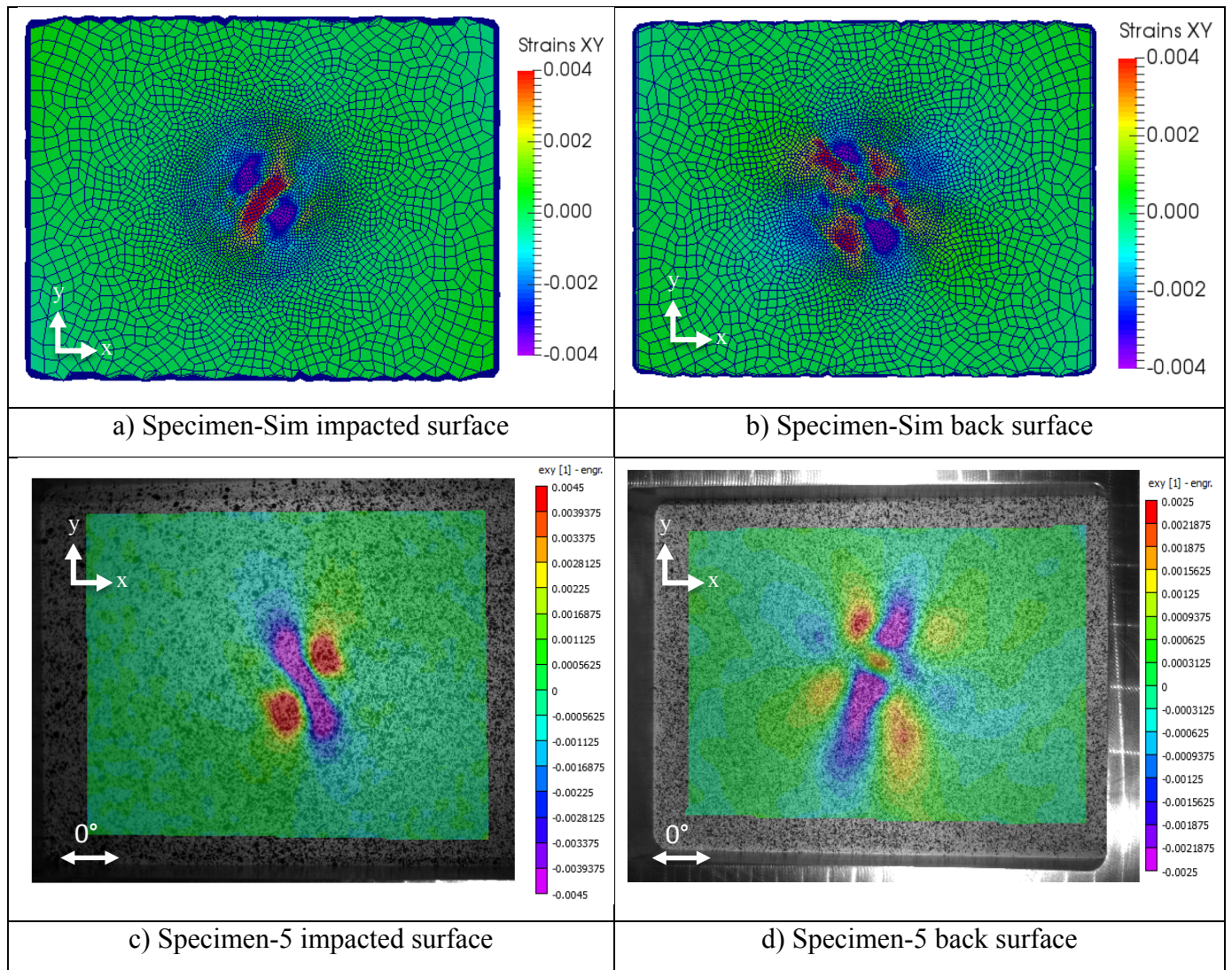


Figure 5.5.4 – Shear strains comparisons between simulation and DIC

5.5.1 Failure Prediction

Delamination patterns obtained from X-ray CT were pre-imposed into a three-dimensional discretized damage model (Figure 5.5.5 and Figure 5.5.6.a). Cracks were also pre-imposed into the model by taking transverse matrix cracks from X-ray CT (Figure 5.5.6.b). The transverse matrix crack selections were prioritized by picking the matrix cracks on the edges of delamination. The morphology of the impacted and back surfaces were obtained using the profilometry of the impacted surface only, and linear interpolations of the node positions were used to represent the damage through the thickness of the composite. Figure 5.5.6.c shows the delaminated pattern of discretized model and overlays the transverse matrix cracks to provide a visual representation of the damage.

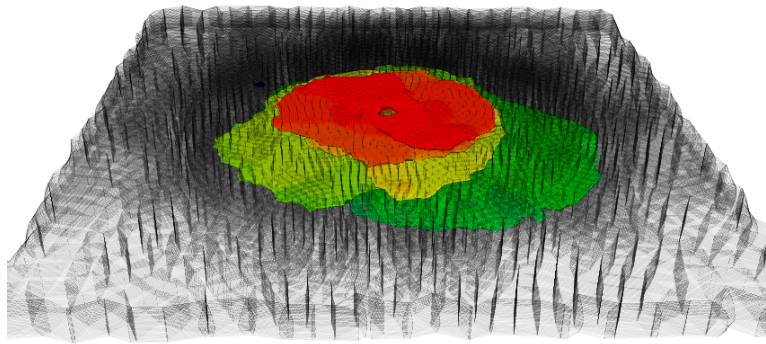


Figure 5.5.5 – 3D Representation of initial delamination

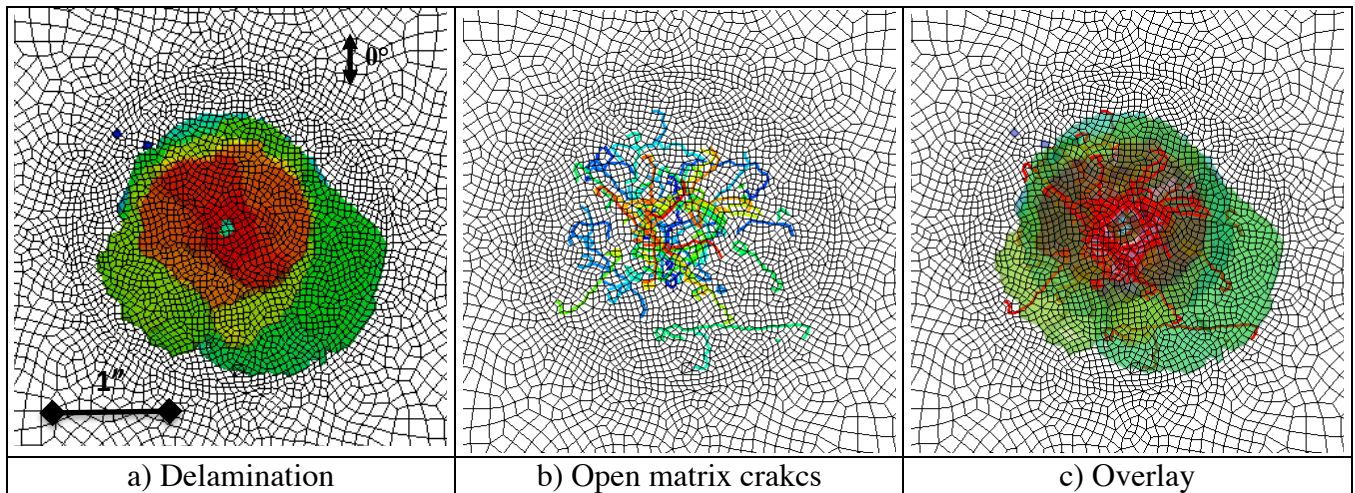


Figure 5.5.6 – Frontal image of initial delamination and open transverse matrix cracks

The simulation shows the effects of the onset and propagation of new cracks. Delamination does grow, but is miniscule compared to the growth of the transverse matrix cracks and fiber breakages. New cracks initiate in the 40th step and the original cracks continue to grow. Progressive fiber failure initiates at the 45th step. Red surfaces through the thickness of the ply represent transverse matrix crack in the images. The black and blue elements represents that the reduction of stiffness of that element has reduced indicated progressive fiber failure. Figure 5.5.7 shows the sequence of events of growth for transverse matrix cracks, delamination, and fiber failure. Figure 5.5.8 shows the sequence of events between transverse matrix cracks and the fiber failure. Fiber failure appeared to occur around transverse

matrix cracks that existed in the 0° plies. It appears that the transverse matrix cracks influence the behavior of fiber failure as new cracks began to be incorporated into the model.

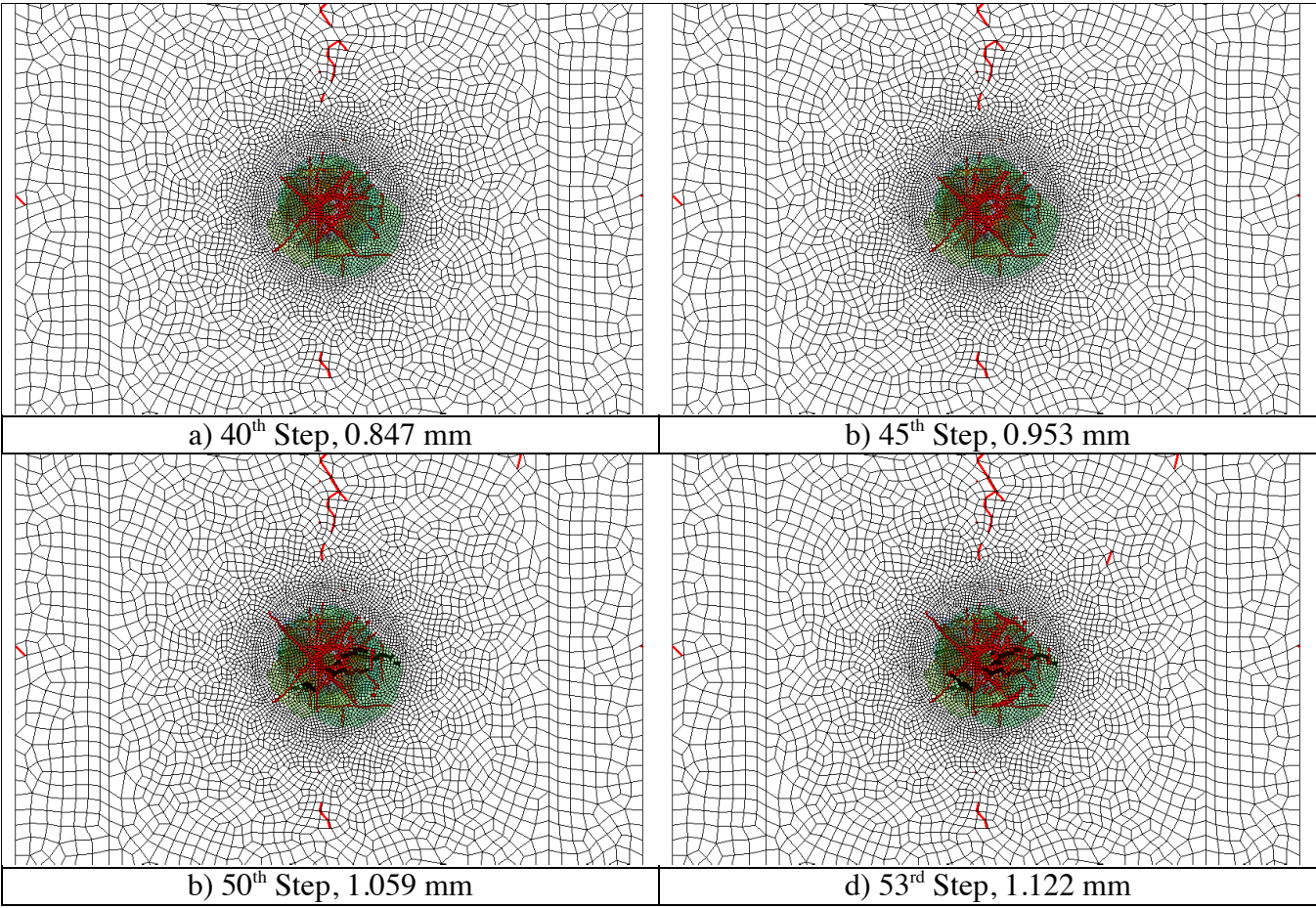


Figure 5.5.7 – Sequence of damage growth for cracks, delamination, and fiber breakage

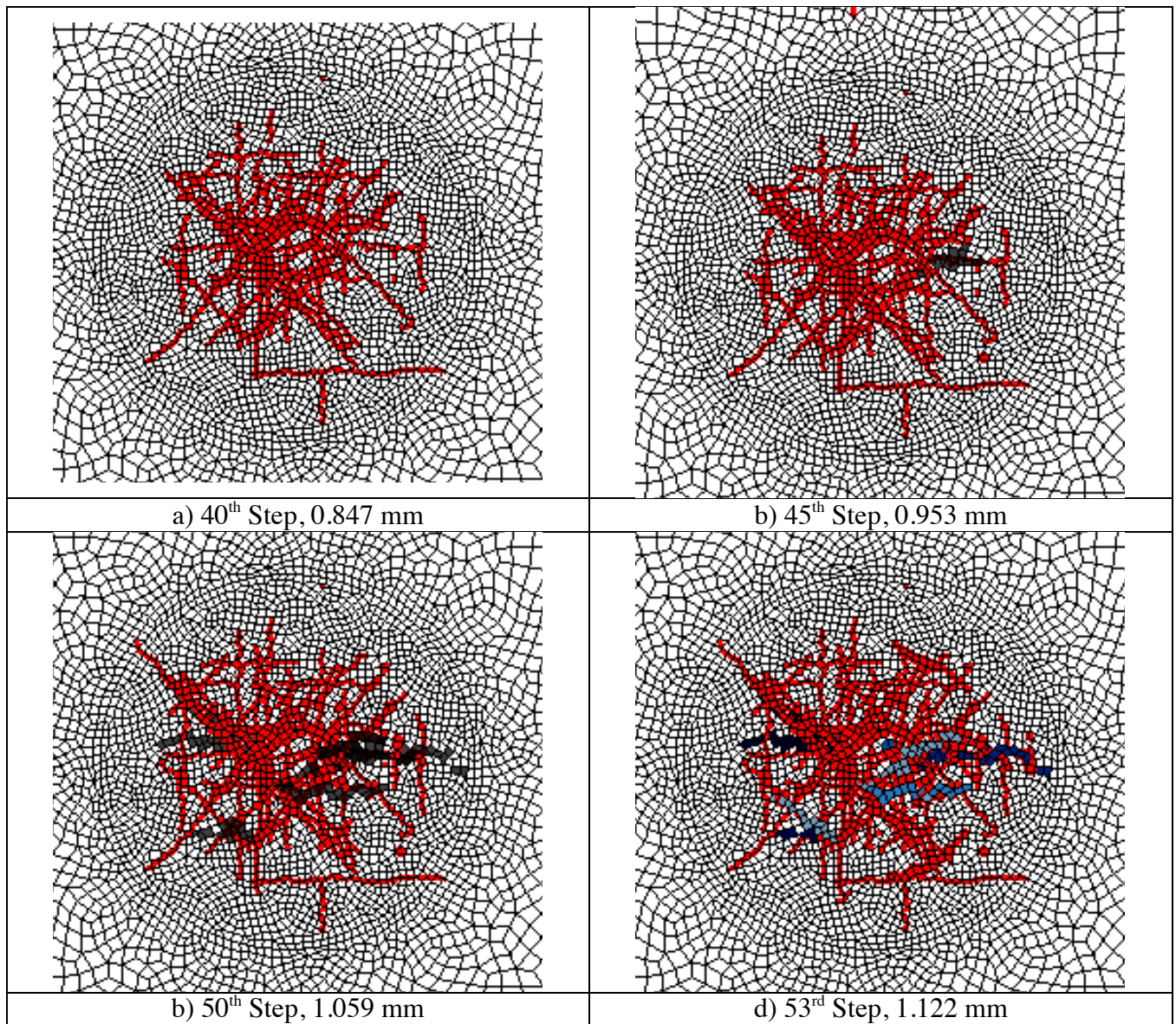


Figure 5.5.8 – Transverse matrix crack and progressive fiber failure

The simulation failed to predict the ultimate failure load due to a numerical instability that is at the time of writing been identified. The overall meaning behind this error is unclear, however, it could indicate that the problem is ill defined due to an underlying boundary condition issue. The simulation converged readily in every step prior to the error. Once the zero on the diagonal error occurred, the problem was unable to compute its next step. As a result, it could not predict damage growth up to ultimate failure. However, it was able to capture progressive fiber failure occurring near transverse

matrix cracks. The model can conclude that progressive fiber failure plays an attributing role to the failure. This corroborates the findings of compression after impact of thin plates.

5.5.2 Ballpark Estimates for Real World Problems

In many real world scenarios, the capability to determine if there are cracks in the composite is not there. Inspection primarily uses C-Scans to determine the amount of delamination within a composite and an engineer makes a judgment on whether it is critical enough to repair. In this problem, cracks are allowed to initiate and propagate using the same laws. Keep in mind; there are no initial cracks that were pre-imposed into the model. The delamination pattern, STL, was scaled to fit the damaged morphology to the selected the nodes that require a weak cohesive zone. The morphology for each lamina of the composite conformed to the line profiles of the impacted surface determined by profilometry. Figure 5.5.9 shows a 3-D representation of the delamination patterns of the composite. Figure 5.5.10 shows the frontal view of the delaminated region of the simulation and also compares the simulation done by an Olympus Omiscan Probe. The Olympus Omniscan Probe is one of the ultrasonic devices that the industry uses to inspect airframes.

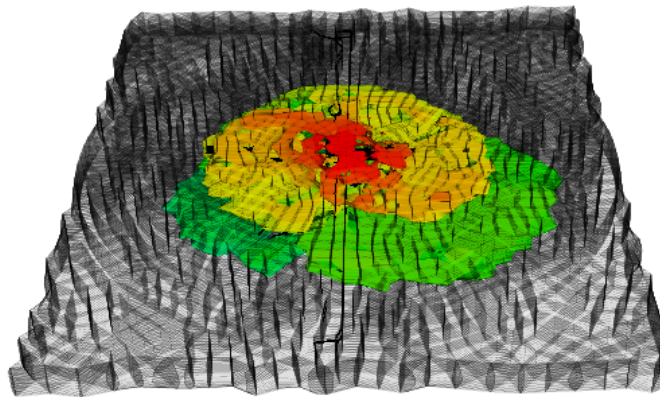


Figure 5.5.9 – Three dimensional representation of the pre-imposed delamination

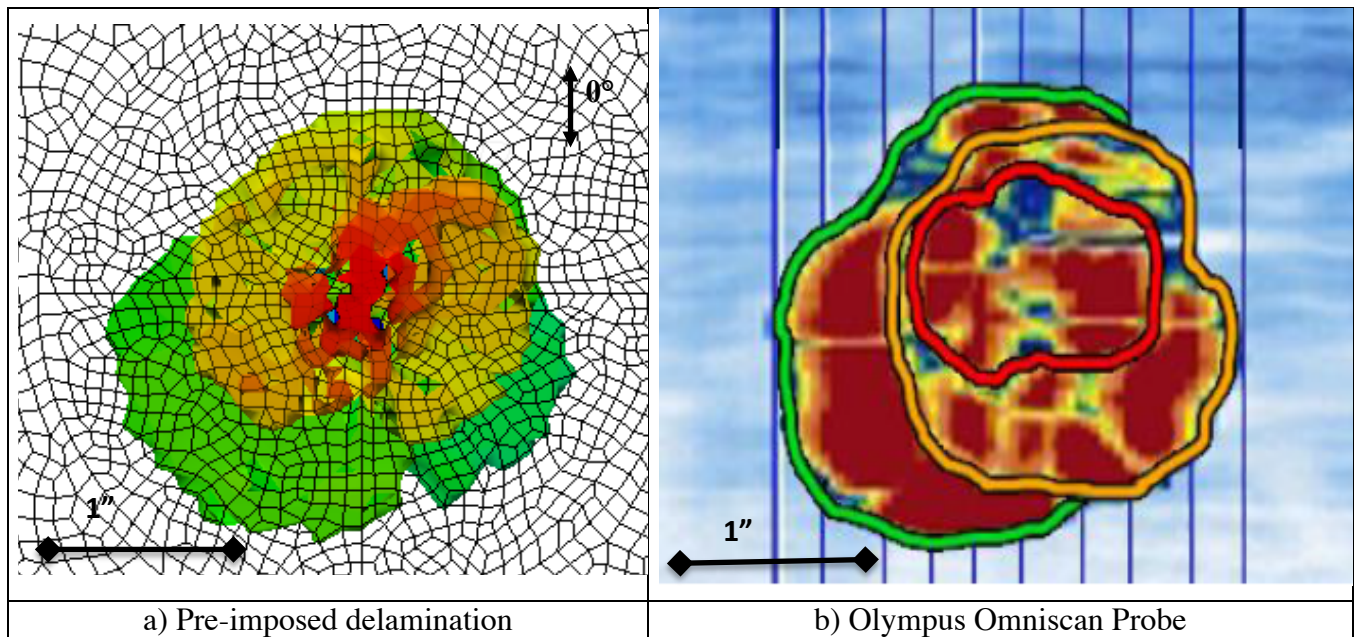


Figure 5.5.10 – Comparison of delamination between the a) simulation and b) Olympus Omniscan Probe

Even when only considering that there are no initial cracks in the composite, the out-of-plane contours match remarkably well with experiment. The out-of-plane displacement for the back surface did not match as well. However, it is suspected that this is because the back curvature was not pre-imposed into the model (instead, the impacted surface profile was projected to the back surface). While the out-of-plane displacements contours for the back surface matched, there were in error by approximately the height of the back surface that was not pre-imposed into the model. The strains are remarkably similar qualitatively to the contour as well (Figure 5.5.12-17). Furthermore, cracks appear to affect the way the contours look. In the previous section cracks on the surface appeared to affect the way it looked. This could primarily be based on the resolution between the model and DIC. Since the resolution on the DIC is lower, DIC has a tendency to smooth the effects of surface cracks.

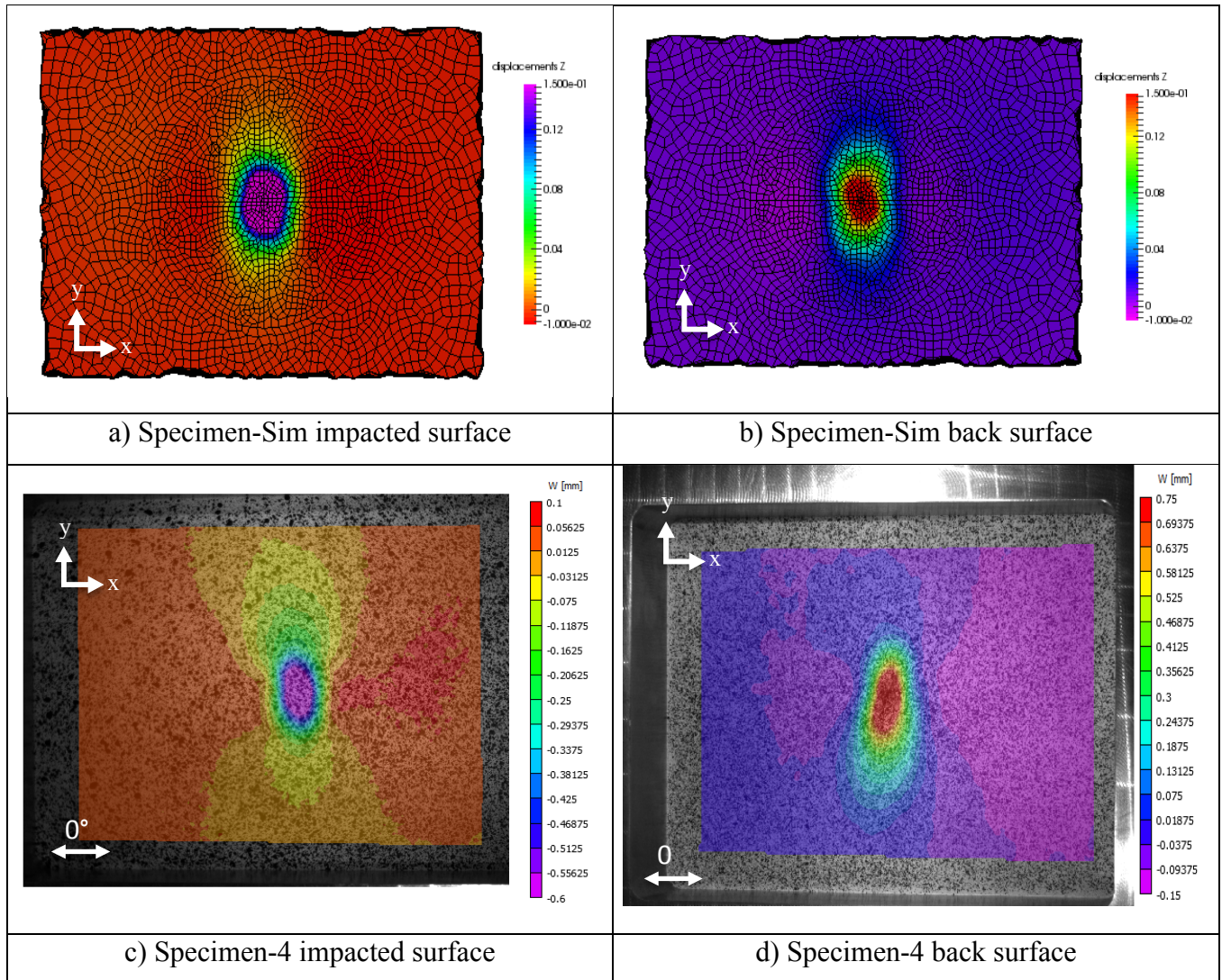


Figure 5.5.11 – Out-of-plane comparisons between simulation and DIC

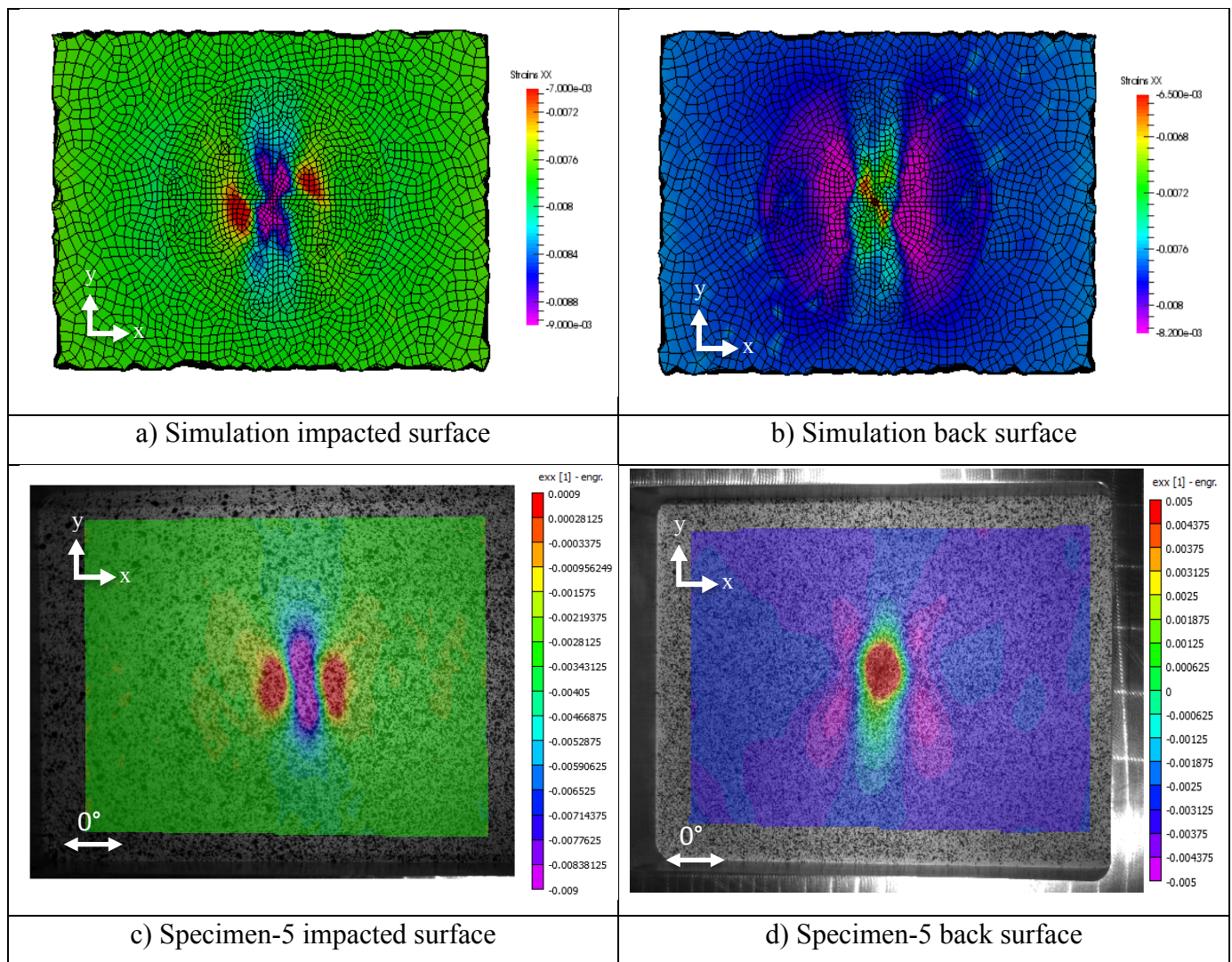


Figure 5.5.12 – Axial strain comparisons between simulation and DIC

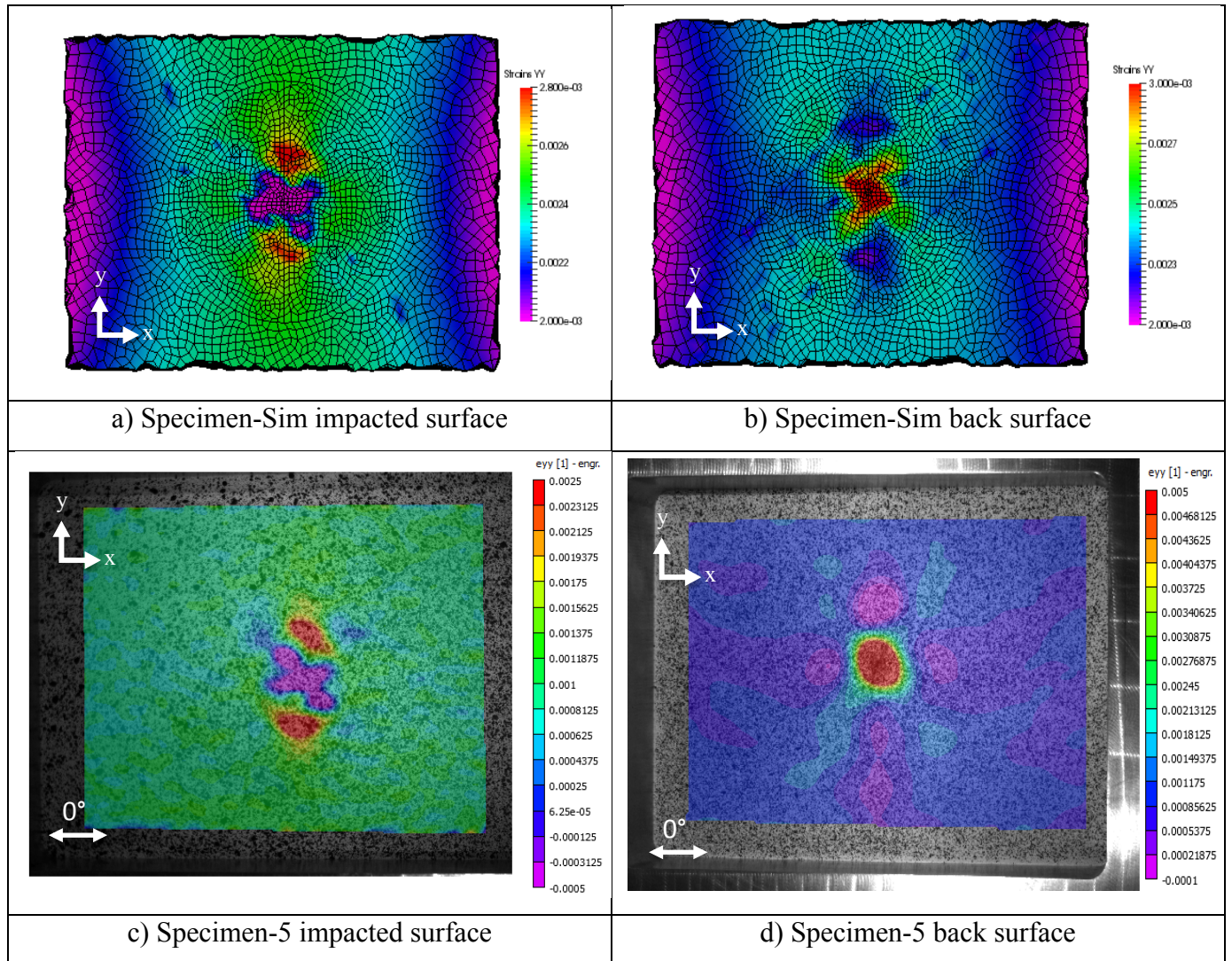


Figure 5.5.13 – Transverse strain comparisons between simulation and DIC

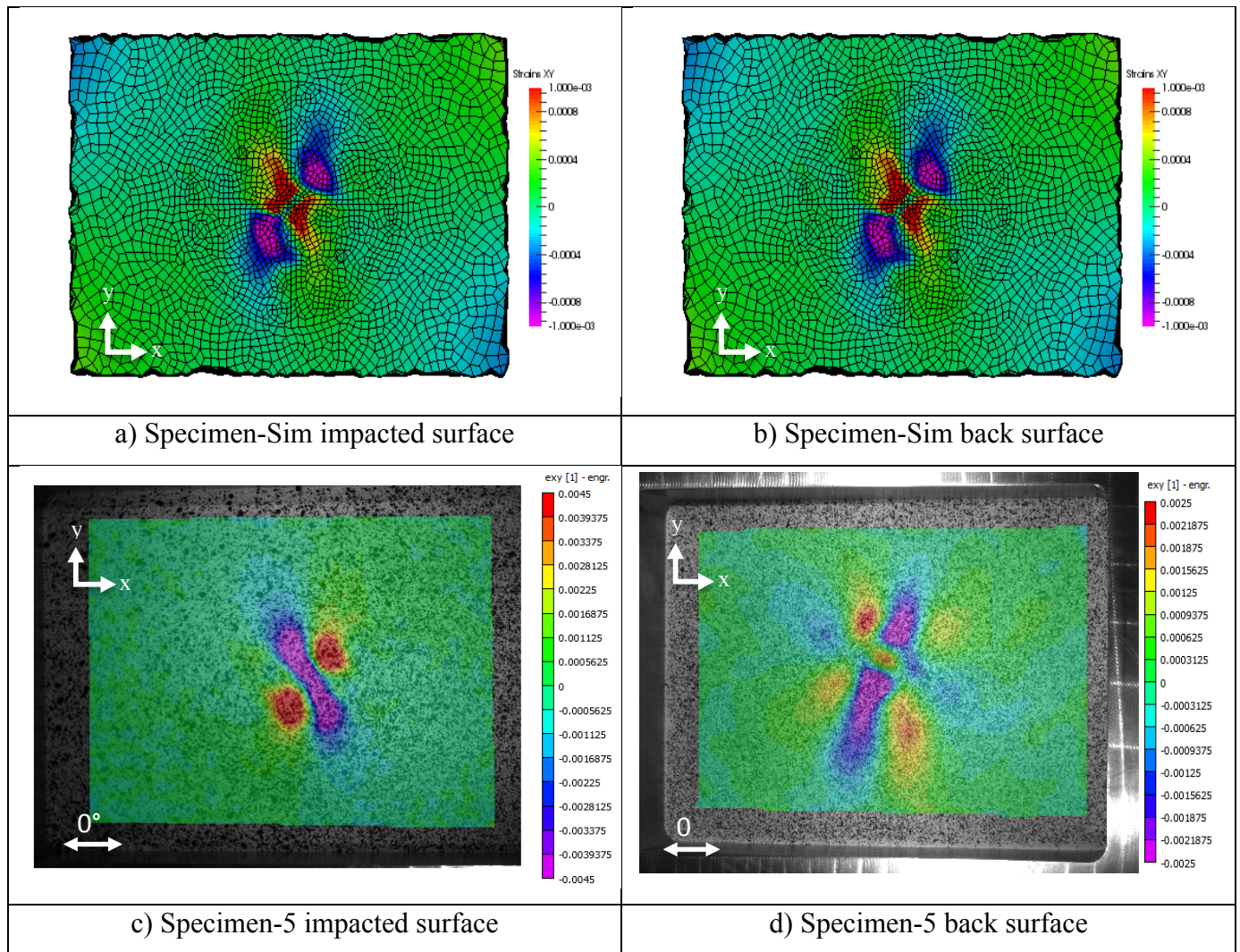


Figure 5.5.14 – Shear strain comparisons between simulation and DIC

Similar to the previous section, progressive fiber failure appears to be the driving mechanism for failure. The simulation is compared to specimen 5 since the delamination are similar. Figure 5.5.15 compares the damage from the simulation to the post damage of specimen-5. The initial delamination (green) did grow towards the end of the simulation. Even with the naked eye, transverse matrix cracks and fiber breakage could be seen on the surface of the digital image. Although fiber breakage (black) only occurred on the 0° plies in the simulation, fiber breakage could influence how the material behaves even in experiment. The simulation found that fiber breakage initiates near transverse matrix cracks (red). Figure 5.5.16 compares the ultimate failure of the specimen between the simulation and

immersion ultrasound. The damage pattern from the ultrasound do have similarities between shape, however, ultrasound only has the capability to assess delamination within a composite.

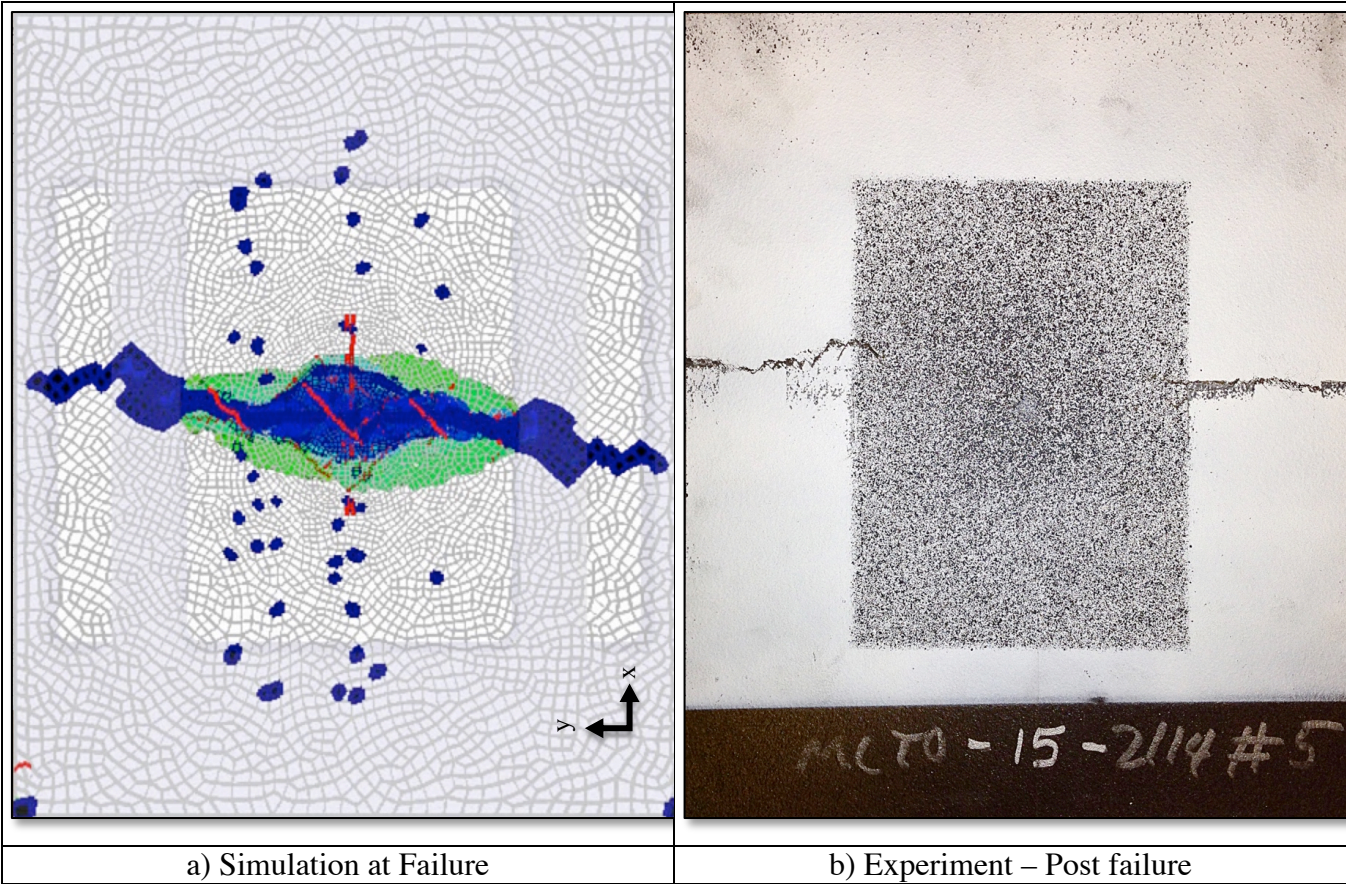


Figure 5.5.15 – Comparison of ultimate failure between a) simulation and b) experiment

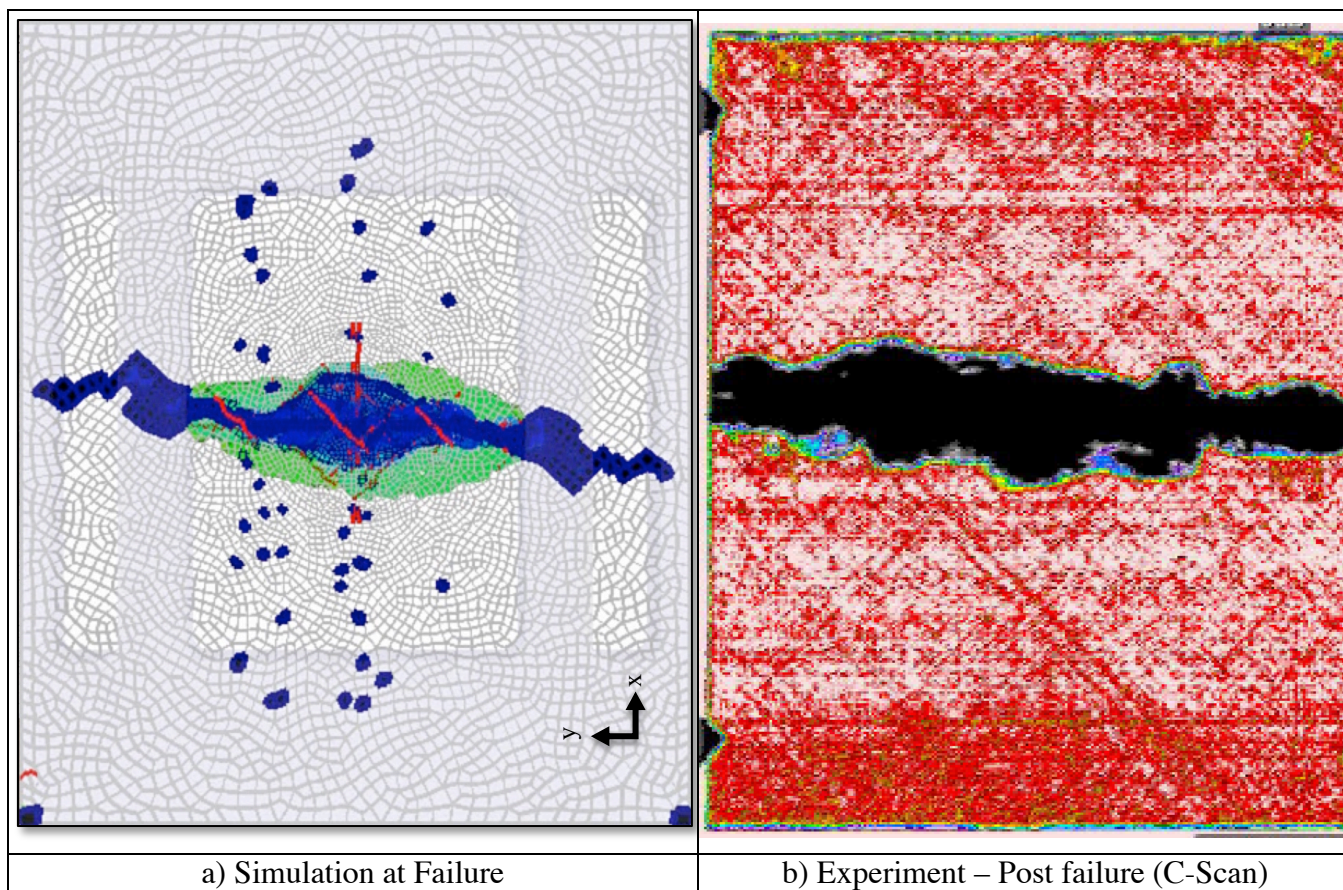


Figure 5.5.16 – Comparison of ultimate failure between a) simulation and b) experiment (c-scan)

Figure 5.5.17 compares the simulation to an X-ray image of specimen-5. What is strikingly similar between the images is that the fiber damage patterns on the left side of the panel. Even though specimen-5 has a different delamination pattern, it appears to capture progressive fiber failure. Even the right side of the image indicates a similar dip. Although, the X-ray makes it appear that the fiber breakage is occurring on the 45° ply, it also shows how fiber breakage is influenced by transverse matrix cracks. This is important because this is what is seen for the 0° plies in the simulation in the previous model.

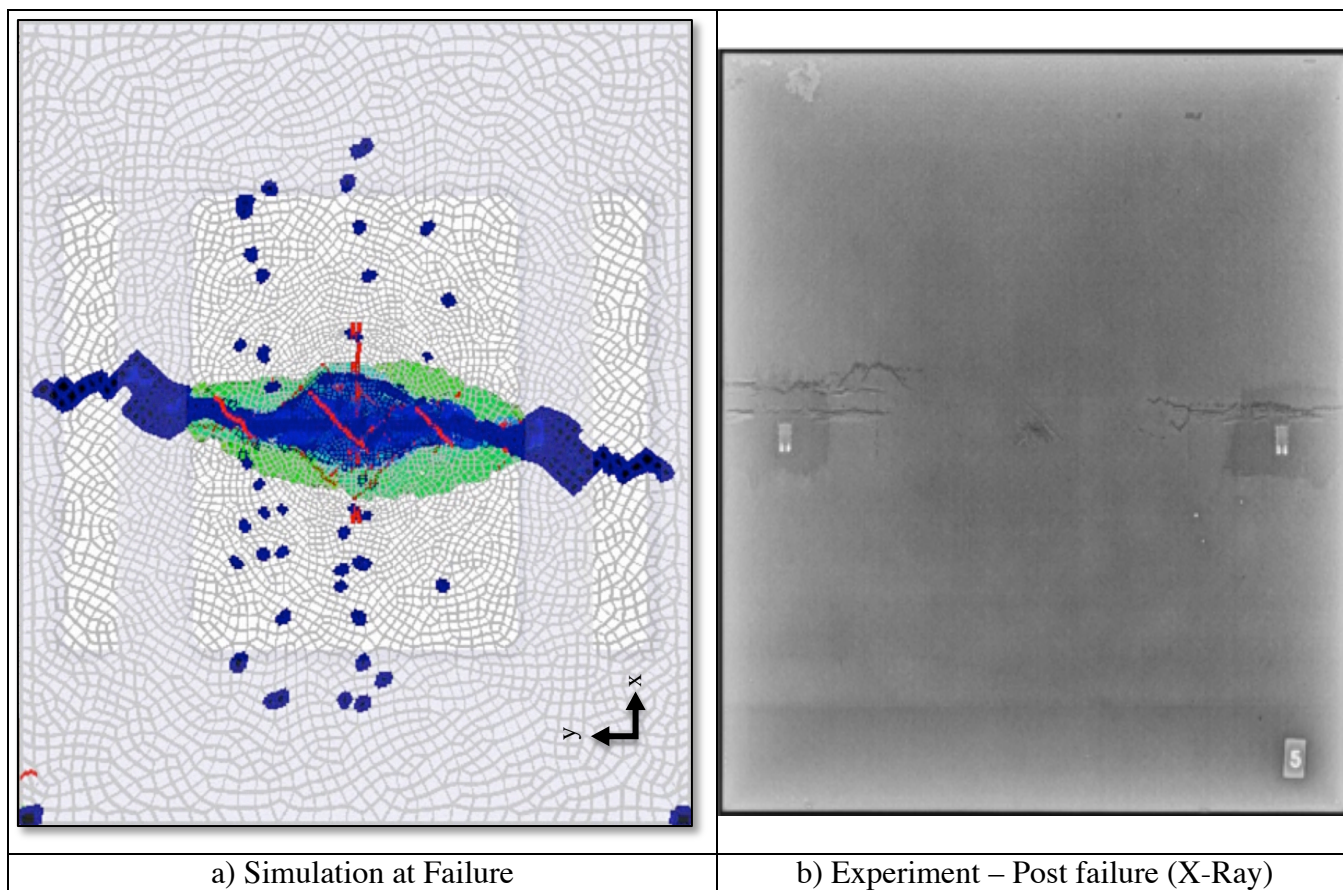


Figure 5.5.17 – Comparison of ultimate failure between a) simulation and b) experiment (X-Ray)

There are remarkable similarities in the contours between the simulation and the experiment. Furthermore, the high fidelity model was able to capture the underlying failure mechanisms for compression after impact. However, the model failed to predict the ultimate failure of the specimen. The model prediction was twice the experimental value (Figure 5.5.18). Without any knowledge of the main mechanical properties, the model predicted the modulus within 7%. Although more information is needed to ensure the strength values are correct, the model predicted the damage without knowing too much about the mechanical properties. Nonlinear parts of the code need to be incorporated to ensure that the model is taking into account of large displacements. However, to conclude that incorporating nonlinearity would be sufficient to solve this problem is still not enough. A process needs to be developed where pre-imposed damage could be inserted by reducing the stiffness of the elements in the region.

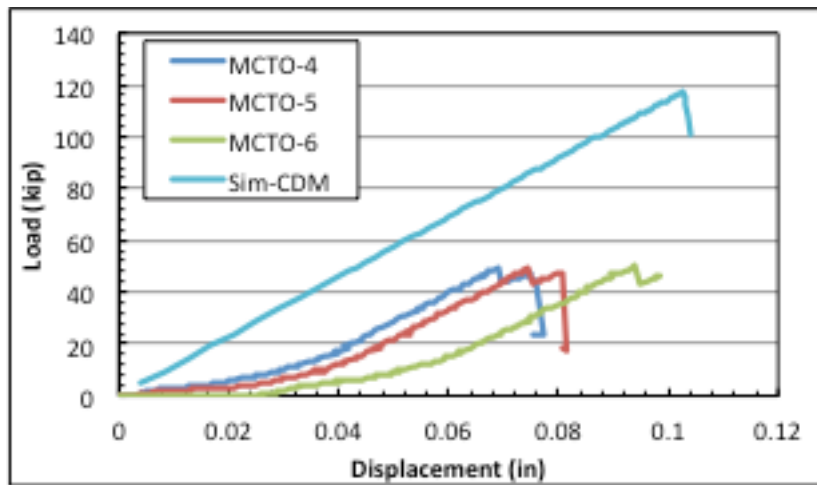


Figure 5.5.17 – Load vs displacement curves for simulation and experiments

5.6 Conclusion

Three composite specimens went through a series of extensive nondestructive techniques and another three specimens went through compression after impact tests. Specimen-1 was compared to specimen-5 because it had similar delamination patterns, which was found using immersion ultrasound. X-Ray CT with zinc iodine penetrant and image segmentation techniques was used to quantify the amount of delamination within the composite to create a 3D representative STL. The STL was used to create a rough estimate of the delamination pattern in the discretized model and crack region. Artificial cracks were pre-imposed by obtaining crack locations obtained from X-Ray CT. The morphology of the impacted region was incorporated into the discretized model by linearly interpolating the nodes from the line profiles of the impacted and back surface obtained through profilometry. The simulation was put through a compressive load to determine the failure mechanisms.

The deformation and the strain contours from the simulation matched remarkably well with the contours from digital image correlation. Since the composite was thicker, the composite rarely seemed to be undergoing sublaminar buckling. This is slightly different in the case of thin composite plates discussed in the previous chapter. During the experiment, there was no indication of damage growth. The ultimate failure happened instantaneously indicating catastrophic failure. The simulation found that the most dominating factor for failure was fiber failure, which coincided with X-ray images.

5.7 Future Work

Future models will incorporate nonlinearity into the model as well as pre-imposed damage to ensure the failure is accurately represented and predicted. Nonlinearity will use a Lagrangian algorithm that analyzed the geometric large displacements of the discretized model. X-ray CT images were used to capture the amount of delamination and matrix cracks that occurred in the composite. Even though it proved to be a usual nondestructive technique in capturing the damage of the composite plate, future models will attempt to incorporate delamination patterns obtained from c-scan images. Many industries heavily rely on c-scan images when inspecting airframes and structures. The reason behind this is to provide quick time solution in modeling the damage of the composite for operational proficiency.

Chapter 6: Conclusion

6.1 Impact Experiments

In Chapter 2, two types of experiments were conducted using different standards. One standard was ASTM 7136, which is commonly performed in academia. Four different stacking sequences were impacted with 10 J of energy with a 1/2" hemispherical tupper using a drop weight tower. Digital image correlation recorded the displacements and strains of the back surface of the composite plates. DIC was able to capture the initiation of a crack for Panel C. Using Y-Displacements, it might be possible to identify crack initiation on a discontinuity in the DIC contour. The key finding from these impact experiments was the damage threshold strain. The significance behind the damage threshold strain is that there was minimal variation between the stacking sequences. This indicates it could be used as a new parameter for impact resistance. The next steps would be impact composite layups based on a specified strain. The strain response at the damage threshold strain could provide engineers information about how the material behaves at a critical event, the initiation of damage. Nondestructive evaluation could be used to characterize the damage at the DTS. Ultrasonic techniques could be used to determine the reduction of modulus of a given volume representative in a given region of interest. This data could be utilized in impact models. In addition to, the effective reduction in modulus data could be pre-imposed into compression after impact simulations. Analyzing impacted specimens at DTS could provide the physical parameters necessary to quantify the damage in terms of delamination, transverse matrix cracks, and reduction of modulus.

Lockheed Martin conducted a series of impact experiments for the larger composite specimens. Six unidirectional carbon fiber composites were impacted with a 1" hemispherical tupper at 55ft-lbs using a drop weight tower. Three of the six specimens went through a series of extensive nondestructive evaluation to obtain high fidelity images of the damage. Immersion ultrasound and infrared flash thermography were done to the other three specimens, which were then put through compression tests.

6.2 Modeling Damage

Chapter 3 described how nondestructive evaluation was used to quantify damage in a way that has never been done before. By taking delamination patterns from X-ray CT, pre-imposed delamination

was inserted into a 3D discretized damage model of a composite flat plat. The information from the X-ray CT correlated well with the C-Scan images. Future work will involve the use of just C-Scan, as this technique is currently used for inspecting damaged composites. C-scans are also able to obtain data quicker than X-ray CT. Artificial cracks were pre-imposed into the model by identifying key transverse matrix cracks from the X-ray CT data. The morphology of the impacted region was modeled by linearly extrapolating the nodes between the line profiles obtained from profilometry. Future simulations will study the affects of pre-imposing continuum damage by reducing the stiffness matrix of elements within the delamination regions. A mesh sensitivity analysis needs to be completed to ensure that the damaged region is accurately represented. The mesh sizing also plays an important role in the growth of the damage region. Nondestructive evaluation could provide overall insight into the optimization of the mesh size.

6.3 Compression Strength After Impact

Chapters 4 and 5 talked about the numerical and experimental investigations into compression strength after impact for two different testing standards. Currently there is little that can be inferred between the damage threshold strain and the compression threshold strain. However, if there is minimal variation in the damage threshold strain between different stacking sequences, then it should be explored further. This could determine if the damage threshold strain impacts the compression threshold strain. Maintenance operators could use this tool to determine if repairs need to be done on the airframe, not to mention the added utility of designing and certifying future advanced composites.

These simulations did not take into account of large displacements that occur due to buckling nor did it consider the material degradation from the impacted region. Therefore, it over-predicted the ultimate strength of the composite. As result, the dominating failure appeared to be fiber failure. During the experiment, there was no indication of delamination growth. The simulations found that the dominating failure mechanism for the tests was fiber failure. This coincided with the images obtained from X-ray CT. C-Scan is usually used to understand damage, however, C-Scan only has the capability to quantify delamination. Therefore, more research needs to go into the mechanistic failures to accurately model damage growth for compression after impact of composites.

6.4 Damage Tolerance and Assessment

It is important to reflect on the underlying limitations of nondestructive evaluation. In addition the limitations of computational models and physical experiments need to be considered. Integrating all these techniques was the foundation for exploring material behavior under compression loading. In this process, limitations of nondestructive techniques found that c-scans could only quantify the amount of delamination within the composite. As a result, every model and experiment assumed that c-scans could only quantify delamination. This has resulted in the basic assumption that failure is delamination driven. Whilst this is not entirely wrong [75-77] but it could potentially lead to an ill posed problem. Alderliesten has previously discussed some of the limitations for designing hybrid materials [78,79]. The interactions between different damage modes has not been explored in great detail. For example, the interactions of fiber/matrix damage with other forms of damage could be further investigated. This will help ensure that the model accurately predicts damage growth. The complexity of the mechanisms that occur cannot be described with the simplicity of the proposed phenomenological methods [79].

Discrete damage modeling could answer some of the questions about the damage growth of composites. In this process, it could determine what is critical damage (conceptually and realistically) and how it plays a role on the structure's integrity. For this reason alone, robust tools that simulate the interaction between damage mechanisms need to be developed.

6.5 Significance of Study

Although this study primarily focused on compression strength after impact, pre-imposing damage into discrete damage models has huge implications for the future. Pre-imposing damage in any form could provide engineers a theoretical understanding on how materials behave at any level. The technology is limitless. It can be used to understand how cracks grow given a metallic grain structure. Artificially pre-imposing damage into a region of a structure that cannot be inspected using nondestructive techniques could pave a new way to design damage tolerant structures. Not only does it help engineers understand the mechanisms of the failure of composites, it could be used to design complex hybrid structures with a fidelity that has never been seen before. The tools created for the use of this project could be utilized to certify composites but also certify structural entities as well. These

tools could be extended to predicting microstructural behavior, where the curing process of composites creates voids or defects. This could be used to help manufacturers design better processing methods. Since DDM also uses a regularized X-FEM to model transverse matrix cracks and are purely geometrical, every structure could already have a discrete 3D model and could reduce time for realtime solutions. As BSAM adds the capability for tetrahedral elements, the capability to use this approach for complex architecture will be available.

References

- [1] Cantell, W.J. and Morton, J., The impact resistance of composite materials – a review, *Composites*, 22, 1998, 347-362
- [2] Abrate, S., *Impact on Composite Structures*, Cambridge University Press, Cambridge UK, 1998.
- [3] Carlsson L.A., Adams, D.F., Pipes, R.B, *Experimental Characterization of Advanced Composite Material*, 4th Edition, CRC Press, 2014.
- [4] Chamis, C.C., Murthy, P.L.N., Minnetyan, L., *Progressive Fracture in Composite Structures, Composite Materials Fatigue and Fracture*, 6th Volume, 1997
- [5] Williams, J.G., *NASA Research in Composite Structure Damage Tolerance and Composite Applications in the Oil Industry*, AIAA/ASME/ASCE/AHS/ASC Structures, Structural Dynamics & Materials Conference, 18-21 April, 2005
- [6] O'Brien, T.K., *Composite Rotorcraft Structures Durability and Damage Tolerance Research*, American Society for Composites 29th Technical Conference, San Diego, CA, September 8-10, 2014
- [7] Olsson, R., Modeling of Impact Damage Zones in Composite Laminates for Strength After Impact, *The Aeronautical Journal*, December 2012, Vol 116, No 1186, p1349-1365
- [8] AC 32-19A, *Airframe Guide for Certification of Part 23 Airplanes*
- [9] Johnson, A.F., Toso-Pentecote, N., Schueler, D., "Numerical modeling of impact and damage tolerance in aerospace structures," *Numerical modeling of failure in advanced composite materials*, 2015, <http://dx.doe.org/10.1016/B978-0-08-100332-9.00018-9>
- [10] Olsson, R., Low- and medium-velocity impact as a cause of failure in polymer matrix composites." *Failure mechanisms, in polymer matrix composites*, 2012, Woodhead Publishing Limited
- [11] Rasuo, B., "Damage tolerance and survivability of composite aircraft structures," *Structural Integrity and Druability of Advanced Compoistes*, (2015), <http://dx.doe.org/10.1016/B978-0-08-100137-1.00032-7>
- [12] Sierakowski, R.L. , "Damage Tolerance: A Status Resport," 46th AIAA/ASME/ASCE/AHS/ASC/ Stuctures, Structural Dynamics & Materials Conference, 18*21 April 2005, Austin, Texas
- [13] Harris, Charles E., Starnes, James H, Jr. and Shuart, Mark J., "Advanced durability and damage tolerance design and analysis methods for composite structures – lessons learned from NASA Technology Development Programs, NASA TM 2003-212420 June 2003.
- [14] Sierakowski, R.L., "Impact Damage Tolerant Composite Structural Design," Chapter 4 in *Imapct Behavior of Fibre-Reinforced Composite Materials and Structures*, Editors, Reid, S.R., Zhou, G., Woodhead Publishing Limited, Cambridge, England, 2000
- [15] Anon, *Aeronautics and Space, Code of Federal Regulations, Title 14*, published by the Office of the Federal Register, Natiional Archives and Records, Administration, U.S. Government Printing Office, Mail Stop SSOP, Washington DC 20402, 1996.
- [16] *Polymer Matrix Composites, Mil-Handbook-17, Volum 3, Chapter 7, Damage Resistance, Durability, and Damage tolerance*, Department of Defense, U.S.A., December 12, 2001.
- [17] Abrate, S., "Impact on laminated composites materials, 1991," *Applied Mechanics*, Volume 44, no. 4, pp 155-190
- [18] Cantell, W.J. and Morton, J., 1998, "The impact resistance of composite materials – a review," *Composites*, 22 , 347-362
- [19] Carlsson L.A., Adams, D.F., Pipes, R.B, "Experimental Characterization of Advanced Composite Material, 4th Edition," CRC Press, 2014.
- [20] Cantwell, W.J., and Morton J. 1985, "Detection of Impact Damage in CFRP laminates," *Composite Structures* 3, 241-247

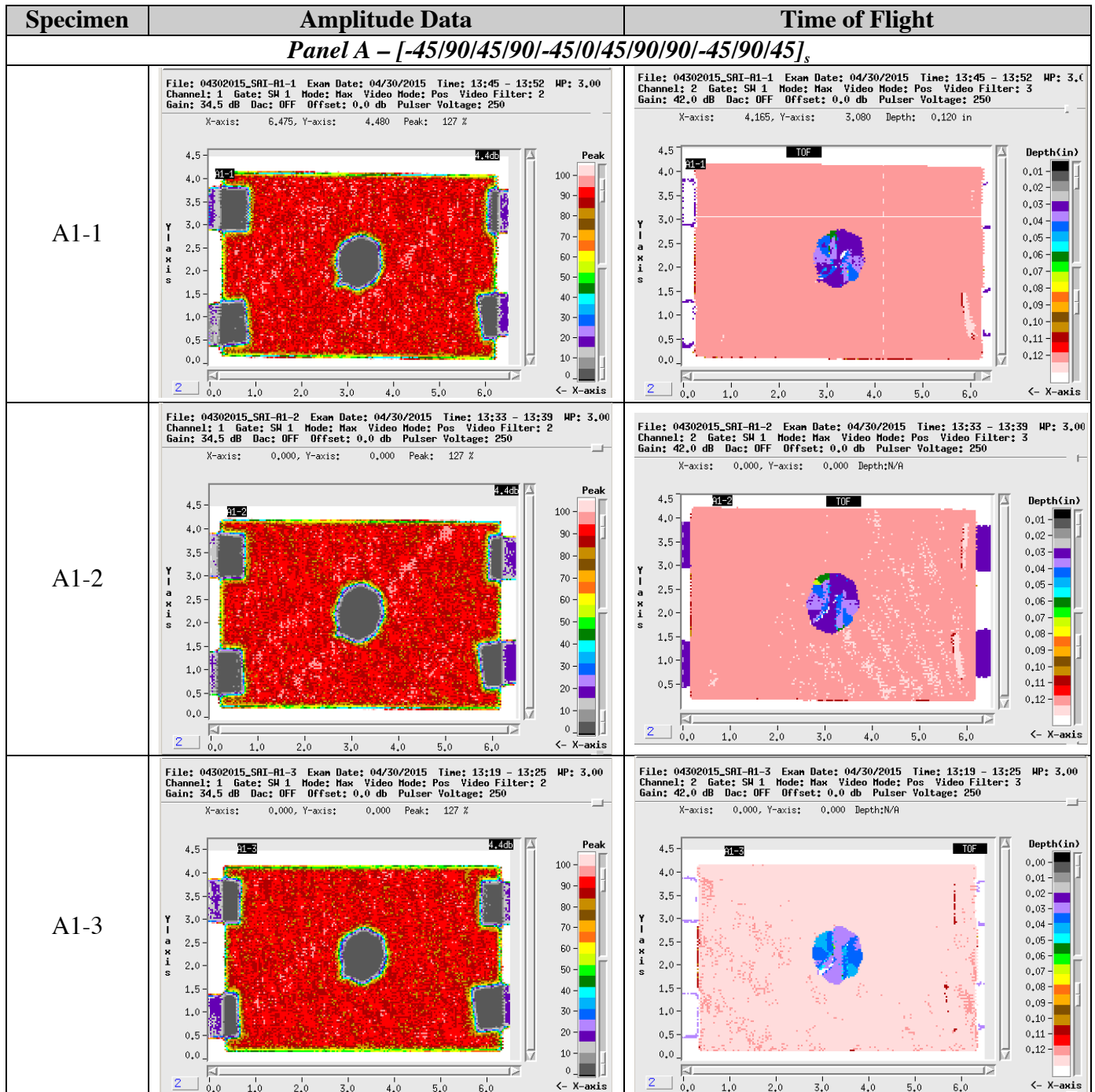
- [21] Takeda, N., Sierakowski, R.L., Ross, C.A., Malvern, L.E., 1982, "Delamination-Crack Propagation in Ballistically Impacted Glass/Epoxy Composite Laminates," *Experimental Mechanics*, Vol 22, Issue 1, pp19-25
- [22] Takeda, N., 1981, "Transverse cracks in glass/epoxy cross-ply laminates impacted by projectiles," *Journal of Material Science*, July 1981, Volume 16, Issue 7, pp 2008-2011
- [23] Chai, H., Knauss, W.G., Babcock, C.D, 1983, "Observation of damage growth in compressively loaded laminates," *Experimental Mechanics*, Sept. 1983, Volume 23, Issue, pp 329-337
- [24] Malvern, L.E., Sierakowski, R.L., Ross, C.A., Cristescu, N, 1979, "Impact Failure Mechanisms in Fiber-Reinforced composite plates", *High Velocity Deformation of Solids International Union of Theoretical and Applied Mechanics*, 1979, pp 120-131.
- [25] Namala KK, Mahanjan P, Bhatnagar N., 2014, "Digital image correlation of low velocity impact on a glass/epoxy composite." *Int J Comput Methods Eng Sci Mech* 2014;15(3):203e17.
- [26] Hayes, S.V., Rybicki, E.F., 1981, "The development of a low velocity impact methodology for hybrid material systems", Naval Air Systems Command Technical Report, July 1981
- [27] Richardson, M.O.W., Wisheart, M.J., 1996, "Review of low-velocity impact properties of composite materials", *Composites: Part A*, 27A, 1996, 1123-1131
- [28] Davies, G., Irving P., 2015, "Impact, post-impact strength and post-impact fatigue behavior of polymer composites," *Polymer Composites of the Aerospace Industry*, 231-259
- [29] Davies, C.K.L, Turner, S., Williamson K.H, 1985, "Flexed plate impact testing of carbon fibre-reinforced polymer composites," *Composites Vol 16 No 4*, 279-285
- [30] Schoeppner, G.A., Abrate, S., 2000, "Delamination threshold loads for low velocity impact of composite laminates," *Composites: Part A*, 31, p 903-915
- [31] Caprino, G., Lopresto, V., Scarponi, C., Briotti, G., 1999, "Influence of material thickness on the response of carbon-fabric/epoxy panels to low velocity impact," *Composite Science and Technology*, 59, 2279-2286
- [32] Caprino, G., Visconti, C.I., Ilio, A.D, 1984, "Elastic behavior of composite structures under low velocity impact," *Composites Vol 15 no3*, 1984, 231-234
- [33] ARAMIS Digital Image Correlation Manual
- Charles E. Anderson Jr.*, Rory P. Bigger, and Carl E. Weiss, 2014, "Crack and Damage Velocities in Ballistic Experiments," *International Journal of Applied Glass Science*, pages 374–383
- [34] Doyle, J.F. 1983, "Further developments in determining the dynamic contact law", *Advances in Aerospace Structures, Materials and Dynamics, A symposium of Composites*
- [35] Timoshenko, S., (1953), "History of Strength of Materials," McGraw-Hill, New York
- [36] LM Aero Composite Durability and Damage Tolerance Test Methodology
- [37] Austin, J., ICM2 Impact Panel NDI Summary
- [38] Julia F. Barrett, Nicholas Keat, "Artifacts in CT: Recognition and Avoidance," *RadioGraphics* 2004; 24:1679–1691, 10.1148/rg.246045065
- [39] Richard A. Ketchum, Romy D. Hanna, "Beam hardening correction for X-ray computed tomography of heterogeneous natural materials," *Computers & Geosciences* 67 (2014) 49–61
- [40] N. Chawla, V.V. Ganesh, B. Wunsch, "Three-dimensional (3D) microstructure visualization and finite element modeling of the mechanical behavior of SiC particle reinforced aluminum composites," *Scripta Materialia*, 51, 2004, p161-165.
- [41] N. Chawla, R.S. Sidhu., V.V. Ganesh, "Three-dimensional visualization and microstructure-based model of deformation in particle-reinforced composites," *Acta Materialia*, 54, 2006, 1541-1548
- [42] E. Coleri, J.T. Harvey, "A fully heterogeneous viscoelastic finite element model for full-scale accelerated pavement testing," *Construction and Building Materials*, 43, 2013, p14-30.

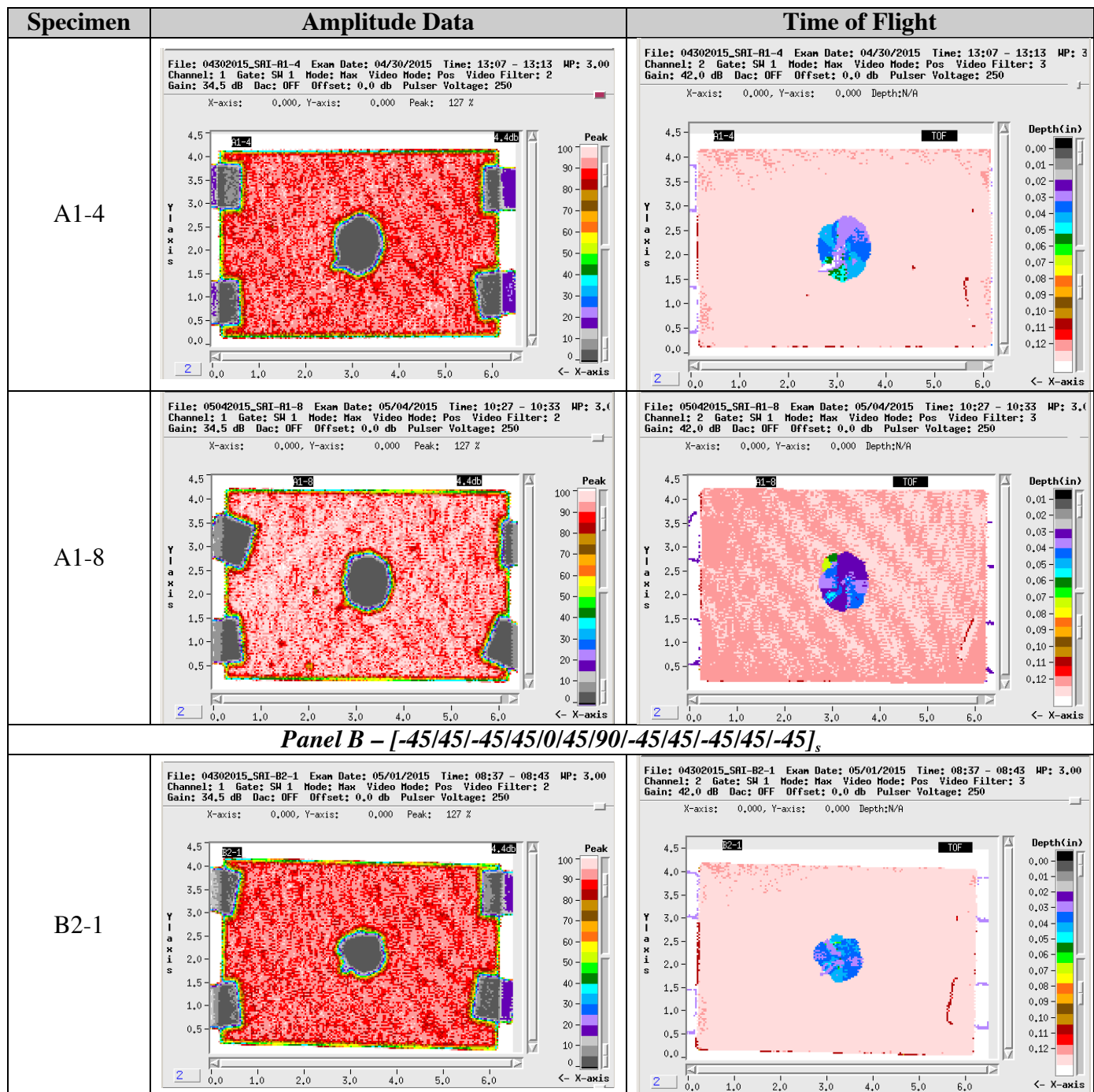
- [43] M.A. Dudek, L. Hunter, S. Kranz, J.J. Williams, S.H. Lau, N. Chawla, "Three-Dimensional (3D) visualization of reflow porosity modeling of deformation in Pb-free solder joints," *Material Characterizations*, 61, 2010, p433-439.
- [44] A.J. Hoyt, C.M. Yakacki, R.S. Fertig III, R.D. Carpenter, C.P. Frick, "Monotonic and cyclic loading behavior of porous scaffolds made from poly(para-phenylene) for orthopedic applications," *Journal of the Mechanical Behavior of Biomedical Materials*, 41, 2015, p135-148
- [45] A. Stienon, A. Fazekas, J.-Y. Buffiere, A. Vincent, P. Daguiet, F. Merchi, "A new methodology based on X-Ray micro-tomography to estimate stress concentration around inclusions in high strength steels," *Materials Science and Engineering A* 513-514, 2009, p376-383
- [46] M.A. Groeber, B.K. Haley, M.D. Uchic, D.M. Dimiduk, S. Ghosh, "3D reconstruction and characterization of polycrystalline microstructures using a FIB-SEM system," *Materials Characterization*, 57 (2006), p259-273
- [47] S. Ghosh, Y. Bhandari, M. Groeber, "CAD-based reconstruction of 3D polycrystalline alloy microstructures from FIB generated serial sections," *Computer-Aided Design*, 40 (2008) p293-310
- [48] J. Thomas, M. Groeber, S. Ghosh, "Image-based crystal plasticity FE framework for microstructure dependent properties of Ti-6Al-4V alloys," *Materials Science and Engineering A*, 553 (2012), p164-175
- [49] G. Loughnane, M. Groeber, M. Uchic, M. Shah, R. Srinivasan, R. Grandhi, "Modeling the effect of voxel resolution of the accuracy of phantom grain ensembles statistics," *Materials Characterization*, 90 (2014) p136-150
- [50] M. Groeber, S. Ghosh, M. D. Uchic, D. M. Dimiduk, "A framework for automated analysis and simulation of 3D polycrystalline microstructures. Part 1: Statistical characterization," *Acta Materialia*, 56 (2008), p1274-1287
- [51] M. Groeber, S. Ghosh, M. D. Uchic, D. M. Dimiduk, "A framework for automated analysis and simulation of 3D polycrystalline microstructures. Part 2: Synthetic Structure generation," *Acta Materialia*, 56 (2008), p1274-1287
- [52] Y. Bhandari, S., Sarkar, M. Groeber, M.D. Uchic, D.M. Dimiduk, S. Ghosh, "3D polycrystalline microstructure reconstruction from FIB generated serial sections for FE analysis," *Computational Materials Science*, 41 (2007), p222-p235
- [53] D. Rodriguez-Galan, I. Sabirov, J. Segurado, "Temperature and strain rate effect on the deformation of nanostructured pure titanium," *International Journal of Plasticity*, 70, 2015, p191-205
- [54] F.P. Rodrigues, J. Li, N. Silikas, R.Y. Ballester, D.C. Watts, "Sequential software processing of micro-XCT dental-images for 3D-FE analysis," *Dental Materials*, 25, 2009, p247-255
- [55] J.J. Williams, J. Segurado, J. Llorca, N. Chawla, "Three dimensional (3D) microstructure-based modeling of interfacial decohesion in particle reinforced metal matrix composites," *Material Science & Engineering A*, 2012, p113-118
- [56] X. Zhu, S. Ai, X. Lu, L. Zhu, B. Liu, "A novel 3D geometrical reconstruction method for aluminum foams and FEM modeling of the material response," *Theoretical & Applied Mechanics Letters* 4, 021006 (2104)
- [57] E. Mikkola, G. Marquis, J. Solin, "Mesoscale modeling of crack nucleation from defects in steel," *International Journal of Fatigue*, Volume 41, August 2012, p64-71
- [58] A. Shigang, F. Daining, H. Rujie, P. Yongmao, "Effect of manufacturing defects on mechanical properties and failure features of 3D orthogonal woven C/C composites," *Composites Part B: Engineering*, Vol 71 (2015), p113-121
- [59] R.A. Kline, G. Cruse, A.G. Striz, E.I. Madaras, "Integrating NDE-derived engineering properties with finite element analysis for structure composite materials," *Ultrasonics*, Vol 31 (1993), p53-59
- [60] A. Castellano, P. Foti, A. Fraddosio, S. Marzano, M.D. Piccioni, "Mechanical characterization of CFRP composites by ultrasonic immersion tests: Experimental and numerical approaches," *Composites: Part B*, 66 (2014), p299-310

- [61] A.A. Fahim, R. Gallego, N. Bochud, G. Rus, "Model-Based damaged reconstruction in composites from ultrasound transmission," *Composites: Part B*, 45 (2013), p50-62
- [62] E. Panettieri, Fanteria D., Firrincieli, "Damage initialization techniques for non-sequential FE propagation analysis of delaminations in composite aerospace structures," *Advances in the Mechanics of Composite and Sandwich Structures*, (2015) 50:2569-2585
- [63] E. Panettieri, D. Fanteria, F. Danzi, "Delaminations growth in compression after impact test simulations: Influence of cohesive elements parameters on numerical results," *Composite Structures*, 137, (2019) 140-147
- [64] E.V. Iarve, M.R. Gurvich, D.H. Mollenhauer, C.A. Rose, C.G. Davila, "Mesh-independent matrix crack and delamination modeling in laminated composites," *Int. J. Numerical Methods in Engineering*, (2011), published online DOI:10.1002/nme.319
- [65] E.V. Iarve, D.H. Mollenhauer, T.J. Whitney, R. Kim, "Strength Prediction in composites with stress concentrations: classical weibull and critical failure volume methods with micromechanical considerations," *Journal of Material Science*, Vol. 41, No.20, Oct. 2006, p5510-6622
- [66] E.V. Iarve, D.H. Mollenhauer, T.J. Whitney, R. Kim, "Strength Prediction in composites with stress concentrations: classical weibull and critical failure volume methods with micromechanical considerations," *Journal of Material Science*, Vol. 41, No.20, Oct. 2006, p5510-6622
- [67] M.J. Swinderman, E.I. Iarve, R.A. Brockman, "Strength prediction in open hole composite laminates by using discrete damage modeling," *AIAA Journal*, 51(4), 2012, p936-945
- [68] D.H. Mollenhauer, L. Ward, E.V. Iarve, S. Putthanarat, K. Hoos, S. Hallett, X. Li, "Simulation of discrete damage in composite overheight compact tension specimens," *Composites Part A*, 43(2010), p1667-167
- [69] C.G. Davila, P.P. Camanho, C.A. Rose, "Failure criteria for FRP laminates," *Journal of Composite Materials*, Vol. 39, No.4 (2005), p323-45
- [70] S.T. Pinho, C.G. Davila, P.P. Camanho, L. Iannuci, P. Robinson, "Failure modes and criteria for FRP under in-plane or three-dimensional stress states including shear nonlinearity," Hampton, VA February 2005, NASA/TM-2005-213530
- [71] A. Turon, P.P. Camanho, J. Costa, C.G. Davila, "A damage model for the simulation of delamination in advanced composites under variable-mode loading," *Mechanics of Materials*, Vol. 38, No. 11, Nov. 2006, p1072-89.
- [72] P.P. Camanho, P. Maimi, C.G. Davila, "Prediction of size effects in notched laminates using continuum damage mechanics," *Composite Science and Technology*, 2007;67, p2715-2727
- [73] P. Maimi, P.P. Camanho, J.A. Mayugo, C.G. Davila, "A continuum damage model for composite laminates: Part I – constitutive model," *Mechanics of Materials*, Vol. 39, No.10, 2007, p897-908
- [74] P. Maimi, P.P. Camanho, J.A. Mayugo, C.G. Davila, "A continuum damage model for composite laminates: Part II– computational implementation and validation," *Mechanics of Materials*, Vol. 39, No.10, 2007, p909-919
- [75] B-Spline Analysis Method User manual (2014)
- [76] Daniel, IM, Ishai, O., "Engineering Mechanics of Composite Materials," Oxford University Press, New York
- [77] Tsai J. and Sun, C.T., "Dynamic compressive strength of polymeric composites," *International Journal of Solids and Structures*, 2004, 41, 3211-3224
- [78] Oguni, K., and Ravichandran, G., "Dynamic compressive behavior of unidirectional E-glass/vinylester composites," *Journal of Materials Science*, 2001, 36, 831-838

Appendix A: NDE – Immersion Ultrasound

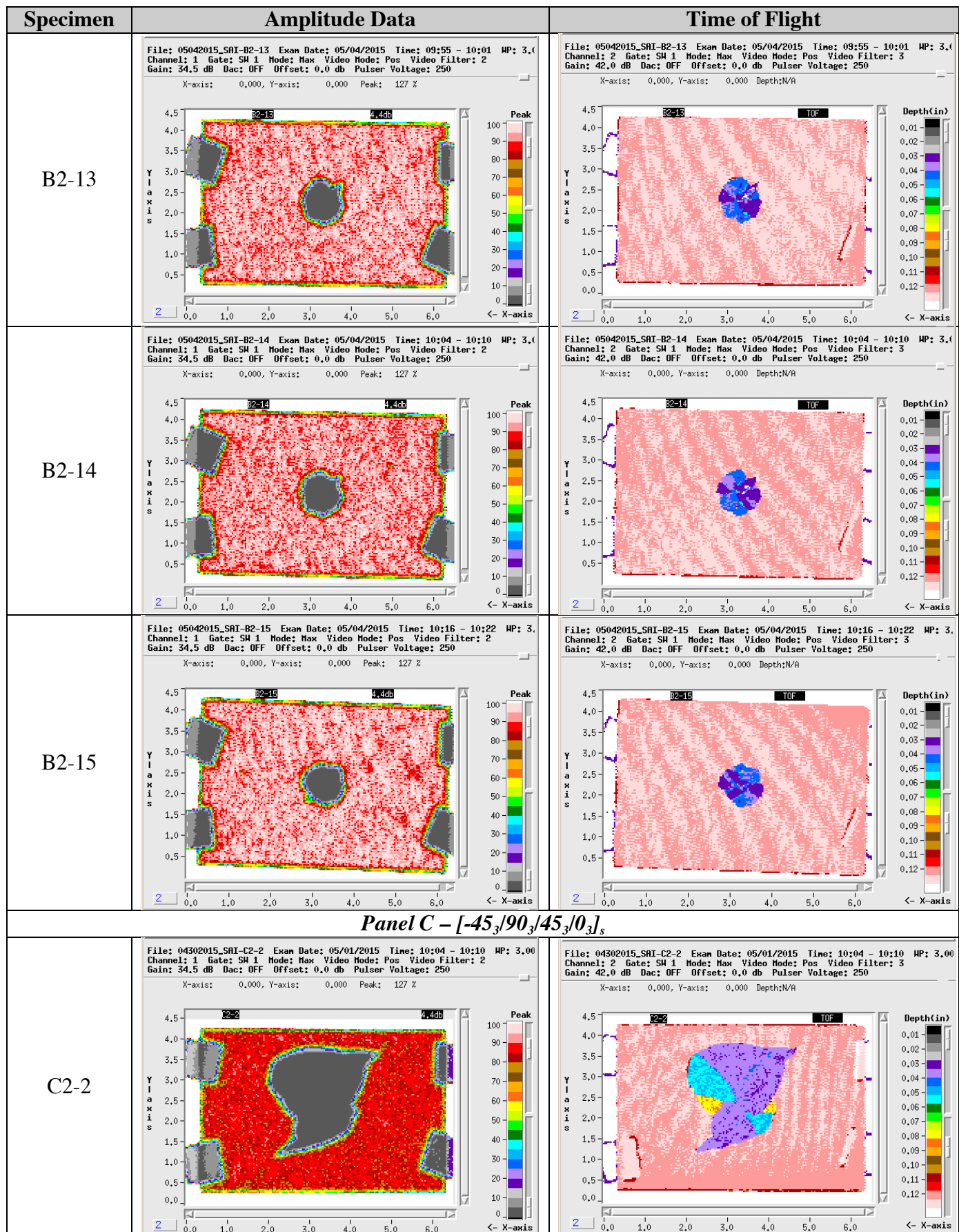
The alpha numeric refers to the panel layout. The number connected to the alpha numeric refers to the panel the specimen was on. The number after the dash refers to the specimen number.

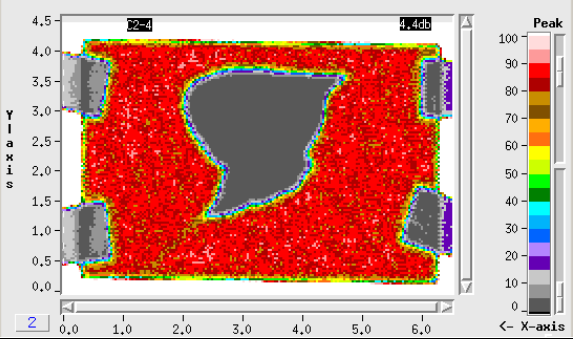
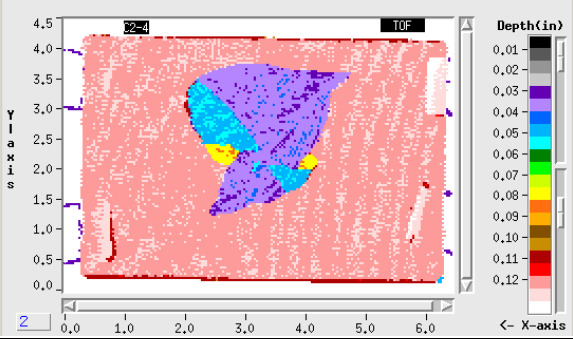
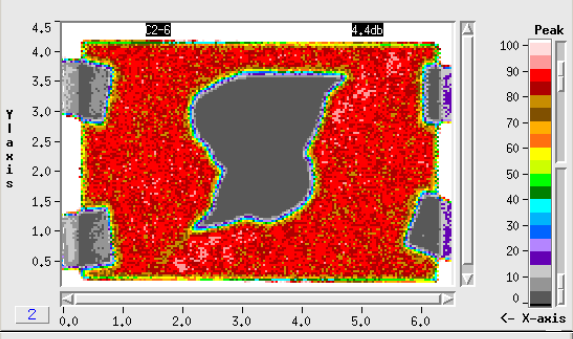
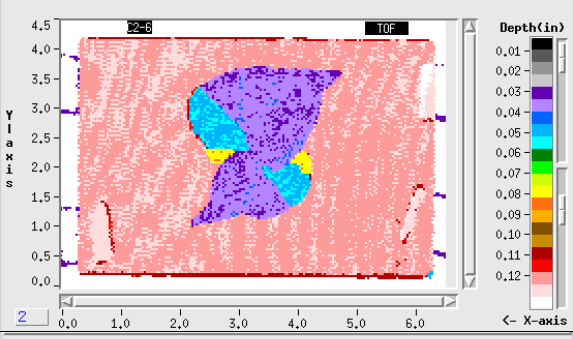
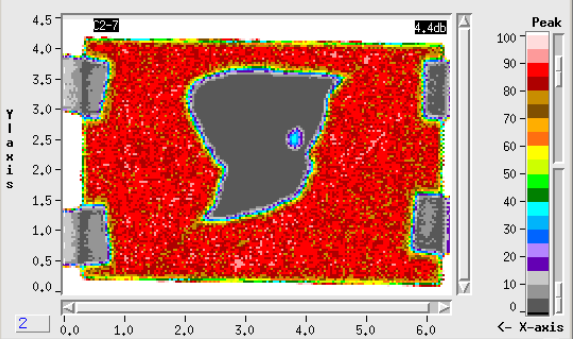
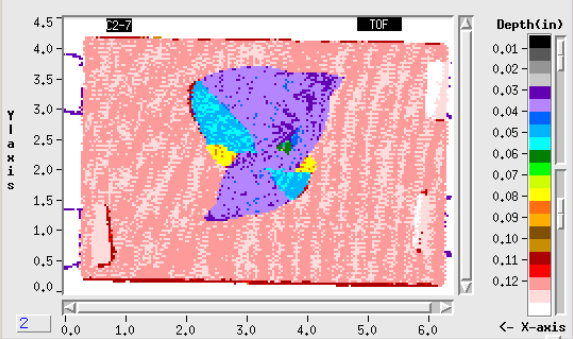
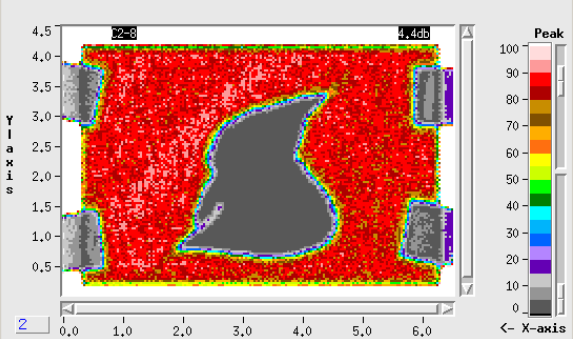
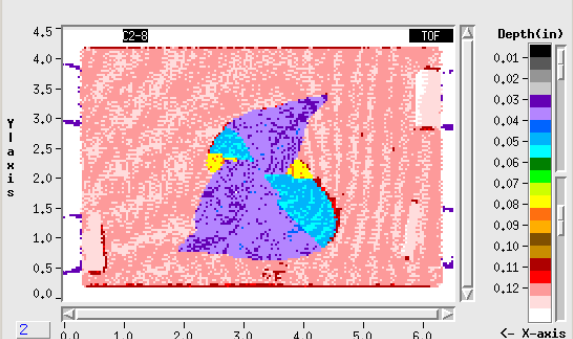




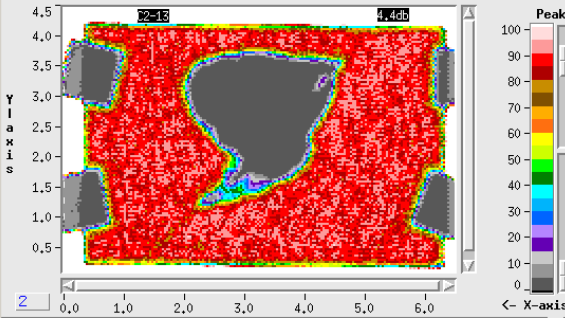
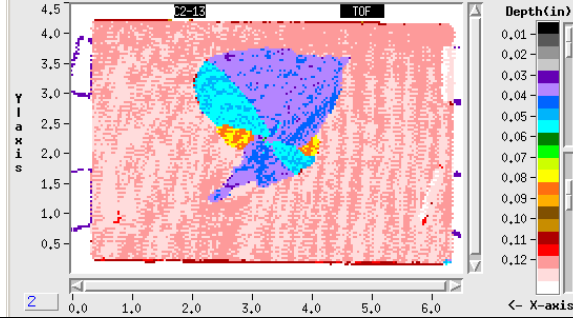
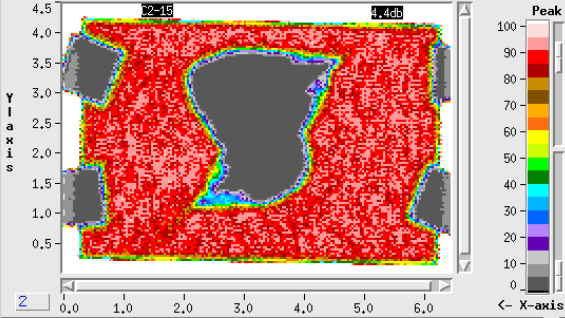
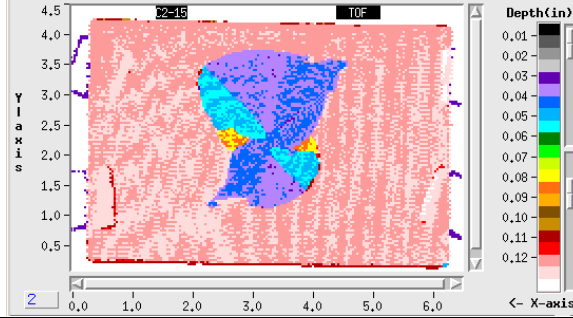
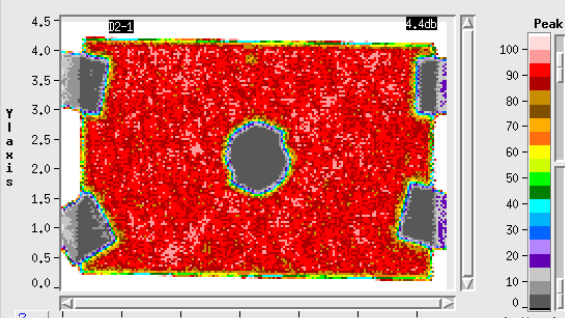
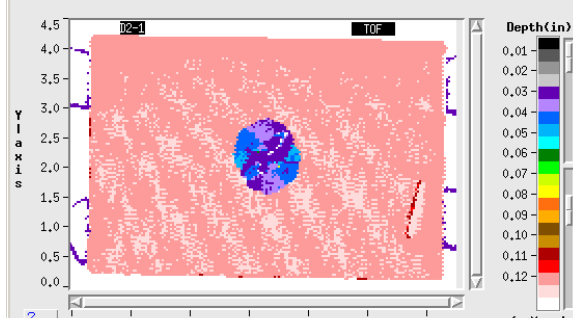
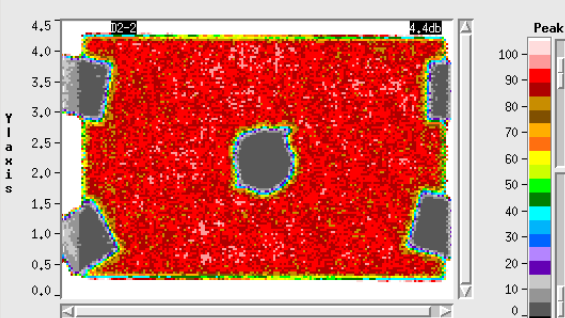
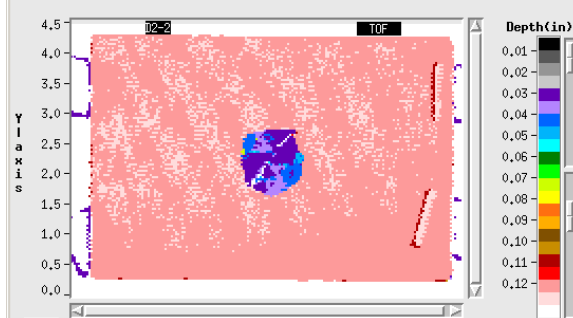
| Specimen | Amplitude Data | Time of Flight |
|----------|-----------------------------------------------------------------------------------------------------------------------------------------------------------------------------------------------------------------------------------------------------------------------|----------------------------------------------------------------------------------------------------------------------------------------------------------------------------------------------------------------------------------------------------------------------|
| B2-2 | <p>File: 04302015_SRI-B2-2 Exam Date: 04/30/2015 Time: 15:16 - 15:22 MP: 3.0 Channel: 1 Gate: SW 1 Mode: Max Video Mode: Pos Video Filter: 2 Gain: 34.5 dB Dac: OFF Offset: 0.0 db Pulser Voltage: 250</p> <p>X-axis: 6.405, Y-axis: 4.480 Peak: 127 %</p> | <p>File: 04302015_SRI-B2-2 Exam Date: 04/30/2015 Time: 15:16 - 15:22 MP: 3.0 Channel: 2 Gate: SW 1 Mode: Max Video Mode: Pos Video Filter: 3 Gain: 42.0 dB Dac: OFF Offset: 0.0 db Pulser Voltage: 250</p> <p>X-axis: 0.000, Y-axis: 0.000 Depth: N/A</p> |
| B2-3 | <p>File: 04302015_SRI-B2-3 Exam Date: 04/30/2015 Time: 15:01 - 15:07 MP: 3.00 Channel: 1 Gate: SW 1 Mode: Max Video Mode: Pos Video Filter: 2 Gain: 34.5 dB Dac: OFF Offset: 0.0 db Pulser Voltage: 250</p> <p>X-axis: 0.000, Y-axis: 0.000 Peak: 127 %</p> | <p>File: 04302015_SRI-B2-3 Exam Date: 04/30/2015 Time: 15:01 - 15:07 MP: 3.00 Channel: 2 Gate: SW 1 Mode: Max Video Mode: Pos Video Filter: 3 Gain: 42.0 dB Dac: OFF Offset: 0.0 db Pulser Voltage: 250</p> <p>X-axis: 0.000, Y-axis: 0.000 Depth: N/A</p> |
| B2-5 | <p>File: 04302015_SRI-B2-5 Exam Date: 04/30/2015 Time: 14:50 - 14:56 MP: 3.00 Channel: 1 Gate: SW 1 Mode: Max Video Mode: Pos Video Filter: 2 Gain: 34.5 dB Dac: OFF Offset: 0.0 db Pulser Voltage: 250</p> <p>X-axis: 0.000, Y-axis: 0.000 Peak: 127 %</p> | <p>File: 04302015_SRI-B2-5 Exam Date: 04/30/2015 Time: 14:50 - 14:56 MP: 3.00 Channel: 2 Gate: SW 1 Mode: Max Video Mode: Pos Video Filter: 3 Gain: 42.0 dB Dac: OFF Offset: 0.0 db Pulser Voltage: 250</p> <p>X-axis: 0.000, Y-axis: 0.000 Depth: N/A</p> |
| B2-6 | <p>File: 04302015_SRI-B2-6 Exam Date: 04/30/2015 Time: 14:39 - 14:45 MP: 3.0 Channel: 1 Gate: SW 1 Mode: Max Video Mode: Pos Video Filter: 2 Gain: 34.5 dB Dac: OFF Offset: 0.0 db Pulser Voltage: 250</p> <p>X-axis: 0.000, Y-axis: 0.000 Peak: 127 %</p> | <p>File: 04302015_SRI-B2-6 Exam Date: 04/30/2015 Time: 14:39 - 14:45 MP: 3.0 Channel: 2 Gate: SW 1 Mode: Max Video Mode: Pos Video Filter: 3 Gain: 42.0 dB Dac: OFF Offset: 0.0 db Pulser Voltage: 250</p> <p>X-axis: 0.000, Y-axis: 0.000 Depth: N/A</p> |

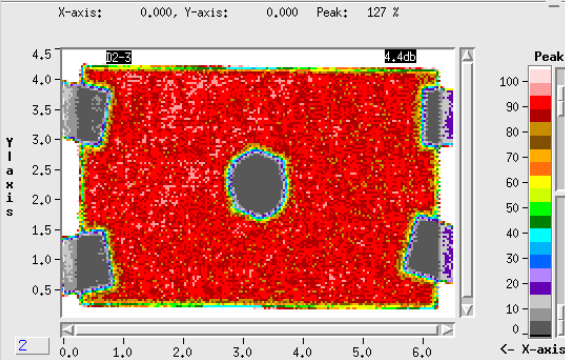
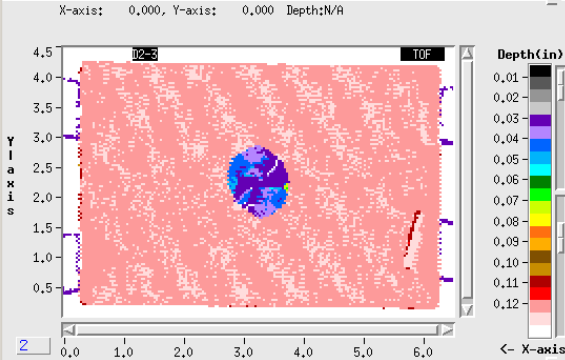
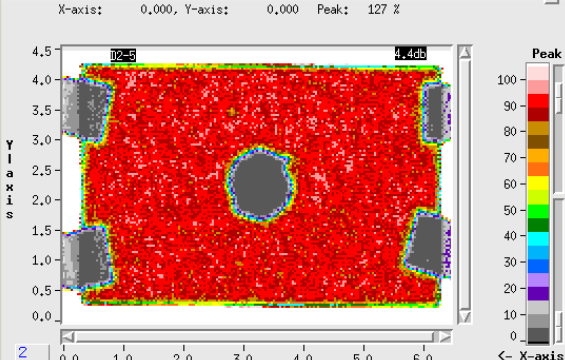
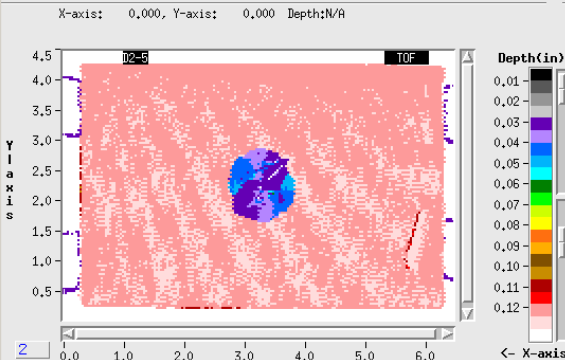
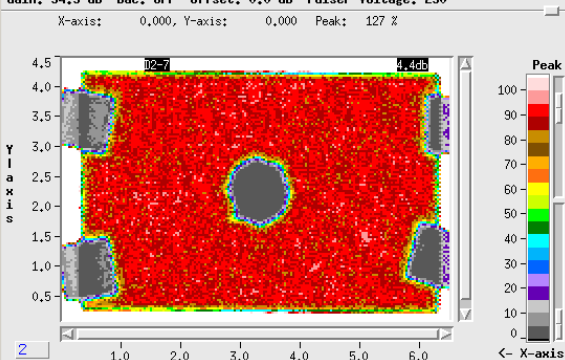
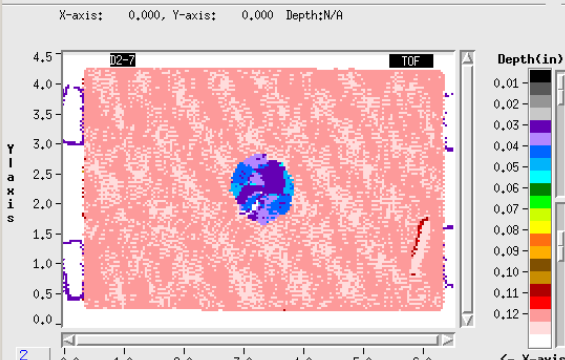
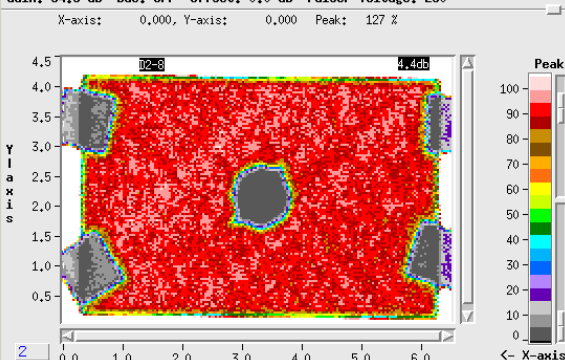
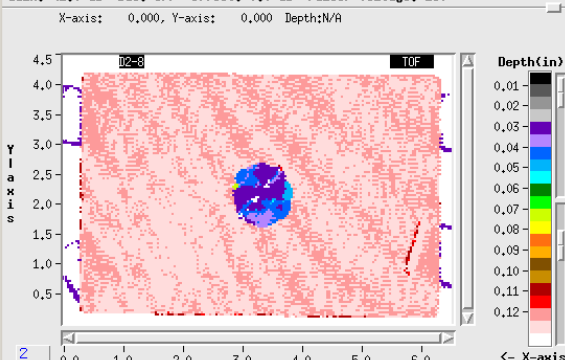
| Specimen | Amplitude Data | Time of Flight |
|----------|--------------------------------------------------------------------------------------------------------------------------------------------------------------------------------------------------------------------------------------------------------------------|-------------------------------------------------------------------------------------------------------------------------------------------------------------------------------------------------------------------------------------------------------------------|
| B2-7 | <p>File: 04302015_SRI-B2-7 Exam Date: 04/30/2015 Time: 14:03 - 14:10 MP: 3.0 Channel: 1 Gate: SW 1 Mode: Max Video Mode: Pos Video Filter: 2 Gain: 34.5 dB Dac: OFF Offset: 0.0 db Pulser Voltage: 250</p> <p>X-axis: 0,000, Y-axis: 0,000 Peak: 127 %</p> | <p>File: 04302015_SRI-B2-7 Exam Date: 04/30/2015 Time: 14:03 - 14:10 MP: 3.0 Channel: 2 Gate: SW 1 Mode: Max Video Mode: Pos Video Filter: 3 Gain: 42.0 dB Dac: OFF Offset: 0.0 db Pulser Voltage: 250</p> <p>X-axis: 0,000, Y-axis: 0,000 Depth:N/A</p> |
| B2-8 | <p>File: 05042015_SRI-B2-8 Exam Date: 05/04/2015 Time: 09:27 - 09:33 MP: 3.0 Channel: 1 Gate: SW 1 Mode: Max Video Mode: Pos Video Filter: 2 Gain: 34.5 dB Dac: OFF Offset: 0.0 db Pulser Voltage: 250</p> <p>X-axis: 0,000, Y-axis: 0,000 Peak: 127 %</p> | <p>File: 05042015_SRI-B2-8 Exam Date: 05/04/2015 Time: 09:27 - 09:33 MP: 3.00 Channel: 2 Gate: SW 1 Mode: Max Video Mode: Pos Video Filter: 3 Gain: 42.0 dB Dac: OFF Offset: 0.0 db Pulser Voltage: 250</p> <p>X-axis: 0,000, Y-axis: 0,000 Depth:N/A</p> |
| B2-10 | <p>File: 05042015_SRI-B2-10 Exam Date: 05/04/2015 Time: 09:37 - 09:43 MP: 3. Channel: 1 Gate: SW 1 Mode: Max Video Mode: Pos Video Filter: 2 Gain: 34.5 dB Dac: OFF Offset: 0.0 db Pulser Voltage: 250</p> <p>X-axis: 0,000, Y-axis: 0,000 Peak: 127 %</p> | <p>X-axis: 0,000, Y-axis: 0,000 Depth:N/A</p> |
| B2-11 | <p>File: 05042015_SRI-B2-11 Exam Date: 05/04/2015 Time: 09:45 - 09:51 MP: 3. Channel: 1 Gate: SW 1 Mode: Max Video Mode: Pos Video Filter: 2 Gain: 34.5 dB Dac: OFF Offset: 0.0 db Pulser Voltage: 250</p> <p>X-axis: 0,000, Y-axis: 0,000 Peak: 127 %</p> | <p>File: 05042015_SRI-B2-11 Exam Date: 05/04/2015 Time: 09:45 - 09:51 MP: 3. Channel: 2 Gate: SW 1 Mode: Max Video Mode: Pos Video Filter: 3 Gain: 42.0 dB Dac: OFF Offset: 0.0 db Pulser Voltage: 250</p> <p>X-axis: 0,000, Y-axis: 0,000 Depth:N/A</p> |



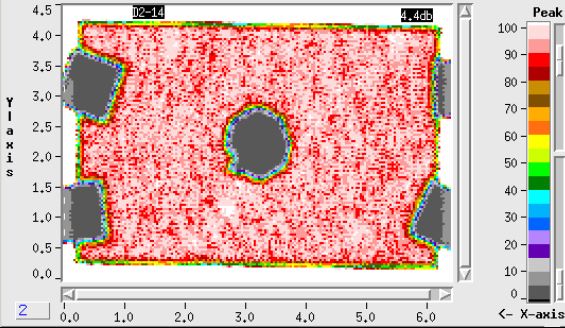
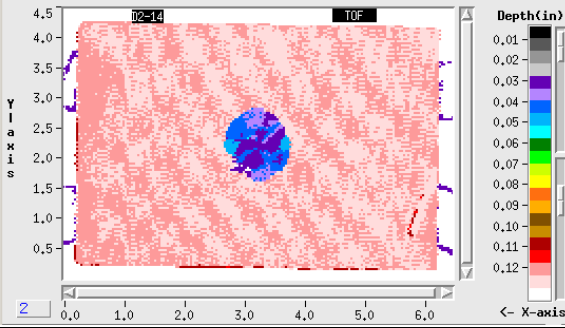
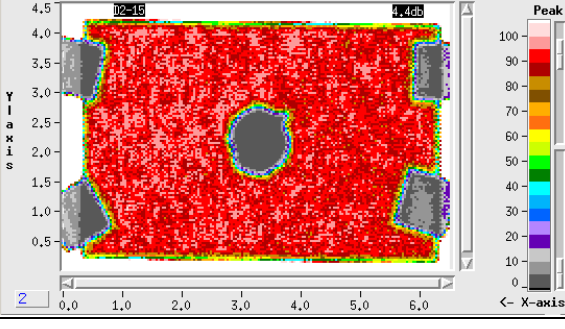
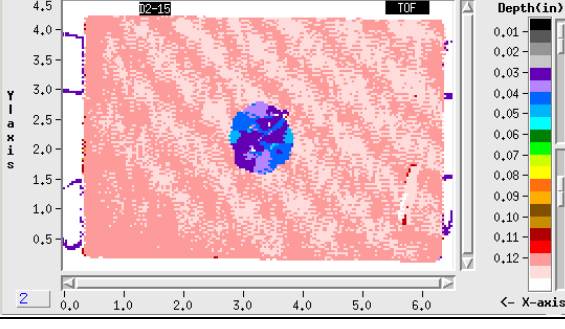
| Specimen | Amplitude Data | Time of Flight |
|----------|-----------------------------------------------------------------------------------------------------------------------------------------------------------------------------------------------------------------------------------------------------------------------------------------------------------------------------------------------------------|----------------------------------------------------------------------------------------------------------------------------------------------------------------------------------------------------------------------------------------------------------------------------------------------------------------------------------------------------------|
| C2-4 | <p>File: 04302015_SRI-C2-4 Exam Date: 05/01/2015 Time: 09:53 - 09:59 MP: 3.04 Channel: 1 Gate: SW 1 Mode: Max Video Mode: Pos Video Filter: 2 Gain: 34.5 dB Dac: OFF Offset: 0.0 db Pulser Voltage: 250</p> <p>X-axis: 0,000, Y-axis: 0,000 Peak: 127 %</p>  | <p>File: 04302015_SRI-C2-4 Exam Date: 05/01/2015 Time: 09:53 - 09:59 MP: 3.0 Channel: 2 Gate: SW 1 Mode: Max Video Mode: Pos Video Filter: 3 Gain: 42.0 dB Dac: OFF Offset: 0.0 db Pulser Voltage: 250</p> <p>X-axis: 0,000, Y-axis: 0,000 Depth:N/A</p>  |
| | <p>File: 04302015_SRI-C2-6 Exam Date: 05/01/2015 Time: 09:39 - 09:45 MP: 3.00 Channel: 1 Gate: SW 1 Mode: Max Video Mode: Pos Video Filter: 2 Gain: 34.5 dB Dac: OFF Offset: 0.0 db Pulser Voltage: 250</p> <p>X-axis: 0,000, Y-axis: 0,000 Peak: 127 %</p>  | <p>File: 04302015_SRI-C2-6 Exam Date: 05/01/2015 Time: 09:39 - 09:45 MP: 3.00 Channel: 2 Gate: SW 1 Mode: Max Video Mode: Pos Video Filter: 3 Gain: 42.0 dB Dac: OFF Offset: 0.0 db Pulser Voltage: 250</p> <p>X-axis: 0,000, Y-axis: 0,000 Depth:N/A</p>  |
| C2-7 | <p>File: 04302015_SRI-C2-7 Exam Date: 05/01/2015 Time: 09:20 - 09:26 MP: 3.1 Channel: 1 Gate: SW 1 Mode: Max Video Mode: Pos Video Filter: 2 Gain: 34.5 dB Dac: OFF Offset: 0.0 db Pulser Voltage: 250</p> <p>X-axis: 0,000, Y-axis: 0,000 Peak: 127 %</p>  | <p>File: 04302015_SRI-C2-7 Exam Date: 05/01/2015 Time: 09:20 - 09:26 MP: 3.1 Channel: 2 Gate: SW 1 Mode: Max Video Mode: Pos Video Filter: 3 Gain: 42.0 dB Dac: OFF Offset: 0.0 db Pulser Voltage: 250</p> <p>X-axis: 0,000, Y-axis: 0,000 Depth:N/A</p>  |
| | <p>File: 04302015_SRI-C2-8 Exam Date: 05/01/2015 Time: 09:10 - 09:16 MP: 3.04 Channel: 1 Gate: SW 1 Mode: Max Video Mode: Pos Video Filter: 2 Gain: 34.5 dB Dac: OFF Offset: 0.0 db Pulser Voltage: 250</p> <p>X-axis: 0,000, Y-axis: 0,000 Peak: 127 %</p>  | <p>File: 04302015_SRI-C2-8 Exam Date: 05/01/2015 Time: 09:10 - 09:16 MP: 3.04 Channel: 2 Gate: SW 1 Mode: Max Video Mode: Pos Video Filter: 3 Gain: 42.0 dB Dac: OFF Offset: 0.0 db Pulser Voltage: 250</p> <p>X-axis: 0,000, Y-axis: 0,000 Depth:N/A</p>  |

| Specimen | Amplitude Data | Time of Flight |
|----------|---------------------------------------------------------------------------------------------------------------------------------------------------------------------------------------------------------------------------------------------------------------------|--------------------------------------------------------------------------------------------------------------------------------------------------------------------------------------------------------------------------------------------------------------------|
| C2-9 | <p>File: 05042015_SRI-C2-9 Exam Date: 05/04/2015 Time: 08:11 - 08:17 MP: 3.0 Channel: 1 Gate: SM 1 Mode: Max Video Mode: Pos Video Filter: 2 Gain: 34.5 dB Dac: OFF Offset: 0.0 db Pulser Voltage: 250</p> <p>X-axis: 0,000, Y-axis: 0,000 Peak: 127 %</p> | <p>File: 05042015_SRI-C2-9 Exam Date: 05/04/2015 Time: 08:11 - 08:17 MP: 3.0 Channel: 2 Gate: SM 1 Mode: Max Video Mode: Pos Video Filter: 3 Gain: 42.0 dB Dac: OFF Offset: 0.0 db Pulser Voltage: 250</p> <p>X-axis: 0,000, Y-axis: 0,000 Depth: N/A</p> |
| C2-10 | <p>File: 05042015_SRI-C2-10 Exam Date: 05/04/2015 Time: 08:22 - 08:28 MP: 3.0 Channel: 1 Gate: SM 1 Mode: Max Video Mode: Pos Video Filter: 2 Gain: 34.5 dB Dac: OFF Offset: 0.0 db Pulser Voltage: 250</p> <p>X-axis: 0,000, Y-axis: 0,000 Peak: 127 %</p> | <p>File: 05042015_SRI-C2-10 Exam Date: 05/04/2015 Time: 08:22 - 08:28 MP: 3.0 Channel: 2 Gate: SM 1 Mode: Max Video Mode: Pos Video Filter: 3 Gain: 42.0 dB Dac: OFF Offset: 0.0 db Pulser Voltage: 250</p> <p>X-axis: 0,000, Y-axis: 0,000 Depth: N/A</p> |
| C2-11 | <p>File: 05042015_SRI-C2-11 Exam Date: 05/04/2015 Time: 08:31 - 08:37 MP: 3.0 Channel: 1 Gate: SM 1 Mode: Max Video Mode: Pos Video Filter: 2 Gain: 34.5 dB Dac: OFF Offset: 0.0 db Pulser Voltage: 250</p> <p>X-axis: 0,000, Y-axis: 0,000 Peak: 127 %</p> | <p>File: 05042015_SRI-C2-11 Exam Date: 05/04/2015 Time: 08:31 - 08:37 MP: 3.0 Channel: 2 Gate: SM 1 Mode: Max Video Mode: Pos Video Filter: 3 Gain: 42.0 dB Dac: OFF Offset: 0.0 db Pulser Voltage: 250</p> <p>X-axis: 0,000, Y-axis: 0,000 Depth: N/A</p> |
| C2-12 | <p>File: 05042015_SRI-C2-12 Exam Date: 05/04/2015 Time: 08:45 - 08:51 MP: 3.0 Channel: 1 Gate: SM 1 Mode: Max Video Mode: Pos Video Filter: 2 Gain: 34.5 dB Dac: OFF Offset: 0.0 db Pulser Voltage: 250</p> <p>X-axis: 0,000, Y-axis: 0,000 Peak: 127 %</p> | <p>File: 05042015_SRI-C2-12 Exam Date: 05/04/2015 Time: 08:45 - 08:51 MP: 3.0 Channel: 2 Gate: SM 1 Mode: Max Video Mode: Pos Video Filter: 3 Gain: 42.0 dB Dac: OFF Offset: 0.0 db Pulser Voltage: 250</p> <p>X-axis: 0,000, Y-axis: 0,000 Depth: N/A</p> |

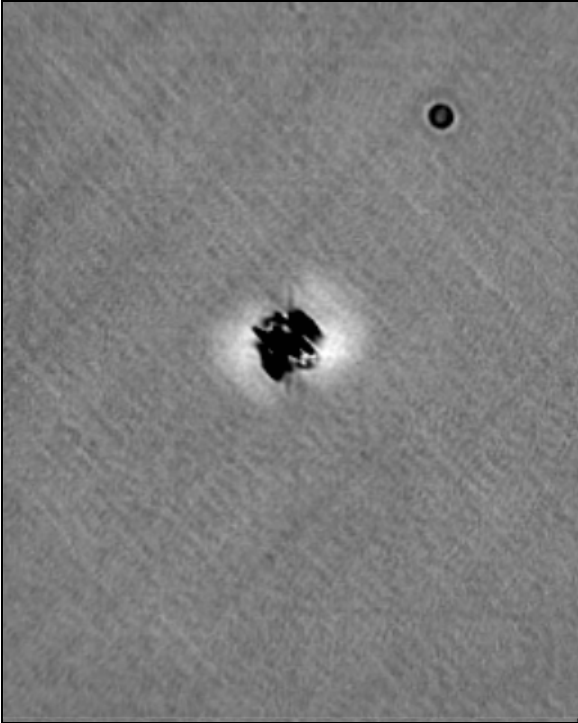
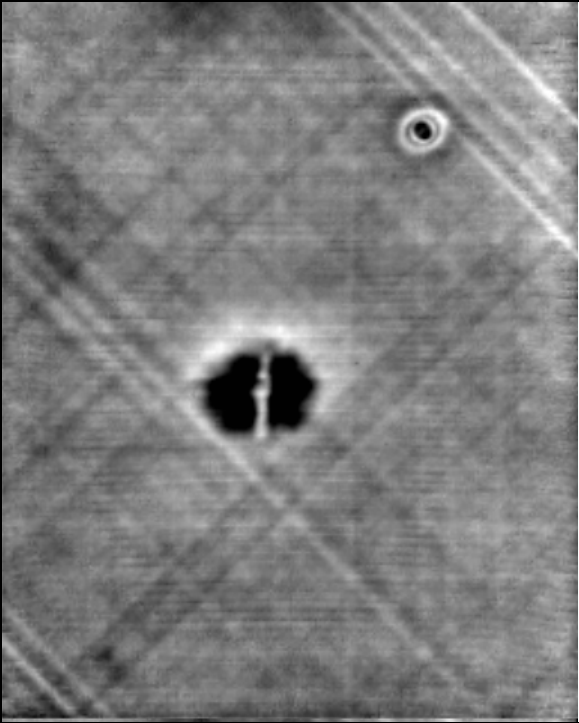
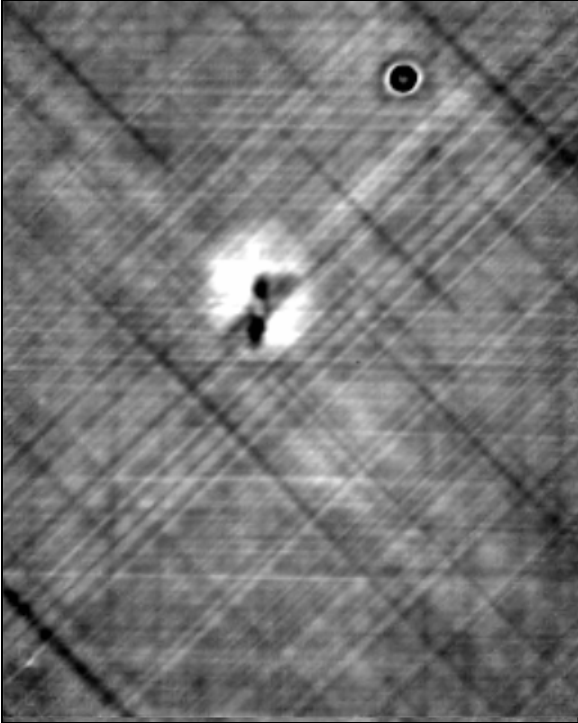
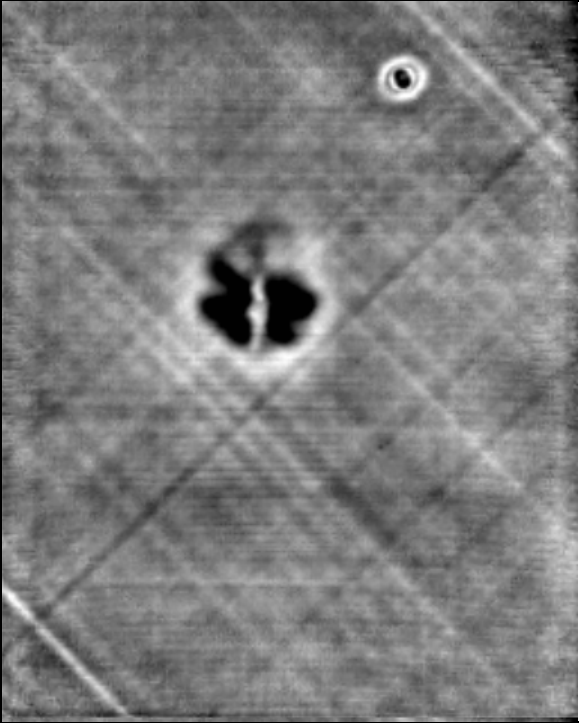
| Specimen | Amplitude Data | Time of Flight |
|---------------------------------------------|---------------------------------------------------------------------------------------------------------------------------------------------------------------------------------------------------------------------------------------------------------------------------------------------------------------------------------------------------------|---------------------------------------------------------------------------------------------------------------------------------------------------------------------------------------------------------------------------------------------------------------------------------------------------------------------------------------------------------|
| C2-13 | <p>File: 05042015_SRI-C2-13 Exam Date: 05/04/2015 Time: 09:03 - 09:09 MP: 3.0 Channel: 1 Gate: SW 1 Mode: Max Video Mode: Pos Video Filter: 2 Gain: 34.5 dB Dac: OFF Offset: 0.0 db Pulser Voltage: 250</p> <p>X-axis: 0.000, Y-axis: 0.070 Peak: 127 %</p>  | <p>File: 05042015_SRI-C2-13 Exam Date: 05/04/2015 Time: 09:03 - 09:09 MP: 3.0 Channel: 2 Gate: SW 1 Mode: Max Video Mode: Pos Video Filter: 3 Gain: 42.0 dB Dac: OFF Offset: 0.0 db Pulser Voltage: 250</p> <p>X-axis: 0.000, Y-axis: 0.070 Depth: N/A</p>  |
| C2-15 | <p>File: 05042015_SRI-C2-15 Exam Date: 05/04/2015 Time: 09:13 - 09:19 MP: 3.0 Channel: 1 Gate: SW 1 Mode: Max Video Mode: Pos Video Filter: 2 Gain: 34.5 dB Dac: OFF Offset: 0.0 db Pulser Voltage: 250</p> <p>X-axis: 0.000, Y-axis: 0.000 Peak: 127 %</p>  | <p>File: 05042015_SRI-C2-15 Exam Date: 05/04/2015 Time: 09:13 - 09:19 MP: 3.0 Channel: 2 Gate: SW 1 Mode: Max Video Mode: Pos Video Filter: 3 Gain: 42.0 dB Dac: OFF Offset: 0.0 db Pulser Voltage: 250</p> <p>X-axis: 0.000, Y-axis: 0.000 Depth: N/A</p>  |
| Panel D - [-45/90/45/0]_{3s} | | |
| D2-1 | <p>File: 04302015_SRI-D2-1 Exam Date: 05/01/2015 Time: 11:20 - 11:26 MP: 3.00 Channel: 1 Gate: SW 1 Mode: Max Video Mode: Pos Video Filter: 2 Gain: 34.5 dB Dac: OFF Offset: 0.0 db Pulser Voltage: 250</p> <p>X-axis: 0.000, Y-axis: 0.000 Peak: 127 %</p>  | <p>File: 04302015_SRI-D2-1 Exam Date: 05/01/2015 Time: 11:20 - 11:26 MP: 3.00 Channel: 2 Gate: SW 1 Mode: Max Video Mode: Pos Video Filter: 3 Gain: 42.0 dB Dac: OFF Offset: 0.0 db Pulser Voltage: 250</p> <p>X-axis: 0.000, Y-axis: 0.000 Depth: N/A</p>  |
| D2-2 | <p>File: 04302015_SRI-D2-2 Exam Date: 05/01/2015 Time: 11:09 - 11:15 MP: 3.0 Channel: 1 Gate: SW 1 Mode: Max Video Mode: Pos Video Filter: 2 Gain: 34.5 dB Dac: OFF Offset: 0.0 db Pulser Voltage: 250</p> <p>X-axis: 0.000, Y-axis: 0.000 Peak: 127 %</p>  | <p>File: 04302015_SRI-D2-2 Exam Date: 05/01/2015 Time: 11:09 - 11:15 MP: 3.0 Channel: 2 Gate: SW 1 Mode: Max Video Mode: Pos Video Filter: 3 Gain: 42.0 dB Dac: OFF Offset: 0.0 db Pulser Voltage: 250</p> <p>X-axis: 0.000, Y-axis: 0.000 Depth: N/A</p>  |

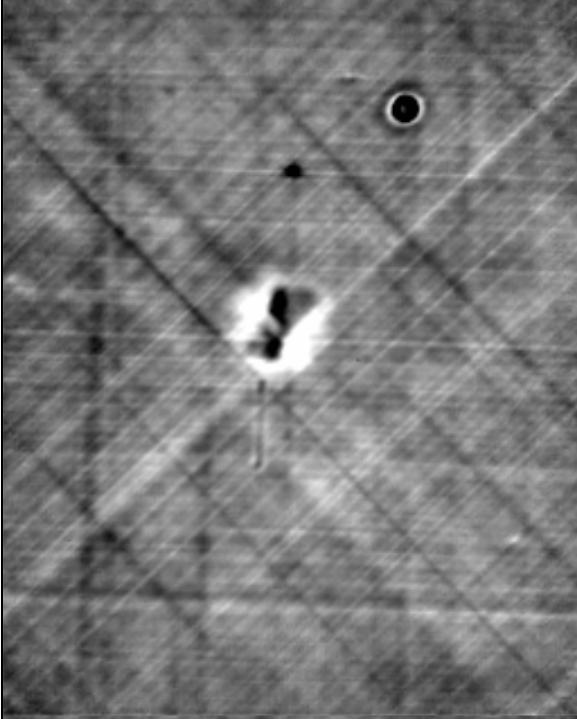
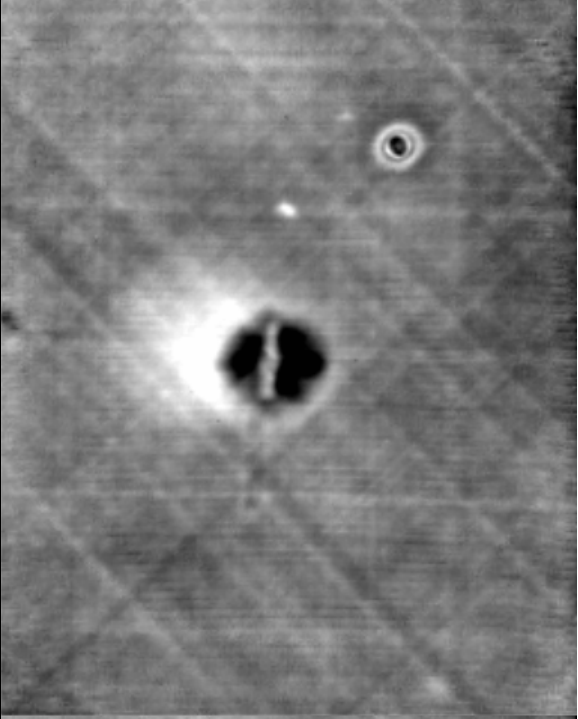
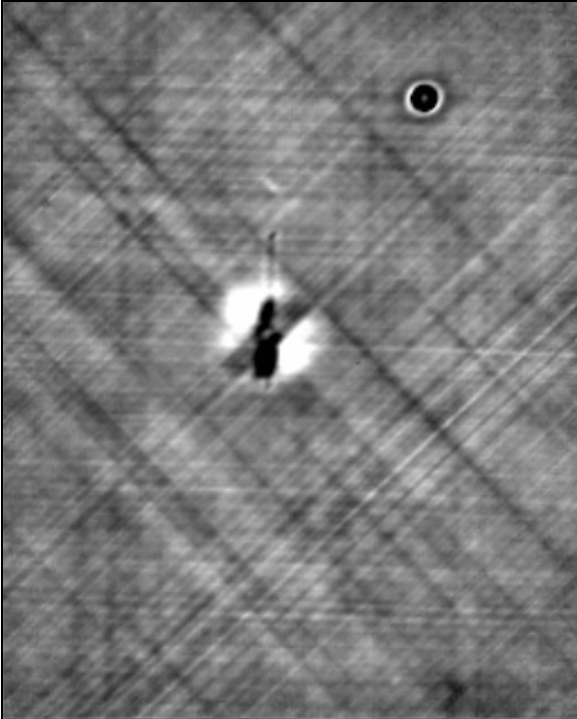
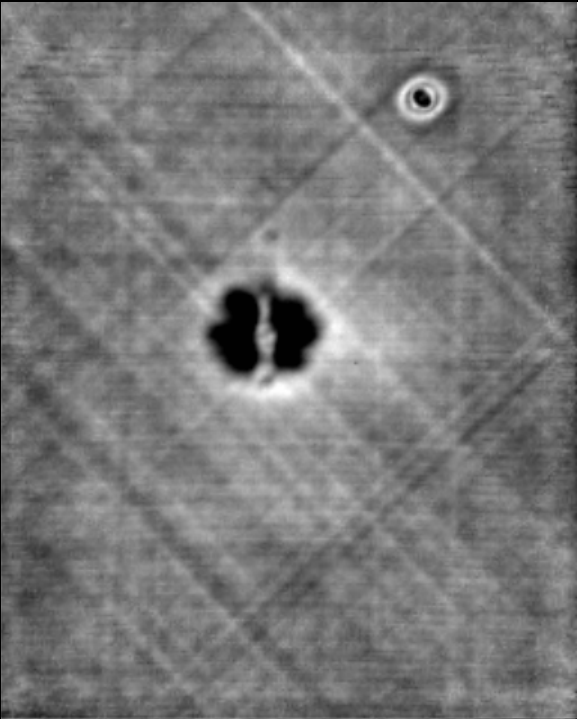
| Specimen | Amplitude Data | Time of Flight |
|----------|----------------------------------------------------------------------------------------------------------------------------------------------------------------------------------------------------------------------------------------------------------------------------------------------------------|-----------------------------------------------------------------------------------------------------------------------------------------------------------------------------------------------------------------------------------------------------------------------------------------------------------|
| D2-3 | <p>File: 04302015_SAI-D2-3 Exam Date: 05/01/2015 Time: 10:59 - 11:05 MP: 3.0 Channel: 1 Gate: SW 1 Mode: Max Video Mode: Pos Video Filter: 2 Gain: 34.5 dB Dac: OFF Offset: 0.0 db Pulser Voltage: 250</p>  | <p>File: 04302015_SAI-D2-3 Exam Date: 05/01/2015 Time: 10:59 - 11:05 MP: 3.0 Channel: 2 Gate: SW 1 Mode: Max Video Mode: Pos Video Filter: 3 Gain: 42.0 dB Dac: OFF Offset: 0.0 db Pulser Voltage: 250</p>  |
| D2-5 | <p>File: 04302015_SAI-D2-5 Exam Date: 05/01/2015 Time: 10:45 - 10:51 MP: 3.0 Channel: 1 Gate: SW 1 Mode: Max Video Mode: Pos Video Filter: 2 Gain: 34.5 dB Dac: OFF Offset: 0.0 db Pulser Voltage: 250</p>  | <p>File: 04302015_SAI-D2-5 Exam Date: 05/01/2015 Time: 10:45 - 10:51 MP: 3.0 Channel: 2 Gate: SW 1 Mode: Max Video Mode: Pos Video Filter: 3 Gain: 42.0 dB Dac: OFF Offset: 0.0 db Pulser Voltage: 250</p>  |
| D2-7 | <p>File: 04302015_SAI-D2-7 Exam Date: 05/01/2015 Time: 10:35 - 10:41 MP: 3.0 Channel: 1 Gate: SW 1 Mode: Max Video Mode: Pos Video Filter: 2 Gain: 34.5 dB Dac: OFF Offset: 0.0 db Pulser Voltage: 250</p>  | <p>File: 04302015_SAI-D2-7 Exam Date: 05/01/2015 Time: 10:35 - 10:41 MP: 3.0 Channel: 2 Gate: SW 1 Mode: Max Video Mode: Pos Video Filter: 3 Gain: 42.0 dB Dac: OFF Offset: 0.0 db Pulser Voltage: 250</p>  |
| D2-8 | <p>File: 04302015_SAI-D2-8 Exam Date: 05/01/2015 Time: 12:22 - 12:29 MP: 3.0 Channel: 1 Gate: SW 1 Mode: Max Video Mode: Pos Video Filter: 2 Gain: 34.5 dB Dac: OFF Offset: 0.0 db Pulser Voltage: 250</p>  | <p>File: 04302015_SAI-D2-8 Exam Date: 05/01/2015 Time: 12:22 - 12:29 MP: 3.0 Channel: 2 Gate: SW 1 Mode: Max Video Mode: Pos Video Filter: 3 Gain: 42.0 dB Dac: OFF Offset: 0.0 db Pulser Voltage: 250</p>  |

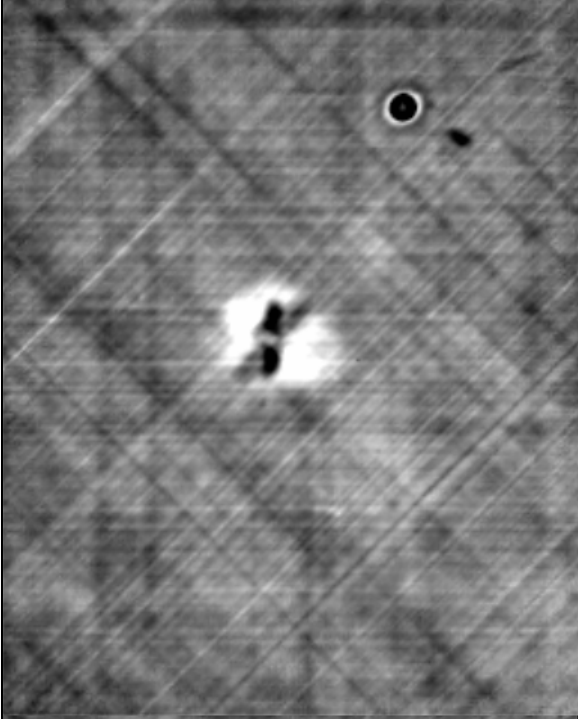

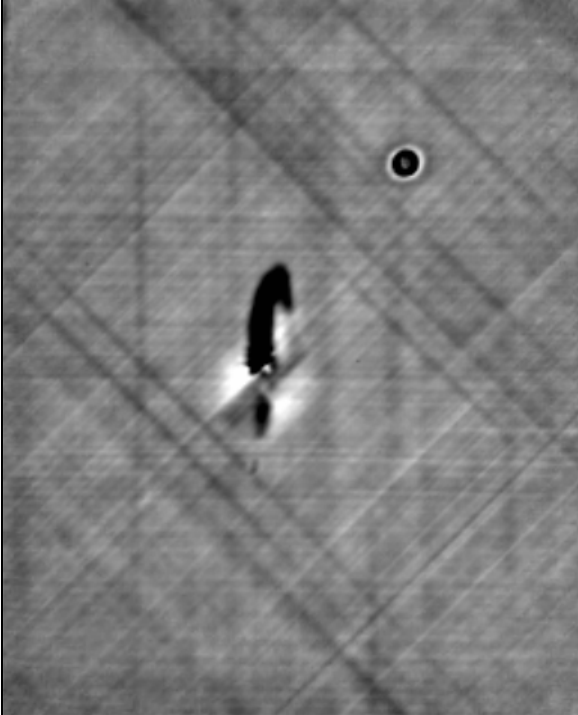
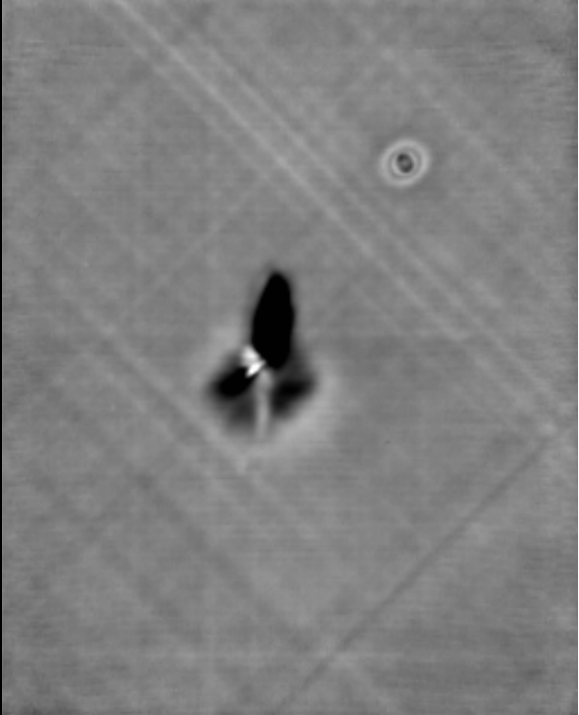
| Specimen | Amplitude Data | Time of Flight |
|----------|----------------------------------------------------------------------------------------------------------------------------------------------------------------------------------------------------------------------------------------------------------------------|---------------------------------------------------------------------------------------------------------------------------------------------------------------------------------------------------------------------------------------------------------------------|
| D2-9 | <p>File: 04302015_SRI-D2-9 Exam Date: 05/01/2015 Time: 12:32 - 12:38 MP: 3.0 Channel: 1 Gate: SM 1 Mode: Max Video Mode: Pos Video Filter: 2 Gain: 34.5 dB Dac: OFF Offset: 0.0 db Pulser Voltage: 250</p> <p>X-axis: 0,000, Y-axis: 0,000 Peak: 127 %</p> | <p>File: 04302015_SRI-D2-9 Exam Date: 05/01/2015 Time: 12:32 - 12:38 MP: 3.0 Channel: 2 Gate: SM 1 Mode: Max Video Mode: Pos Video Filter: 3 Gain: 42.0 dB Dac: OFF Offset: 0.0 db Pulser Voltage: 250</p> <p>X-axis: 0,000, Y-axis: 0,000 Depth:N/A</p> |
| D2-10 | <p>File: 04302015_SRI-D2-10 Exam Date: 05/01/2015 Time: 12:41 - 12:47 MP: 3.0 Channel: 1 Gate: SM 1 Mode: Max Video Mode: Pos Video Filter: 2 Gain: 34.5 dB Dac: OFF Offset: 0.0 db Pulser Voltage: 250</p> <p>X-axis: 0,000, Y-axis: 4,480 Peak: 127 %</p> | <p>File: 04302015_SRI-D2-10 Exam Date: 05/01/2015 Time: 12:41 - 12:47 MP: 3.0 Channel: 2 Gate: SM 1 Mode: Max Video Mode: Pos Video Filter: 3 Gain: 42.0 dB Dac: OFF Offset: 0.0 db Pulser Voltage: 250</p> <p>X-axis: 0,000, Y-axis: 4,480 Depth:N/A</p> |
| D2-11 | <p>File: 05042015_SRI-D2-11A Exam Date: 05/04/2015 Time: 11:05 - 11:11 MP: 3.0 Channel: 1 Gate: SM 1 Mode: Max Video Mode: Pos Video Filter: 2 Gain: 34.5 dB Dac: OFF Offset: 0.0 db Pulser Voltage: 250</p> <p>X-axis: 0,000, Y-axis: 0,000 Peak: 127 %</p> | <p>File: 05042015_SRI-D2-11A Exam Date: 05/04/2015 Time: 11:05 - 11:11 MP: 3.00 Channel: 2 Gate: SM 1 Mode: Max Video Mode: Pos Video Filter: 3 Gain: 42.0 dB Dac: OFF Offset: 0.0 db Pulser Voltage: 250</p> <p>X-axis: 0,000, Y-axis: 0,000 Depth:N/A</p> |
| D2-12 | <p>File: 05042015_SRI-D2-12A Exam Date: 05/04/2015 Time: 10:55 - 11:02 MP: 3.0 Channel: 1 Gate: SM 1 Mode: Max Video Mode: Pos Video Filter: 2 Gain: 34.5 dB Dac: OFF Offset: 0.0 db Pulser Voltage: 250</p> <p>X-axis: 0,000, Y-axis: 0,000 Peak: 127 %</p> | <p>File: 05042015_SRI-D2-12A Exam Date: 05/04/2015 Time: 10:55 - 11:02 MP: 3.0 Channel: 2 Gate: SM 1 Mode: Max Video Mode: Pos Video Filter: 3 Gain: 42.0 dB Dac: OFF Offset: 0.0 db Pulser Voltage: 250</p> <p>X-axis: 0,000, Y-axis: 0,000 Depth:N/A</p> |

| Specimen | Amplitude Data | Time of Flight |
|----------|--------------------------------------------------------------------------------------------------------------------------------------------------------------------------------------------------------------------------------------------------------------------------------------------------------------------------------------------------------|-------------------------------------------------------------------------------------------------------------------------------------------------------------------------------------------------------------------------------------------------------------------------------------------------------------------------------------------------------|
| D2-14 | <p>File: 05042015_SRI-D2-14A Exam Date: 05/04/2015 Time: 10:47 - 10:53 MP: 3 Channel: 1 Gate: SM 1 Mode: Max Video Mode: Pos Video Filter: 2 Gain: 34,5 dB Dac: OFF Offset: 0,0 db Pulser Voltage: 250</p> <p>X-axis: 0,000, Y-axis: 0,000 Peak: 127 %</p>  | <p>File: 05042015_SRI-D2-14A Exam Date: 05/04/2015 Time: 10:47 - 10:53 MP: 3 Channel: 2 Gate: SM 1 Mode: Max Video Mode: Pos Video Filter: 3 Gain: 42,0 dB Dac: OFF Offset: 0,0 db Pulser Voltage: 250</p> <p>X-axis: 0,000, Y-axis: 0,000 Depth:N/A</p>  |
| D2-15 | <p>File: 04302015_SRI-D2-15 Exam Date: 05/01/2015 Time: 11:30 - 11:37 MP: 3,0 Channel: 1 Gate: SM 1 Mode: Max Video Mode: Pos Video Filter: 2 Gain: 34,5 dB Dac: OFF Offset: 0,0 db Pulser Voltage: 250</p> <p>X-axis: 0,000, Y-axis: 0,000 Peak: 127 %</p>  | <p>File: 04302015_SRI-D2-15 Exam Date: 05/01/2015 Time: 11:30 - 11:37 MP: 3,0 Channel: 2 Gate: SM 1 Mode: Max Video Mode: Pos Video Filter: 3 Gain: 42,0 dB Dac: OFF Offset: 0,0 db Pulser Voltage: 250</p> <p>X-axis: 0,000, Y-axis: 0,000 Depth:N/A</p>  |
| | | |

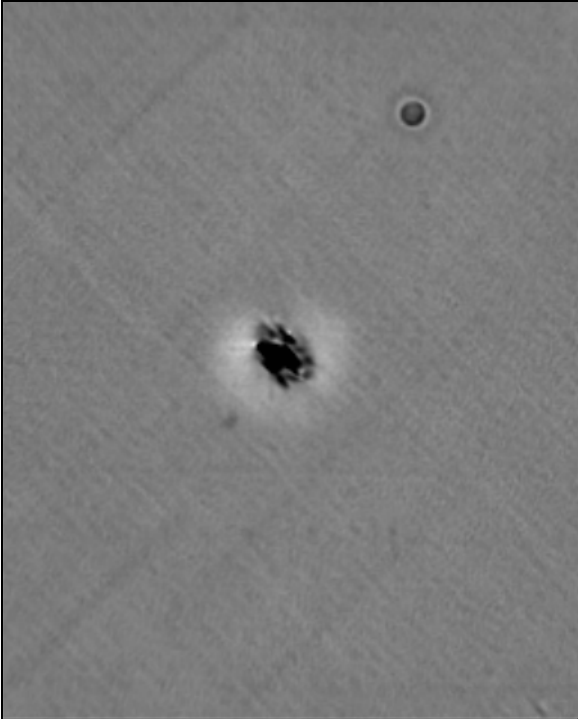
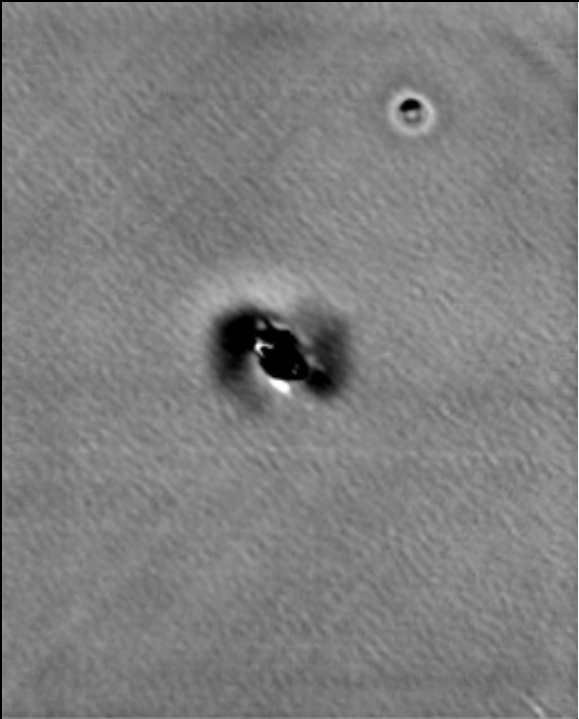
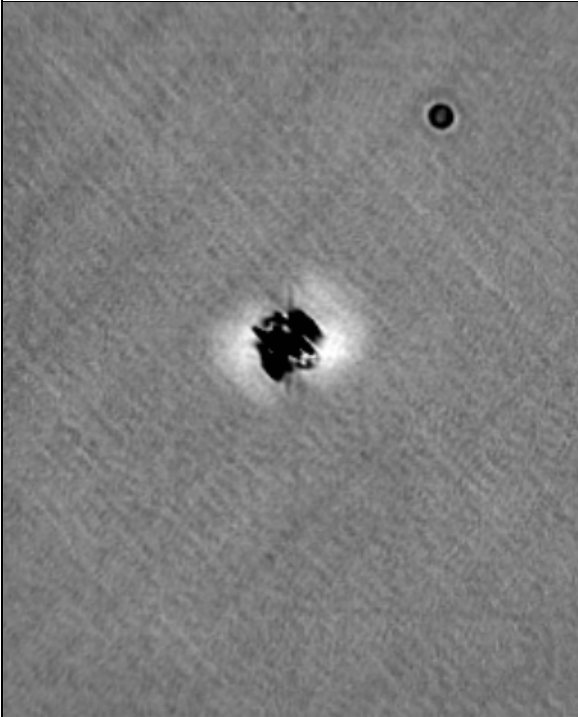
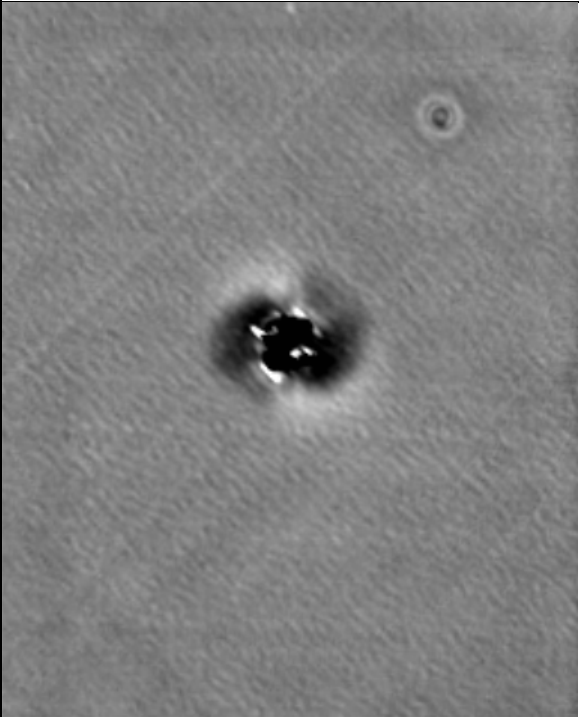
Appendix B: Flash Thermography of Impacted Surface

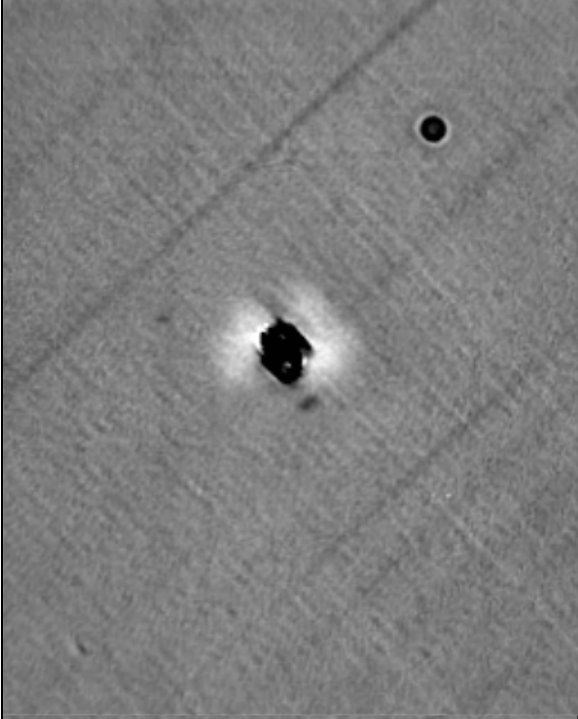
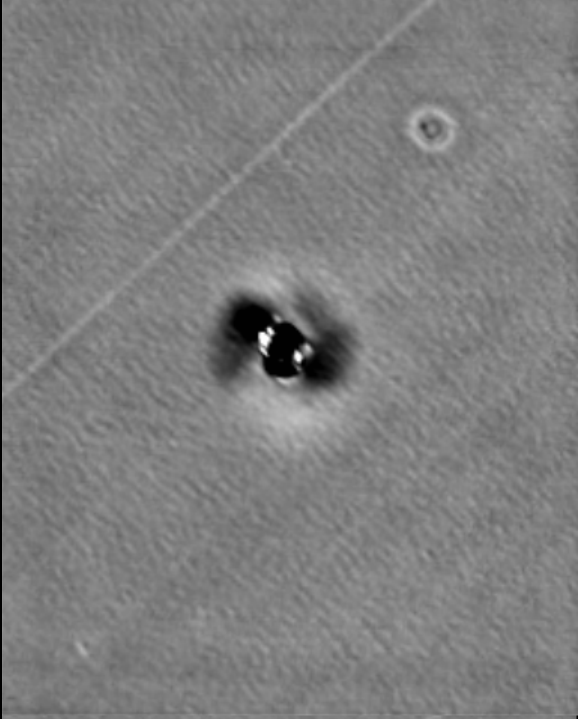
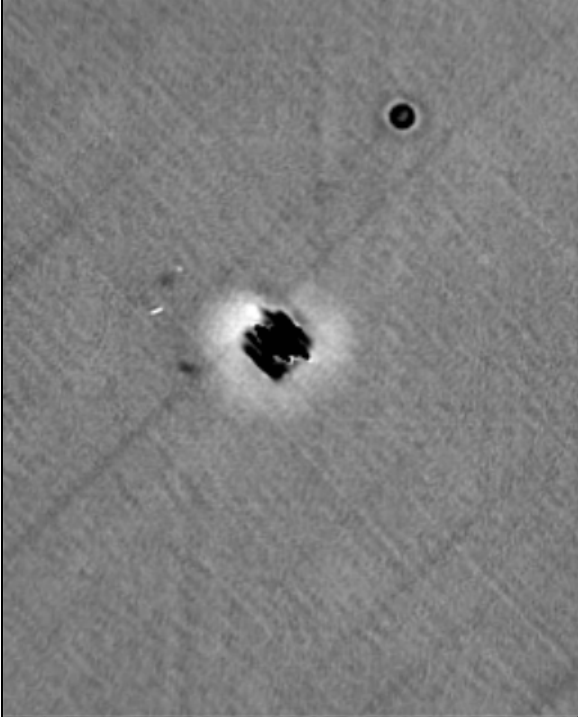
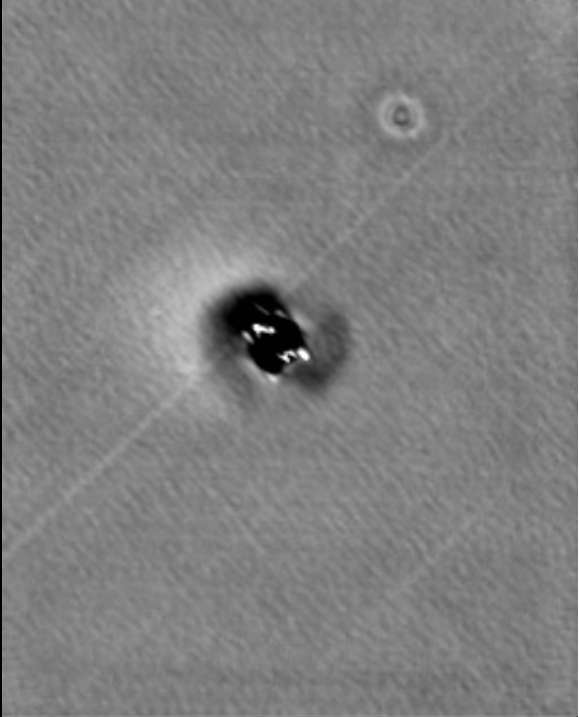
| Specimen-#1 | |
|-------------------------------------------------------------------------------------|--------------------------------------------------------------------------------------|
| 2D at 0.400 | 2D at 1.500 |
|  |  |
| Specimen-#2 | |
| 2D at 0.400 | 2D at 1.500 |
|  |  |

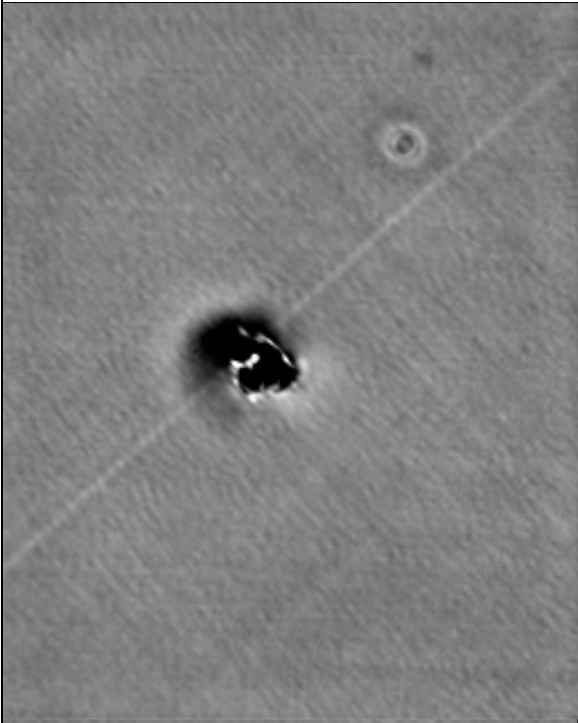
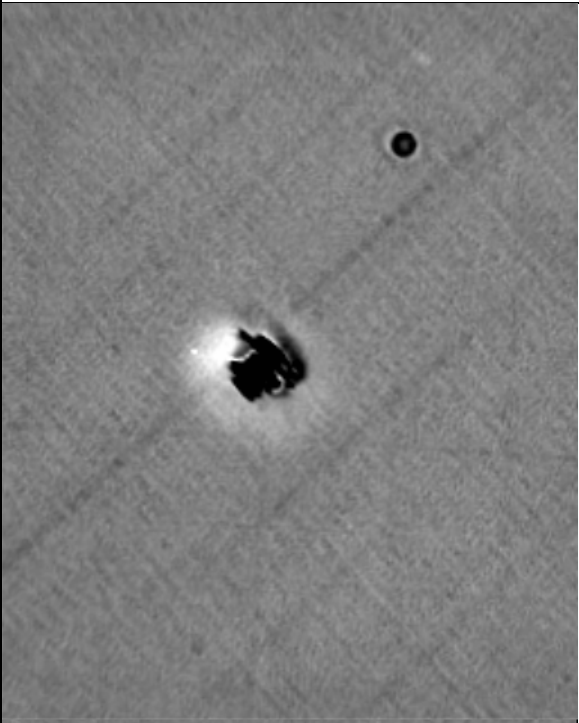
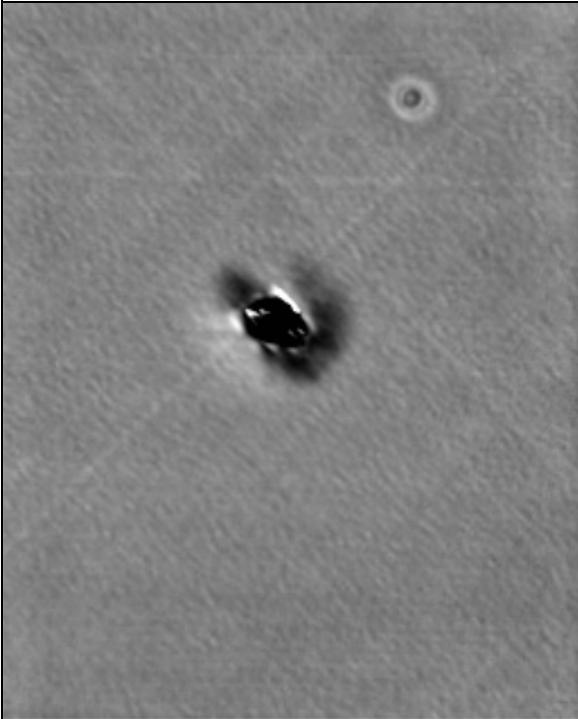
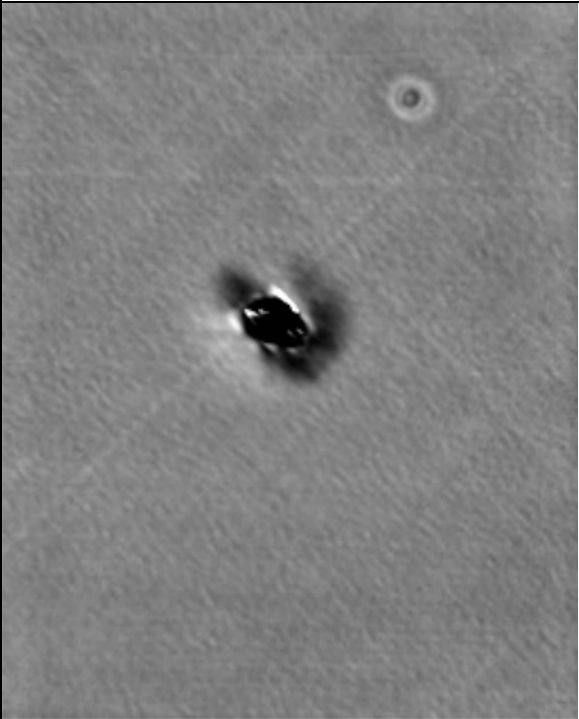
| Specimen-#3 | |
|-------------------------------------------------------------------------------------|--------------------------------------------------------------------------------------|
| 2D at 0.400 | 2D at 1.500 |
|  |  |
| Specimen-#4 | |
| 2D at 0.400 | 2D at 1.500 |
|  |  |

| Specimen-#5 | |
|-------------------------------------------------------------------------------------|--------------------------------------------------------------------------------------|
| 2D at 0.400 | 2D at 1.500 |
|  |  |
| Specimen-#6 | |
| 2D at 0.400 | 2D at 1.500 |
|  |  |

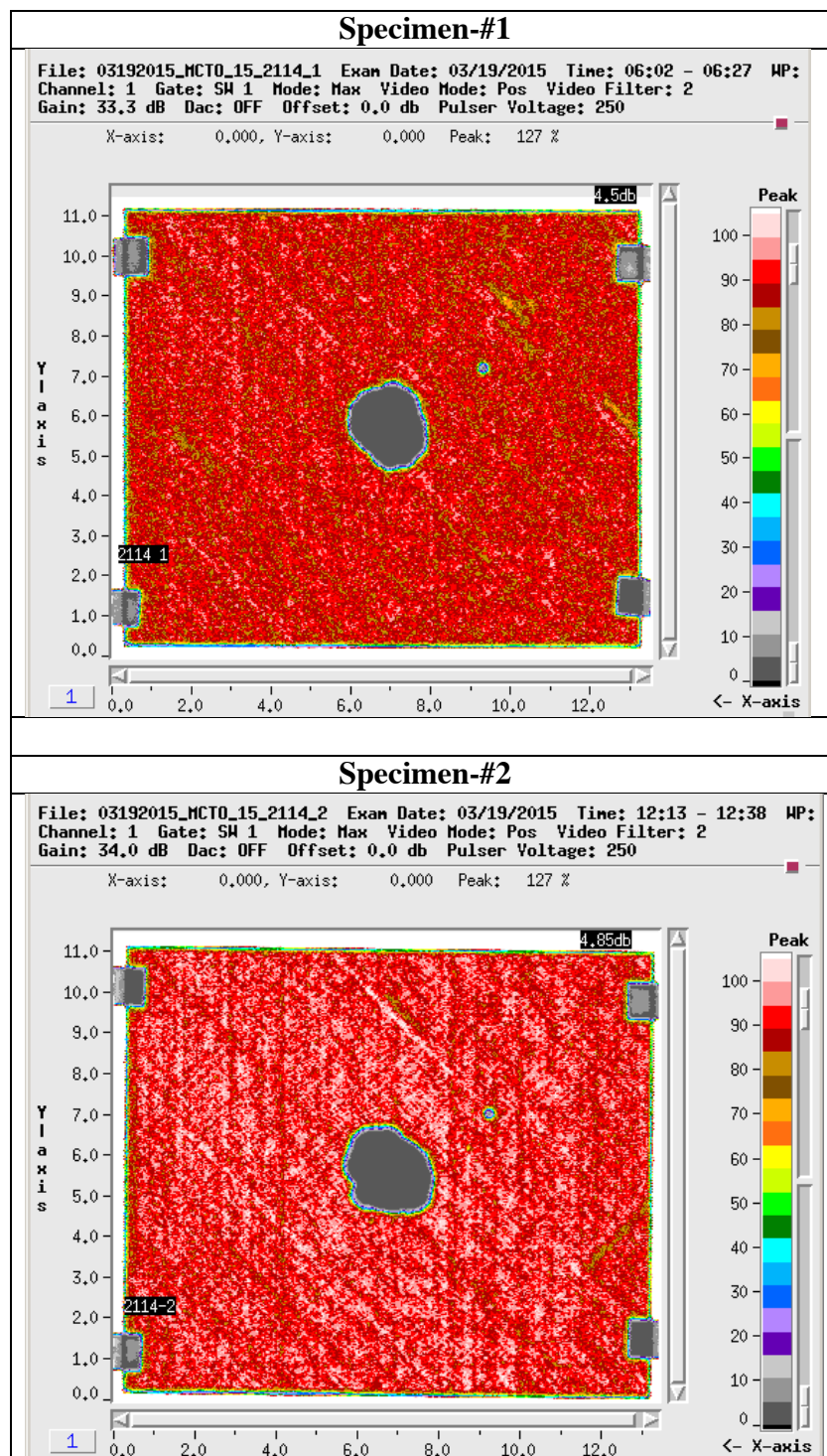
Appendix C: Flash Thermography of Back Surface

| Specimen-#1 | |
|-------------------------------------------------------------------------------------|--------------------------------------------------------------------------------------|
| 2D at 0.400 | 2D at 1.500 |
|  |  |
| Specimen-#2 | |
| 2D at 0.400 | 2D at 1.500 |
|  |  |

| Specimen-#3 | |
|-------------------------------------------------------------------------------------|--------------------------------------------------------------------------------------|
| 2D at 0.400 | 2D at 1.500 |
|  |  |
| Specimen-#4 | |
| 2D at 0.400 | 2D at 1.500 |
|  |  |

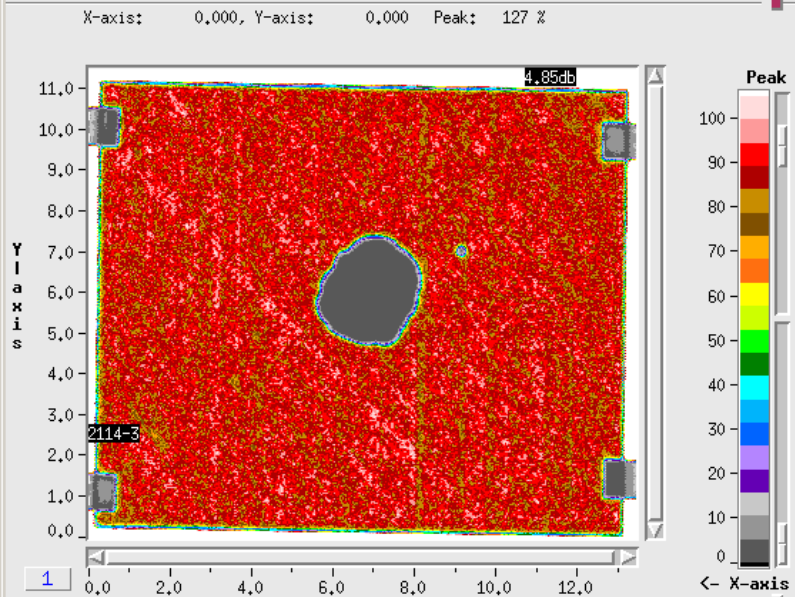
| Specimen-#5 | |
|-------------------------------------------------------------------------------------|--------------------------------------------------------------------------------------|
| 2D at 0.400 | 2D at 1.500 |
|  |  |
| Specimen-#6 | |
| 2D at 0.400 | 2D at 1.500 |
|  |  |

Appendix D: Immersion Ultrasound – Amplitude Data



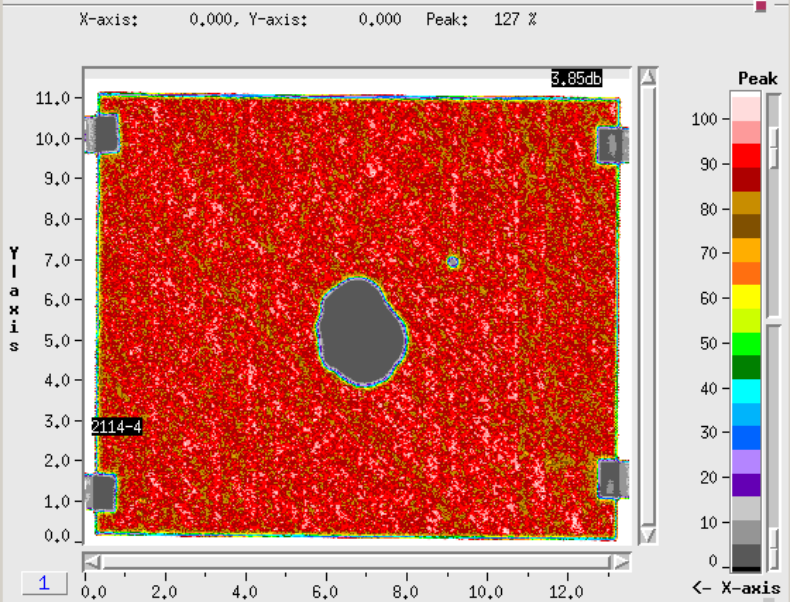
Specimen-#3

File: 03192015_MCT0_15_2114_3 Exam Date: 03/19/2015 Time: 11:15 - 11:40 WP:
Channel: 1 Gate: SW 1 Mode: Max Video Mode: Pos Video Filter: 2
Gain: 34.0 dB Dac: OFF Offset: 0.0 db Pulser Voltage: 250



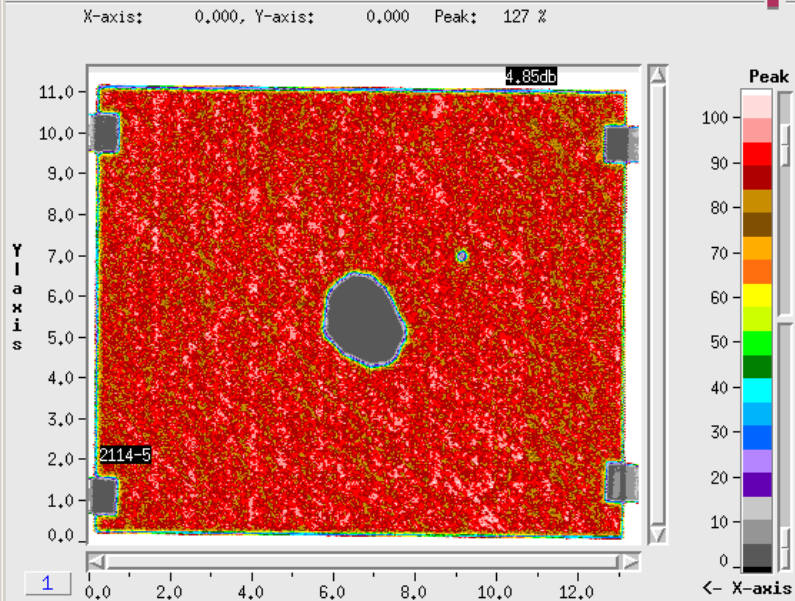
Specimen-#4

File: 03192015_MCT0_15_2114_4 Exam Date: 03/19/2015 Time: 10:19 - 10:43 WP:
Channel: 1 Gate: SW 1 Mode: Max Video Mode: Pos Video Filter: 2
Gain: 34.0 dB Dac: OFF Offset: 0.0 db Pulser Voltage: 250



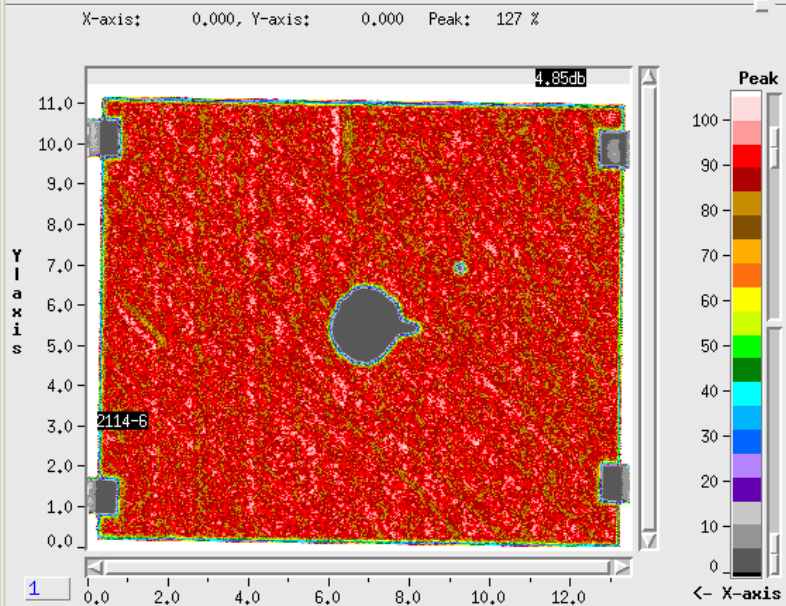
Specimen-#5

File: 03192015_MCT0_15_2114_5 Exam Date: 03/19/2015 Time: 09:45 - 10:10 WP:
Channel: 1 Gate: SW 1 Mode: Max Video Mode: Pos Video Filter: 2
Gain: 34.0 dB Dac: OFF Offset: 0.0 db Pulser Voltage: 250

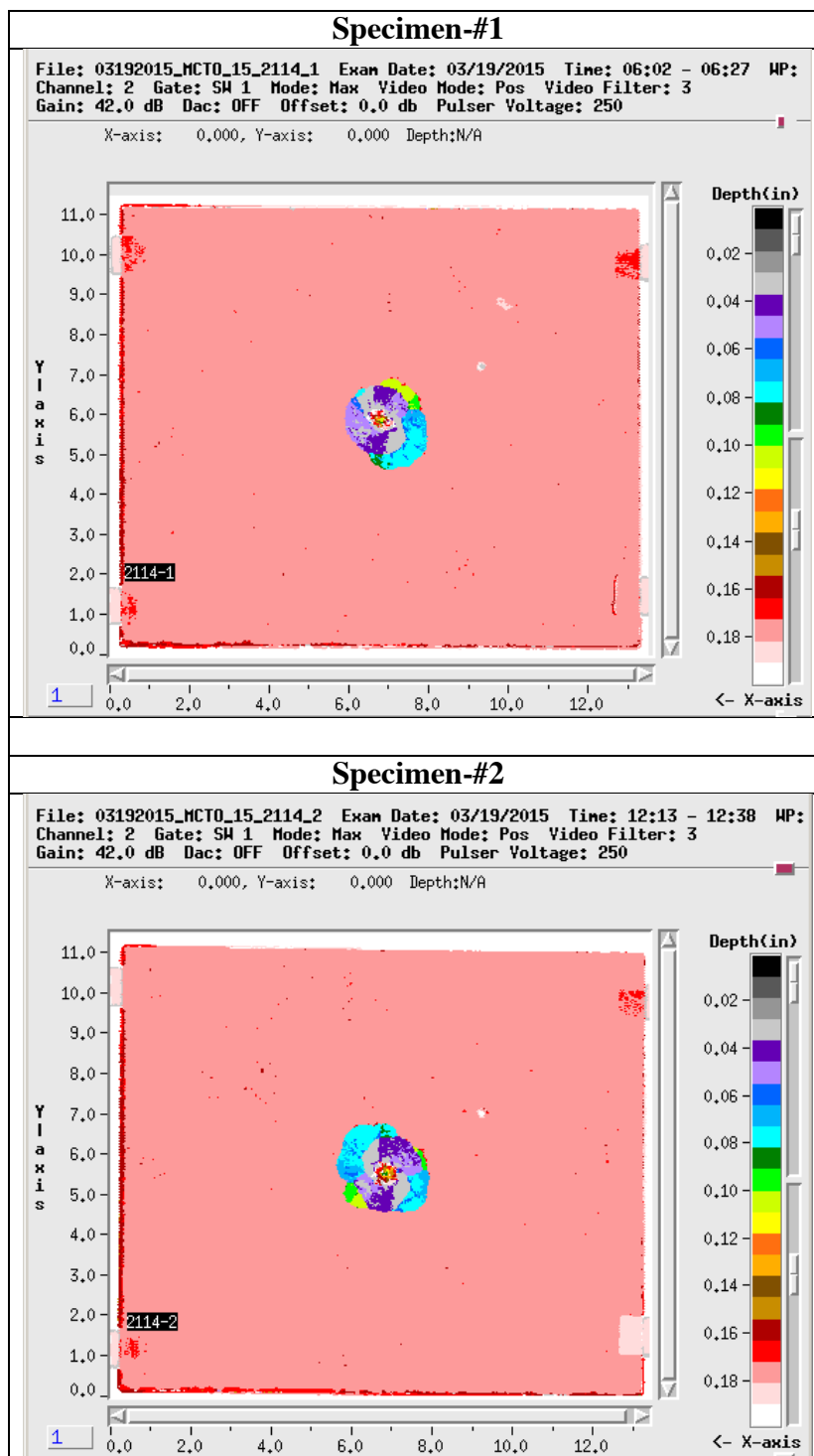


Specimen-#6

File: 03192015_MCT0_15_2114_6 Exam Date: 03/19/2015 Time: 08:42 - 09:07 WP:
Channel: 1 Gate: SW 1 Mode: Max Video Mode: Pos Video Filter: 2
Gain: 34.0 dB Dac: OFF Offset: 0.0 db Pulser Voltage: 250



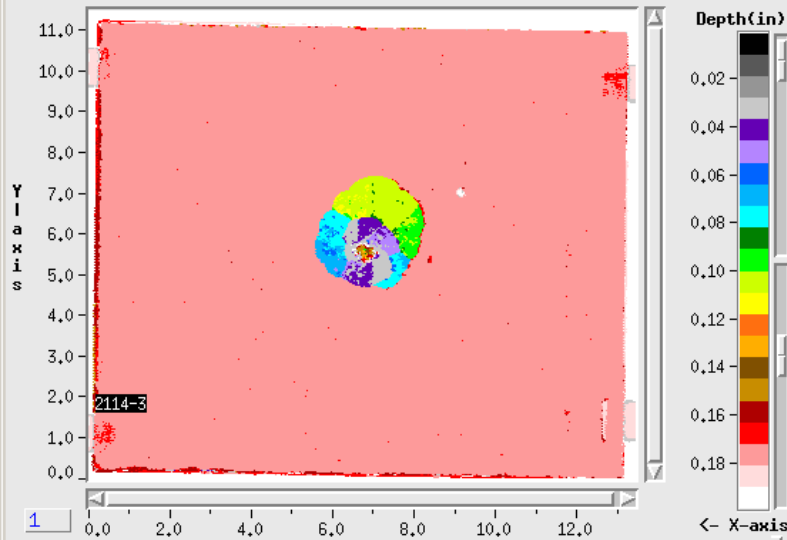
Appendix E: Immersion Ultrasound – Time of Flight Data



Specimen-#3

File: 03192015_MCT0_15_2114_3 Exam Date: 03/19/2015 Time: 11:15 - 11:40 WP:
Channel: 2 Gate: SM 1 Mode: Max Video Mode: Pos Video Filter: 3
Gain: 42.0 dB Dac: OFF Offset: 0.0 db Pulser Voltage: 250

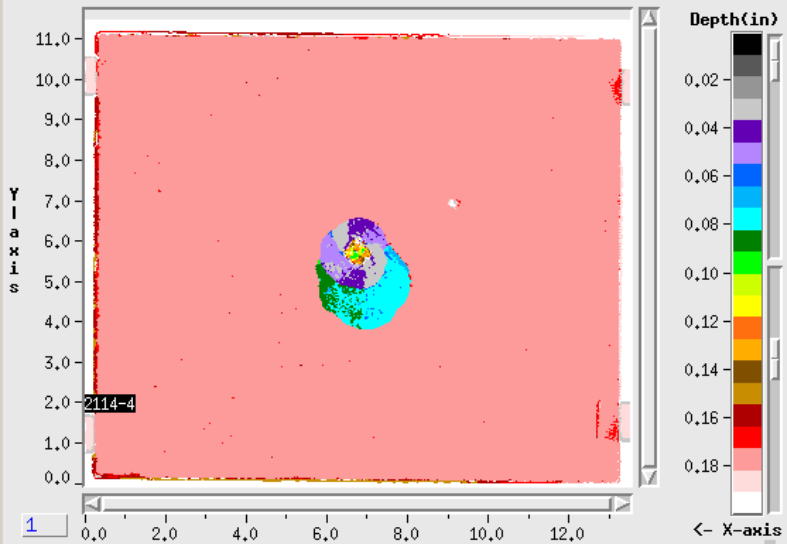
X-axis: 0.000, Y-axis: 0.000 Depth:N/A



Specimen-#4

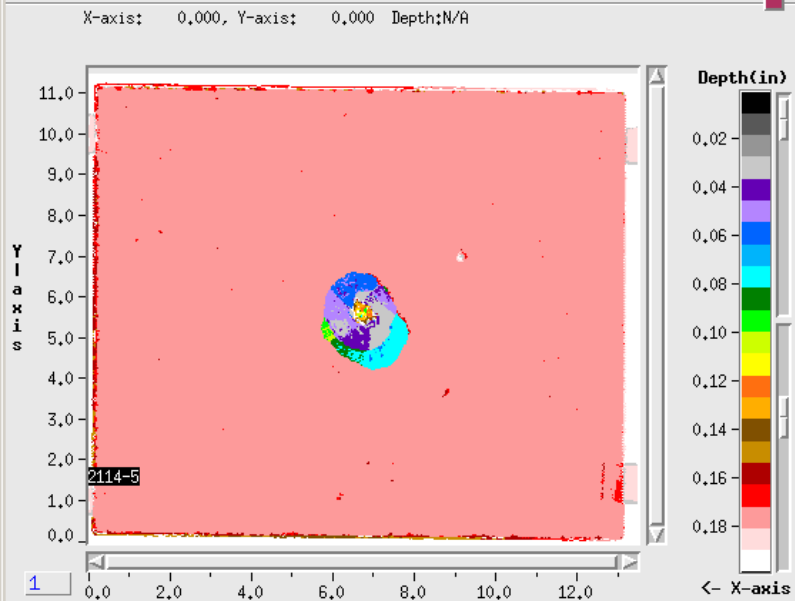
File: 03192015_MCT0_15_2114_4 Exam Date: 03/19/2015 Time: 10:19 - 10:43 WP:
Channel: 2 Gate: SM 1 Mode: Max Video Mode: Pos Video Filter: 3
Gain: 42.0 dB Dac: OFF Offset: 0.0 db Pulser Voltage: 250

X-axis: 0.000, Y-axis: 0.000 Depth:N/A



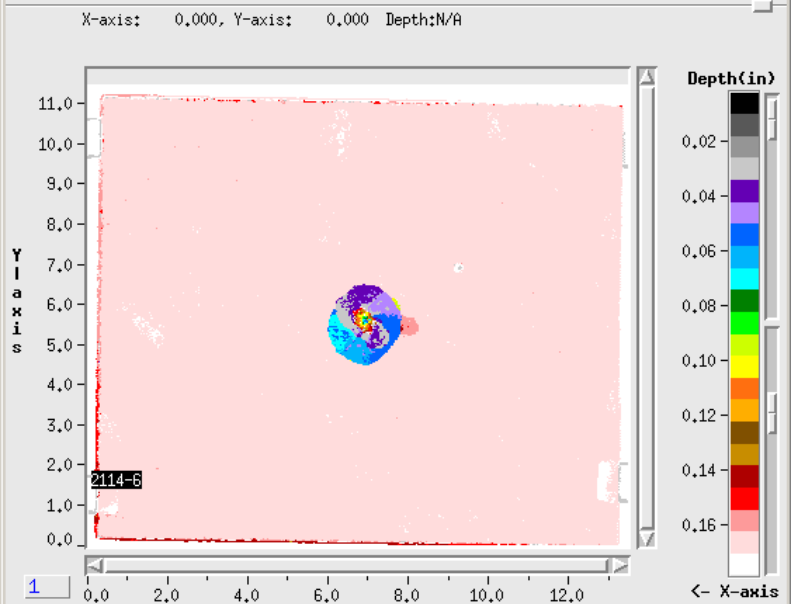
MCTO-15-2114-#5

File: 03192015_MCTO_15_2114_5 Exam Date: 03/19/2015 Time: 09:45 - 10:10 WP:
Channel: 2 Gate: SW 1 Mode: Max Video Mode: Pos Video Filter: 3
Gain: 42.0 dB Dac: OFF Offset: 0.0 db Pulser Voltage: 250

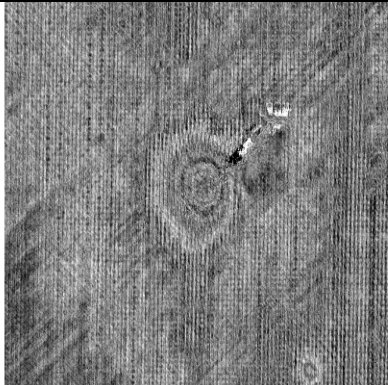

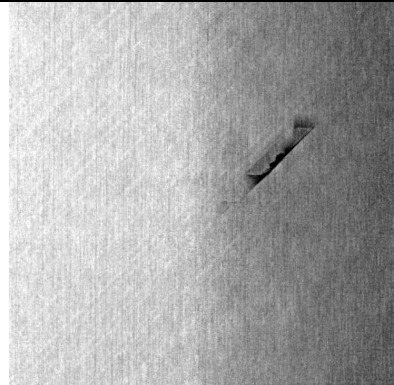
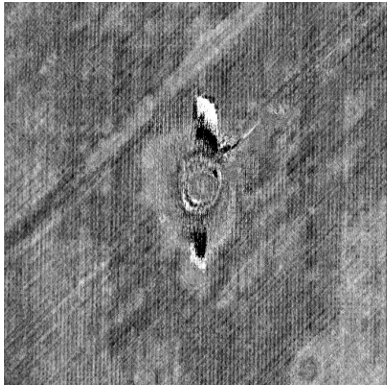
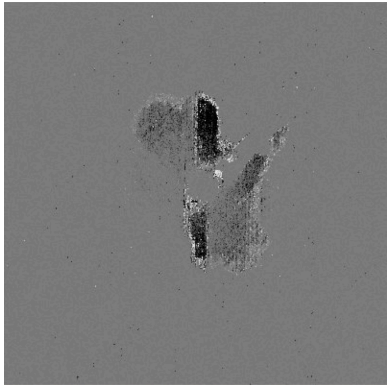
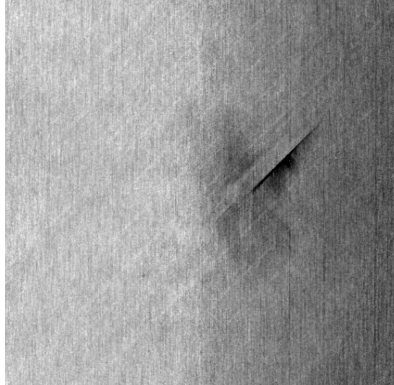
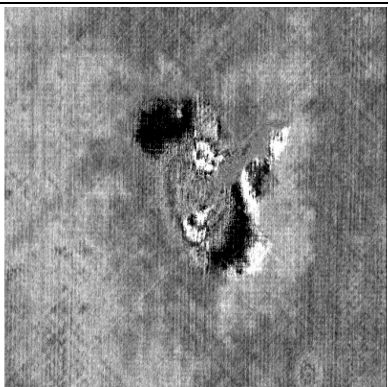
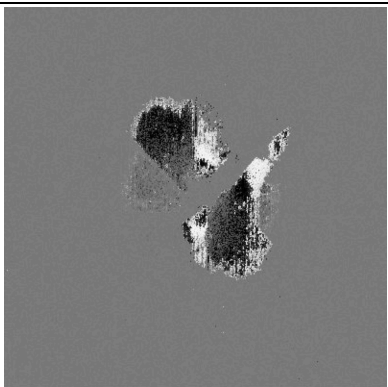
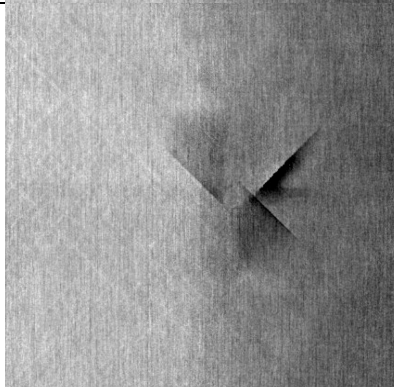

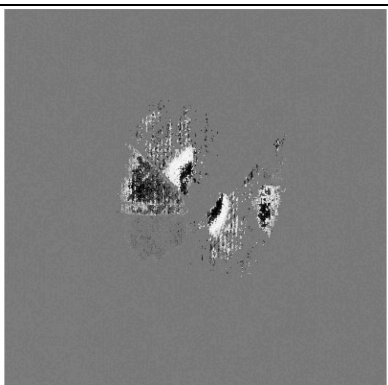
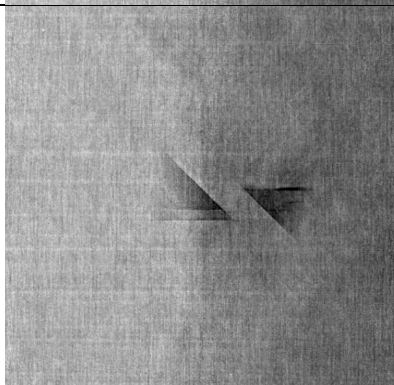


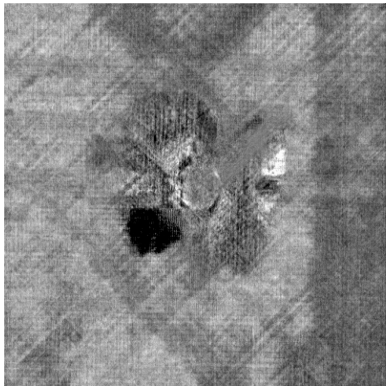
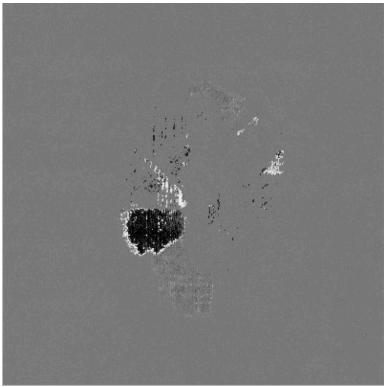
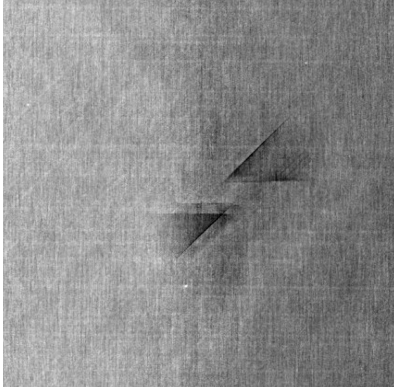
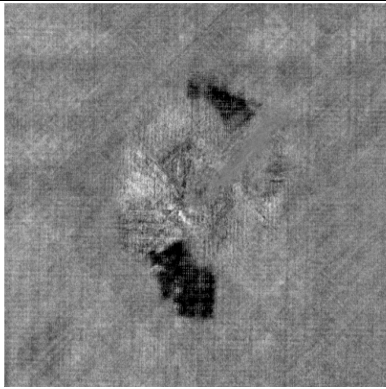
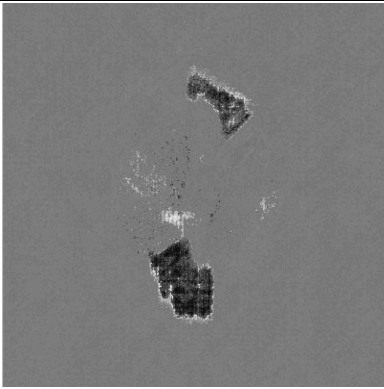
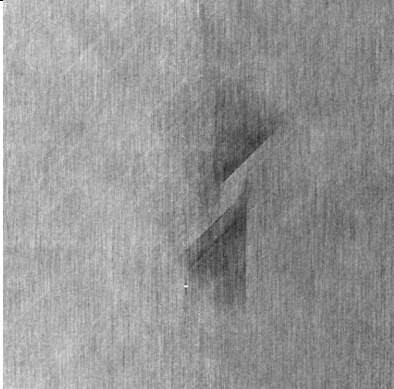
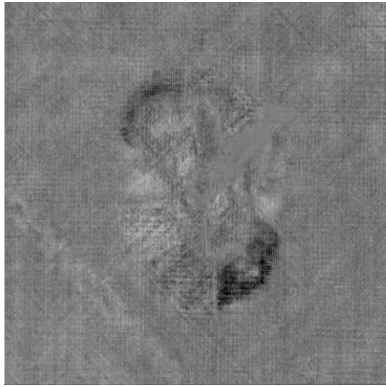
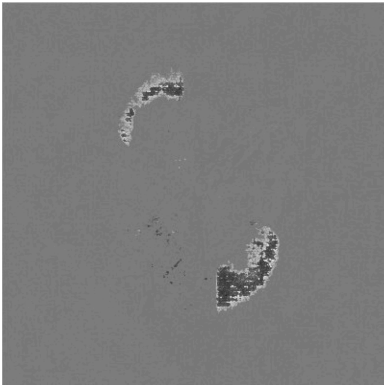
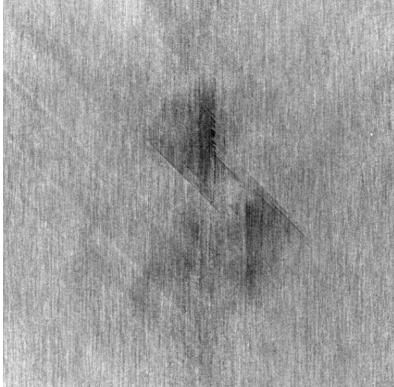
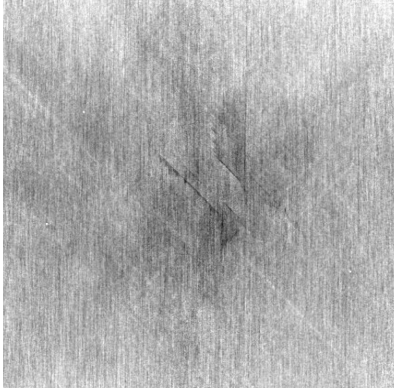
MCTO-15-2114-#6

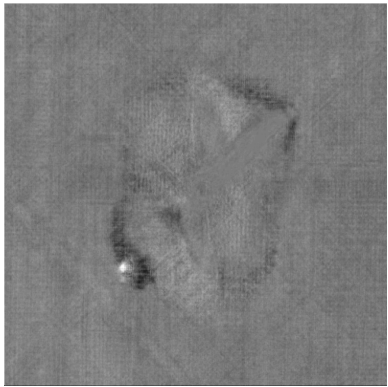
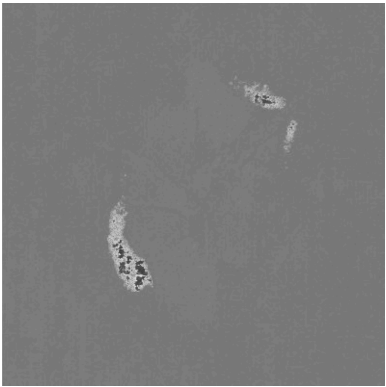

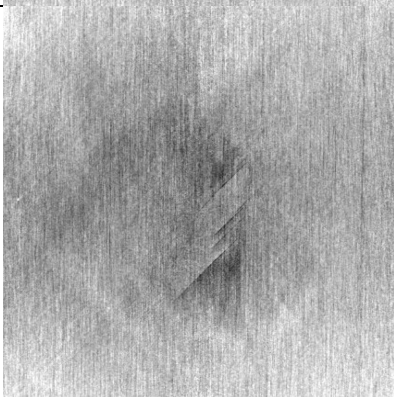
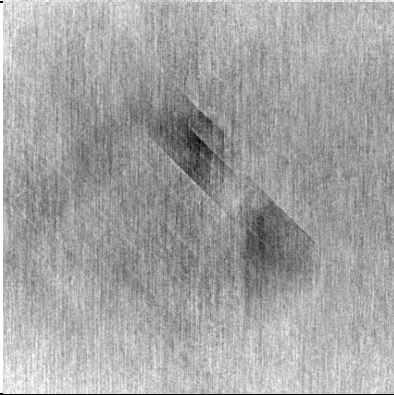
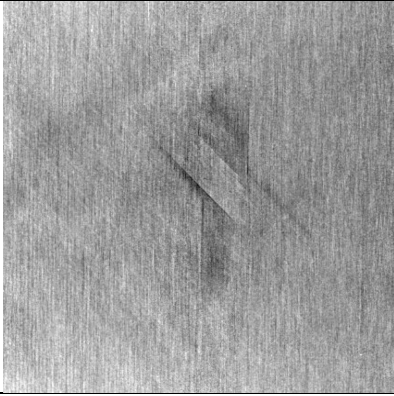
File: 03192015_MCTO_15_2114_6 Exam Date: 03/19/2015 Time: 08:42 - 09:07 WP:
Channel: 2 Gate: SW 1 Mode: Max Video Mode: Pos Video Filter: 3
Gain: 42.0 dB Dac: OFF Offset: 0.0 db Pulser Voltage: 250

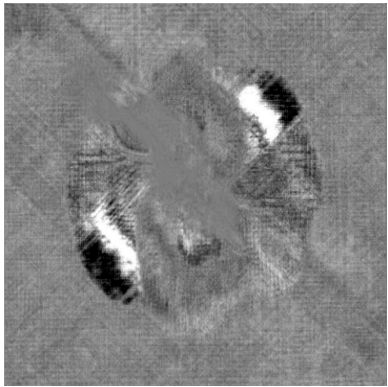
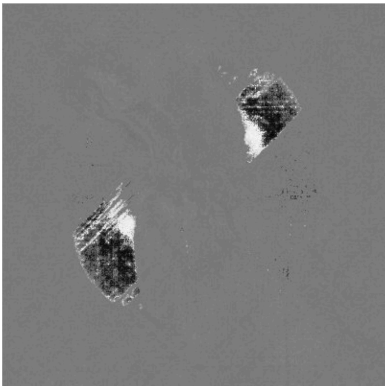
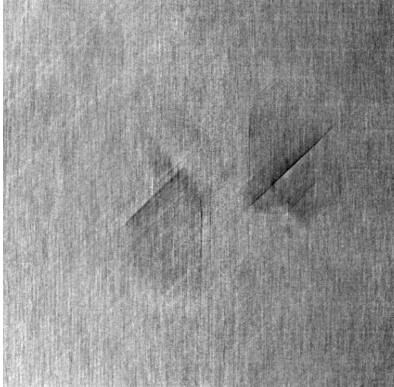
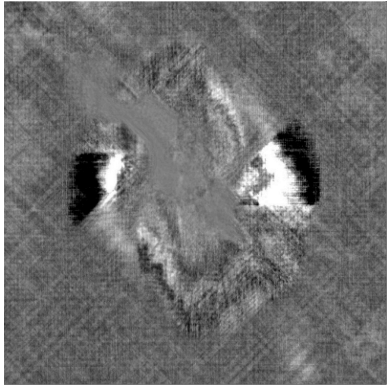
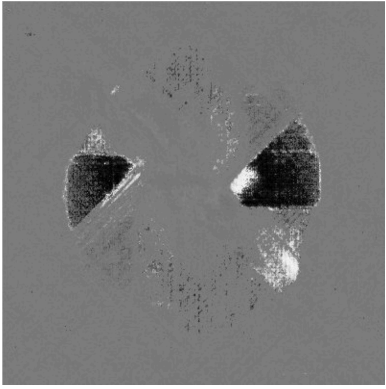
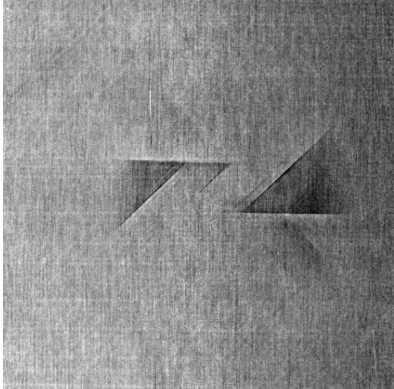

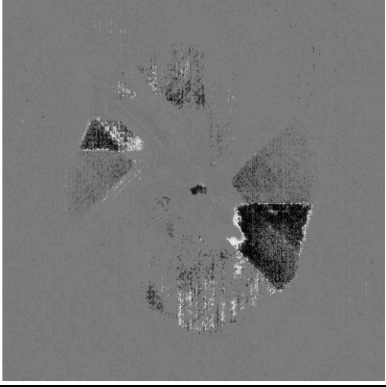
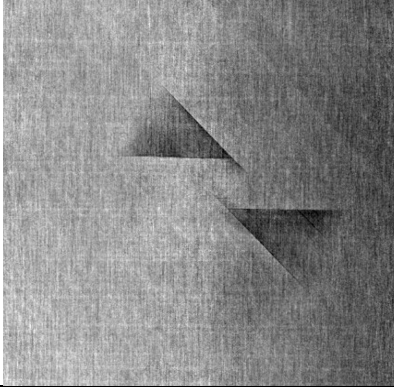
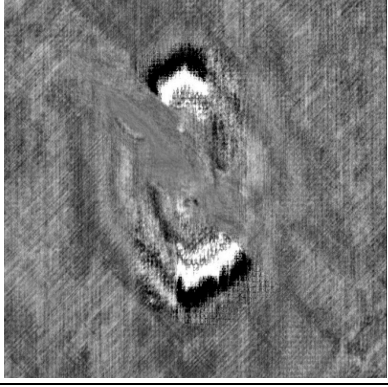
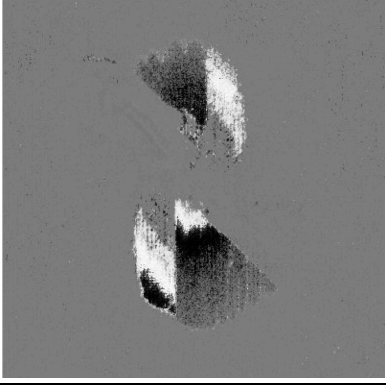
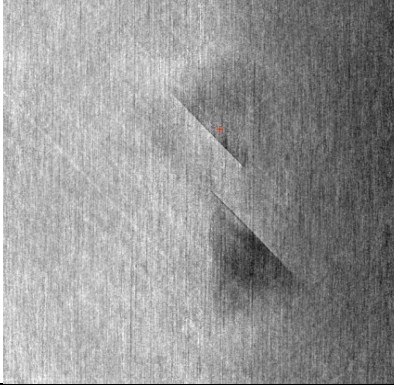


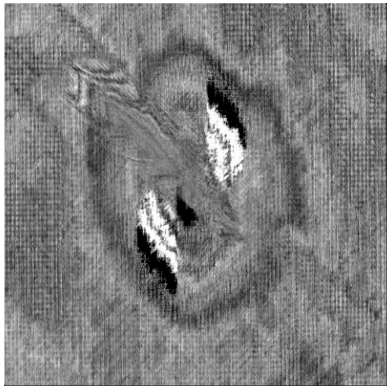
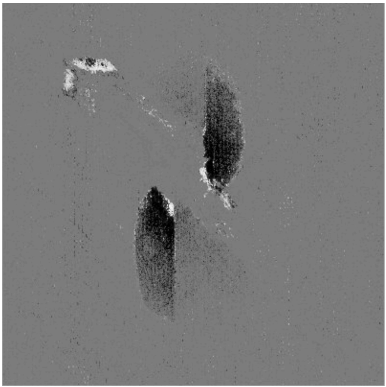

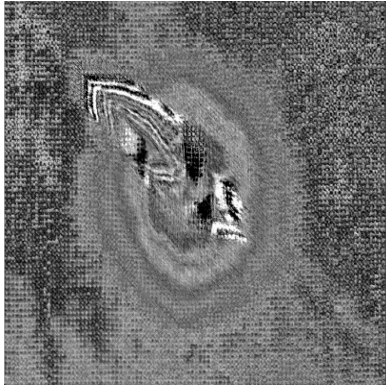
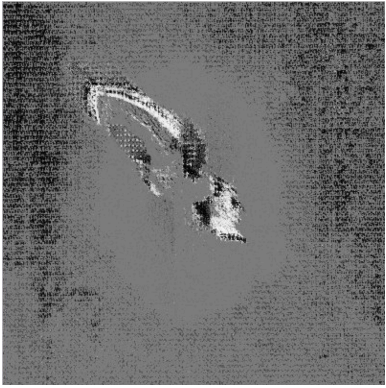
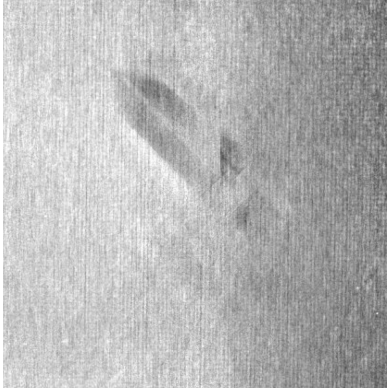
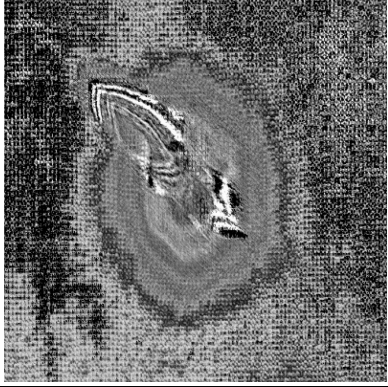
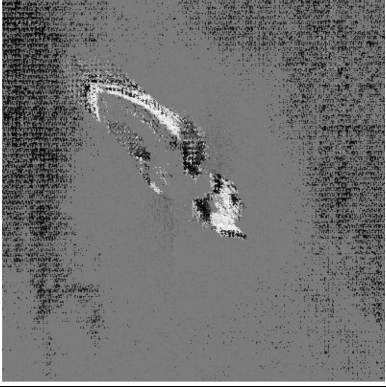
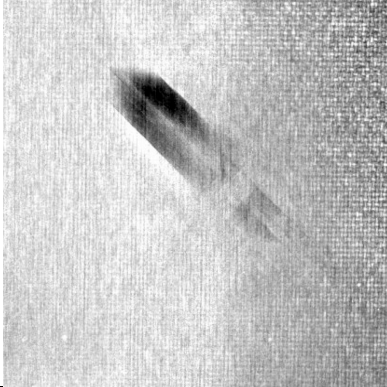
Appendix F: Image Segmentation C-Scan/X-Ray CT Analysis of Panel A

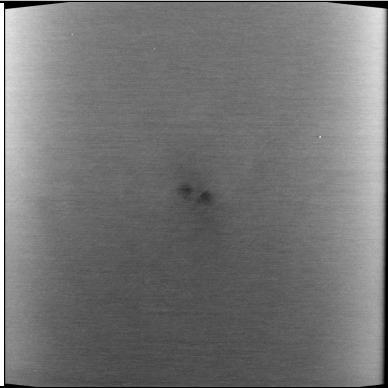
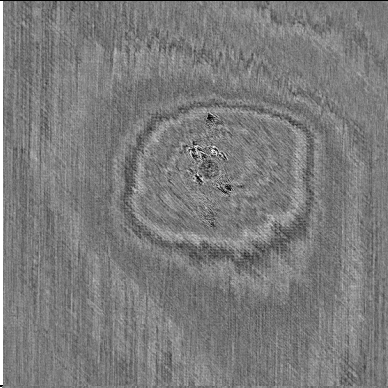

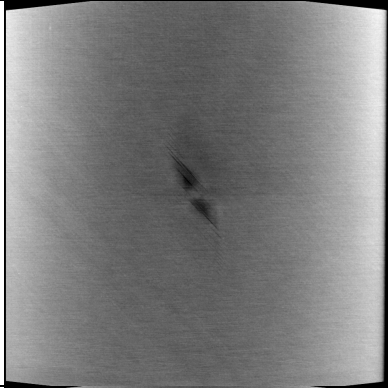
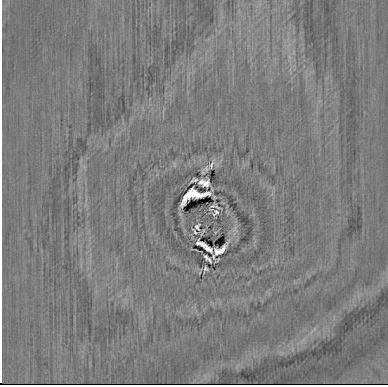
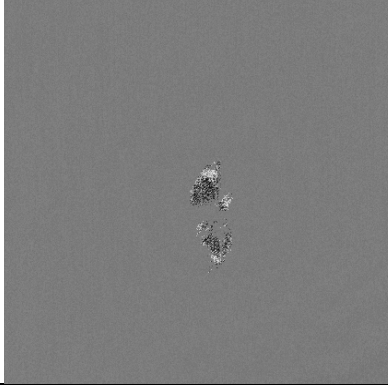
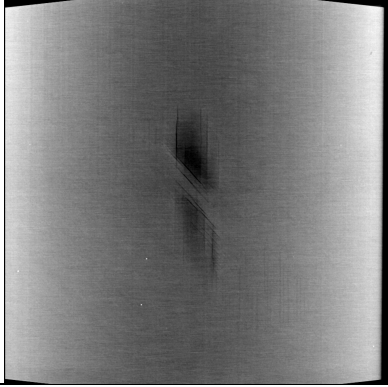
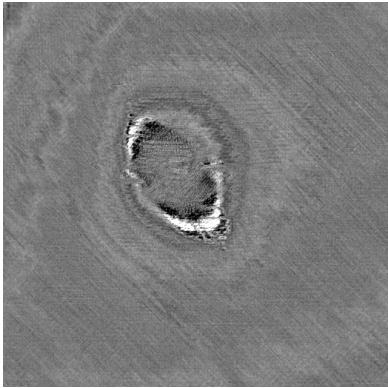
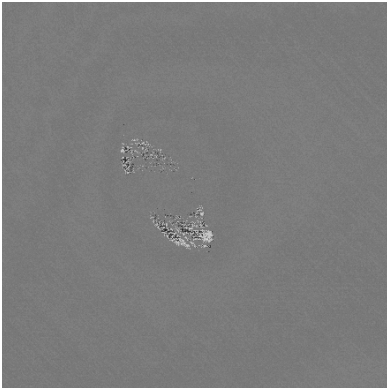
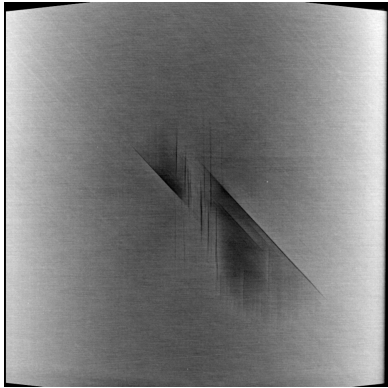
| Panel A - [-45/90/45/90/-45/0/45/90/90/-45/90/45] _s | | | |
|----------------------------------------------------------------|-------------------------------------------------------------------------------------|--------------------------------------------------------------------------------------|---------------------------------------------------------------------------------------|
| | C-Scan | Filtered C-Scan | X-Ray CT |
| 90/45 |  |  |  |
| 90/45 |  |  |  |
| 45/90 |  |  |  |
| 90/-45 |  |  |  |

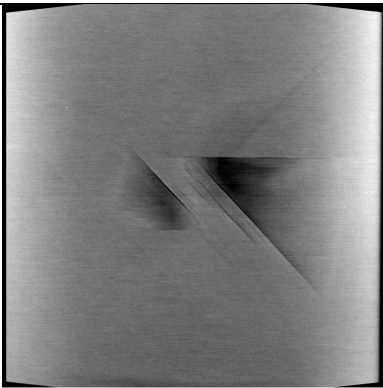
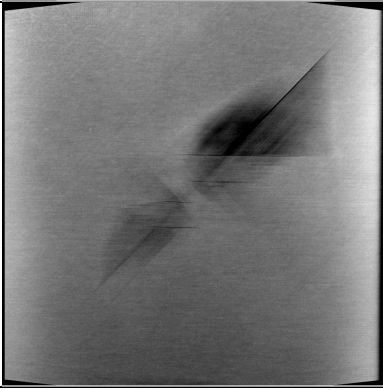
| Panel A - [-45/90/45/90/-45/0/45/90/90/-45/90/45] _s | | | |
|----------------------------------------------------------------|------------------------------------------------------------------------------------|-------------------------------------------------------------------------------------|---------------------------------------------------------------------------------------|
| | C-Scan | Filtered C-Scan | X-Ray CT |
| -45/0 |  |  |  |
| -45/90 |  |  |  |
| 90/-45 |  |  |  |
| -45/90 | | |  |

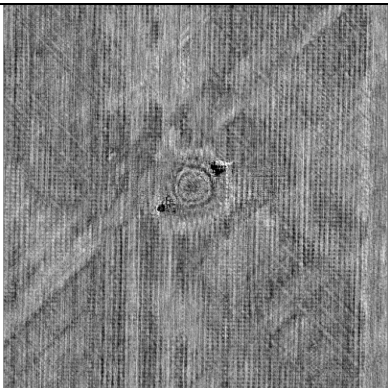
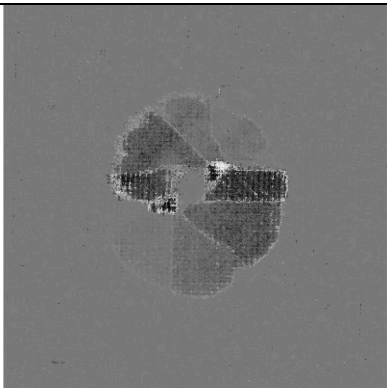
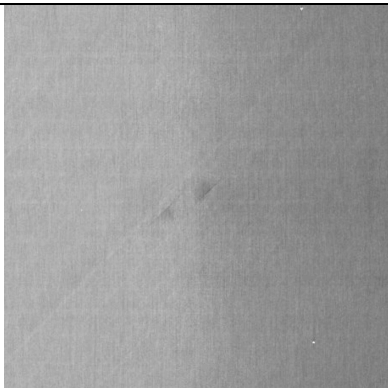
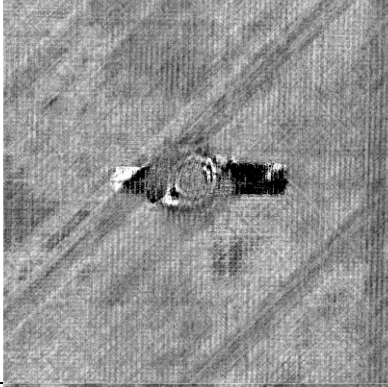
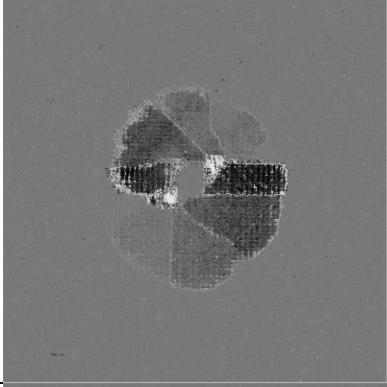
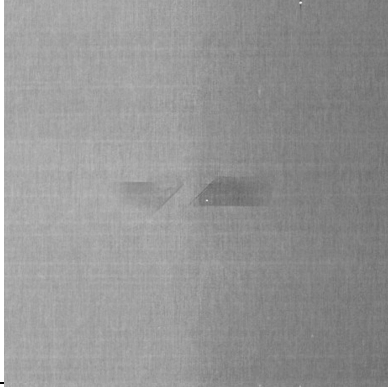

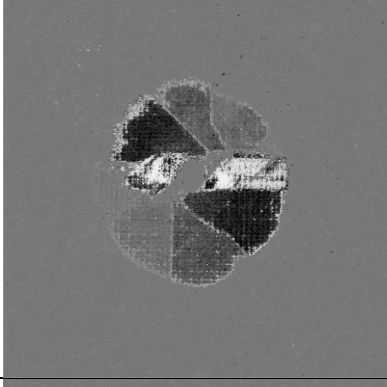
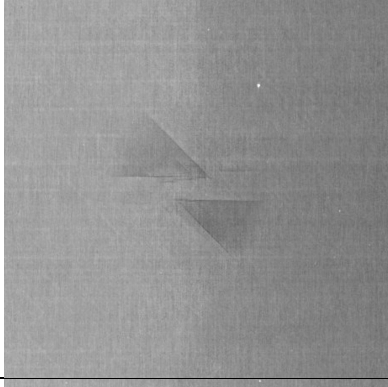

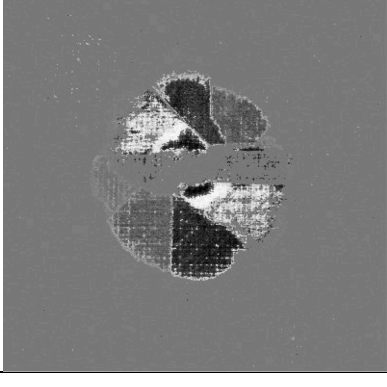
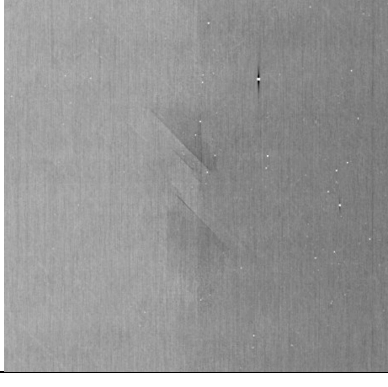
| Panel A - [-45/90/45/90/-45/0/45/90/90/-45/90/45] _s | | | |
|----------------------------------------------------------------|-----------------------------------------------------------------------------------|------------------------------------------------------------------------------------|---------------------------------------------------------------------------------------|
| | C-Scan | Filtered C-Scan | X-Ray CT |
| 90/45 |  |  |  |
| 90/45 | | |  |
| -45/90 | | |  |
| 90/-45 | | |  |

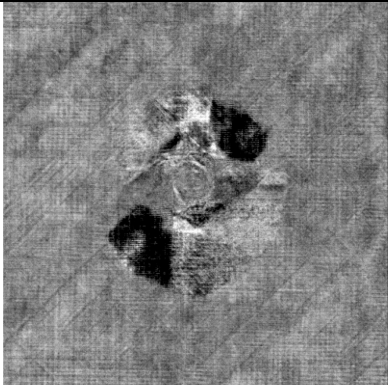
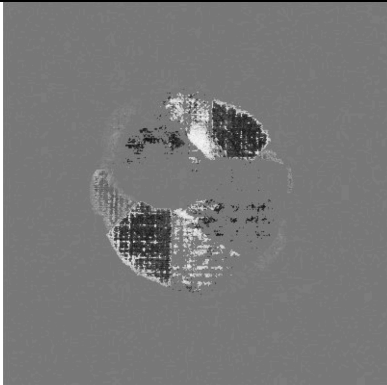
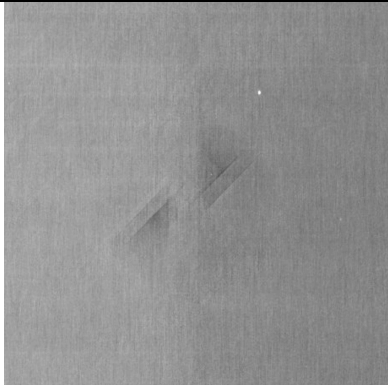
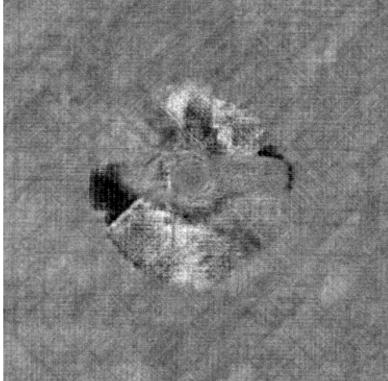
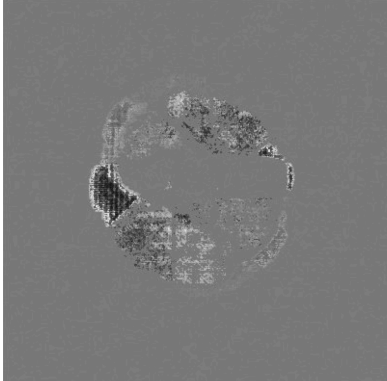
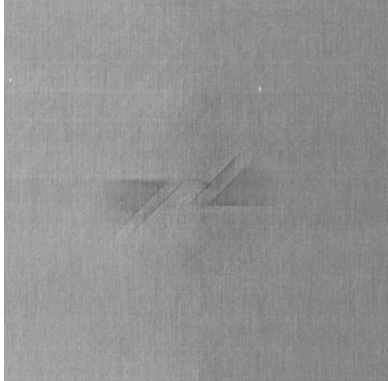
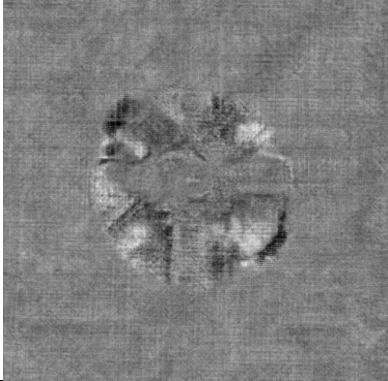
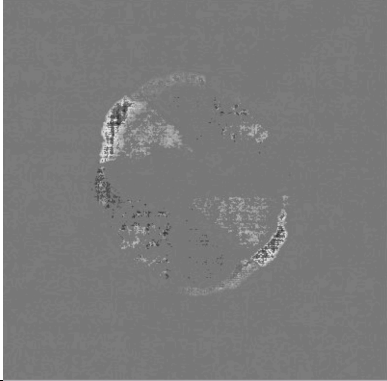
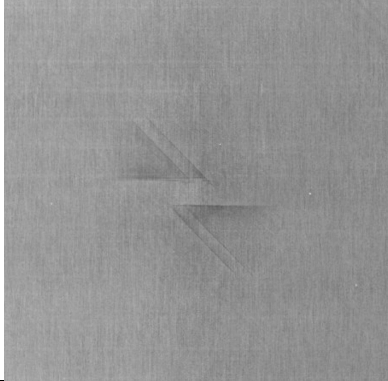
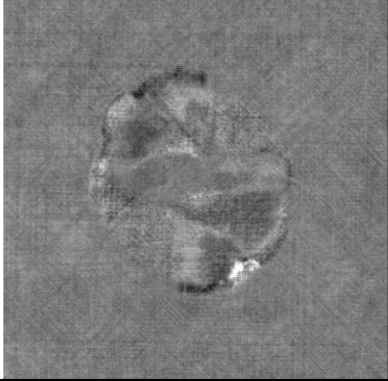

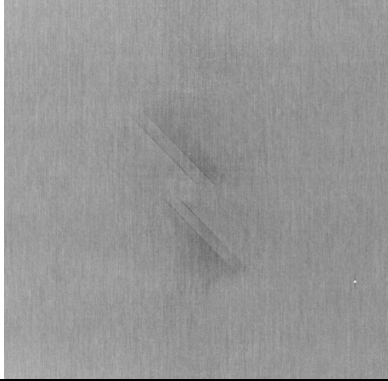
| Panel A - [-45/90/45/90/-45/0/45/90/90/-45/90/45] _s | | | |
|----------------------------------------------------------------|-------------------------------------------------------------------------------------|--------------------------------------------------------------------------------------|---------------------------------------------------------------------------------------|
| | C-Scan | Filtered C-Scan | X-Ray CT |
| 45/90 |  |  |  |
| 0/45 |  |  |  |
| -45/0 |  |  |  |
| 90/-45 |  |  |  |

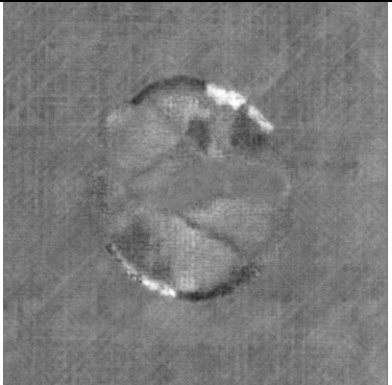
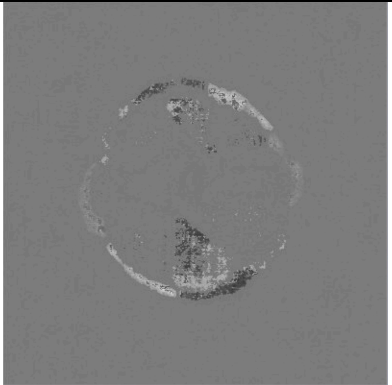
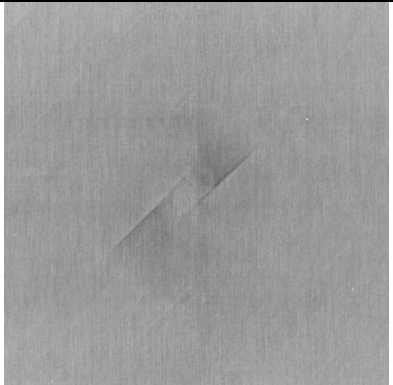
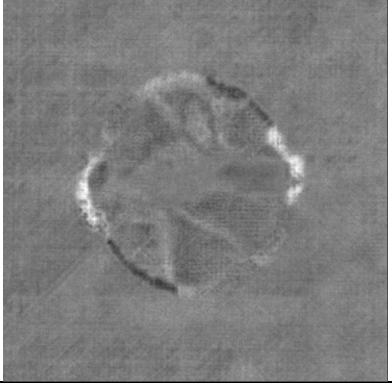
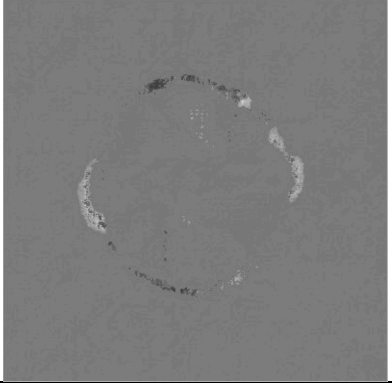
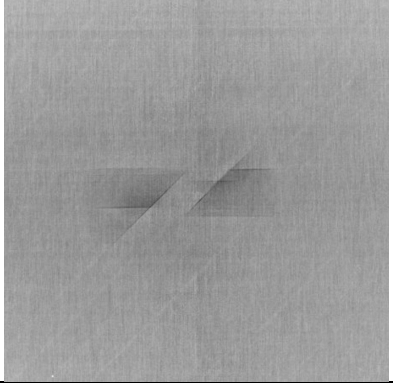
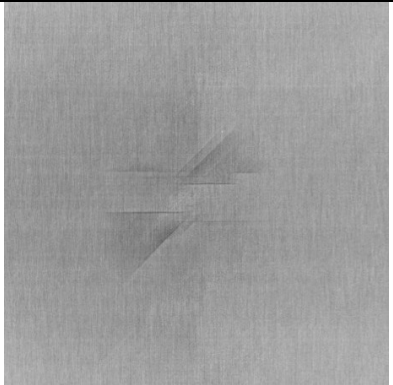
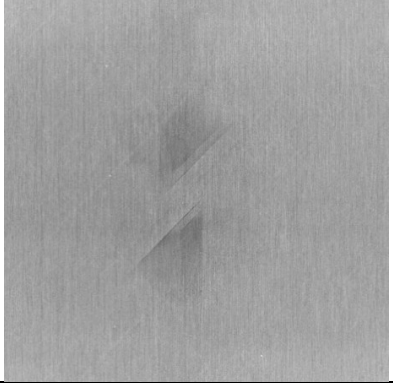
| Panel A - [-45/90/45/90/-45/0/45/90/90/-45/90/45] _s | | | |
|----------------------------------------------------------------|------------------------------------------------------------------------------------|-------------------------------------------------------------------------------------|--------------------------------------------------------------------------------------|
| | C-Scan | Filtered C-Scan | X-Ray CT |
| 45/90 |  |  |  |
| 90/45 |  |  |  |
| -45/90 |  |  |  |

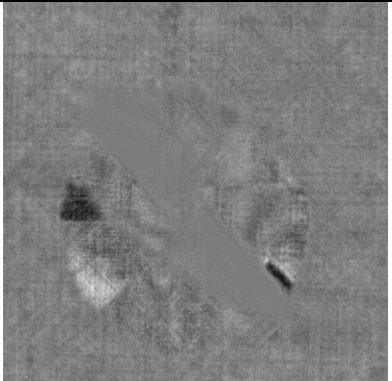
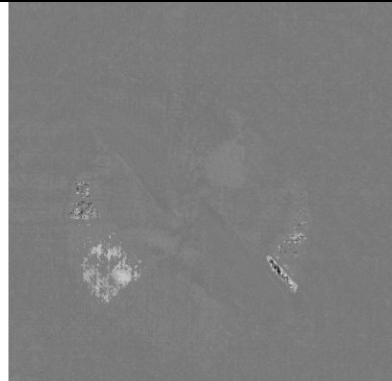
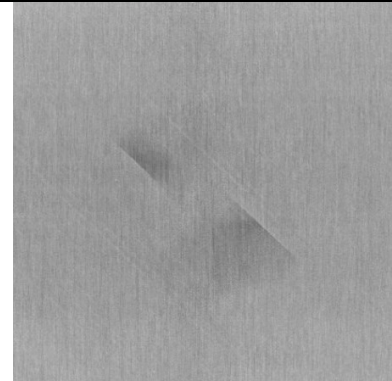
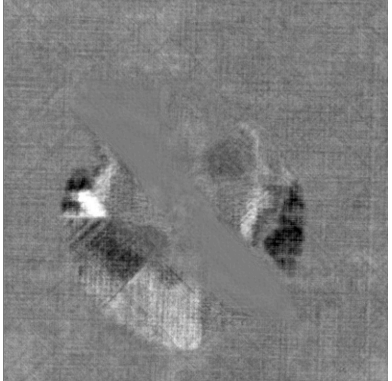
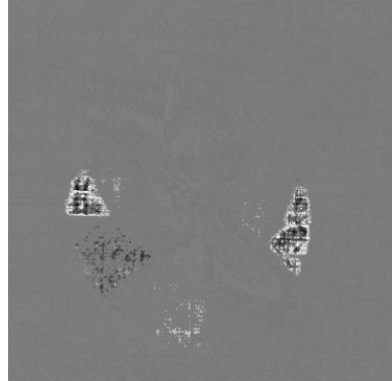
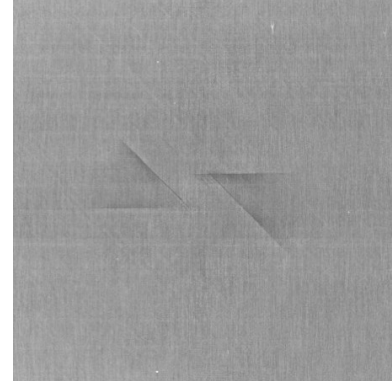

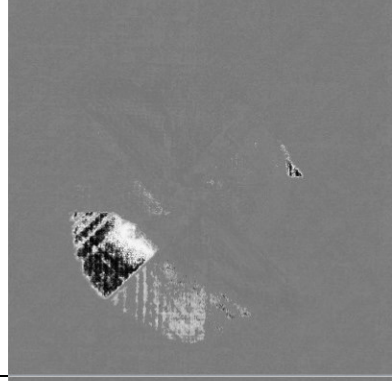
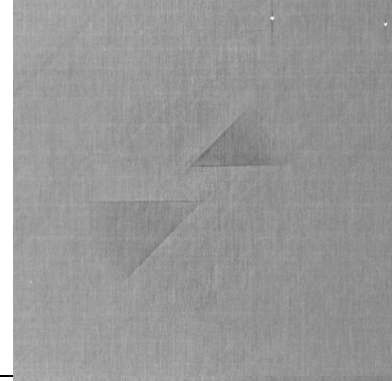
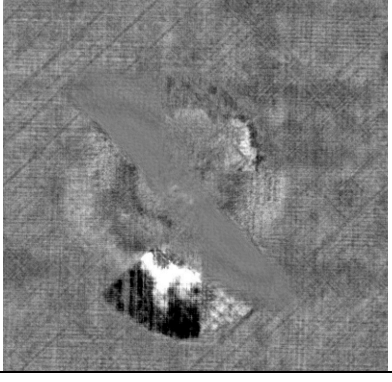
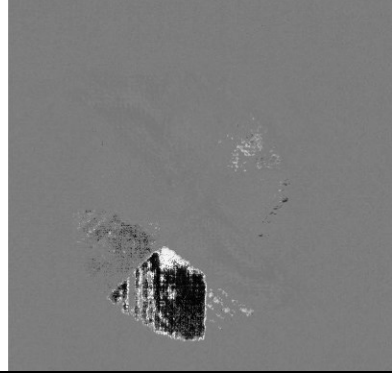
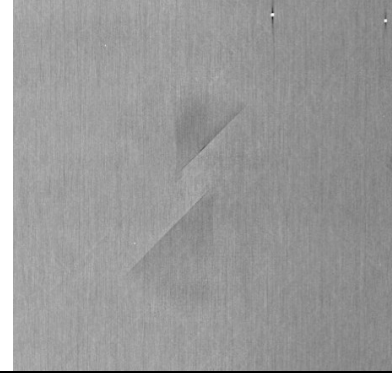
| Panel C - [-45 ₃ /90 ₃ /45 ₃ /0 ₃] _s | | | |
|----------------------------------------------------------------------------------------------|-------------------------------------------------------------------------------------|--------------------------------------------------------------------------------------|---------------------------------------------------------------------------------------|
| | C-Scan | Filtered C-Scan | X-Ray CT |
| -45/90 | | |  |
| 90/45 |  |  |  |
| 45/0 |  |  |  |
| 0/0 | | | |
| 0/45 |  |  |  |

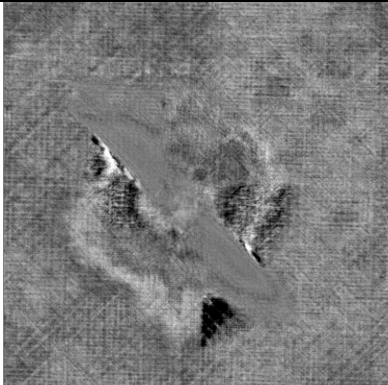
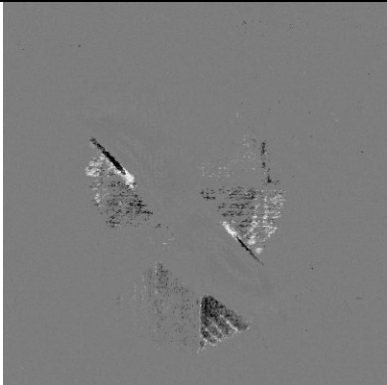
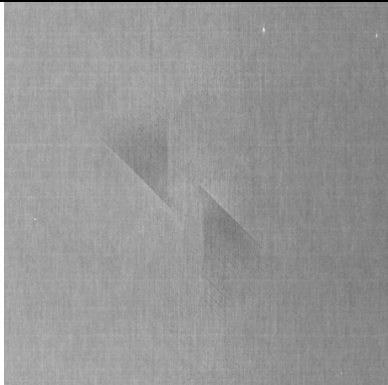
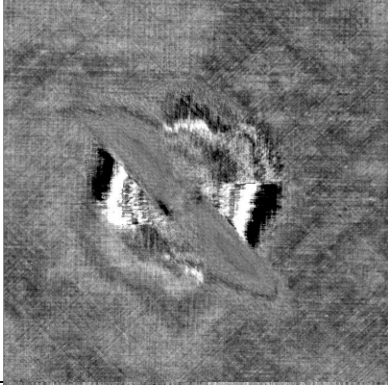
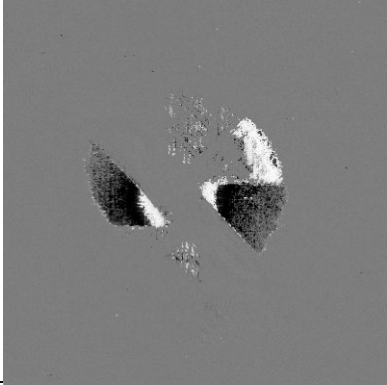
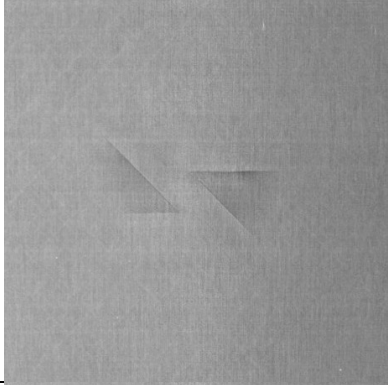
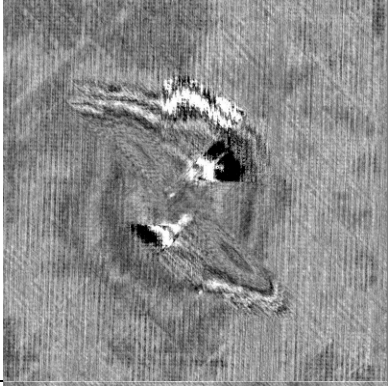
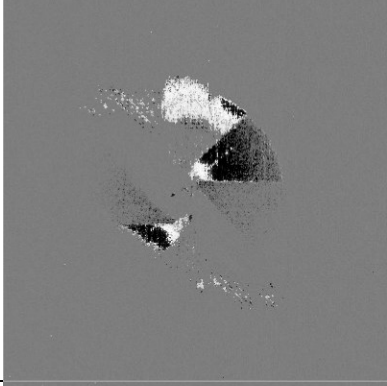
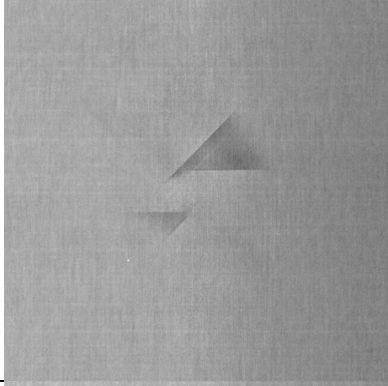
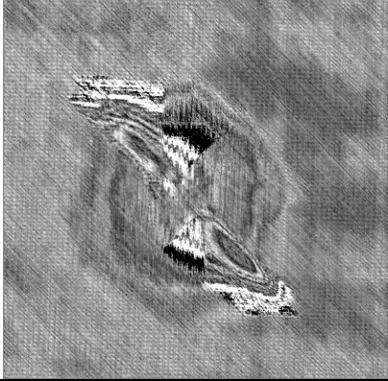
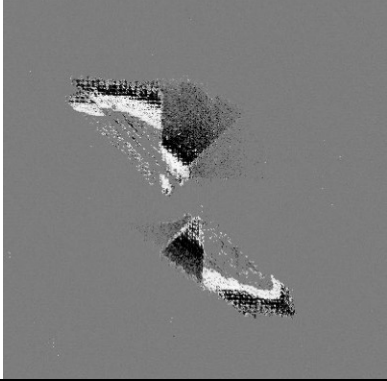
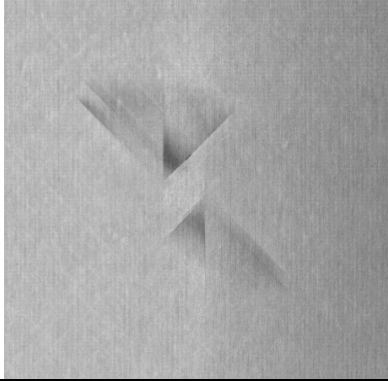
| | | | |
|--------|--|--|-------------------------------------------------------------------------------------|
| 45/90 | | |  |
| 90/-45 | | |  |

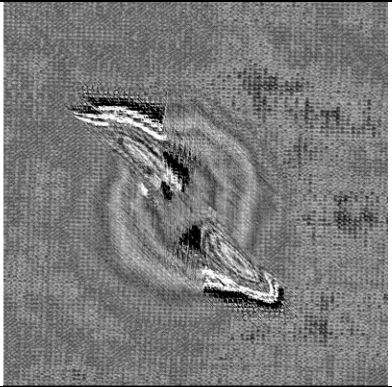
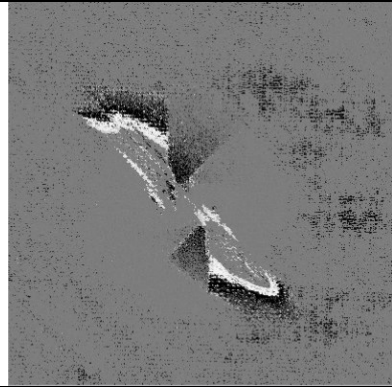
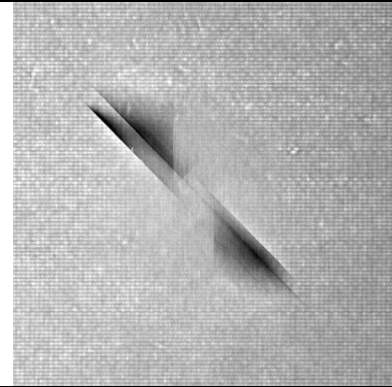
| Panel D – [-45/90/45/0] _{3s} | | | |
|---------------------------------------|-------------------------------------------------------------------------------------|--------------------------------------------------------------------------------------|---------------------------------------------------------------------------------------|
| | C-Scan | Filtered C-Scan | X-Ray CT |
| -45/90 | | | |
| 90/45 |  |  |  |
| 45/0 |  |  |  |
| 0/-45 |  |  |  |
| -45/90 |  |  |  |

| Panel D – [-45/90/45/0] _{3s} | | | |
|---------------------------------------|-------------------------------------------------------------------------------------|--------------------------------------------------------------------------------------|---------------------------------------------------------------------------------------|
| | C-Scan | Filtered C-Scan | X-Ray CT |
| 90/45 |  |  |  |
| 45/0 |  |  |  |
| 0/-45 |  |  |  |
| -45/90 |  |  |  |

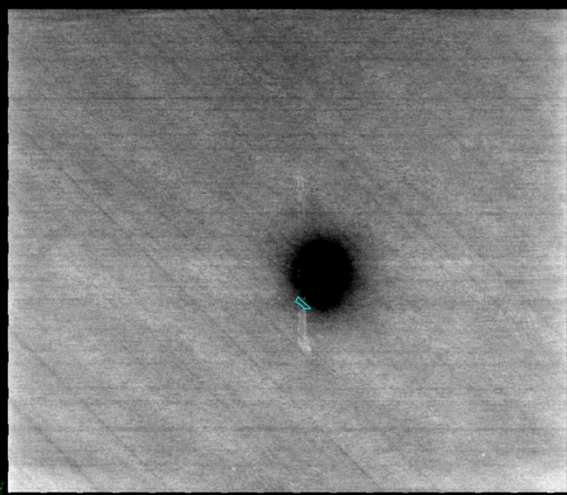
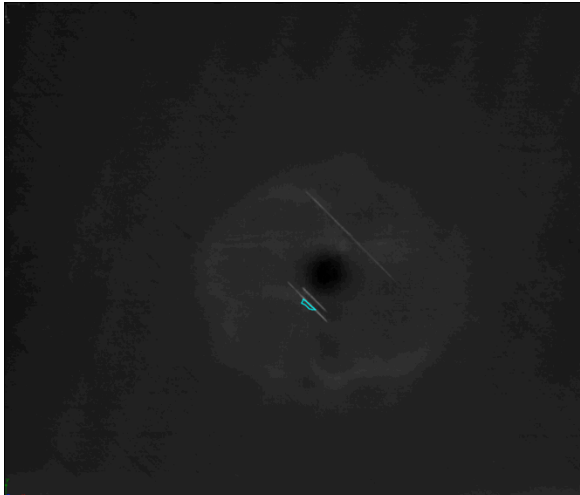
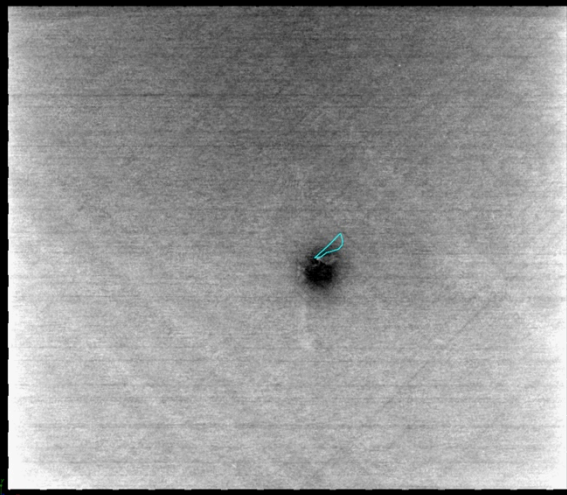
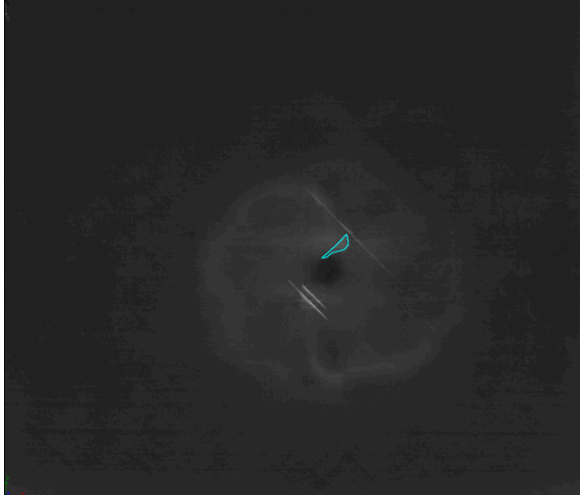
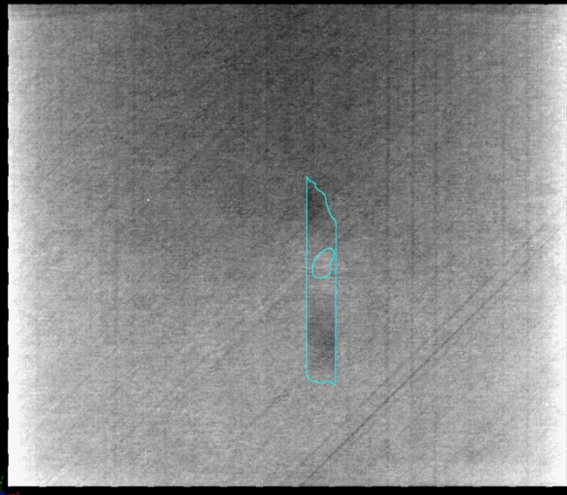
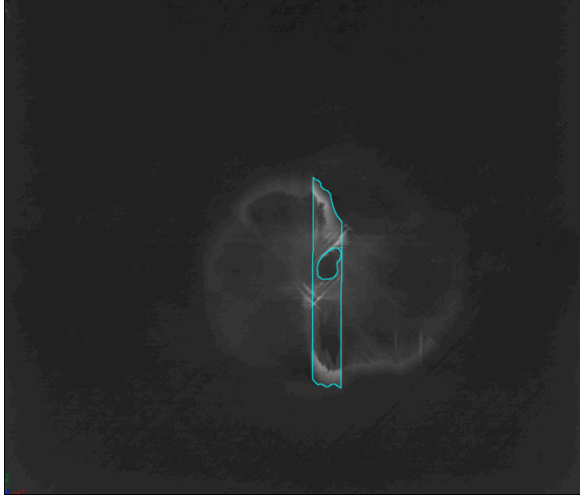
| Panel D – [-45/90/45/0] _{3s} | | | |
|---------------------------------------|-----------------------------------------------------------------------------------|------------------------------------------------------------------------------------|---------------------------------------------------------------------------------------|
| | C-Scan | Filtered C-Scan | X-Ray CT |
| 90/45 |  |  |  |
| 45/0 |  |  |  |
| 0/0 | | | |
| 0/45 | | |  |
| 45/90 | | |  |

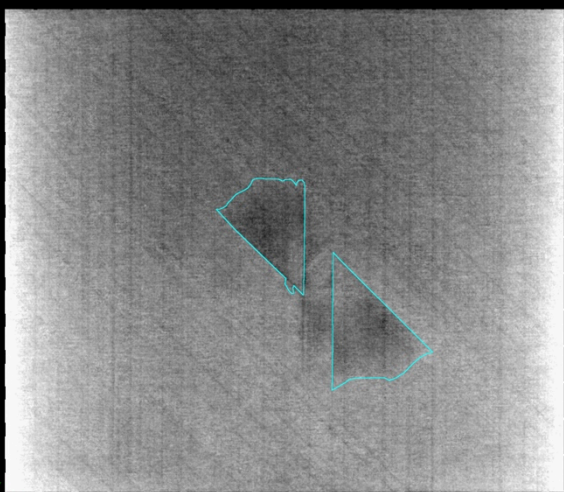
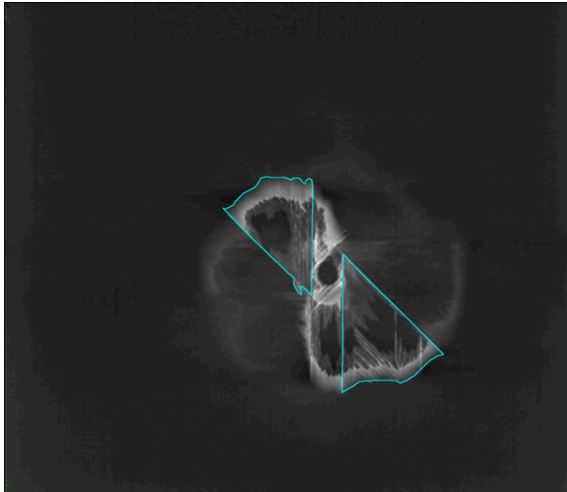
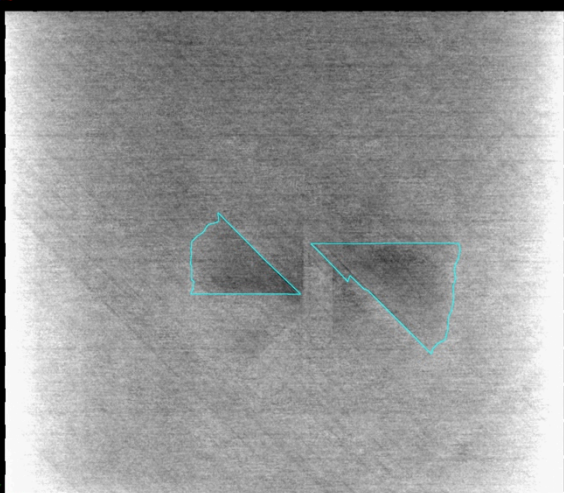
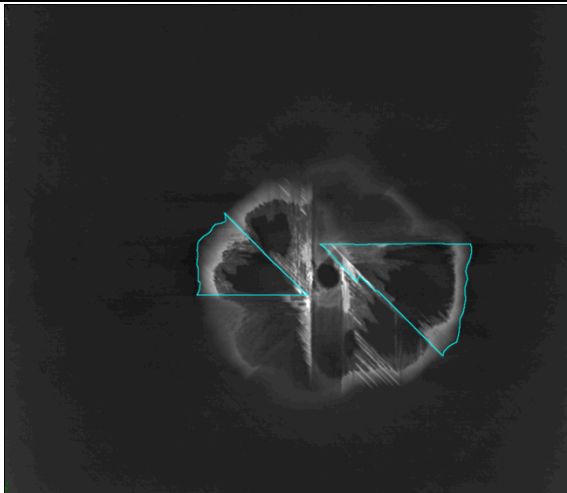
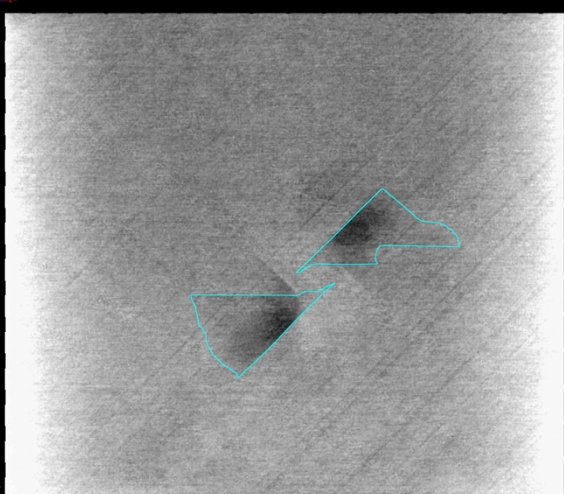
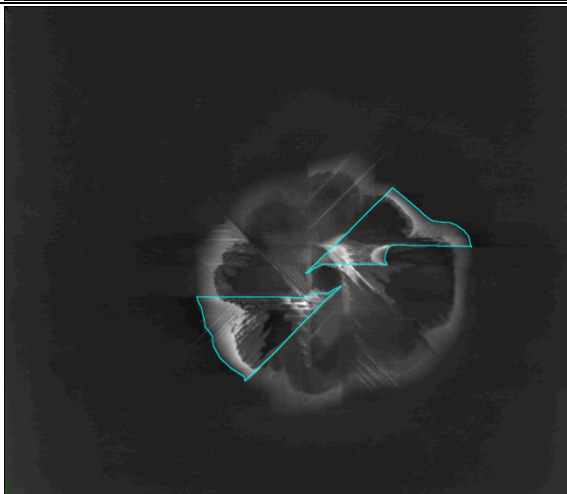
| Panel D – [-45/90/45/0] _{3s} | | | |
|---------------------------------------|-------------------------------------------------------------------------------------|--------------------------------------------------------------------------------------|---------------------------------------------------------------------------------------|
| | C-Scan | Filtered C-Scan | X-Ray CT |
| 90/-45 |  |  |  |
| -45/0 |  |  |  |
| 0/45 |  |  |  |
| 45/90 |  |  |  |

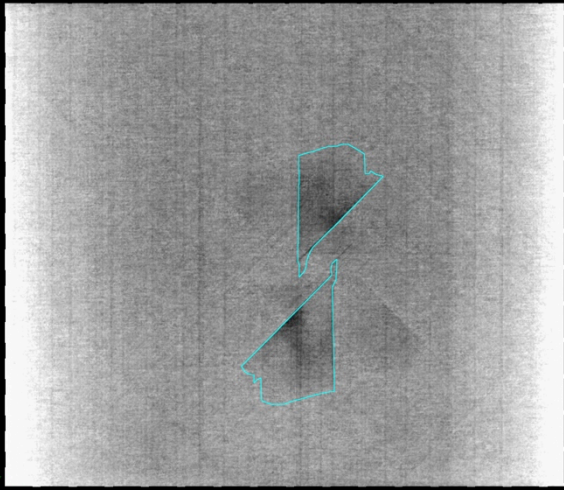
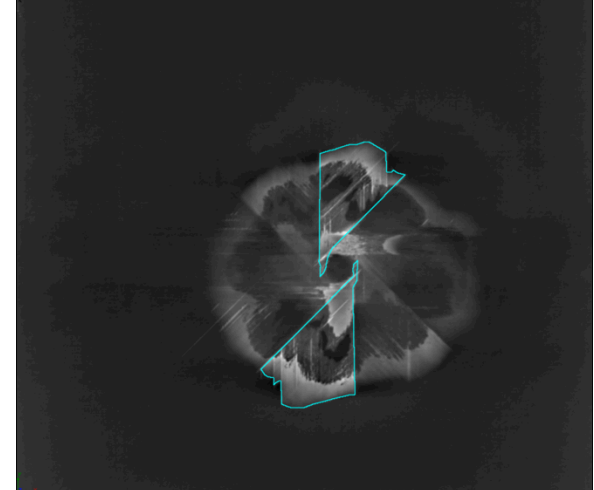
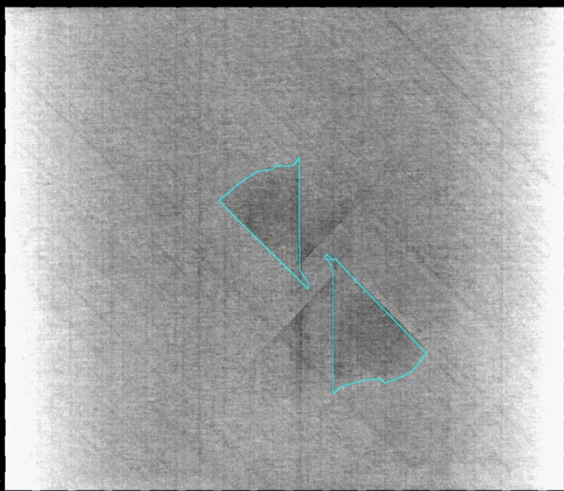
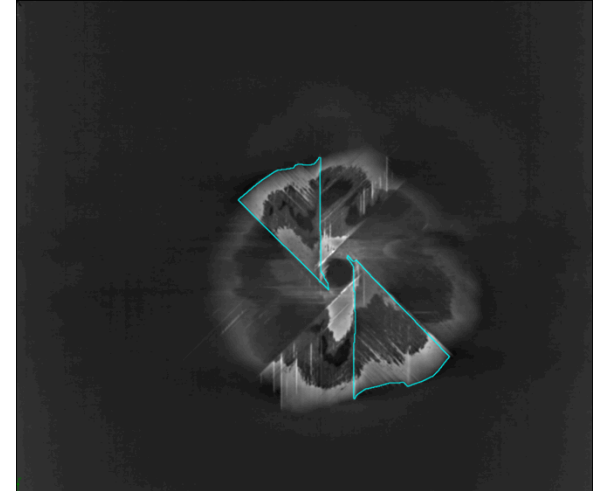
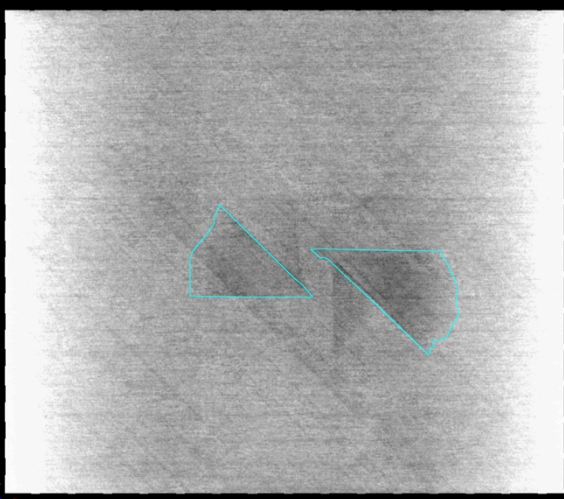
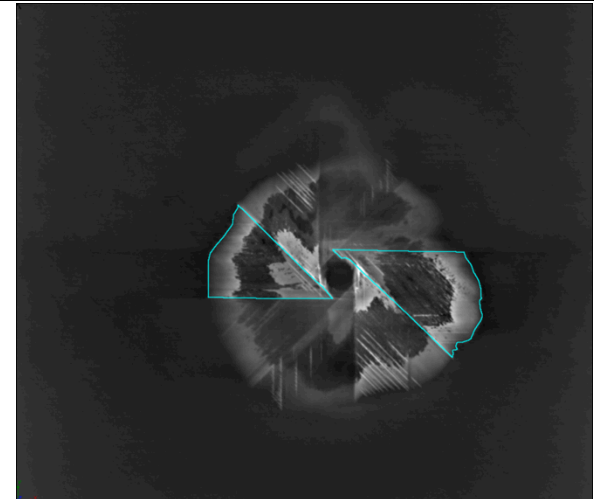
| Panel D – [-45/90/45/0] _{3s} | | | |
|---------------------------------------|-------------------------------------------------------------------------------------|--------------------------------------------------------------------------------------|---------------------------------------------------------------------------------------|
| | C-Scan | Filtered C-Scan | X-Ray CT |
| 90/-45 |  |  |  |
| -45/0 |  |  |  |
| 0/45 |  |  |  |
| 45/90 |  |  |  |

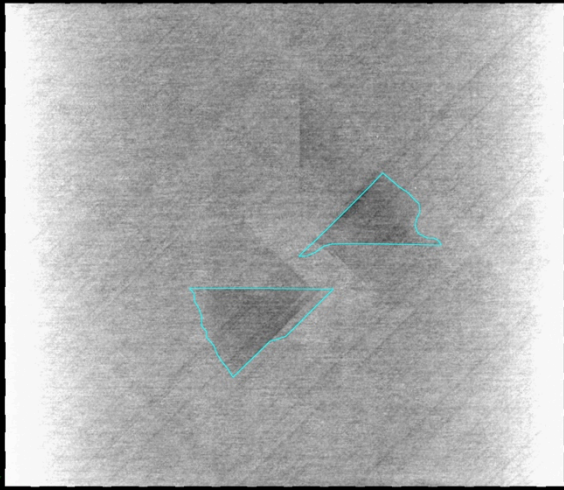
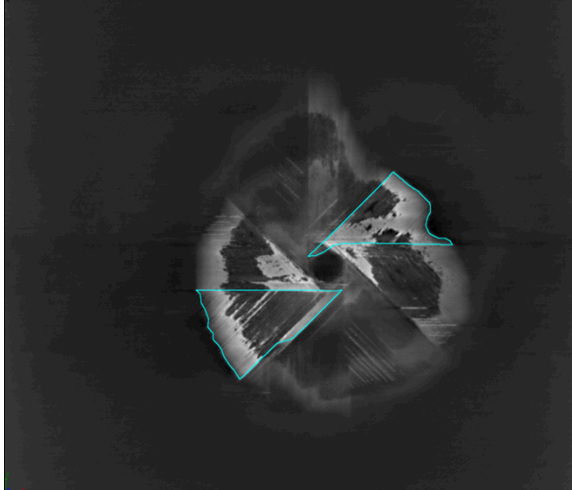
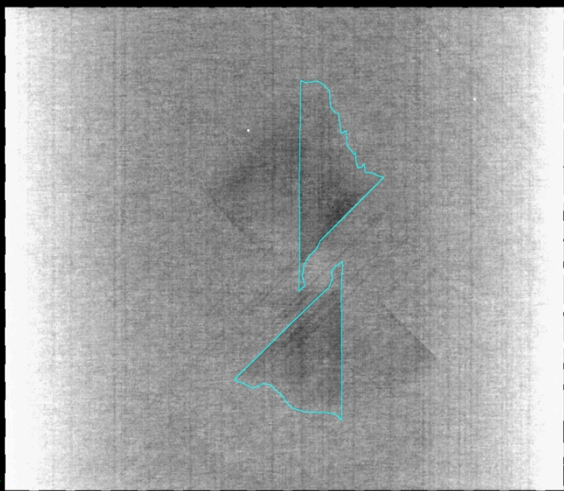
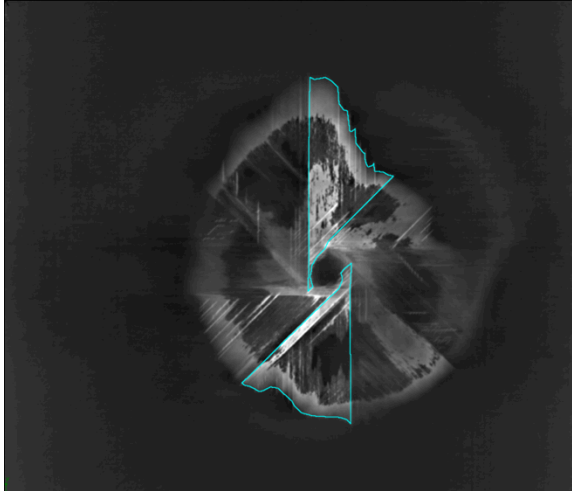
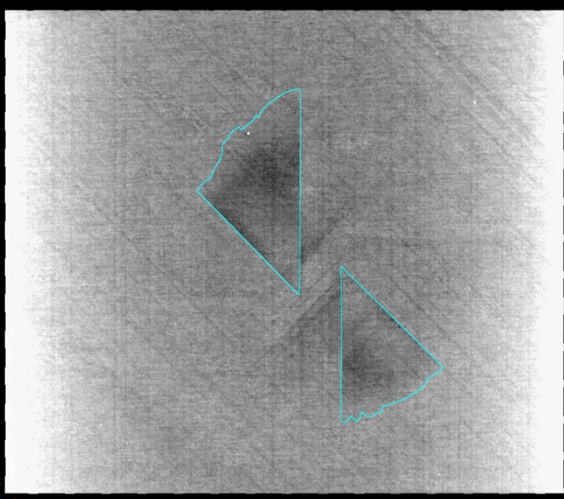
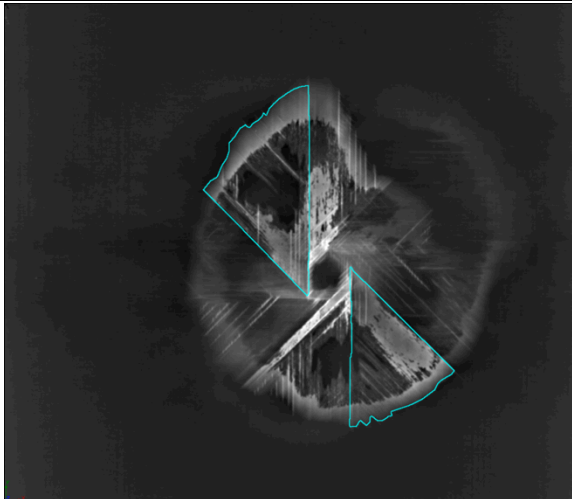
| Panel D – [-45/90/45/0] _{3s} | | | |
|---------------------------------------|-----------------------------------------------------------------------------------|------------------------------------------------------------------------------------|-------------------------------------------------------------------------------------|
| | C-Scan | Filtered C-Scan | X-Ray CT |
| 90/-45 |  |  |  |

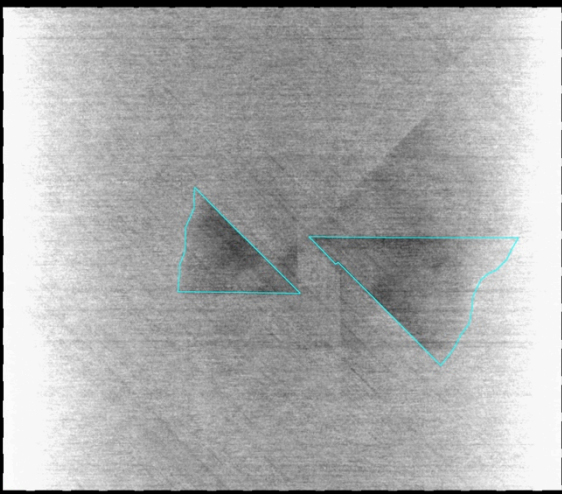
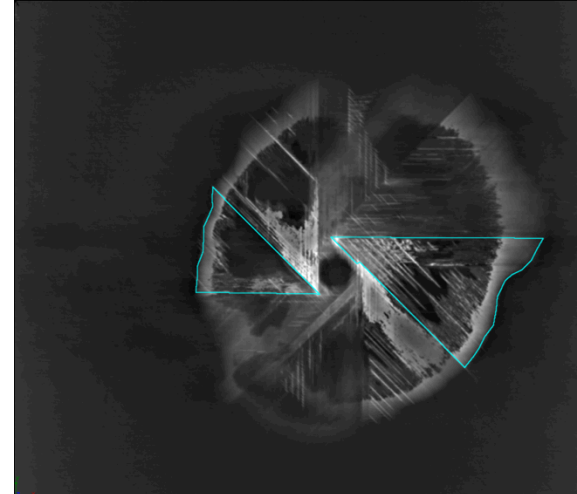
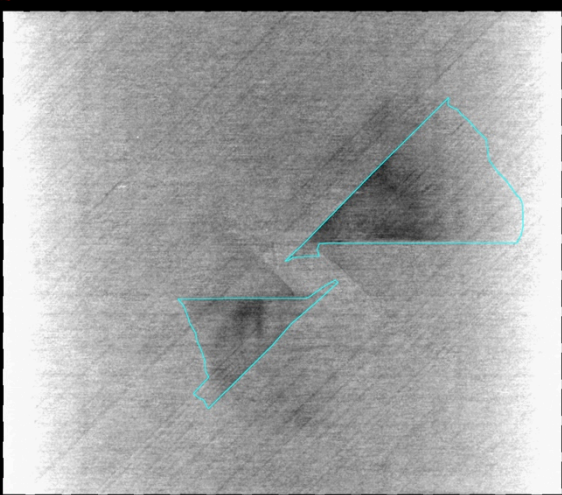
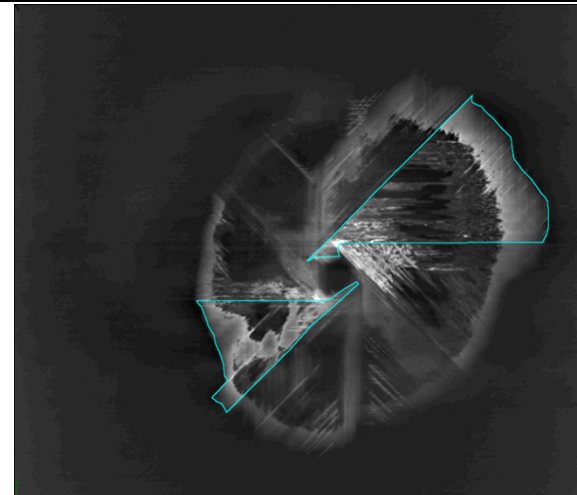
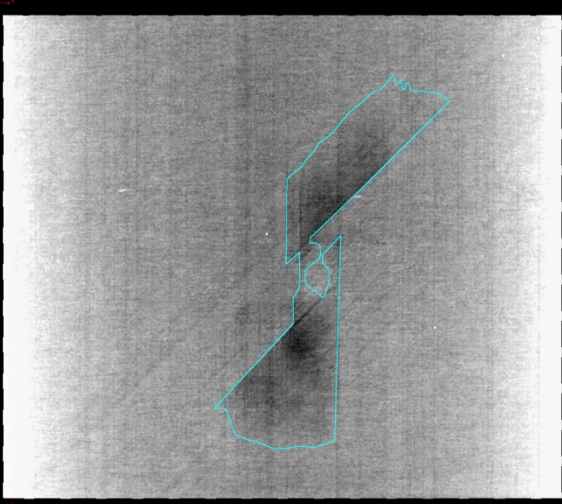

Appendix G: Image Segmentation Specimen-1 X-Ray CT Analysis

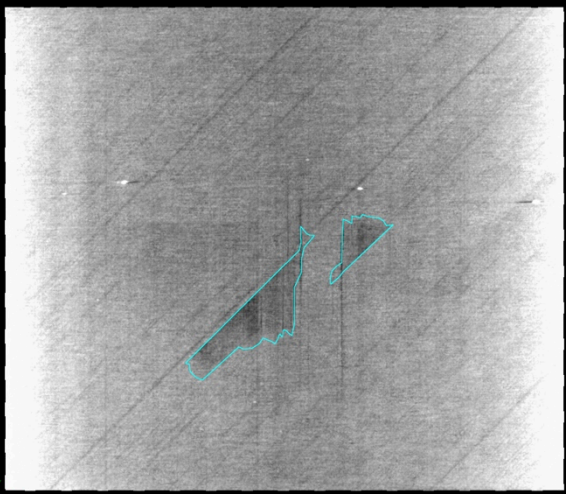
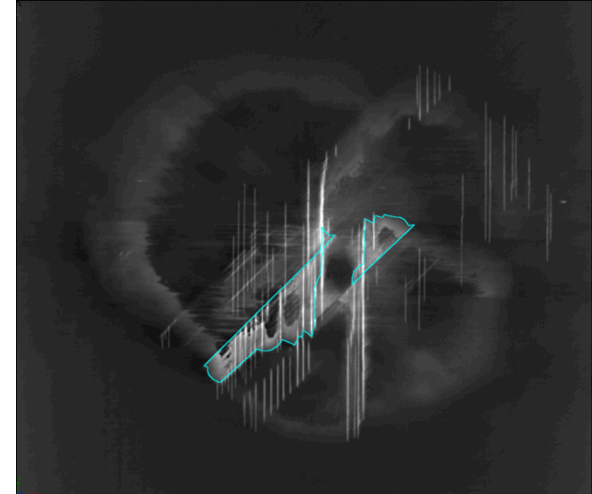
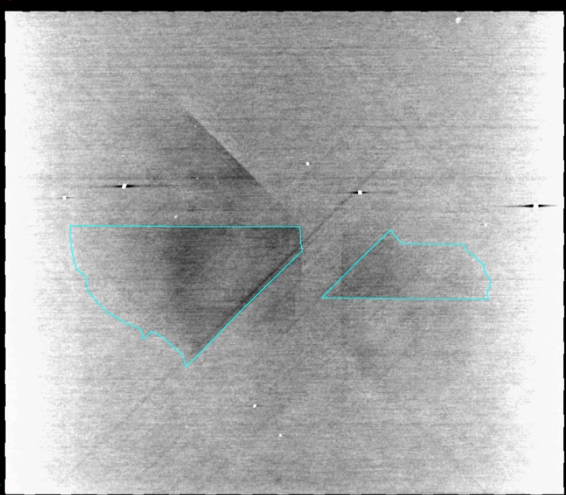
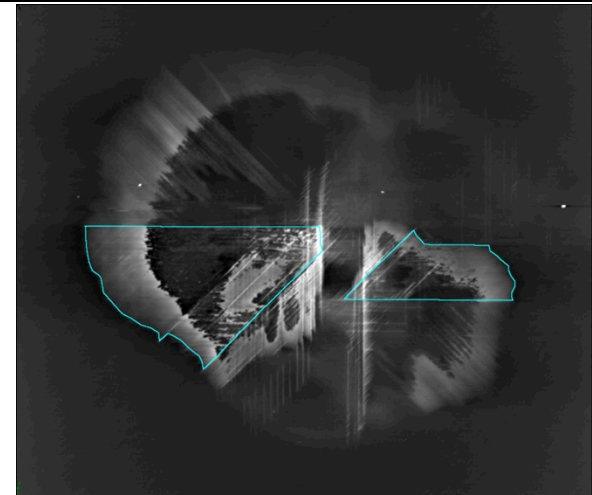
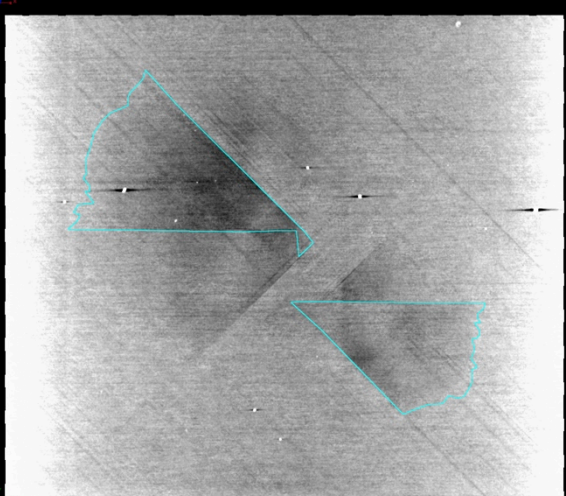
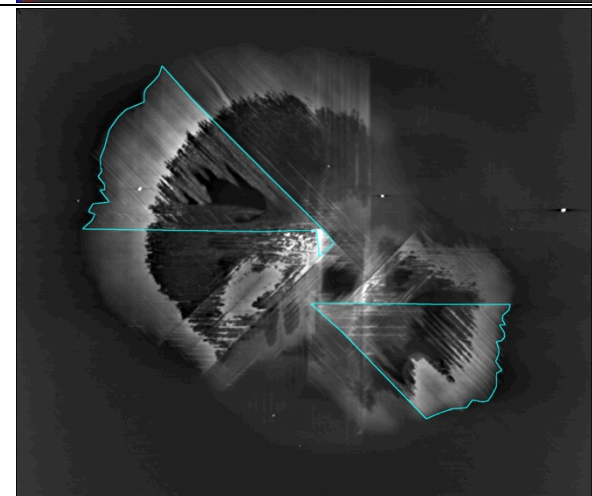
| Interface | X-Ray | X-Ray Zinc Iodide |
|-----------|-------------------------------------------------------------------------------------|--------------------------------------------------------------------------------------|
| 1 |  |  |
| 2 |  |  |
| 3 |  |  |

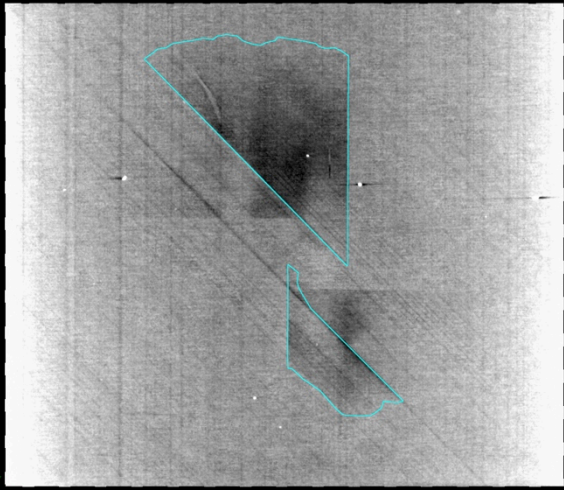
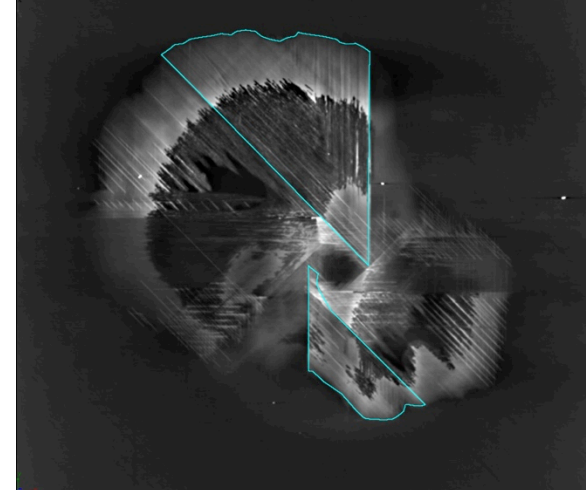
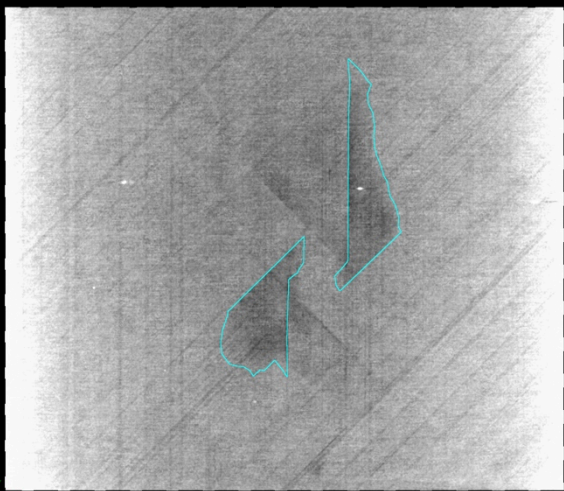

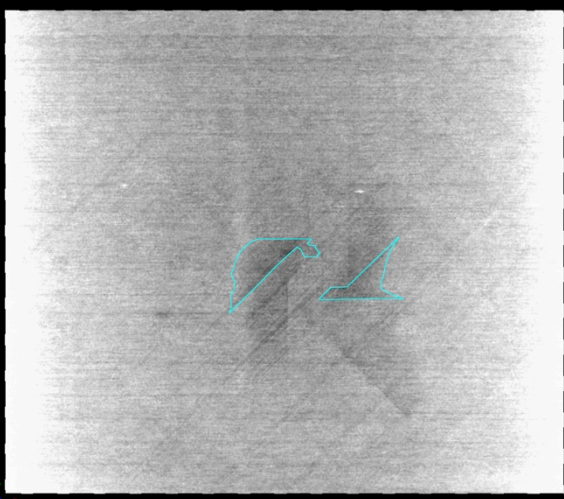
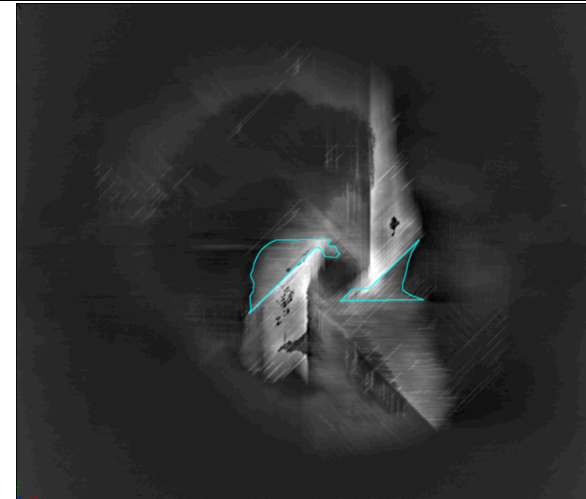
| Interface | X-Ray | X-Ray Zinc Iodide |
|-----------|-------------------------------------------------------------------------------------|--------------------------------------------------------------------------------------|
| 4 |  |  |
| 5 |  |  |
| 6 |  |  |

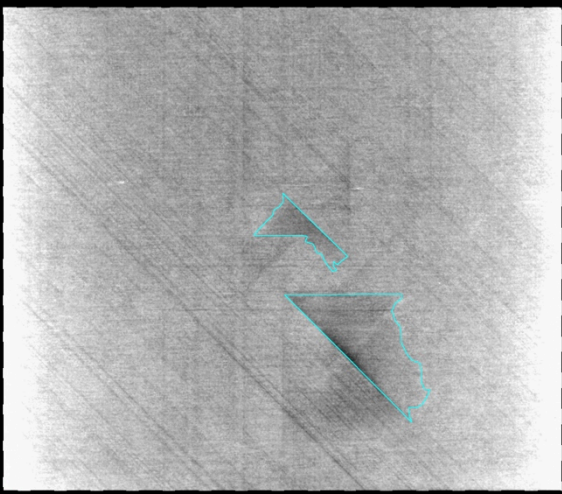
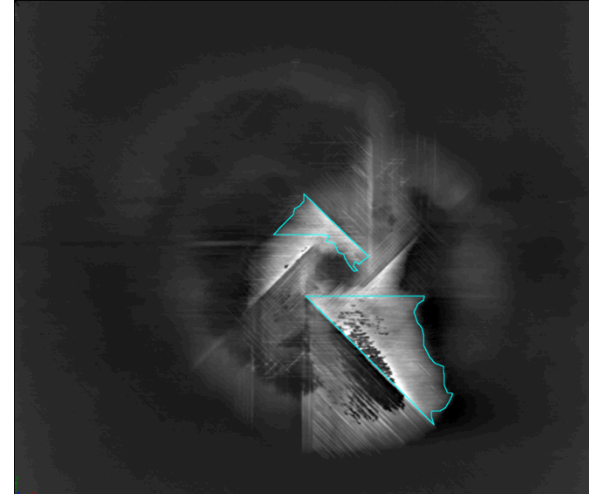
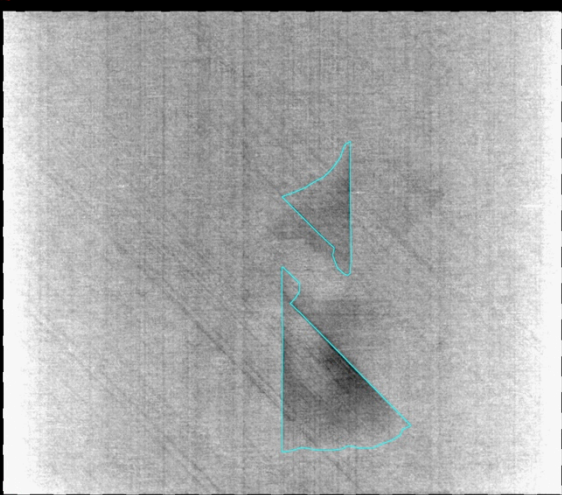
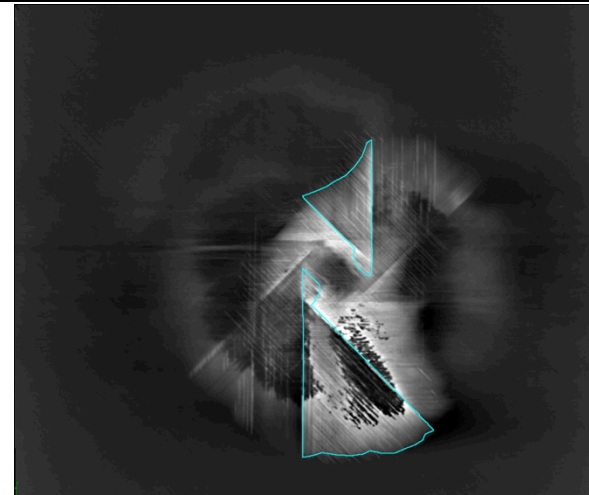
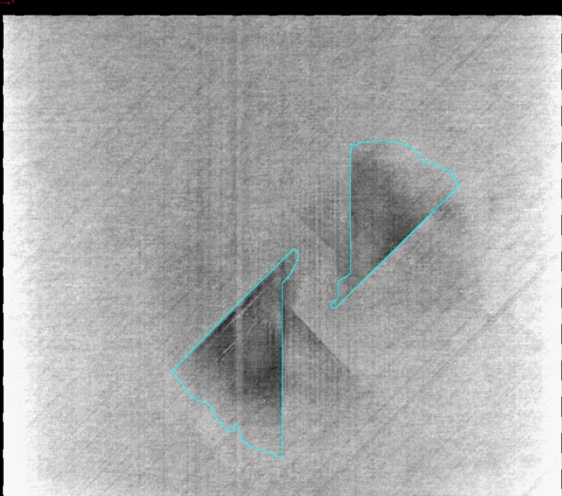
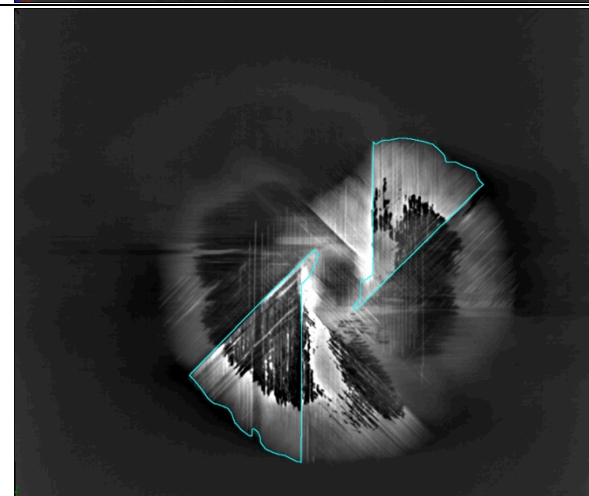
| Interface | X-Ray | X-Ray Zinc Iodide |
|-----------|-------------------------------------------------------------------------------------|--------------------------------------------------------------------------------------|
| 7 |  |  |
| 8 |  |  |
| 9 |  |  |

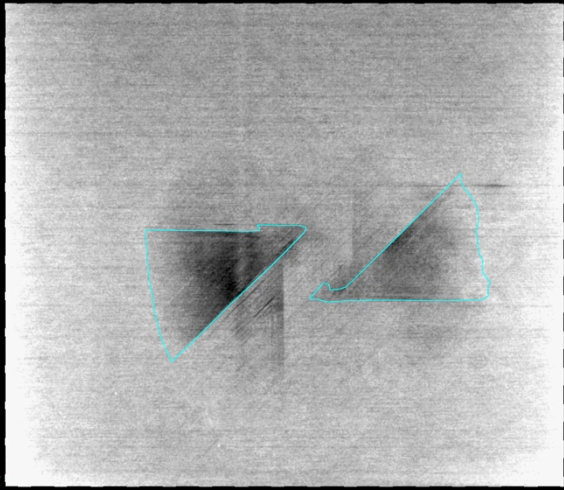
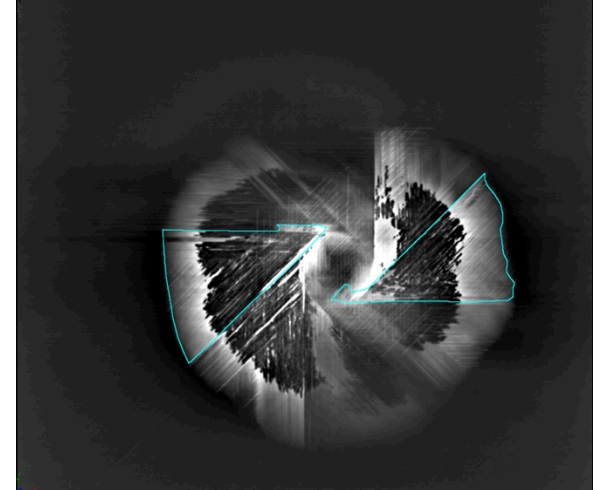
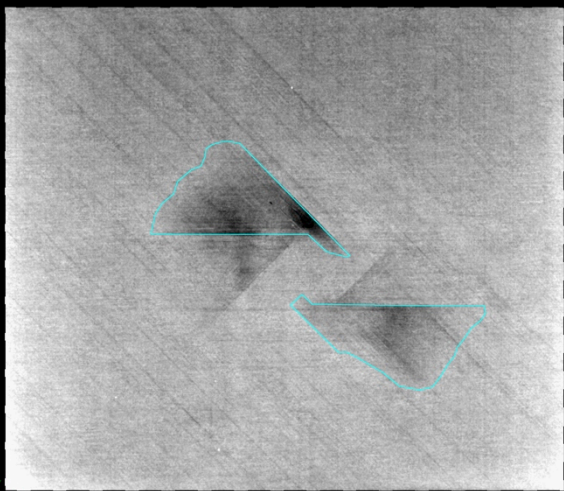
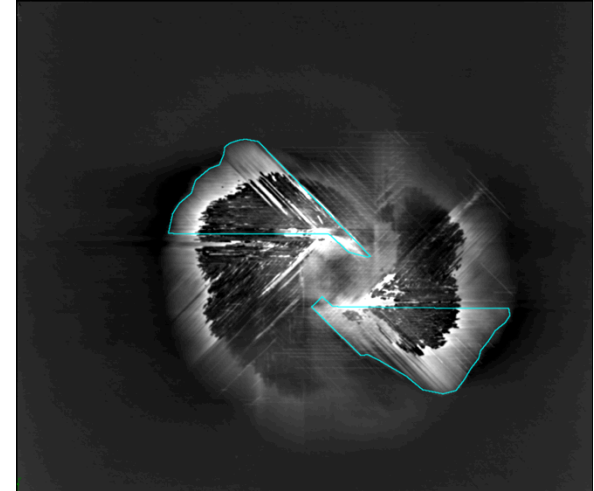
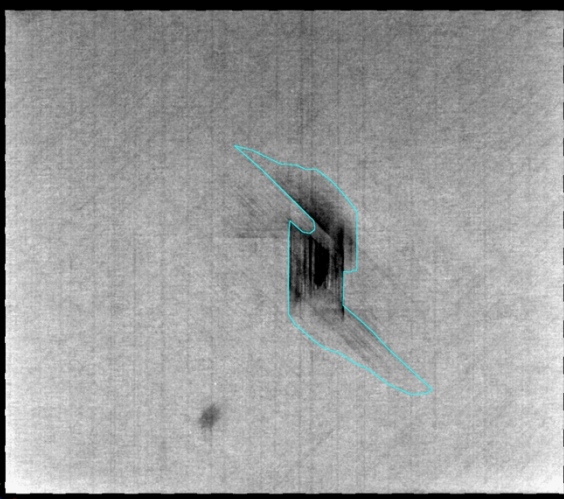
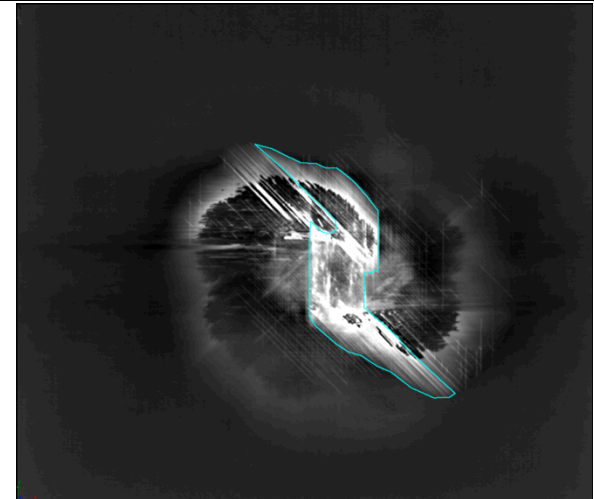
| Interface | X-Ray | X-Ray Zinc Iodide |
|-----------|-------------------------------------------------------------------------------------|--------------------------------------------------------------------------------------|
| 10 |  |  |
| 11 |  |  |
| 12 |  |  |

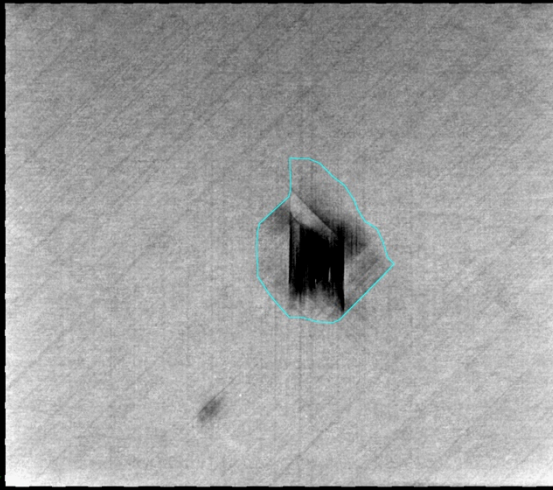
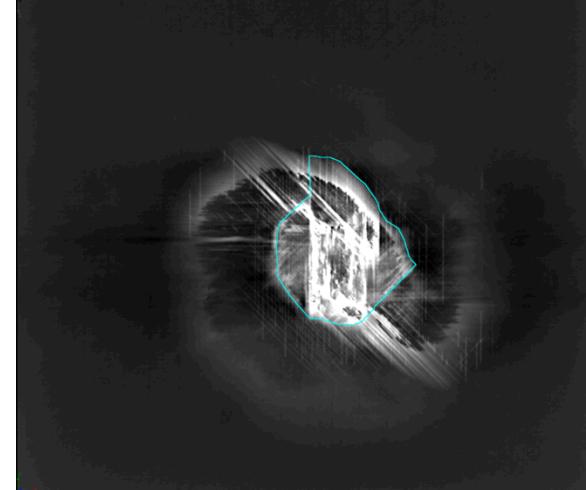
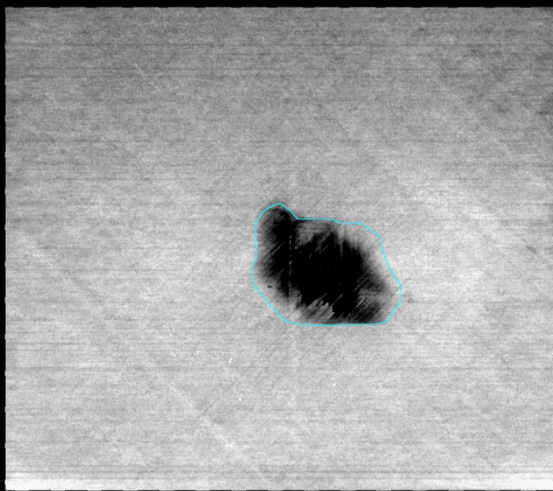
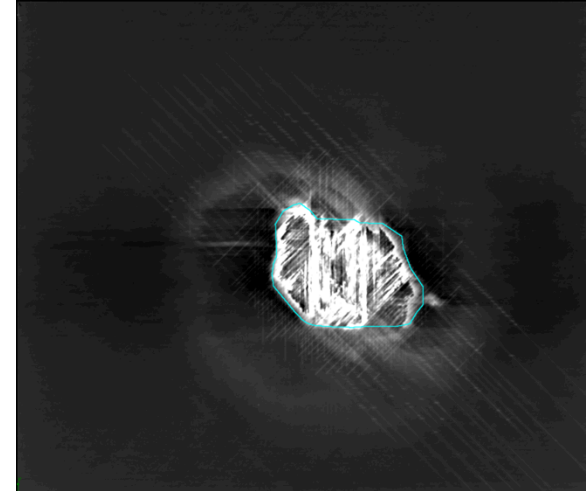
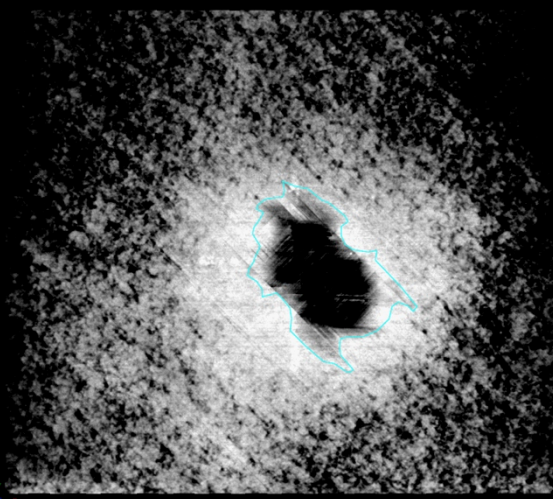
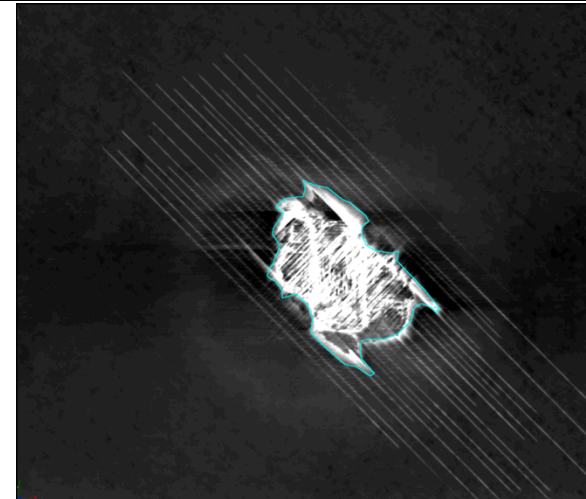
| Interface | X-Ray | X-Ray Zinc Iodide |
|-----------|-------------------------------------------------------------------------------------|--------------------------------------------------------------------------------------|
| 13 |  |  |
| 14 |  |  |
| 15 |  |  |

| Interface | X-Ray | X-Ray Zinc Iodide |
|-----------|-------------------------------------------------------------------------------------|--------------------------------------------------------------------------------------|
| 17 |  |  |
| 18 |  |  |
| 19 |  |  |

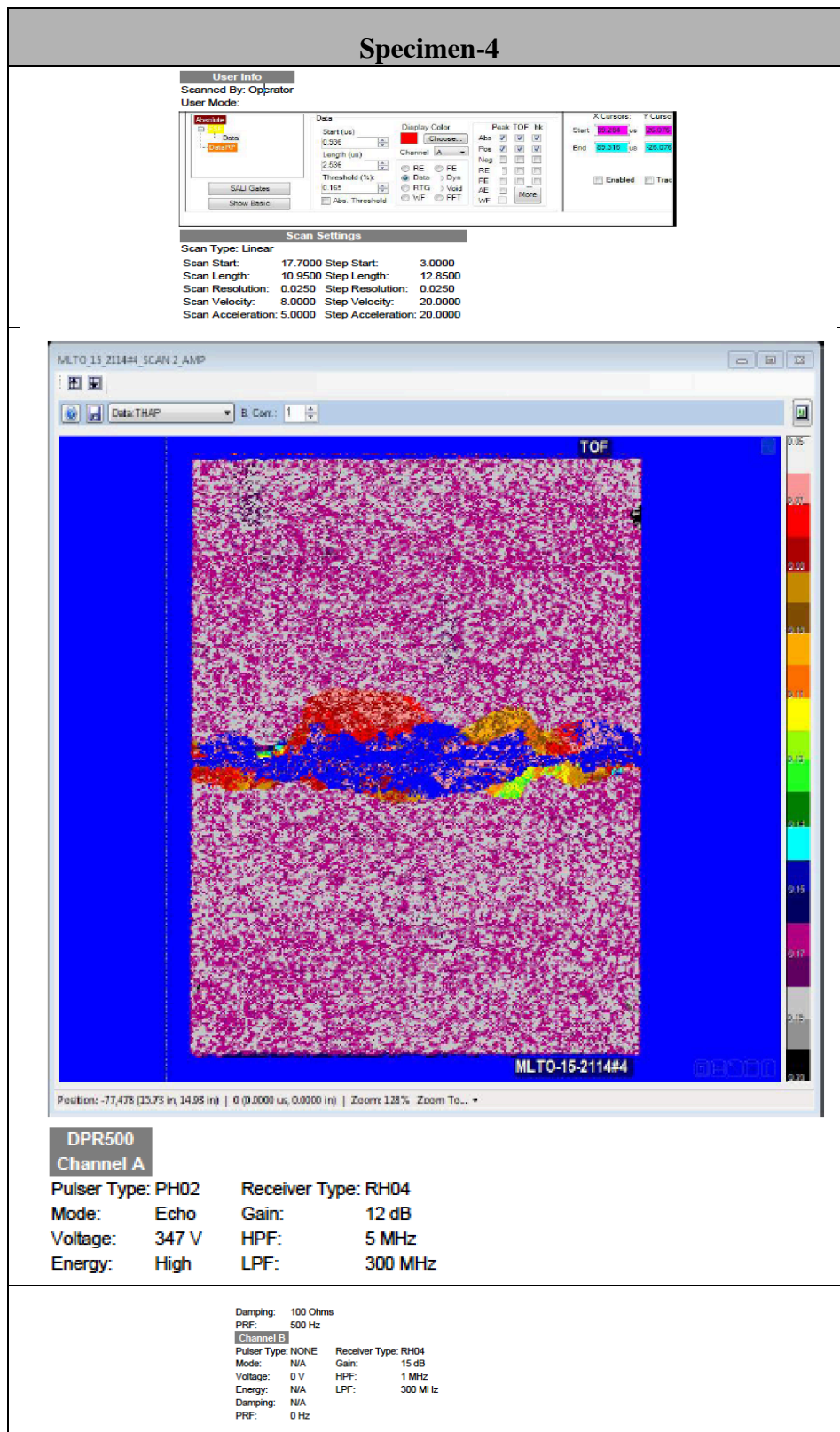
| Interface | X-Ray | X-Ray Zinc Iodide |
|-----------|-------------------------------------------------------------------------------------|--------------------------------------------------------------------------------------|
| 20 |  |  |
| 21 |  |  |
| 22 |  |  |

| Interface | X-Ray | X-Ray Zinc Iodide |
|-----------|-------------------------------------------------------------------------------------|--------------------------------------------------------------------------------------|
| 23 |  |  |
| 24 |  |  |
| 25 |  |  |

| Interface | X-Ray | X-Ray Zinc Iodide |
|-----------|-------------------------------------------------------------------------------------|--------------------------------------------------------------------------------------|
| 26 |  |  |
| 27 |  |  |
| 28 |  |  |

| Interface | X-Ray | X-Ray Zinc Iodide |
|-----------|-------------------------------------------------------------------------------------|--------------------------------------------------------------------------------------|
| 29 |  |  |
| 30 |  |  |
| 31 |  |  |

Appendix H: Post Compression Failure C-Scan Images – Time of Flight



Specimen-6

User Info
Scanned By: Operator
User Mode:

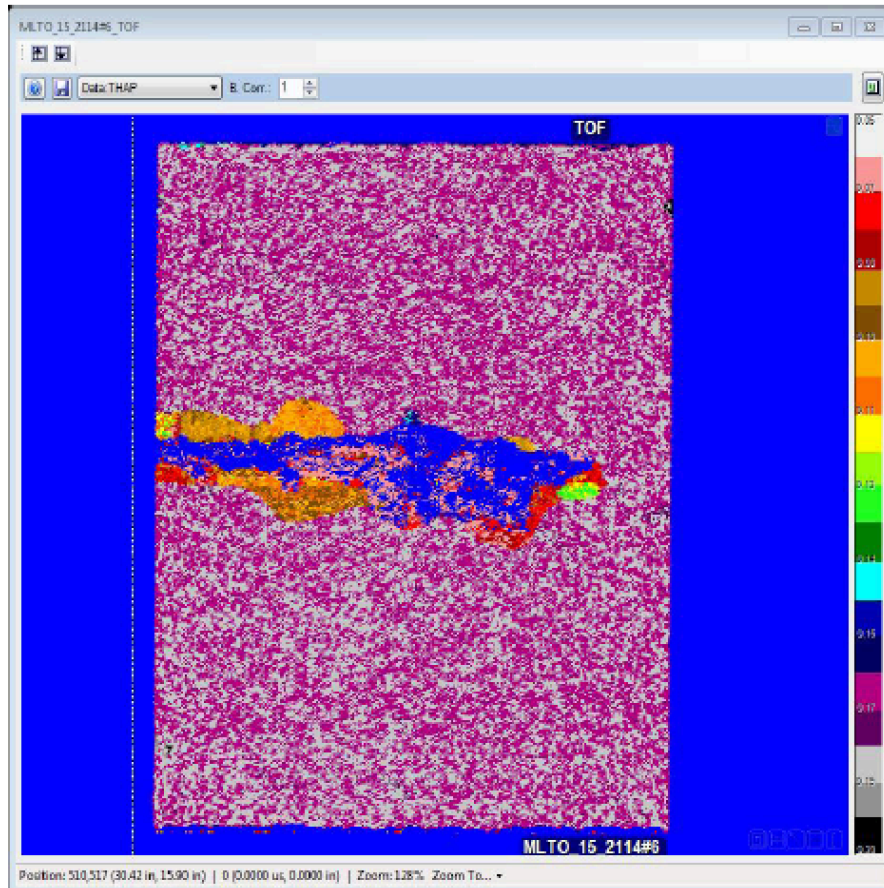
Acquire
Start (us): 0.036
Length (us): 2.536
Threshold (%): 0.165
SQU Gates
Show Basic

Display Color
Channel: A
RE ☒ FE ☒
Data ☒ Dyn ☒
RTG ☒ VRF ☒
Abs Threshold ☒

Peak TOP
Abs ☒ Pos ☒
Neg ☒ RE ☒
FE ☒ AE ☒
VF ☒ More

X Cursors
Start: 0.036 us
End: 20.016 us
Enabled ☐ Trace ☐

Scan Settings
Scan Type: Linear
Scan Start: 17.7000 Step Start: 3.0000
Scan Length: 10.9500 Step Length: 12.8500
Scan Resolution: 0.0250 Step Resolution: 0.0250
Scan Velocity: 8.0000 Step Velocity: 20.0000
Scan Acceleration: 5.0000 Step Acceleration: 20.0000

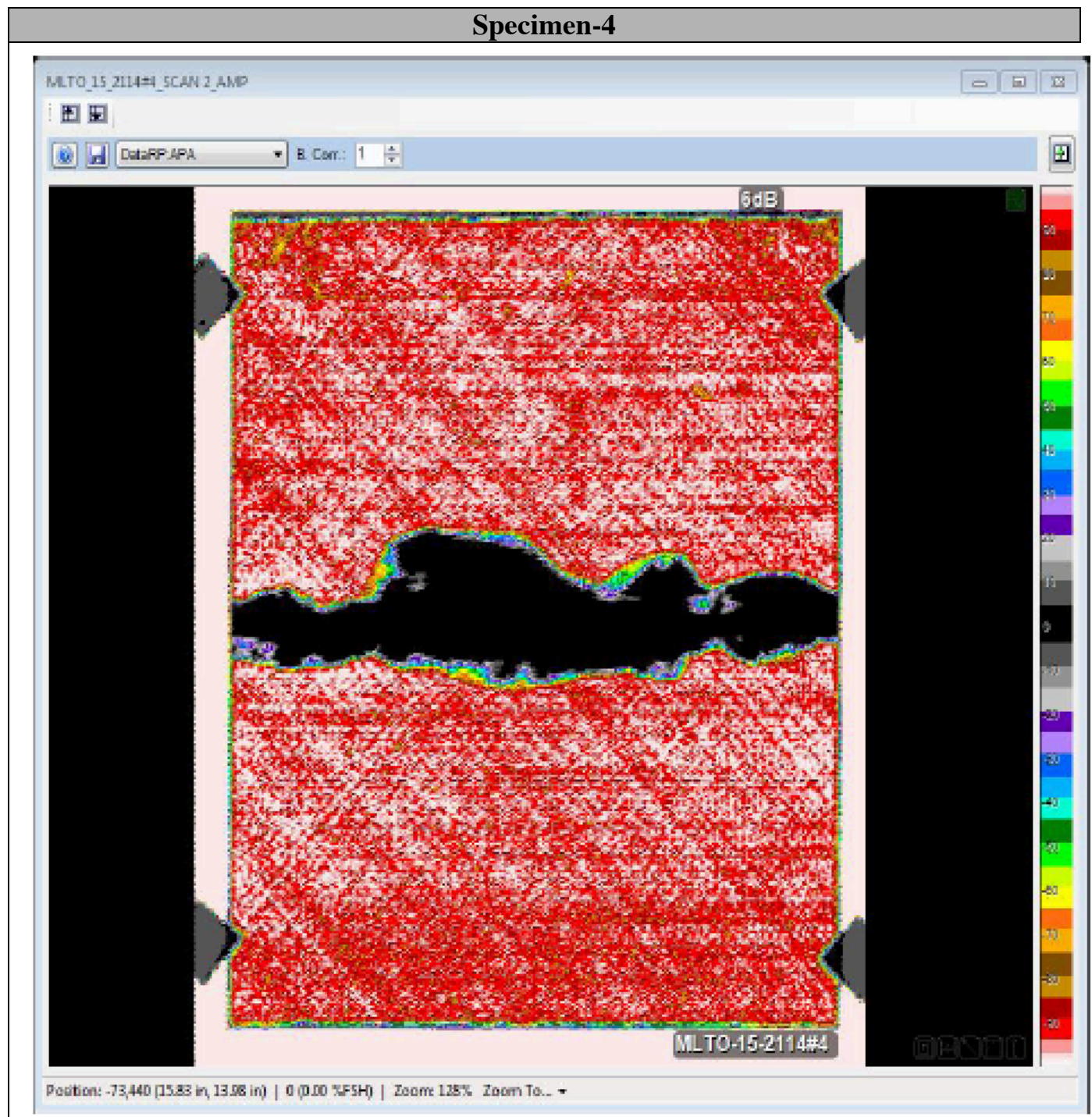


DPR500 Channel A

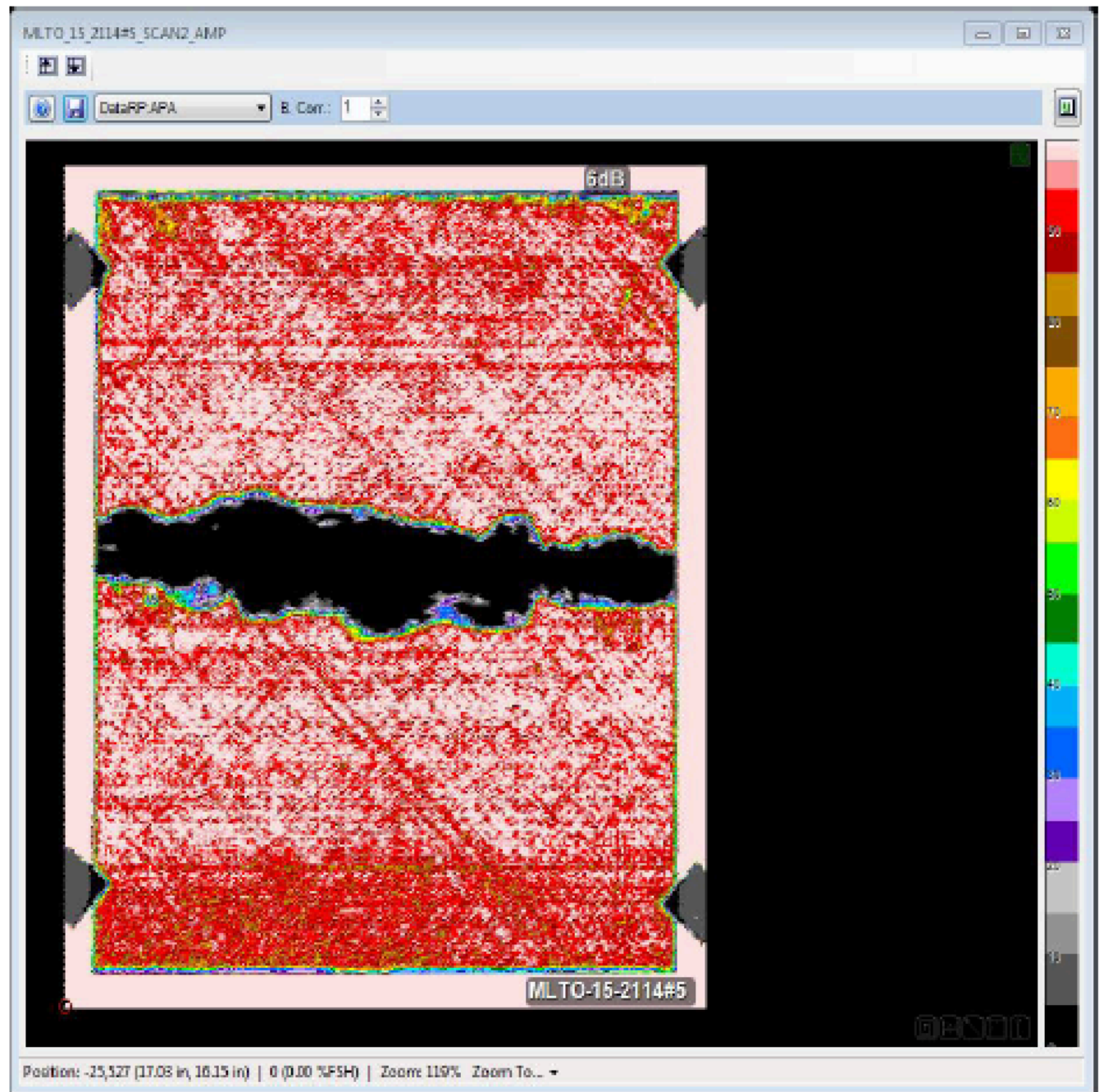
| | |
|-------------------|---------------------|
| Pulser Type: PH02 | Receiver Type: RH04 |
| Mode: Echo | Gain: 12 dB |
| Voltage: 347 V | HPF: 5 MHz |
| Energy: High | LPF: 300 MHz |

Damping: 100 Ohms
PRF: 500 Hz
Channel B
Pulser Type: NONE
Mode: N/A
Voltage: 0 V
Energy: N/A
Damping: N/A
PRF: 0 Hz
Receiver Type: RH04
Gain: 15 dB
HPF: 1 MHz
LPF: 300 MHz

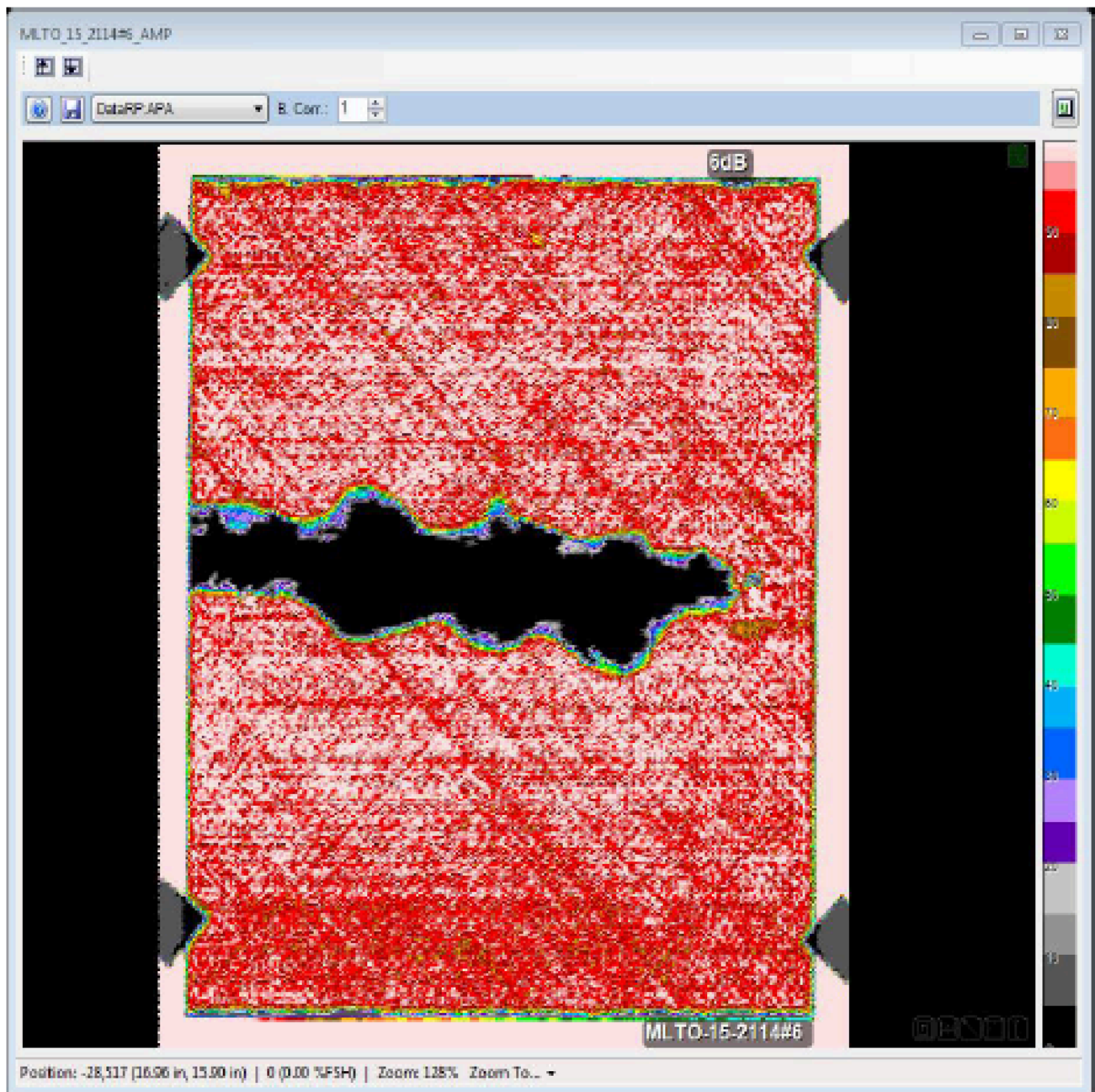
Appendix I: Post Compression Failure C-Scan Images – Amplitude



Specimen-5



Specimen-6



Appendix J: Post Compression Failure X-Ray Images



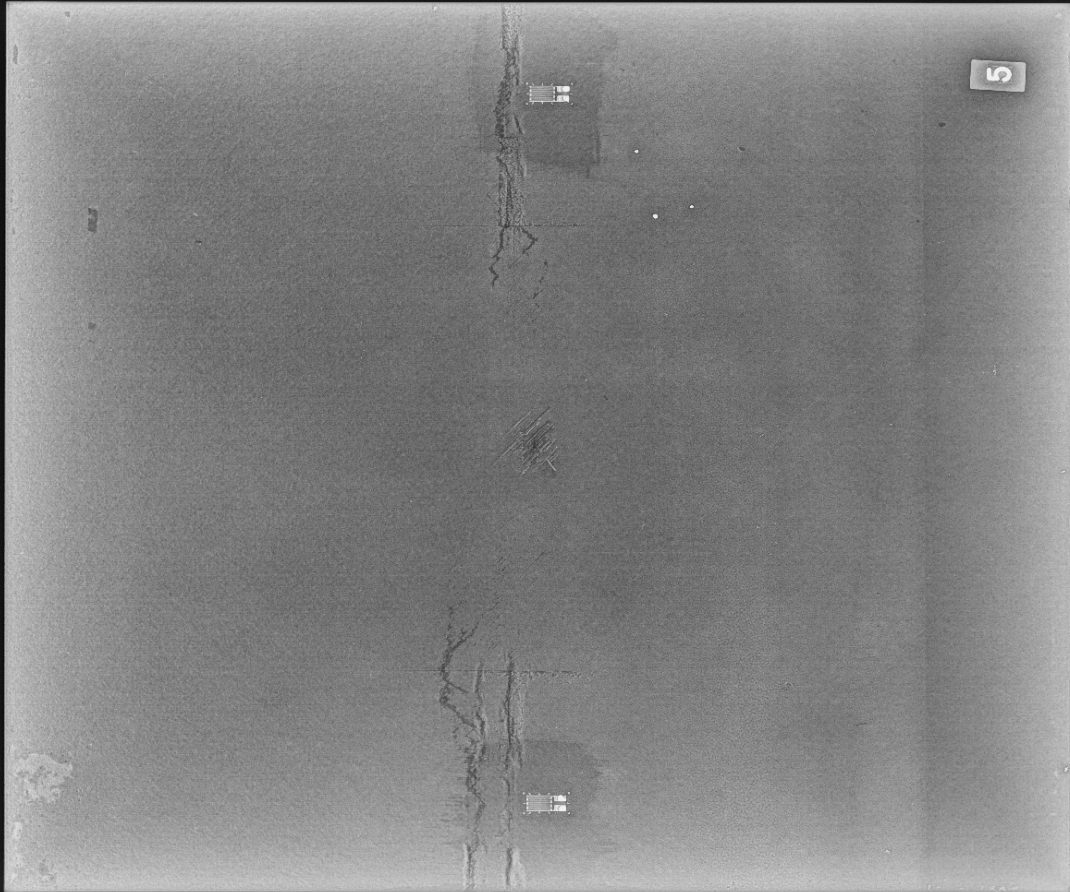
Specimen-5

Impact Panels
Task 413
Shot 4
Panel MCTO 15 2114 #5

Filter: Application Filter
AFRL/RXSAS

Roberts UTC

20150811 133656
8/11/2015 1:38:41 PM



C32272
W73232

23.000kV
3.000mA
30000msec
48inches

res: 050\,050
CRxFlex (CRxFlex�)

Specimen-6

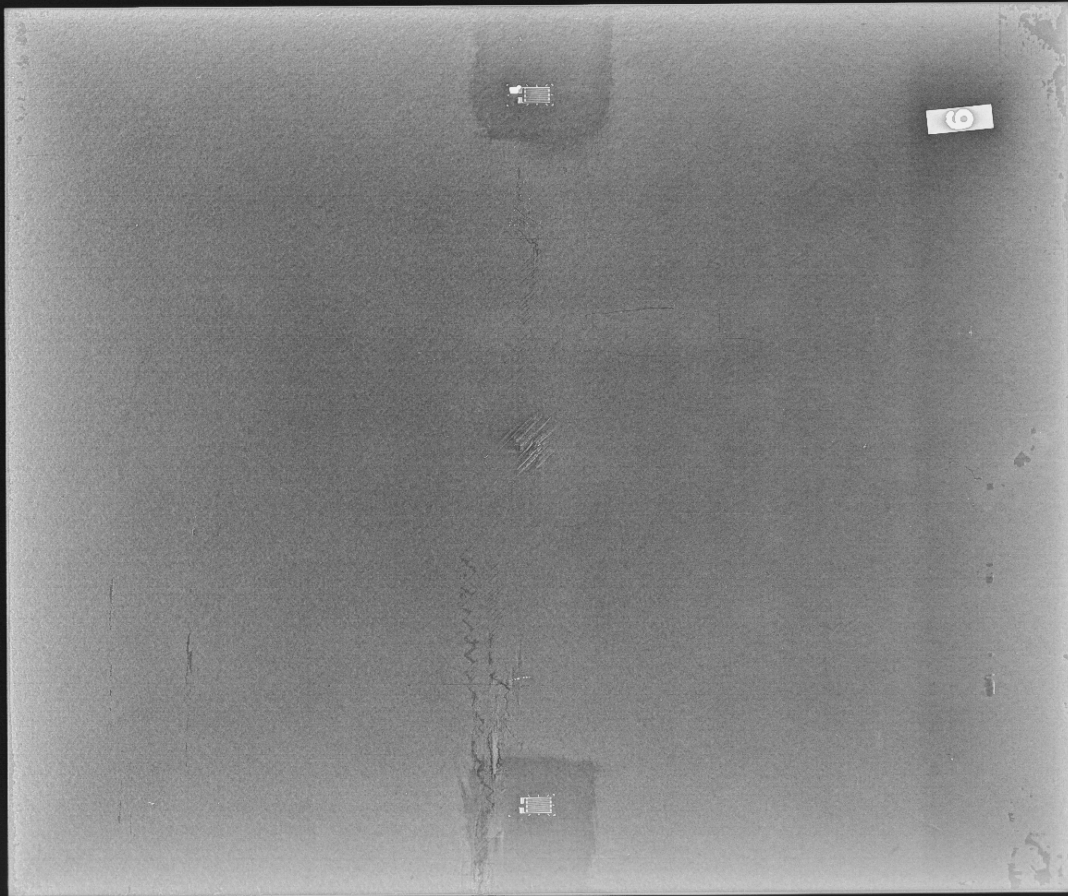
Impact Panels
Task 413

Filter: Application Filter
AFRL/RXSAS

Roberts UTC

Shot 3
Panel MCTO 15 2114 #6

20150811 133656
8/11/2015 1:38:41 PM



C32272
W73232

23.000kV
3.000mA
30000msec
48inches

res: 050\, 050
CRxFlex (CRxFlex�.)

Vita

Mark D. Flores was born and raised in El Paso, TX. Mark graduated from J.M. Hanks High School in the year 2000 and decided to attend the University of Texas at El Paso (UTEP) to obtain a mechanical engineering degree. During his undergraduate studies, he was able to participate in several competitions and internships. In 2003, he worked for General Motors as an Intern at the Moraine Assembly Plant, which was known for building high quality SUVs such as the Buick Rainer, Trailblazer, and Envoy. In 2004, he worked for ATK Thiokol working as an Intern near Salt Lake City, Utah under a quality engineer to determine if the rockets were meeting design requirements. In 2005, Mark participated in the Texas Space Grant Consortium on designing an unpressurized manned vehicle using an elastic mobility system. After graduating UTEP with a Bachelors Degree in Mechanical Engineering, he spent the next four years working for Lockheed Martin as a Satellite Systems Engineer. During his professional career he worked for three satellite programs in which he was responsible for operating, maintaining, building plans, and testing for various segments such as satellite subsystems, ground systems, and command and control systems. After working a little more than 4 years with the company, Mark decided to go back to his roots and pursue his master's degree under Dr. Jack Chessa investigating the impact resistance of high temperature ceramics elevated to over 1000 degrees Celsius. Mark then switched gears to Civil Engineering to pursue a doctorate under the guidance of Dr. L. Roy Xu, investigating the mechanical degradation of marine composites when exposed to seawater. During his years in academia, he has been able to obtain an internship with Air Force Research Laboratory (AFRL). In 2012, he computationally investigated oxide growth of a substrate using level set method. In 2014, received a research opportunity with AFRL under damage tolerance and assessment of unidirectional carbon fiber composites. During this time he discovered they are damage threshold strains of composite materials. He was also able to take realistic damage obtained from nondestructive evaluation and integrate it into a discrete damage model to understand the behavior of damage while under loading. After Mark obtains his PhD, he is excited to enter the work force designing new applications for the civil, mechanical, electrical, and aerospace industries.

Permanent address: 11240 Pony Soldier
El Paso, TX 79936

This dissertation was typed by Mark D. Flores